UNIVERSIDADE DA BEIRA INTERIOR

Aerodynamic Control of the Mixing of Confined, Plane and Co-axial Jets

Fernando Manuel da Silva Pereira das Neves

Submitted in partial fulfillment of the requirements
for the degree of Doctor of Philosophy in
Aeronautical Engineering

Faculdade de Engenharia
Universidade da Beira Interior
Covilhã, Portugal, November, 2012

This research was supported in part by the FCT-Fundação para a Ciência e Tecnologia under the scope of the *AeroG – Aeronautics and Astronautics Research Center* (Project MECH-Centro-Covilhã-4034, 2008-2011) and the AEROG-Aeronautics and Astronautics Research Group (RG-Centro-50022-3875) of the Research Line of Aeronautics and Space (RL-EME-LA22-159) of the LAETA-Associated Laboratory in Energy, Transports and Aeronautics (contract LA-LVT-22, 2011-2012), Project PTDC/EME-MFE/64493/2006 (2008-2010), grant BII/AeroG/05/2010 (2010) and Project Pest-OE/EME/LA0022/2011 (2011-present).

The author was also the recipient of a grant of the Faculty of Engineering of the UBI-Universidade da Beira Interior (2011).

The views and conclusions contained here are those of the author and should not be interpreted as necessarily representing the official policies or endorsements, either express or implied, of FCT, *AeroG*, AEROG, LAETA, UBI, or the Portuguese Government or any of its agencies.

Keywords: aerodynamic control of recirculating flows, confined coaxial jets, turbulence, recirculating flows

Resumo

A mistura turbulenta de jactos coaxiais confinados é um complexo processo dinâmico com muitas aplicações práticas, como em ejectores, bombas a jacto, queimadores industriais, câmaras de combustão de motores a jacto, foguetes nucleares gasosos, câmaras de mistura, pós-queimadores (afterburners), motores turbofan. Nestas ultimas aplicações, o confinamento é também de interesse fundamental, porque envolve certos fenómenos de interacção de escoamentos turbulentos, cujos detalhes não estão ainda quantitativamente completamente entendidos (Ahmed e Sharma, 2000).

Tem havido estudos sobre o comportamento aerodinâmico de jactos coaxiais em diferentes tipos de geometria e com diferentes parâmetros operacionais com diferentes motivações. Enquanto uma escala de relações de diâmetros foi investigada no passado, não existem praticamente registos de trabalhos para diâmetros inferiores a 2, que é o caso dos motores turbofan com muito baixo *bypass*, com razões de *bypass* de 0.3 ou inferior. Somente Ahmed e Sharma (2000) relataram recentemente detalhadas medições em velocimetria laser das componentes de velocidade média e turbulenta, bem como da pressão total e estática, numa escala de rácios de velocidade com relevância no contexto actual. No seu trabalho, foi analisada a influência da relação da velocidade sobre o processo de mistura turbulenta, mas existem muitos outros parâmetros que influenciam o processo de mistura turbulenta.

Esta investigação estuda o processo de mistura turbulenta de jactos parietais sem recurso a efeitos de rotação (*swirl)* nem a "*bluff bodies*". Na sequência de um estudo numérico realizado anteriormente, pretende-se aumentar a compreensão de interacções entre alguns fenómenos de escoamento turbulento em jactos coaxiais, de forma poder controlar a sua mistura de uma forma exclusivamente aerodinâmica. Neste trabalho estuda-se experimentalmente uma geometria bidimensional, avaliando-se a influência de parâmetros geométricos e iniciais com vista à obtenção do controlo do escoamento: confinamento, ângulo de inclinação e intensidade de turbulência do escoamento exterior.

Abstract

Turbulent mixing of confined coaxial jets is a complex dynamic process with many practical applications such as ejectors, jet pumps, industrial burners, jet engine combustion chambers, gaseous nuclear rockets, mixing chambers, afterburners, and turbofan engine mixing chambers. In this latter applications the confinement is also of basic interest because it involves a certain interacting turbulent flow phenomena, the details of which are not yet fully understood quantitatively (Ahmed and Sharma, 2000).

There have been studies of different geometric and operating parameters on the turbulent mixing process of confined coaxial jets with different motivations. While a wide range of diameter ratios has been investigated in the past, no work was reported on diameter ratios below 2, which is the case with many low bypass turbofan engines with bypass ratios of 0.3 and less. Only Ahmed and Sharma (2000) reported recently detailed LDV measurements of mean and turbulence components of velocity as well as the total and static pressures over a range of velocity ratios with relevance in the present context. In their work they analyse the influence of velocity ratio on the turbulent mixing process, but there are many other parameters which influence the turbulent mixing process.

This research is dedicated to the study of the turbulent mixing of parietal jets without any generated effect of swirl and without the presence of bluff bodies. The major objective was to design mixing control strategies using purely aerodynamic tools. Following a work on axisymmetric geometries, a two-dimensional geometry was adopted to study the influence of geometric and initial parameters to control the flow: confinement, inclination angle and turbulence intensity of the outer flow.

Acknowledgments

With deep sense of gratitude, I would like to truly thank my supervisor Professor Jorge Manuel Martins Barata for many suggestions, continuous guidance, unreserved support, valuable advice and follow up he has been making during this work. His overly enthusiasm and integral view on research and his mission for providing only high quality work has made a deep impression on me. The confidence and dynamism with which he guided the work has no elaboration. I owe him lots of gratefulness for having me shown this way of research. Besides of being an excellent advisor, I appreciate his approach as close as relative to openly discuss social affairs too.

I wish to pay my thanks to Professor André Resende Rodrigues da Silva for his all given support. I also wish to pay my thanks to Engª Maria Emilia da Silva Baltazar for her moral support during some more difficult stages. I wish to pay my thanks at the Universidade da Beira Interior (UBI) in particular at the Departamento de Ciências Aeroespaciais (DCA) by all given support during this work. I wish to pay my thanks to the Faculdade de Engenharia of Universidade da Beira Interior (FE-UBI) for one year of research Grant financial support. I wish to pay my thanks at the Instituto Superior Técnico (IST) in particular by all given research support supply during this work. I wish to pay my thanks to all my colleagues and *AeroG-Aeronautics and Astronautics Research Center* members: Paulo Machado, Samuel Galvão, Pedro Santos and Joel Fonseca. I wish to pay my thanks to the DCA laboratory technician Mr. Rui Manuel Tomé Paulo for its components parts production and to DCA administrative assistant, Mrs. Ana Almeida. In general, I pay my thanks to all who have contributed to this work. Failing to mention all the contributions, I intend also to record a special thanks to all who sought to create a good working environment and helped me to overcome the most difficult obstacles. I also wish to express my gratitude for the understanding and soul-support of my family during all phases of this work.

This work was made possible through the FCT, Fundação para a Ciência e a Tecnologia financial support.

Fernando Manuel da Silva Pereira das Neves

Covilhã and UBI, October 2011

Index

Resumo ..... **v**

Abstract ..... **vii**

Acknowledgments ..... **ix**

Index ..... **xi**

Figure Index ..... **xv**

Table Index ..... **xxiii**

Nomenclature ..... **xxiv**

Chapter 1. Introduction **1-1**

1.1. Early Studies 1-2

1.1.1. Experimental investigations *1-3*

1.1.2. Numerical and theoretical investigations *1-63*

1.2. Thesis Statement 1-91

1.3. Outline of the Thesis 1-93

Chapter 2. Experimental Setup **2-1**

2.1. Introduction 2-1

2.2. Facility description 2-1

2.2.1. Engine and Fan *2-1*

2.2.2. Diffuser *2-3*

2.2.3. Settling Chamber *2-4*

2.2.4. Contraction cone *2-4*

2.2.5. Test section *2-5*

2.2.6. Electronic frequency converter device *2-5*

2.2.7. Digital micromanometer *2-5*

2.2.8. Cyclone *2-6*

2.3. Laser Doppler Anemometry (LDA) description 2-6

2.3.1. Introduction *2-7*

2.3.2. Principles of LDA *2-10*

2.3.2.1. Laser beam 2-10

2.3.2.2. Doppler Effect 2-11

2.3.2.3. Frequency to velocity conversion 2-13
2.3.2.4. Optical principle 2-15
2.3.2.5. Transmitting and receiving systems 2-15
2.3.2.6. Directional ambiguity / Frequency shift 2-16
2.3.2.7. The fringe model 2-17
2.3.2.8. Measurement volume 2-18
2.3.2.9. Seeding 2-19
2.3.2.10. Signal characteristics 2-21
2.3.3. LDA operational procedure 2-23
2.4. Flow Configuration 2-24
2.5. Calibration and experimental facility setup tests 2-27
2.6. Visualization 2-30
2.7. Errors estimation of LDA measurements 2-31
2.7.1. Hardware errors 2-31
2.7.2. Velocity bias 2-31
2.7.3. Fringe bias 2-32
2.7.4. Fringe distortion effects 2-32
2.7.5. Results accuracy 2-39

Chapter 3. Results 3-1

3.1. Introduction 3-1
3.2. Horizontal profiles of the horizontal velocity 3-2
3.3. Horizontal profiles of the vertical velocity 3-5
3.4. Vertical profiles of horizontal velocity 3-7
3.4.1. Unconfined A_1 and confined B_1 jets 3-7
3.4.2. Unconfined A_2 and confined B_2 jets 3-12
3.4.3. Convergent 11^o C_1 and convergent 22^o D_1 jets 3-18
3.4.4. Convergent 11^o C_2 and convergent 22^o D_2 jets 3-22
3.5. Vertical profiles of vertical velocity 3-26
3.5.1. Unconfined A_1 and confined B_1 jets 3-26
3.5.2. Unconfined A_2 and confined B_2 jets 3-31
3.5.3. Convergent 11^o C_1 and convergent 22^o D_1 jets 3-36
3.5.4. Convergent 11^o C_2 and convergent 22^o D_2 jets 3-39
3.6. Vertical profiles of streamwise fluctuation velocity 3-43
3.6.1. Unconfined A_1 and confined B_1 jets 3-43
3.6.2. Unconfined A_2 and confined B_2 jets 3-49

3.6.3. Convergent 11° C_1 and convergent 22° D_1 jets 3-55
3.6.4. Convergent 11° C_2 and convergent 22° D_2 jets 3-59
3.7. Vertical profiles of transverse fluctuation velocity 3-63
3.7.1. Unconfined A_1 and confined B_1 jets 3-63
3.7.2. Unconfined A_2 and confined B_2 jets 3-69
3.7.3. Convergent 11° C_1 and convergent 22° D_1 jets 3-75
3.7.4. Convergent 11° C_2 and convergent 22° D_2 jets 3-79
3.8. Vertical profiles of shear stress 3-83
3.8.1. Unconfined A_1 and confined B_1 jets 3-83
3.8.2. Unconfined A_2 and confined B_2 jets 3-88
3.8.3. Convergent 11° C_1 and convergent 22° D_1 jets 3-93
3.8.4. Convergent 11° C_2 and convergent 22° D_2 jets 3-97
3.9. Vertical profiles of anisotropy 3-101
3.9.1. Unconfined A_1 and confined B_1 jets 3-101
3.9.2. Unconfined A_2 and confined B_2 jets 3-106
3.9.3. Convergent 11° C_1 and convergent 22° D_1 jets 3-112
3.9.4. Convergent 11° C_2 and convergent 22° D_2 jets 3-116
3.10. Vertical profiles of correlation coefficient 3-120
3.10.1. Unconfined A_1 and confined B_1 jets 3-120
3.10.2. Unconfined A_2 and confined B_2 jets 3-126
3.10.3. Convergent 11° C_1 and convergent 22° D_1 jets 3-132
3.10.4. Convergent 11° C_2 and convergent 22° D_2 jets 3-136

Chapter 4. Conclusions 4-1

References 5-1

Figure Index

Figure 1.1. Example of subsonic coaxial jets. (Visualization created by the Technische Universität Berlin Computational Fluid Dynamics). 1-1

Figure 1.2. Initial region of coaxial, confined jets. 1-3

Figure 1.3. Example of a Vortex Breakdown with good perception of the complicated recirculation inside the bubble. (Visualization created by the Scientific Computing and Imaging (SCI) Institute, University of Utah). 1-36

Figure 1.4. Extend of modelling for certain types of turbulent models 1-68

Figure 1.5. Detail of a low bypass turbofan engine. 1-91

Figure 1.6. Detail of coaxial jets and 2D jets. 1-92

Figure 2.1. Detail of the engine (left) and the attached fan (middle and right). 2-2

Figure 2.2. General panoramic of the wind tunnel photograph. 2-3

Figure 2.3. Simplified chronology of 40 years of Laser Doppler Velocimeter. 2-8

Figure 2.4. Scheme of a back scattered LDA. 2-9

Figure 2.5. Electromagnetic spectrum. 2-9

Figure 2.6. Laser beam with Gaussian distribution. 2-11

Figure 2.7. left) light scattering from a moving seeding particle; right) Scattering of two incoming laser beams.left) light scattering from a moving seeding particle; right) Scattering of two incoming laser beams. 2-11

Figure 2.8. Superposition of two light waves .Superposition of two light waves. 2-12

Figure 2.9. Scheme of the Doppler effect. 2-13

Figure 2.10. Frequency to velocity conversion scheme. 2-14

Figure 2.11. Photo-detector receiving light scattered from the surface of a reflecting spherical seeding particle. 2-15

Figure 2.12. Transmitting and receiving systems of a LDA. 2-16

Figure 2.13. Bragg cell (left); Directional ambiguity without frequency shift (right, red line); Solved directional ambiguity using frequency shift (right, blue line). 2-17

Figure 2.14. Example of a fringe model detail. 2-18

Figure 2.15. Measurement ellipsoid volume with a Gaussian intensity 3 dimensions distribution δ_x, δ_y and δ_z. 2-19

Figure 2.16. Polar plot of scattered light intensity versus scattering angle with intensity shown on a logarithmic scale. 2-21

Figure 2.17.Typical single and multiple-particle Doppler bursts: left - Doppler burst; middle – filtered Doppler burst; right – multi-particles. 2-22

Figure 2.18. Smoke machine (middle), the remote control (left) and the seeding used for tracer (right). 2-24

Figure 2.19. Induced flow by a trip wire. 2-25

Figure 2.20. Tested flow configurations. 2-26

Figure 2.21. Diagram of the LDA positioning and the experimental setup for the confined jets case. 2-26

Figure 2.22. Left: electronic frequency converter device; middle: micromanometer; right: smoke machine.....2-28

Figure 2.23. Pressure variation with the tested frequency.....2-29

Figure 2.24. Variation of the laser velocity with the tested pressure. 2-29

Figure 2.25. Unconfined jets visualization (top: A_1 case, f=30 Hz); Confined jets (middle: the B_1 case, f=30 Hz; bottom: the B_2 case, f=40Hz).....2-30

Figure 2.26. Left; Convergent 11^o jets visualization (top: C_1 case, f=30 Hz; bottom: C_2 case, f=40Hz.); Right; Convergent 22 ^{o} jets visualization (top: D_1 case, f=30 Hz; bottom: D_2 case, f=40Hz).....2-30

Figure 2.27. Fringe distortion effects: a) both beam waist placed before the measurement volume center (distance z_1). This kind of distortion exist with both beam waist placed after the measurement volume center; b) one beam waist placed before the measurement volume center and one beam waist placed after the measurement volume center; c) astigmatism: displacements of all four focal points on two laser beams (A and B) from the measurement volume (one-time refraction); d) tracer partices interference distortion in the fringe pattern.....2-33

Figure 2.28. Geometrical and optical specifications of the Gaussian beam. 2-34

Figure 2.29. Radius of Gaussian curvature of beam wave front and the fringe distortion number. 2-37

Figure 2.30. Overestimation of the standard deviation in function of the real flow turbulence and the fringe distortion number. 2-39

Figure 2.31. Calibration Doppler burst signal.....2-40

Figure 2.32. Gaussian pdf distribution of a jet flow measured by LDA method. 2-40

Figure 3.1. Horizontal profiles of horizontal velocity for A_1 and B_1 test cases. 3-2

Figure 3.2. Horizontal profiles of horizontal velocity for A_2 and B_2 test cases. 3-3

Figure 3.3. Horizontal profiles of horizontal velocity for C_1 and D_1 test cases. 3-3

Figure 3.4. Horizontal profiles of horizontal velocity for C_2 and D_2 test cases. 3-3

Figure 3.5. Horizontal profiles of vertical velocity for A_1 and B_1 test cases. 3-5

Figure 3.6. Horizontal profiles of vertical velocity for A_2 and B_2 test cases. 3-5

Figure 3.7. Horizontal profiles of vertical velocity for C_1 and D_1 test cases. 3-5

Figure 3.8. Horizontal profiles of vertical velocity for C_2 and D_2 test cases. 3-6

Figure 3.9. Vertical profiles of horizontal velocity for A_1 and B_1 test cases at stations x=8, 50, 100 and 150 mm..... 3-7

Figure 3.10. Vertical profiles of horizontal velocity for A_1 and B_1 test cases at stations x=200, 245, 295 and 395 mm. 3-9

Figure 3.11. Vertical profiles of horizontal velocity for A_1 and B_1 test cases at stations x=490, 540, 640 and 735 mm. 3-10

Figure 3.12. Vertical profiles of horizontal velocity for A_1 and B_1 test cases at stations x=985 and 1235 mm. 3-11

Figure 3.13. Vertical profiles of horizontal velocity for A_2 and B_2 test cases at stations x=8, 50, 100 and 150 mm..... 3-12

Figure 3.14. Vertical profiles of horizontal velocity for A_2 and B_2 test cases at stations x=200, 245, 295 and 395 mm. 3-14

Figure 3.15. Vertical profiles of horizontal velocity for A_2 and B_2 test cases at stations x=490, 540, 640 and 735 mm. 3-16

Figure 3.16. Vertical profiles of horizontal velocity for A_2 and B_2 test cases at stations x=985 and 1235 mm. 3-17

Figure 3.17. Vertical profiles of horizontal velocity for C_1 and D_1 test cases at stations x=100, 200, 295 and 395 mm. 3-18

Figure 3.18. Vertical profiles of horizontal velocity for C_1 and D_1 test cases at stations x=490, 540, 735 and 985 mm. 3-20

Figure 3.19. Vertical profiles of horizontal velocity for C_1 and D_1 test cases at station x=1235 mm. 3-21

Figure 3.20. Vertical profiles of horizontal velocity for C_2 and D_2 test cases at stations x=100, 200, 295 and 395 mm. 3-22

Figure 3.21. Vertical profiles of horizontal velocity for C_2 and D_2 test cases at stations x=490, 540, 735 and 985 mm. 3-24

Figure 3.22. Vertical profiles of horizontal velocity for C_2 and D_2 test cases at station x=1235 mm. 3-25

Figure 3.23. Vertical profiles of vertical velocity for A_1 and B_1 test cases at stations x=8, 50, 100 and 150 mm..... 3-26

Figure 3.24. Vertical profiles of vertical velocity for A_1 and B_1 test cases at stations x=200, 245, 295 and 395 mm. 3-28

Figure 3.25. Vertical profiles of vertical velocity for A_1 and B_1 test cases at stations x=490, 540, 640 and 735 mm. 3-29

Figure 3.26. Vertical profiles of horizontal velocity for A_1 and B_1 test cases at stations x=985 and 1235 mm. 3-30

Figure 3.27. Vertical profiles of vertical velocity for A_2 and B_2 test cases at stations x=8, 50, 100 and 150 mm. 3-31

Figure 3.28. Vertical profiles of vertical velocity for A_2 and B_2 test cases at stations x=200, 245, 295 and 395 mm. 3-32

Figure 3.29. Vertical profiles of vertical velocity for A_2 and B_2 test cases at stations x=490, 540, 640 and 735 mm. 3-33

Figure 3.30. Vertical profiles of vertical velocity for A_2 and B_2 test cases at stations x=985 and 1235 mm. 3-35

Figure 3.31. Vertical profiles of vertical velocity for C_1 and D_1 test cases at stations x=100, 200, 295 and 395 mm. 3-36

Figure 3.32. Vertical profiles of vertical velocity for C_1 and D_1 test cases at stations x=490, 540, 735 and 985 mm. 3-38

Figure 3.33. Vertical profiles of vertical velocity for C_1 and D_1 test cases at station x=1235 mm. 3-39

Figure 3.34. Vertical profiles of vertical velocity for C_2 and D_2 test cases at stations x=100, 200, 295 and 395 mm. 3-39

Figure 3.35. Vertical profiles of vertical velocity for C_2 and D_2 test cases at stations x=490, 540, 735 and 985 mm. 3-41

Figure 3.36. Vertical profiles of vertical velocity for C_2 and D_2 test cases at station at x=1235 mm. 3-42

Figure 3.37. Vertical profiles of streamwise velocity fluctuation for A_1 and B_1 test cases at stations x=8, 50, 100 and 150 mm. 3-43

Figure 3.38. Vertical profiles of streamwise velocity fluctuation for A_1 and B_1 test cases at stations x=200, 245, 295 and 395 mm. 3-45

Figure 3.39. Vertical profiles of streamwise velocity fluctuation for A_1 and B_1 test cases at stations x=490, 540, 640 and 735 mm. 3-46

Figure 3.40. Vertical profiles of streamwise velocity fluctuation for A_1 and B_1 test cases at stations x=985 and 1235 mm. 3-48

Figure 3.41. Vertical profiles of streamwise velocity fluctuation for A_2 and B_2 test cases at stations x=8, 50, 100 and 150 mm. 3-49

Figure 3.42. Vertical profiles of streamwise velocity fluctuation for A_2 and B_2 test cases at stations x=200, 245, 295 and 395 mm. 3-51

Figure 3.43. Vertical profiles of streamwise velocity fluctuation for A_2 and B_2 test cases at stations x=490, 540, 640 and 735 mm. 3-53

Figure 3.44. Vertical profiles of streamwise velocity fluctuation for A_2 and B_2 test cases at stations x=985 and 1235 mm. 3-54

Figure 3.45. Vertical profiles of streamwise velocity fluctuation for C_1 and D_1 test cases at stations x=100, 200, 295 and 395 mm. 3-55

Figure 3.46. Vertical profiles of streamwise velocity fluctuation for C_1 and D_1 test cases at stations x=490, 540, 735 and 985 mm. 3-56

Figure 3.47. Vertical profiles of streamwise velocity fluctuation for C_1 and D_1 test cases at station x=1235 mm. 3-58

Figure 3.48. Vertical profiles of streamwise velocity fluctuation for C_2 and D_2 test cases at stations x=100, 200, 295 and 395 mm. 3-59

Figure 3.49. Vertical profiles of streamwise velocity fluctuation for C_2 and D_2 test cases at stations x=490, 540, 735 and 985 mm. 3-61

Figure 3.50. Vertical profiles of streamwise velocity fluctuation for C_2 and D_2 test cases at station x=1235 mm. 3-62

Figure 3.51. Vertical profiles of vertical velocity fluctuation for A_1 and B_1 test cases at stations x=8, 50, 100 and 150 mm. 3-63

Figure 3.52. Vertical profiles of vertical velocity fluctuation for A_1 and B_1 test cases at stations x=200, 245, 295 and 395 mm. 3-65

Figure 3.53. Vertical profiles of vertical velocity fluctuation for A_1 and B_1 test cases at stations x=490, 540, 640 and 735 mm. 3-66

Figure 3.54. Vertical profiles of vertical velocity fluctuation for A_1 and B_1 test cases at stations x=985 and 1235 mm. 3-68

Figure 3.55. Vertical profiles of vertical velocity fluctuation for A_2 and B_2 test cases at stations x=8, 50, 100 and 150 mm. 3-69

Figure 3.56. Vertical profiles of vertical velocity fluctuation for A_2 and B_2 test cases at stations x=200, 245, 295 and 395 mm. 3-71

Figure 3.57. Vertical profiles of vertical velocity fluctuation for A_2 and B_2 test cases at stations x=490, 540, 640 and 735 mm. 3-72

Figure 3.58. Vertical profiles of vertical velocity fluctuation for A_2 and B_2 test cases at stations x=985 and 1235 mm. 3-74

Figure 3.59. Vertical profiles of vertical velocity fluctuation for C_1 and D_1 test cases at stations x=100, 200, 295 and 395 mm. 3-75

Figure 3.60. Vertical profiles of vertical velocity fluctuation for C_1 and D_1 test cases at stations x=490, 540, 735 and 985 mm. 3-77

Figure 3.61. Vertical profiles of vertical velocity fluctuation for C_1 and D_1 test cases at station x=1235 mm. 3-78

Figure 3.62. Vertical profiles of vertical velocity fluctuation for C_2 and D_2 test cases at stations x=100, 200, 295 and 395 mm. 3-79

Figure 3.63. Vertical profiles of vertical velocity fluctuation for C_2 and D_2 test cases at stations x=490, 540, 735 and 985 mm. 3-81

Figure 3.64. Vertical profiles of vertical velocity fluctuation for C_2 and D_2 test cases at station x=1235 mm. 3-82

Figure 3.65. Vertical profiles of shear stress for A_1 and B_1 test cases at stations x=8, 50, 100 and 150 mm. 3-83

Figure 3.66. Vertical profiles of shear stress for A_1 and B_1 test cases at stations x=200, 245, 295 and 395 mm. 3-85

Figure 3.67. Vertical profiles of shear stress for A_1 and B_1 test cases at stations x=490, 540, 640 and 735 mm. 3-86

Figure 3.68. Vertical profiles of shear stress for A_1 and B_1 test cases at stations x=985 and 1235 mm. 3-87

Figure 3.69. Vertical profiles of shear stress for A_2 and B_2 test cases at stations x=8, 50, 100 and 150 mm. 3-88

Figure 3.70. Vertical profiles of shear stress for A_2 and B_2 test cases at stations x=200, 245, 295 and 395 mm. 3-89

Figure 3.71. Vertical profiles of shear stress for A_2 and B_2 test cases at stations x=490, 540, 640 and 735 mm. 3-91

Figure 3.72. Vertical profiles of shear stress for A_2 and B_2 test cases at stations x=985 and 1235 mm. 3-92

Figure 3.73. Vertical profiles of shear stress for C_1 and D_1 test cases at stations x=100, 200, 295 and 395 mm. 3-93

Figure 3.74. Vertical profiles of shear stress for C_1 and D_1 test cases at stations x=490, 540, 735 and 985 mm. 3-95

Figure 3.75. Vertical profiles of shear stress for C_1 and D_1 test cases at station x=1235 mm.. 3-96

Figure 3.76. Vertical profiles of shear stress for C_2 and D_2 test cases at stations x=100, 200, 295 and 395 mm. 3-97

Figure 3.77. Vertical profiles of shear stress for C_2 and D_2 test cases at stations x=490, 540, 735 and 985 mm. 3-98

Figure 3.78. Vertical profiles of shear stress for C_2 and D_2 test cases at station x=1235 mm.. 3-100

Figure 3.79. Vertical profiles of anisotropy for A_1 and B_1 test cases at stations x=8, 50, 100 and 150 mm. 3-101

Figure 3.80. Vertical profiles of anisotropy for A_1 and B_1 test cases at stations x=200, 245, 295 and 395 mm. 3-102

Figure 3.81. Vertical profiles of anisotropy for A_1 and B_1 test cases at stations x=490, 540, 640 and 735 mm. 3-104

Figure 3.82. Vertical profiles of anisotropy for A_1 and B_1 test cases at stations x=985 and 1235 mm. 3-105

Figure 3.83. Vertical profiles of anisotropy for A_2 and B_2 test cases at stations x=8, 50, 100 and 150 mm. 3-106

Figure 3.84. Vertical profiles of anisotropy for A_2 and B_2 test cases at stations x=200, 245, 295 and 395 mm. 3-108

Figure 3.85. Vertical profiles of anisotropy for A_2 and B_2 test cases at stations x=495, 540, 640 and 735 mm. 3-110

Figure 3.86. Vertical profiles of anisotropy for A_2 and B_2 test cases at stations x=985 and 1235 mm. 3-111

Figure 3.87. Vertical profiles of anisotropy for C_1 and D_1 test cases at stations x=100, 200, 295 and 395 mm. 3-112

Figure 3.88. Vertical profiles of anisotropy for C_1 and D_1 test cases at stations x=490, 540, 735 and 985 mm. 3-114

Figure 3.89. Vertical profiles of anisotropy for C_1 and D_1 test cases at stations station x=1235 mm. 3-115

Figure 3.90. Vertical profiles of anisotropy for C_2 and D_2 test cases at stations x=100, 200, 295 and 395 mm. 3-116

Figure 3.91. Vertical profiles of anisotropy for C_2 and D_2 test cases at stations x=490, 540, 735 and 985 mm. 3-118

Figure 3.92. Vertical profiles of anisotropy for C_2 and D_2 test cases at station x=1235 mm.... 3-119

Figure 3.93. Vertical profiles of correlation coefficient for A_1 and B_1 test cases at stations x=8, 50, 100 and 150 mm. 3-120

Figure 3.94. Vertical profiles of correlation coefficient for A_1 and B_1 test cases at x=200, 245, 295 and 395 mm. 3-122

Figure 3.95. Vertical profiles of correlation coefficient for A_1 and B_1 test cases at x=495, 540, 640 and 735 mm. 3-123

Figure 3.96. Vertical profiles of correlation coefficient for A_1 and B_1 test cases at x=985 and 1235 mm. 3-125

Figure 3.97. Vertical profiles of correlation coefficient for A_2 and B_2 test cases at stations x=8, 50, 100 and 150 mm. 3-126

Figure 3.98. Vertical profiles of correlation coefficient for A_2 and B_2 test cases at stations x=200, 245, 295 and 395 mm. 3-127

Figure 3.99. Vertical profiles of correlation coefficient for A_2 and B_2 test cases at stations x=490, 540, 640 and 735 mm. 3-129

Figure 3.100. Vertical profiles of correlation coefficient for A_2 and B_2 test cases at stations x=985 and 1235 mm. 3-131

Figure 3.101. Vertical profiles of correlation coefficient for C_1 and D_1 test cases at stations x=100, 200, 295 and 395 mm. 3-132

Figure 3.102. Vertical profiles of correlation coefficient for C_1 and D_1 test cases at stations x=490, 540, 735 and 985 mm. 3-133

Figure 3.103. Vertical profiles of correlation coefficient for C_1 and D_1 test cases at station x=1235 mm. 3-135

Figure 3.104. Vertical profiles of correlation coefficient for C_2 and D_2 test cases at stations x=100, 200, 295 and 395 mm. 3-136

Figure 3.105. Vertical profiles of correlation coefficient for C_2 and D_2 test cases at stations x=490, 540, 735 and 985 mm. 3-138

Figure 3.106. Vertical profiles of correlation coefficient for C_2 and D_2 test cases at station x=1235 mm. 3-139

Table Index

Table 1.1. Summary of the experimental investigations related to coaxial jets.....1-40
Table 1.2. Computational Methods and Turbulence Models.....1-67
Table 1.3. Summary of the numerical investigations related to coaxial jets.....1-81
Table 2.1. Centrifugal Fan Data Table. 2-2
Table 2.2. Main characteristics of the LDA. 2-10
Table 2.3. Typically seeding materials for air flows..... 2-20
Table 2.4. Calibration data. 2-28
Table 3.1. Experimental conditions. 3-1
Table 3.2. Stations studied summary..... 3-2

Nomenclature

Symbol

A_1	Unconfined jets, f=30 Hz test case
A_2	Unconfined jets, f=40 Hz test case
B_1	Confined jets, f=30 Hz test case
B_2	Confined jets, f=40 Hz test case
BS	Beam splitter
C_1	Convergent 11° jets, f=30 Hz test case
C_2	Convergent 11° jets, f=40 Hz test case
D	Diameter, mm
D_1	Convergent 22° jets, f=30 Hz test case
D_2	Convergent 22° jets, f=40 Hz test case
D_i	Diameter of the inner jet, mm
D_o	Diameter of the outer jet, mm
d_p	Particle diameter
e_1, e_2	Unit vectors of directions of the laser beams
e_i, e_s	Unit vectors describing direction of incoming and scattered light respectively
e^{-2}	Beam diameter, mm
f	Frequency, Hz; Focal length of focusing lens, mm
f_D	Doppler frequency
f_{sc}	Frequency shift
k	Turbulent kinetic energy, m^2/s^2
K	Velocimeter transfer constant, MHz/ms^{-1}
l	Wavelength of laser light, nm
N_f	Fringes number
Re	Reynolds number, dimensionless

Ro	Ross number, dimensionless
s	Beam spacing, mm
S	Swirl number, ms^{-1}
Sc	Schmidt number, dimensionless
St	Strouhal number, dimensionless
U_f	Flow velocity, ms^{-1}
U_i	Horizontal velocity of the inner jet, ms^{-1}
U_{mean}	Mass average velocity, ms^{-1}
U_o	Horizontal velocity of the outer jet, ms^{-1}
U_∞	Horizontal velocity of the external flow, ms^{-1}
U_p	Particle velocity, ms^{-1}
$\vec{U}$	Instantaneous velocity vector
$\sqrt{\overline{u'^2}}$	Streamwise velocity fluctuations, ms^{-1}
$\overline{u'\,v'}$	Shear stress, ms^{-1}
$\sqrt{\overline{u'^2}}/\sqrt{\overline{v'^2}}$	Anisotropy, ms^{-1}
$\frac{\overline{u'v'}}{\sqrt{\overline{u'^2}}\sqrt{\overline{v'^2}}}$	K_{uv} Correlation factor, ms^{-1}
V	Vertical velocity, ms^{-1}
$\sqrt{\overline{v'^2}}$	Transverse velocity fluctuations, ms^{-1}

Greek symbols

ε	Turbulent dissipation
ρ	Specific mass, kg/m^3
ρ_f	Flow Specific mass
ρ_p	Particle specific mass
λ	Velocity ratio ($\lambda = U_o / U_i$), Chapter 1, Chapter 3
λ	Wavelength, Chapter 2
θ	Half of beam laser intersection angle, °
θ_B	Bragg cell tilt angle, °
ν	Cinematic viscosity
δ_f	Fringe spacing, µm
$\delta_x, \delta_y, \delta_z$	height, width and length of the measuring volume
ω	Angular frequency

Chapter 1. Introduction

The turbulent mixing of coaxial confined jets is a complex dynamic process that is applied in a large number of devices such as the engineering ejectors, pumps jet, industrial burners, combustion chambers of jet engines, nuclear rockets gas, mixing chambers of turbofans or afterburners. Previous work indicate that there are various parameters (geometrical and operating) that influence the process of turbulent mixing such as velocity, temperature or density ratios, compressibility effects, levels of turbulence of jets, pressure gradient and shape of the duct. Swirl and bluff bodies have been used by many researchers to generate recirculation, allowing so a greater mix of jets in a shorter space thus increasing the efficiency of practical devices.

The main objective of this research is to achieve enhanced mixing without any effect of swirl caused and without the presence of bluff body. It sought the understanding of interactions between some phenomena in turbulent coaxial jets in order to control the mix in a purely aerodynamic form.

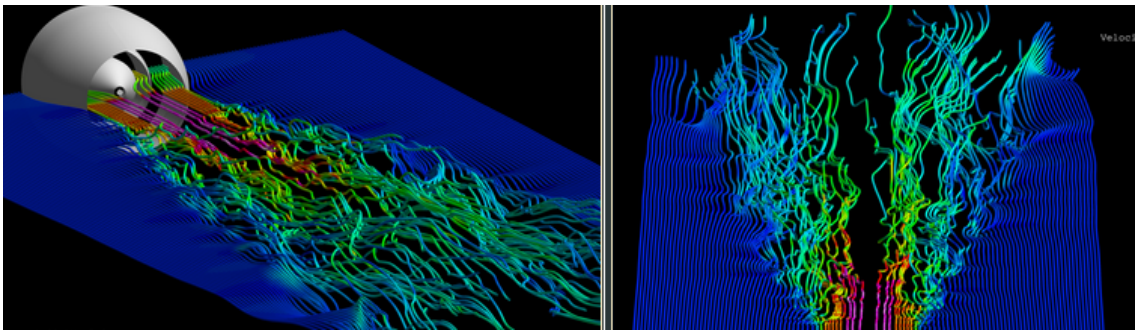

Figure 1.1. Example of subsonic coaxial jets[1]. (Visualization created by the Technische Universität Berlin Computational Fluid Dynamics).

Recently, much interest has concentrated on engineering applications of a swirling coaxial jet in a variety field of aerospace technologies and industrial manufacturing processes. Some of the major applications of swirling coaxial jets are enhancement of the mixing between two streams, improvement of plasma jet cutting performance and flame stabilization of combustion technologies (Lee *et al*, 2004). Coaxial jets are present in several practical applications, especially in the field of combustion where the mixing process is largely controlled by the flow dynamics. The process of turbulent mixing of coaxial jets finds application in a variety of engineering devices. Study of the aerodynamic behaviour of coaxial jets in different types of confinement is also of basic interest because it involves a number of interacting turbulent flow phenomena, the details of which are not yet understood quantitatively. The factors that are involved in a mixing process and are also primarily responsible for the complexity are: the velocity ratio, temperature ratio, density ratio,

[1] http://www.cfd.tu-berlin.de/~panek/cfd/Simulation.html#cfd [accessed on 16.06.2010].

compressibility and turbulence levels of the two streams, swirl, pressure gradient, interaction between wall-bounded and free shear flows, mixing duct to core jet diameter ratio and thickness of the core duct wall. Conventional coaxial jet consists of a central or an inner nozzle surrounded by an annulus connected to separate supply sources. A two layers model describes the jet. The outer layer of the jet is a shear layer with single sign of vorticity. The inner layer is characterized by opposite signs of vorticity due to the merging of a wake profile and a shear layer profile and is therefore susceptible to instabilities. The length of the potential core and dynamic interaction between the inner and outer layers is governed by the ratio of jets velocity and the state of boundary layer on the walls of nozzle and the annulus (Champagne and Wygnanski, 1971; Dahm *et al*, 1992). The inner jet issued from a nozzle of diameter D_i and an outer annular jet issued from an outer annulus of diameter D_o ($D_o > D_i$). U_o and U_i designate the respective velocities of the inner and outer jets. One of the important parameters characterizing the coaxial jet dynamics is the ratio between the outer to the inner jet momentum flux, $M = \rho_o U_o^2 / \rho_i U_i^2$ where ρ_i and ρ_o are, respectively, the inner and outer density. For constant density jets ($\rho_i = \rho_o$), the momentum flux ratio reduces to the velocity ratio $\lambda = U_o / U_i$. These jets are situated in-between two limiting cases: a single round jet ($\lambda = 1$) and a purely annular jet ($\lambda \rightarrow \infty$). Purely annular jets are characterized by the presence of a big recirculation bubble near the jet axis. Since this backflow is absent for small enough values of λ, there exists a critical velocity ratio λ_c which separates the two different main flow regimes, without recirculation bubble for $1 < \lambda < \lambda_c$ and with recirculation bubble for $\lambda > \lambda_c$.

1.1. Early Studies

Coaxial jets have been investigated since 1925. Initial investigations were concerned mainly with laminar jets (Kulik *et al*, 1969). Coaxial jets experimental work has begun since the 1950s. Forstall and Shapiro (1950), Stark (1953), Chigier and Beer (1964) studied the mixture of a circular jet with an annular coaxial jet for various nozzles diameters and velocities ratios. Measurements were taken using a Pitot tube. They found results proving that the nozzles diameters and velocities ratios were the most significant parameters which determined the jet configuration and the average velocity profiles of the flow. The common characteristic of all these investigations is that they were concerned only by the mean velocity field rather than the turbulent flowfields structure.

Turbulent mixing of confined coaxial jets is a complex dynamic process which finds application in a number of engineering devices such as ejectors, jet pumps, industrial burners, jet engine combustion chambers, gaseous nuclear rockets, turbofan engine mixing chambers, afterburners, etc. The study of aerodynamic behaviour of coaxial jets in different types of confinement is also of basic interest because it involves a certain interacting turbulent flow phenomena, the details of which are not yet fully understood quantitatively. In all of the above applications, the need for performance enhancement and optimization makes desirable an improved understanding of the interaction of the competing dynamical

mechanisms that arise in swirling jets and govern their evolution. Their axial velocity profiles allow shear-induced instabilities similar to those encountered in non-swirling flows. However, the additional presence of swirl results in an azimuthal shear layer and centrifugal instability when the circulation decreases outwards. Finally, under certain conditions, *i.e.* when the swirl rate is high enough, swirling jets are known to produce vortex breakdown events. The complex three-dimensional and unsteady structure of the breakdown of slender vortices has been a great challenge for experimentalists since the first observations by Peckham and Atkinson, 1957. Improved understanding of these mechanisms and their mutual coupling is expected to pave the way for the development of passive and active flow control strategies employing sound, changes in nozzle geometry and motion.

1.1.1. Experimental investigations

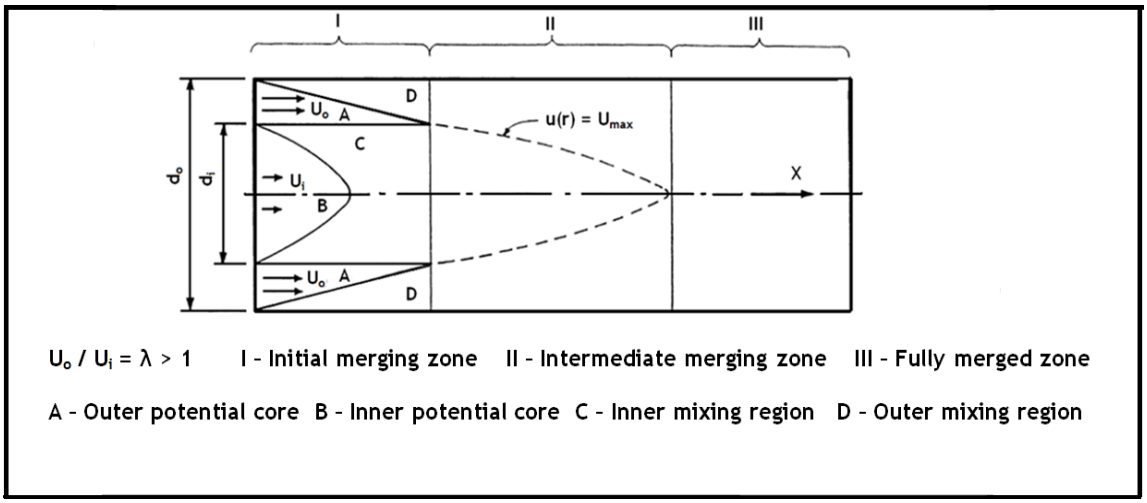

Figure 1.2. Initial region of coaxial, confined jets.

The complex nature of the near field structure of a ducted coaxial jets configuration can be appreciated from **Erro! A origem da referência não foi encontrada.**, which refers to a typical condition with comparable inner and outer jet areas. The flow field that arises from the interaction of coaxial jets and their mixing can be considered to comprise of three main zones of flow development as shown in the figure. Zone I is the initial merging zone wherein the core and the annular streams enter the mixing duct with different uniform axial velocities. The initial zone consists of two different potential flow regions, A and B, and two different shear flow regions, *i.e.* the jet shear and the boundary layer regions, C and D, respectively. The shear regions increase in size and the potential flow regions decrease in size in the flow direction. The annular stream potential core disappears when the shear region and the wall boundary layer meet. Zone II is the intermediate merging zone, where the largest momentum exchange between the jets takes place. The central potential flow region no longer exists in this zone for $\lambda > 1$, while for $\lambda < 1$; it exists but continues to decrease. Zone III is the fully merged zone, in which the flow conditions become progressively similar to

those of a single jet, in agreement with the work of Acharya (1954) and Razinsky and Brighton (1971). Further downstream, flow becomes fully developed and self-similar (a similarity exists between velocity profiles at each cross-section along the streamwise axis) and a boundary layer type analysis usually fits the experimental data well. The simplified picture of the complex flow presented in Figure 1.2, is further complicated by the presence of boundary layers on both the surfaces of the inner duct wall (splitter plate) and the subsequent annular wake trailing from the inner duct into the initial merging zone. The initial jet spreading rate and the length of zone I are sensitive to the inner duct (nozzle) geometry and the inlet flow conditions; vortex shedding from thick nozzle wall may accelerate the erosion of the potential core and enhance mixing with the entrained stream (Albayrak *et al.*, 1990). In the literature several studies such as Razinsky and Brighton (1971), Acharya (1954), Mikhail (1960), Gibson (1986) and Albayrak *et al.,* (1990) indicate that there are other parameters (geometrical and operating) that influence the process of turbulent mixing such as velocity, temperature or density ratios, compressibility effects, levels of turbulence of jets, pressure gradient, interaction between the walls and the jets or the ration between the diameters of the mixing duct and the internal jet nozzle. Acharya (1954) conducted a comprehensive review of progress on the mixing of jets between 1864 and 1951 and found that all of the studies published during that period were concentrated on unconfined jets. He performed a detailed and quantitative research to study the influence of the velocity and temperature ratios on the mixing with confinement, and concluded that the shear friction between the two turbulent currents is greater in confined jets than in unconfined jets.

Zawacki and Weinstein (1968) made an experimental study of axially symmetric, turbulent, incompressible, co-flowing streams using hot-wire anemometry techniques to make measurements in three systems: one homogeneous system with a resultant density ratio of 1, and two heterogeneous systems, with an inner to outer stream density ratio of 4 to 1 (ρ_o / ρ_i = 0.25) Freon 12-air system, and 7 to 1 (ρ_o / ρ_i = 0.143) Freon C318-air system. They varied the outer stream velocity from 12 to 50 fts^{-1} and the inner stream was changed to provide outer to inner stream velocity ratios of from 1 to 40. They presented results for the relative axial turbulence intensity, relative radial turbulence intensity, and turbulent shear stress for various velocity ratios in the homogeneous system, in both the initial mixing region and the downstream or similar region. In the homogeneous case they present six different outer to inner stream velocity ratios, respectively 39.5, 28.5, 16, 8, 3.4 and 1. The Reynolds numbers for 39.5, 28.5, and 16 were correspondingly, 435, 583, and 1060, which indicate that the flow in the tube should be laminar. Upon further investigation they found that with no flow in the inner stream and full flow in the external stream, large fluctuations exist in the inner tube and that an average component was found to exist, indicating that a circulation pattern existed inside the tube. They found that for high velocity ratios, or low inner stream velocities, these circulations and fluctuations are super-imposed on the mean flow, stating that the nature of this phenomenon were not clear. In the first heterogeneous case they present eleven different velocity ratios for the Freon 12 – air system. For the higher

presented velocity ratio (36.8) the same circulation phenomenon occurs, with the centreline velocity exhibiting the characteristic of decreasing, increasing and decreasing again before finally increasing. They also concluded that for all comparable velocity ratios, the heterogeneous system produced larger values of the relative turbulence intensity than the homogeneous system.

Ko and Kwan (1976) presented an experimental investigation within coaxial subsonic air jets that mix externally. Using a constant-temperature type of hot-wire anemometer and a microphone, they measured mean velocity, turbulence intensity and pressure. The central nozzle, which generated the primary jet, had D_i = 2.10 cm diameter and the area contraction ratio were 13:1, with a maintained 60 ms^{-1} velocity. The secondary or outer jet has a D_o = 4 cm diameter, with an area contraction ratio of 8:1. Their experiments consisted in three mean-velocity ratios of λ = 0.3, 0.5 and 0.7. Their investigation domain was mostly confined within the first seven diameters of the central jet. They obtained results that showed similarity of the mean velocity and turbulence-intensity profiles of the three mixing regions, inside the initial merging and fully-merged zones. In the intermediate zone, no similarity was founded. The dominance of either type of vortices or both depended of the velocity ratio. At λ = 0.3, the high-frequency vortices were found more dominant. At λ = 0.5, the high-frequency were still dominant, but the dominance of low-frequency was increasing, while at λ = 0.7, the low-frequency vortices became the only dominant ones.

Albayrak *et al* (1990) by hot-wire anemometer investigated experimentally turbulence intensity distributions and axial velocities in the mixing region of the coaxial jets. Using independent sources to obtain inner and outer jets, they studied the mixing and entrainment of the jets for various outer to inner velocity ratios (∞, 1.45, 1, 0.48). The test area consisted on two pipes with 50 and 110 mm in diameter and the inner wall thickness had 1.5 mm. They run three different experiments: single jet, annular jet and coaxial jets. For the single jet experiment the maximum velocity was 22 ms^{-1} corresponding to a Reynolds number on the pipe diameter and centreline velocity of Re = 68700. For the annular jet experiment the maximum velocity was 12.5 ms^{-1}, with the Reynolds number based on the hydraulic diameter of the annulus and the peak velocity was Re = 48250. For the coaxial jets experiment, the maximum velocities of both jets was U_i = 18.4 and U_o = 26.5 ms^{-1}, with the respective Reynolds numbers Re_{id} = 55200 and Re_{od} = 101400. In their measurements with both turbulent jets, when the annular jet velocity was higher than the central jet, a vortex region was setup causing a reverse flow with respect to the central jet. The same phenomena occur for the case of the pure annular flow λ = ∞. For the case of equal velocity jets, they obtained two jets merged to form an equivalent single jet at the downstream of the jets. For the case of higher velocity in the central jet, the core jet begins to draw in the annular jet in order to satisfy its entrainment requirements. For their case of λ = 0.48 with both turbulent jets, the annular jet is completely absorbed with the confines of the core jet at the downstream of the exit.

Durão and Whitelaw (1973) performed an experimental work of turbulent mixing in the developing region of air coaxial jets. Using a Pitot tube, a Preston tube, normal and 45° hot-wire probes, they measured mean velocity, the three normal stresses and Reynolds shear stress in three velocity ratios: U_i / U_o = 0, 0.23 and 0.62. Their facility was with an inner pipe 2.83 m long with 16.13 mm inner diameter and 21.59 outer diameters, and the outer jet was 2.00 m long with 44.50 mm inner diameter and 50.44 mm outer diameter. The apparatus was designed to provide fully developed turbulent flow at the exit from both the annulus and pipe. The pipe Reynolds numbers were Re_i = 1.7 x 10^4 and 2.8 x 10^4 and the Re_o = 6.6 x 10^4 and 6.4 x 10^4. They investigated the developing region of coaxial jets at downstream distances up to 17 outer diameters. Their results showed that coaxial jets tend to reach a self-preserving state much more rapidly than axisymmetric single jets. The attainment of the fully developed state was a function of the velocity ratio and zero velocity ratios leads to the most rapid development. Their experiments showed that the flow possesses locations of zero mean-velocity gradients which were not coincident with locations of zero shear stress. They stated that as the coaxial jet flow tented to its self-preservation, it was clear that turbulent kinetic energy was a suitable property with which to characterize the flow, and it was of interest to consider that the kinetic energy was directly related to the local shear stress, as was already proposed by previous authors.

Warda *et al* (1999a) investigated experimentally the near-field region of a free turbulent coaxial jet using LDA. They measured the axial variations of both mean and fluctuating longitudinal velocities of a double concentric jets with a velocity ratio of λ = 0.64 (U_i = 5.2 ms^{-1}, Re_D = 0.27 x 10^4 for the inner jet; U_o = 8.1 ms^{-1}, Re_D = 0.93 x 10^4 for the outer jet, respectively). They proceeded their study with more three velocity ratios by maintaining the central jet velocity fixed at 20 ms^{-1}, and by decreasing the annular jet velocity to 10, 6 and 4.5 ms^{-1}, (λ = 2, 3.3 and 4.5) with Reynolds number for the annular jet Re_{DO} = 1.15x10^4, 0.7 x 10^4 and 0.51 x 10^4, respectively. They concluded that coaxial jets with the velocity ratio less than unity develop faster than that with λ > 1 and also that the inner potential core of the coaxial jets strongly depends on the velocity ratio while the outer core of coaxial jets with velocity ratios greater than unity seems to be insensitive to the velocity ratio.

Warda *et al* (2001) investigated experimentally the influence of the magnitude of two initial velocities of a coaxial turbulent jet. Using a LDA they measured the axial mean velocity and axial turbulence intensity. The effect of absolute value of each stream velocity, on the flow field, was investigated by means of achieving the velocity ratio, λ = 2, three times with two different velocities each time (U_i / U_o = 20/10, 14/7 and 10/5 ms^{-1}). For these cases the Reynolds number was Re_D = 10200, 7100 and 5100 respectively and Re_{DO} = 11500, 8000 and 5700 respectively. Moreover, they compared the similarity of the axial mean velocity profiles, for two other values of λ (3.3 and 4.5), and compared with the results of the single jet. They found that for the same velocity ratio, when the velocity of each stream (inner and outer) was reduced, the growth of the half width of coaxial jets with λ > 1 was increased. They concluded also that the velocity ratio, λ, affects the evolution and the structure of coaxial

jets affecting as well the absolute values of the velocity of each stream, particularly in the region $10 \leq x / D \geq 20$. Their reduction in the absolute values of the velocities of both streams while keeping the same velocity ratio, λ constant made the jet decay faster along the centreline.

Matsumoto *et al* (1973) performed experimental studies for air-air double concentric jets. Using an X-array probe, they measured turbulent intensity and turbulent shear stress, axial velocity and static pressure. The test section was a 100 mm diameter circular duct. The air for the central jet was supplied by a compressor and spurts pout to the test section from a nozzle with a 5.2 mm diameter. The velocity profile at the outlet of the nozzle was a fully developed turbulent profile. They tested four velocity ratios, limited to the case that the central jet has a higher velocity than the external stream λ = 0.24, 0.42, 0.54 and 0.82, with an average velocity of the inner jet at the outlet of the nozzle of 100, 57, 44.4 and 29.3 ms^{-1} and with a central velocity of the inner jet at the outlet of the nozzle of 122.5, 68.5, 52.5 and 35 ms^{-1}, respectively. Considering the flow pattern in the duct, the Reynolds number of the jet lies in the range of about 1.1 to 3.2 x 10^4. At the entrance of the test section the external stream had a uniform velocity of 24 ms^{-1}. They observed that the flow pattern in the duct was divided into three regions: (I) – initial region, (II) – main region and (III) – the region in which jet boundary was interfered by boundary layer on circular duct. In the main region, the dimensionless radial velocity profiles fit the cosine curve independently of values of dimensionless thickness of the nozzle wall $\bar{\delta}$, λ and the dimensionless axial coordinate, $\bar{x}$, They concluded too, that for larger values of the dimensionless thickness of the nozzle wall $\bar{\delta}$, a large recirculation was recognized behind the nozzle wall and the external stream showed a curved shape. They found that for small values of λ, the velocity decay on the central axis and the intensity of turbulence were hardly affected by the wall thickness, while for large values of λ, the tendency of velocity decay becomes remarkable and the turbulence intensity is affected heavily by the wake behind the nozzle wall with an increase in the wall thickness.

Escudier and Keller (1985) made an experimental study in the recirculation phenomena of the swirling water flow. The diameter of annular segment was with inner and outer diameters of 20 and 40 mm, while the diameter of the tube was D = 60 mm for the visualization case and D = 55 mm for the measurements case, always with a total length 350 mm. They made visualization using a fluorescent dye (fluorescein), at a low Reynolds number (1352) to ensure the reduced rate which dye was dispersed. For the velocity measurements it was installed a nozzle element with inner diameter 32 mm and an exit contraction with variable diameter D_E. Others variable parameters were the guide vane angle ϕ and the volumetric flow rate Q. Using LDA, they measured the mean axial and swirl velocities at a considerably high Reynolds number (7008) to ensure an acceptably high data rate acquisition. The visualization was made for ϕ = 60 and 70 deg, corresponding to a swirl number S = 2.28 and 11.8, respectively. In the first case it was observed a separated wake and breakdown recirculation zones, and in the second case the data showed combined wake and recirculation zones. The measurements were made for two different values of ϕ. For the case of ϕ = 62

deg corresponding to a swirl number S = 2.74, they studied the D_E / D = 1 and 0.455 (D_E = 40 mm). For the case ϕ = 70 deg corresponding to a swirl number S = 11.8, they studied the D_E / D = 1. 0.855, 0.727 and 0.455 (D_E = 55, 47, 40 and 25 mm respectively). In the case of ϕ = 62 for both studies, the data showed that the flow recovers to supercritical after breakdown, and the exit contraction appears to represent a major change of the downstream of the vortex tube. For the ϕ = 70, for the four studies, they observed that exit contraction have a strong influence on the entire flowfield. For strong exit contractions, the recirculation zone assumed a mushroom shape, even more pronounced if the upstream centre body was reduced.

Nikitopoulos *et al* (2003) performed an experimental work by comparing circular and square coaxial jets with low velocity ratio and with a turbulent initial state. Using a pulsed laser sheet seeding with $TiCl_4$, they made visualization. A hot-wire traversing the centre (in the case of the square jets at a square side and at a square diagonal) was used for local velocity measurements, at a Reynolds number of 1.9 x 10^4 (based on the outer nozzle hydraulic diameter and average velocity), and the inner-to-outer velocity ratio was 0.3. For the circular coaxial nozzle, the inner and outer hydraulic diameter jet was 15.24 and 19.05 mm respectively. For the square nozzles, the hydraulic diameters were the same, for a proper near-field comparison between the two nozzles. The inner to outer area ratio was preserved at 0.213. They made four strategy seeding to visualize selectively the shear layers in the near-field of the nozzles: in strategy 1 and 2, the outer jet was maintained with $TiCl_4$, while the inner jet was H_2O (v) in the first strategy and dry air in the second; in strategy 3 and 4, the inner jet was maintained with $TiCl_4$, while the outer jet was H_2O (v) in the third strategy and dry air in the fourth. Scaling of the mean velocity and turbulence profiles for the three shear layers formed in the near-field of axisymmetric and square flows was found to be consistent between the two geometries and with previously reported trends for axisymmetric coaxial jets. Large-scale periodic structures were identified for both nozzle configurations in the midfield of the inner mixing region, with wake characteristics. They observed that the spectral characteristics of the circular and square nozzle combinations were qualitatively similar, and that the outer mixing region, which was initially highly turbulent, showed no signs of an organized structure. They also found a slight increase on the mixing on square nozzles compared with the coaxial nozzles, which they attributed to the different initial velocity profiles between the configurations.

Bitting *et al* (2001) using high-resolution, reactive Mie scattering laser-sheet visualization, two-colour DPIV and thermal anemometry measurements, compared air flows on axisymmetric coaxial nozzles and square nozzles. Their visualization results were obtained for three square coaxial configurations and a reference circular coaxial nozzle at two Reynolds numbers of the outer jet (19000 and 29000) and for inner to outer jet velocity ratios of 0.15, 0.22 and 0.3. The three square nozzles experiments varied in the orientation of the inner square jet with respect to the outer square jet giving a centreline angular orientation offset of 22.5° (square I), 0° (square II) and 45° (square). The coaxial nozzles had an effective

hydraulic inner and outer jet diameters of respectively, d_i = 15.26 and d_o = 19.05 mm. The wall thickness of the inner nozzle had 1.905 mm. For the square nozzles the hydraulic diameters was the same, with the outer/inner area ratio preserved at 4.69. Axial velocity and instantaneous vorticity were measured by DPIV, and visualization was carried out using a pulsed laser sheet and with $TiCl_4$. They observed that the non-mixed internal region decreases with the decrease of velocity ratio and also observed instable recirculation and reversal flow phenomena at the end of the internal core of the jet for low velocity ratios. The inner and coflowing unmixed regions disappear sooner in the square II case than the axisymmetric one, and the inner and outer shear-layer growth appears to be faster. A recirculation was observed at λ = 0.15 and 0.22 in both square II and the axisymmetric jets, while was absent at λ = 0.3 for both Reynolds numbers examined.

Villermaux (1998) studied the effects on mixing in a confined turbulent flow of a low density jet with low velocity in the inner ring with a fast and light annular jet on the annular ring. The jet outer fluid was air and the inner fluid was water with diameters D_o = 5.5 and D_i = 4 cm, respectively. One of the main goals of this work, was to study the rockets engines that operated at a momentum flux ratio ($M = \rho_o U_o^2/\rho_i U_i^2$) of the order to 10. He made visualization for the velocity ratios λ = 3 and 15 (M = 9 and 225) using dye injection in the central jet. He made measurements of radial mean and rms velocity and made connections with known results in the airblast atomization and with several experimental facts, both in one and two-phase flows. He concluded that with the increasing density ratios for this case, $\rho_1\rho_2$ the instability was progressively damped. He observed that the shape of the profile of velocities in the outer ring and the thickness of vorticity influences the growth rate of the instability. When the ratio of moments (energy) between the phases was above M critical, M > 35, a transition occurs for a recirculation flow. Above the critical M, the size of the recirculation bubble was gradually increased and reached a size of the order of D_i when $M \rightarrow \infty$.

An experimental study of two mixed confined coaxial jets made by Zhdanov *et al* (2006) using one-component LDV and LIF (scalar field). The experiment was made in a water closed-circuit channel. The facility included a tube 1 (D = 50 mm) and steel nozzle 2 with the inner diameter d = 10 mm. Nozzle 2 was fixed in detachable block 3 with length 430 mm. Tube 4 of 50 mm inner diameter had a movable joint with the flanges of block 3 via circular seals. Owing to this, the angular position, of nozzle 2 relative to tube 1 could be varied by rotating tube 4 relative to fixed tube 1. For all cases, the nozzle jet was turbulent at the Reynolds number Re_d equal to 10000. They investigated the distance range between $0.1 \leq x / D \leq 9.1$. They presented profiles of an averaged velocity and velocity fluctuations in the mixer cross-sections at three angular positions of the nozzle (0º, 90º, and 180º). Over the investigated distance range, they found that the uniform averaged velocity field has no time to form, although when the recirculation zone was formed, the uniform averaged velocity distribution was set along the larger part of the mixer cross-section. The authors stated that the obtained data of the analysis of the mixing development in the recirculation zone

revealed some flow features that have not been discussed previously in their available literature. These features were: existence of two different types of the flow in the recirculation region; oscillating backflow fluid, i.e., averaged unsteady flow; fluid oscillating in the antiphase near the opposite walls and flow asymmetry. They found that there were flow regions within the recirculation zone where the inertial convective sub-range in the scalar fluctuation spectrum exists, and concluded that this zone was a superposition of unsteady vortices of different length and time scales. They also stated that the theoretical models used to calculate the mixing should account for the existence of different length scales in the recirculation zone and a strong unsteady behaviour of the flow and the most appropriate candidates for this is large Eddy simulation (LES).

Rehab *et al* (1997) experimentally showed that the coaxial jet dynamics and its vortex topology are strongly dependent on the shape of the inlet nozzle. The experimental set-up consists of coaxial axisymmetric water jets discharging into a tank where the fluid (water) is at rest. Their nozzle configuration have inner and outer diameters of D_i = 2 cm and D_o = 2.7 cm, contraction ratios of 2 and 4 respectively and an area ratio at the nozzle exit of 1.82. The inner and the outer jet covered an exit velocity range of respectively $0 \leq U_i \leq 1$ ms^{-1}, and $0.3 \leq U_o \leq 4$ ms^{-1}. They studied three velocity ratios: λ = 2, 3 and 4 with the outer jet fixed to 2 ms^{-1} and the Reynolds number around 7000, and had observed that the fast outer jet dominates the dynamics. Mean and turbulent velocity measurements were made with a constant-temperature hot-film anemometer. Mean static pressure measurements, with respect to the local hydrostatic pressure, were made with a pressure probe linked to an HMB-KWS differential pressure sensor. The visualizations have been realized by a laser-induced-fluorescence technique, using disodium fluorescein dye as a passive tracer, excited by an argon-ion laser sheet. They found that above a critical velocity ratio λ_c, the inner potential cone was truncated by a reverse flow and a wake-type regime was active, characterized by the existence of an unsteady recirculation bubble that oscillates with low frequency and with large amplitude compared to the Kelvin-Helmholtz mode. The size of the recirculating bubble increases with λ and reaches a maximum length for $\lambda = \infty$ (U_i = 0), typically equal to one inner jet diameter D_i. The mean reverse flow velocity was proportional to U_o.

Dahm *et al* (1992) made an experimental investigation in to the vortex patterns and the dynamics of their interactions for the incompressible flow in the near field of a coaxial jet issuing into a quiescent ambient flow. They also attempted to simulate numerically the explanation for the role of the absolute velocities through the thinning of the vorticity layers. Their water facility was 33 x 33 x 63 in. interior dimensions with 1 in. thick 31 x 31 in. glass windows on four sides. A two-coloured planar LIF technique was used for visualisation, recorded with ciné photography. The outer nozzle had a 3.01 in. interior diameter, while the inner nozzle had a 2.10 in. interior diameter and the wall thickness had 0.05 in., giving the nozzle exit diameter ratio equal to 1.40 and the annular-to-inner nozzle exit area ratio of 0.94. The contraction ratio of the inner stream was 9.9:1, while the outer stream experiment a contraction ratio of 10.6:1. Their experiments consisted in seven different pairs of

velocities of the inner and outer jet. They varied the inner jet in velocities between the range 2.5 < U_i < 20 cms^{-1}, and the outer jet between the range 6.5 < U_o < 20 cms^{-1}, running the λ velocity ratio of 0.59, 0.71, 1.00 (two times), 1.14, 2.56 and 4.16. For all the results, the overall jet far-field Reynolds number were Re < 15000, and the nozzle boundary layer Reynolds number Re_δ < 200. Their facility consisted also in a third jet exterior to the others with velocity $U_3 \neq 0$ and $U_3 = 0$, but only presenting results for the case of $U_3 = 0$. For the λ = 0.59, the velocity jump across both layers the same sign and were roughly the magnitude. They observed that the shear layer vortices formed a helical vortex structure of the near-field, for about the first two diameters downstream. For the λ = 0.71, the velocity jump across both layers still had the same sign, but differed in magnitude by more than a factor of two. In this case the subsequent development appears to be much more strongly dominated by the vortical structures, with the outer layer forming shear-layer-like vortices, which suggested in the author's the idea of near-field structure consisted in vortex rings with a tentacle appearance in the potential core, rather than the helical structures in the first case. For the λ = 1.00, the velocity jump was zero across the inner layer. They found that the outer layer developed into shear-layer-like vortex rings and that the core length was considerably greater than the previous case. For the λ = 1.14, the velocity jump across the two layers showed opposing signs. The rollup of the inner layer started to look more shear-layer-like than wake-like and the interactions whit the shear-layer vortices, became significant. The outer layer still appears to govern the dynamics through vortex rings pairings with less success in consuming the potential core that for λ = 0.71 case. The overall core length was roughly the same as in the previous case. For the λ = 2.56, the resulting shear-layer vortices in the two layers again presented opposing senses of circulation, with the assumption of the authors that they developed independently of each other. The asymmetries showed in this velocity ratio were more effective at consuming the potential core, that presented long tentacle features and was shorter than for the case of λ = 0.71. For the λ = 4.16 case, the velocity jump across the inner and outer layers with opposite signs but with at about roughly the same magnitude. The potential core ends abruptly at about one and a half diameters downstream. The authors suggested that the two layers do not develop independently.

Fink (1997) made an experimental and theoretical study concerning the influence of external turbulence on mixing of axisymmetric coaxial jets. He used a theoretical *"k-ε"* turbulence model for physical considerations, measured the mean velocities with Pitot tubes and axial turbulence fluctuations with single normal wires. Measurements were performed in a wind tunnel using 13 different grids to produce distinct levels and scales of background turbulence. Jets with different momentum thickness were discharged from a long tube with *D* = 6 mm in the centre of the tunnel cross-section and coaxial to the main flow. The jet was introduced at a distance of 10 mesh lengths downstream of a bi-plane grid. The ratio of size to thickness of the square bars was 40/10, corresponding this to a solidity ratio of σ = 0.43. He presented results for three jet-pair of different strengths at 6 cross-sections, with velocity ratios of jet exit velocity/velocity of the external flow U_0 / U_∞= 3.10, 4.50 and 5.75. The

Reynolds number based on the jet exit velocity were respectively Re = 8500, 13000 and 15700. In the presence of a suitable external turbulence, for the axial development of the velocity scale, he concluded that the mean velocities decreased and the half widths increased more rapidly. Related with axial development of the shear stress parameter, he concluded that the ratio of the maximum shear stress to the maximum defected velocity increased more rapidly. About the theoretical observations he also found that more reliable predictions could be achieved by using a phenomenological concept borrowed from the theory of relative diffusion, according to which the width of the jet corresponds to a wavelength in the inertial sub range of the external turbulence, stating for this, that the detailed mechanism of the external turbulence effects on the shear layer of the jets, was not adequately understood.

Lima and Palma (2002) using LDA/LIF, studied experimentally the mixing of coaxial water confined cylindrical jets with velocities ratio annular/internal U_a / U_{in} = 3.2 and 6.5 and Reynolds number of about 3 x 10^4, based on the bulk velocity and inner diameter of the outer tube. The test section was 2 m long with a 42 mm internal diameter. Simultaneous measurements of velocity, turbulence intensity and concentration in coaxial jets were made. The velocity ratio was obtained by maintaining the outer jet at 0.83 ms^{-1}, and varying the inner jet: 0.26 and 0.13 ms^{-1}. In the higher velocity ratio they found a recirculation region, prevailed at a distance of 1 inner diameter from the jet outlet with consequences on the jets near field. They concluded that mixture was enhanced as the velocity ratio increased, showing the dependence between mixture and the intensity of the shear layer between the two flows. In case of backflow they found that the axial turbulence intensity exhibited two peak values, at the location where the axial velocity reached its minimum and where the longitudinal gradient of axial velocity was larger. Their quadrant analysis showed that the negative axial turbulent flux was restricted to a region around the centreline, after the end of the inner core. They stated that the occurrence of this backflow region was in agreement with previous studies in non-confined flows and that apparently, the confinement played no role in the onset of a region with axial negative velocity.

Champagne and Wygnanski (1971) using a hot-wire anemometer in their turbulent coaxial jets research, measured mean velocity, turbulence intensity and turbulent shear stress. Their experimental set-up had a centrifugal blower that supplied the airflow for both nozzles. The contraction ratios were 144:1 for the inner nozzle and 100:1 for the outer nozzle. All measurements were made at subsonic speed with the larger initial velocities being approximately 60 ms^{-1}, with the inner nozzle diameter of 1 inch. Measurements were made with outer/inner velocity ratio U_o / U_i = 0, 0.5, 5.0, and 10, for both areas ratio of A_o / A_i = 1.28 and 2.94, with the corresponding Reynolds numbers ranging based on the nozzle diameters from 0 to about 10^5 for both nozzles. They showed that the length of each core decreases with downstream distance, and that sufficiently far downstream, the velocity profiles become similar. They also proved that the external potential core length seems to be independent of velocities ratios and equal to eight times the annular tube thickness. However, the inner potential core length was strongly dependent on velocities and nozzles

surfaces ratios. They stated that for a fixed A_o / A_i, the U_o / U_i should be greater than one to enhance rapid mixing between the two streams.

Dahm and Dimotakis (1987) using LIF techniques (Laser-induced fluorescence) in conjunction with an isothermal acid-base reaction, visualized and measured the time-dependent character (mean radial concentration, radial rms concentration fluctuations) of the free turbulent water jets entrainment and mixing. Their water facility was 33 x 33 x 63 in. interior dimensions with 1 in. thick 31 x 31 in. glass windows on four sides. The jet fluid issued from the plenum through a ¾ in. long axisymmetric nozzle with a $1/10^{th}$ in. interior diameter and a smooth, axisymmetric faired inlet. All the experiments were made at a Schmidt number, Sc ≈ 600. They made three measurements: time-dependent characteristics of the jet mixing, with the Reynolds number Re = 10000 and the stoichiometric mixture ratio ϕ = 15; instantaneous radial profile of concentration, with the water fixed at pH = 9 and Re = 1500 and 5000, and the unmixed ambient fluid on the jet axis, with Re = 1500 and 5000. Their results showed a quantitative assessment in the presence of an organization of large-scale mixing, similar to turbulent jets. The instantaneous composition of the mixed fluid along the jet was approximately uniform in large regions, but had areas of non-mixing along the jet. The probability of finding fluid outside the jet increases at regular intervals, with a tendency to periodicity. By increasing the Reynolds number, decreases the probability of finding fluid outside the jet.

Ahmed and Sharma (2000) presented an experimental investigation concerning on the effect of velocity ratio on turbulent mixing of confined, coaxial jets with low rate of "bypass". Using LDV they measured mean velocity and streamwise and transverse turbulence intensity for seven velocity ratio, λ = 0.3, 0.6, 1.3, 1.5, 3.0, 6.0 and 10.0. The experiments were obtained in a closed circuit all-steel wind tunnel. The contractions had equal lengths of 1200 mm and their inner diameters of 1100 and 900 mm at the inlet smoothly reduced to 380 and 330 mm, respectively at the exit. The wall thickness had 5 mm. The contraction ratios of the outer and inner streams were respectively about 13.3 and 7.4. The velocity of the outer jet was varied between the range $12.9 < U_o < 84.5$ ms^{-1}, and the inner jet between the range $8.45 < U_i < 37.65$ ms^{-1}. The Reynolds number based on the mass average velocity and in the diameter of the test section varied between the range $4.2 \times 10^5 < Re < 7.0 \times 10^5$. They concluded that the process of turbulent mixing depends strongly on the velocity ratio between the two jets, and found that the drop in total pressure was bigger when the velocity gradient between the jet increases, while for velocity ratios close to 1, the pressure drop was minimal. They also concluded that for the jets with smaller (outer to inner) diameter ratio, the mixing process also depended strongly on the interaction between the boundary layer, mixing layer and main flow. For the high velocity ratios cases, the velocity of the inner stream reduced considerably in the core region due to the entrainment effect, before the mixing layer reaches the centre of the duct. For λ = 10, the reduction was found to be of the order of 40%. It was found that the rate of mixing gets enhanced when the outer stream had higher velocity.

Ribeiro and Whitelaw (1976) in their experimental work, with hot-wire anemometry obtained measurements in a free coaxial jet flow of a mean velocity ratio of unity (mean and rms velocity fluctuations), and cross-wire for higher order correlation measurements. They focused their attention to the region of flow in the wake of the wall of the inner pipe to assess its influence on the mixing and on assumptions which are frequently made in turbulence modelling. Their facility was with an inner pipe 2.83 m long with 16.13 mm inner diameter and 21.59 outer diameters, and the outer jet was 2.00 m long with 44.50 mm inner diameter and 50.44 mm outer diameter. The apparatus was designed to provide fully developed turbulent flow at the exit from both the annulus and pipe. The Reynolds numbers on the wire ranged between 150 and 200, and the $Re_i = 3.49 \times 10^4$ and $Re_o = 5.02 \times 10^4$. They concluded that for equal maximum initial velocities the coaxial jet develops faster than a single jet due to dissipation of turbulent kinetic energy that caused considerable diffusion, and the conditions for self-preserving were almost satisfied for the mean velocity radial profiles at seventeen outer diameters but the radial profiles of the Reynolds shear stress up to 30 diameters did not conform to the self-preserving pattern at this location.

Buresti *et al* (1994) using a LDA system and hot-wire measured mean and rms velocities of a coaxial jet configuration. The inner/outer diameters of their experience were $D_i / D_o = 0.485$ with a 76.2 mm inner diameter and a 5 mm wall thickness duct given an outer/inner area $A_o / A_i = 2.97$. Their tests were performed with a velocity ratio of inner/outer jet $U_i / U_o = 0.67$, at a Reynolds number based on the inner diameter and velocity $Re_{Di} = 1.04 \times 10^5$. They normalized the Strouhal number using the wall thickness and the average velocity, obtaining $St_t = 0.24$. Their hot-wire spectral analysis permitted them to recognize the presence of a particular set of structures in the near-exit region of the inner mixing layer, which they stated as probably connected with the alternate shedding of vortices downstream caused by the thickness of the wall duct. At $St_t = 0.24$ frequency, their available data suggested them that two sheets of alternating vortices were shed from the two sides of the inner duct wall within an axial distance between 1 and 2 jet diameters (nearly 20 times the wall thickness). Those vorticity sheets were engulfed and annihilated within the larger mixing layer between the two jets. As this phenomenon was found to have a significant influence on the mixing between the two jets, the authors decided to analyze its dependence on the velocity ratio of the jets by keeping the velocity of the outer jet at 30 ms^{-1} and reducing progressively the inner jet velocity, covering the $0.3 < U_i / U_o < 0.67$ range. They concluded also that for the $U_i / U_o \geq 0.44$ the same phenomenon affected the near-field mixing between the two flows.

Favre-Marinet *et al* (1999) made an experimental investigation in the near-field of the coaxial jet with large density ratios. Using LDV and hot/cold wire and laser sheet, they made visualization and measured centreline mean and rms axial velocities and made comparison of the obtained results. Their investigation was focused on the structure of the flow in the near-field region and on the identification of the different flow regimes by using various experimental methods with particular attention to density effects on the onset of

recirculation. Their experimental set-up consists of a pair of concentric axisymmetric nozzles discharging into quiescent ambient air. The inner jet (D_i = 20 mm) was supplied by air or SF_6, and had the Reynolds number, based on the total momentum flux varied between 7300 < Re_M < 7800. The outer jet (D_o = 27 mm) was supplied by air or helium (D_o / D_i = 1.35), and had the Reynolds number, based on the total momentum flux varied between 2100 < Re_M < 2400. The external Reynolds number for U_o = 16 ms^{-1} was Re_{ext} = 3200 for the helium/air jets and Re_{ext} = 11000 for the air/air or air/SF_6 jets. They slightly diverged (3º) the final part of the central nozzle to reduce the wall thickness (0.2 mm). The density ratio 0.028 < S < 1, the specific momentum flux ratio varied between 1 < M < 200, and the bulk velocity ratio was varied from 3 to 70, obtained by changing the inner velocity and by keeping the outer velocity at 16 ms^{-1} for the case of helium and at 6 ms^{-1} for the case of the air. The three experimental techniques used were in agreement and showed that the dynamical of coaxial jets were essentially governed by the outer to inner jet flux momentum ratio M. Their results confirm that for helium/SF_6 jets, the critical momentum ratio M_c was higher than 100 and the boundaries of the recirculation bubble were shifted in the downstream direction. (100 < M_c < 140) for helium/SF_6 jets (density ratio: 0.028). For the case of coaxial jets with density ratio much smaller than one (helium/air, S = 0.14; air/SF_6, S = 0.21), they observed a regime of a recirculation above the critical momentum ratio (M_c ≈ 50).

Favre-Marinet and Schettini (2001) made an experimental investigation of the density field of coaxial jets with large density differences. Their experimental set-up consists of a pair of concentric axisymmetric nozzles discharging into quiescent ambient air. The inner jet (D_i = 20 mm) was supplied by air or SF_6. The outer jet (D_o = 27 mm) was supplied by air or helium (D_i / D_o = 1.35). They slightly diverged (3º) the final part of the central nozzle to reduce the wall thickness (0.2 mm). The density ratio 0.028 < S < 1, the specific momentum flux ratio varied between 1 < M < 200, and the bulk velocity ratio was varied from 3 to 70, obtained by changing the inner velocity and by keeping the outer velocity at 16 ms^{-1}. The Reynolds number, based on the total momentum flux varied between 2100 < Re_M < 2400, and proportional to the external Reynolds number for U_e = 16 ms^{-1} was Re_{ext} = 3200. Mean and rms density along the jet axis was determined by a thermo-anemometric (hot-wire) method based on an aspirating probe. They concluded that the density field was strongly affected by the dynamics of the flow; however, their measurements showed that density effects on mixing were rather well taken into account by considering the outer to inner jet flux momentum ratio, instead of the velocity ratio and the density ratio separately. For the measurements obtained in coaxial helium-air jets the near-field was not affected by viscous effects. A regime of recirculation occurs for M higher than a critical value (M_c ≈ 50).

Ahmed and Sharma (2006) using LDV and Pitot tubes, performed detailed total pressure, streamwise and transverse velocity and turbulence measurements regarding the effect of directing part of the annular stream towards the core region at an angle of 20º, with the help of a chute mixer. Their experimental facility was the same reported in their previous investigation (Ahmed and Sharma, 2000). Their annular to core area ratio was 0.26 and the

chutes constitute 16% of the annular area and direct 12% of the mass of annular stream towards the core region. Their annular and core streams velocity were respectively velocity of 66 ms^{-1} and 36 ms^{-1} corresponding to λ = 1.8, and a Reynolds number of about 7.4 x 10^5 based on the mixing duct diameter. The boundary layer thicknesses on either side of the nozzle rim were about 2 mm and both turbulent. They found that the transverse turbulence component was much stronger immediately downstream of the chute exit, causing rapid mixing in the transverse direction and observed the formation of two distinct shear regions as the streams interact at the end of the chute mixer. The total turbulence generation were more than twice with chutes compared to the case without chutes and the streams were found to mix completely over a length of 2.2 times the radius of the mixing duct. However they concluded that the total pressure loss was of 1.71% which they stated as the penalty to be paid for the improved mixing and reduction in mixer length.

Giannadakis *et al* (2008) made an experimental study, using a facility that consists of 3% diverging conical swirler with a D_i = 28 mm exit diameter and a coaxial annular duct from which parallel flow was introduced into the chamber. The wall thickness of the inner nozzle had 1.5 mm. The test chamber consists of a 400 mm long tube of D_o = 100 mm inner diameter. With the use of 2D-DPIV and hot-wire, they presented measurements of velocity, turbulent velocity, turbulent vorticity, vorticity and Reynolds stress. They studied six experimental conditions using three tangential and two annular mass flow rates, for swirling jet spatially mean longitudinal velocity values of 1.30, 1.58 and 1.80 ms^{-1}, and for annular flow spatially mean longitudinal velocity values of 3.00 and 4.00 ms^{-1}. In this work, the authors generated a recirculation by a swirling under the influence of a coaxial stream, and discuss the mean and turbulent characteristics of this phenomena flowfield, laying emphasis on the structure of the recirculation bubble and its effect on the interaction and mixing of the two streams. Their results of the mean and turbulent flow field demonstrate an important role of the recirculation bubble on flow dynamics and the mixing process between the swirling jet and the annular flow. High recirculating velocities were observed at the central area of the bubble, the amplitude of which increased with the Rossby number ((annular flow mean longitudinal velocity minus swirling mean longitudinal velocity) divided by the swirling mean tangential velocity). They found that the bubble interior was characterized by low turbulent kinetic energy, and that vorticity diffusion from the shear layer to the vortex ring results to the creation of a second region of high mean azimuthal vorticity Ω_0 and high values of azimuthal vorticity fluctuations $\sqrt{w_0^{'2}}$ at the vortex ring core plane. Characteristics of mean and turbulent flow depicted one zone that was dominated by the recirculation bubble and the vortex ring dynamics while one second zone was located downstream the aft of the bubble acquired wake flow characteristics.

Buresti *et al* (1998) made an experimental investigation on the turbulent near-field of coaxial jets. Using a two-component LDA, they simultaneously measured the axial and radial velocity. Measurements with hot-wire anemometry were also carried out, and the relevant

time histories of the two velocity components were used for spectral analyses. With a coaxial jet configuration having an inner to outer diameter ratio D_i / D_o = 0.5 they studied two values of velocity ratio: U_i / U_o = 0.30 and 0.67, by maintaining the outer jet velocity at 30 ms^{-1}. The tests were performed both with the 5 mm thick inner duct wall, and with a sharp inner duct with a 2.5º angle at the outlet. In all cases, they used Fourier and wavelet spectra of hot-wire signals to obtain the dominating frequencies of the fluctuations in various regions of the near-field. The Reynolds number based on the inner diameter and velocity was Re = 1.04 x 10^5. They concluded that the sharpening of the inner duct outlet produced a reduction in the radial fluctuations and Reynolds stresses in the near-field of the inner shear layer, particularly for the case U_i / U_o = 0.67, at which a regular vortex shedding occurs when the duct was 5 mm thick. They concluded also that the prevailing frequencies estimated from the spectra of the time histories of both velocity components seem to confirm the dominance of the stronger vortices of the outer shear layer, and for the higher velocity ratio suggest a possible coupling of the velocity fluctuations in the inner core to those present at its downstream boundary.

Leithem *et al* (1969) performed an experimental investigation in the mixing region between ducted coaxial streams. Their apparatus consisted in a vertical column 8 in. square cross section divided in three sections: the entrance region with 34 in. long, enough to provide a parallel flowfield without too much boundary layer buildup; a 36 in. long test section where the mixing of the two streams took place and a third section 12 in. long filled with card board honeycomb to prevent any swirling of the fluid due to exit effects. The inner stream had 0.75 in. in diameter and the wall thickness had 0.0135 inch. They divided their experiments in four different velocity ratios (5.8, 10. 14.7 and 30.0) for the case of the homogeneous jets, and four different velocity ratios (4.9, 9.5, 13.8 and 29.2) for the heterogeneous case, in both cases with absolute velocities from 1.5 to 40 fts^{-1}. Their used outer stream gas was air, and the inner jet gas was air and Freon 12. Their outer jet was always faster. Using a constant temperature hot-film anemometer, they measured average velocity, radial and axial turbulence intensity both near and far downstream for the homogeneous cases, and average velocity, density and axial turbulence intensity as well as mass holdup data both near and far downstream for the heterogeneous cases. For the homogeneous case, the radial turbulence intensity profiles were similar in shape to the axial turbulence intensity curves, while the ratio of axial to radial turbulence intensity was about 1.5, the same as found for unconfined coaxial flow. The shapes of axial turbulence intensity profiles were similar for both cases, but showed a larger magnitude for the homogeneous case. The flow system was found to be one of combined wake-coaxial flow with possible backflow.

Rozenman and Weinstein (1970) performed an experimental study initial region in a turbulent coaxial jet flow, limited to low speed coaxial jets which can be considered incompressible. Using a hot-wire anemometer and static pressure probes, they made their measurements of average velocity and turbulence intensity in the initial region, and centre

line and radial distribution of static pressure. Their apparatus was the same used by Leithem *et al* (1969). Their outer stream velocity was kept constant at a value 48 fts^{-1} while the inner velocity was varied from 0 to 48 fts^{-1}, (presenting results for 27 different velocity ratios) ranging velocity ratios between 1 to ∞. They examined two cases: a homogeneous case, where the inner and outer streams were both air, and a heterogeneous case, with Freon-12 in the inner jet and air in the outer stream. The density ratio of Freon-12 to air is four. They observed that a back flow region was formed at outer to inner stream velocity ratio of 13 for the homogeneous jet and at outer to inner stream velocity ratio of 26 for the heterogeneous jet, observing also that the that region was at first very unstable with an intermittent flow component. For higher velocity ratio they also observed an established circulating toroidal vortex which enhances the mixing between the inner and outer streams.

Kulik *et al* (1970) made an experimental investigation concerning the mixing of turbulent air ducted coaxial streams. Using a constant-temperature hot-wire anemometer, they measured mean velocities and axial rms velocity fluctuations while a cross probe arrangement was used to measured the $u'v'$ correlation as well as the radial rms velocity fluctuations. The inner tube jet had a 2.8 in. inner diameter, while the outer tube jet had a 6.0 in. inner diameter. The inner tube extended 6 in. down into the outer tube so that there was a 2.5 ft turbulent mixing text section. The inner air stream was pressure fed in the top end of the tube through a fritted glass disk to achieve a uniform flow. To reduce the turbulence and temperature effects of the blower, the outer air stream was sucked through the test section. The velocity ratio tested was 5.8, with the outer stream moving faster than the inner stream. At the initial region they observed three zones. In the potential core region the inner stream loses its pipe flow properties and merges with the outer stream. The $u'v'$ correlation was positive with u' and v' not varying much and the velocity profiles had changed from that of the pipe flow to that of the central portion of the mixing region. In the second zone the $u'v'$ correlation was negative with u' and v' showing maximum values and the mean velocity profiles showed inflection points and large gradients. The correlation, u' and v' all raises rapidly approaching the wall (peak) and then fall to a zero value at the wall.

Sadr and Klewicki (2003) studied the near-field region of a coaxial jet flow for D_i / D_o = 30/75 mm = 0.39 and for λ = 1.11, 0.8, 0.48, and 0.18 using molecular tagging velocimetry (MTV) nonintrusively, they measured velocity. The wall thickness of the central jet nozzle measured 1.5 mm. The experiments were performed in a closed recirculating water flow facility with a 0.5 x 0.5 x 0.6 m acrylic test section. The central jet velocity was held fixed at a maximum centreline velocity of U_i = 1.39 ms^{-1} in all of the experiments, giving a core flow Reynolds number $Re_i = 4.1 \times 10^4$. They concluded that in the region very close to the jet exit the profiles of axial intensity and velocity gradient intensity support earlier results, indicating the existence of two trains of vortices shed from the two sides of inner jet wall. They also concluded that the magnitude of these intensities on each side of the inner jet wall depends on the absolute velocity of the corresponding jet. The wake component of the inner mixing region was identifiable in all λ, and its magnitude and extent depended on λ. Their calculated

shear stress combined with the gradient of the mean velocity indicates that the turbulent characteristics of the flow in a coaxial jet are a function of λ for both the inner and outer shear layers. This is in agreement with the results of the axial intensity measurements suggesting that the rate of increase of turbulence intensity in each shear layer depends on the velocity ratio for that shear layer.

Talamelli and Gavarini (2006) presented a numerical and experimental work concerning the linear instability characteristics of incompressible coaxial jets. They developed their numerical code assuming that the fluid was inviscid, incompressible and axisymmetric with only the axial velocity component different from zero where the equations governing the stability problem were the continuity equation and the Euler equation expressed in cylindrical coordinates. They made visualization with an Nd-Yag laser sheet, seeding only the external annular jet and using hot-wire measured the axial and radial velocity and spectral density. In their analysis, they kept constant the radius of the outer/inner jets R_e^*/R_i^* = 2 (inner radius = 38.1 mm) and the radial positions r_1^*/R_i^* = 0.7, r_2^*/R_i^*= 1.5 and r_3^*/R_i^*= 1.7. For simplicity the momentum of the thicknesses of the three shear layers were kept equal to $\theta_1^* = \theta_2^* = \theta_3^* = \theta^*$. Their velocity ratios were well below the critical value, λ_c. The tests were performed in air at a Reynolds numbers, Re = 10^5 with two different wall thicknesses, with the external velocity was kept at 30 ms^{-1} and the velocity ratio varied in the range from 1.2 to 3.3. The visualization showed the presence of an alternate vortex shedding behind the duct wall separating the two jets. The shear-layers thicknesses changed the extension of the region where the flow remained absolutely unstable, affecting also the absolute growth rate of the instability. They observed three different unstable modes: one corresponding to the external shear layer and two associated with the presence of the inner duct wall wake. Mode I, a “jet mode”, which was the most unstable one and was characterized by a unison displacement of the critical layers; mode II, a “wake mode”, which was the least unstable and was associated with an opposite displacement of the critical layers, and mode III, the “classical” unstable mode, due to the inflection point in the external shear layer.

Ko and Chan (1978) divided the initial region of an annular high-pressured air jet and obtained axial mean velocity and turbulent intensity measurement using a hot-wire anemometer. The first configuration was the basic annular nozzle without any protrusion or bullet at the nozzle exit, the second and the third included a conical and an ellipsoidal bullet-like protrusion. The annular jet outer diameter was D_o = 6.2 cm and the inner diameter was D_i = 2.8 cm, and the length of the conical and ellipsoidal bullet was 1.5 D_o, and the domain of their work was mostly confined to the first seven outer diameters downstream of the nozzle exit. They made experiments with exit velocity of 50 ms^{-1} and 30 ms^{-1}. They used a single wire for mean velocity and turbulence intensity measurements. Measurements were made in the outer mixing region within the initial region of the annular, conical and ellipsoidal jets type permitted the isolation of three separated zones: the initial merging, the intermediate and the fully merged zone. For all cases, they observed that the initial merging zone was

within the first two outside diameters downstream of the nozzle exit, the zone where the annular potential core exited. The intermediate zone, where the mixing of the high velocity flow inherited from the potential core occurred, was observed within the next three outside diameters downstream. A fully merged zone was observed after five outside diameters, and they observed that the flow became fully merged and behaved like a combined jet.

Using a forward scattered LDA, Mergheni *et al* (2008) studied the flow field of a coaxial jet configuration. They used diameter ratio $D_i / D_o = 0.33$. (round central jet $D_i = 6$ mm and annular jet with $D_o = 18$ mm) and studied four values of the velocity ratios $U_i / U_o = 5.17$, 1.13, 0.77, and 0.54, with Reynolds numbers respectively 11893, 4545, 2839 and 2968. They measured axial mean velocity, axial turbulence intensities, and shear stress for the initial and fully zones. Their coaxial jet was directed vertically downward and the vertical jet flow discharged in still ambient air. In contrast to the majority of the previous investigations, that involved inner jet Reynolds numbers greater and comparable values for the annular Reynolds numbers, they used lower values of Reynolds numbers for both jets thus, expanding the available data range to cover the lack of data in double concentric jets of low Reynolds numbers. They found that the inner potential core length of the coaxial jet strongly depends on the velocity ratio while the outer potential core for jets having velocity ratios greater than unity seems to be insensitive to the velocity ratio. They concluded too, that coaxial jets with the velocity ratio less than unity develop faster than that with $U_i / U_o > 1$ and enhanced rapid mixing between the two streams.

Cenedese *et al* (1994) made an experimental work in free jets. Their visualization was performed from Re ≈ 2000 to 25000 corresponding to velocities from 0.8 to 10 ms^{-1} for the circular shape and 3.5 to 40 ms^{-1} for the annular one. A turbulent jet was generated from a subsonic open-loop wind tunnel. The air was accelerated toward the outlet section of circular shape (diameter ≈ 3.6 cm). The annular jet configuration was obtained by inserting a cone in the middle of the outlet section (diameter ≈ 2.8 cm), connected to the walls by thin wires (diameters ≈ 0.3 mm). The LDA and PIV velocity and vorticity measurements were compared at Re ≈ 5000 for the annular jet and Re ≈ 15000 for the circular one. For the case of the circular jet, with Re ≈15000, recirculating region was observed at the jet interface. The authors decided to perform another tests at a different Reynolds number (Re ≈ 25000) in this jet. They observed recirculating regions with higher velocity values. For the case of the annular jet with Re ≈ 5000, recirculations and perturbation of the velocity field were observed very close to the outlet. They stated that their results were in good agreement in describing the flow configuration. However they observed a disagreement in the region which the flow reversal occurs. They felt a problem of how seeding particles can be used to measure velocity field in domains with high vorticity values and stated that the use of particles with different density and diameter can point out the main characteristics of this approximation.

Curtet and Ricou (1964) investigated the mixing of two-dimensional and axisymmetric ducted jets. Using a hot-wire anemometer and Pitot probes they measured mean and

fluctuating velocities and shear stress. The two fluids were both of the same nature and incompressible. In its experiments, they varied the initial velocity ratio while they kept a constant radius ratio (between the nozzle/duct radii, h / a = 13.5), using their work for a fundamental verification of the theoretical studies of confined jets made by Craya and Curtet (1955; 1958 and 1960). Their primary jet circuit comprised a medium-pressure blower discharging into a damping chamber, with a valve and a heater (620 mm H_2O, 50 ls^{-1}). Their secondary (ambient) fluid circuit comprised an intake chamber that draws ambient air through its top and an elliptical-meridian secondary flow contraction. In their four experiences, the initial jet velocity was 38.3, 69.6, 103.2 102.3 ms^{-1}. The ambient temperatures and pressures remained between 20 and 28° C and between 735 and 750 mm Hg, throughout the tests. According to their experimental study the mean velocities appear to tend towards an equilibrium profile, but not the velocity fluctuations, indicating a certain lack of self-preservation tendencies in the flow throughout the considered measurements region, from the nozzle to the cross section at which the jet meets the boundary layer at the duct wall.

Wygnanski and Fiedler (1969) made some measurements in the self-preservating jet. They investigated the axisymmetric turbulent incompressible and isothermal jet by the use of linearized constant-temperature hot-wire anemometers. They presented measurements of the mean velocity, turbulence stress, intermittency, skewness and flatness factors, correlations, scales, low-frequency spectra and convection velocity. The jet emerged from a nozzle with 1.04 in. in diameter at a Reynolds number of 10^5. The velocity of the jet was maintained constant to accuracy better than 1%, and the temperature was maintained constant to within 1° F. The air was cleaned using an electrostatic precipitator, which removed particles and hydrocarbons in the air down to 0.04 microns of diameter. It was established that the jet was truly self-preserving some 70 diameters downstream of the nozzle and most of the measurements were made in excess of this distance. The velocity of the jet at the nozzle in most cases was 51 ms^{-1}, although some measurements were also made at 72 ms^{-1}. They found that the rms values of the various velocity fluctuations differ from those measured previously as a result of lack of self-preservation and insufficient frequency range in the instrumentation of the previous investigations, and that their energy balance, calculated from the various measured quantities presented the results quite different from measures made by other authors (Sami, 1967), which were obtained 20 diameters downstream from the nozzle.

Yamashita *et al* (1996) presented an experimental study made on the transition and mixing processes of a coaxial jet into a coflowing water stream, visualized by a LIF technique. The facility consisted in a horizontal water tunnel with a 100 x 100 mm square cross-section with 1000 mm length, with a transparent wall made in acrylic resin to allow for laser access and to collect induced fluorescence. In the axis of the tunnel they placed a water injector with fluorescent dye with 6 and 7 mm inside and outside diameter, respectively. They conducted two different velocities of coflowing water: U = 0.02 and 0.04 ms^{-1} with Reynolds

number varying from 120 to 4800 and the Schmidt number at a value nearly 2000. They study the time dependent behaviour of the jet, in a way to understand the transition mechanism from laminar to turbulent flow, and the mixing characteristics in the downstream transitional and turbulent regions. The distribution becomes bimodal for Re = 2400, for which turbulence was ejected into the jet intermittently. They found that the transition was caused by the helical mode Kelvin-Helmholtz instability and that the mixing process in the transitional region, downstream of the transition point, was mostly governed by the large scale fluctuation induced by the transition. They already found that in the mixing process in the further downstream turbulent region, the roll of small scale turbulence becomes more important.

Ribeiro and Whitelaw (1980), made an experimental work using hot-wire anemometry. They measured mean velocity, axial and radial turbulence intensities and Reynolds shear stress for coaxial jets with and without swirl. The length of the pipes assured fully-developed pipe and annular flows at the exit plane. The inner pipe had 2.83 m long and an inner and outer diameter of respectively 1.61 and 2.16 cm, and the outer pipe had 2.00 m long and 4.49 cm in inside diameter. For coaxial jet without swirl (S = 0), they performed three velocity ratios of U_i / U_o = 0.65, 1.00 and 1.48, with the Reynolds number based on the average velocities at outlets of pipe Re_i = 25600, 31300 and 41000 respectively, and the annulus Re_o = 58900, 46800 and 41500 respectively. For the case of the coaxial jet with swirl (S = 0.26), the value of the velocity ratio was U_i / U_o = 0.71, Re_o = 53900 and Re_i = 27700. In the case of the jet without swirl, they observed that the annular flow does not have influence in the mean velocity at the centreline inside the first three diameters, but affected slightly the Reynolds stresses. Between three and six diameters, they observed a centreline decay of mean velocity asymptotes to a value inversely proportional to the inlet distance. After six diameters, the profiles of the axial and radial turbulence followed a trend towards self-similarity, and at fifteen diameters, the behaviour of the mean flow and of the Reynolds stresses were no longer dependent on the initial conditions. In the presence of the swirl, they observed that the coaxial jet developed at faster rate. They observed also that non-swirling flow configuration approach a self-similar state in a much smaller distance than that of the round jet, due to the mixing layer and vortex shedding that occurred in the region downstream of the separation wall between the two streams.

Wicker and Eaton (1994) made an experimental investigation in the near field of a coaxial jet with and without excitation. They used a laser sheet (24 cm, four annular jet diameters) to illuminate the flow for instantaneous photographs and a single hot-wire probe for turbulent intensities measurements. Their outer nozzle exit diameter was 6 cm. The core nozzle had a knife-edge exit boundary of 1.3 mm exit wall thickness that yielded an annular width of 2 cm. The exit annular to core diameter ratio was 3 and the annular to core ratio was 8. They conducted the experiments for four velocity ratios of U_o / U_i = 0.55, 0.71, 1.23 and 1.45, by holding the inner jet fixed at 10 ms^{-1}, with a core flow Reynolds number Re_i = 13 x 10^5. For the case of the axially forced jet, the outer layer was excited at a frequency

corresponding to a Strouhal number $St_{Do} \approx 0.5$. For the natural jet development, they observed that for $U_o / U_i = 0.55$ the velocity jump across each shear layer had the same sign and approximately the same magnitude, while for $U_o / U_i = 0.71$ still had the same sign but different magnitudes. For $U_o / U_i = 1.23$ and 1.45 the velocity had opposite signs and different magnitudes. The annular flow appears to dominate the inner flow by approximately four inner diameters. For the excited flow, they observed that for all cases the annular flow produced large-scale outer layer structures similar to a single jet, which provide a strong coupling between the outer and inner layers.

Ko and Au (1987) made an experimental work in coaxial jets of different mean velocity ratios. Using a hot-wire anemometer (constant-temperature type), they measured the axial turbulence intensity, and the static pressure fluctuations were obtained by a condenser microphone fitted with a standard nose cone. The central nozzle which generated the inner jet, had a $D_i = 20$ mm diameter, while the outer jet that was produced by an annular nozzle, had an outer diameter Do = 40 mm and an inner diameter $D_i^{'} = 22$ mm, which gave an outer to inner area ratio of 2.73. The area contractions for the inner and outer nozzles were respectively 13 and 8, and the lip thickness was 1 mm. The jet exit boundary layers of the two nozzles were laminar. The experiments were made with the mean exit velocity $\overline{U}_o = 50 ms^{-1}$, while the inner jet was varied between the range $0.15 < \lambda^{-1} (=\overline{U}_i / \overline{U}_o) < 0.8$. The Reynolds number based on the outer diameter was $Re = 1.4 \times 10^5$. They presented also a flow visualization (dye flow) of coaxial jets in a closed-circuit water tunnel for the case of $\lambda^{-1} = 0.45$ at Reynolds number from $Re = 1 \times 10^4$ to 4×10^4, with the outer nozzle diameter of 63 mm, and with the others diameters of coaxial nozzles approximately scaled to those of air coaxial jets. They founded that the flow within the inner missing region was λ^{-1} dependent, and that the shedding mode of the initial vortices observed had important bearings on the development of the coherent structures downstream. For $\lambda^{-1} \leq 0.5$, they found coflowing-wake-vortices and that the coalescence of these phenomena brings out the evolution of another train of w-vortices. The situation of disappearance of the coflowing-wake-vortices observed at higher λ^{-1}, makes the authors stated that deserved second thoughts based on a consideration of the relationship observed between the large scale structures and the far field jet noise.

An experimental investigation was made by Gladnick *et al* (1990). Using a two-component Phase-Doppler particle Analyzer (PDPA) they measured mean and rms axial and radial velocity and shear stress, and using laser Rayleigh scattering they obtained the spectral properties of concentration. The flow consisted in a tube with an inside diameter $d = 18.3$ mm and 102 cm length and 0.7 mm thick, surrounded by a primary annulus with 56 mm, already with 0.7 mm thick and a secondary annulus with 80 mm in diameter. CFC-12 was supplied to the central jet, while air was supplied to the co annular jets, all the jets passed through pressure regulators in order to maintain a constant flow rate. The outer tube wall was tapered at 7 deg to a knife-edge at the exit. The CFC-12 was through a temperature bath, providing that the temperature fluctuation were between the range $28 \mp 2°$ C. In the

central jet exit, the Reynolds number was held constant at about 16000 (2.43 ms^{-1}). They studied also free jets of CFC-12, air, helium, in order to compare the mean axial velocity decay with other author's studies and to observe the effects of density differences (helium Re = 4000). The velocity ratio (λ) had been defined as the ratio of bulk velocity in the coannular stream to that in the central jet, and they studied three different values (λ = 0.64, 1.00 and 2.00). They concluded that the exit velocity profile of a jet with a turbulent, pipe-flow-type decay more rapidly than a jet with a top-hat exit profile. For $\lambda \leq 1$, they observed that the vortical structures were apparently not periodic. The mixing and entrainment were also found to increase with increasing velocity differences. For λ = 1, their results were consistent with the presence of pairs of counter-rotating vortices, typical of a wake flow. For $\lambda \geq 1$, the results were consistent with the presence of an annular vortex ring with negative vorticity. They concluded also that their results also support the hypothesis that the near-field mixing of a jet in a coflowing stream was dominated by the large-scale structures, which evolved from an instability in the shear layer occurring at the interface between the central and the coflow jets.

Cohen and Wygnanski (1987) made an experimental investigation concerning the evolution of instabilities in the axisymmetric jet. The experiments were performed using an air-jet facility with a chamber approximately with 80 cm long and 30 cm of circular cross-section. The flow exits through a nozzle ending with a diameter of 5 cm. The jet velocity was varied between the range 3 < U_j < 8,5 ms^{-1}, and the Reynolds number based on the exit diameter of the nozzle changed from 10^4 to 2.9 x 10^4. A speaker was used to generate controlled axisymmetric disturbances at the exit plane of the nozzle. Hot-wire anemometers were used in conjunction with Disa Model 55P11 sensors for mean velocity flow measurements. A linear model was used as a transfer function to predict the spectral distribution of the velocity perturbations in a jet. They found that the axisymmetric jet column surrounded by a thin shear layer admitted the evolution of an infinite number of helical instabilities in addition to the axisymmetric instability, which was found independent of the azimuthal coordinate. They found also that an increase in the relative thickness of the shear layer limits the number of unstable modes and only the helical mode remained unstable at the end of the potential core.

Kwan and Ko (1977) made an experimental work concerning the initial region of subsonic jets. Using a single normal wire, a microphone and cross-wires probes they measured the axial component of the flow, axial and radial velocity fluctuations and pressure measurements. The primary nozzle had a 2.04 cm diameter and the tests were run with a primary jet efflux velocity $\bar{U}_t$ = 60 ms^{-1}. They investigated three different velocity ratios: 0.3, 0.5 and 0.7. The secondary nozzle had an outer diameter of 4 cm. The area ratio between secondary/primary nozzles was 2.67. Their investigation was within the first eight diameter of the primary jet downstream from the nozzle exit. The authors presented a simple model for coaxial jets proposed by them (Kwan and Ko, 1976) and made single-point correlations, two-point correlations and comparisons with their previous model, related with pressure

fluctuations p', axial velocity fluctuations u' and radial velocity fluctuations v'. The single-point correlations measurements on the core side of the vortices gave the followed phase relationship: - p' leads u' by a small angle, p' leads v' by approximately 90º and v' leads u' by an angle slightly less than 90º; and on the entrainment side of the vortices was observed that p' and u' were approximately in phase, p' leads v' by approximately 90º and v' lags u' by an angle slightly greater than 90º. In the mixing region they found that u' and v' were in phase. In the two-point correlation signals showed that p' and v' do not undergo any phase change during a traverse from the core side of a mixing region to the entrainment side. The signal of u' undergoes inversion. They concluded also that these obtained relationship basically were in agreement with the experimental results for single jets, which indicates that the coherent structures in coaxial and single jets were physically similar.

Park and Chen (1989) presented an experimental and theoretical investigation of confined turbulent jets. Using LDA they measured mean axial and fluctuations velocities and differential wall pressures. The data were compared with predictions of the standard *"k-ε"* turbulence model. The experimental set-up consisted of a coaxial injector with an inside diameter of 12.7 mm and an outer diameter of 25.4 mm. The wall thickness was 3.1 mm. The contraction of the inner jet was 36:1, while the outer jet was 30:1. They studied two flow conditions: the flow I, with a Reynolds number Re = 9400 at the inner jet exit (based on air viscosity, mean velocity = 11.4 ms^{-1} and inner diameter) and Re = 6900 at the annular jet exit. The corresponding Reynolds number for flow II were Re = 18800 (inner) and 6900, (outer) respectively. The flow I had an equal velocity at the coaxial jets exit, while the flow II presented a higher velocity at the central jet. They identified three flow regimes: the potential core, main flow and recirculation flow. It was identified a sharp decrease in the mean velocities near the injector exit, probably due to pressure gradient associated with the sudden expansion geometry. It was also identified a steep decrease in wall pressures immediately downstream of the injector followed a near constant value for x / d up to 5. The potential core extends to x / d around 4 and the re-attachment point appeared at x / d around 13.5. Flow II presented a shorter potential core and higher fluctuation velocities. The minimum pressure was observed in the recirculation zone. Their predictions yielded realistic estimates of wall pressure and velocities, overestimated the rate of the flow development and underestimated turbulent intensities and the length of the recirculation zone.

Khodadadi and Vlachos (1989) made an experimental and numerical study of confined coaxial turbulent jets. They used a two-equation *"k-ε"* turbulence model for testing selected experimental previous data and a LDA for the axial mean and rms velocities measurements. Their facility consisted in a regulated airflow allowed to develop in a 1 in. pipe diameter for 48 diameters before reaching the primary nozzle with a contraction area ratio of 4:1, and the nozzle wall thickness were 0.1 in. They used two different tubes for the secondary stream: 4.25 and 6.5 in. and made three different velocity ratio measurements for each case. For the case of the secondary stream with 4.25 in. diameter, the inner jet velocity tested were 5.0, 28.3 and 62.2 ms^{-1} with the respectively pair velocity of the outer stream of 1.0, 2.3 and 5.1

ms^{-1}, with the Reynolds number based on the mean velocity varying between 6.7 x 10^3 and 4.2 x 10^4. For the case of the secondary stream with 6.5 in. diameter, they varied only the velocity of the secondary stream: 0.4, 1.2 and 2.6 ms^{-1}, with the Reynolds number between the values of 4.5 x 10^3 and 3.2 x 10^4. Three of these six cases were selected for computations. They concluded that the evolution of the axial velocities, the separation size and the near-wall behaviour of the rms velocity were in excellent agreement with the computations. The velocity spectra in the initial mixing zone demonstrated the existence of coherent structures. The velocity spectra in the initial mixing zone had demonstrated the existence of coherent structures. The Strouhal number range of 0.33 to 0.51 was in excellent agreement with the previous works reports.

Warda *et al* (1999) performed an experimental investigation of the near-field region of the free turbulent round central and annular jets. Using LDA, they measured radial, mean and fluctuating longitudinal velocities. Their coaxial air jet flowfield was generated by two double concentric profiled nozzles. The profile of the inner wall of the inner nozzle had a nozzle inlet diameter D_i = 40 mm and a nozzle exit diameter D_o = 8 mm, the profile of the outer wall of the inner nozzle had D_i = 50 mm and D_o = 12 mm and the profile of the inner wall of the outer jet had D_i = 70 mm and D_o = 18 mm. They studied the central jet for two velocities: 14 and 25 ms^{-1}, with a Reynolds number based on the jet exit velocity and inner diameter of the inner nozzle Re_i = 0.72 x 10^4 and 1.3 x 10^4. The annular jet velocity was 12 ms^{-1}, with the corresponding Re_o = 1.36 x 10^4. For the central jet, they concluded that the core length depended on the turbulent intensity of the flow at the exit plane as well as the exit profiles of the mean velocity. They observer that the maximum turbulence intensity occurred near the points of the inflection of the mean velocity profiles and that by increasing the jet exit velocity results in a reduction of the jet growth rate. For the outer jet, they founded that the reattachment point was located at a further downstream distance than the corresponding point reported previously by others authors. After the reattachment point they observed that the jet expanded in the same manner as in the single jet.

Kiwata *et al* (2006) performed an experimental investigation of a coaxial jet with and without tabbed annular nozzle. Using a two-color LIF, a hot-film anemometry and a 2D and stereoscopic PIV, they made the visualization and measured the axial mean and fluctuating velocities. Their experimental set-up consisted of a coaxial axisymmetric water jet discharging into an open tank (435 x 435 x 100 mm) where water was at rest. The annular jet had an outer diameter D_o = 40 mm and an inner diameter of 24 mm, while the inner jet had an inner diameter D_i = 16 mm. They placed six semi elliptic tabs (5 x 4 x 10 mm) at the nozzle exit on the outer side wall of the outer nozzle, which gave a blocked area of about 9%. The pipe was sufficiently long to yield fully developed velocity profiles at the exit plane of the inner jet. The experiments were run with a mean exit bulk velocity of the annular jet of $U_o \cong$ 8 cms^{-1}, with the Reynolds number of the annular jet, based on the outer diameter Re = 3000. The mean velocity ratio was fixed at U_i / U_o = 0.6. They studied the interaction between axisymmetric and streamwise vortices in the unexcited and excited coaxial jets, in both cases

with and without tabs. In the case of the excited jets with tabs, the jet was wider than the excited jet without tabs, due to streamwise vortices that significantly developed from the nozzle exit. In this case, it was found also that enhanced axisymmetric and streamwise vortex structures increased the jet spreading. In the case of an unexcited jet with tabs, streamwise vortices evolve from near the jet exit, but the two fluid streams do not mixed well and the turbulent intensity in the inner mixing region was no higher than that of the coaxial jet without tabs. Axisymmetric vortices in shear layer do not form clearly because streamwise vortices caused by the tabs prevented the evolution of axisymmetric vortices.

Dziomba and Fiedler (1985) studied the effect of initial conditions on two-dimensional free shear layers. They used single-hot-wire probes for all measurements. Momentum thicknesses and spreading rates were calculated with FORTRAN programs, graphically checked. They measured the streamwise fluctuations, u' and $\frac{\sqrt{u'^2}}{u_2-u_1}$ velocities and presented autocorrelations and frequency spectra of the shear layer. The investigations were carried out in both a suction and a blower wind tunnel, where the ratio of the two velocities U_i and U_o at the either side of the splitter plate was such that $0 < U_i / U_o < 1$. The maximum Reynolds number was Re = 8.5 x 10^5. In all measurements, the higher velocity jet was fixed at U_o = 13 ms^{-1}, while the other jet was varied for velocities u_1 = 3.9, 5.2 and 7.9, which gives a velocity ratio of U_i / U_o = 0.3, 0.4 and 0.6, respectively. They studied the shear layer with disturbances, the effect of the trip wire and the effect of the trailing-edge thickness. The angle of the splitter plate in the blower tunnel was ≈ 3° and in the suction tunnel was approximately 4°. They found that while disturbing frequencies can influence the shear layer at almost any downstream position, only the developing region was influenced by the splitter-plate boundary layers or the trailing-edge thickness. They stated that only ideal laminar or turbulent splitter-plate boundary layers lead to a development of the shear layer was expected from theory. Each external disturbance in the initial range changed the shear layers characteristics in the developing region as compared to the ideal case. They also concluded that the realization of an experimental shear layer appeared much more difficult than what might been expected.

Antonia and Bilger (1979) made an experimental study concerning the heated round jet in a coflowing stream. The mean and fluctuating temperatures were obtained with a 3 μm diameter platinum-coated tungsten wire (cold wire) and mean and fluctuating velocities were obtained with a 5 μm diameter wire of similar material (hot-wire). The air jet was supplied at a high pressure and heated electrically before entering a 50 mm diameter supply pipe which contracts to the diameter of the brass nozzle (d = 15.9 mm). At the exit from the nozzle the jet temperature was maintained at approximately 170° C above the ambient temperature. The jet velocity controlled was kept at U_j = 45.7 ms^{-1}. The external air jet was supplied at a temperature of approximately 20° C. They used three values of external air velocity, U_l, giving ratio velocities U_j / U_l = 16.8, 5.6 and 3.0. They found that beyond about 20 diameters from the jet outlet, normalized mean and fluctuating temperature and velocity profiles

showed almost no influence of either axial distance or of velocity ratio and closely resembled those found for the jet into still air and axisymmetric heated wake. For higher values of U_j / U_l, the rms axial velocity fluctuations were very close to those found for a jet into still air and for low values of U_j / U_l, and large axial distance, they tend to toward the much higher values found in wakes.

Yu *et al* (2004) performed an experimental investigation concerning the near-field of a confined square jet. Their experiments were made in a gravity-driven water facility. The flow was guided by two concentric 500 mm length contractions into the test section. At the inlet the contractions had circular shapes with inners diameters of 260 and 130 mm respectively, that smoothly transform into square shapes at the exit, with the inner side width of the two nozzles of D_i = 16 and D_o = 32 mm, and with the lip thickness of 1 mm. The area ratio was A_o / A_i = 2.73. The temperature of the water was kept at 21ºC during the experiments. Using a LDA, they measured mean and rms velocities and Reynolds normal and shear stress. In their experiments, they kept the internal jet velocity at U_i = 0.70 ms^{-1} and varied the outer jet velocity in three different values, U_o = 0.70, 0.35 and 1.40 ms^{-1}, which gave the velocity ratio U_o / U_i = 1.0, 0.5 and 2.0. The respective Reynolds number based on the equivalent jet velocity, was Re_M = 2.43 x 10^4, 1.53 x 10^4 and 4.20 x 10^4. Their results showed that the inner potential core length was greatly affected by the velocity ratio, increasing slightly as U_o / U_i was increased. The U_o / U_i = 0.5 case had achieved the largest spreading rates among the three cases. Under the similar condition flow, the extent of the potential core was very similar but at least one diameter shorter than for the circular coaxial jet case.

Abrosimov *et al* (2007) presented an experimental investigation concerning to the control of coaxial jet mixing through the action of microjets on the mixing layer. The velocity of the central jet was U = 100 ms^{-1}, while the velocity of the external jet W = 20ms^{-1}. Control jets were blown out into the central jet, into the external jet, and into both jets concurrently. The number of control jets was n = 60, 72, 90 and 135. The diameter of the control jet nozzles was d = 0.6, 0.75 and 0.9 mm. The angle of the control jet blowing-out was a = 90, 120 and 135º. The range of variation in the velocity of the control jet blowing-out was V = 120-250 ms^{-1}. Using an oriented Pitot tube and a hot-wire anemometer they measured mean velocity and turbulent intensity. They found that for each control jet nozzle diameter exist an optimal number of these nozzles, at which the reduction of the length of the initial section of the central jet will be the largest. The variation of the angle of the control jets from 90 to 135º decreases the velocity along the central jet axis by 3 to 5%. The experimental results had confirmed the hypothesis on the possibility of controlling the jet mixing process by acting on vortex formation near the nozzle edge made by others previous authors.

Sharma and Ahmed (1998) made an experimental investigation on the mixing of coaxial jets with small annular area in a short duct. Using LDV, they measures mean velocity and turbulence intensities. A Furness Controls manometer was used for the wall pressure distributions measures. The experiments were carried out in a closed-circuit all-steel wind

tunnel consisted in two concentric contractions discharging airstream into the test section with 1000 mm length. The outer jet had a diameter of 380 mm, while the inner jet had a 330 mm diameter. The inner nozzle wall thickness was 5 mm. Without changing the net mass flow, they studies the outer/inner velocity ratios λ = 0.3 and 3.0, with a mass-average velocities of U_m = 30.8 and 31.3, respectively. The Reynolds number based on the mass-average velocity was about 5.7 x 10^5. For the lower velocity ratio, λ = 0.3, their results showed a continuous rise in pressure with mild gradient, and that at higher velocity ratio, λ = 3.0, the wall proximity effect become particularly pronounced, resulting in a significant pressure loss across the duct length contrary to the expected pressure rise due to mixing and production of high turbulence that enables intense mixing to occur at fine scale.

Owen (1976) made an experimental investigation concerning two coaxial turbulent recirculating jet air flows. Using a laser velocimeter, he measured the mean velocity, rms turbulent intensity and turbulent shear stress. He observed a free and a confined expansion geometrical configurations. The confined configuration had an inlet flow of the inner stream of 2.5 in. inner diameter and the outer flow had a 3.5 in. inner diameter. In each case the outer and inner peak velocities were 96.0 and 8.0 fts^{-1}, with the Reynolds number based on the jet diameter of 1.5 x 10^5 and 0.08 x 10^5. In both cases the velocity ratio was sufficient to produce a recirculation zone in the initial mixing region above the centre jet. The confined expansion had a tube with 5.0 in. diameter and 48.0 in. long. He found larges differences between the two configurations. The size and the recirculation mass flux were significantly larger in the confined flow than in the free expansion. The mean radial velocities measured in both initial mixing regions were at the same order of magnitude as the mean axial velocities. In the confined case an additional recirculation zone occurred in the corner between the outer jet and the confining duct. The measured turbulent intensities and shear stress distributions in the recirculation regions showed that local turbulence equilibrium models were inadequate.

Ivanic *et al* (2003) made an experimental investigation of the near-field structure of four different configurations coaxial flows: coaxial jets without rotation, outer flow rotation only, inner-jet rotation only and co-rotation jets. The investigations were performed in a cylindrical water tunnel, with an independent rotation of the two flows. Laser tomography was used to document the flowfield and time mean velocity profiles were obtained with the use of PIV. The apparatus consisted in vertical swirling flows, generated by a pump. Each flow arrives into the swirler, composed by two coaxial chambers each containing 36 blades permitting the adjustment of the angular velocity. To rotate the jets, the blade inclination was held constant to 30º. The contraction ratios were designed to reduce the turbulence level and the boundary layer thickness at nozzle exit. The inner jet diameter had a 40 mm diameter, while the outer jet had a 95 mm diameter. For all the four cases, the Reynolds number was Re = 2000 and the inner/outer velocity ratio, U_i / U_o was 2.5. For the case of the coaxial jets without rotation, the initial instabilities rolled up into the axisymmetric vortex rings, played an essential role in the development of the axisymmetric mixing layer. For the

case of the outer flow rotation only, in spite of the amount of the introduced swirl being very small, they observed only small differences in the axial velocity profiles, while the flow dynamics had some important changes and the introduction of any amount of swirl, showed strong influences in the vortex dynamics. For the case of the inner-jets rotation only, the axial velocity profiles were greatly influenced by the introduction of the swirl, characterized by the acceleration of the centreline velocity. For the co-rotation jets case, they observed a similar flow dynamics as in the case of the inner-jets rotation only.

Ahmed and Bangash (2009) performed an investigation of axisymmetric water coaxial synthetic jets. They used a laser-induced fluorescent for visualization and PIV for mean velocities measurements. Spectral contents were measured with an anemometer and a hot film probe. The measurements were made in the near-field of piston driven axisymmetric coaxial synthetic jets emanated from an orifice and surrounded annulus of equal exit areas and cavity volumes. The results were obtained for two different diameters of the orifice (D = 6.35 and 3.2 mm) and four spacing (d = 0, 0.5, 1 and 2D). They obtained the results for two cases of forced frequencies: 80 and 120 Hz. For both cases, the piston velocity was 20 mms^{-1}, and the maximum centreline velocity of the jet for the 80 Hz case, was 410, 270 and 320 mms^{-1}, respectively for the d = 0, 0.5, 1D, respectively. For the case of 120 Hz and the maximum centreline velocity of the jet was 390, 300 and 315 mms^{-1}, respectively for the d = 0, 0.5, 1 D. They found that the recirculation region between orifice and annulus could be adjusted to control effectively the spreading of the jet. They observed that the spacing d, driver frequency and amplitude had strong influence on the jet characteristics for a given cavity volume and that periodic strains in the vortex lines were responsible for non-uniform distribution of vorticity. For up to ten diameters, they observed also that the decay of the centreline velocity and the growth of the jet width, followed trends of conventional jets.

Villermaux and Rehab (2000) made an experimental investigation concerning the mixing in coaxial jets. Using a fluorescent dye and hot-film anemometry with a TSI probe, they made visualization, velocity and rms fluctuation concentration measurements. Their experimental set-up consisted in two coaxial injectors supplied with water by a constant-head reservoir, which discharged into a large tank of water at rest. The inner and outer nozzles had D_i = 2 and D_o = 2.7 cm, with a contraction ratio of 2 and 4, respectively. The mean velocities at the nozzle exit were in the range of $0.1 < U_i < 1$ and $0.3 < U_o < 4$ ms^{-1}, respectively. Their main goal was in the regime for the ratio of the maximal velocities of the outer/inner jet λ larger than unity. For these cases, the Reynolds number defined from the net momentum input was of the order of 5.4×10^3 to 7×10^4, and for the Reynolds number constructed on the gap thickness $e = (D_o - D_i) / 2$ and the annular momentum dominating stream velocity U_o, $Re = U_o e / \upsilon$ ranged from 10^3 to 1.4×10^4. The Schmidt number based on the kinematic viscosity υ to the molecular diffusivity of the dye was about $Sc \approx 2000$. The vorticity thickness δ of the rapid stream at the lip of the injector exit was $\delta/e = 9.5\ Re^{-0.5}$, which gives a Reynolds number $Re_\delta = u_2 \delta / \upsilon$ was about 800 at u_2 = 2 ms^{-1}. They observed that for a given gap width e, the vorticity thickness δ of the annular velocity profile become

smaller as u_2 was increased, and the instabilities of each shear layer developed progressively, independently of each other.

Razinsky and Brighton (1971) performed an experimental investigation concerning confined jet mixing for nonseparating conditions. Their experimental apparatus had a centrifugal blower that supplied room air to the primary nozzle. They used two interchangeable nozzles with inner exit diameters of 1 and 2 inches. The secondary flow was provided by the inherent momentum transfer from the primary stream and a centrifugal blower located at the end of the apparatus. The mixing tube had 30 ft long and 6 in. inner diameter. Measurements were made for the two jet radius (1 and 2 inches), both for five different initial secondary velocities of 15, 25, 50, 75 and 100 fts^{-1}, giving velocity ratios of 9, 5, 2, 1 and 0.5, respectively. Using a micromanometer and a stainless steel impact tube they measured mean velocity. Longitudinal velocity fluctuations and Reynolds stresses were measured with a constant-temperature hot-wire and static pressure was obtained from the wall pressure taps. They observed that the length of the core becomes shorter with the increasing of the velocity ratio and also that the spread and magnitude of the change of the Reynolds stress with axial distance followed essentially the same pattern at the longitudinal velocity fluctuations.

Kulik *et al* (1969) performed an experimental investigation concerning the effect of free stream turbulence on coaxial mixing. Their apparatus was the same used by Leithem *et al* (1969). They studied both homogeneous air-air and heterogeneous air-Freon-12 systems, with a density ratio of 1 and 4, respectively. In most of the tests the outer stream velocity was kept constant at U_o = 51 fts^{-1} and the mass average velocity ratios U_o / U_i was varied from 2 to 20. However, they presented also results for the heterogeneous case of U_o = 31.2 fts^{-1} and U_o / U_i =12.25. Using two independent constant-temperature anemometer channels they measured velocity, axial turbulence intensity and concentrations. For six Reynolds numbers from 6110 to 29400 the volumetric flow rates were determined for Freon-12 concentrations of 0.0, 0.2, 0.4, 0.5, 0.6, 0.8, and 1.0. For the homogeneous case, data was taken with a 64 mesh screen in the outer stream, both near and far downstream. To determine the dominating effect of the screen, a boundary layer trip device was used to effect the boundary layer separation without reducing the free stream turbulence. For the homogeneous case they observed that for low velocity ratios there was less momentum transfer from the outer to the inner stream with the screen and the boundary layer trip device than without such devices. For large velocity ratios there was no observable affect of either the screen or the boundary layer trip device. For the heterogeneous system, with the mass balance they concluded that standing circulation patterns do exit.

Singh *et al* (1989) performed an experimental investigation concerning the contra-swirling coaxial, confined jets. The coaxial jets were supplied with air from a single centrifugal blower and operated with a mass flow of 0.034 and 0.31 kgs^{-1}. The ratio of bulk velocities was 1.6 and pipe and annulus Reynolds numbers of 6.2 x 10^4 and 2.4 x 10^5, respectively. The central pipe was 60 diameters long (fully developed flow) and the annulus

was 2.25 hydraulic diameters long. The inner and outer diameters of the central pipe were 39 and 42 mm respectively and the inner diameter of the annulus was 100 mm. The diameter of the confining pipe was 200 mm (expansion ratio = 2). Their annular swirlers had vane angles fixed at -15º, -30º and -45º to the axial and the hubless swirlers had angles of 15º, 30º and 45º. Using a water tube manometer, they measured total head and static pressures. With the use of 3-hole probe, they measured the axial and circumferential mean velocities. They concluded that the introduction of swirl in the central jet had enhanced the merger whereas higher swirl in the annulus enhanced both mixing and flow development. On qualitative comparisons with previous similar investigations, with the imposition of pressure gradient in form of expanded confinement enhanced the capability of formation of central recirculation core. The wall static pressure distribution showed an indication of the wall recirculation size.

Altgeld *et al* (1983) made an experimental investigation concerning the confined swirl driven recirculating air flow. The configuration employed consisted in a 300 mm long circular tube of 100 mm of diameter. Swirl was generated by a gas-turbine aerodynamic swirler and the flow was representative of that found in the primary zone of many practical combustors. Its upstream end was closed by a flange with a build-in aerodynamic vaned swirler of 42 mm outer diameter, 21 mm hub diameter and an outlet vane angle of 45º. Their experiments studied two configurations: in the first the fuel injector was removed and a central core jet entered the chamber via the resulting circular hole in the centre of the swirler. In the second case the injector was retained but a circular baffle was located at the exit plane, with the outflow occurring at the annulus. For the core jet flow configuration, the swirler to the jet mass flow rate was 4.99 and the average velocity was 3.3 ms^{-1}. For the baffle configuration, the swirler to the jet mass flow rate was slightly higher and the average velocity was 3.9 ms^{-1}. Using a LDA they measured axial, radial and circumferential velocities. All measurements were made with a swirl number $S = 0.78$. The flow patterns set up in the two cases were quite different. In the core jet case regions of recirculation were confined to within the first one combustor diameter whereas with the baffle configuration two large recirculation regions encompassing most of the chamber arose.

Chang and Kim (2001) using PIV techniques performed an experimental investigation in a circular tube with and without swirling flow. For the two cases the Reynolds number was varied at Re = 10000, 15000 and 20000. They measured axial velocity and turbulence intensity. Using a centrifugal pump, water was drawn through a swirl generating chamber. The isothermal test section was a cylindrical tube with 50.8 mm inside diameter and a 3 m length. They concluded that in the most cases it appears that the turbulence intensities decreased with the distance along the test tube, which was compatible with the decay of the swirl. Some preliminary measurements indicated that over the first four diameters, two regions of flow reversal were set-up and at highest Reynolds numbers, the maximum values of the measured axial velocity components had moved toward the test tube wall and produced more flow reversal at the centre at the tube. As the Reynolds was increased, the turbulence intensity of swirling flow at the tube inlet also increased.

Grandmaison *et al* (1996) performed an experimental investigation concerning the scalar mixing in turbulent concentric round jets. Using Marker nephelometry, they measured mean velocity and the mean and fluctuation concentration field were estimated with three jet markings (centre jet marked, annular jet marked and both jets marked). The Reynolds number for the centre jet ranged from 1.01 x 10^4 to 3.25 x 10^4, and the Reynolds for the annular jet in excess of 5 x 10^4. These flow conditions were close to those of Durão and Whitelaw (1973) and Ribeiro and Whitelaw (1973). The centre jet had an inside diameter D_i = 35.4 mm and an outside diameter D_{io} = 35.1 mm. Their experiments were for three velocity ratios between centre / annular jet, U_i / U_o = 0.188, 0.519 and 0.911, with the Reynolds number Re_i = 10100, 22800 and 32500 and Re_o = 77000, 62800 and 51000, respectively. They concluded that for the initial mixing behaviour between the jets was better for the lower velocity ratio although further downstream there was better transverse mixing between the jets with the higher velocity ratio.

Kornev *et al* (2008) performed an experimental and numerical investigation concerning on the scalar macro and microstructures in a confined jet. Using PLIF they measured mixture fractions (concentration). The *"k-ε"* model was used to for estimations. The flowfield investigated was a turbulent axisymmetric jet developing in a coflow confined by a pipe of diameter D = 50 mm with 5000 mm length. The inner tube had a diameter d = 10 mm and a length of 600 mm. Both flows were water. The Reynolds number based on the jet exit velocity U_d was Re = 10^4. The jet can be considered as a fully-developed turbulent jet. They performed two sets of measurements, with recirculation zone (r-mode) and without recirculation zone (j-mode). For the r-mode the jet exit velocity U_d = 1.0 ms^{-1} and the velocity of the outer jet was U_D = 0.06 ms^{-1}. For the j-mode the jet exit velocity U_d = 1.0 ms^{-1} and the velocity of the outer jet was U_D = 0.1 ms^{-1}. The flow rate values were $\dot{V}_D$ / $\dot{V}_d$ = 1.3 and 5.0 respectively. They observed that the macrostructures of the flow in a confined jet configuration depended strongly on the flow mode. In the j-mode the structures were similar to those of the free jet. In the r-mode the coherent vortex structures with dominant streamwise components of vorticity caused oscillations containing a dominating long period mode. The fine scalar structures with scales sufficiently less than the integral scale were strongly influenced by large scale motions. For the r-mode case, the fine structures become smaller behind the recirculation zone and were difficult to recognize visually at the end of the test section. On the contrary, for the j-mode the fine structures were clearly identified up to x / D = 7. In the scalar field, they found the presence of structures (cliffs) with a rapid change of the scalar that causes small-scale intermittency which was strongly dependent on the flow mode. The intermittency was most pronounced in the front of the recirculation zone and become weaker on the centreline and downstream.

Jackson and Lilley (1985) performed an experimental and numerical investigation concerning the turbulence characteristics of swirling flowfields. Their confined test facility consisted in air that flows through an axial flow with adjustable speed. The air then enters a flow straightened and turbulence management section consisted of mesh screens and packed

straws. Next was the contoured nozzle that leads to the test section, designed to produce a minimum adverse pressure gradient in the boundary layer to avoid the unsteadiness phenomenon associated with local separation regions. The test section consisted of either 15 or 30 cm diameter tube depending on which expansion ratio was desirable, D / d = 1 or 2. Using a six orientation (differences of 30°) hot-wire, they measured U, V, W, U'_{rms}, V'_{rms}, W'_{rms}, $\overline{u'v'}$, $\overline{v'w'}$, eddy dissipation rate, kinetic turbulent energy and turbulent dissipation. The predictions were obtained by mean of the "*k-ε*" turbulence model. Their investigation were made using swirl vane angles ∅ = 0 (swirler removed), 38, 45, 60 and 70 degrees. The Reynolds number based on the throat diameter was up to Re = 6 x 10^5. The reduction of expansion ratio D / d = 1 caused a tangential velocity domination for all tested swirling cases. No recirculation zones were found in the nonexpanded flowfield across the entire section. For the expansion cases, they concluded that the existence, size and shape of both corner recirculation zone and the central toroidal recirculation zone were affected by the degree of swirl. Their measurements showed that increasing the swirl strength from zero to medium swirl produced shorter corner regions and the generation of a central bubble extending to approximately 1.5 chamber diameters downstream of the jet exit.

Grandmaison and Becker (1982) performed an experimental investigation concerning the turbulent mixing in free swirling jets. The jet source consisted of a flow-nozzle fitted to the exit of a wind tunnel settling chamber, providing an area, contraction of 150:l. The nozzle throat diameter was 7.14 cm. Swirl vanes with blade angles varied at 30, 45, 60 and 65° were mounted in a short tubular extension attached to the nozzle. The system was operated at nozzle Reynolds numbers over 100000. The jet source air was marked with an oil condensation smoke to facilitate investigation of the nozzle fluid concentration field by marker nephelometry. Their direct measurement of the axial and angular momentum fluxes for these jets indicated swirl numbers of S = 0.22, 0.36. 0.61 and 0.68, respectively. They found that the two lower levels of swirl (S < 0.6) were insufficient to induce a recirculation bubble or eddy in the core of the jet downstream of the nozzle exit. In their field of mean concentration and concentration fluctuation intensity measurements presented dashed curves, which they called "*the recirculation envelop*". They found that inside this envelope the turbulent mixing was dominated by the recirculation of jet mainstream fluid from downstream, while on the outside it was dominated by the entrainment of ambient fluid into the mainstream. The results for the recirculation region of the jets with recirculation (S = 0.61 and 0.68) were found fairly consistent with previous investigations on the velocity field. They evidence that the downstream limit of the recirculation eddy was around $x \approx 10\ r_o$. At $x > 10\ r_o$ these jets fairly rapidly approach a self-preserving form similar to that observed in weakly swirling jets.

Sarpkaya (1971) performed an experimental investigation on stationary and travelling vortex breakdowns. The experimental equipment consisted in a water tank with 130 x 35 x 35 cm inner measures maintained under of 8 cm of water pressure by a simple overflow pipe in a box attached to the top of the tank. The test section was constituted by a diverging

cylindrical tube with 25.4 cm in length and with an initial radius of 1.905 cm. The angle of the divergence of the tube was chosen to be 1.434 degrees (tan a = 0.025). A bell-mouth joined the diverging test tube through a 5.72 cm long and 1.905 cm radius cm radius uniform section. A round tube was smoothly coupled to the downstream end of the test section. The other end of the tube was connected through a 4 cm long smooth reducer embedded in the tank wall, to a 2.54 cm inner diameter pipe outside the tank. He imparted swirl to the fluid by the use of 32 streamlined foils placed symmetrically in a circular array around the inlet piece. Each vane was set at any desirable angle between 0 to 60 degrees. Using fluorescent dye injection and hypodermic tubes he measured the circumferential and axial velocity distributions. The maximum average velocity in the tank, outside the test pipe was approximately 0.25 cms^{-1}, while the average velocity of the flow between the vanes ϕ = 60 degrees was approximately 7 cms^{-1}. For the observation of stationary vortex breakdowns, the ratio of the tangential to axial velocity was varied by the adjustable vanes maintaining the flow rate (Re = 5000). For the observations of the travelling vortex breakdowns he produced several changes: or increased the inlet flow rate, or releasing a small air bubble from one of the side vanes, or oscillating one of the vanes, or oscillating the hypodermic tube used for the eccentric dye injection, or by varying the settings of all vanes. He found three basic types of stationary vortex breakdowns: double helix, spiral, and axisymmetric, and that the type and shape of the intermediate forms depended upon the particular combination of the Reynolds and circulation numbers. For certain values of Reynolds and circulation numbers, he observed a second region fairly well defined in which only the spiraling type of breakdowns occurred. The axisymmetric breakdown evolves either from double helix or from a spiral, or directly from an axisymmetric swelling of the vortex core. The mode of evolution depended on the particular region defined by the Reynolds and circulation numbers. For a sufficiently high Reynolds and circulation numbers the axisymmetric bubbles evolves only from a symmetric swelling of the vortex core, enclosing an ovoid region of circulating fluid. The observation reported that the vortex-breakdown phenomenon was governed by two basic and conceptually different mechanisms: hydrodynamic instability and finite-transition to a sequent state. Instability manifested itself for emphatically at low Reynolds and high circulation numbers. The finite-transition type if behaviour of the axisymmetric breakdown was brought more clearly in an unsteady swirling flow (created by the perturbation of the circulation) than in a swirling steady flow. He observed as well that no simple explanation could be offered regarding the difference in sense of the rotation of the spiral breakdown relative to that of the ambient flow in a tube and a leading-edge vortex.

Brücker and Althaus (1992) performed an experimental investigation concerning vortex breakdown. Using particle tracking velocimetry (PTV), they measured two-dimensional velocity and vorticity. For the visualization of the vortex axis and the known appearance of its breakdown, fluorescent dye was injected into the flow through a thin injection tube placed on the axis of the apparatus. Their experimental facility was a vertical low speed water channel at the. They generated a swirling flow by 12 guidevanes which were starlike

arranged around the centreline and were positioned at the top inlet of a tube with a diameter of 8.4 cm. The Reynolds number, based on the characteristic core radius *r* of the initial vortex and the axial velocity *U* was Re = 150, and a Rossby number Ro = 1.2 based on the characteristic rotation rate of the vortex core representing the ratio of the characteristic axial to swirl velocity (Spall et al. 1990). These definitions of the Re and Ro numbers were usual in the case of vortical flows. The results of the experiments showed a single vortex ring in the lower part of the bubble which was tilted against the centreline and gyrates around it. The authors referred that this behaviour was responsible for the fluid exchange at the open end of the bubble as first noted Sarpkaya (1971). Within the bubble the interior region was characterized by a strong axial reversal flow. The undisturbed vortical flow was bulged over the bubble and a stagnation point was generated. However, the vortex axis seemed to remain at the centreline. Downstream of the bubble, the axial vorticity was intensified and the characteristic vortical size was decreased.

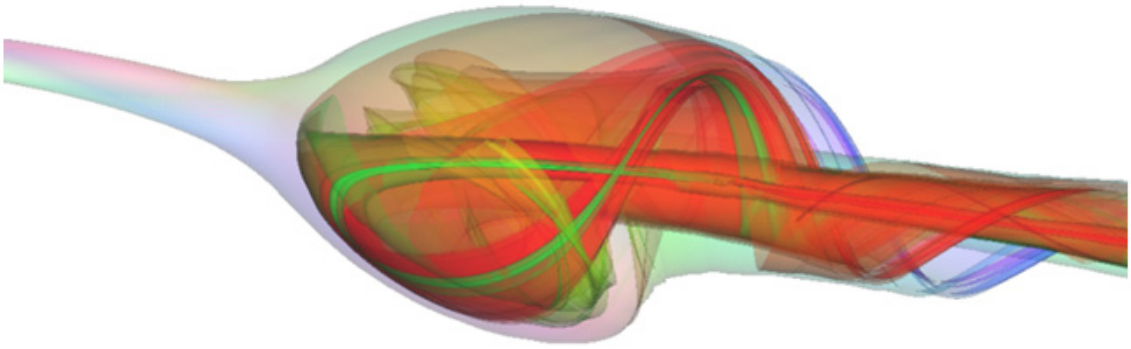

Figure 1.3. Example of a Vortex Breakdown[2] with good perception of the complicated recirculation inside the bubble. (Visualization created by the Scientific Computing and Imaging (SCI) Institute, University of Utah).

Sheen *et al* (1996) presented an experimental investigation concerning recirculation zones of unconfined and confined annular swirling jets. Using a LDA, they measured axial, radial and azimuthal velocities (*U, V, W*) for the annular swirling and nonswirling jet flows. Smoke was used to visualize the detailed flow patterns of the recirculation zone and the vortex breakdown. The annular airflow region had an inner diameter *d* = 21.7 mm and an outer diameter *D* = 45.3. For the confined case, a sudden-expansion tube with an inner diameter D_E = 130 mm was placed at the exit of the annular pipe, with an expansion ratio D_E / *D* = 2.87. For the unconfined case, the experiments were carried out with the sudden-expansion tube removed. The airflow passed through a curved settling chamber into a 16-guide-vane swirl generator. The angle of the guide vane was adjusted from 0 to 56 deg with a

[2] - http://www.siam.org/books/series/csecover.php [accessed on 23.06.2010.]

0.1 deg resolution. The swirl values, were between the range $0 < S < 0.6$, and the Reynolds number between the range $60 < Re < 6000$. Their results indicated that the recirculation zones for unconfined and confined cases could be classified into seven typical flow patterns based on the Reynolds number and swirl number: stable flow, vortex shedding, transition, prepenetration, penetration, vortex breakdown and attachment. In the attachment regime (stagnation point joined with the apex of the recirculation bubble), they observed that the central recirculation zone for the confined case was larger than that for the unconfined case. Their results indicated that the recirculation length was inversely proportional to the ratio of the azimuthal velocity to the axial velocity.

Billant *et al* (1998) made an experimental study of vortex breakdown in swirling jets. The main goal of their study was to characterize the various breakdown states that take place in a swirling water jet. Using LDA, they measured axial and azimuthal velocities and the visualization was made with LIF technique. The experimental set-up consisted in a vertical swirling jet discharging into a large water tank (120 x 40 x 40 cm). The maximum water temperature differences were kept below 0.2° C. A swirl velocity component was imparted to the jet by means of a motor and two concentric cylinders: an outer cylinder fixed, and an inner cylinder set into rotational motion, with 40 cm long and 18.5 cm in diameter. They used two different contraction zones for comparison: D_1 = 40 mm and D_2 = 25 mm. The swirl number was varied between the range $0 < S < 1.42$ maintaining the Reynolds number between the range $300 < Re < 1200$. When S was increased with a maintained Re, strong asymmetric disturbances were observed and gradually develop to form a steady helix configuration. When S reached the critical value $Sc \approx 1.3 - 1.4$, independently of the Re for both nozzles, they observed that a stagnation point appeared in region of the swirling jet concurrently with the development of a localized recirculation zone. They founded that this breakdown process could give birth to for distinct configurations: the bubble, the cone, the asymmetric bubble and the asymmetric cone, which they stated that the cone configurations does not seemed to have been previously identified. Both asymmetric states were observed at large low Reynolds and for $Re \leq 800$ only bubble and cone prevailed.

Champagne and Kromat (2000) made an experimental study on the formation of a recirculation zone in swirling coaxial jets with 5° half-angle diffusers supplied by two independent centrifugal blowers. The outer chamber was 0.91 m diameter cylinder with 0.91 m long. The exit diameter of the outer jet was 101.6 mm. The inner chamber was 0.3 m diameter acrylic tube. The flow exits this chamber through a nozzle with a 144:1 contraction ratio (25.4 mm). The inner nozzle walls near the exit plane had 0.5 mm. The axial velocity component at the exit plane was set in a range of 1 to 15 ms^{-1} for the inner jet and of 3 to 25 ms^{-1} for the outer jet. They measured the mean and rms axial and azimuthal velocity field using X-wires calibrated over a range of yaw angles $-30° \leq a \leq 30°$, at velocity magnitudes from approximately 1.5 to 15 ms^{-1}. They used also a Pitot-static tube for their static pressure measures. The mass flow rate was kept ay $35.4 < m_r < 36.9$. The swirl number was varied over a range of $0.00 < S < 0.75$ while the Reynolds number was 6.7×10^3 for the inner jet and 2.6 x

10^4 for the outer jet. The results showed that for swirl numbers greater than the minimum (0.55), with low mass flow ratios, the inner jet had sufficient axial momentum flux to overcome the negative pressure gradient and the recirculation does not occur. They concluded that the vorticity dynamics model for vortex breakdown proposed by Brown and Lopez (1990) provides a plausible mechanism which leads to the formation of its internal recirculation zone in the studied flow.

Huang and Tsai (2001) made an experimental work on flow structures and turbulence properties of air-air double concentric jets with a large separation between the central jet and swirling annular flows using the smoke-wire flow visualization technique and a two component LDV. Their cylindrical test section was with a D_o = 40 mm diameter and was attached to the exit of the nozzle. A circular diameter disk with 30 mm diameter and 1 mm of thickness was placed concentrically at the exit of the cylindrical test section. The blockage ratio was 0.563. Measures and discussion of velocity distributions, velocity vectors, streamlines and turbulence properties were made. They identified the fundamental flow pattern at Re_c. Their experience was made for four values of swirl, S = 0.1259, 0.1644, 0.2076 and 0.4260 with the values of the exit Reynolds number of the annular flow respectively 144, 346, 234 and 528. They found that a large spatial separation (blockage ratio greater than 0.11) at the exit between the central and swirling annular jets can expedite the formation of a recirculation zone at low swirl and Re number, with various structures inside. In the recirculation zone, they found four flow modes: single bubble, dual rings, vortex breakdown and vortex shedding. It was also observed an off-axis saddle point surrounded with a particularly large turbulence intensities and shear stress. Their streamline patterns of the dual-ring mode show no stagnation point existing on the central axis, which was different from the non-swirling concentric jets. Large central jet velocity induces a large entrainment of the fluid in the recirculation zone and thus reduces the size of the recirculation bubble.

Wang and Bai (2004) performed an experimental and numerical investigation concerning a confined turbulent swirling flow in a model dump combustor. Mean and rms velocities were made using a LDV and LES was used to compare the obtained results. Their investigation consisted in three test cases with the Reynolds number based on the diameter of the guiding pipe and the bulk velocity U_b varied between the range from 10000 to 20000 and the swirl number varied, S = 0, 0.33 and 0.43. Their experimental apparatus consisted in a inlet section with a radius of R_1 = 25.3 mm, a test section with a radius of R_2 = 49.1 mm and an outlet contraction section with radius $R_3 = R_1$. The bulk velocity for the three cases were U_b = 1.59, 1.57 and 2.72 ms^{-1}. The turbulent Reynolds based on the integral length and u_{rms}, was in the range of 150-1500. With a sufficient grid resolution and suitable inflow and outflow boundary conditions, LES successfully predicted the experimental results for the three test cases. They found that vortex breakdown occurred when the swirl number was high enough and lead to an internal recirculation zone (IRZ) generated near the axis. The IRZ was found to move upstream as the swirl number increases and becomes more oscillatory at a dominant low frequency. In the nonswirling flow turbulence was mostly generated in the shear layer

near the sudden expansion. In the swirling flows turbulence was not only produced in the shear layer near the sudden expansion, but also in the IRZ. The decay rate increased as the swirl number was increased.

Alekseenko *et al* (2008) performed an experimental investigation concerning the effect of axisymmetric forcing on the structure of a swirling water free turbulent jet. Using a Stereo PIV, they measured instantaneous velocity fields and spatial distributions of the mean velocity and components of turbulent kinetic energy (TKE). Their experimental set-up consisted in a hydrodynamic loop equipped with a rectangular working section, a pump, a flowmeter and a temperature stabilizing device. The temperature of the water was kept at a 26° C ($\pm$ 0.2°C). The mean flow rate velocity was U_o = 0.52 ms^{-1}, and the nozzle diameter was d = 15 mm. The Reynolds number based on the mean flow rate and the nozzle diameter was Re = 8900. They reported results of forced swirling jets for S = 0, 0.41 and 1. For all cases, including on the jets without swirl, they made experiments with forced frequencies corresponding to a Strouhal number, St = 0.52 and 1.2. The obtained results showed that for both non-swirling and low swirl jets (S = 0 and 0.41) forced at St = 0.52 leads to an increased generation of turbulent kinetic energy with growth in the forcing amplitude, and for St =1.2, this effect was significantly less. For the case of the jet with swirl S = 1 and St = 0.52 the jet structure suffer only a minor effect. For the case of the jet with swirl S = 1 and St = 1.2, an abrupt change in turbulence structure was observed. The total kinetic energy and the azimuthal component were significantly increased. They concluded as well that combined application of external forcing and high swirl could be used as a tool for effective control of turbulent structures in jet flows. For both cases of S = 1, they observed a recirculation zone caused by vortex breakdown detected near the nozzle exit.

Table 1.1. Summary of the experimental investigations related to coaxial jets.

Authors	Experience	Techniques	Results	Comments
Alekseenko *et al* (2008) (water)	Swirling free turbulent jets Re = 8900 $0 < S < 1.0$ St = 0.52 and 1.2	SPIV	• Instantaneous velocity • Axial and azimuthal mean velocity • Azimuthal component of turbulent kinetic energy (TKE).	• For the case S = 1 and St = 1.2 the total kinetic energy and the azimuthal component were significantly increased • Application of external forcing and high swirl could be used as a tool for effective control of turbulent structures in jet flows. • Recirculation zone caused by vortex breakdown detected near the nozzle exit.
Zawacki and Weinstein (1968) air, Freon 12; Freon, C318	Homogeneous and two heterogeneous coaxial jets systems $435 < Re < 1060$	Hot-wire	• Turbulence intensities in the near and far downstream • Turbulent shear stress. • Velocity	• Homogeneous case, for high velocity ratios or inner low stream velocities, a circulation phenomenon appears. • Heterogeneous case of Freon 12-air system (ρ_o/ρ_i = 0.25), for velocity ratio 36.8, the same circulation phenomenon occurs. • Heterogeneous system produces larger values of relative turbulence than the homogeneous system.
Rehab *et al* (1997) (water)	Coaxial jets with different shapes of the inlet nozzle $Re \cong 7000$. $0 \leq U_i \leq 1$ ms^{-1} $0.3 \leq U_o \leq 4$ ms^{-1} λ = 2, 3 and 4	LIF Pressure tube Constant-temperature anemometer	• Turbulent velocity • Static pressure • Mean velocity	• Above λ_c (critical) the inner potential core was truncated by a reverse flow. • Size of the recirculating bubble increases with λ and reaches a maximum length for $\lambda = \infty$ (U_i = 0), typically equal to one inner jet diameter D_i.
Buresti *et al* (1998)	Coaxial jet with thick and sharp inner duct wall $Re = 1.04 \times 10^5$ λ = 0.30 and 0.67	LDA Hot-wire	• Axial and radial velocity • Statistical moments	• Sharp inner duct outlet produced a reduction in the radial fluctuations and Reynolds stresses in the near-field of the inner shear layer, particularly for the case λ = 0.67, at which a regular vortex shedding occurs when the duct was 5 mm thick. • Prevailing frequencies seem to confirm the dominance of the stronger vortices of the outer shear layer

Table 1.1. Summary of the experimental investigations related to coaxial jets. (Cont.)

Authors	Experience	Techniques	Results	Comments
Albayrak *et al* (2008)	Coaxial jets mixing region $\lambda = \infty$, 1.45, 1, 0.48 $Re_{id} \leq 55200$ $Re_{od} \leq 101400$ $U_i \leq 18.4\ ms^{-1}$ $U_o \leq 26.5\ ms^{-1}$	Hot-wire	• Turbulence intensity • Axial velocity	• For both turbulent jets, whit annular jet velocity higher than the central jet, a vortex region was setup causing a reverse flow with respect to the central jet. • Same phenomena occurs for the case of the pure annular flow $\lambda = \infty$ • For equal velocity jets, two jets merged to form an equivalent single jet at the downstream of the jets. • With a higher velocity in the central jet, the core jet begins to draw in the annular jet in order to satisfy its entrainment requirements. • For $\lambda = 0.48$ with both turbulent jets, the annular jet is completely absorbed with the confines of the core jet at the downstream of the exit.
Warda *et al* (1999a)	Near-field region of a free double concentric jets $0.64 < U_i/U_o < 4.5$ $Re_{DO} \leq 1.15x10^4$	LDA	• Fluctuating velocities • Mean velocity	• The inner potential core of the coaxial jets strongly depends on the velocity ratio while the outer core of coaxial jets with $\lambda > 1$ seemed to be insensitive to the velocity ratio. • Coaxial jets with the velocity ratio less than unity develop faster than that with $\lambda > 1$
Warda *et al* (2001)	Coaxial turbulent jets $\lambda = 2$, 3.3 and 4.5 $5100 < Re_D < 10200$ $5700 < Re_{DO} < 11500$	LDA	• Mean turbulent velocity • Mean velocity	• For the same velocity ratio, when the velocity of each stream (inner and outer) was reduced, the growth of the half width of coaxial jets with $\lambda > 1$ was increased. • The velocity ratio affects the evolution and the structure of coaxial jets affecting as well the absolute values of the velocity of each stream, particularly in the region $10 \leq x/D \geq 20$. • Reduction in the absolute values of the velocities of both streams while keeping λ constant made the jet decay faster along the centreline.
Villermaux (1998) outer fluid: air inner fluid: water	Mixing and spray formation in coaxial jets $D_o = 5.5$ cm; $D_i = 4$ cm λ=3 and 15	Visualization Dye injection	• Radial mean velocity • Rms velocity	• With the increasing density ratios, the instability was progressively damped. • The shape of the profile of velocities in the outer ring and the thickness of vorticity influences the growth rate of the instability. • When the ratio of moments (energy) between the phases was above M critical, M > 35, a transition occurs for a recirculation flow. • Above the critical M, the size of the recirculation bubble was gradually increased and reached a size of the order of D_1 when $M \rightarrow \infty$.

Table 1.1. Summary of the experimental investigations related to coaxial jets. (Cont.)

Authors	Experience	Techniques	Results	Comments
Matsumoto *et al* (1973) (air-air)	Double concentric jets $0.24 \leq U_o/U_i \leq 0.82$ $1.1x10^4 \leq Re \leq 3.2x10^4$	X-array probe	• Turbulent intensity • Turbulent shear stress • Axial velocity • Static pressure	• Flow pattern in the duct was divided into three regions: (I) - initial region, (II) - main region and (III) - the region in which jet boundary was interfered by boundary layer on circular duct. • In the main region, the dimensionless radial velocity profiles fit the cosine curve independently of values of dimensionless thickness of the nozzle wall $\bar{\delta}$, λ and the dimensionless axial coordinate, $\bar{x}$. • For larger values of the dimensionless thickness of the nozzle wall $\bar{\delta}$, a large recirculation was recognized behind the nozzle wall and the external stream showed a curved shape. • For small values of λ, the velocity decay on the central axis and the intensity of turbulence were hardly affected by the wall thickness, while for large values of λ, the tendency of velocity decay becomes remarkable and the turbulence intensity is affected heavily by the wake behind the nozzle wall with an increase in the wall thickness.
Escudier and Keller (1985) (water)	Recirculation in swirling flow Re = 7008 Variables: exit contraction D_E guide vane angle ϕ volumetric flow rate Q	Fluorescent dye LDA Visualization	• Mean axial and swirl velocities	• Visualization was made for ϕ = 60 and 70 deg, corresponding to a swirl number S = 2.28 and 11.8, respectively. In the first case it was observed a separated wake and breakdown recirculation zones, and in the second case the data showed combined wake and recirculation zones. • For the case of ϕ = 62 for both studies, the data showed that the flow recovers to supercritical after breakdown, and the exit contraction appears to represent a major change of the downstream of the vortex tube. • For the ϕ = 70, for the four studies, they observed that exit contraction have a strong influence on the entire flowfield. For strong exit contractions, the recirculation zone assumed a mushroom shape, even more pronounced if the upstream centerbody was reduced.
Kulik *et al* (1970)	Mixing of turbulent air ducted coaxial streams λ = 5.8	Hot-wire Cross-wires	• Mean velocity • Axial rms velocity fluctuations • $u'v'$ correlation • Radial rms velocity fluctuations	• At the initial region were observed three zones. • In the potential core region the inner stream loses its pipe flow properties and merges with the outer stream. The $u'v'$ correlation was positive with u' and v' not varying much and the velocity profiles had changed from that of the pipe flow to that of the central portion of the mixing region. • In the second zone the $u'v'$ correlation was negative with u' and v' showing maximum values and the mean velocity profiles showed inflection points and large gradients. • The correlation, u' and v' all raises rapidly approaching the wall (peak) and then fall to a zero value at the wall.

Table 1.1. Summary of the experimental investigations related to coaxial jets. (Cont.)

Authors	Experience	Techniques	Results	Comments
Nikitopoulos *et al* (2003)	Comparisons of circular and square coaxial jets Re = 1.9×10^4 Inner/outer velocity = 0.3 Inner/outer area = 0.213	Pulsed laser sheet Hot-wire Visualization	• Mean velocity • Turbulent intensity • Spectral velocity	• Scaling of the mean velocity and turbulence profiles for the three shear layers formed in the near-field of axisymmetric and square flows was found to be consistent between the two geometries and with previously reported trends for axisymmetric coaxial jets • Large-scale periodic structures were identified for both nozzle configurations in the midfield of the inner mixing region, with wake characteristics. • The spectral characteristics of the circular and square nozzle combinations were qualitatively similar, and the outer mixing region, which was initially highly turbulent, showed no signs of an organized structure. • It was found a slight increase on the mixing on square nozzles compared with the coaxial nozzles, which was attributed to the different initial velocity profiles between the configurations.
Bitting *et al* (2001) (air)	Circular and square coaxial nozzles Re = 19000 and 29000 Inner/outer velocity ratios = 0.15, 0.22 and 0.3	DPIV Laser sheet Thermal anemometry Visualization	• Axial velocity • Instantaneous vorticity	• The non mixed internal region decreases with the decrease of λ and was observed an instable recirculation and reversal flow phenomena at the end of the internal core of the jet for low λ. • The inner and coflowing unmixed regions disappear sooner in the square II case than the axisymmetric one, and the inner and outer shear-layer growth appears to be faster. • A recirculation was observed at λ = 0.15 and 0.22 in both square II and the axisymmetric jets, while was absent at λ = 0.3 for both Re numbers examined.
Zhdanov *et al* (2006) (water closed-circuit channel)	Mixing of confined coaxial flows Re_d = 10000 Angular positions of the nozzle (0°, 90°, and 180°) Range investigation $0.1 \leq x/D \leq 9.1$	LDV LIF	• Average velocity • Velocity fluctuations	• Between $0.1 \leq x/D \leq 9.1$ the uniform averaged velocity field has no time to form, although when the recirculation zone was formed, the uniform averaged velocity distribution was set along the larger part of the mixer cross-section. • The mixing development in the recirculation zone revealed some flow features that have not been discussed previously in the available literature: oscillating backflow fluid, i.e., averaged unsteady flow; fluid oscillating in the antiphase near the opposite walls and flow asymmetry. • Recirculation zone was a superposition of unsteady vortices of different length and time scales.

Table 1.1. Summary of the experimental investigations related to coaxial jets. (Cont.)

Authors	Experience	Techniques	Results	Comments
Lima and Palma (2002) (water)	Mixing in coaxial confined jets of large velocity ratio Annular/internal U_a/U_{in} = 3.2 and 6.5 Re_{bulk} about $3x10^4$	LDA LIF Visualization	• Velocity • Turbulence intensity • Concentration	• For higher velocity ratio a recirculation region was found, prevailed at a distance of 1 inner diameter from the jet outlet with consequences on the jets near field. • Mixture was enhanced as the velocity ratio increased, showing the dependence between mixture and the intensity of the shear layer between the two flows. • In case of backflow the axial turbulence intensity exhibited two peak values, at the location where the axial velocity reached its minimum and where the longitudinal gradient of axial velocity was larger. • The quadrant analysis showed that the negative axial turbulent flux was restricted to a region around the centreline, after the end of the inner core. • The occurrence of the backflow region was in agreement with previous studies in non-confined flows and apparently, the confinement played no role in the onset of a region with axial negative velocity.
Champagne and Wygnanski (1971)	Coaxial turbulent jets A_o/A_i = 1.28 and 2.94 U_o/U_i = 0, 0.5, 5.0 and 10 $0 < Re < 10^5$ based on the nozzle diameters	Hot-wire	• Mean velocity • Turbulence intensity • Turbulent shear stress	• The length of each core decreases with downstream distance, and sufficiently far downstream, the velocity profiles become similar. • The external potential core length seems to be independent of velocities ratios and equal to eight times the annular tube thickness. • The inner potential core length was strongly dependent on velocities and nozzles surfaces ratios. • For a fixed A_o/A_i, the U_o/U_i should be greater than one to enhance rapid mixing between the two streams.
Sadr and Klewicki (2003) (closed recirculated water flow)	Near-field flow development in coaxial jet $Re_i = 4.1x10^4$ λ = 1.11, 0.8, 0.48, and 0.18	MTV	• Velocity	• In the region very close to the jet exit the profiles of axial intensity and velocity gradient intensity support earlier results, indicating the existence of two trains of vortices shed from the two sides of inner jet wall. • The magnitude of these intensities on each side of the inner jet wall depends on the absolute velocity of the corresponding jet. • The wake component of the inner mixing region and its magnitude and extent, depended on λ. • Shear stress combined with the gradient of the mean velocity indicates that the turbulent characteristics of the flow in a coaxial jet were a function of λ for both the inner and outer shear layers.

Table 1.1. Summary of the experimental investigations related to coaxial jets. (Cont.)

Authors	Experience	Techniques	Results	Comments
Ahmed and Sharma (2006)	Turbulent mixing enhancement in coaxial jets with a 20° chute mixer $\lambda = 1.8$ $Re = 7.4x10^5$	LDV Pitot tubes	• Mean Velocity • Rms velocity • Total Pressure	• The transverse turbulence component was much stronger immediately downstream of the chute exit, causing rapid mixing in the transverse direction and a formation of two distinct shear regions as the streams interact at the end of the chute mixer was observed. • The total turbulence generation were more than twice with chutes compared to the case without chutes and the streams were mix completely over a length of 2.2 times the radius of the mixing duct. • Total pressure loss was of 1.71%, considered as a penalty to be paid for the improved mixing and reduction in mixer length.
Giannadakis *et al* (2008)	A swirling jet under the influence of a coaxial flow	2D-DPIV Hot-wire	• Mean velocity • Turbulent velocity • Vorticity • Turbulent vorticity • Reynolds stress	• The mean and turbulent flow field demonstrate an important role of the recirculation bubble on flow dynamics and the mixing process between the swirling jet and the annular flow. • High recirculating velocities were observed at the central area of the bubble, the amplitude of which increased with the Rossby number ((annular flow mean longitudinal velocity minus swirling mean longitudinal velocity) divided by the swirling mean tangential velocity). • The bubble interior was characterized by low turbulent kinetic energy, and the vorticity diffusion from the shear layer to the vortex ring results to the creation of a second region of high mean azimuthal vorticity and high values of azimuthal vorticity fluctuations at the vortex ring core plane. • Characteristics of mean and turbulent flow depicted one zone that was dominated by the recirculation bubble and the vortex ring dynamics while one second zone was located downstream the aft of the bubble acquired wake flow characteristics.
Rozenman and Weinstein (1970) <u>Cases:</u> Homogeneous Heterogeneous	Recirculation patterns in the initial region of coaxial jets λ from 1 to ∞ air-air inner jet: Freon 12 outer jet: Air	Hot-wire Static pressure tubes	• Average velocity • Turbulence intensity	• A back flow region was formed at outer to inner stream velocity ratio of 13 for the homogeneous jet and at outer to inner stream velocity ratio of 26 for the heterogeneous jet, • That region was at first very unstable with an intermittent flow component. • For higher velocity ratio was also observed an established circulating toroidal vortex which enhances the mixing between the inner and outer streams.

Table 1.1. Summary of the experimental investigations related to coaxial jets. (Cont.)

Authors	Experience	Techniques	Results	Comments
Buresti et al (1994)	Velocity field of a coaxial configuration $A_o/A_i = 2.97$ $U_i/U_o = 0.67$ $Re_{Di} = 1.04x10^5$ $St_t = 0.24$	LDA	• Mean Velocity • Rms velocity	• Hot-wire spectral analysis permitted to recognize the presence of a particular set of structures in the near-exit region of the inner mixing layer, which was probably connected with the alternate shedding of vortices downstream caused by the thickness of the wall duct. • At $St_t = 0.24$ frequency, the data showed that two sheets of alternating vortices were shed from the two sides of the inner duct wall within an axial distance between 1 and 2 jet diameters (nearly 20 times the wall thickness). Those vorticity sheets were engulfed and annihilated within the larger mixing layer between the two jets, with a significant influence on the mixing between the two jets. • For $U_i/U_o \geq 0.44$ the same phenomenon affected the near-field mixing between the two flows.
Favre-Marinet *et al* (1999) Inner jet: air or SF_6 Outer jet: air or helium	Coaxial jet with large density ratios (D_i = 20 mm) $7300 < Re_M < 7800$ (D_o = 27 mm) $2100 < Re_M < 2400$	Laser sheet Hot-wire Cold-wire LDV Visualization	• Mean velocity • Rms axial velocity	• The three experimental techniques used were in agreement and showed that the dynamical of coaxial jets were essentially governed by the outer to inner jet flux momentum ratio M. • The results confirm that for helium/SF_6 jets, the critical momentum ratio M_c was higher than 100 and the boundaries of the recirculation bubble were shifted in the downstream direction. ($100 < M_c < 140$) for helium/SF_6 jets (density ratio: 0.028). • For the case of coaxial jets with density ratio much smaller than one (helium/air, S = 0.14; air/SF_6, S = 0.21), a regime of a recirculation above the critical momentum ratio ($M_c \approx 50$) was observed.
Favre-Marinet *et al* (2001) Inner jet: air or SF_6 Outer jet: air or helium	Coaxial jets with large velocity and large density differences (D_i = 20 mm) $7300 < Re_M < 7800$ (D_o = 27 mm) $2100 < Re_M < 2400$	(hot-wire) method based on an aspirating probe.	• Mean density • Rms density	• Density field was strongly affected by the dynamics of the flow; however, • Density effects on mixing were rather well taken into account by considering the outer to inner jet flux momentum ratio, instead of the velocity ratio and the density ratio separately. • For the measurements obtained in coaxial helium-air jets the near-field was not affected by viscous effects. • A regime of recirculation occurs for M higher than a critical value ($M_c \approx 50$).

Table 1.1. Summary of the experimental investigations related to coaxial jets. (Cont.)

Authors	Experience	Techniques	Results	Comments
Leithem *et al* (1969) Cases: Homogeneous Heterogeneous	Turbulent in the mixing region between ducted coaxial streams λ = 5.8, 10, 14.7 and 30.0 λ = 4.9, 9.5, 13.8 and 29.2	Hot-wire	• Average Velocity • Radial and axial turbulence intensities	• For the homogeneous case, the radial turbulence intensity profiles were similar in shape to the axial turbulence intensity curves, while the ratio of axial to radial turbulence intensity was about 1.5, the same as found for unconfined coaxial flow. • The shapes of axial turbulence intensity profiles were similar for both cases, but showed a larger magnitude for the homogeneous case. • The flow system was found to be one of combined wake-coaxial flow with possible backflow.
Mergheni *et al* (2008)	Different mean velocity ratios on the dynamics of a coaxial jet U_i / U_o = 5.17, 1.13, 0.77, and 0.54 Re = 11893, 4545, 2839 and 2968	LDA	• Axial mean velocity • Axial turbulence intensities • Shear stress	• The inner potential core length of the coaxial jet strongly depends on the velocity ratio while the outer potential core for jets having velocity ratios greater than unity seems to be insensitive to the velocity ratio. • Coaxial jets with the velocity ratio less than unity develop faster than that with $U_i / U_o > 1$ and enhanced rapid mixing between the two streams.
Del Taglia *et al* (2004) (Numerical and Experimental investigation)	Annular jet flow with large blockage D_o = 85 mm blockage ratio = 0.89 Re = 4400 U_o = 13.2 ms^{-1}	3D LDA URANS	• Mean axial and radial velocities • Axial velocity fluctuation	• The computed velocity fluctuations were in very good agreement with the experiments. • The experiments and simulations proved the existence of an asymmetric flow field inside of the recirculation zone, with a preferential flow direction. • The fluctuations in the recirculation zone manly consisted of fluctuations of large scale vortices, having the necessity of performing the computations in an unsteady manner. • The steady computations clearly underestimated the total fluctuations.
Owen (1976)	Free and confined turbulent recirculation flows $0.08x10^5 \leq Re \leq 1.5x10^5$ Inner peak velocities 96.0 and 8.0 fts^{-1}	Laser velocimeter	• Mean velocity • Rms turbulence intensity • Turbulent shear stress	• The size and the recirculation mass flux were significantly larger in the confined flow than in the free expansion. • The mean radial velocities measured in both initial mixing regions were at the same order of magnitude as the mean axial velocities. • In the confined case an additional recirculation zone occurred in the corner between the outer jet and the confining duct. • The measured turbulent intensities and shear stress distributions in the recirculation regions showed that local turbulence equilibrium models were inadequate.

Table 1.1. Summary of the experimental investigations related to coaxial jets. (Cont.)

Authors	Experience	Techniques	Results	Comments
Curtet and Ricou (1964)	Mixing of two-dimensional and axisymmetric ducted jets jet velocity = 38.3, 69.6, 103.2 102.3 ms^{-1}	Hot-wire Pitot probes	• Mean velocity • Velocity fluctuations • Shear stress	• According to their experimental study the mean velocities appear to tend towards an equilibrium profile, but not the velocity fluctuations, indicating a certain lack of self-preservation tendencies in the flow throughout the considered measurements region, from the nozzle to the cross section at which the jet meets the boundary layer at the duct wall.
Wygnanski and Fiedler (1969)	Measurements in the self-preservating jet Jet velocity = 51 and 72 ms^{-1}. Re = 10^5	Hot-wire	• Mean velocity • Turbulence stress • Convection velocity • Low-frequency spectra	• Rms values of the various velocity fluctuations differ from those measured previously as a result of lack of self-preservation and insufficient frequency range in the instrumentation of the previous investigations • Energy balance, calculated from the various measured quantities presented the results quite different from measures made by other authors (Sami, 1967), which were obtained 20 diameters downstream from the nozzle.
Ko and Chan (1978) (air)	Similarity in the initial region of annular jets <u>Nozzles:</u> Annular jet Annular jet conical Annular jet ellipsoidal D_o = 6.2 cm; D_i = 2.8 cm exit velocity = 50 and 30 ms^{-1}	Single wire	• Mean velocity • Turbulence intensity	• For all cases, the initial merging zone was within the first two outside diameters downstream of the nozzle exit, the zone where the annular potential core exited. • The intermediate zone, where the mixing of the high velocity flow inherited from the potential core occurred, was observed within the next three outside diameters downstream. • A fully merged zone was observed after five outside diameters, and they observed that the flow became fully merged and behaved like a combined jet.
Villermaux and Rehab (2000)	Mixing in coaxial jets Re=10^3 to $1.4x10^4$ *Sc* ≈ 2000	Fluorescent dye Hot-film anemometry with a TSI probe Visualization	• Velocity and rms fluctuation • Concentration measurements	• For a given gap width e, the vorticity thickness δ of the annular velocity profile become smaller as u_2 was increased, and the instabilities of each shear layer developed progressively, independently of each other.

Table 1.1. Summary of the experimental investigations related to coaxial jets. (Cont.)

Authors	Experience	Techniques	Results	Comments
Ribeiro and Whitelaw (1980)	Coaxial jets with and without swirl Without swirl: U_i/U_o = 0.65, 1.0, 1.48 Re_i = 25600 to 41000 Re_o = 58900 to 41500 With swirl (S = 0.26): U_i/U_o = 0.71 Re_o = 53900 Re_i = 27700	Hot-wire	• Mean velocity • Axial and radial turbulence intensities • Reynolds shear stress	• In the case of the jet without swirl, the annular flow does not have influence in the mean velocity at the centreline inside the first three diameters, but affected slightly the Reynolds stresses. • Between 3 and 6 diameters, was observed a centreline decay of mean velocity asymptotes to a value inversely proportional to the inlet distance. After six diameters, the profiles of the axial and radial turbulence followed a trend towards self-similarity, and at fifteen diameters, the behaviour of the mean flow and of the Reynolds stresses were no longer dependent on the initial conditions. • With swirl presence, it was observed that the coaxial jet developed at faster rate. • The non-swirling flow configuration approach a self-similar state in a much smaller distance than that of the round jet, due to the mixing layer and vortex shedding that occurred in the region downstream of the separation wall between the two streams.
Wicker and Eaton (1994)	Coaxial jet with and without axial excitation U_o/U_i = 0.55, 0.71, 1.23 and 1.45 $Re_i = 13x10^5$ $St_{Do} \approx 0$ - forced jet	Laser sheet Hot-wire Visualization	• Turbulence intensity	• For the natural jet development, was observed that for U_o/U_i = 0.55 the velocity jump across each shear layer had the same sign and approximately the same magnitude, while for U_o/U_i = 0.71 still had the same sign but different magnitudes. • For U_o/U_i = 1.23 and 1.45 the velocity had opposite signs and different magnitudes. The annular flow appears to dominate the inner flow by approximately four inner diameters. • For the excited flow, was observed that for all cases the annular flow produced large-scale outer layer structures similar to a single jet, which provide a strong coupling between the outer and inner layers.
Dahm and Dimotakis (1987) (water)	Entrainment and mixing in turbulent jets Sc ≈ 600 1500 ≤ Re ≤10000	LIF Visualization	• Mean radial concentration • Radial rms concentration fluctuations	• The results showed a quantitative assessment in the presence of an organization of large-scale mixing, similar to turbulent jets. • The instantaneous composition of the mixed fluid along the jet was approximately uniform in large regions, but had areas of non-mixing along the jet. • The probability of finding fluid outside the jet increases at regular intervals, with a tendency to periodicity. • Increasing Reynolds number decreases the probability to find fluid outside the jet.

Table 1.1. Summary of the experimental investigations related to coaxial jets. (Cont.)

Authors	Experience	Techniques	Results	Comments
Ribeiro and Whitelaw (1976)	Near-exit mixing of coaxial jets $Re_i = 3.49x10^4$ $Re_o = 5.02x10^4$	Hot-wire Cross-wire	• Mean velocity • Rms velocity fluctuations	• For equal maximum initial velocities the coaxial jet develops faster than a single jet due to dissipation of turbulent kinetic energy that caused considerable diffusion. • The conditions for self-preserving were almost satisfied for the mean velocity radial profiles at seventeen outer diameters but the radial profiles of the Reynolds shear stress up to 30 diameters did not conform to the self-preserving pattern at this location.
Ko and Kwan (1976)	Initial region of subsonic coaxial jets λ = 0.3, 0.5 and 0.7 Inner jet maintained at 60 ms^{-1}	Hot-wire Microphone	• Mean velocity • Turbulence intensity • Pressure	• The results showed similarity of the mean velocity and turbulence-intensity profiles of the three mixing regions, inside the initial merging and fully-merged zones. • In the intermediate zone, no similarity was founded. The dominance of either type of vortices or both depended of the velocity ratio. • At λ = 0.3, the high-frequency vortices were found more dominant. • At λ = 0.5, the high-frequency were still dominant, but the dominance of low-frequency was increasing. • At λ = 0.7, the low-frequency vortices became the only dominant ones.
Fink (1997) Experimental and theoretical investigation	Influence of external turbulence on mixing of axisymmetric coaxial jets jet exit velocity / velocity of the external flow U_0/U_∞ = 3.10, 4.50 and 5.75 Re_o = 8500, 13000 and 15700	*k*- ε model Pitot tubes Single normal wires	• Mean velocity • Axial turbulence fluctuations	• In the presence of a suitable external turbulence, for the axial development of the velocity scale, mean velocities decreased and the half widths increased more rapidly. • Related with axial development of the shear stress parameter, the ratio of the maximum shear stress to the maximum defected velocity increased more rapidly. • About the theoretical observations was found that more reliable predictions could be achieved by using a phenomenological concept borrowed from the theory of relative diffusion, according to which the width of the jet corresponds to a wavelength in the inertial sub range of the external turbulence, stating for this, that the detailed mechanism of the external turbulence effects on the shear layer of the jets, was not adequately understood.
Sharma and Ahmed (1998)	Confined coaxial jets in a short length duct λ = 0.3 and 3.0 U_m = 30.8 and 31.3 $Re_M = 5.7x10^5$	LDV Furness Controls manometer	• Mean velocity • Turbulence intensities • Wall pressure	• For λ = 0.3, the results showed a continuous rise in pressure with mild gradient. • For λ = 3.0 the wall proximity effect become particularly pronounced, resulting in a significant pressure loss across the duct length contrary to the expected pressure rise due to mixing and production of high turbulence that enables intense mixing to occur at fine scale.

Table 1.1. Summary of the experimental investigations related to coaxial jets. (Cont.)

Authors	Experience	Techniques	Results	Comments
Ko and Au (1987)	Coaxial jets of different mean velocity ratios $\overline{U}_0$ = 50ms^{-1} (fixed) 0.15 < $\overline{U}_i/\overline{U}_0$ < 0.8 $Re_o = 1.4x10^5$	Dye flow Hot-wire Microphone Visualization	• Axial turbulence intensity • Static pressure fluctuations	• The flow within the inner missing region was λ^{-1} dependent, and the shedding mode of the initial vortices observed had important bearings on the development of the coherent structures downstream. • For $\lambda^{-1} \leq 0.5$, the coflowing-wake-vortices and that the coalescence of these phenomena brings out the evolution of another train of w-vortices. • The situation of disappearance of the coflowing-wake-vortices observed at higher λ^{-1}, makes deserved second thoughts based on a consideration of the relationship observed between the large scale structures and the far field jet noise.
Gladnick *et al* (1990).	Near-field characteristics of a turbulent coflowing jet Inner jet: CFC-12 Re = 16000 (2.43 ms^{-1}) Outer jet: Air Ratio of bulk velocity in the coannular stream /central jet (λ=0.64, 1.00 and 2.00)	PDPA Laser Rayleigh	• Mean velocity • Rms axial and radial velocity • Shear stress • Spectral concentration properties	• The exit velocity profile of a jet with a turbulent, pipe-flow-type decay more rapidly than a jet with a top-hat exit profile. • For $\lambda \leq 1$, was observed that the vortical structures were apparently not periodic. • The mixing and entrainment were increased with increasing velocity differences. • For $\lambda = 1$, the results were consistent with the presence of pairs of counter-rotating vortices, typical of a wake flow. • For $\lambda \geq 1$, the results were consistent with the presence of an annular vortex ring with negative vorticity. • The results support the hypothesis that the near-field mixing of a jet in a coflowing stream was dominated by the large-scale structures, which evolved from an instability in the shear layer occurring at the interface between the central and the coflow jets.
Sheen *et al* (1996)	Recirculation zones of unconfined and confined annular swirling jets 0 < S < 0.6 60 < Re < 6000	Smoke LDA Visualization	• Axial, radial and azimuthal velocities *U*, *V*, *W*	• The results indicated that the recirculation zones for unconfined and confined cases could be classified into seven typical flow patterns based on the Reynolds number and swirl number: stable flow, vortex shedding, transition, prepenetration, penetration, vortex breakdown and attachment. • In the attachment regime (stagnation point joined with the apex of the recirculation bubble), was observed that the central recirculation zone for the confined case was larger than that for the unconfined case. • The recirculation length was inversely proportional to the ratio of the azimuthal velocity to the axial velocity.

Table 1.1. Summary of the experimental investigations related to coaxial jets. (Cont.)

Authors	Experience	Techniques	Results	Comments
Villermaux and Rehab (2000)	Mixing in coaxial jets $0.1 < U_i < 1$ ms^{-1} $0.3 < U_o < 4$ ms^{-1} $10^3 <$ Re $< 1\ 1.4 \times 10^4$ Sc ≈ 2000 $D_i = 2$ cm; $D_o = 2.7$ cm	Fluorescent dye Hot-film anemometry	• Mean velocity • Turbulent intensity • Total pressure	• For a given gap width e, the vorticity thickness δ of the annular velocity profile become smaller as u_2 was increased, and the instabilities of each shear layer developed progressively, independently of each other.
Dahm *et al* (1992) water	Vortex structure and dynamics in the near field of a coaxial jet Inner jet: $2.5 < U_i < 20$ cms^{-1} Outer jet: $6.5 < U_o < 20$ cms^{-1} λ =0.59, 0.71, 1.00, 1.14, 2.56 and 4.16 Re < 15000	Two-color Planar LIF recorded with ciné photography	• Absolute velocity	• For the $\lambda = 0.59$, the velocity jump across both layers the same sign and were roughly the magnitude. The shear layer vortices formed a helical vortex structure of the near-field, for about the first two diameters downstream. • For the $\lambda = 0.71$, the velocity jump across both layers still had the same sign, but differed in magnitude by more than a factor of two. • For the $\lambda = 1.00$, the velocity jump was zero across the inner layer. The outer layer developed into shear-layer-like vortex rings and the core length was considerably greater than the previous case. • For the $\lambda = 1.14$, the velocity jump across the two layers showed opposing signs. The rollup of the inner layer started to look more shear-layer-like than wake-like and the interactions whit the shear-layer vortices, became significant. The outer layer still appears to govern the dynamics through vortex rings pairings with less success in consuming the potential core that for $\lambda = 0.71$ case. The overall core length was roughly the same as in the previous case. • For the $\lambda = 2.56$, the resulting shear-layer vortices in the two layers again presented opposing senses of circulation, with the assumption of the authors that they developed independently of each other. The asymmetries showed in this velocity ratio were more effective at consuming the potential core, that presented long tentacular features and was shorter than for the case of $\lambda = 0.71$. • For the $\lambda = 4.16$ case, the velocity jump across the inner and outer layers with opposite signs but with at about roughly the same magnitude. The potential core ends abruptly at about one and a half diameters downstream, suggesting that the two layers do not develop independently.

Table 1.1. Summary of the experimental investigations related to coaxial jets. (Cont.)

Authors	Experience	Techniques	Results	Comments
Billant *et al* (1998) (water)	Vortex breakdown in swirling jets $0 < S < 1.42$ $300 < Re < 1200$ $D_i = 40$ mm $D_o = 25$ mm	LIF LDA Visualization	• Axial velocity • Azimuthal velocity	• When S was increased with a maintained Re, strong asymmetric disturbances were observed and gradually develop to form a steady helix configuration. • When S reached the critical value $Sc \approx 1.3$-1.4, independently of the Re for both nozzles, it was observed that a stagnation point appeared in region of the swirling jet concurrently with the development of a localized recirculation zone. • The breakdown process could give birth to for distinct configurations: the bubble, the cone, the asymmetric bubble and the asymmetric cone • The cone configurations do not seemed to have been previously identified. • Both asymmetric states were observed at large low Reynolds and for $Re \leq 800$ only bubble and cone prevailed.
Cohen and Wygnanski (1987) (air-jet)	Evolution of instabilities in the axisymmetric jet $3 < U_j < 8,5$ ms^{-1} $10^4 < Re < 2.9x10^4$	Hot-wire Linear model	• Mean velocity • Spectral velocity perturbation	• The axisymmetric jet column was surrounded by a thin shear layer and admitted the evolution of an infinite number of helical instabilities in addition to the axisymmetric instability, which was found independent of the azimuthal coordinate. • An increase in the relative thickness of the shear layer limits the number of unstable modes and only the helical mode remained unstable at the end of the potential core.
Kwan and Ko (1977)	Single-phase confined turbulent jets $\overline{U}_i = 60$ ms^{-1} $\lambda = 0.3$, 0.5 and 0.7	Single normal wire Cross-wires Microphone	• Axial velocity • Axial and radial velocity fluctuations • Pressure	• The single-point correlations measurements on the core side of the vortices gave the followed phase relationship: - p' leads u' by a small angle, p' leads v' by approximately 90° and v' leads u' by an angle slightly less than 90°; • On the entrainment side of the vortices was observed that: p' and u' were approximately in phase, p' leads v' by approximately 90° and v' lags u' by an angle slightly greater than 90°. • In the mixing region was found that u' and v' were in phase. • In the two-point correlation signals showed that p' and v' do not undergo any phase change during a traverse from the core side of a mixing region to the entrainment side. The signal of u' undergoes inversion. • The obtained relationship basically was in agreement with the experimental results for single jets, which indicates that the coherent structures in coaxial and single jets were physically similar.

Table 1.1. Summary of the experimental investigations related to coaxial jets. (Cont.)

Authors	Experience	Techniques	Results	Comments
Park and Chen (1989) Experimental and theoretical investigation	Confined Turbulent jets: single data Flow I: Mean velocity=11.4 ms^{-1} Re_i = 9400 Re_o = 6900 Flow II: Re_i = 18800 Re_o = 6900	LDA k-ε turbulence model	• Mean axial and fluctuations velocities • Differential wall pressures	• Three flow regimes were identified: potential core, main flow and recirculation flow. • It was identified a sharp decrease in the mean velocities near the injector exit, probably due to pressure gradient associated with the sudden expansion geometry. • The potential core extends to x/d around 4 and the re-attachment point appeared at x/d around 13.5. • Flow II presented a shorter potential core and higher fluctuation velocities. The minimum pressure was observed in the recirculation zone. • The predictions yielded realistic estimates of wall pressure and velocities, overestimated the rate of the flow development and underestimated turbulent intensities and the length of the recirculation zone.
Khodadadi and Vlachos (1989) Experimental and numerical work	Confined coaxial turbulent jets Secondary streams: d = 4.25 in 5.0, 28.3 and 62.2 ms^{-1} R =$6.7x10^3$ and $4.2x10^4$ d = 6.5 in 0.4, 1.2 and 2.6 ms^{-1} Re=$4.5x10^3$ and $3.2x10^4$	LDA k-ε model	• Axial mean velocity • Rms velocities	• The evolution of the axial velocities, the separation size and the near-wall behaviour of the rms velocity were in excellent agreement with the computations. The velocity spectra in the initial mixing zone demonstrated the existence of coherent structures. • The velocity spectra in the initial mixing zone had demonstrated the existence of coherent structures. • The Strouhal number range of 0.33 to 0.51 was in excellent agreement with the previous works reports.
Warda *et al* (1999)	Near-field region of free turbulent round central and annular jets Inner jet: 14 and 25 ms^{-1} $0.72x10^4 \leq Re_i \leq 1.3x10^4$ D_i = 18 mm Outer jet: 12 ms^{-1} D_o = 70 mm Re_o = $1.36x10^4$	LDA	• Mean velocity • Radial velocity • Fluctuating velocity	• For the central jet was concluded that the core length depended on the turbulent intensity of the flow at the exit plane as well as the exit profiles of the mean velocity. • The maximum turbulence intensity occurred near the points of the inflection of the mean velocity profiles and by increasing the jet exit velocity resulted in a reduction of the jet growth rate. • For the outer jet, the reattachment point was located at a further downstream distance than the corresponding point reported previously by others authors. • After the reattachment point was observed that the jet expanded in the same manner as in the single jet.

Table 1.1. Summary of the experimental investigations related to coaxial jets. (Cont.)

Authors	Experience	Techniques	Results	Comments
Yu *et al* (2004) Gravity-driven water facility	Near-field of a confined coaxial jet λ =1.0, 0.5 and 2.0 $1.53x10^4 \leq Re_M \leq 4.20x10^4$ D_i = 16 mm D_o = 32 mm	LDA	• Mean velocity • Rms velocity • Reynolds normal and shear stress	• Their results showed that the inner potential core length was greatly affected by the velocity ratio, increasing slightly as U_o/U_i was increased. • The U_o/U_i = 0.5 case had achieved the largest spreading rates among the three cases. • Under the similar condition flow, the extent of the potential core was very similar but at least one diameter shorter than for the circular coaxial jet case.
Sarpkaya (1971)	Stationary and travelling vortex breakdowns Re = 5000 ϕ = 0 to 60 degrees	Fluorescent dye injection Hypodermic tubes	• Circumferential and axial velocity distributions	• It was found three basic types of stationary vortex breakdowns: double helix, spiral, and axisymmetric, and that the type and shape of the intermediate forms depended upon the particular combination of the Reynolds and circulation numbers. • For certain values of Reynolds and circulation numbers, was observed a second region fairly well defined in which only the spiralling type of breakdowns occurred. The axisymmetric breakdown evolving either from double helix or from a spiral, or directly from an axisymmetric swelling of the vortex core. • The mode of evolution depended on the particular region defined by the Reynolds and circulation numbers. For a sufficiently high Reynolds and circulation numbers the axisymmetric bubbles evolves only from a symmetric swelling of the vortex core, enclosing an ovoid region of circulating fluid. • The observation reported that the vortex-breakdown phenomenon was governed by two basic and conceptually different mechanisms: hydrodynamic instability and finite-transition to a sequent state. Instability manifested itself for emphatically at low Reynolds and high circulation numbers. The finite-transition type if behaviour of the axisymmetric breakdown was brought more clearly in an unsteady swirling flow (created by the perturbation of the circulation) than in a swirling steady flow. • No simple explanation could be offered regarding the difference in sense of the rotation of the spiral breakdown relative to that of the ambient flow in a tube and a leading-edge vortex.

Table 1.1. Summary of the experimental investigations related to coaxial jets. (Cont.)

Authors	Experience	Techniques	Results	Comments
Yamashita *et al* (1996)	Transition and mixing processes of a coaxial jet into a coflowing water stream U = 0.02 and 0.04 ms^{-1} $120 \leq Re \leq 4800$ $Sc \approx 2000$	LIF Visualization	• Visualization	• The distribution becomes bimodal for Re = 2400, for which turbulence was ejected into the jet intermittently. • The transition was caused by the helical mode Kelvin-Helmholtz instability and the mixing process in the transitional region, downstream of the transition point, was mostly governed by the large scale fluctuation induced by the transition. • The mixing process in the further downstream turbulent region, the roll of small scale turbulence becomes more important.
Ahmed and Sharma (2000)	Velocity ratio on turbulent mixing of confined, co-axial jets λ = 0.3, 0.6, 1.3, 1.5, 3.0, 6.0 and 10.0 $12.9 < U_o < 84.5$ ms^{-1} $8.45 < U_i < 37.65$ ms^{-1} $4.2x10^5 < Re < 7.0x10^5$ d_o = 380 mm d_i = 330 mm	LDV	• Mean velocity • Streamwise and transverse turbulence intensity	• The process of turbulent mixing depends strongly on the velocity ratio between the two jets and the drop in total pressure was bigger when the velocity gradient between the jet increases, while for velocity ratios close to 1, the pressure drop was minimal. • For the jets with smaller (outer to inner) diameter ratio the mixing process also depended strongly on the interaction between the boundary layer, mixing layer and main flow. • For the high velocity ratios cases the velocity of the inner stream reduced considerably in the core region due to the entrainment effect before the mixing layer reaches the centre of the duct. • For λ = 10, the reduction was found to be of the order of 40%. • The rate of mixing gets enhanced when the outer stream had higher velocity.
Abrosimov *et al* (2007)	Control of coaxial jet mixing Central jet U = 100 ms^{-1} External jet W = 20ms^{-1} a = 90, 120 and 135°	Pitot tube Hot-wire	• Mean velocity • Turbulent intensity	• It was found that for each control jet nozzle diameter exists an optimal number of these nozzles, at which the reduction of the length of the initial section of the central jet will be the largest. • The variation of the angle of the control jets from 90 to 135° decreases the velocity along the central jet axis by 3 - 5%. • The experimental results had confirmed the hypothesis on the possibility of controlling the jet mixing process by acting on vortex formation near the nozzle edge made by others previous authors.

Table 1.1. Summary of the experimental investigations related to coaxial jets. (Cont.)

Authors	Experience	Techniques	Results	Comments
Ivanic *et al* (2003) water coaxial four different configurations	Dynamics of swirling jet flows D_i = 40 mm D_o = 95 mm Re = 2000 U_i/U_o = 2.5	Laser tomography PIV Visualization	• Visualization • Mean velocity	• For the case of the coaxial jets without rotation, the initial instabilities rolled up into the axisymmetrical vortex rings, played an essential role in the development of the axisymmetric mixing layer. • For the case of the outer flow rotation only, in spite of the amount of the introduced swirl being very small, they observed only small differences in the axial velocity profiles, while the flow dynamics had some important changes and the introduction of any amount of swirl, showed strong influences in the vortex dynamics. • For the case of the inner-jets rotation only, the axial velocity profiles were greatly influenced by the introduction of the swirl, characterized by the acceleration of the centreline velocity. • For the co-rotation jets case, they observed a similar flow dynamics as in the case of the inner-jets rotation only.
Ahmed and Bangash (2009)	Axisymmetric coaxial synthetic jets D = 6.35 and 3.2 mm	LIF PIV Hot-film probe Visualization	• Visualization • Mean velocity • Spectral contents	• It was found that the recirculation region between orifice and annulus could be adjusted to control effectively the spreading of the jet. • With the spacing d, driver frequency and amplitude had strong influence on the jet characteristics for a given cavity volume and that periodic strains in the vortex lines were responsible for non-uniform distribution of vorticity. • For up to ten diameters, the decay of the centreline velocity and the growth of the jet width, followed trends of conventional jets.
Durao and Whitelaw (1973)	Turbulent mixing in the developing region of coaxial jets U_i/U_o = 0, 0.23 and 0.62 $Re_i = 1.7x10^4$ and $2.8x10^4$ $Re_o = 6.6x10^4$ and $6.4x10^4$	Pitot tube, Normal and 45° hot-wire probes	• Mean velocity • Reynolds normal stress • Reynolds shear stress	• The results showed that coaxial jets tend to reach a self-preserving state much more rapidly than axisymmetric single jets. • The attainment of the fully developed state was a function of the velocity ratio and zero velocity ratios leads to the most rapid development. • The experiments showed that the flow possesses locations of zero mean-velocity gradients which were not coincident with locations of zero shear stress. • They stated that as the coaxial jet flow tented to its self-preservating, it was clear that turbulent kinetic energy was a suitable property with which to characterize the flow, and it was of interest to consider that the kinetic energy was directly related to the local shear stress, as was already proposed by previous authors.

Table 1.1. Summary of the experimental investigations related to coaxial jets. (Cont.)

Authors	Experience	Techniques	Results	Comments
Hassel *et al* (2006) Numerical and experimental	Mixing in a coaxial jet mixer Re_d = 10000 r-mode $\dot{V}_D/\dot{V}_d$ =1.3 j-mode $\dot{V}_D/\dot{V}_d$ =5.0	LES models (DGM and DMM) RANS models (SST, k-ε and RSM-LRR-IP LIF LDV	• Radial mean velocity • Rms velocity	• A good agreement with measurements for averaged characteristics was achieved by RANS SST and LES DMM models for both r-mode and j-mode cases, while the other models LES DGM, k-ε and RSM gave rather poor results. • The LES DMM calculations of the rms values showed also a satisfactory agreement with measurements. • It was reported the confirmation of the qualitative observations of Barchilon and Curtet (1964) and revealed that the flow had a pronounced unsteady character and contained dominating long period oscillations occurring in an opposition-of-phase mode. • The recirculation zone contained unsteady large-eddy structures (many vortices of various sizes), that causes the intermittency of the scalar field.
Razinsky and Brighton (1971)	Confined jet mixing for nonseparating conditions λ=9, 5, 2, 1 and 0.5	Micromanometer Stainless steel impact tube Hot-wire Wall pressure taps	• Mean velocity • Longitudinal velocity fluctuations • Reynolds stresses • Static pressure	• The length of the core becomes shorter with the increasing of the velocity ratio and also that the spread and magnitude of the change of the Reynolds stress with axial distance followed essentially the same pattern at the longitudinal velocity fluctuations.
Kulik *et al* (1969) air-air air-Freon-12	Effect of free stream turbulence on coaxial mixing U_o = 51 fts^{-1} U_o/U_i=2 to 20 U_o = 31.2 fts^{-1} U_o/U_i =12.25 6110≤Re≤29400	Two independent constant-temperature anemometer channels	• Velocity • Axial turbulence intensity • Concentrations	• For the homogeneous case, data was taken with a 64 mesh screen in the outer stream, both near and far downstream. To determine the dominating effect of the screen, a boundary layer trip device was used to effect the boundary layer separation without reducing the free stream turbulence. • For the homogeneous case it was observed that for low velocity ratios there was less momentum transfer from the outer to the inner stream with the screen and the boundary layer trip device than without such devices. For large velocity ratios there was no observable affect of either the screen or the boundary layer trip device. • For the heterogeneous system, with the mass balance it was concluded that standing circulation patterns do exit.

Table 1.1. Summary of the experimental investigations related to coaxial jets. (Cont.)

Authors	Experience	Techniques	Results	Comments
Singh *et al* (1989)	Contra-swirling coaxial, confined jets Pipe Re=6.2 x 10^4 Annulus Re=2.4 x 10^5 Swirlers angles=15, 30 and 45 degrees	water tube manometer 3-hole probe	• Total head and static pressures • Axial and circumferential mean velocities	• The introduction of swirl in the central jet had enhanced the merger whereas higher swirl in the annulus enhanced both mixing and flow development. • On qualitative comparisons with previous similar investigations, with the imposition of pressure gradient in form of expanded confinement enhanced the capability of formation of central recirculation core. • The wall static pressure distribution showed an indication of the wall recirculation size.
Altgeld *et al* (1983)	Confined swirl driven recirculating air flow S = 0.78	LDA	• Axial, radial and circumferential velocities	• The flow patterns set up in the two cases were quite different. In the core jet case regions of recirculation were confined to within the first one combustor diameter whereas with the baffle configuration two large recirculation regions encompassing most of the chamber arose.
Grandmaison *et al* (1996)	Scalar mixing in turbulent concentric round jets Center jet Re=1.01x10^4 to 3.25x10^4 Annular Re in excess of 5x10^4	Marker nephelometry Three jet markings	• Mean velocity • Mean and fluctuation concentration	• It was concluded that for the initial mixing behaviour between the jets was better for the lower velocity ratio although further downstream there was better transverse mixing between the jets with the higher velocity ratio.
Chang and Kim (2001)	Circular tube with and without swirling flow Re=10000, 15000 and 20000	PIV	• Axial velocity • Turbulence intensity	• In the most cases it appears that the turbulence intensities decreased with the distance along the test tube, which was compatible with the decay of the swirl. • Some preliminary measurements indicated that over the first four diameters, two regions of flow reversal were set-up and at highest Reynolds numbers, the maximum values of the measured axial velocity components had moved toward the test tube wall and produced more flow reversal at the centre at the tube. • As the Reynolds was increased, the turbulence intensity of swirling flow at the tube inlet also increased.

Table 1.1. Summary of the experimental investigations related to coaxial jets. (Cont.)

Authors	Experience	Techniques	Results	Comments
Wang and Bai (2004) Numerical and Experimental	Confined turbulent swirling flow in a model dump combustor Re from 10000 to 20000 S = 0, 0.33 and 0.43	LES LDV	• Mean velocity • Rms velocity	• Vortex breakdown occurred when the swirl number was high enough and lead to an internal recirculation zone (IRZ) generated near the axis. • The IRZ was found to move upstream as the swirl number increases and becomes more oscillatory at a dominant low frequency. • In the nonswirling flow turbulence was mostly generated in the shear layer near the sudden expansion. • In the swirling flows turbulence was not only produced in the shear layer near the sudden expansion, but also in the IRZ. • The decay rate increased as the swirl number was increased.
Kornev *et al* (2008) Numerical and Experimental (water)	Scalar macro and microstructures in a confined jet Re = 10^4 $\dot{V}_D/\dot{V}_d$ = 1.3 and 5.0	PLIF k-ε model	• Mixture fractions	• Macrostructures of the flow in a confined jet configuration depended strongly on the flow mode. In the j-mode the structures were similar to those of the free jet. • In the r-mode the coherent vortex structures with dominant streamwise components of vorticity caused oscillations containing a dominating long period mode. • For the r-mode case, the fine structures become smaller behind the recirculation zone and were difficult to recognize visually at the end of the test section. • For the j-mode in the scalar field, it was found the presence of structures (cliffs) with a rapid change of the scalar that causes small-scale intermittency which was strongly dependent on the flow mode. • The intermittency was most pronounced in the front of the recirculation zone and become weaker on the centreline and downstream.
Jackson and Lilley (1985) Numerical and Experimental	Turbulence characteristics of swirling flowfields ϕ = 0, 38, 45, 60 and 70 degrees Re = $6x10^5$	Hot-wire k-ε turbulence model	• U, V, W, U'_{rms}, V'_{rms}, W'_{rms}, $\overline{v'w'}$, $\overline{u'v'}$ • Eddy dissipation rate, • kinetic turbulent energy • turbulent dissipation	• No recirculation zones were found in the nonexpanded flowfield across the entire section. • For the expansion cases, it was concluded that the existence, size and shape of both corner recirculation zone and the central toroidal recirculation zone were affected by the degree of swirl. • Measurements showed that increasing the swirl strength from zero to medium swirl produced shorter corner regions and the generation of a central bubble extending to approximately 1.5 chamber diameters downstream of the jet exit.

Table 1.1. Summary of the experimental investigations related to coaxial jets. (Cont.)

Authors	Experience	Techniques	Results	Comments
Brücker and Althaus (1992)	Vortex breakdown Re = 150 Ro = 1.2	PTV fluorescent dye Visualization	• Two-dimensional velocity • Vorticity	• The results of the experiments showed a single vortex ring in the lower part of the bubble which was tilted against the centerline and gyrates around it. The authors referred that this behaviour was responsible for the fluid exchange at the open end of the bubble as first noted Sarpkaya (1971). • Within the bubble the interior region was characterized by a strong axial reversal flow. The undisturbed vortical flow was bulged over the bubble and a stagnation point was generated. However, the vortex axis seemed to remain at the centreline. • Downstream of the bubble, the axial vorticity was intensified and the characteristic vortical size was decreased.
Grandmaison and Becker (1982)	Turbulent mixing in free swirling jets S=0.22, 0.36. 0.61 and 0.68	Marker nephelometry	• Axial and angular momentum fluxes	• It was found that the two lower levels of swirl ($S < 0.6$) were insufficient to induce a recirculation bubble or eddy in the core of the jet downstream of the nozzle exit. In their field of mean concentration and concentration fluctuation intensity measurements presented dashed curves, which the authors called "the recirculation envelop". • Inside this envelope the turbulent mixing was dominated by the recirculation of jet mainstream fluid from downstream, while on the outside it was dominated by the entrainment of ambient fluid into the mainstream. • The results for the recirculation region of the jets with recirculation (S = 0.61 and 0.68) were found fairly consistent with previous investigations on the velocity field. Authors made evidence that the downstream limit of the recirculation eddy was around $x \approx 10\ r_o$. At $x > 10\ r_o$ these jets fairly rapidly approach a self-preserving form similar to that observed in weakly swirling jets.
Talamelli and Gavarini (2006) Numerical and experimental	Incompressible coaxial jets Re = 10^5 $1.2 \leq U_o/U_i \leq 3.3$ external velocity kept at 30 ms^{-1}	Nd-Yag laser sheet Hot-wire Visualization	• Axial and radial velocity • Spectral density	• Visualizations showed the presence of an alternate vortex shedding behind the duct wall separating the two jets. • The shear-layers thicknesses changed the extension of the region where the flow remained absolutely unstable, affecting also the absolute growth rate of the instability. • Three different unstable modes were observed: Mode I, a "jet mode", which was the most unstable one and was characterized by a unison displacement of the critical layers. Mode II, a "wake mode", which was the least unstable and was associated with an opposite displacement of the critical layers, and mode III, the "classical" unstable mode, due to the inflection point in the external shear layer.

Table 1.1. Summary of the experimental investigations related to coaxial jets. (Cont.)

Authors	Experience	Techniques	Results	Comments
Huang and Tsai (2001) air-air	Swirling double concentric jets S = 0.1259, 0.1644, 0.2076 and 0.4260 blockage ratio = 0.563 Re = 144, 346, 234 and 528	Smoke-wire LDV Visualization	• Mean velocity • turbulence intensities	• At a large spatial separation (blockage ratio greater than 0.11) at the exit between the central and swirling annular jets can expedite the formation of a recirculation zone at low swirl and *Re* number, with various structures inside. • In the recirculation zone was founded four flow modes: single bubble, dual rings, vortex breakdown and vortex shedding. • It was observed an off-axis saddle point surrounded with a particularly large turbulence intensities and shear stress. • The streamline patterns of the dual-ring mode show no stagnation point existing on the central axis, different from the non-swirling concentric jets. • Large central jet velocity induces a large entrainment of the fluid in the recirculation zone and thus reduces the size of the recirculation bubble.
Cenedese *et al* (1994)	Free jets 0.8 to 10 ms^{-1} inner jet 3.5 to 40 ms^{-1} annular jet Re ≈ 2000 to 25000	LDA PIV Visualization	• Axial and transverse velocity • Vorticity	• For the case of the circular jet, with Re ≈ 15000, a recirculating region was observed at the jet interface. For Re ≈ 25000 recirculating regions were observed with higher velocity values. • For the case of the annular jet with Re ≈ 5000, recirculations and perturbation of the velocity field were observed very close to the outlet. • The results were in good agreement in describing the flow configuration. However a disagreement was observed in the region which the flow reversal occurs. • A problem was felt of how seeding particles can be used to measure velocity field in domains with high vorticity values because the use of particles with different density and diameter can point out the main characteristics of this approximation.
Champagne and Kromat (2000)	Recirculation zone in swirling jets 1 to 15 ms^{-1} inner jet 3 to 25 ms^{-1} outer jet $Re_i = 6.7x10^3$ $Re_o = 2.6x10^4$ $0.00 < S < 0.75$	X-wire Pitot tube Visualization	• Vmean velocity • Rms axial and azimuthal velocity • Static pressure	• The results showed that for swirl numbers greater than the minimum (0.55), with low mass flow ratios, the inner jet had sufficient axial momentum flux to overcome the negative pressure gradient and the recirculation does not occur. • The vorticity dynamics model for vortex breakdown proposed by Brown and Lopez (1990) provides a plausible mechanism which leads to the formation of its internal recirculation zone in the studied flow.

1.1.2. Numerical and theoretical investigations

Most of the current research has been dedicated to the study of turbulent flows. Almost any naturally occurring flow is turbulent, and hence it is important to be able to model turbulent flows accurately. The complex behaviour of turbulence is the consequence of a fairly simple set the Navier-Stokes equations. However, analytical solutions to even the simplest turbulent flows do not exist. Numerical studies of coaxial jets are very rare and are often restricted to 2D cases, due to the need for massive computer resources (Silva *et al,* 2003). The difficulty in achieving predictive simulations is perhaps best illustrated by the wide range of approaches that have been developed and are still being used by the turbulence modelling community, such as the RANS[3]-based turbulence models, the Large Eddy Simulation (LES)[4] models, the Detached Eddy Simulation (DES)[5] models, the Direct Numerical Simulation (DNS)[6] models, the Turbulence near-wall modelling and Turbulence free-stream boundary conditions (see Table 2). The RANS-based turbulence models include the linear eddy viscosity models, the non linear eddy viscosity models and the Reynolds Stress models (RSM). The linear eddy viscosity models include the algebraic models, the one equation models and two-equation models. There are four Algebraic[7] models: the Cebeci-Smith[8], the Baldwin-Lomax[9], the Johnson-King[10] and the roughness-dependent[11] models. There are three One Equation models: the Prandtl's[12], the Baldwin-Barth[13] and the Spalart-Allmaras[14] models. The Two Equations models include the *"k-ε"* models, the *k-ω* models, and the Realisability issues

[3] - Reynolds Averaging of Navier-Stokes equations.

[4] - LES resolves large scales of the flow field solution. LES operates on the Navier-Stokes equations to reduce the range of length scales of the solution, reducing the computational cost.

[5] - An example of a hybrid technique attempt that combines the use of the best aspects of RANS and LES methodologies in a single solution strategy.

[6] - Navier-Stokes equations are numerically solved without any turbulence model. Whole range of spatial and temporal scales of the turbulence must be resolved. All the spatial scales of the turbulence must be resolved in the computational mesh, from the smallest dissipative scales associated with the motions containing most of the kinetic energy.

[7] - Algebraic turbulence models or zero-equation turbulence models are models that do not require the solution of any additional equations, and are calculated directly from the flow variables.

[8] - Suitable for high-speed flows with thin attached boundary-layers, typically present in aerospace applications.

[9] - Suitable for high-speed flows with thin attached boundary-layers, typically present in aerospace and turbomachinery applications.

[10] - This model incorporates the solution of an ordinary differential equation.

[11] - Three different versions: Two-equation k-ε eddy viscosity model, one-equation eddy viscosity model and Algebraic eddy viscosity model.

[12] - The original one-equation model. Solve one turbulent transport equation.

[13] - One-Equation Turbulence Transport Model for High Reynolds Number Wall-Bounded Flows.

[14] - One equation model which solves a transport equation for a viscosity-like variable *v*.

models. And all these models have different variants. For instance, k-ε[15] includes four variants: the standard[16] model, the realisable[17] model, the RNG[18] model and the near-wall treatment[19] for k-ε model. The k-ω[20] includes the Wilcox's[21] k-ω, the Wilcox's[22] modified k-ω, the SST[23] k-ω and the near-wall treatment[24] for k-ω models. The Two Equation turbulence model constraints and limiters includes the Kato-Launder[25] modification model, the Durbin's[26] realisability constraint model, the Yap correction[27] model and the Realisability and Schwarz'[28] inequality model versions. The non linear eddy viscosity models includes the $\overline{v^2}$-f [29] and the ζ-f [30] or zeta model. The Reynolds stress models (RSM)[31] involves calculation of the individual Reynolds stresses, $\rho\overline{u_i'u_j'}$ using differential transport equations. LES includes six major variant

[15] - The first transported variable is turbulent kinetic energy, k. The second transported variable is the turbulent dissipation; ε. It doesn't perform well in cases of large adverse pressure gradients (Wilcox, David, C., "Turbulence Modeling for CFD". 2nd Ed. Anaheim: DCW Industries, 1998. pp. 174.)

[16] - Model Constants: $C_1 = 1.44$; $C_2 = 1.92$; $\sigma_k = 1.0$; $\sigma_\varepsilon = 1.3$. Default value of Prandtl Number Pr_t is 0.85.

[17] - Model Constants: $C_1 = 1.44$; $C_2 = 1.9$; $\sigma_k = 1.0$; $\sigma_\varepsilon = 1.2$. Default value of Prandtl Number Pr_t is 0.85.

[18] - Re-Normalisation Group (RNG). Renormalised Navier-Stokes equations. Model Constants: $C_1 = 1.42$; $C_2 = 1.68$; $\sigma_k = 0.7194$; $\sigma_\varepsilon = 0.7194$.

[19] - Low Reynolds k-ε models. Literature refers hundreds of low Reynolds models.

[20] - The first transported variable is turbulent kinetic energy, k. The second transported variable in this case is the specific dissipation, ω.

[21] - This form of two-equation models is sometimes used because vorticity magnitude Ω is usually readily available in most Navier-Stokes codes.

[22] - There are no specific farfield boundary conditions recommended for this model. This model exhibits some sensitivity to freestream boundary conditions on ω.

[23] - Shear stress transport (SST) formulation combines the use of a k-ω formulation in the inner parts of the boundary layer which makes the model directly usable all the way down to the wall through the viscous sub-layer. It can be used as a Low-Re turbulence model without any extra damping functions.

[24] - The wall boundary conditions for the k equation in the k-ω models are treated in the same way as the k equation is treated when enhanced wall treatments are used with the k- ε models.

[25] - The modification was originally developed for transient simulations of vortex-shedding behind square cylinders, where the normal k-ε model tends to produce too much turbulent energy in stagnation regions and in the small regions with strong acceleration and deceleration around the square corners. Kato and Launder replaced one of the strain-rates, S, in the turbulent production term with the vorticity, Ω.

[26] - No observations was found except the article; Durbin, P. A. (1996), "On the k-epsilon Stagnation Point Anomaly", International Journal of Heat and Fluid Flow, 1996, Vol. 17, pp. 89-90.

[27] - The Yap correction consists of a modification of the ε equation. The Yap source term contains the explicit distance to the nearest wall. This distance is sometimes difficult to efficiently calculate in complex geometries.

[28] - Realisability is the minimum requirement to prevent a turbulence model generating non-physical results. For a model to be realisable the normal Reynolds stresses must be non-negative.

[29] - Similar to the Standard k-ε. Additionally, it incorporates some near-wall turbulence anisotropy as well as non-local pressure-strain effects. It is a general turbulence model for low Reynolds-numbers that does not need to make use of wall functions because it is valid up to solid walls.

[30] - Instead of using the wall-normal velocity fluctuation as the velocity scale, the normalized wall-normal velocity scale ζ. This turbulence variable can be regarded as the ratio of the two time scales: isotropic and anisotropic.

[31] - The Reynold's Stress Model (RSM) is a higher level, elaborate turbulence model. It is usually called a *Second Order Closure*. In RSM, the eddy viscosity approach has been discarded and the Reynolds stresses are directly computed. The exact Reynolds stress transport equation accounts for the directional effects of the Reynolds stress fields.

models: the Smagorinsky-Lilly[32] model, the dynamic subgrid-scale[33] model, the RNG-LES[34] model, the Wall-Adapting Local Eddy-viscosity (WALE)[35] model, the kinetic energy subgrid-scale[36] model and the near-wall treatment[37] for LES model. Turbulence near-wall modelling[38] is based on law of the wall and uses low-Re resolved boundary layers. Turbulence free-stream boundary conditions[39] include two variants: Turbulence intensity[40] and Turbulence length scale[41].

The three major types of turbulence methodologies are DNS, LES and "*k*-ε" modelling. DNS is a simulation in which the Navier-Stokes equations are numerically solved without any turbulence model, therefore the whole range of spatial and temporal scales of the turbulence must be resolved. This approach is extremely expensive, if not intractable, for complex problems on modern computing machines, hence the need for models to represent the smallest scales of fluid motion. That is, to resolve all spatial and temporal scales, the spatial and temporal grids would need to be extremely small, resulting in a problem which would take an extraordinarily long time to solve with today's technology. LES was used first by Joseph Smagorinsky to simulate atmospheric air currents and implemented in the 1970s by atmospheric scientists to study the weather. Since that time it has been used in almost every engineering field. LES seeks to directly solve large spatial scales like DNS, while modelling the smaller scales "*k*-ε". The "*k*-ε" model is one of the most common turbulence models. It includes two extra transport equations to represent the turbulent properties of the flow. This

---

[32] - Constant C_S = 0.1-0.2 and the the eddy viscosity is modeled by a subgrid-scale.

[33] - The DSGS model may be viewed as a modification of the Smagorinsky model, as the dynamic model allows the Smagorinsky constant C_S to vary in space and time.

[34] - Based on Renormalization Group Theory, where constant C_{rng} = 0.157.

[35] - WALE model is invariant to any coordinate translation or rotation and only local information is needed. It is well-suited for LES in complex geometries. Constant C_w = 0.325. (Nicoud, F., Ducros, F., "Subgrid-scale stress modeling based on the square of velocity gradient tensor", Flow, Turbulence and Combustion, April 1999.)

[36] - Subgrid-scale kinetic energy k_{sgs} were defined subgrid-scale eddy viscosity μ_t were computed using k_{sgs}.

[37] - Standard Smagorinsky model eddy viscosity is nonzero at solid boundaries, contrary to the notion that the eddy viscosity should be zero where there is no turbulence. To solve that problem, it was added a Van Driest-style damping function into the length scale.

[38] - Low-Reynolds simulation using fully resolved boundary layers requires a refined boundary layer mesh with the first cell at the walls at a $y^+ < 1$. Stretching of the following cells outside of a wall should usually be kept below something like 1.25.

[39] - Estimating the turbulence model variables, like turbulent energy, dissipation or Reynolds stresses, directly is often difficult. Instead it is easier to think in terms of variables like the incoming turbulence intensity and turbulent length scale or eddy viscosity ratio. These properties are more intuitive to understand and can more easily be related to physical characteristics of the problem.

[40] - Turbulence intensity or turbulence level is defined by u' / U, where *u'* is the root-mean-square of the turbulent velocity fluctuations and *U* is the mean velocity.

[41] - Turbulent length *l* scale should normally not be larger than the dimension of the problem, since that would mean that the turbulent eddies are larger than the problem size. Contant $C\mu = 0.09$ and $l = C\mu^{3/4} \times (k^{3/2} / \varepsilon)$.

allows a two equation model to account for history effects like convection and diffusion of turbulent energy. The first transported variable is turbulent kinetic energy, *k*. The second transported variable in this case is the turbulent dissipation, ε. It is the variable that determines the scale of the turbulence, whereas the first variable, *k*, determines the energy in the turbulence. This methodology simply attempts to model the turbulence by performing time or space averaging. As described in Bardina *et al*. (1997), the *k*-ε model has been shown

Table 1.2. Computational Methods and Turbulence Models.

RANS – Reynolds-averaged Navier–Stokes			
Linear eddy viscosity models	Algebraic models:	• Cebeci-Smith • Baldwin-Lomax • Johnson-Kingl • A roughness-dependent	
	One equation models:	• Prandtl's one-equation • Baldwin-Barth • Spalart-Allmaras	
	Two equation models:	• k-ε models	• Standard k- ε • Realisable k- ε • RNG k- ε • Near-wall treatment
		• k-ω models	• Wilcox's k- ω • Wilcox's modified k- ω • SST k- ω • Near-wall treatment
		• Realisability issues	• Kato-Launder modification • Durbin's realizability constraint • Yap correction • Realisability and Schwarz' inequality
Nonlinear eddy viscosity models	Explicit nonlinear constitutive relation:	• Cubic k- ε • Explicit algebraic Reynolds stress models (EARSM)	
v^2 - f models	• v^2 – f model • ζ – f model		
• Reynolds stress model (RSM)			
LES - Large Eddy Simulation			
• Smagorinsky-Lilly model • Dynamic subgrid-scale model • RNG-LES model • Wall-adapting local eddy-viscosity (WALE) model • Kinetic energy subgrid-scale model • Near-wall treatment for LES models			
DES - Detached Eddy Simulation			
DNS - Direct Numerical Simulation			
Turbulence near-wall modeling			
Turbulence free-stream boundary conditions			
• **Turbulence intensity** • **Turbulence length scale**			

to be useful for free-shear layer flows with relatively small pressure gradients. Similarly, for wall-bounded and internal flows, the model gives good results only in cases where mean pressure gradients are small; accuracy has been shown experimentally to be reduced for flows containing large adverse pressure gradients. One might infer then, that the "*k-ε*" model would be an inappropriate choice for problems such as inlets and compressors. Under certain conditions this method can be very accurate, but it is not suitable for transient flows, because the averaging process wipes out most of the important characteristics of a time-dependent solution.

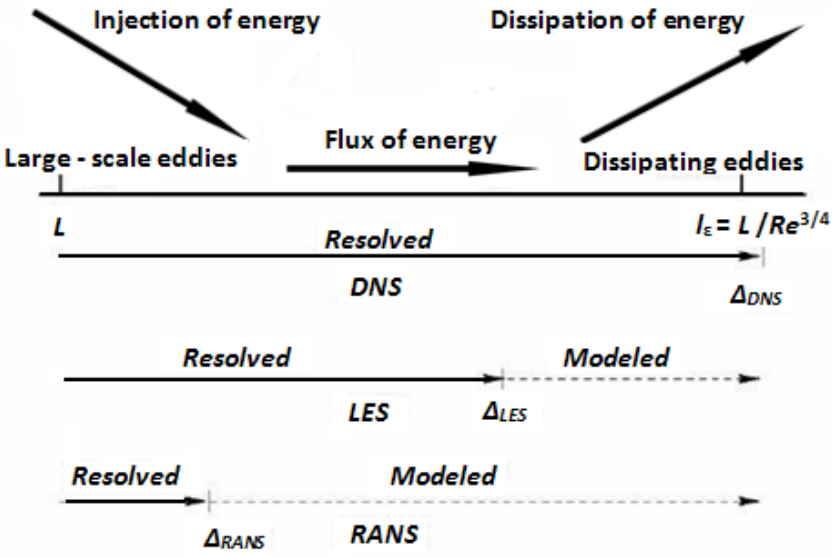

Figure 1.4. Extend of modelling for certain types of turbulent models[42] .

Habib and Whitelaw (1985) presented a numerical work investigation concerning the confined coaxial-jet flows. They applied three different turbulence models to the prediction of the flow properties: a two-equation "*k-ε*" model and two Reynolds stress models. They made their calculations for two velocity ratio of the annulus maximum velocity/maximum pipe velocity equal to 3 and 1. They computed the axial mean velocity normalized by the mean velocity value on the axis at the exit plane of the coaxial jets and compared with previous measurements data of Habib (1980). Using under-relaxation to improve the convergence, they stated that the computation time required by the Reynolds-stress models was larger than that of the "*k-ε*" model to achieve the same convergence. They found that the agreement between experimental data and the predicted results of the three models varied according to the flow conditions, for instance the mean velocity distribution near and inside the recirculation zone was better predicted by the Reynolds-stress models than the eddy viscosity model. Significant discrepancies exist and the size of the recirculation zone

[42] - Sodja, J., Podgornik R., Turbulence Models in CFD, Faculty for Mathematics and Physics, Department of University of Physics, University of Ljubljana, 2007.

was underpredicted by the three models with the Reynolds-stress models giving lower discrepancy. The normal stress was underestimated by the three models particularly near the centre-line and the rate of dissipation was overestimated. They found that the discrepancies were associated with the streamline curvature and that appropriate modifications to the Reynolds stress equations and the equation for the rate of dissipation were required.

Balarac and Si-Ameur (2005) presented a numerical investigation using DNS applied to the mixing and coherent vortices in turbulent coaxial jets studies, and validated by comparison against laboratory experiments. The velocity ratio between the outer and the inner jet was $r_u = \lambda = 5$. The domain size was 10.8 D_i x 10.65 D_i x 10.65D_i the streamwise direction was (x) and two transverses directions (y, z) and the Reynolds and Schmidt numbers were Re =U_o / D_i / υ = 3000 (with the velocity of the outer jet U_o) and Sc = υ / k =1, respectively. They solve numerically the full incompressible Navier–Stokes equations written in Cartesian coordinates in the parallelepipedic computational domain consisting in 231 × 384 × 384 points with a uniform mesh size in all three directions. The spatial discretization was performed with the help of a sixth-order compact finite difference scheme in the streamwise. They computed isosurfaces coloured by axial and tangential vorticity, mean axial velocity and rms axial velocity. The mixing process was studied by seeding a numerical passive tracer first in the outer annular jet, and after in the inner jet. For the case of the tracer seeded in the annular jet, the turbulent mixing process begun by an engulfment of species through both shear layers due to Kelvin-Helmholtz vortices. Further downstream, the mixing process showed an intermittent character as a result of fluid injections caused by counter-rotating vortices along the flow. For the tracer in the inner jet case, the mixing process was only due to the inner vortices. The tracer remained confined in the jet centre. Finally, a large amount of fluid from the outer jet invaded the inner jet.

Chen and Kim (1987) performed a numerical investigation using an extended *"k-ε"* turbulence closure model in several turbulent flows with different characteristics. A second-order accurate finite difference boundary layer code and a nearly second-order accurate finite difference elliptical flow solver were used for their numerical computations. For the confined swirling flow case, their simulations consisted of two coaxial inlet pipes with the swirling guide vanes installed between the inner and outer pipes. They simulated the axial centreline velocity. The inner and outer pipes had radii of 12.5 and 29.5 mm, respectively. The inlet channel was followed by a sudden pipe expansion with expansion ratio around 1:2. The radius of the downstream pipe, R_o, was 61 mm. The inlet swirling velocity generated by the swirling guide vane created a central recirculation zone along the pipe centre line downstream of the expansion plane. This central recirculation zone was accompanied by a corner recirculation region downstream of the step. They simulated results for static pressure, mean and axial velocity, turbulent kinetic energy and shear stress. They compared results of the sizes of the central recirculation zones computed with their modified *"k-ε"* model with the standard *"k-ε"* model. They concluded that their modified model predicted

much better results than that of the standard model and the obtained results with the standard *"k-ε"* model were similar to those reported in some previous investigations.

Lin (1998) presented a numerical investigation concerning the modelling of the confined swirling coaxial jet. The case computed was previously investigated experimentally by Roback and Johnson (1983), where the swirl number S = 0.41 and the Reynolds number based on the inlet jet velocity was 80300. Passive scalar was supplied through the centre tube and swirling flow was imposed on the annular duct. This case was also investigated numerically with LES by Pierce and Moin (1998). He used a computational framework based on the Reynolds averaged equation approach and the eddy-viscosity type turbulence models adapted (*"k-ε"* and k-ε-v^2-f). The main goal of Lin (1998) was to identify the causes of discrepancies and to investigate the influences of grid density and turbulence modelling on the predicted results. He simulated axial and tangential velocity. The dominant features of the flow were the annular recirculation zone after the expansion and the extensive central recirculation zone due to the effect of the swirling coaxial jet. The presence of the centre and corner recirculation zones was crucial to the stabilization of the combustion zone within the combustor. Based in the simulation results, he concluded that the excessive level of mixing of the scalar field at the region bordering the central recirculation zone predicted numerically by other authors, may be due to the insufficient grid density adopted in the solution domain. Regarding the effects of turbulence modelling, he observed that both *"k-ε"* and k-ε-v^2-f models predicted well the development of the mixing layer near before the central recirculation bubble. LES results presented a slightly higher level of diffusive transport in the near field of the mixing layer. The strength of the central jet predicted by the *"k-ε"* model was the strongest, followed by the LES simulations. The *"k-ε-v²-f"* prediction was slightly diffusive, with a presence of the reverse flow along the centreline in some locations. The overall better predictions of the scalar fields were with the use of LES.

Del Taglia *et al* (2004) made a numerical and experimental investigation of an annular jet with large blockage. Using 3-D LDA they measured mean values of axial and radial velocity and axial velocity fluctuations. For their numerical investigation they used Unsteady Reynolds Averaged Navier-Stokes (URANS) simulation technique. For the simulation of the annular jet flow they used three different models for the Reynolds stress: the standard *"k-ε"* model based on the Boussinesq approximation; the Reynolds Stress Model of Speziale, Sarkar and Gatski a no-model approach, for which the Reynolds stresses are assumed to be zero. The inner tube diameter D_o = 85 mm and the disk diameter D = 80 mm (blockage ratio = 0.89) and the Reynolds number based on the hydraulic diameter and the jet exit velocity was 4400. The air flow was fixed at such a rate that the axial bulk velocity at the slot exit was U_o = 13.2 ms^{-1}. At these flow conditions, different points were measured and mean and rms velocity values were computed, with the simulations based on the three-dimensional unsteady RANS technique. A comparison of the mean velocities presented significant differences between the simulated and measured values, which they stated to prove to be the effect of asymmetries in the experimental jet exit velocities. Their computed velocity fluctuations were in very

good agreement with the experiments. Their experiments and simulations proved the existence of an asymmetric flow field inside of the recirculation zone, with a preferential flow direction. They observed that the fluctuations in the recirculation zone manly consisted of fluctuations of large scale vortices, having the necessity of performing the computations in an unsteady manner. The steady computations clearly underestimated the total fluctuations.

Barata *et al* (2007; 2007a; 2009) presented a numerical investigation concerning the numerical study of the mixing of the coaxial jets. Using a standard "k-ε" turbulence model, they simulated the experimental investigation condition of Ahmed and Sharma (2000). They computed mean radial velocity, turbulent kinetic energy, with the main goal to study the effect of the initial levels of turbulence of each coaxial jet for diameter ratios less than 2, which is the case of very low bypass turbine engines. The outer and annular jet had a diameter of 380 mm while the inner jet had diameter of 330 mm. The simulations were made for velocity ratios λ = 0.3, 1.5 and 6.0 and the results were compared with the experimental values (Barata *et al*, 2007). The outer jet velocity was U_o = 12.9, 55.7 and 80.8 ms^{-1} respectively, while the inner jet velocity was U_i = 37.65, 36.3 and 13.1 ms^{-1}, respectively. The Reynolds number based on the mass average velocity was Re_M = 5.6 x 10^5, 7.0 x 10^5 and 5.0 x 10^5, respectively. The computed results showed agreement with the experimental results for λ = 0.3, 1.5. For the λ = 6.0 case, the computed results showed the presence of a large recirculation zone. They also concluded that the turbulent mixing process of confined coaxial jets strongly depended from the velocity ratio. The mix rate increased with outer jet velocity greater than the inner jet velocity. As a consequence of the recirculation appearance for the case of λ = 6.0, Barata *et al* (2007a; 2009) studied numerically a dimensionless parameter, ratio of the turbulence intensity, θ, defined as the square root of the value of the turbulent kinetic energy of the outer jet/turbulent kinetic energy of the inner jet, $\theta = (k_{ext}/k_{int})^{0.5}$. In order to study the influence of the initial turbulence intensity, the conditions of one of the jets was kept constant, and the turbulence intensity of the other jet was varied successively by one order of magnitude. As a consequence, the effect of θ, was analyzed for two sets of eleven orders of magnitude of initial intensity of turbulence, from 10^{-5} to 10^5. The results revealed that for relatively high turbulence intensities of the outer jet a vortex was always present for velocity ratios of 6 or larger, and that this was independent of the turbulence intensity ratio. When the turbulence intensity of the inner jet was kept constant and the ratio of turbulence intensities was increased, the recirculation zone decreases in size, its centre moves further upstream until it disappears completely.

Balarac and Métais (2005) by DNS, characterized the respective thicknesses of the inner and outer shear layers by their momentum thicknesses θ_{01} and θ_{02}, and investigated the influence of θ_{01} on the transitional processes in the near field of coaxial jets. They measured the axial velocity and the turbulent kinetic energy. The domain size was 10.8D_i x 10.65 D_i x 10.65 D_i along the streamwise (x). The two transverses directions were (y, z) and the Reynolds numbers were Re = U_o / D_i / υ = 3000 (with the velocity of the outer jet U_o) and the ratio of the outer to inner diameter was D_o / D_i, respectively. The ratio of the outer radius to

the outer initial shear layer momentum thickness was fixed with R_o / θ_{02} = 25. They presented 20 different runs for the velocity ratio range between 3 ≤ λ ≤ 30. The numerical results were compared with two different experiments of others authors. They identified two distinct jet regimes: $\lambda > \lambda_c$, where a recirculation bubble was present near the jet inlet and $\lambda < \lambda_c$, without any recirculation. For the $\lambda < \lambda_c$, the outer vortices imposed their shedding frequency to the inner vortices and the latter were trapped between two consecutive larger vortex rings. The critical value λ_c, separating the regime without and with recirculation bubble was found to be strongly dependent on θ_{01}. For $\lambda > \lambda_c$, the shape and the length of the recirculation bubble was strongly affected by the shape of the inlet profile: the bubble was significantly shortened when θ_{01} was small.

Chen and Kim (1987) performed a numerical investigation using an extended *"k-ε"* turbulence closure model in several turbulent flows with different characteristics. A second-order accurate finite difference boundary layer code and a nearly second-order accurate finite difference elliptical flow solver were used for their numerical computations. For the confined swirling flow case, their simulations consisted of two coaxial inlet pipes with the swirling guide vanes installed between the inner and outer pipes. They simulated the axial centreline velocity. The inner and outer pipes had radii of 12.5 and 29.5 mm, respectively. The inlet channel was followed by a sudden pipe expansion with expansion ratio around 1:2. The radius of the downstream pipe, R_o, was 61 mm. The inlet swirling velocity generated by the swirling guide vane created a central recirculation zone along the pipe centre line downstream of the expansion plane. This central recirculation zone was accompanied by a corner recirculation region downstream of the step. They simulated results for static pressure, mean and axial velocity, turbulent kinetic energy and shear stress. They compared results of the sizes of the central recirculation zones computed with their modified *"k-ε"* model and with the standard *"k-ε"* model. They concluded that their modified model predicted much better results than that of the standard model and the obtained results with the standard *"k-ε"* model were similar to those reported in some previous investigations.

Balarac *et al* (2007) performed a DNS investigation concerning the flow dynamics and the mixing properties of natural unforced and excited coaxial jets. The domain size was 10.8 D_i x 10.65 D_i x 10.65 D_i along the streamwise (x). The two transverses directions were y and z and the Reynolds number was Re = U_o / D_i / υ = 3000. The inlet jet velocity was defined by the velocity ratio λ = 5 and with the momentum thickness, D_i / θ_{01} = D_i / θ_{02} = 25. The Schmidt number was Sc = 1. Their computations consisted in three different flows: a natural coaxial jet, a purely axisymmetric excitation and a combined axisymmetric and azimuthal excitation, both of moderated amplitude. For the last case, several microjets (N = 5, 10 and 15) were placed circumferentially around the outer nozzle and ejecting periodically. The excitations were applied to the outer shear layer with a frequency corresponding to the periodic passage of the outer vortical structures. Using species injected in the outer jet alone, they made visualization. The computed results were reported to the mean velocity, radial and azimuthal turbulent kinetic energy and rms streamwise vorticity. In the natural jet, was

observed that the transition process begins with the development of Kelvin-Helmholtz vortices on the outer and inner shear layers. There was a domination of the outer Kelvin-Helmholtz vortices which impose their frequency to the inner ones. Further downstream, counter-rotating pairs of streamwise vortices appear allowing the ejections of these species, characterized by mushroom-type structures. For the purely axisymmetric excitation case the excitation was made at the most unstable frequency of the outer shear layer allowing a faster development of Kelvin-Helmholtz instability of both outer and inner layers. These intense vortices allowed the engulfment of the outer stream from the beginning of the jet. Furthermore, a faster transition was observed since streamwise vortices were formed earlier and so the ejection phenomenon of the outer species was faster as compared to the unforced case. For the last case, similarly with the purely axisymmetric case, the excitation was applied at the outer shear layer most amplified frequency. They also concluded that this triggers a rapid development of the outer and inner Kelvin-Helmholtz vortices implying an efficient engulfment of the outer species. The azimuthal disturbance yields an azimuthal deformation of the outer Kelvin- Helmholtz vortices leading to the early formation of counter rotating streamwise vortices.

Del Taglia *et al* (2004) made a numerical and experimental investigation of an annular jet with large blockage. Using 3-D LDA they measured mean values of axial and radial velocity and axial velocity fluctuations. For their numerical investigation they used Unsteady Reynolds Averaged Navier-Stokes (URANS) simulation technique. For the simulation of the annular jet flow they used three different models for the Reynolds stress: the standard "k-ε" model based on the Boussinesq approximation; the Reynolds Stress Model of Speziale, Sarkar and Gatski a no-model approach, for which the Reynolds stresses are assumed to be zero. The inner tube diameter D_o = 85 mm and the disk diameter D = 80 mm (blockage ratio = 0.89) and the Reynolds number based on the hydraulic diameter and the jet exit velocity was 4400. The air flow was fixed at a rate that the axial bulk velocity at the slot exit was U_o = 13.2 ms^{-1}. At these flow conditions, different points were measured and mean and rms velocity values were computed, with the simulations based on the three-dimensional unsteady RANS technique. A comparison of the mean velocities presented significant differences between the simulated and measured values, which they stated to prove to be the effect of asymmetries in the experimental jet exit velocities. Their computed velocity fluctuations were in very good agreement with the experiments. Their experiments and simulations proved the existence of an asymmetric flow field inside of the recirculation zone, with a preferential flow direction. They observed that the fluctuations in the recirculation zone manly consisted of fluctuations of large scale vortices, having the necessity of performing the computations in an unsteady manner. The steady computations clearly underestimated the total fluctuations.

Xu *et al* (2002) performed a numerical LES for a confined square and annular coaxial jet. They imposed the fully developed turbulent conditions on the inlet of the jet and used the temporal approach. The Reynolds number $Re_{bulk} = U\ h\ /\ \upsilon$ = 4921 in the square case and 2534 in the annular case. The total integration time, T_{total} was 40 s for each case with a time

step $\Delta t = 5.0 \times 10^{-4}$ s. They validated and verified the code with previous experimental and analytical works. They computed mean velocity, streamwise and transverse turbulence intensity and instantaneous distributions of streamwise vorticity. They found that their centre-velocity decay rate was in agreement with the previous measurements of Chua and Lua (1998), and that the decay rate in confined square jet was significantly lower than the one in a free jet. They stated that the turbulence statistics in the confined square jets bear some resemblance in the near field to those in square free jets, while some significant deviations were found in the far field.

Ben Cheikh *et al* (2007) studied numerically an air-air turbulent coaxial jet for different velocity ratios ranging between 1 and 10. Their code validation was done through the experimental configuration of the work of Ribeiro *et al* (1980). Using the standard *"k-ε"* first order model, they computed the axial velocity for four different velocity ratio (λ = 1, 3, 4 and 10). The internal nozzle had D_{iint} = 16.1 mm of internal diameter and D_{iext} = 21.6 mm of external diameter, while the outer nozzle had D_{oint} = 44.9 mm and D_{oext} = 50.4, respectively. Their *x* and *y* dimension domain were respectively 60 and 10 times the inner diameter of the external jet D_{oint}. For $\lambda < 3$ there was the presence of a low pressure area which migrates to the jet axis when *r* tends to 3. For $\lambda \geq 3$ they noted the presence of a recirculation zone that approaches to the initial zone of the jets when *r* was increased. The size of the recirculation zone increases in function of the velocity ratio.

Pope and Whitelaw (1976) presented a numerical investigation concerning the near-wake flows with and without recirculation's. Their computations were made using three different turbulence models: the first comprised transport equations for turbulence kinetic energy and the rate of turbulence dissipation *"k-ε"* and the second and third comprised equations for the rate of turbulence dissipations and two forms of Reynolds-stress equations characterized by different redistribution terms Using this turbulence models, they simulated the available data of experimental results of other investigations, such as Chevray (1968), Chevray and Kovasznay (1969), Carmody (1964), Durao and Whitelaw (1974) and Durao (1975, private communication). They computed results of velocity and correlations of velocity. They found significant discrepancies between measurements and predictions, that may be attributed both to inaccurate measurements, leading to erroneous boundary conditions and to deficiencies in the turbulence models. In the turbulence models, they found two particular defects in the prediction of the recirculating flow: the length of the recirculation region was underpredicted as was the rate at which the wake decays. Their results showed that for wakes without recirculation the particular turbulence model was less important than the boundary condition assumed in the plane of the trailing edge of the body, though the Reynolds-stress models do provided a better representation of the individual normal stresses.

Salvetti *et al* (1996) carried out DNS of transitional axisymmetric water coaxial jets. They investigated the sensitivity of the numerical solution to the domain size, pointing out the feedback effect of the boundary conditions on the pressure at the inlet, and the effects of the Reynolds number on the characteristics of the flow. They made simulations for Re =

500, 1000, 1500, 2000, 2500 and 3000. They computed four different size domains: 4, 8, 12 and 16 R_i. The used internal radius had R_i = 2.73 cm and the velocity on the axis of the inner jet in the simulations was V_i = 11 cms^{-1}, for the case of Re = 3000. The ratio between the maximum velocity of the internal and the external jet was V_e/V_i = 0.71 and the ratio between the external and internal radius was R_e / R_i = 1.41. They computed values of mean axial velocity, pressure and vorticity. They found that boundary conditions affected the dynamics of the jets, through a feedback effect by the pressure field that becomes negligible as the axial size of the computational domain was increased. The Reynolds number affected clearly the flow. The evolution of the large startup vortex was found to be independent of the Reynolds number, whereas the circulation per unit length at the centre of this vortex increases with the Reynolds number.

Zhu and Shih (1993) presented a numerical investigation concerning of confined coflow jets with three different turbulence models. They used a RNG-based *"k-ε"* model and a realizable Reynolds stress algebraic equation model and made comparisons with the standard *"k-ε"* model calculations in axial mean velocity calculations. The numerical credibility of the solutions was assured by the use of the second-order accurate differencing schemes and sufficiently fine grids. The inlet jet and the ambient velocities were taken from the experiment of Barchilon and Curtet (1964). The velocity of the jet was varied between the range of 1253.8 ≤ U_J ≤ 1298.8 cms^{-1}, while the ambient velocity was varied between range of 7.42 ≤ U_a ≤ 84.48 cms^{-1}. The diameters of the jet were respectively D_o = 16 cm and d_o = 1.2 cm. The flow considered involved recirculation with infixed separation and reattachment points and severe adverse pressure gradients. Detailed comparisons with experiments showed that the realizable Reynolds stress algebraic equation model consistently had work better than the standard "k-ε" model in capturing the essential flow features. The RNG-based *"k-ε"* model do not demonstrated any improvements over the standard "k-ε" model under the flow conditions considered.

Hassel *et al* (2006) presented a numerical and experimental investigation concerning the mixing in a coaxial jet mixer. Using two LES models (DGM and DMM) and three RANS models (SST, *"k-ε"* and RSM-LRR-IP of Launder *et al* 1975, they compared with LIF and LDV radial mean and rms velocities measurements. The experiments were carried out in closed water channel. They injected an aqueous solution through the nozzle (d = 10 mm) into the water coflow (D = 50 mm). Simulations and measurements were taken for the j-mode (jet mode, without recirculation zone) and for the r-mode (with the massive separation and creation of the recirculation zone). For the r-mode case, tests were performed at Re_d = 10000 and with a flow rate ratio $\dot{V}_D/\dot{V}_d = 1.3$, whereas for the j-mode case these parameters were Re_d = 10000 and with flow rate ratio $\dot{V}_D/\dot{V}_d = 5.0$, respectively. A good agreement with measurements for averaged characteristics was achieved by RANS SST and LES DMM models for both r-mode and j-mode cases, while the other models LES DGM, *"k-ε"* and RSM gave rather poor results. The LES DMM calculations of the rms values showed also a satisfactory agreement with measurements. In consequence of these results LIF measurements and LES

DMM were used for study of flow physics in the r-mode. They reported the confirmation of the qualitative observations of Barchilon and Curtet (1964) and revealed that the flow had a pronounced unsteady character and contained dominating long period oscillations occurring in an opposition-of-phase mode. The recirculation zone contained unsteady large-eddy structures (many vortices of various sizes), that causes the intermittency of the scalar field. Common Reynolds averaged characteristics were not quite informative quantitative to describe this flow property.

Jahnke *et al* (2005) presented a numerical study of influence of different parameters on mixing in a coaxial jet mixer using LES. The studied parameters were: Influence of the Re_d, influence of the flow rate, influence of different density ratios, influence of heat and transfer and mixing of gases versus mixing of liquids. They computed rms temperature fluctuations and the degree of mixedness along the pipe. In terms of diameter, their computational domain had the 7.645 x 1 x 2π in a cylindrical coordinate system (x, r, θ). The diameter ratio of the nozzle was d / D = 0.32, coaxially arranged at the inlet of the pipe. The bulk velocity of the co-flow, U_1 was varied between the range of 2.5 and 20 ms^{-1}, while the bulk velocity within the nozzle, U_2 was varied between the range of 12.5 and 50 ms^{-1}, with the corresponding Reynolds number $Re_d = U_2\ d\ /\ \upsilon_2$ varying between 5214 and 160000, respectively. For the case of the influence of the Reynolds number, they testes two situations: $\upsilon_i\ /\ \upsilon_o$ = 0.5 and $\upsilon_o\ /\ \upsilon_i$ = 0.5, maintaining the flow rate constant $R = Q_2\ /\ Q_1$ = 0.57. For the different density ratios, they tested two cases: air-methane and methane air (ρ_i/ρ_o = 0.62 and 1.61). For the mixing of gases versus mixing of liquids, they used air (Schmidt number, Sc = 0.7) and water (Schmidt number, Sc = 1000). The Reynolds number increased from 10430 to 160000 when air was replaced by water. The influence of the heat transfer on mixing was studied for the liquid mixture test case, water at flow rate R = 0.57, with U_i = 5ms^{-1} and U_o = 25 ms^{-1}. The temperature of the coflow was maintained at T_i = 293K and the jet temperature varied in two values: T_o = 275 and 360 K, for cases with adiabatic wall temperature of 350 K. The numerical simulations showed that the influence of the Reynolds number was negligible after a distance larger than 6 based on the pipe diameter. For the different density ratio, numerical solutions showed an enhancement of the overall mixing along the first three diameters of the pipe if the density in the jet was lower than that in the coflow. For the mixing characteristics of gas and liquid mixtures, while the Schmidt number reduced the role of micro-mixing in the overall mixing, the Reynolds number leaded to a strong enhancement of the mixing process. The influence of the temperature on the integral mixing characteristics in liquid mixtures was rather poor but there was a notable influence on higher moments of temperature and velocity fluctuations.

Silva *et al* (2003) performed a numerical investigation concerning the transition in high velocity ratio coaxial jets analyzed from DNS. They carried out two simulations for two different velocity ratios: $\lambda = U_o\ /\ U_i$ = 3.3 and 23.5, both with a coflow that $U_3\ /\ U_o$ = 0.04. In both simulations the Reynolds number and the ratio of outer/inner jet diameters was $Re_{D1} = U_o\ D_i\ /\ \upsilon$ = 3000 and $D_o\ /\ D_i$ = 2. The Strouhal number based on the initial momentum thickness

at the inner shear layers were Str_θ^i = 0.011 and 0.01, and at the outer layers were Str_θ^o = 0.028 and 0.03, respectively for U_2 / U_1 = 3.3 and 23.5. They computed streamwise velocity and vorticity. For both flows the Kelvin-Helmholtz instability in the inner and outer shear layers resulted in a formation of vortex rings that further downstream formed an inner and outer helical structure. They observed that the inner rings were "locked" into the outer ones. For the case of U_o / U_i = 23.5, the inner potential core does not exist due to the formation of a large recirculation region in x / D_i <5.

Mitsuishi *et al* (2006) performed a DNS investigation of scalar transport and mixing in a coaxial round jet issued into a small model of methane/air combustor. The outer-to-inner bulk mean velocity was fixed at 6.4 and the Reynolds number based on the diameter and bulk mean velocity of the outer annular jet was Re=1320. The computational model used was a coaxial central and annular jets issued to an expanded cylindrical space. They computed mean and rms fluctuations of axial velocity, azimuthal vorticity and concentration. The diameter ratio of the outer/inner jets was D_o / D_i = 2 (2 and 1cm), the expansion ratio was equally 2 and the outer/inner momentum flux ratio was 41, which corresponded to the equivalence ratio of 0.72. The Schmidt number of the passive scalar was assumed as Sc = 1, which nearly corresponded to the diffusion of methane into air at the standard temperature and pressure. An intelligent nozzle was modelled as a spatiotemporal change of the inlet velocity profile with an amplitude of flapping motion ε = 0, 0.001, 0.01 and 0.0125, with the Strouhal number varying between the range of $0.5 \leq St_a \leq 1.5$. For the natural jet, they tested four velocity ratios, 6.4, 9.1, 16 and 32. They observed that the intelligent modelled nozzle generated various types of flow patterns and concentration profiles depending the amplitude and frequency of the contraction. For the best mixing case (St_a = 0.9 and ε = 0, 0.0125), they observed a pair of counter-rotating two-dimensional vortex rings synchronously discharged with the controlled input, distorted by the streamwise vortices near the centerline. Finally, the inner vortex rings become three-dimensional and breakdown.

Dianat *et al* (2006) performed a numerical investigation in a confined coaxial jet. They made an implementation of a passive scalar transport equation into a LES code. Both second order accurate TVD (Total Variation Diminishing) and higher order accurate DRP (Dispersion Relation Preservating) schemes were assessed. The measured data of Lima and Palma (2002) was used to their examination. They measured mean axial velocity and rms fluctuations. The central axisymmetric pipe had an inner diameter of 17 mm and an outer diameter of 19 mm, while the confining outer pipe had a diameter of 42 mm. The fluid used was water. The unsteady scalar mixing performance of the LES code (using the TDV scheme) was validated against published DNS data for a slightly heated channel flow. They also provided RANS "k-ε" model predictions for comparison. They obtained an excellent agreement between the results of LES and DNS, both for dynamic and scalar fields. Their simulations had a considerable improvement over the standard eddy viscosity RANS approach. The downstream development of the scalar field in the rapid mixing region was much better predicted by LES approach.

Nallasamy (1987) performed a numerical investigation on the prediction of recirculation zones in isothermal coaxial jet flows relevant to combustors. The experimental configuration used by Owen (1976) was reproduced for this investigation and consisted in a 6.35 cm central jet surrounded by an 8.89 cm annular jet. Both jets were discharged into a 12.7 cm diameter chamber with 121.9 cm long. The outer and inner peak velocities were 29.26 and 2.44 ms^{-1} respectively, corresponding to a Reynolds numbers based on respective diameters of 1.5 x 10^5 and 0.08 x 10^5. For the velocity ratios of 12, 9, 6 and 3, he simulated axial mean velocity and axial turbulence intensity using a *"k-ε"* model. He concluded that for a given geometrical configuration, the velocity ratio determined the axial location of the central toroidal recirculation (CTRZ) zone. For the geometrical configuration studied the length of the corner recirculation decreases with increase in the velocity ratio in contrast to the results obtained by Habib and Whitelaw, 1979; 1980. For a velocity ratio of 3, the experimental configuration of Owen (1976) resulted in the formation of a CTRZ, while the configurations of Habib and Whitelaw, 1979; 1980 and Johnson and Bennett, 1981 produced no CTRZ. The *"k-ε"* turbulence model predicted the location, shape and size of the recirculation zones fairly well. In these regions, the predicted axial and radial mean velocities and axial turbulence intensity were in good agreement with the measurements. However, the redevelopment of the flow beyond the reattachment on the centreline was slow compared to the measurements.

Srinivasan and Mongia (1980) performed a numerical computation investigation in swirling recirculating flow. Their computational program consisted in three tasks: I, II and III. In all cases, they simulated the axial and tangential velocity profiles including the total pressure for the last case. In Task I, using the original version of a *"k-ε"* model, only the geometry of the test apparatus and the mass flow rates and vane angles were specified. For the co-swirl case, the inner flow had a 29.65 ms^{-1} axial velocity and a swirl number S = 0.577 while the outer flow had respectively 20.3 ms^{-1} and S = 0.536. For the counterswirl case, the inner jet had 30.33 ms^{-1} and a swirl number S = 0.49 while the outer flow had respectively 20.2 ms^{-1} and S = - 0.507. In Task II, the measured velocity profiles at the centre stream exit plane were used as boundary conditions. Predictions were obtained using the original *"k-ε"* turbulence model and a modified *"k-ε"* model (with Richardson number effects). In Task III, a modified 2-D elliptic program was employed to include the effects of interaction between the inner and outer streams. The geometry of the experimental apparatus consisted of a central 3.72 cm diameter swirling jet mixing into a coaxial co-swirl or counterswirling flow with 14.6 cm outer diameter. The inner tube had a swirl generator consisted of 12 equally spaced vanes with a 68.5 degree swirl angle and a vane thickness of 0.5 cm. The outer channel had 76 cm radial inflow passage with 24 adjustable vane swirlers that allowed the produce of any desirable swirl direction and velocity. In Task I, the inlet profiles for the mixing region were estimated by neglecting the elliptic effects of the interaction between the two coaxial streams. They found uncorrected values near the axis of the tube and the predictions further downstream did not show any flow reversal. In Task II, the inlet profiles for the mixing region

were prescribed from the test data. The original *"k-ε"* model did not predict any recirculation. The modified *"k-ε"* model predicted a recirculation bubble near the axis of the tube in the counterswirl case, when the measured velocity profiles were used as input. The predicted recirculation bubble was elongated in the axial direction. In the co-swirl case, the modified 2-D elliptic program predicted a recirculation bubble, while the measurements did not indicate any flow reversal. The modified 2-D elliptic program predictions for the counterswirl case were in agreement with other author's experimental data and predicted a recirculation zone.

Fröhlich *et al* (2008) performed a numerical investigation concerning to a turbulent swirling jet. They simulated the same geometry of the experimental investigation conducted by Bender and Büchner, 2005: two annular jets exiting into still ambient. The outer main jet accounted for 90% and the inner jet for 10% of the mass flux. The total swirl number was S = 0.93, determined at the jet exit. The swirl number of the pilot jet alone was S = 2 at x / R = -0.73. The Reynolds number based on the bulk velocity of the main jet and its outer radius R was Re_b = 81000. They computed two different cases: without retraction of the pilot jet and with retraction of the pilot jet. In each of the annuli a passive scalar was introduced both with Schmidt number Sc = 1. They used a dynamic Smagorinsky model with an additional bounded HLPA scheme and an eddy diffusivity model. They simulated the mean axial and mean tangential velocity and mean concentration. They found that in the retraction of the pilot jet case, energetic large-scale structures were present and were generated by the retraction of the pilot jet into the tube of the main annular jet, having this a strong impact on the mixing process. In a reacting flow, they would alter considerably the combustion process.

Yang and Ma (2003) performed a numerical investigation for confined swirling coaxial jets, using linear and nonlinear turbulence models. They used the simulation conditions of the experimental investigation of Roback and Johnson, 1983. Eleven turbulence models were used to compare with the experimental results. All models were compared under the same numerical platform, with the same discretization scheme and iterative solver. Mean velocity profiles, streamline patterns and passive scalar were compared. A nonswirling inner jet and a swirling annular jet were discharged into a sudden-expansion larger pipe. Passive scalar was supplied with the inner jet. The inlet Reynolds number based on the overall mass flow rate and the jet diameter was Re = 80300. The inlet swirl number was S = 0.41. The results indicated that for flows with low inlet swirl number (S < 0.5), the linear *"k-ε"* models performed very well the prediction of the mean flow properties, while almost all nonlinear models overpredicted the strength of recirculation and could provide satisfactory results. They also concluded that a fully developed rotating pipe flow does not contain enough flow physics to calibrate the cubic-order turbulence model correctly. The calibration of cubic terms was still a topic of investigation. The explicit algebraic stress models (EASM) provide an effective approach to predict swirling flows, however, requiring fewer calibrations.

Ranga Dinesh and Kirkpatrick (2009) performed a numerical investigation concerning the study of jet precession, recirculation and vortex breakdown in turbulent jets using LES. Their simulations were based on the Sydney swirl burner with a 60 mm diameter annulus in the primary swirling air stream surrounding a circular bluff body of 50 mm of diameter with a 3.6 mm diameter central fuel jet. The jet fluid for the isothermal cases was air. The conditions of their simulations were made by maintaining the velocity of the central jet at 66 ms^{-1}, with the respective Reynolds number of 14300, for two values of the bulk axial velocity of the annulus of 16.3 and 29.7 ms^{-1}. For the first case, they varied the swirl number from, S = 0.57 to 0.91, with the Reynolds number Re = 2400. For the second case they varied the swirl number from, S = 0.28 to 0.45, with the Reynolds number Re = 59000. They simulated mean axial velocity and mean centerline axial velocity and power spectrum. They observed that appears to be a relation between the central jet precessions and the axial extent of the vortex bubble, however, further investigation was required to explore the relationship between the central jet precession and the downstream vortex bubble. The simulations of their study showed that LES seemed to be suitable for investigating instabilities in swirling jets, which they considered an important finding, since there is a need for more fundamental LES investigations on the mechanisms of instability modes and PVC in combustion systems.

Table 1.3. Summary of the numerical investigations related to coaxial jets.

Authors	Experience	Techniques	Results	Comments
Del Taglia *et al* (2004) (Numerical and Experimental investigation)	Annular jet flow with large blockage D_o = 85 mm blockage ratio = 0.89 Re = 4400 U_o = 13.2 ms^{-1}	3D LDA URANS	• Mean axial and radial velocities • Axial velocity fluctuation	• The computed velocity fluctuations were in very good agreement with the experiments. • The experiments and simulations proved the existence of an asymmetric flow field inside of the recirculation zone, with a preferential flow direction. • The fluctuations in the recirculation zone manly consisted of fluctuations of large scale vortices, having the necessity of performing the computations in an unsteady manner. • The steady computations clearly underestimated the total fluctuations.
Fink (1997) Experimental and theoretical investigation	Influence of external turbulence on mixing of axisymmetric coaxial jets jet exit velocity / velocity of the external flow U_0/U_∞ = 3.10, 4.50 and 5.75 Re_o = 8500, 13000 and 15700	"*k*- ε" model Pitot tubes Single normal wires	• Mean velocity • Axial turbulence fluctuations	• In the presence of a suitable external turbulence, for the axial development of the velocity scale, mean velocities decreased and the half widths increased more rapidly. • Related with axial development of the shear stress parameter, the ratio of the maximum shear stress to the maximum defected velocity increased more rapidly. • About the theoretical observations was found that more reliable predictions could be achieved by using a phenomenological concept borrowed from the theory of relative diffusion, according to which the width of the jet corresponds to a wavelength in the inertial sub range of the external turbulence, stating for this, that the detailed mechanism of the external turbulence effects on the shear layer of the jets, was not adequately understood.
Khodadadi and Vlachos (1989) Experimental and numerical work	Confined coaxial turbulent jets <u>Secondary streams:</u> *d* = 4.25 in 5.0, 28.3 and 62.2 ms^{-1} R =6.7x10^3 and 4.2x10^4 *d* = 6.5 in 0.4, 1.2 and 2.6 ms^{-1} Re=4.5x10^3 and 3.2x10^4	LDA "*k*-ε" model	• Axial mean velocity • Rms velocities	• The evolution of the axial velocities, the separation size and the near-wall behaviour of the rms velocity were in excellent agreement with the computations. The velocity spectra in the initial mixing zone demonstrated the existence of coherent structures. • The velocity spectra in the initial mixing zone had demonstrated the existence of coherent structures. • The Strouhal number range of 0.33 to 0.51 was in excellent agreement with the previous works reports.

Table 1.3. **Summary of the numerical investigations related to coaxial jets. (Cont.)**

Authors	Experience	Techniques	Results	Comments
Park and Chen (1989) Experimental and theoretical investigation	Confined Turbulent jets: single data Flow I: Mean velocity=11.4 ms^{-1} Re_i = 9400 Re_o = 6900 Flow II: Re_i = 18800 Re_o = 6900	LDA "k-ε" turbulence model	• Mean axial and fluctuations velocities • Differential wall pressures	• Three flow regimes were identified: potential core, main flow and recirculation flow. • It was identified a sharp decrease in the mean velocities near the injector exit, probably due to pressure gradient associated with the sudden expansion geometry. • The potential core extends to x/d around 4 and the re-attachment point appeared at x/d around 13.5. • Flow II presented a shorter potential core and higher fluctuation velocities. The minimum pressure was observed in the recirculation zone. • The predictions yielded realistic estimates of wall pressure and velocities, overestimated the rate of the flow development and underestimated turbulent intensities and the length of the recirculation zone.
Yang and Ma (2003)	Confined swirling coaxial jets Re=80300 S=0.41	Eleven turbulence models	• Mean velocity • Streamline patterns • Passive scalar	• The results indicated that for flows with low inlet swirl number (S<0.5), the linear "k-ε" models performed very well the prediction of the mean flow properties, while almost all nonlinear models overpredicted the strength of recirculation and could provide satisfactory results. • A fully developed rotating pipe flow does not contain enough flow physics to calibrate the cubic-order turbulence model correctly. • The explicit algebraic stress models (EASM) provide an effective approach to predict swirling flows, however, requiring fewer calibrations.
Barata *et al* (2007; 2007a; 2009)	Mixing of the coaxial jets λ = 0.3, 1.5 and 6.0 U_o=12.9, 55.7 and 80.8 ms^{-1} U_i=37.65, 36.3 and 13.1 ms^{-1} Re_M =5.6x10^5, 7.0x10^5 and 5.0x10^5 θ from 10^{-5} to 10^5	"k-ε" standard model	• Mean radial velocity • Turbulent kinetic energy	• For the λ = 6.0 case, the computed results showed the presence of a large recirculation zone. • The turbulent mixing process of confined coaxial jets strongly depended from the velocity ratio. The mix rate increased with outer jet velocity greater than the inner jet velocity. • The results revealed that for relatively high turbulence intensities of the outer jet a vortex was always present for velocity ratios of 6 or larger, and that this was independent of the turbulence intensity ratio. • When the turbulence intensity of the inner jet was kept constant and the ratio of turbulence intensities was increased, the recirculation zone decreases in size, its centre moves further upstream until it disappears completely.

Table 1.3. **Summary of the numerical investigations related to coaxial jets. (Cont.)**

Authors	Experience	Techniques	Results	Comments
Balarac and Si-Ameur (2005)	Coherent vortices in turbulent coaxial jets studies λ=5 Re = 3000 *Sc* =1	DNS	• Mean axial velocity • Rms axial velocity	• For the case of the tracer seeded in the annular jet, the turbulent mixing process begun by an engulfment of species through both shear layers due to Kelvin-Helmholtz vortices. • Further downstream, the mixing process showed an intermittent character as a result of fluid injections caused by counter-rotating vortices along the flow. • For the tracer in the inner jet case, the mixing process was only due to the inner vortices. The tracer remained confined in the jet centre. Finally, a large amount of fluid from the outer jet invaded the inner jet.
Balarac and Métais (2005)	Near field of coaxial jets Re = 3000 velocity ratio range between $3 \leq \lambda \leq 30$	DNS	• Axial velocity • Turbulent kinetic energy	• It was identified two distinct jet regimes: for $\lambda > \lambda_c$, a recirculation bubble was present near the jet inlet; for $\lambda < \lambda_c$, no recirculation was found. • For the $\lambda < \lambda_c$, the outer vortices imposed their shedding frequency to the inner vortices and the latter were trapped between two consecutive larger vortex rings. • The critical value λ_c, separating the regime without and with recirculation bubble was found to be strongly dependent on θ_{01}. • For $\lambda > \lambda_c$, the shape and the length of the recirculation bubble was strongly affected by the shape of the inlet profile: the bubble was significantly shortened when θ_{01} was small.
Xu *et al* (2002)	Confined square and annular coaxial jet Re_{bulk} = 4921 square Re_{bulk} = 2534 annular	LES	• Mean velocity • Streamwise and transverse turbulence intensity • Instantaneous distributions of streamwise vorticity	• The centre-velocity decay rate was in agreement with previous measurements made by Chua and Lua (1998). • The decay rate in confined square jet was significantly lower than the one in a free jet. • Turbulence statistics in the confined square jets bear some resemblance in the near field to those in square free jets, while some significant deviations were found in the far field.

Table 1.3. **Summary of the numerical investigations related to coaxial jets. (Cont.)**

Authors	Experience	Techniques	Results	Comments
Ben Cheikh *et al* (2007)	air-air turbulent coaxial jet λ = 1, 3, 4 and 10	Standard "k-ε" first order model	• Axial velocity	• For λ < 3 there was the presence of a low pressure area which migrates to the jet axis when r tends to 3. • For $\lambda \geq 3$ it was observed the presence of a recirculation zone that approaches to the initial zone of the jets when λ was increased. • The size of the recirculation zone increases in function of the velocity ratio.
Talamelli and Gavarini (2006) Numerical and experimental	Incompressible coaxial jets Re = 10^5 $1.2 \leq U_o/U_i \leq 3.3$ external velocity kept at 30 ms^{-1}	Nd-Yag laser sheet Hot-wire	• Visualization • Axial and radial velocity • Spectral density	• Visualizations showed the presence of an alternate vortex shedding behind the duct wall separating the two jets. • The shear-layers thicknesses changed the extension of the region where the flow remained absolutely unstable, affecting also the absolute growth rate of the instability. • Three different unstable modes were observed: Mode I, a "jet mode", which was the most unstable one and was characterized by a unison displacement of the critical layers. Mode II, a "wake mode", which was the least unstable and was associated with an opposite displacement of the critical layers, and mode III, the "classical" unstable mode, due to the inflection point in the external shear layer.
Balarac *et al* (2007)	Natural unforced and excited coaxial jets Re = 3000 λ = 5 $D_i/\theta_{01} = D_i/\theta_{02}$ = 25 Sc = 1	DNS	• Rms streamwise vorticity • Mean velocity • Visualization • Radial and azimuthal turbulent kinetic energy	• Computations consisted in a natural coaxial jet, a purely axisymmetric excitation and a combined axisymmetric and azimuthal excitation, both of moderated amplitude. • In the natural jet was observed a domination of the outer Kelvin-Helmholtz vortices which impose their frequency to the inner ones, characterized by mushroom-type structures. It was observed a faster development of Kelvin-Helmholtz instability of both outer and inner layers. • For the purely axisymmetric excitation jet intense vortices were observed that allowed the engulfment of the outer stream from the beginning of the jet. Furthermore, a faster transition was formed earlier compared to the unforced case. • For the last case, the excitation was applied once more at the outer shear layer most amplified frequency. This triggers a rapid development of the outer and inner Kelvin-Helmholtz vortices implying an efficient engulfment of the outer species. The azimuthal disturbance yields an azimuthal deformation of the outer Kelvin- Helmholtz vortices leading to the early formation of counter rotating streamwise vortices.

Table 1.3. Summary of the numerical investigations related to coaxial jets. (Cont.)

Authors	Experience	Techniques	Results	Comments
Zhu and Shih (1993)	Confined coflow jets with three different turbulence models $1253.8 \leq U_J \leq 1298.8 cms^{-1}$ $7.42 \leq U_a \leq 84.48\ cms^{-1}$ D_o=16 cm; d_o=1.2 cm	Models RNG-based "*k-ε*" Realizable Reynolds stress algebraic eq. Standard "*k-ε*"	• Axial mean velocity	• The flow considered involved recirculation with infixed separation and reattachment points and severe adverse pressure gradients. • Detailed comparisons with experiments showed that the realizable Reynolds stress algebraic equation model consistently had work better than the standard "k-ε" model in capturing the essential flow features. • The RNG-based "*k-ε*" model do not demonstrated any improvements over the standard "*k-ε*" model under the flow conditions considered.
Hassel *et al* (2006) Numerical and experimental	Mixing in a coaxial jet mixer Re_d = 10000 r-mode $\dot{V}_D / \dot{V}_d$ =1.3 j-mode $\dot{V}_D / \dot{V}_d$ =5.0	LES models DGM DMM RANS models SST "*k-ε*" RSM-LRR-IP LIF LDV	• Radial mean velocity • Rms velocity	• A good agreement with measurements for averaged characteristics was achieved by RANS SST and LES DMM models for both r-mode and j-mode cases, while the other models LES DGM, "*k-ε*" and RSM gave rather poor results. • The LES DMM calculations of the rms values showed also a satisfactory agreement with measurements. • It was reported the confirmation of the qualitative observations of Barchilon and Curtet (1964) and revealed that the flow had a pronounced unsteady character and contained dominating long period oscillations occurring in an opposition-of-phase mode. • The recirculation zone contained unsteady large-eddy structures (many vortices of various sizes), that causes the intermittency of the scalar field.
Jahnke *et al* (2005)	Mixing in a coaxial jet mixer $2.5 \leq U_i \leq 20\ ms^{-1}$ $12.5 \leq U_o \leq 50\ ms^{-1}$ $5214 \leq Re_d \leq 160000$	LES	• Rms temperature fluctuations • Degree of mixedness	• For the different density ratio, numerical solutions showed an enhancement of the overall mixing along the first three diameters of the pipe if the density in the jet was lower than that in the coflow. • For the mixing characteristics of gas and liquid mixtures, while the Schmidt number reduced the role of micro-mixing in the overall mixing, the Reynolds number leaded to a strong enhancement of the mixing process. • The influence of the temperature on the integral mixing characteristics in liquid mixtures was rather poor but there was a notable influence on higher moments of temperature and velocity fluctuations.

Table 1.3. Summary of the numerical investigations related to coaxial jets. (Cont.)

Authors	Experience	Techniques	Results	Comments
Silva *et al* (2003)	Transition in high velocity ratio coaxial λ =3.3 and 23.5 Re_{D1}=3000 D_o/D_i=2	DNS	• Streamwise velocity • Vorticity	• For both flows the Kelvin-Helmholtz instability in the inner and outer shear layers resulted in a formation of vortex rings that further downstream formed an inner and outer helical structure. • It was observed that the inner rings were "locked" into the outer ones. For the case of U_2/U_1 = 23.5, the inner potential core does not exist due to the formation of a large recirculation region in x/D_1 <5.
Mitsuishi *et al* (2006) Intelligent nozzle	Scalar transport and mixing in a coaxial round jet Re=1320 D_o/D_i=2 Sc=1 λ=6.4, 9.1, 16 and 32	DNS	• Mean and rms fluctuations of axial velocity • Azimuthal vorticity • Concentration	• The intelligent modelled nozzle generated various types of flow patterns and concentration profiles depending the amplitude and frequency of the contraction. • For the best mixing case (St_a = 0.9 and ε = 0, 0.0125), it was observed a pair of counter-rotating two-dimensional vortex rings synchronously discharged with the controlled input, distorted by the streamwise vortices near the centerline. • Finally, the inner vortex rings become three-dimensional and breakdown.
Chen and Kim (1987)	Several turbulent flows with different characteristics inner and outer pipes radii=12.5; 29.5 mm Expansion ratio ≈ 1:2	Models Extended "k-ε" turbulence closure Standard "k-ε"	• Static pressure • Mean and axial velocity • Turbulent kinetic energy • Shear stress	• The modified model predicted much better results than that of the standard model. • The obtained results with the standard "k-ε" model were similar to those reported in some previous investigations.
Ranga Dinesh and Kirkpatrick (2009)	Jet precession, recirculation and vortex breakdown in turbulent jets Re=2400 to 59000 S=0.28 to 0.91	LES	• Mean axial velocity • Mean centreline axial velocity • Power spectrum	• It was observed that appears to be a relation between the central jet precessions and the axial extent of the vortex bubble, however, further investigation was required to explore the relationship between the central jet precession and the downstream vortex bubble. • The simulations of their study showed that LES seemed to be suitable for investigating instabilities in swirling jets, which they considered an important finding, since there is a need for more fundamental LES investigations on the mechanisms of instability modes and PVC in combustion systems.

Table 1.3. Summary of the numerical investigations related to coaxial jets. (Cont.)

Authors	Experience	Techniques	Results	Comments
Lin (1998)	Modelling of the confined swirling coaxial jet	Reynolds averaged eq. approach "k-ε" k-ε-v^2-f	• Axial and tangential velocity	• The dominant features of the flow were the annular recirculation zone after the expansion and the extensive central recirculation zone due to the effect of the swirling coaxial jet. • The presence of the centre and corner recirculation zones was crucial to the stabilization of the combustion zone within the combustor. • Regarding the effects of turbulence modelling, it was observed that both "k-ε" and k-ε-v^2-f models predicted well the development of the mixing layer near before the central recirculation bubble. • The overall better predictions of the scalar fields were with the use of LES.
Dianat *et al* (2006)	Confined coaxial jet	LES (assessed with TVD and DRP) DNS RANS	• Mean axial velocity • Rms fluctuations	• It was obtained an excellent agreement between the results of LES and DNS, both for dynamic and scalar fields. • The simulations had a considerable improvement over the standard eddy viscosity RANS approach. • The downstream development of the scalar field in the rapid mixing region was much better predicted by LES approach.
Wang and Bai (2004) Numerical and Experimental	Confined turbulent swirling flow in a model dump combustor Re from 10000 to 20000 S = 0, 0.33 and 0.43	LES LDV	• Mean velocity • Rms velocity	• Vortex breakdown occurred when the swirl number was high enough and lead to an internal recirculation zone (IRZ) generated near the axis. • The IRZ was found to move upstream as the swirl number increases and becomes more oscillatory at a dominant low frequency. • In the nonswirling flow turbulence was mostly generated in the shear layer near the sudden expansion. • In the swirling flows turbulence was not only produced in the shear layer near the sudden expansion, but also in the IRZ. • The decay rate increased as the swirl number was increased.

Table 1.3. Summary of the numerical investigations related to coaxial jets. (Cont.)

Authors	Experience	Techniques	Results	Comments
Fröhlich *et al* (2008)	Turbulent swirling jet S=0.93 Re_b=81000 Sc=1	Smagorinsky model with an additional bounded HLPA scheme Eddy diffusivity model	• Mean axial velocity • Mean tangential velocity • Mean concentration	• It was found that in the retraction of the pilot jet case, energetic large-scale structures were present and were generated by the retraction of the pilot jet into the tube of the main annular jet, having this a strong impact on the mixing process. In a reacting flow, they would alter considerably the combustion process.
Kornev *et al* (2008) Numerical and Experimental (water)	Scalar macro and microstructures in a confined jet Re = 10^4 $\dot{V}_D/\dot{V}_d$ = 1.3 and 5.0	PLIF "k-ε" model	• Mixture fractions	• Macrostructures of the flow in a confined jet configuration depended strongly on the flow mode. In the j-mode the structures were similar to those of the free jet. • In the r-mode the coherent vortex structures with dominant streamwise components of vorticity caused oscillations containing a dominating long period mode. • For the r-mode case, the fine structures become smaller behind the recirculation zone and were difficult to recognize visually at the end of the test section. • For the j-mode in the scalar field, it was found the presence of structures (cliffs) with a rapid change of the scalar that causes small-scale intermittency which was strongly dependent on the flow mode. • The intermittency was most pronounced in the front of the recirculation zone and become weaker on the centreline and downstream.
Nallasamy (1987)	Prediction of recirculation zones in isothermal coaxial jet flows relevant to combustors	Standard "k-ε" model	• Axial mean velocity • Axial turbulence intensity	• For a given geometrical configuration, the velocity ratio determined the axial location of the central toroidal recirculation (CTRZ) zone. • The turbulence model predicted the location, shape and size of the recirculation zones fairly well. In these regions. • The predicted axial and radial mean velocities and axial turbulence intensity were in good agreement with the measurements. • However, the redevelopment of the flow beyond the reattachment on the centrelin was slow compared to the measurements.

Table 1.3. Summary of the numerical investigations related to coaxial jets. (Cont.)

Authors	Experience	Techniques	Results	Comments
Srinivasan and Mongia (1980)	Swirling recirculating flow Co-swirl case U_i=29.65 ms^{-1} S_i = 0.577 U_o= 20.3 ms^{-1} S_o = 0.536 Counterswirl case U_i=30.33 ms^{-1} S_i = 0.49 U_o= 20.2 ms^{-1} S_o = 0.507	Original "k-ε" turbulence model Modified "k-ε" model (with Richardson number effects) Modified 2-D elliptic program	• Axial velocity	• In Task I, the inlet profiles for the mixing region were estimated by neglecting the elliptic effects of the interaction between the two co-axial streams. Uncorrected values were found near the axis of the tube and the predictions further downstream did not show any flow reversal. • In Task II, the inlet profiles for the mixing region were prescribed from the test data. The original "k-ε" model did not predict any recirculation. The modified "k-ε" model predicted a recirculation bubble near the axis of the tube in the counterswirl case, when the measured velocity profiles were used as input. The predicted recirculation bubble was elongated in the axial direction. • In the co-swirl case, the modified 2-D elliptic program predicted a recirculation bubble, while the measurements did not indicate any flow reversal. The modified 2-D elliptic program predictions for the counterswirl case were in agreement with other author's experimental data and predicted a recirculation zone.
Jackson and Lilley (1985) Numerical and Experimental	Turbulence characteristics of swirling flowfields ϕ=0, 38, 45, 60 and 70 degrees Re = 6x10^5	Hot-wire "k-ε" turbulence model	• $\overline{v'w'}$, $\overline{u'v'}$ • U, V, W, U'_{rms}, V'_{rms}, W'_{rms}, • Eddy dissipation rate • k, ε	• No recirculation zones were found in the nonexpanded flowfield across the entire section. • For the expansion cases, it was concluded that the existence, size and shape of both corner recirculation zone and the central toroidal recirculation zone were affected by the degree of swirl. • Measurements showed that increasing the swirl strength from zero to medium swirl produced shorter corner regions and the generation of a central bubble extending to approximately 1.5 chamber diameters downstream of the jet exit.

Table 1.3. Summary of the numerical investigations related to coaxial jets. (Cont.)

Authors	Experience	Techniques	Results	Comments
Salvetti *et al* (1996)	Transitional axisymmetric water coaxial jets Re=500, 1000, 1500, 2000, 2500 and 3000	DNS	• Mean axial velocity • Pressure • Vorticity	• The boundary conditions affected the dynamics of the jets, through a feedback effect by the pressure field that becomes negligible as the axial size of the computational domain was increased. • The Reynolds number affected clearly the flow. • The evolution of the large startup vortex was found to be independent of the Reynolds number, whereas the circulation per unit length at the center of this vortex increases with the Reynolds number.
Habib and Whitelaw (1985)	Confined coaxial-.jet flows. U_a/U_p = 3 and 1	"k-ε" model two Reynolds stress models	• Axial mean velocity	• The agreement between experimental data and the predicted results of the three models presents variations according to the flow conditions. • Significant discrepancies exist and the size of the recirculation zone was underpredicted by the three models with the Reynolds-stress models giving lower discrepancy. • The normal stress was underestimated by the three models particularly near the centre-line and the rate of dissipation was overestimated. • The discrepancies were associated with the streamline curvature.
Pope and Whitelaw (1976)	Near-wake flows with and without recirculation's	"k-ε" model Two Reynolds stress models	• Velocity • Correlations of velocity	• Significant discrepancies were found between measurements and predictions, that may be attributed both to inaccurate measurements, leading to erroneous boundary conditions and to deficiencies in the turbulence models. • In the turbulence models, two particular defects in the prediction of the recirculating flow were observed: the length of the recirculation region was underpredicted as was the rate at which the wake decays. • Results showed that for wakes without recirculation the particular turbulence model was less important than the boundary condition assumed in the plane of the trailing edge of the body, though the Reynolds-stress models do provided a better representation of the individual normal stresses.

1.2. Thesis Statement

The turbulent mixing of confined coaxial jets is a complex process that has a wide practical application, as described above. For most of the real engineering flows, it is desirable to achieve its complete mixing in the shortest possible length in order to get better efficiencies. One way to achieve this rate is ranging highlight the difference in speed between the two flows. And this application in fuel injection systems is quite interesting due to better mixing of fuel-air mixture, leading it to better yields and efficiencies.

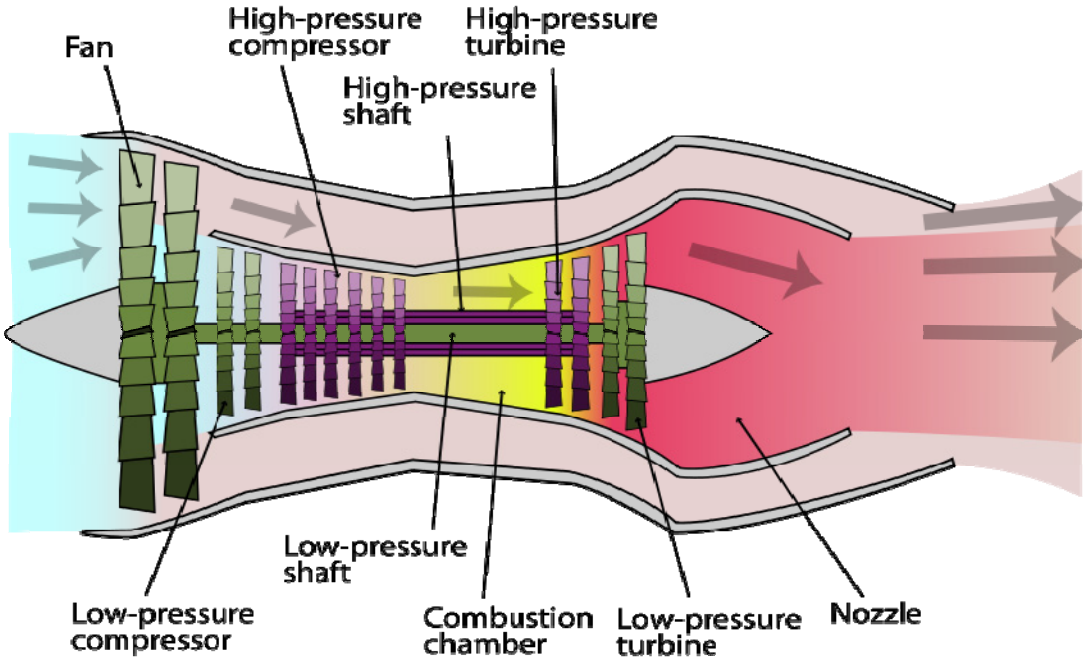

Figure 1.5. Detail of a low bypass turbofan engine.

In the specific case of the turbofan engines there has a particular interest in reducing the temperature gradient between the jet engine to be output and ambient temperature, thus achieving a lower formation of noise. There have been several studies related to the aerodynamic behavior of coaxial jets with different geometries and also with different operating parameters with different motivations. Although a wide diameters range were investigated in the past, before Ahmed and Sharma (2000) there were no reported studies for ratio diameters bellow 2, which is the case of low-bypass turbofan engines, with bypass ratios of 0.3 or lower. The present study was based on experimental work results with that aeronautics application interest made by Ahmed and Sharma (2000), where they studied the velocity ratio influence. However, there are many parameters that had influence in the mixture process.

The hypothesis of this thesis was presented in Barata *et al* (2007, 2007a), that report a numerical research using the "k-ε" to model turbulence for the Ahmed and Sharma (2000) experimental results (λ = 0.3, 1.5 and 6.0). In the numerical work a recirculation zone were

detected for the velocity ratio λ = 6.0, a situation that was not verified in the experimental work.

These facts lead this investigation towards the numerical study of the influence of the turbulence intensity on the coaxial jets with and without the favorable pressure gradient (see also Barata *et al., 2009)*. The experimental setup used by Ahmed and Sharma (2000) had a clear favourable longitudinal pressure gradient that could be the responsible to the wash away of the recirculation zone. This was confirmed in present work using the same favorable pressure gradient of the experiments, and it was than confirmed the absence of the recirculation zone reported by Ahmed and Sharma (2000). In this axisymmetric case, it was found that the axial pressure gradient plays an important role in the flow development. Additionally, the area variation in the radial direction may also be another relevant factor. To isolate any axisymmetric effect in the present study a two-dimensional geometry was adopted (see Figure 1.6).

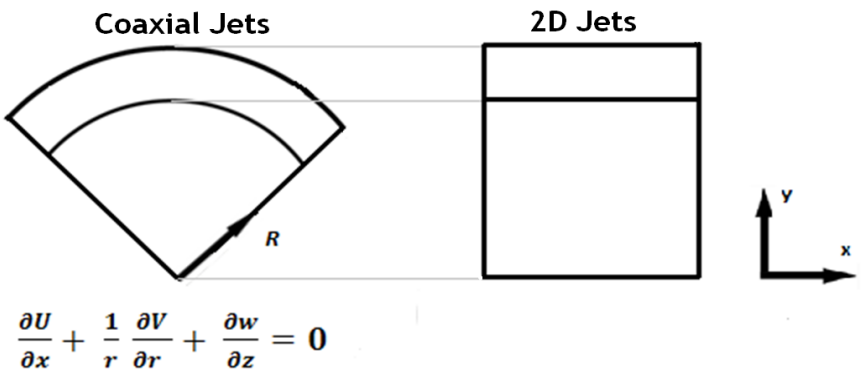

Figure 1.6. Detail of coaxial jets and 2D jets.

The width of inner and outer jets is proportional to those of the Ahmed and Sharma (2000) experimental work. In this experimental work, it was decided to study the behavior of the confined and unconfined planar jets. Since no recirculation zone emerged from the measurements of those configurations and with the previous acknowledgement that for this jets ratios and velocity ratios λ>1 the outer jet is predominant due mainly to its high turbulence intensity levels, it was then decided to vary the outer jets angle toward the inner jet in a way to accelerate the mixing propagation between jets with different velocities and thus to obtain measurements of a recirculating flow.

This result set up the reverse question: ***is it possible to generate experimentally the recirculation zone detected numerically for near zero pressure gradient? To investigate this hypothesis, the present work used a two-dimensional configuration with three parietal jets representing the inner and outer flows.***

1.3. Outline of the Thesis

The thesis is organized in four main chapters, including the present introduction. Chapter 2 describes the experimental setup and the measurement techniques used. The results are presented and discussed in Chapter 3. Finally, chapter 4 presents the main findings and conclusions of this thesis together with some future work proposals.

Chapter 2. Experimental Setup

This Chapter describes the experimental facility and other devices used in this work. The facility is described in detail together with a general description of all components of the laser velocimeter LDA technology, the flow configuration, the calibration and experimental facility setup tests as well as the used visualization technique

2.1. Introduction

The experimental facility includes a "jet"-type, subsonic open wind tunnel, with a variable speed engine attached to a centrifugal fan, the diffuser, the settling chamber, the contraction and the test section.

The flow was measured using a Flowlite 2D Laser Doppler Anemometer, a BSA F60 Flow Processor of Dantec Dynamics, interfaced to a Compaq Presario 6000 microcomputer. The LDA measurement volume was positioned with a remote controlled transversing mechanism. The flow seeding was obtained with the help of a smoke generating machine, and a purpose-built cyclone.

The wind tunnel used for this work was built thinking of a fairly wide range of experiences. The test section is very versatile. It was designed without the top and both side walls. The original test section is an open section, only with a bottom wall. The wind tunnel was entirely built in DCA - Departamento de Ciências Aeroespaciais da Universidade da Beira Interior. Its construction was made almost entirely of wood. This fact in addition to the economical costs reduction has the added advantage of being more easily include the strengthening of wall thickness with side bars, allowing a significant reduction of vibration inherent in its operation period.

Since all measurements had to be performed with laser light, it would be desirable the least possible interference from outside light. Therefore, all measurements for this study, either for the facility calibration or for the parametric study purpose were carried out in similar lightness conditions. Therefore, to avoid any laser disruption the laboratory was always kept in the dark regardless the measurements daily time period.

2.2. Facility description

2.2.1. Engine and Fan

A centrifugal fan, with a maximum flow rate of 3000 m^3/h was driven by a Siemens engine with 15 kW of nominal power (see Table 2.1 for details). For the speed control of the flow, it was used a MICROMASTER 430 electronic frequency converter device.

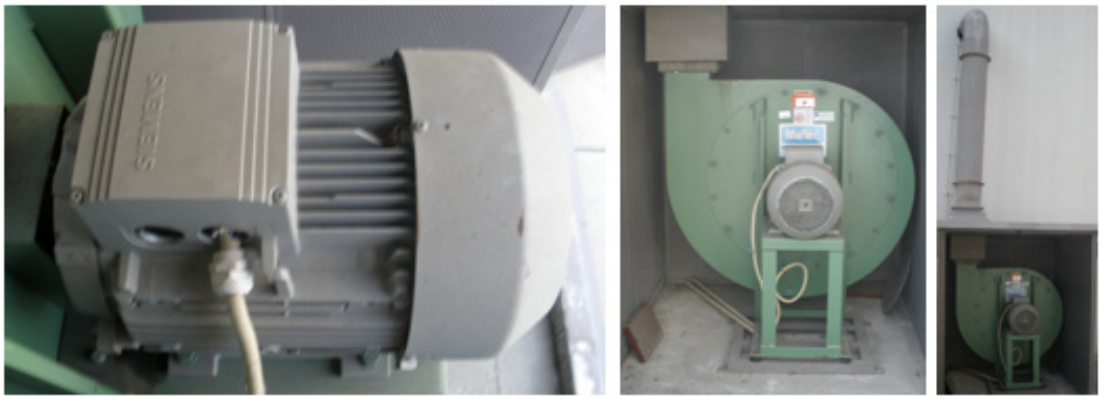

Figure 2.1. Detail of the engine (left) and the attached fan (middle and right).

The tunnel entrance was an adaptation of the circular profile of the nozzle from the fan for the rectangular section of the entry of the divergent. The adaptation was performed on metal tube, with the side of the circular profile with 300 mm diameter and rectangular output dimensions 184 x 300 mm. Figure 2.2 illustrates a general wind tunnel panoramic. The test section configurations are detailed presented in Figure 2.20.

Table 2.1. Centrifugal Fan Data Table.

Capacity	3000 m^3/h
Pressure	1200 mm of water column Static Discharge
Dynamic Pressure	54 mmca
Total Pressure	1254 mm of water column
Rotation Speed	2935 rpm
Maximum Power	15 kW
Eficiency	73 %

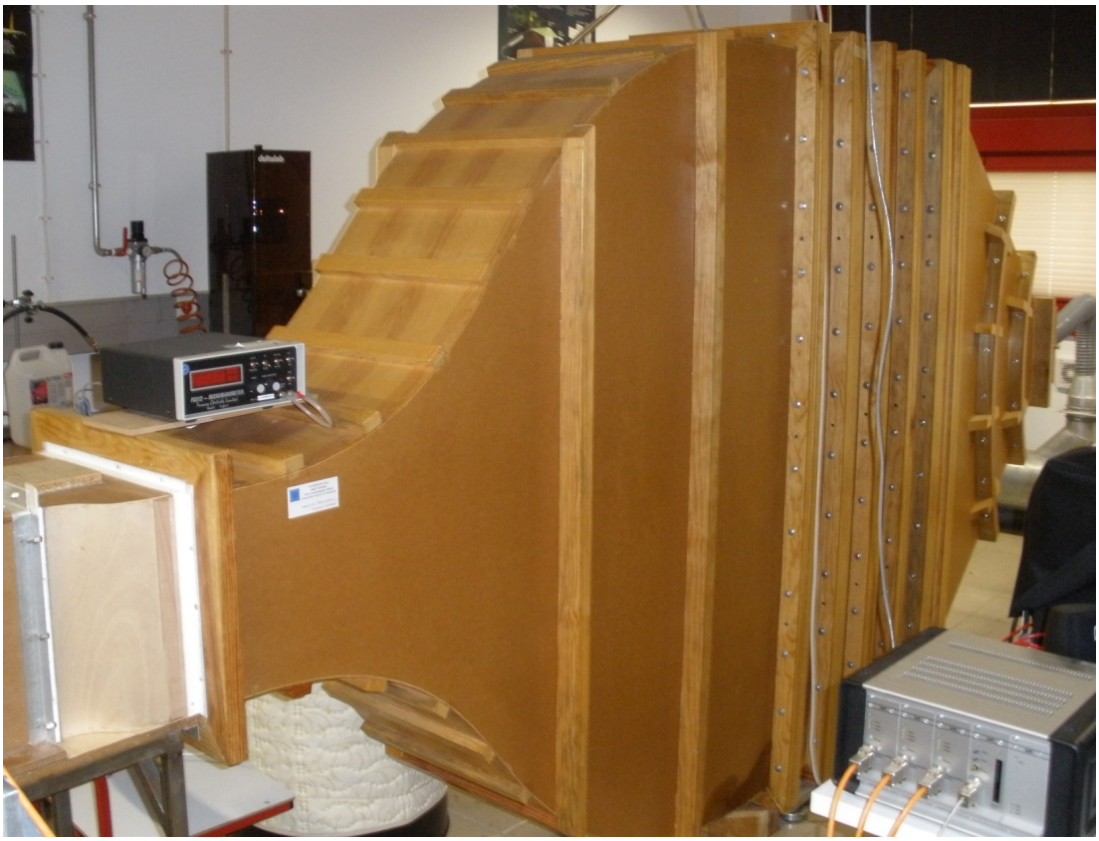

Figure 2.2. General panoramic of the wind tunnel photograph.

2.2.2. Diffuser

Despite the widely usage of diffusers, their flow characteristics are still not fully understood. The flow through a diffuser inevitably depends on its geometry, defined by vast important parameters: area ratio, wall expansion angle, cross-sectional shape, wall contours, and conditions at entry and exit and eventually boundary layer control devices. Even so, it becomes difficult to predict the flow through a diffuser with an arbitrary combination of these parameters. And even so, it becomes further complicated by the occasional presence of boundary layer separation caused by the adverse pressure gradients necessarily present in diffusers.

The design of this diffuser was take into account some critical points: the angle of expansion should not be greater than 7º (Mehta and Bradshaw, 1979), preferably below 5º (Barlow, Rae and Pope, 1999) to prevent separation of the flow. In this case, the angle of the vertical walls is only 4.146º, but in the case of the lower and upper walls angle is ± 30.237º to limit the diffuser length, which implies the use of screens to control the turbulent nature of flow and prevent their separation[43]. The four most important parameters in a wide-angle diffuser are (Mehta and Bradshaw, 1979): the area ratio, A; the diffuser angle, 2θ; the

[43] - Castro, P., "Estudo Experimental da Interacção de um Jacto de Parede e uma Camada Limite", Projecto Final de Curso, Departamento de Ciências Aeroespaciais, Universidade da Beira Interior, Covilhã, 2004.

number of screens within the diffuser, n and the total pressure drop coefficient of all screens, K_{sum}.

The design of the diffuser was taken into account other important aspects such as inlet conditions, screen positioning, wall shape, screen shape and cross-sectional shape. Through observation of different graphical displays (Mehta and Bradshaw, 1979), it was concluded that for this case, the ideal is the use of three screens that can ensure the complete control of the boundary layer.

2.2.3. Settling Chamber

The settling chamber usually includes a honeycomb flow straightener and wire mesh smoothing screens that produce a smooth airflow. The usual arrangement of a honeycomb (with about 25000 cells) followed by screens, the number and K-value depending on the turbulent level requirements. If a severe yaw or swirl is expected in the flow from the wide-angle diffuser, it is advisable to install one screen upstream of the honeycomb, so that the flow angles are reduced (Mehta and Bradshaw, 1979).

Beyond these considerations, was also taken into account that a screen combination with a spacing equivalent to about 0.2 settling chamber diameters performs successfully. To calculate the open area ratio (β), the ratio of pressure drop (K), and to choose the material to use, it was followed the recommendations of Mehta, 1985. A screen with K=1.5 reduces yaw and swirl angles by a factor of about 0.7 for swirl angles of about 40º. The honeycomb should be installed some way downstream of the wide-angle diffuser exit, so that the flow static pressures and angles have had a chance to become more uniform. A more detailed analysis carried out by Batchelor (1953) showed that the speed excess is eliminated to K≈2.8. The options for the screen turned in favour to stainless steel, with a β value slightly above 0.57 as recommended to avoid instabilities. The value of K was slightly higher than 2.8, causing only a small increase in the pressure loss. The honeycomb is effective in removing the lateral variable side of the mean velocity and in removing the rotational movements of the flow, since the angle of incidence in the comb does not exceed 10º. According to Mehta and Bradshaw (1979), it is desirable to have at about 150 cells per settling chamber diameter. The elimination of turbulent undesirable effects is achieved with a honeycomb length near to 6-8 cell diameters. According to Barlow, Rae and Pope (1999), the hexagonal shape is the one that ensures better results. It was adopted the option of an aluminium honeycomb with a length equal to 8 times its diameter, with about 30000 cells[43].

2.2.4. Contraction cone

The contraction cone's purpose is to take a large volume flow of low velocity air and reduce it to a small volume of high velocity air without creating turbulence. A contraction increases the mean velocity which allows the honeycomb and screens to be placed in a low speed region, thus reducing pressure losses and reduces both mean and fluctuating velocity variations to a smaller fraction of the average speed (Mehta and Bradshaw, 1979). The design

of a contraction is centred on the on the uniform and steady stream production at its outlet and requires the flow separation avoidance. The most important single parameter in determining these effects is *c*, the contraction ratio. Two more desirable criteria include minimum exit boundary thickness and minimum contraction length.

The contraction cone design of this wind tunnel was based on the Morel (1975) method, detailed in Morel (1977). Its contraction ratio is 6:1. It has been designed so that the airflow coming from the settling chamber, leads to the test section with a cap-type profile, thus enabling a laminar boundary layer at the test section entrance[43]. This requirement stems from the desired fact to provoke an entirely controlled boundary layer transition, and thus to be able to obtain previously specified turbulent flows.

2.2.5. Test section

The test section requires such a manufacturing and assembly care, allowing so the best flow uniformity, free from angles and with minimal eddies (Fox and McDonalds, 1998). The overall objective is to get a streamlined constant parallel flow in this section, with uniform speed, as much as possible. For this study, it was created four different configurations to be tested in the test section. These settings are detailed in the Figure 2.20.

2.2.6. Electronic frequency converter device

For the speed control of the flow, it was used a MICROMASTER 430 electronic frequency converter device (Figure 2.22, left). With its features and default settings the MICROMASTER 430 is particularly suitable for use in pumps and fans. The inverters are microprocessor controlled and use IGBT (Insulated Gate Transistor Bipolar) last generation, making them reliable and versatile. A special method for modulation band pulse, with selectable pulse rate, provides silent operation of the engine. The extensive protection features available to them, provide excellent protection from both the converter, as the engine.

2.2.7. Digital micromanometer

The digital micromanometer used was a FCO12 (model 2) of Furness Controls Limited. This micromanometer (Figure 2.22) was connected to a Pitot tube, placed at the test section entrance. Its scale is from 0 - 20 mmH_20 with a ± 1% precision, with a measuring speed range from 0 to 18 ms^{-1}. The velocities were calibrated using the micromanometer and the laser. To control de mean velocity it was decided to maintain identical the values of the micromanometer pressure, for each frequency value (0.53 mmH_2O for 30 Hz and 0.99 mmH_2O for 40 Hz).

2.2.8. Cyclone

The seeding insemination of the flow to study is done through a cyclone created for this work. This device is connected to the smoke machine by one of the extremity of a rubber tube with about 4 cm of circular section. The smoke machine is connected to a compressor that will charge the constant 1 bar pressure in all measurements to be made. The other end of this tube enters the main body of the cyclone with a slope of about 45º up. This tube end was also designed to make possible that the flow exhaustion to the cyclone could be made with a minimum angle with respect to the cyclone wall, in a way to avoid flow perturbation. After that, the flow then rises in spiral form in a circular cross section of 16 inches, which leads to a conical contraction that ends with a circular cross section of about 6.5 mm. The output of this little section is the end of the cyclone. Hence, the flow goes through a connecting rubber pipe with the same circular cross section. This connecting tube is connected to a similar circular cross-section metal tube that will be used to perform the work measurements, the seeding tube. The seeding tube pierces the south/north test section in the middle and has longitudinally and in the same direction, spaced small holes of 1 mm circular cross-section. All these holes were 1 cm spaced between them. The north end of the seeding tube is sealed and its working position is with the holes facing in favour of the motion of the flow to study.

2.3. Laser Doppler Anemometry (LDA) description

Turbulent motion has proven to be one of the most difficult problems to solve in the physical sciences over the last century. As basically, almost all industrial flows and in general almost all flows that occur naturally on land, sea or atmosphere are turbulent, it is of utmost importance to understand the underlying mechanisms in these complex flows as this issue has a vast range of interest and applications in many fields of engineering and science. Claude-Louis Navier[44] and George Gabriel Stokes[45] developed a set of equations capable of describing liquids and gases flow. These equations establish that changes in momentum and acceleration of a fluid particle are simply the result of pressure changes and dissipative viscous forces that act within the fluid. Together with supplemental equations such as the conservation of mass equation and well formulated boundary conditions, these Navier–Stokes equations seem to

[44] - Claude Louis Marie Henri Navier (10.02.1785 - 21.08.1836) was a French engineer and physicist who specialized in mechanics. In 1819 he succeeded in determining the zero line of mechanical stress, finally allowing correcting Galileo Galilei´s incorrect results. In 1821 he formulated the general theory of elasticity in a mathematically usable form making it available to the field of construction with sufficient accuracy for the first time. In 1822 he has his major contribution, which remains the Navier–Stokes equations, central to fluid mechanics. In 1826 he established the elastic modulus as a property of materials independent of the second moment of area.

[45] - Sir George Gabriel Stokes (13.08.1819 – 01.02.1903) was an Irish mathematician and physicist. At Cambridge he made important contributions to optics, and mathematical physics. It´s major contribution was central to fluid dynamics (Navier–Stokes equations). He was secretary, then president, of the Royal Society.

model fluid motion accurately. A solution of these equations is the velocity field or flow field, which is the description of the velocity of the fluid at a given point in space and time.

On average, even turbulent flows seem to agree with real world observations. However, theoretical understanding of the Navier-Stokes equations is incomplete. Nevertheless and in these turbulent cases, the solutions of these equations remains one of the greatest unsolved problems in physics despite its immense importance in science and engineering knowledge, maybe even impossible to solve.

Measurements by LDA, on the other hand are easier to make, and cover several fairly broad research fields. In industrial field could be useful to investigate technical problems, to check technical specifications and to verify and/or improve performance. In the engineering areas could be used to determine parameters in turbulence mode, develop, extend, and refine models or to investigate models limits. On the Fluid Mechanics Theory could be used on the forecasting of models investigations, theoretical investigations of the predictions and verification of new concepts. In terms of ideas conceptualization could stimulate demand of new ideas.

This subchapter presents a very brief historical presentation of the Laser Doppler Anemometry as well as some generic characteristics and applications of LDA, details of principles of the used LDA, and the operational procedure of the used LDA for this work.

2.3.1. Introduction

Usually a LDA basic equipment consists of a laser beam generator, a optical transmitter, a optical receiver, a signal processor unit through a manual or automatic mechanism for transmitting and receiving optics, an oscilloscope, a seeding generator and a relatively large capacity hard drive computer with a management and data acquisition software for data manipulation. These non-intrusive optical instruments for the fluid flow structures in liquids and gases investigations owe their existence of the invention of the gas laser in the early sixties. It is a technique that has ranged from the simple technique of smoke and dye injection for flow path visualization to more sophisticated schlieren and interferometer methods, which actually measured one-dimensional integral values of a density field but permit velocity information to be extracted from the relationship between the density field and the velocity distribution.

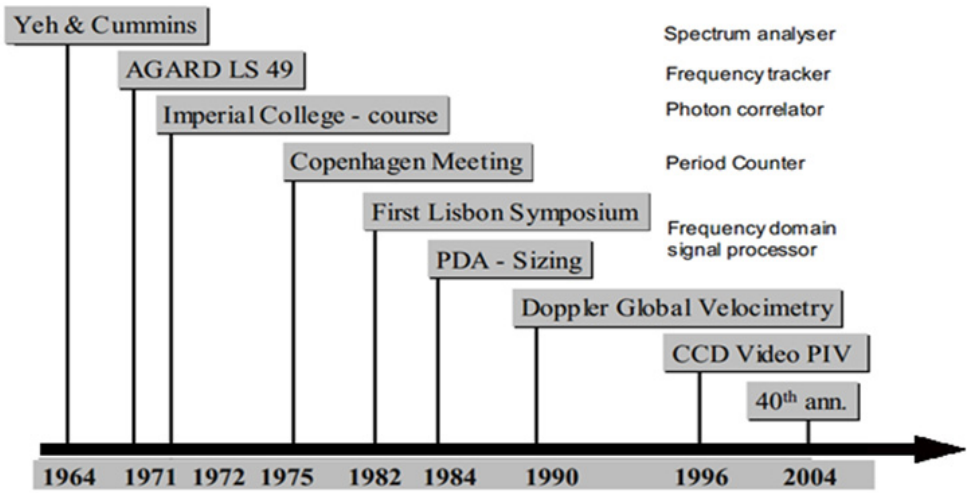

Figure 2.3. Simplified chronology of 40 years of Laser Doppler Velocimeter.

This optical technique (reference-beam LDA) with no calibration required was first reported by Yeh and Cummins (1964) and in its simplest form consists on crossing two beams of collimated, monochromatic, and coherent laser light in the flow of the fluid being measured. Figure 2.3 summarizes the LDA 40 years of history (Riethmuller, M. L., Von Kármán Intitute for Fluid Dynamics, & Boutier, A., ONERA DSG/GS). These two beams are usually obtained by splitting a single beam, ensuring coherency between them, and are made to intersect at their waists (the focal point of a laser beam), where they interfere and generate a measurement volume with a set of straight fringes[46]. One sensor is then aligned to the flow such that the fringes are perpendicular to the flow direction. Small liquid entrained particles are inseminated in the flow to study. As these particles pass through the fringes, they produce a burst of reflected light into a photodetect. By measuring the Doppler frequency-shift of the scattered light, it is possible to calculate the velocity of the tracer particle and thus the flow velocity. This technique has a very high accuracy, a very high spatial resolution due to small measurement volume; however tracer particles are required. Its applications could be extended to laminar and turbulent flows, investigations on aerodynamics, supersonic flows, turbines, automotive, liquid flows, surface velocity and vibration measurement, hot environments (flames, plasma etc.) and velocity of particles.

[46] - Two intersecting beams intersect and form the measurement volume with a fringe pattern of high and low intensity which looks like bright and dark stripes/planes, leading this to become known by the fringe model (Figure 2.3.12). When the particle traverses this fringe pattern, the scattered light fluctuates in intensity with a frequency equal to the velocity of the particle divided by the fringe spacing.

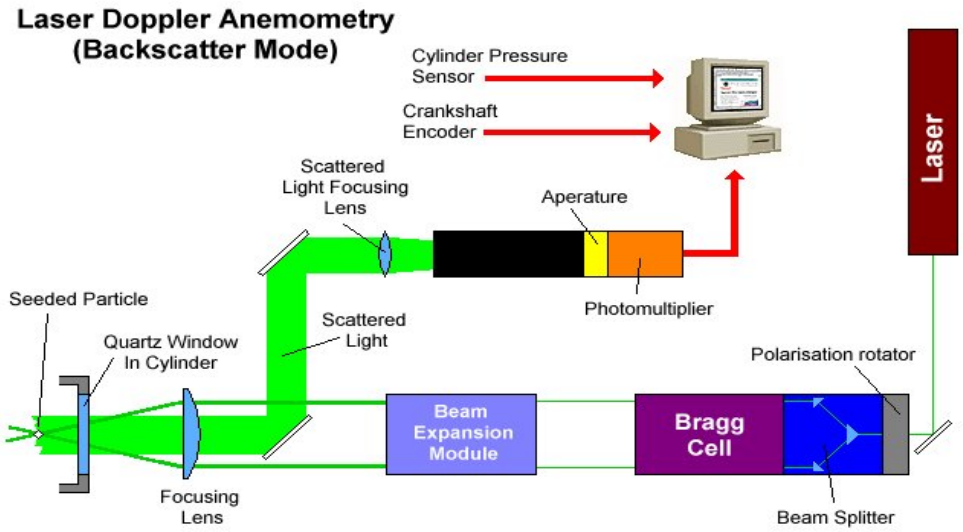

Figure 2.4. Scheme of a back scattered LDA[47].

For this work, it was used a Flowlite 2D backscattering LDA from Dantec Dynamics. The backscattering LDA allows for the integration of transmitting and receiving optics in a common housing, saving the user time-consuming work aligning separate units. The main characteristics of the used 2D LDA for this work are described in table 2.2. The red laser operates at 632.8 nm and the green laser operates at 532 nm.

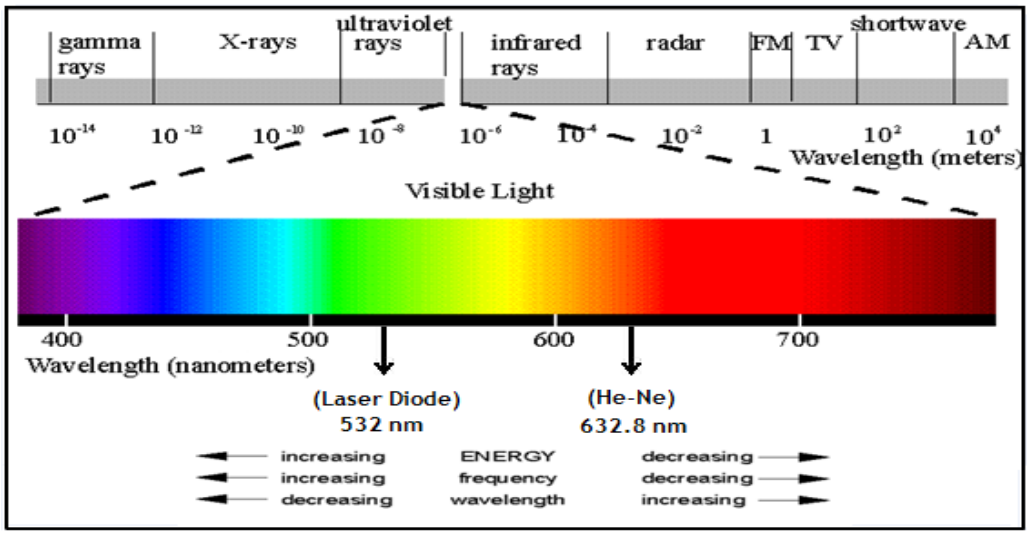

Figure 2.5. Electromagnetic spectrum.

[47] - http://www.eng.warwick.ac.uk/oel/courses/engine/ic036.htm [accessed on 12.05.2010].

Table 2.2. Main characteristics of the LDA.

Wavelength, λ [nm]	632.8 (He-Ne)	532 (Laser Diode)
Focal length of focusing len, f [mm]	400	400
Beam diameter based on the e^{-2} intensity, [mm]	1.35	1.35
Beam spacing, s [mm]	38.87	39.13
Calculated half-angle at the beam intersection, θ [°]	2.78	2.8
Fringe spacing, δ_f [μm]	6.53	5.45
Velocimeter transfer constant, K [MHz/ms^{-1}]	0.153	0.183
Diameter of the measurement volume [mm]	0.135	0.112
Number of fringes	21	21

2.3.2. Principles of LDA

The principles of an LDA rely in three parts: a scattering system which is considered to consist of a fixed light source, a moving object (i.e. a small particle) and a fixed observer to receive the light scattered by the moving particle.

2.3.2.1. Laser beam

Although the laser beam visually straight and constant thickness appearance, his real form is more like the Figure 2.6 type. All measurements take place in the beam waist to get optimal performance from any LDA equipment. Along the cross section, the intensity has a Gaussian[48] distribution and the width of the beam is usually defined by the edge-intensity being e^{-2} = 13% of the core intensity. The beam waist is a location along the propagation direction where the beam radius has its minimum. The waist of the laser beam coincides with the focal point of the lens on the LDA head, as well as the crossing of two laser beams in a beam pair at the beam waists has been thus ensured. At this point the cross section attains its smallest value and the laser beam is uniquely described by the size and position, i.e., with a known wavelength λ of the laser light, the laser beam is uniquely described by the d_0 size and the position of the beam waist.

[48] - Johann Carl Friedrich Gauss (30.04.1777 – 23.021855) was a German mathematician and scientist who contributed significantly to many fields, including number theory, statistics, analysis, differential geometry, geodesy, geophysics, electrostatics, astronomy and optics. Gaussian distribution is a continuous probability distribution that is often used as a first approximation to describe real-valued random variables that tend to cluster around a single mean value. The graph of the associated probability density function is “bell”-shaped, and is known as the Gaussian function or bell curve.

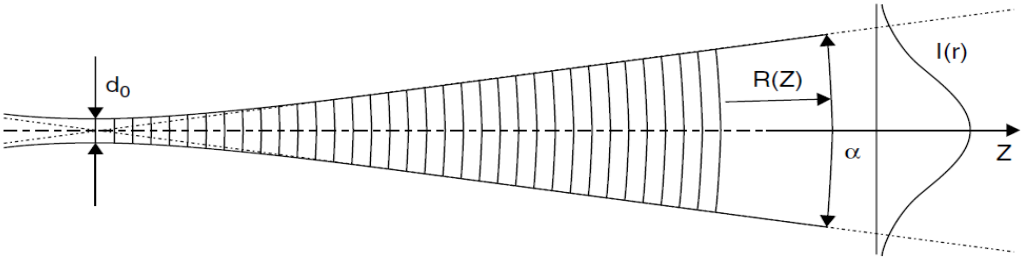

Figure 2.6. Laser beam with Gaussian distribution[49].

2.3.2.2. Doppler[50] Effect

As indicated by the Laser Doppler Anemometry name, Doppler effect plays an important role. LDA utilizes the Doppler effect to measure instantaneous particle velocities. When particles suspended in a flow are illuminated with a laser beam, the frequency of the light scattered (and/or refracted) from the particles is different from that of the incident beam. This difference in frequency, the Doppler shift, is linearly proportional to the particle velocity. This principle is showed at Figure 2.7, left), where *U* represent the particle velocity, and the e_i and e_s are unit vectors describing the direction of incoming and scattered light respectively. According to the Lorenz-Mie[51] scattering theory, the light is scattered in all directions at once, but the users can only consider the light reflected in the direction of the LDA receiver. In the intersection beams case, the scattered light is a result of the light scattered from two intersecting laser mixed beams e_1 and e_2 (Figure 2.7, right). And as a result of this incoming both laser beams are scattered towards the receiver, but with slightly different frequencies due to the different angles of the two laser beams.

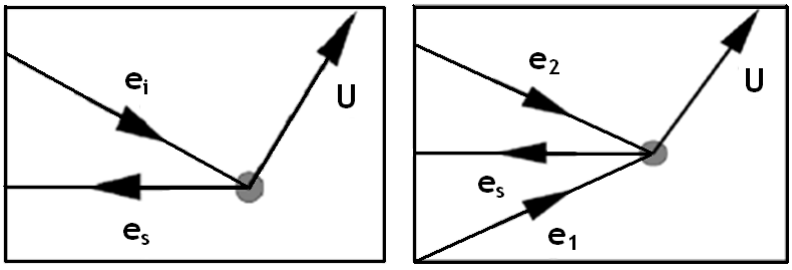

Figure 2.7. left) light scattering from a moving seeding particle; right) Scattering of two incoming laser beams.left)[52] light scattering from a moving seeding particle; right)[53] Scattering of two incoming laser beams.

[49] - BSA Flow Software, Installation & user´s guide, Vol. 1.

[50] - Named after Christian Andreas Doppler (29.11.1803 - 17.03.1853), an Austrian mathematician and physicist who proposed it in 1842 in Prague. Doppler effect or Doppler shift is a change in frequency of emitted waves produced by motion of an emitting source relative to an observer.

[51] - Mie solution to Maxwell's equations (also known as the Lorenz-Mie solution, the Lorenz-Mie-Debye solution or Mie scattering) describes the scattering of electromagnetic radiation by a sphere.

[52] - BSA Flow Software, Installation & user´s guide, Vol. 1.

The superposition of two light waves of different frequencies leads to the optical interference (Figure 2.8). According to that illustration, the two harmonic waves a) of the laser beam E_a, and b) of the laser beam E_b assumed to have different amplitudes and frequencies. At a given time the spatial distribution of this superimposed wave can be obtained, as shown in Figure 2.8c). For simplicity only the plane waves are considered, which propagate in the *x*-direction. In that direction, the flux density is proportional to E_m^2 and oscillates with an angular frequency of $2\omega_m = \omega_a - \omega_b$ which is known as the beat frequency (Figure 2.8d). As a consequence of these super-imposed two wave trains of slightly different frequency, the result is that they are intermittently interfering with each other constructively and destructively, generating the beat frequency or the Doppler frequency phenomenon.

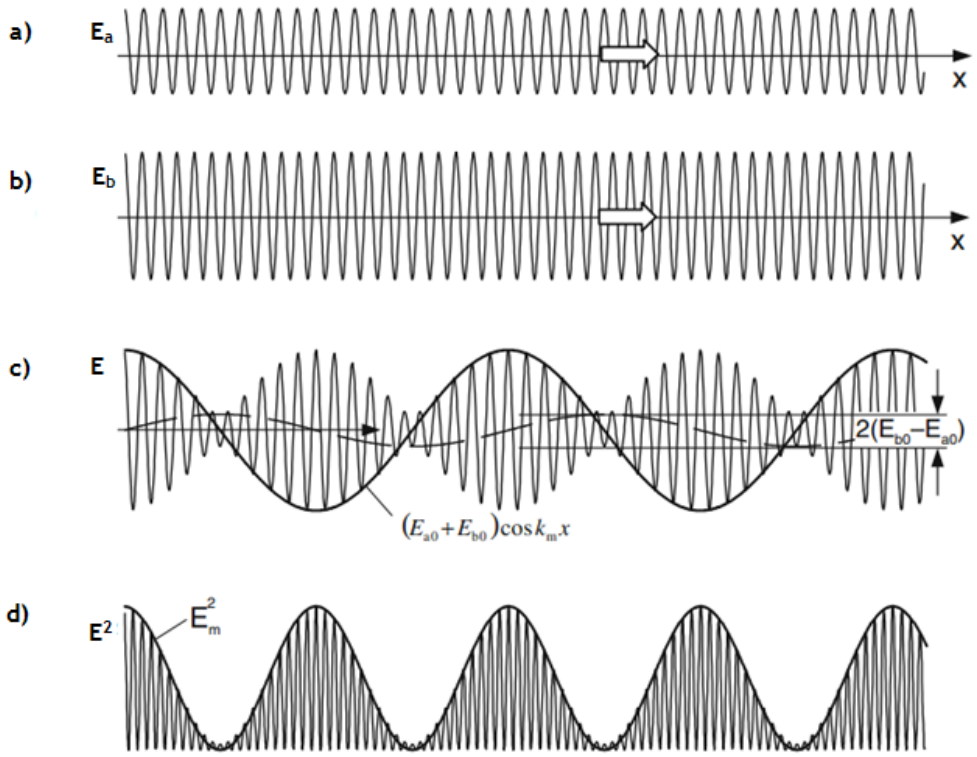

Figure 2.8. Superposition of two light waves .Superposition of two light waves[54].

LDA is a measuring technique that enables to follow instantaneous velocity of the fluid by the detecting the frequency shift of laser light that has been scattered by small particles suspended in the flow (Figure 2.9). Thereafter, Doppler effect could be described using the following vector formula:

[53] - BSA Flow Software, Installation & user´s guide, Vol. 1.

[54] - Zhang, Zh., "LDA Application Methods, Laser Doppler Anemometry Fluid Dynamics", e-ISBN 978-3-642-13514-9, Springer-Verlag Berlin Heidelberg 2010.

$$f_{sc} = f_l + \frac{\vec{U}}{\lambda}(\vec{e}_2 - \vec{e}_1) \quad (1)$$

and its scalar representation:

$$f_D = f_{sc} - f_l = \frac{2}{\lambda} U_x \sin\left(\frac{\theta}{2}\right) \quad (2)$$

Where:

$\vec{U}$	Instantaneous velocity vector;
$\vec{e}_1,\ \vec{e}_2$	Unit vectors of directions of the laser beams;
f_l, f_{sc}	Frequencies of the laser beams and light scattered by moving object, respectively;
θ	Angle between laser beams;
l	Wavelength of laser light;
f_D	Doppler frequency (Doppler shift of frequency);
U_x	Velocity component lying in the plane created by laser beams and perpendicular to the line that halves the angle θ.

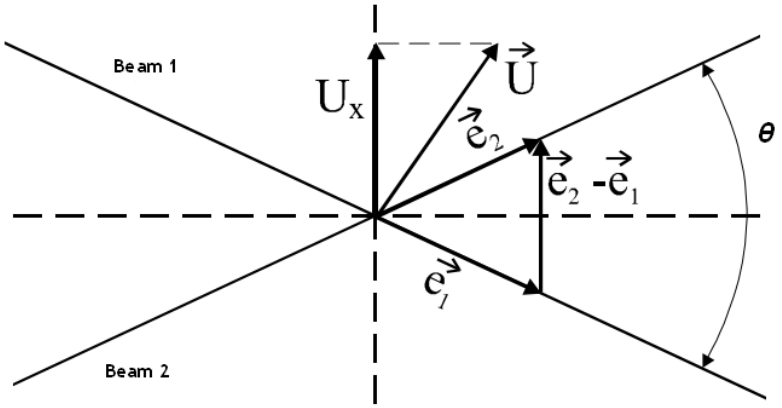

Figure 2.9. Scheme of the Doppler effect.

2.3.2.3. Frequency to velocity conversion

The Doppler frequency is equal to the dot product of the particle velocity with the difference between the scattered and the incident wave vectors. When observed at a single detector, the direction of the scattered wave vectors (causing both Doppler shifts) is the same. Therefore, the Doppler frequency created by the two Doppler shifts is equal to the dot product of the particle velocity and the difference of the incident wave vectors. This Doppler frequency is no longer a function of the angle of detection. The relation obtained using the Doppler shift model yields the same result that was obtained using the interference model:

the constant of proportionality between velocity and Doppler frequency is the calibration factor (*K*). The frequency to velocity conversion is illustrated in Figure 2.10.

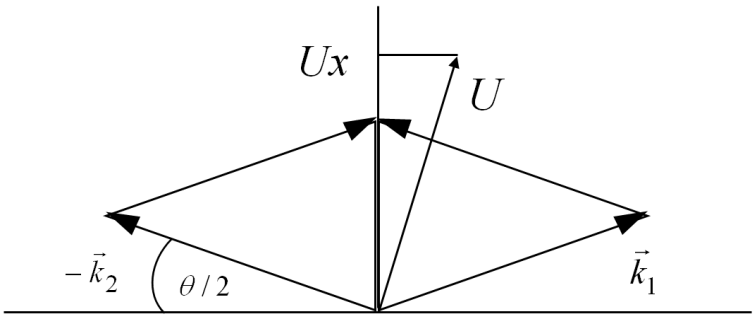

Figure 2.10. Frequency to velocity conversion scheme[55].

The frequency of the *Doppler burst* f_D is the velocity of the particle normal to the fringes U_x divided by the fringe spacing δ_f,

$$f_D = \frac{U_x}{\delta_f} \quad (3)$$

Since the fringe spacing is a function of the laser wavelength λ and crossing angle θ, the Doppler frequency becomes:

$$f_D = \frac{2U_x}{\lambda \sin\,(\theta/2)} \quad (4)$$

The Doppler–frequency is directly proportional to the x-component of the particle velocity, and the velocity can thus be calculated directly from f_D:

$$U_x = \frac{\lambda}{2\sin\,(\theta/2)} f_D \quad (5)$$

And the Calibration factor, *K*:

$$K = \frac{\lambda}{2\sin\left[atan\,(\frac{s}{2L})\right]} \quad (6)$$

where:

s is the beam spacing, and

L is the front lens focal lenght.

[55] - http://faculty.ksu.edu.sa/azzeer/Documents/534%20PHYS/LN7_LDA_s.pdf

2.3.2.4. Optical principle

A flow is seeded with small, neutrally buoyant particles that scatter light. When a particle passes through the intersection volume formed by the two coherent laser beams, the scattered light, received by a detector, has components from both beams. The components interfere on the surface of the detector. Due to changes in the difference between the optical path lengths of the two components, this interference produces pulsating light intensity, as the particle moves through the measurement volume.

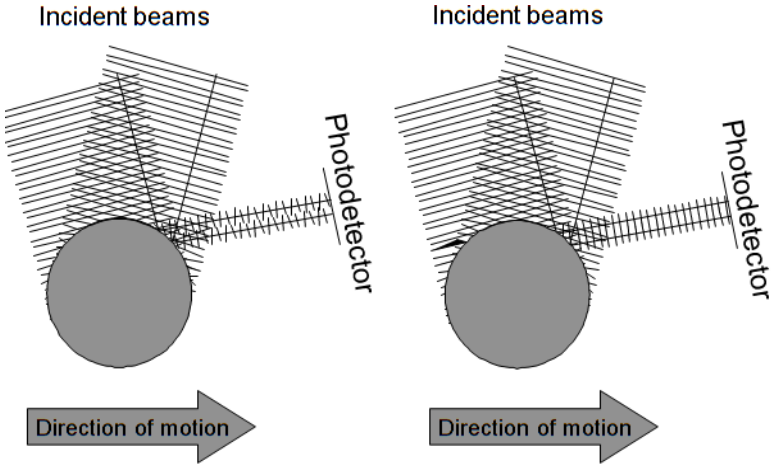

Figure 2.11. Photo-detector receiving light scattered[56] from the surface of a reflecting spherical seeding particle.

2.3.2.5. Transmitting and receiving systems

Generically, the transmitting system has two main functions: measuring the volume formation and the introduction of a frequency shift. A basic model of the transmitting optics, consist of a beam splitter (BS, Figure 2.12, left) and achromatic lens. The beam splitter is adjusted to divide the beam from the laser and split into two identical beams with approximately the same intensity. In one of the beams, an acoustical-optical Bragg[57] cell is inserted. This component introduces a fixed frequency shift in the particular beam, allowing the users to determine the sign of the measured velocity and the flow direction. The front lens deflects the two beams so they intersect. A combination of lenses in front of or replacing the front lens converts the beams exiting the optical system to beams of greater width. At the same time the spacing between the two laser beams is increased, since the beam expander also increase the aperture. Providing that the focal length (F, see Figure 2.12)

[56] - http://faculty.ksu.edu.sa/azzeer/Documents/534%20PHYS/LN7_LDA_s.pdf

[57] - William Henry Bragg (02.07.1862 - 10.03.1942) was a British physicist, chemist and mathematician. His son, William Lawrence Bragg (31.03.1890 - 01.07.1971) was an Australian-born British physicist and X-ray crystallographer, discoverer (1912) of the Bragg law of X-ray diffraction, which is basic for the determination of crystal structure. In 1915 father and son were jointly awarded the Nobel Prize in Physics for their studies, using the X-ray spectrometer, of X-ray spectra, X-ray diffraction, and of crystal structure. The mineral Braggite is named after William Henry Bragg and William Lawrence Bragg.

remain unchanged, the larger beam spacing will increase the θ angle, thus reducing the size of the measuring volume and increase power density. In the intersecting volume, seeding particles will scatter the incoming laser light.

The receiving optics system (Figure 2.12, right) is composed mainly by the receiving optics, a fibre cable (connecting the probe and acting as a spatial filter), an interference filter and a detector composed by photodetectors (photomultipliers) and photodiodes. Part of the incoming light is scattered backwards toward the front lens and is split into colours and directed to particular photodetectors, which are able to distinguish the information from different velocity components.

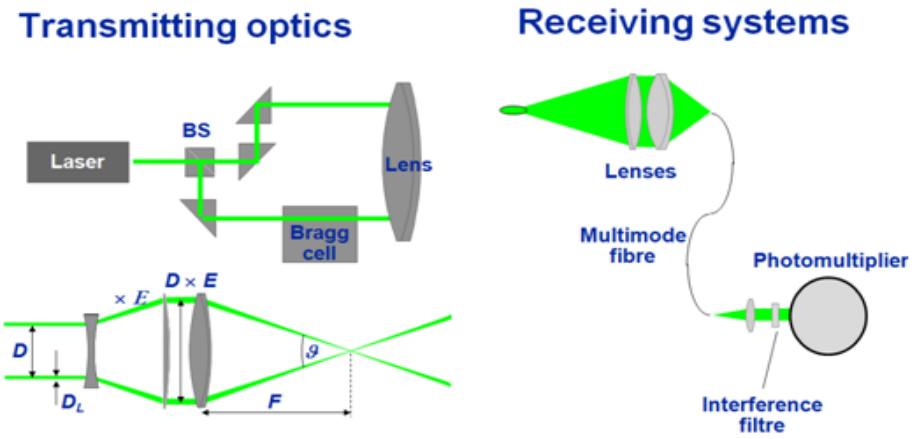

Figure 2.12. Transmitting and receiving systems of a LDA[58].

2.3.2.6. Directional ambiguity / Frequency shift

Particles moving in either the forward or reverse direction will produce identical signals and frequencies. Once that negative velocities $U_x<0$ will produce negative frequencies $f_D<0$, the receiver system could not distinguish between positive and negative frequencies, and as a consequence of that it will be ambiguity in the measured velocities (Figure 2.13, right, top).

In order to solve the directional ambiguity problem, a slab of glass kwon as Bragg cell is introduced in path of one of the laser beams. On one of its side, an electro-mechanical transducer driven by an oscillator produces an acoustic wave propagating through the slab, generating a periodic moving pattern of high and low density. The opposite side of the slab is shaped to minimize reflection of the acoustic wave and is attached to a material absorbing the acoustic energy. The incident light beam hits a series of travelling wave fronts which act as a thick diffraction grating. The interference of the scattered light by each acoustic wave front causes a maximal intensity to be emitted in several directions. By adjusting the

[58] - http://faculty.ksu.edu.sa/azzeer/Documents/534%20PHYS/LN7_LDA_s.pdf

acoustical signal intensity and the tilt angle θ_B, of the Bragg cell, the intensity balance between the direct beam and the first order diffraction can be adjusted.

The Bragg cell adds a fixed frequency shift f_0 to diffracted beam (Figure 2.13, right, bottom). And since the particle velocity does not introduce a negative frequency shift numerically larger than f_0, the Bragg cell will ensure a measurable positive Doppler frequency, f_D. This frequency shift allows measurements of velocities without directional ambiguity down to:

$$U_x > -\frac{\lambda f_0}{2 \sin(\theta/2)} \quad (7)$$

As typical values might be λ = 500 nm, f_0 = 40 MHz, θ = 20°, allowing for a measurement of negative velocity component down to:

$$U_x > -\frac{500 \cdot 10^{-9} m \cdot 40 \cdot 10^{6} s^{-1}}{2 \sin(20°/2)} \quad (8)$$

which gives U_x>-57.6 ms^{-1}. Upwards the maximum measurable velocity is limited only by the response-time of the photo-multiplier and the following signal-conditioning electronics. Resuming, with frequency shift in one beam relative to the other, the interference fringes appear to move at the shift frequency and with frequency shifting negative velocities can be distinguished.

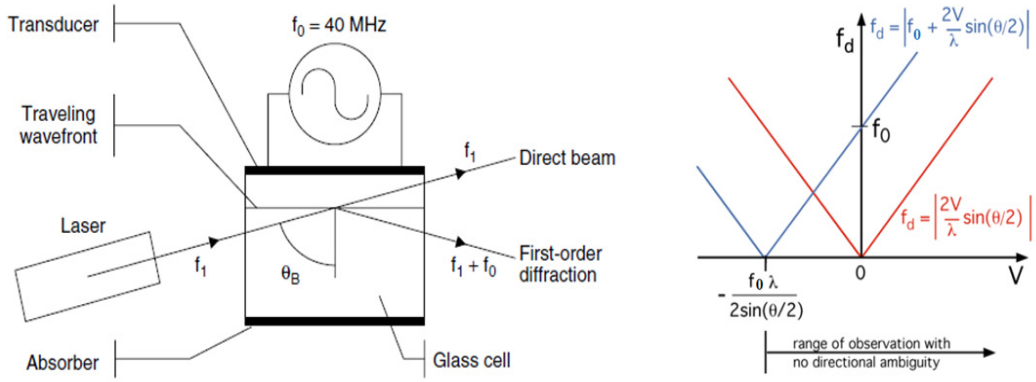

Figure 2.13. Bragg cell (left)[59]; Directional ambiguity without frequency shift (right, red line)[60]; Solved directional ambiguity using frequency shift (right, blue line).

2.3.2.7. The fringe model

When two coherent laser beams intersect, they will interfere in the measurement volume. If the beams intersect in their respective beam waists, the wave fronts are approximately plane, and consequently the interference produce parallel planes of light and

[59] - BSA Flow Software, Installation & user´s guide, Vol. 1.

[60] - http://web.mit.edu/fluids-modules/www/exper_techniques/LDA.text.pdf

darkness as shown in Figure 2.14. The interference planes are known as fringes, and the distance between them δ_f, depend on the wavelength and the angle between the incident beams:

$$\delta_f = \frac{\lambda}{2\sin(\theta/2)} \quad (9)$$

The fringe model assumes as a way of visualisation that the two intersecting beams form a fringe pattern of high and low intensity and when the particle traverses this fringe pattern, the burst detector records a signal burst whose amplitude is modulated by the fringe pattern. Burst detectors, which are used with counter type LDA processors, generally require a minimum number of signal periods above a fixed trigger level and are able to determine when a signal is present which the rest of the instrument can analyze for velocity and size information. This frequency of the modulation is the Doppler frequency, where it is possible to acquire the velocity component perpendicular of the particle in relation to the fringes.

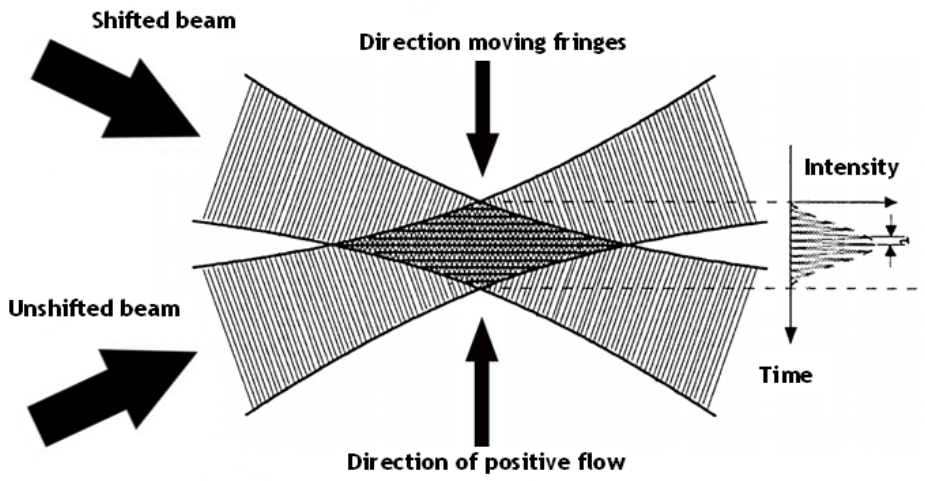

Figure 2.14. Example of a fringe model detail.

2.3.2.8. Measurement volume

Measurements take place in the intersection between the two incident laser beams in the measuring volume, which has an optical geometry defined by the intersection of the crossing region of the two incident laser beams. Such volume has a modulation depth higher than e^{-2} times the peak core value and due to the Gaussian intensity distribution in the beams and presents an ellipsoid form. This is the image region onto the collection optics spatial filters. For this work, the measurement volume has a calculated axis dimensions of the e^{-2} locations, were of 135 x 6.54 x 6.53 μm and of 112 x 5.46 x 5.45 μm. Its size can be calculated from the beam waist diameter δ_f of the focused laser beam and the angle θ between them:

$$\delta_x = \frac{\delta_f}{\cos(\theta/2)} \quad (10)$$

$$\delta_y = \delta_f \quad (11)$$

$$\delta_z = \frac{\delta_f}{\sin(\theta/2)} \quad (12)$$

where δ_x is the height, δ_y is the width and δ_z is the length of the measuring volume. From the height δ_x of the measuring volume and from the fringe spacing δ_f, it can be calculated the total number of the fringes:

$$N_f = \frac{\delta_x}{\delta_f} = \frac{2\delta_f}{\lambda}\tan(\theta/2) \quad (13)$$

LDA sensitive to velocity gradients within the measuring volume. For such a small dimensions measurement volume being traversed by tracer particles, there must be a very tight control of particle size tracers; since that LDA measure the velocity of suspended particles in the flow, they must be small enough to track the flow accurately and large enough to scatter sufficient light to be able to detect the Doppler frequency. This limitation of the particles size in a way to have the ability to effectively scatter laser light implies that the particles diameter must be at least the same size of the laser light wavelength.

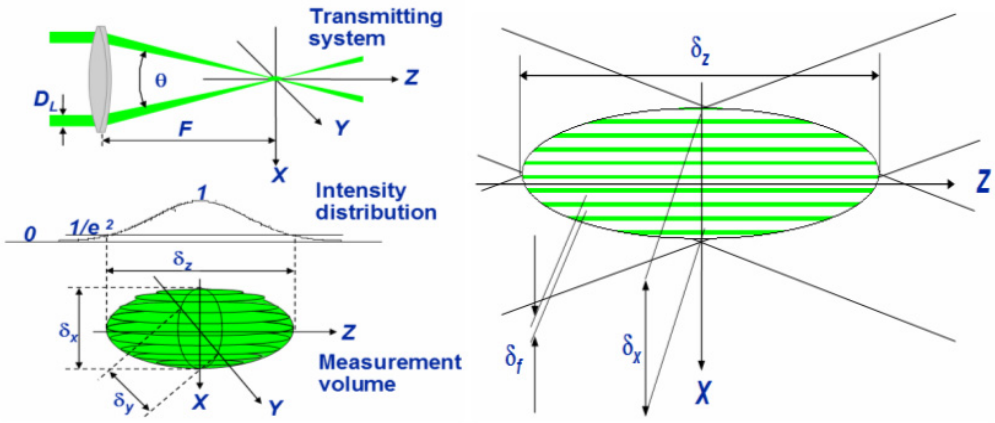

Figure 2.15. Measurement ellipsoid volume[61] with a Gaussian intensity 3 dimensions distribution δ_x, δ_y and δ_z.

2.3.2.9. Seeding

The source of LDA signals is a scattering particle. In a LDA it is not the flow velocity that is measured, but the velocity of the suspended particles on the flow, so seeding particles can be considered to be the velocity probes. And as a consequence of that, all physical properties of that particle, such as particle size, composition, specific mass, shape and

[61]- http://faculty.ksu.edu.sa/azzeer/Documents/534%20PHYS/LN7_LDA_s.pdf

concentration influence the signal quality. This leads to some important considerations about seeding selection.

Generically, the particles whose motion are used to represent the fluid motion should be able to follow the flow, good light scatterers, chemically inactive, conveniently generated, non-toxic, non-corrosive, non-abrasive, non-volatile or slow to evaporate, clean and cheap. However as referred before, its motion in a fluid are also affected by the particle shape, particle size, relative density of particle and fluid, concentration of particles in the fluid and body forces. The shape of the particles affect the drag exerted on the particle by the surrounding fluid and its size along with their relative density influence their response to velocity changes of the surrounding fluid. The concentrations of particles affect the particle motion through interaction between different particles; once that the concentrations very low, this interaction could be neglected. Body forces such as gravity, could be also ignored since this work will not study very slow flows. Furthermore external forces such as gravitational, centrifugal and electrostatic forces could be ignored.

Table 2.3. Typically seeding materials for air flows[62].

Material	Particle Diameter [μm]	Comments
Al_2O_3	< 8	Generated by fluidization. Useful for seeding flames on account of a high melting point.
Glycerine	1 - 5	Usually generated using an atomizer.
Silicone Oil	1 - 3	Very satisfactory.
SiO_2 Particles	1 - 5	Spherical particles with a very narrow size distribution. Better light scattered than TiO_2, but not good as glycerine.
TiO_2 Powder	Submicrons - tens of microns	Good light scattered and stable in flames up to 2500 °C. Very wide size distribution and lumped particle shapes.
Water	1 - 2	Generated by atomization. Evaporation inhibitor must be added.

Since the shape of the particles has a direct influence in the scattering light, only spherical particles in an infinite fluid could be analyzed. The "real" particles could not be modelled properly. With particles size comparable to the wavelength of light, the Lorenz-Mie light scattering theory could be applied. This theory only considers spherical particles and describes only the dependency on particles sizes (Figure 2.16); in practice also considers that the shape and the orientation of seeding particles play a major role in the light scattering. However, the restriction of the Mie-formulae to spherical particles remains a barrier to complete, quantitative interpretations of laser-Doppler signals. The ability to follow the flow is demonstrated by the particle frequency response formula above:

[62] - Jensen, K. D., "Flow Measurements", *Journal of the Brazilian Society of Mechanical Sciences and Engineering*, Vol. 26, No. 4, pp. 400-419, ISSN 1678-5878, 2004.

$$\frac{d}{dt}U_p = -18\,\frac{\upsilon}{d_p^2}\,\frac{U_p - U_f}{\rho_p - \rho_f} \quad (14)$$

where

ν	Kinematics viscosity;
d_p	Particle diameter;
U_p - U_f	Particle velocity minus flow velocity;
ρ_p - ρ_f	Particle specific mass minus flow specific mass.

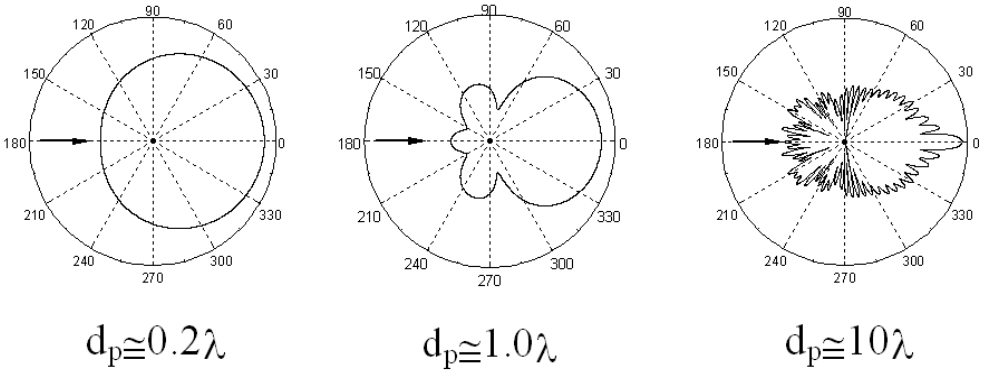

Figure 2.16. Polar plot of scattered light intensity versus scattering angle with intensity shown on a logarithmic scale[63].

2.3.2.10. Signal characteristics

The main goal of the LDA experimentalist is to create an environment in which accurate measurement results can be obtained with minimum cost and effort. Obtaining this goal requires a thorough understanding of the conflicting requirements previously described, along with an understanding of the capabilities of the LDA signal processor used. This leads to the most important considerations in evaluating the performance of an LDA signal processor. The primary result of a LDA measurement is a current pulse from the photodetector, which contains the frequency information related to the velocity to be measured and contains also noise that could become from several sources such as photodetection shot noise, secondary electronic noise, thermal noise from preamplifier circuit, higher-order laser modes (optical noise), light scattered from outside the measurement volume, dirt, scratched windows, ambient light, multiple particles, unwanted reflections (windows, lenses, mirrors, etc.).

The number of seeding particles simultaneously present in the measuring volume it is very important for the quality of the signal, and the performance of the signal processor. If on average much less than one particle is present in the volume, a typical burst-type Doppler signal appears. Figure 2.17 middle, shows the filtered signal which is actually input to the signal processor. The DC part, which was removed by the high-pass filter, is known as the

[63] - http://faculty.ksu.edu.sa/azzeer/Documents/534%20PHYS/LN7_LDA_s.pdf

Doppler pedestal, and it is often used as a trigger signal, which starts sampling of an assumed burst signal. The envelope of the Doppler-modulated current reflects the Gaussian intensity distribution in the measuring volume. If more particles are present in the measuring volume simultaneously, it appears a multiparticle signal (Figure 2.17, right). The detector current is the sum of the current bursts from each individual particle within the illuminated region. Since the particles are located randomly in space, the individual current contributions are added with random phases, and the resulting Doppler signal envelope and phase will fluctuate. Most LDA processors are designed for single-particle bursts, and with a multiparticle signal, they will normally estimate the velocity as a weighted average of the particles within the measuring volume. One should be aware, however, that the random-phase fluctuations of the multiparticle LDA signal add a phase noise to the detected Doppler frequency, which is very difficult to remove.

With the advent of fast digital electronics, the fast Fourier transform of digitized Doppler signals can be performed at hundreds of kHz rates.

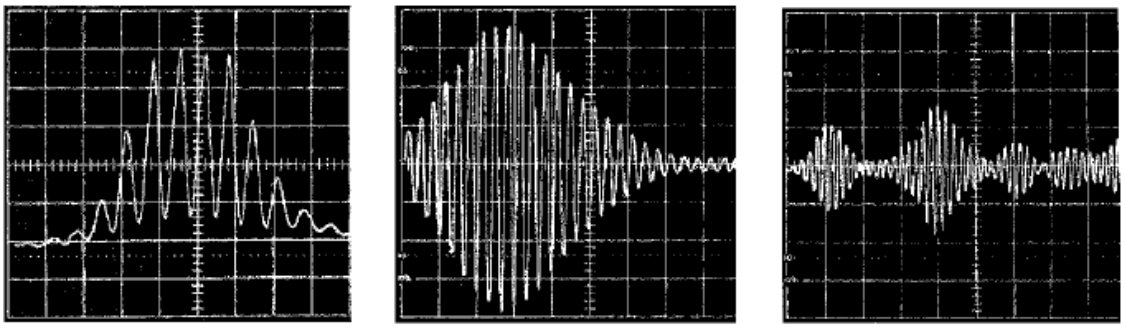

Figure 2.17.Typical single and multiple-particle Doppler bursts: left - Doppler burst; middle – filtered Doppler burst; right – multi-particles[64].

The total light power scattered by a small particle can be obtained by the integral over a sphere surface of R radius. For particles with sphericity less than 0.7, the estimation of the settling velocity is complicated by the fact that its flow orientation is a function of the Reynolds number. The light intensity should be assumed as constant inside the measuring volume to simplify the analyses. The particle spends a very short time interval inside the measuring volume; within this interval time, many photons will be scattered in all directions. The number of electrons leaving the cathode of the photodetector is giving by multiplying the number of collected photons with the quantum efficiency of the photodetector. The total number of photons scattered per particle passage is so a function of the available laser power, the scattering properties of the particle, the particle size and of the focusing properties of the transmitting optics. Only a small proportion of the scattered photons will reach the photodetector due to the finite collection efficiency of the light collecting system. Burst detectors which are used with counter type LDA processors, generally require a

[64] - http://faculty.ksu.edu.sa/azzeer/Documents/534%20PHYS/LN7_LDA_s.pdf

minimum number of signal periods above a fixed trigger level. The burst detector determines a signal present which the rest of the instrument can analyze for velocity and size information.

2.3.3. LDA operational procedure

In this work, the velocity probe used is seeding particles suspended in the flow, with diameters between 0.1 and 5 *μm*. For the effect was used a Techno-Fog JEM smoke generator machine. This machine generated smoke from appropriated liquid for that purpose. The smoke generated was expelled from that machine and with the aid of a compressor working with a pressure value of 1 bar was sent by a pipeline to a cyclone. In this cyclone the smoke was accelerated and sent up in spiral till find a tapered contraction. After the contraction the smoke was sent to a thin pipe, placed inside the test section. This pipe was perforated in a way to allow the seeding insemination into the studied flow. It is necessary to use low concentrations of seeding, since the particle concentration affects particle motion through interaction between different particles. The velocity field was measured with a two-colour (two-component) laser-Doppler velocimeter (Dantec Flowlite 2D), which comprised a 10 *mW* He-Ne and a 25 *mW* diode-pumped frequency doubled Nd: YAG lasers. Bragg-cell frequency shifting at f_o = 40 *MHz* was used in both channels to detect the flow reversals. The half-angle between the beams was 2.8º and the scattered light was collected in backward scattering mode with a focal lens of 400 mm. The measurement volume with calculated axis dimensions at the e^{-2} intensity locations of 135 x 6.54 x 6.53 *μm* and 112 x 5.46 x 5.45 *μm* was positioned at the required location by use of a computer remotely driven X-Y-Z traversing unit with a precision of ± 0.1 mm. The horizontal velocity and vertical velocities, $\overline{U}$ and $\overline{V}$, the mean and turbulent velocities, $\sqrt{\overline{u'^2}}$, $\sqrt{\overline{v'^2}}$ together with shear stress $\overline{u'v'}$, anisotropy $\sqrt{\overline{u'^2}}/\sqrt{\overline{v'^2}}$ and correlation factor $K_{uv}= \frac{\overline{u'v'}}{\sqrt{\overline{u'^2}}\sqrt{\overline{v'^2}}}$ were determined by a two-channel Dantec BSA F60 processor.

The seeding control emission on the flow is done by operating the smoke machine remote control (see Figure 2.18, left). The “Ready” LED (green) is on when the machine is up to operating temperature and capable of producing fog. The timer is switched on by rotating the timer control clockwise until the green timer led is on. At this point the repetition rate of the timed pulse is minimum. Rotating the control clockwise causes the repetition rate to increase. The duration of the pulse is fixed, only the frequency can be changed. When combined with the output level control this provides a simple way to maintain a constant level of fog. By pressing the fog switch (at any time since the “Ready” LED is on), turn possible to get the fog currently set with the output level control. The “Heat” LED is on when power is being supplied to the heat exchanger. When the maximum operating temperature is reached the LED is off. The “Output Level Control” is rotated clockwise to increase the fog output level and reduces automatically as the heat exchanger cools, allowing longer run times.

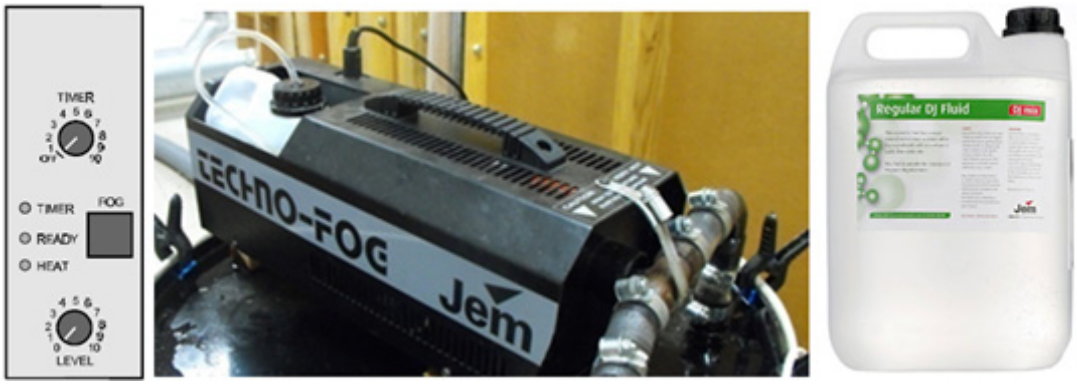

Figure 2.18. Smoke machine (middle), the remote control (left) and the seeding used for tracer (right).

For the visualization results, it is used a Timer and a Heat value equal to 3. The fog button was held down to maintain a strong seeding injection in the flow, to be recorded in a photograph. The used tracer is a monopropylene glycol with demineralised water manufactured by the same manufacturer of the smoke machine.

2.4. Flow Configuration

An experimental study of four different part configurations was made (see Figure 2.20) and for each a part was built: unconfined jets (runs A_1 and A_2), confined jets (runs B_1 and B_2), convergent jets with 11° (runs C_1 and C_2) and convergent jets with 22° (runs D_1 and D_2). The summary of this experimental work test case is resumed in the table 3.1.1. The unconfined configuration part served for the unconfined experiment and served as a main part for all runs. Its interior dimensions are: height 303 mm, width 400 mm and depth 200 mm. This part is divided into three sections: one at the centre, with height of 260 mm to permit the flow passage of the U_i inner jet and two sections at north and south each with 20.5 cm to permit the flow passage of the outer jet, U_o. These two sections have four vertical plate divisions that divide the flow in small sections of equal size and were implemented in a way to straighten the external flow. The division plates have 1 mm thickness each.

For testing, the facility engine is put to work with the converter electronic device indicating the highest frequency chosen for measurements, f = 40 Hz. The velocity of the flow indicated that the flow was laminar. It was decided then to provoke a laminar/turbulent transition with vortex generators implementation. And once there is a low velocity, the trip wire Gibbings criterion could be followed. The Gibbings criterion states that the wire diameter cannot be too big, in a way to create unnecessary flow perturbation and states that the wire diameter cannot be too small, in order to introduce a perturbation strong enough to induce the transition. According to this criterion, the wire Reynolds number should not be inferior to 826, as shows the equation.

$$Re_{wire} = \frac{U_e\, d_{wire}}{\nu} \geq 826 \quad (15)$$

The wire produces a flow similar effect as shown in the figure, which induces a highly unstable velocity profile inflection point with large deficits in momentum. These two mechanisms produce a jump from a given Re_x to a Re_θ. This correlation was proposed by Cebeci and Smith, and according that the transition occurs when the transition Reynolds $Re_\theta = U_e\theta/\nu$ and $Re_x = U_e x/\nu$ were related by:

$$Re_{\theta_{tr}} = 1.174\left(1 + \frac{22400}{Re_{x_{tr}}}\right) Re_{x_{tr}}^{0.46} \quad (16)$$

For the wire diameters calculations, all values were considered for a standard temperature equal to 15º C. The observed velocity for the inner jet is U_i=2.5 ms^{-1} and the outer jet is U_o=20 ms^{-1}. The results for the inner jet wire diameter is d≥4.85 mm. The used wire has d=5 mm, from which the Re_{wire} is still below 900. The results for the outer jet wire diameter is d≥0.6 mm. The used wire has d=0.6 mm.

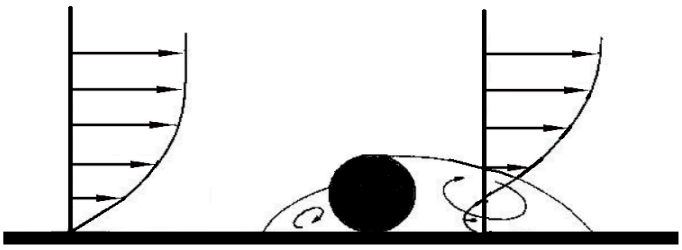

Figure 2.19. Induced flow by a trip wire[65].

Another aim of this work is to obtain an outer jet with higher velocity than the inner jet several times with a single engine feeding the two jets simultaneously. This effect was created with the construction of a structure consisting of two sections of honeycomb divided by three glass wool screens. This structure was tested for the velocities intended to be the chosen for all the experiments, i.e., with the electronic frequency converter device showing the f=30 and *f* = 40 Hz values. For the f = 30 Hz frequency, the velocity ratio is $\lambda = U_o / U_i = 3$ and for the *f* = 40 Hz frequency, the velocity ratio is λ = 3.8.

Each of the three other configurations was adapted in the extension of unconfined jets configuration. The confined part (Figure 2.20, top right) is the unconfined part plus a north and a south wall of a 1500 x 400 mm. The convergent jet with 11º is the unconfined plus a north and south part convergent of 400 x 90 mm and with an 11º angle. Its thickness increases 11 mm. The convergent jet with 22º is the unconfined plus a north and south part convergent of 400 X 90 mm and with a 22º angle. Its thickness increases 22 mm. For each

[65] - Brederode, V., "Fundamentos de Aerodinâmica Incompressível", IDMEC, Instituto Superior Técnico, Lisboa 1997, ISBN 972-97402-0-8.

configuration this study reports the results of the horizontal profiles for *U* and *V* and the vertical profiles for *U*, *V*, $\sqrt{\overline{u'^2}}$, $\sqrt{\overline{v'^2}}$, , $\overline{u'v'}$, $\sqrt{\overline{u'^2}}/\sqrt{\overline{v'^2}}$ and $\frac{\overline{u'v'}}{\sqrt{\overline{u'^2}}\sqrt{\overline{v'^2}}}$.

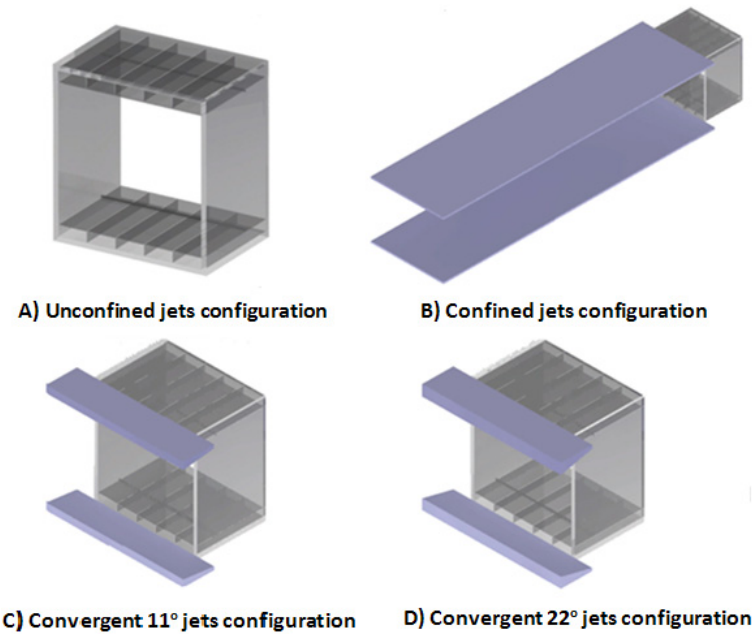

Figure 2.20. Tested flow configurations.

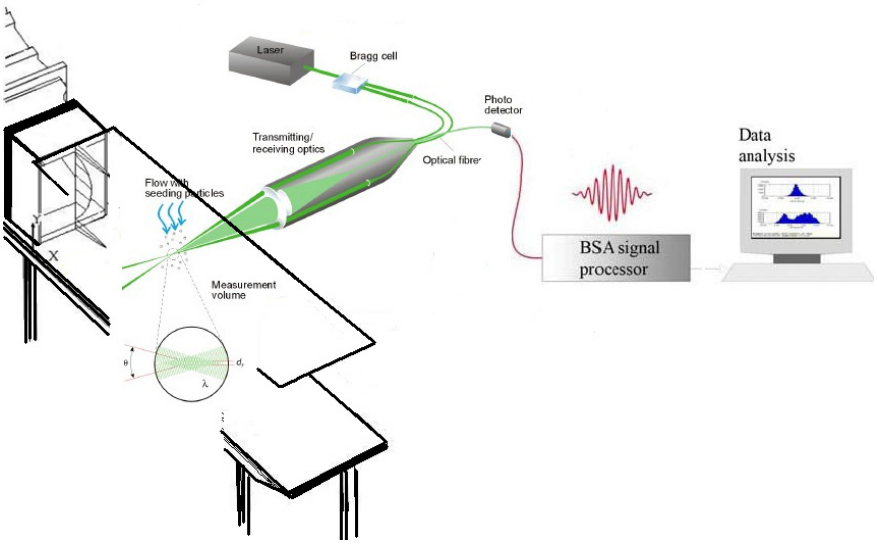

Figure 2.21. Diagram of the LDA positioning and the experimental setup for the confined jets case.

For the test case B_1 and B_2 of confined jets, all measurements were made with the green laser parallel to the upper wall. Relaying on the LDA basis, the green laser had to be rotated its half angle half-angle at the beam intersection.

$$\alpha_{green} = \frac{4\ x\ 532\ x\ 10^{-9}}{\pi\ x\ 1.35\ x\ 10^{-3}} = 502\ x\ 10^{-6} \quad (17)$$

And since the beam spacing divided by the focal length gives:

$$\left(\sin\frac{\theta}{2}\right)_{green} = \frac{39.13\ mm\ /2}{400\ mm} = 0.0489125 \quad (18)$$

And the wavelength divided by two times this value gives the fringe spacing:

$$\delta_f = \frac{532\ x\ 10^{-9}}{2\sin\left(\frac{\theta}{2}\right)} = 5.45\ \mu\mu m \quad (19)$$

This half-angle rotation implies that all the velocity measurement has changed. Thus, for the case of confined jets the algorithm of the program was amended to correct the picked up velocities, as shows the equation:

$$V = V'\cos\frac{\theta}{2} = 0.9988\ V' \quad (20)$$

The traverse table has a maximum travel throughput of 250 mm. The farthest vertical velocity profile is 1235 mm far from the jets exit. For all test cases, the traverse table was put in five sequential courses: the six nearest profiles x = 8, 50,100, 150, 200 and 245 mm were measured in its first course; the x = 295, 395 and 490 mm profiles were measured in its second course; the x = 540 and 640 mm profiles were measured in its third course and the last two profiles x = 985 and 1235 mm were respectively measured in its fourth and fifth course. The horizontal profiles of vertical and horizontal velocity *U* and *V* were measured at the symmetry axis y = 0 and the two more distant profiles were not measured. Each change of the transverse table position was duly recorded on the laboratory floor. The relationship between the velocity of the laser light scatter centre, considering it equal to the flow velocity, and the Doppler frequency, is:

$$U = K\ f_D \quad (21)$$

where f_D is the instantaneous frequency caused by a particle, and K is the velocimeter transfer constant showed in table 2.3.1. The measurement volume positioning accuracy was less than 0.1 mm, the smallest possible step in all three laser axis.

2.5. Calibration and experimental facility setup tests

The calibration of the wind tunnel was developed by varying the mean jet velocity with the help of electronic frequency converter device, and by measuring the velocity in the

same points of the domain, in the symmetry axis. The velocities were calibrated using the micromanometer and the laser. To control de mean velocity it was decided to maintain identical the values of the micromanometer pressure, for each frequency value (0.53 mmH_2O for f = 30 Hz and 0.99 mmH_2O for f = 40 Hz). The digital micromanometer used was connected to a Pitot tube, placed at the test section entrance. It was used a smoke machine and seeding as tracer element. This smoke machine was connected to a compressor, working at 1 bar pressure. The output of the smoke machine was connected by a tube to a cyclone, with the aim to accelerate the flow tracer that spirals up into a pipe that leads directly to the test section.

Figure 2.22. Left: electronic frequency converter device; middle: micromanometer; right: smoke machine.

The calibration of the wind tunnel is a task that aims to understand the limits of the facility and provide support for all measurements to be made. With the help of electronic frequency converter device, measurements were made for five frequencies: f = 30, 35, 40, 45 and 47.5 Hz. The values for each frequency tested in the calibration of this work, are shown in the Table 2.4.

Table 2.4. Calibration data.

Frequency (Hz)	Δp (mmH_2O)	Micromanometer velocity (ms^{-1})	Laser velocity (ms^{-1})
30	0.53	2.93	2.52
35	0.75	3.46	3.07
40	0.99	3.98	3.59
45	1.25	4.49	4.06
47.5	1.38	4.71	4.26

All measurements for these five runs were made at the same point coinciding with the symmetry axis at the jets exit, in the vertical plane x = 8mm. All these values were obtained with a no less acquisition of 10000 samples and a 120 s limit time. Measurements were repeated with the acquisition of 50000 and 30000 samples for comparison. The red laser is

the LDA_1 and measures the horizontal velocities with a verification signal of minus (-) on the flow direction and consequently positive (+) in the opposed direction. The green laser is the LDA_2 and measures the vertical velocities with a verification signal of minus (-) in favor to north direction and a positive (+) in the south direction. The calibration was set in a way to obtain a good Doppler burst, which requires some experience. The instructions were mainly followed by the BSA Flow Software, Installation & user´s guide, Vol. 1.

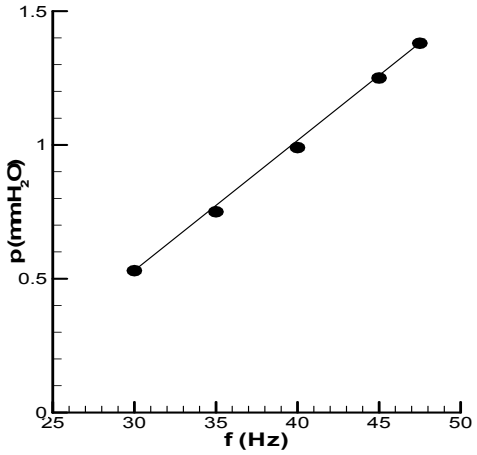

Figure 2.23. Pressure variation with the tested frequency.

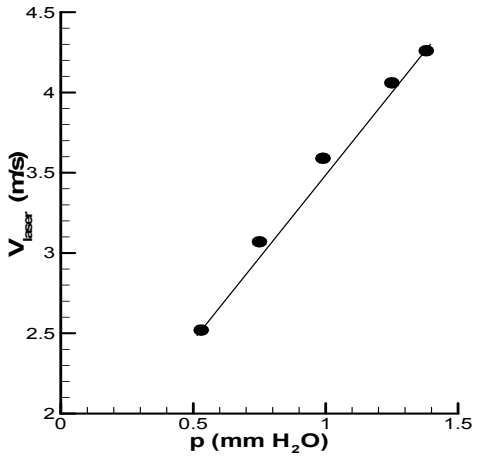

Figure 2.24. Variation of the laser velocity with the tested pressure.

All the measurements were recorded in *txt* files and saved in the Compaq Presario 6000 computer. All the files were turned into *data* files and with the help of the Tecplot 8 program all the data from those files were transferred to graphics, showed in the Chapter 3 of this work.

2.6. Visualization

The qualitative description of the studied flows was made with the aid of a visualization technique. For the visualization recording was used a smoke generator for the confined jets case and for all the other configurations was also used a two convergent He-Ne laser light beam with 10 mW of nominal power, operating at 632.8 nm. These beams of light were made to match a cylindrical lens so as to generate a light plane (Figure 2.25 and Figure 2.26). The results of this light plane were recorded in photography for all the runs that this work includes. The used camera was a Nikon D3000. The resolution was 2896 x 1944 and the speed was 3", 4" and 5", using 24-bit depth, 300 dpi, f-stops varied from f/4.8 and f/6.3 and using colour and black and white exposure with a 1600ASA sensitivity.

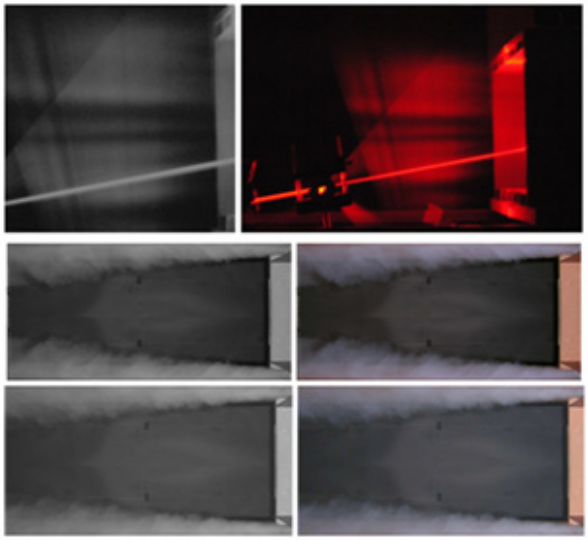

Figure 2.25. Unconfined jets visualization (top: A_1 case, f=30 Hz); Confined jets (middle: the B_1 case, f=30 Hz; bottom: the B_2 case, f=40Hz).

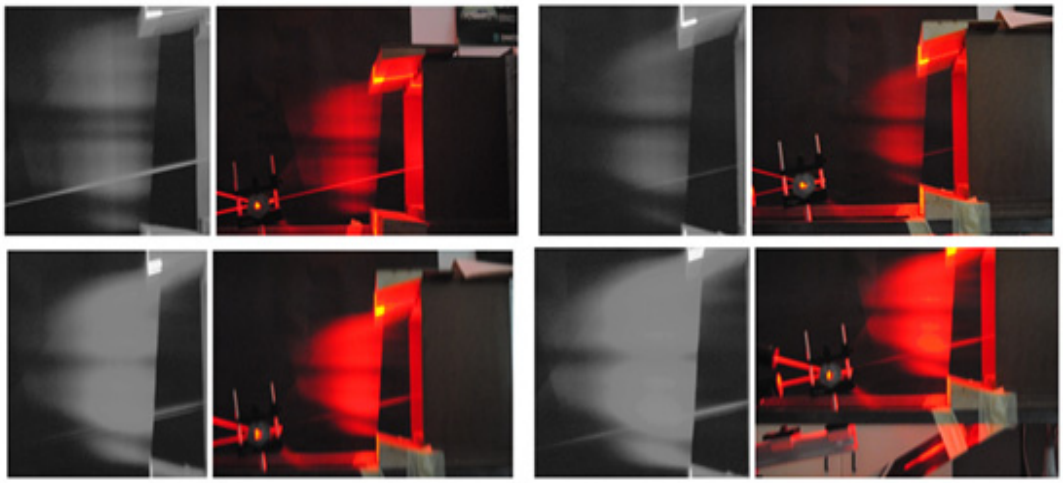

Figure 2.26. Left; Convergent 11° jets visualization (top: C_1 case, f=30 Hz; bottom: C_2 case, f=40Hz.); Right; Convergent 22 ° jets visualization (top: D_1 case, f=30 Hz; bottom: D_2 case, f=40Hz).

For all visualized situations, the obtained photos illustrated an intensive mixing jet immediately after the jets exit, situation that led to chose several velocity profiles very close to each others in this initial region.

2.7. Errors estimation of LDA measurements

As indicated in the Figure 2.15, the major axis δ_z is much bigger than δ_x and δ_y, rendering the measuring volume an elipsoidal shape. This makes the backscattered LDA sensitive to velocity gradients within the measuring volume. For such a small dimensions measurement volume being traversed by tracer particles, there must be a very tight control of particle size tracers; since that LDA measure the velocity of suspended particles in the flow, they must be small enough to track the flow accurately and large enough to scatter sufficient light to be able to detect the Doppler frequency. This limitation of the particles size in a way to have the ability to effectively scatter laser light implies that the particles diameter must be at least the same size of the laser light wavelength.

Although the LDA technique has many advantages compared to methods such as hot-wire and hot-film anemometry, the resulting measurements may contain some errors particular to this technique, such as hardware errors, velocity bias, fringe bias and fringe distortion effects.

2.7.1. Hardware errors

The first common source of errors is the hardware errors. Due to the frequency and internal timer limitations of the signal processor, there were errors of 1 % and 3.6 % for the mean velocity and turbulent fluctuating component respectively as specified by the manufacturer of the LDA system. The accuracy of the beam spacing and the focal length on the fibber optic probe can also affect the calculation of velocity, where the half intersection angle is calculated based on the ratio of the half beam spacing and the focal length. In the existing LDA system, assuming ±0.2 mm misalignment on the beam spacing and focal length, an error of 1 % may be introduced in the calculation of velocities. However, the error due to uncertainty of the optical configuration is constant and affects all measurements equally.

2.7.2. Velocity bias

Another well-known source of uncertainty is velocity bias that is related with a higher probability of getting more particles with a high velocity component crossing the measurement volume in a given sampling time, than particles with a lower velocity component. The system observes particles with larger velocities more often than those with smaller velocities. As a consequence, the symmetry of the histogram constructed from LDA measurements is always more or less disturbed by this velocity bias effect (Zhang, 2010). Higher velocities result in more “detectable” data samples than lower velocities. In a turbulent flow situation, the statistical averaging process for the velocity leads to a bias

towards the higher velocities; thus resulting in an overestimation of velocities, also called broadening effect (Zhang, 2010).

2.7.3. Fringe bias

Finally the source of errors associated with the direction of seeding particles within the measuring volume, known as fringe bias, was evaluated. Under a fixed signal to noise (S/N) ratio, a "detectable" Doppler burst signal is dependent on the signal level above the background noise level as well as the minimum number of fringes presented in the burst signal. The maximum number of fringes within the burst can normally be achieved when the particle trajectory at the centre of the measuring volume intersects the fringes perpendicularly. However, when the measuring volume is in places such as near-wall and flow recirculation regions, particles could travel parallel to the fringes in the measuring volume. This phenomenon often occurs during the multi-dimensional LDA measurements and will lead to insufficient number of fringes presented in Doppler signals for those particles. This subsequently causes a reduction in data rate and is a source of error for the particle velocity statistics.

2.7.4. Fringe distortion effects

Fringe distortions in LDA measurement volumes have been historically considered as the consequence of improper optical layout. Quantitative evaluations of linear fringe distortion effect on the flow measurement accuracy in the measurement volume were performed by Zhang and Eisele (1997; 1998). Figure 2.27 illustrates four fringe distortion types related in literature. The three first types (Figure 2.27a, b and c), were observed by Zhang, 2010. The first type (Figure 2.27a) takes place when the tangential velocity of the flow in a circular pipe is measured without matching the refractive index of the fluid. The second type (Figure 2.27b) is considered as merely a matter of the improper optical layout. The third type (Figure 2.27c) is related to the astigmatism due to laser beam refractions and illustrates the displacements of all four focal points on two laser beams (A and B) from the measurement volume (one-time refraction). Because of the irregular distribution of the beam waists around the LDA measurement volume and hence the complexity of the form of respective wave front of two laser beams, this type of fringe distortion may not yet be well characterized. Ruck (1991) with the help of microscope optics observed a further type of fringe distortion in the measurement volume known as the local fringe distortion and it is caused by the laser light diffraction through particles in the transmission path of the laser beam. This type of fringe distortion provokes interference on fringe pattern (Figure 2.27d). In this figure in the 1-3 photogram's it is observed the interference fringe pattern in the middle of the measurement volume distorted by a latex particle of 4.8 μm diameter at different locations: particle displacement referring to the middle of the measurement volume: 1) in middle plane, no distortion; 2) 100 μm before middle, inside volume; 3) 1000 μm before middle, outside measurement volume. At Figure 2.27d), in the 4-9 photogram's it is observed

the interference fringe pattern in the middle of the measurement volume distorted by a latex particle of 10 μm diameter at different locations: particle displacement referring to the middle of the measurement volume: 4) in middle plane, no distortion; 5) 100 μm before middle, inside volume; 6) 1000 μm before middle, outside measurement volume; 7) 2000 μm before middle, outside measurement volume; 8) 3000 μm before middle, outside measurement volume; and at 9) 4000 μm before middle, outside measurement volume.

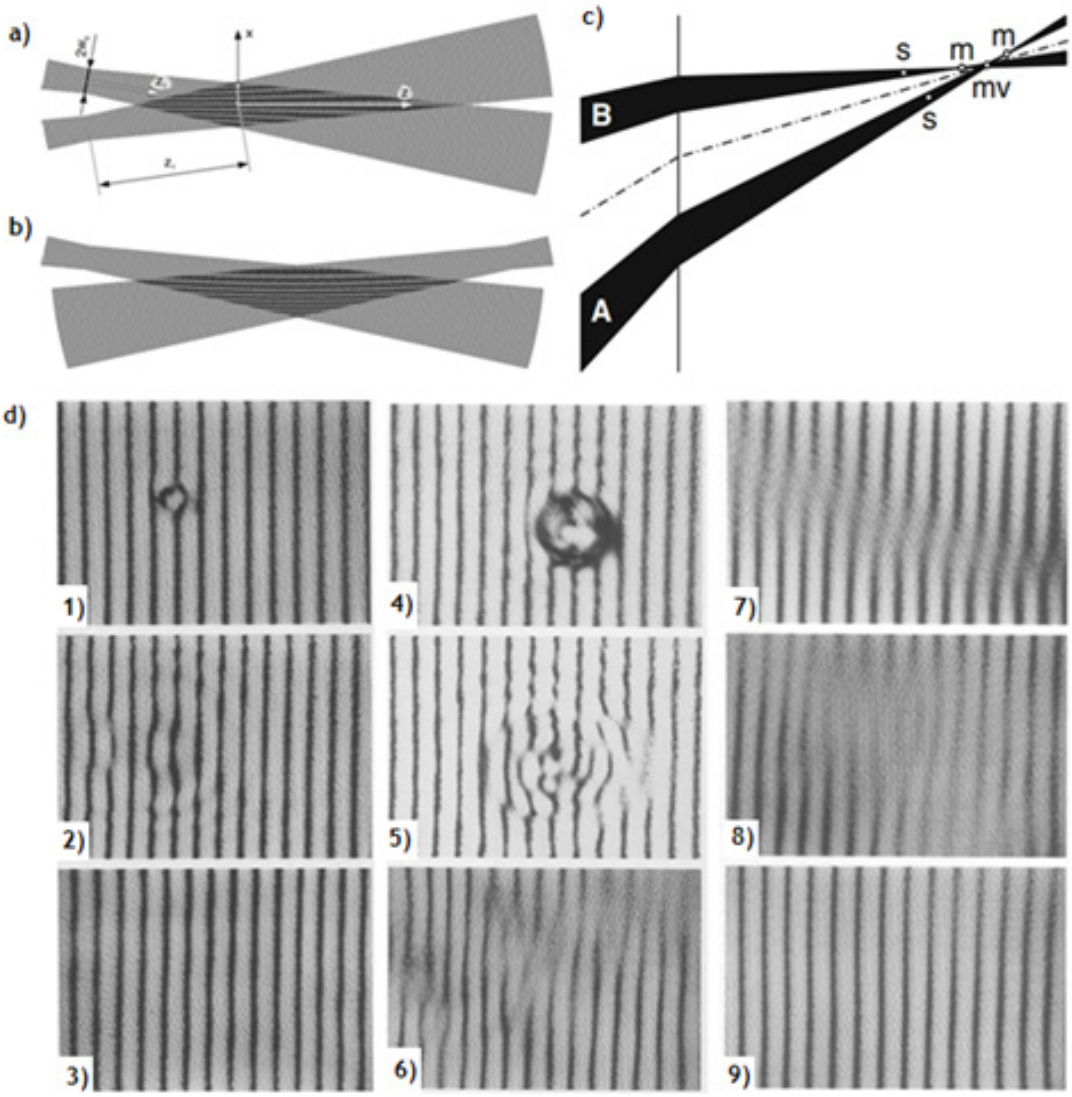

Figure 2.27. Fringe distortion effects: a) both beam waist placed before the measurement volume centre (distance z_1). This kind of distortion exist with both beam waist placed after the measurement volume centre; b) one beam waist placed before the measurement volume centre and one beam waist placed after the measurement volume centre; c) astigmatism: displacements of all four focal points on two laser beams (A and B) from the measurement volume (one-time refraction); d) tracer particles interference distortion in the fringe pattern.

From these four different fringe distortion effects, only the first type was already study in error quantification. As Figure 2.27a) illustrates the two Gaussians crossing beams occurs after their respective waists located at equal distance from the beam intersection point. The same fringe distortion with the same consequence in LDA flow measurements occurs when the beam crossing is prior to both beam waists (Zhang, 2010). Their linear distribution assumption of the fringe spacing in the LDA measurement volume is based on earlier investigations of this type of fringe distortion and contributes to the simplification of calculations.

The uniform velocity distribution within the measurement volume length is assumed (Zhang, 2010). From its measurement by $u = \Delta x \ \nu_D$ with non-uniform fringe spacing, the related non-uniform Doppler frequency is:

$$\frac{1}{\nu_D}\frac{d(\nu_D)}{dz} = -\frac{1}{\Delta x}\frac{d(\Delta x)}{dz} \quad (22)$$

Where:

ν_D is the Doppler frequency,

dz is the window thickness at z coordinate,

Δx is the fringe spacing

According to Hanson (1973; 1975) from accounting for the relative shift Doppler frequency, the fringe spacing gradient is expressed as:

$$\frac{1}{\Delta x}\frac{d(\Delta x)}{dz} = \frac{1}{R} \quad (23)$$

where R is the curvature radius of the wave front at the beam crossing point.

Usually this is a small value because $\Delta z << R$, and specifies the relative change in the fringe spacing at the end of the measurement volume ($z=\Delta/2$) against that at the measurement volume centre ($z=0$).

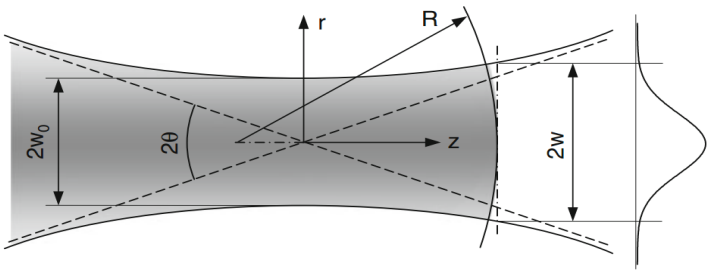

Figure 2.28. Geometrical and optical specifications of the Gaussian beam[66].

[66] - Zhang, Zh., LDA Application Methods, Laser Doppler Anemometry Fluid Dynamics, e-ISBN: 978-3-642-13514-9, Springer-Verlag Berlin Heidelberg 2010.

Light beams with Gaussian distribution always comprise a well-defined beam waist. This property indicates that the Gaussian beam is a focused beam. In fact, such a light beam is geometrically completely describable by merely using the beam waist diameter (Zhang, 2010). According to Figure 2.28, the geometrical feature of a Gaussian beam mainly includes the curvature radius *R* of the wave front and the beam thickness 2*w* representing the beam divergence. The wave front is considered as a surface on which the phase is constant. From the wave optics the curvature radius of the front surface of a Gaussian beam and the beam thickness at the distance *z* from the beam waist are given by:

$$R = z\left[1 + \left(\frac{\pi w_0^2}{\lambda z}\right)^2\right] \quad (24)$$

and

$$w = w_0\sqrt{1 + \left(\frac{\lambda z}{\pi w_0^2}\right)^2} \quad (25)$$

respectively. For large values of the distance *z* the thickness of the light beam linearly increases with the distance. With a spot size (radius w_0) at the beam waist and with the distance from the beam waist to the beam crossing point (z_1, Figure 2.28, *R* follows:

$$R = z_1\left[1 + \left(\frac{\pi w_0^2}{\lambda z_1}\right)^2\right] = z_1\left[1 + \left(\frac{z_R}{z_1}\right)^2\right] \quad (26)$$

where z_R represents the Rayleigh length.

From Eq. 23 it can be shown that by assuming $|z/R| << 1$ within the region of the measurement volume, the longitudinal fringe spacing varies linearly over the length of the measurement volume (Zhang, 2010). According to Hanson (1973) this value of fringe spacing is equal to that in the undistorted measurement volume (Eq. 9). Assuming a uniform flow of velocity u_0 through the measurement volume and with the measured Doppler frequency and the specified constant fringe spacing in the software, the flow velocity is inversely related to the fringe spacing which linearly changes along the measurement volume (Zhang, 2010):

$$u = \Delta x_0 v_D = \Delta x_0 \frac{u_0}{\Delta x} \quad (27)$$

The ensemble average velocity *u* from measurements is different to the actual flow velocity u_0 (Zhang, 2010). For the general case a turbulent flow with random velocity fluctuations is considered to have a mean velocity equal to $\bar{u}$. The apparent mean velocity is calculated by the arithmetic average as:

$$\bar{u}_{app} = \Delta x_0 \frac{1}{N} \sum_{i=1}^{N} \frac{u_i}{\Delta x_i} \quad (28)$$

On the side of the measurement volume, the measurement volume will longitudinally be divided into *m* partial volumes of equal distance. In each partial volume, the fringe spacing can be considered to be constant. On the side of the flow, the same and constant statistical flow properties are assumed to exist among all partial volumes. This also includes the assumption that particles have equal probability in passing through every partial volume (Zhang, 2010). With respect to $N = m \cdot n$ and the mean velocity equal to $\bar{u}$, Eq. 28 is then written as:

$$\bar{u}_{app} = \Delta x_0 \frac{1}{N} \sum_{j=1}^{m} \left(\frac{1}{\Delta x_j} \sum_{i=1}^{n} u_i \right) = \Delta x_0 \bar{u} \frac{1}{m} \sum_{j=1}^{m} \frac{1}{\Delta x_j} \quad (29)$$

With $\Delta z/2$ as the half length of the measurement volume and extending *m* to infinity, the summation can be presented as an integral calculation:

$$\bar{u}_{app} = \bar{u} \frac{\Delta x_0}{\Delta z} \int_{-\Delta z/2}^{\Delta z/2} \frac{dz}{kz + \Delta x_0} \quad (30)$$

Where *k* is the angular wave number of light.

According to Zhang 2010, the fringe distortion on the measurement volume influences the mean velocities measurements even in the linear longitudinal distribution of the fringe spacing case. The relative change of the fringe spacing at the end of the measurement volume is known by the fringe distortion number, γ and in its simplest form could be defined as a pure function of geometric parameters:

$$\gamma = \frac{k\Delta z/2}{\Delta x_0} = \frac{\Delta z/2}{R} \quad (31)$$

The relation between the apparent mean velocity and the mean velocity fluctuation:

$$\frac{\bar{u}_{app}}{\bar{u}} = \frac{1}{2\gamma} \ln \frac{1+\gamma}{1-\gamma} \approx 1 + \frac{1}{3} \gamma^2 \quad (32)$$

The fringe distortion number can be written as:

$$\gamma = \frac{\Delta z/2}{z_1 \left[1 + (z_R/z_1)^2\right]} \quad (33)$$

For laser beams with given beam waist thickness $2w_0$ and hence given Raleigh length z_R the fringe distortion number has been shown as the function of the distance z_1 between the beam waist and the measurement volume centre (Zhang 2010).

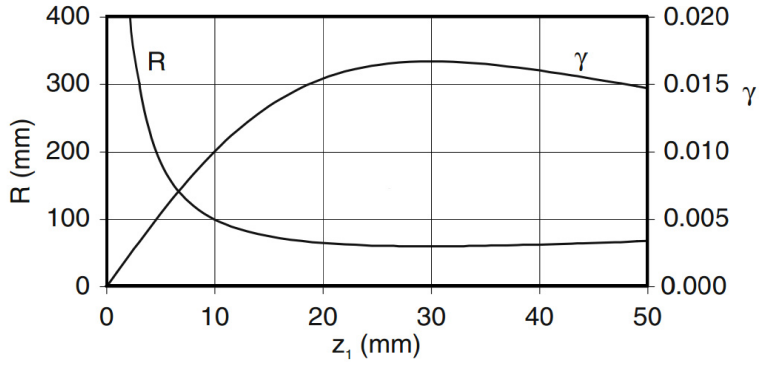

Figure 2.29. Radius of Gaussian curvature of beam wave front and the fringe distortion number[67].

Based on parameter quantifications in this example the fringe distortion number has been confirmed to be in the range of usually not exceeding 0.02. In applying this limit, the error in the mean velocity is very small, mostly negligible because of γ << 1 (Zhang 2010).

In order to quantify the overestimation of all relevant turbulence from the statistics viewpoint, the connection between the mean velocity, $\bar{u}$ and the fluctuation velocity, σ (standard deviation) is given according:

$$\sigma^2 = \overline{u^2} - \bar{u}^2 \quad (34)$$

Where $\overline{u^2}$ is the mean square of the velocity component u.

This relation is also applied in the case of velocity data from measurements undergoing the effect of fringe distortion in the measurement volume. Corresponding velocities are thus apparent, as:

$$\sigma_{app}^2 = \overline{u_{app}^2} - \bar{u}_{app}^2 \quad (35)$$

The overestimation of the turbulence intensity and the related quantities as a result of the fringe distortion in the measurement volume is then determined by:

$$\sigma_{app}^2 - \sigma^2 = \left(\overline{u_{app}^2} - \overline{u^2}\right) - \left(\bar{u}_{app}^2 - \bar{u}^2\right) \quad (36)$$

---

[67] - Zhang, Zh., LDA Application Methods, Laser Doppler Anemometry Fluid Dynamics, e-ISBN: 978-3-642-13514-9, Springer-Verlag Berlin Heidelberg 2010.

The apparent mean square velocities in the above equation are basically calculated in analogy to Eq. 28:

$$\overline{u_{app}^2} = (\Delta x_0)^2 \ \frac{1}{N}\sum_{i=1}^{N}\left(\frac{u_i}{\Delta x_i}\right)^2 \quad (37)$$

And by dividing the measurement volume into *m* partial volumes of equal distance and based on same assumption that led to Eq. 29, the above equation is converted into:

$$\overline{u_{app}^2} = (\Delta x_0)^2 \ \overline{u^2} \ \frac{1}{m} \sum_{j=1}^{m} \frac{1}{(\Delta x_j)^2} \quad (38)$$

By extending *m* to infinity, the summation in the above equation can be presented by corresponding:

$$\overline{u_{app}^2} = (\Delta x_0)^2 \ \overline{u^2} \ \frac{1}{\Delta z} \int_{-\Delta z/2}^{\Delta z/2} \frac{dz}{(kz+\Delta x_0)^2} \quad (39)$$

Using the fringe distortion number:

$$\overline{u_{app}^2} = \frac{1}{1-\gamma^2} \approx \left(1 + \gamma^2\right) \overline{u^2} \quad (40)$$

Substitution of Eq. 32 and Eq. 40 in Eq. 36 and with, and with respect to $\overline{u^2} = \sigma^2 + \bar{u}^2$ lead to:

$$\frac{\sigma_{app}^2 - \sigma^2}{\bar{u}^2} = \gamma^2 \left(\frac{\sigma^2}{\bar{u}^2} + \frac{1}{3}\right) \quad (41)$$

Because of $\sigma_{app} + \sigma \approx 2\sigma$ (with exception for $\sigma = 0$) this eq. can also be written as:

$$\frac{\Delta\sigma}{\bar{u}} = \frac{1}{2} \gamma^2 \ \frac{\bar{u}}{\sigma} \left(\frac{\sigma^2}{\bar{u}^2} + \frac{1}{3}\right) \quad (42)$$

with $\Delta\sigma = \sigma_{app} - \sigma$ as the overestimation of the standard deviation of the mean flow velocity. Figure 2.30 illustrates the overestimation of flow turbulence. For typical fringe distortion γ < 0.02, the overestimation of the flow turbulence has been found to be not significant, especially in the measurements of flows with high turbulence intensity (Zhang, 2010).

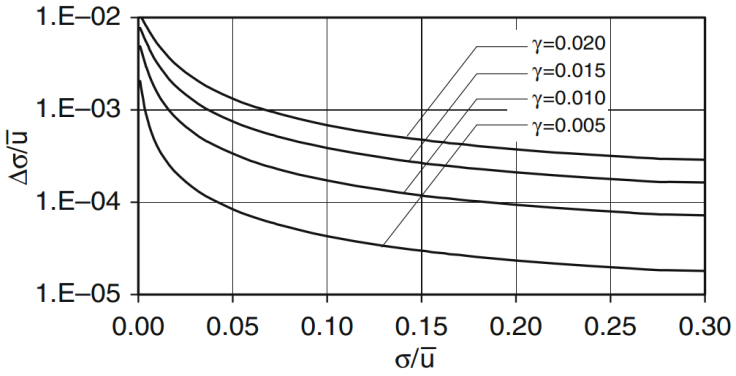

Figure 2.30. Overestimation of the standard deviation in function of the real flow turbulence and the fringe distortion number[68].

2.7.5. Results accuracy

The essential task that every Doppler signal processor is confronted with is to estimate the frequency of the oscillating part of the Doppler signal. Reaching this goal is always hampered by the presence of the noise in the Doppler signal, that comes from different noise sources effects, such as the modulation noise of the laser, the optical path difference of the incoming laser beams, the phase front distortion by tracer particles in the incoming beams, the distortion of the laser beams in the measurement volume due to the tracer particle, the quantization noise of the photocurrent, the amplification noise of the photocurrent or the electronic noise in the filters and amplifiers of the processor. The result accuracy depends on those measurement conditions, signal quality, care taken by the experimentalist, etc.

Because of this, the shape of a Doppler burst signal is determined by the size, shape and surface properties of the particles, as well as the optical system alignment and the actual path that the particle takes as it passes through the measurement volume. The calibration for this work was set in a way to obtain a good Doppler burst. That requires some experience. The instructions were mainly followed by the BSA Flow Software, Installation & user's guide, Vol. 1. This manual referred that the validation rate is a good indicator of a good Doppler burst. Those instructions were used to obtain a good data rate and validation by adjusting the high voltage, gain settings and record length settings under the range and gain properties.

[68] - Zhang, Zh., LDA Application Methods, Laser Doppler Anemometry Fluid Dynamics, e-ISBN: 978-3-642-13514-9, Springer-Verlag Berlin Heidelberg 2010.

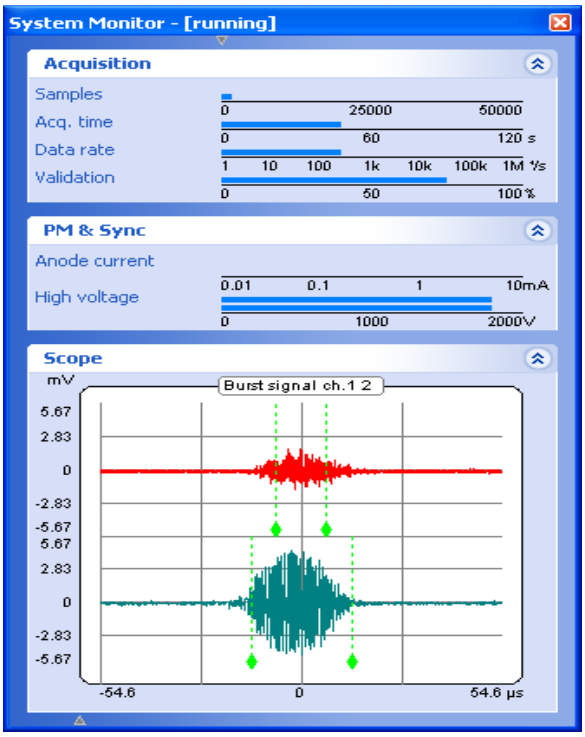

Figure 2.31. Calibration Doppler burst signal.

The calibration result is illustrated in Figure 2.31, a good Doppler burst signal, as referred by the user's guide book. The illustration shows a signal for the f = 35 Hz frequency during the calibration settings. The calibration signal for f = 30, 40, 45 and 47.5 were identical. It is then decided to make a comparative velocity study for all measurements for the frequencies f = 30 and f = 40 Hz. During all measurements of this work, it was able to maintain such an identical signal successfully. Also, during all measurements of this work the *pdf* for each profile presented the Figure 2.32 configuration. All noise velocities that appeared out of this "bell-shape" were removed in a way to a more accurate velocity results presentation. Such as referred at Subchapter 2.1 of this work, all measurements were made with the same similar lightness conditions.

Figure 2.32. Gaussian pdf distribution of a jet flow measured by LDA method.

Tracer particles emission was always controlled with the button “LEVEL” at value 2.5 and with the button “TIMER” at value 2 (Figure 2.18 left). The button “HEAT” was only used to produce smoke at the visualization procedures. Every time that the measurements started, the initial procedure was to repeat the last measurements for results comparison. All measurements had this procedure. Every time that measurement process suffer a break disrupt, those points measurements were repeated with at least 10000 samples. Several times were used the Repetitive acquisition mode as a way of get continuously updated BSA output properties without acquiring data. The main parameters to optimize BSA property settings are the validation and the data rate. The validation was always high, sometimes superior to 90% and the data rate was very good, presenting 10000 samples in less than 120 s at the farthest measured stations. The LDA focal lens was always maintained clean with its proper liquid cleaner.

All the horizontal and vertical velocity profile values for this work were collected in coincidence to enable the Reynolds shear stress values to be estimated, and all with at least 10000 velocity samples collected which leads to a result in a maximum relative statistical error for a 95% confidence interval of approximately 0.5% in the mean velocity and 1.4% in the turbulence intensity according to Yanta *et al.*, 1978.

Chapter 3. Results

3.1. Introduction

This Chapter is divided in ten subchapters: subchapter 3.1 regards a small introduction; subchapters 3.2 and 3.3 presents respectively horizontal profiles graphics for the horizontal velocity and vertical velocity distribution along the symmetry axis plane y=0 mm for all test cases. In subchapter 3.4 to 3.10, all graphics present vertical profiles between -50≤y≤200 mm, traversing the symmetry axis plane y=0 mm. Subchapter 3.4 presents the horizontal velocity results. Subchapter 3.5 presents vertical velocity results. Subchapter 3.6 presents the streamwise velocity fluctuation results. Subchapter 3.7 presents the transverse velocity fluctuation results. Subchapter 3.8 presents the shear stress results. Subchapter 3.9 presents the anisotropy results. Subchapter 3.10 presents the correlation coefficient results. This experimental study involves four configurations shown in table 3.1.1 and their measurements at all stations mentioned at table 3.1.2. The reference axis system is centred on the middle of the symmetry axis at the inlet test section. All measurements were made in the vertical symmetry plane, z=0 mm.

Table 3.1. Experimental conditions.

Test Case	Geometry	Reference[(a)]	U_o (ms^{-1})	U_i (ms^{-1})	U_{mean} (ms^{-1})	$\lambda = U_o/U_i$
A	Unconfined	1	15.06	5.35	6.73	2.8
		2	19.24	5.42	7.38	3.5
B	Confined	1	15.33	5.1	6.55	3.0
		2	19.5	5.0	7.41	3.9
C	Convergent 11°	1	13.9	5.0	6.26	2.8
		2	19.0	6.0	7.84	3.2
D	Convergent 22°	1	15.56	5.0	6.50	3.1
		2	19.9	6.0	7.97	3.3

Reference: (1, f=30 Hz); (2,f=40 Hz).

Table 3.2. Stations studied summary.

Test Case	Station exit distance *x*, (mm)													
A_1	8	50	100	150	200	245	295	395	490	540	640	735	985	---
A_2	8	50	100	150	200	245	295	395	490	540	640	735	985	---
B_1	8	50	100	150	200	245	295	395	490	540	640	735	985	1235
B_2	8	50	100	150	200	245	295	395	490	540	640	735	985	1235
C_1	---	---	100	---	200	---	295	395	490	540	---	735	985	1235
C_2	---	---	100	---	200	---	295	395	490	540	---	735	985	1235
D_1	---	---	100	---	200	---	295	395	490	540	---	735	985	1235
D_2	---	---	100	---	200	---	295	395	490	540	---	735	985	1235

Both unconfined and confined jets A_1 and B_1 test cases such as A_2 and B_2 are inserted into the same graphics. Regarding the 11° and 22° convergent jets C_1 and D_1 test cases such as C_2 and D_2 are inserted into the same graphics optionally, not only to save space in this work but in a way to turn easier its comparison.

3.2. Horizontal profiles of the horizontal velocity

This subchapter graphics presents the relation between the dimensionless horizontal velocity U in its vertical coordinate, along the distance of 39 measured points at the exit jets on its horizontal coordinate within $10<x\leq750$ mm. The obtained values are located along the symmetry axis plane y=0 mm. As mentioned at subchapter 2.5, the LDA_1 red laser measures the horizontal velocities with verification signal of minus (-) on the flow direction and positive (+) in the opposed direction. For that reason, all the U velocity data values obtained present negative values, which is a simple direction question. As a matter of consistency and graphics simplification, the four presented graphics of this subchapter presents positive velocities. Nevertheless, all vertical graphics axis have a $-0.1\leq U/U_{mean}\leq1.6$ interval.

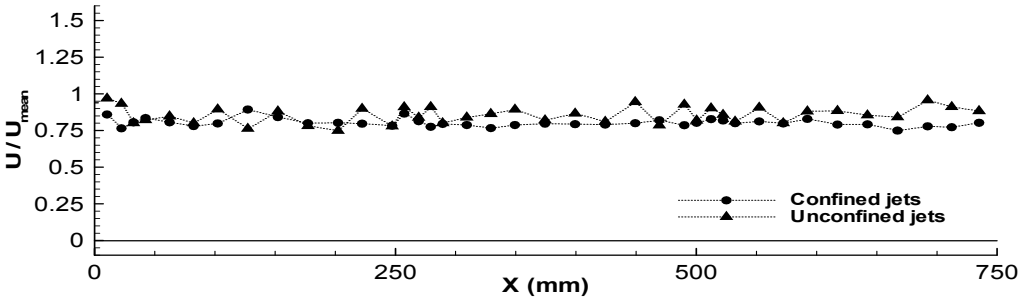

Figure 3.1. Horizontal profiles of horizontal velocity for A_1 and B_1 test cases.

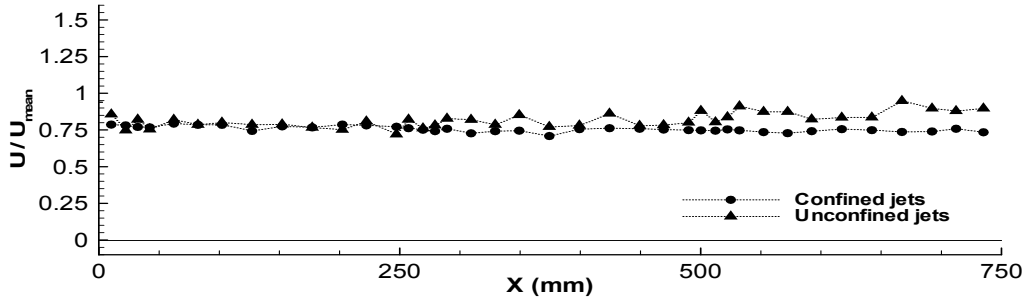

Figure 3.2. Horizontal profiles of horizontal velocity for A_2 and B_2 test cases.

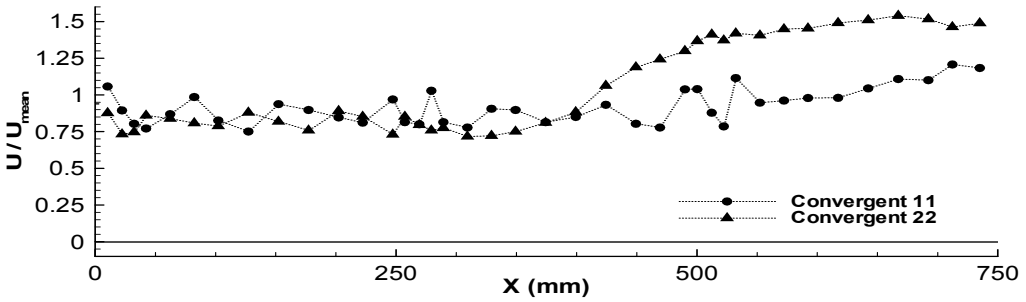

Figure 3.3. Horizontal profiles of horizontal velocity for C_1 and D_1 test cases.

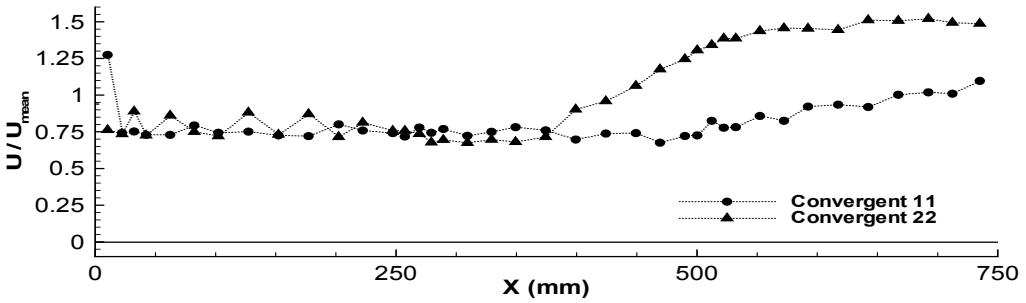

Figure 3.4. Horizontal profiles of horizontal velocity for C_2 and D_2 test cases.

Figure 3.1 presents the obtained results for the confined jets (B_1 test case f=30 Hz) and unconfined jets (A_1 test case f=30 Hz). The confined jets results show values within the interval $0.75<U/U_{mean}<0.9$ along the $10\leq x\leq 735$ mm symmetry axis plane. The initial and final values are practically identical. The unconfined jets results show values within the interval $0.75<U/U_{mean}<1$ along the $10\leq x\leq 735$ mm symmetry axis plane. The initial and final values are also practically identical. Generically, this graphic presents slightly higher values for the unconfined jets case.

Figure 3.2 presents the obtained results for the confined jets (B_2 test case f=40 Hz) and unconfined jets (A_2 test case f=40 Hz). The confined jets results show values within the interval $0.75<U/U_{mean}<0.8$ along $10\leq x\leq 735$ mm symmetry axis plane. All values are practically identical. The unconfined jets results show values within the interval $0.75<U/U_{mean}<1$ along the $10\leq x\leq 735$ mm symmetry axis plane, with final values slightly higher than the initial ones. At region $10\leq x\leq 250$ mm both test cases presented identical values. At region $250\leq x\leq 500$ mm the unconfined jets present very slightly higher values than confined jets and at region $500\leq x\leq 750$ mm, it is slightly notable the ascent of the unconfined jets values.

Figure 3.3 presents the obtained results for both convergent jets 11° (C_1 test case f=30 Hz) and 22° (D_1 test case f=30 Hz). C_1 test case show values within the interval $0.75<U/U_{mean}<1.21$ along $10\leq x\leq 735$ mm symmetry axis plane. Near x=500 mm, the velocity value suffer some sudden perturbation with the posterior measured points having slight gradual increased velocity. The outer jets velocity are U_o=13.9 m/s and the inner jet velocity is U_i=5.0 m/s. At this jets exit distance the outer jets had an acceleration influence on the inner jet at the symmetry axis. Both jets are mixed. C_1 test case show values within the interval $0.71<U/U_{mean}<1.54$ 21 along $10\leq x\leq 735$ mm symmetry axis plane. From x=0 to x=300 mm, all values have slight velocity differences. At region $300\leq x\leq 750$ mm, values ascent from $0.71<U/U_{mean}<1.54$. The outer jets velocity are U_o=15.56 m/s and the inner jet velocity is U_i=5.0 m/s. The outer jets velocity had influence acceleration at the symmetry axis near x=300 mm. The obtained results between both C_1 and D_1 test cases, reveals that the angle increase from 11° to 22° influenced earlier the increase of velocity at the symmetry axis.

Figure 3.4 presents the obtained results for both convergent jets 11° (C_2 test case f=40 Hz) and 22° (D_2 test case f=40 Hz). C_2 test case show values within the interval $0.72<U/U_{mean}<1.09$ along $10\leq x\leq 735$ mm symmetry axis plane. The outer jets velocity are U_o=19.0 m/s and the inner jet velocity is U_i=6.0 m/s. Along $10\leq x\leq 500$ mm all obtained values are identical, within $0.72<U/U_{mean}<0.8$ interval. At the x=500 mm region, the velocity begin to rise up till U/U_{mean}=1.09 in the farthest point. For this C_2 test case the outer jets velocity begin to influence the symmetry axis inner jet velocity at x=500 mm. For D_2 test case the results are within the interval $0.67<U/U_{mean}<1.52$ $10\leq x\leq 735$ mm symmetry axis plane. The outer jets velocity are U_o=19.9 m/s and the inner jet velocity is U_i=6.0 m/s. At region $10\leq x\leq 375$ mm, all values have slight velocity differences, between $0.67<U/U_{mean}<0.88$. At region $400\leq x\leq 750$ mm, the measured points gradually gain velocity from U/U_{mean}=0.9 to U/U_{mean}=1.52 at the x=692 mm, with a slight descendant values at the two farthest points. The outer jets velocity had influence acceleration at the symmetry axis near at x=375 mm. The obtained results between both C_2 and D_2 test cases, reveals that the angle increase from 11° to 22° influenced earlier the increase of velocity at the symmetry axis, as shows the graphic. Figure 3.4 shows also that immediately before the visible velocity acceleration effect at the symmetry axis, and for the two test cases (C_2 and D_2) both values experiment a very slight slowdown results.

3.3. Horizontal profiles of the vertical velocity

Similarly to subchapter 3.2, this subchapter graphics presents the relation between the dimensionless vertical velocity V in its vertical coordinate, along the distance of 39 measured points at the exit jets on its horizontal coordinate within 10<x≤750 mm. The obtained values are located along the symmetry axis plane y=0 mm. As mentioned at subchapter 2.5, green laser LDA_2 measures the vertical velocities with a verification signal of minus (-) in favour to upwards direction and a positive (+) to the symmetry axis plane direction. In these subchapter four graphics, the vertical velocity distribution values are presented in both positive and negative values, from $-0.1 \leq V/U_{mean} \leq 0.1$ along the symmetry axis. The general appearance of all four graphics shows that the obtained values are almost in favour to upwards.

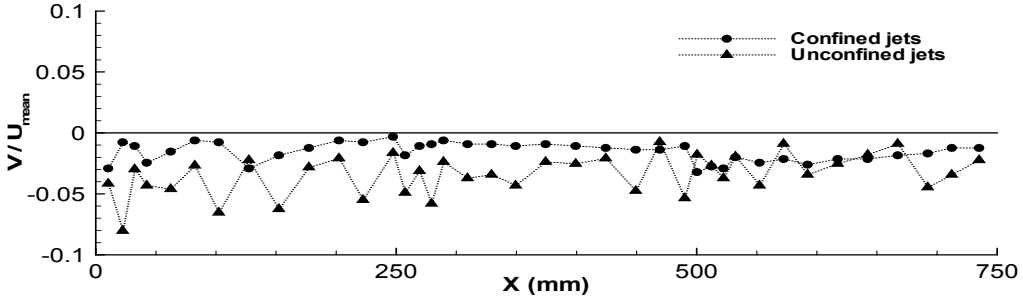

Figure 3.5. Horizontal profiles of vertical velocity for A_1 and B_1 test cases.

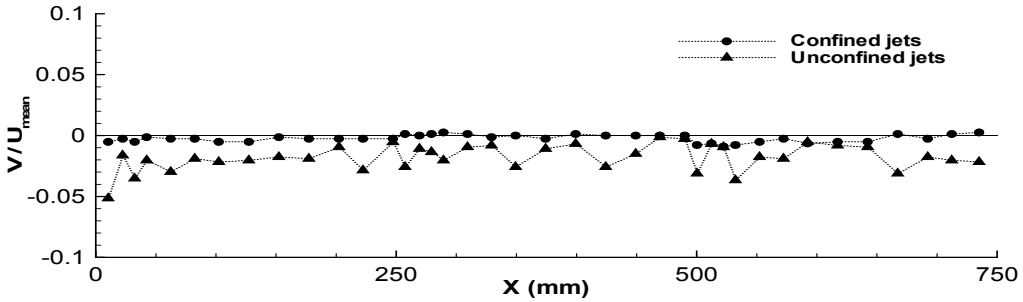

Figure 3.6. Horizontal profiles of vertical velocity for A_2 and B_2 test cases.

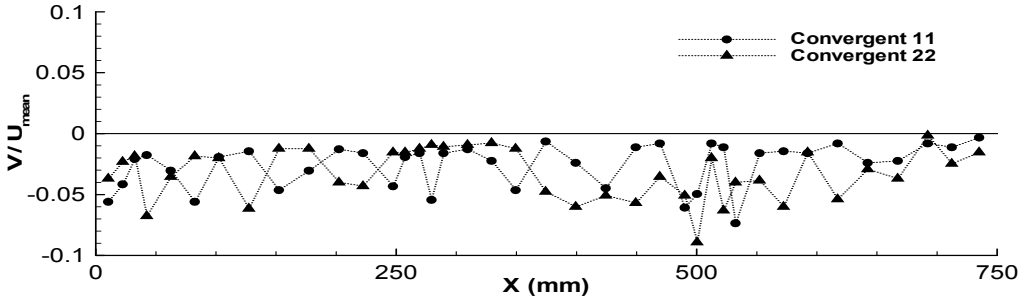

Figure 3.7. Horizontal profiles of vertical velocity for C_1 and D_1 test cases.

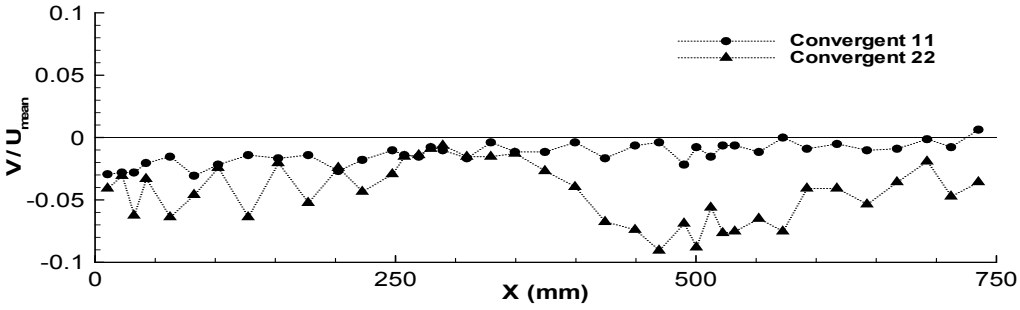

Figure 3.8. Horizontal profiles of vertical velocity for C_2 and D_2 test cases.

Figure 3.5 presents the obtained results for the B_1 confined and A_1 unconfined jets. The confined test case, show values within the $-0.02901<V/U_{mean}<-0.00305$ interval, with lowers values -0.02901 present at x=10 mm, x=127.25 mm and x=522.25 mm points. The velocity variation is lower for this case than for the unconfined case. The unconfined test show values within the $-0.08024<V/U_{mean}<-0.00743$ interval. When compared the two intervals, it could be verified that the unconfined jets interval it is almost 2.75 times the confined jets interval amplitude. However, all velocities are near zero.

Figure 3.6 presents the obtained results for the B_2 confined and A_2 unconfined jets. The confined test case, show values within the $-0.00912<V/U_{mean}<+0.002584$. This interval range is about $V/U_{mean}=0.003496$. From x=250 to x=500 mm, the obtained values are almost positive, which reveals the velocity tendency in favour to the axis plane direction. For the unconfined jets, all values are in a negative interval within $-0.05149<V/U_{mean}<-0.00136$. This interval range is about $V/U_{mean}=0.051626$, nearly 14 times the range interval of the confined jets case. Compared with the results of Figure 3.5, it could be concluded that the increase of horizontal velocity is connected with a less perturbation of the flow, the decrease of vertical velocity. All velocities are near zero.

Figure 3.7 presents the obtained results for both C_1 convergent jets 11° and D_1 convergent jets 22°. C_1 test case follows the tendency of negative values, with all values between $-0.07348<V/U_{mean}<-0.00319$. This range interval is about $V/U_{mean}=0.07029$. These oscillations are expected, due to the perturbation caused by the convergent jets. D_1 test case follows the tendency of negative values, with all values between $-0.8923<V/U_{mean}<-0.00154$. This range interval is about $V/U_{mean}=0.08769$. These oscillations were increased by the velocity increase. It was verified that in all A and B test cases the increase of horizontal velocity produces the opposite effect.

Figure 3.8 presents the obtained results for both C_2 convergent jets 11° and D_2 convergent jets 22°. C_2 test case follows the tendency of negative values with exception for the farthest point. All values are between the $-0.03061<V/U_{mean}<+0.006378$ interval, with a range of $V/U_{mean}=0.036988$. D_2 test case follows the tendency of negative values. All values are between the $-0.09056<V/U_{mean}<-0.00638$ interval, with a range of $V/U_{mean}=0.08418$, nearly 2.2 times the C_2 test case interval. Figure 3.5 to 3.8 reveal velocities near zero.

3.4. Vertical profiles of horizontal velocity

This subchapter presents all obtained results for vertical profiles of horizontal velocity distribution at the horizontal axis in each studied station between -50<y<200 mm. All graphics are dimensionless form by mass average velocity U_{mean}. For all presented graphics the verification velocity signals are inverted, thus to obtain positive velocity values. Minus verification signal (-) obtained favouring the flow direction did not appear and horizontal velocity distribution values presents only positive values between $0 \leq U/U_{mean} \leq 3$. Confined jets limit values ends at y=148.50 mm due to its wall confinement. Unconfined jets limit values ends at y=182.25 mm.

3.4.1. Unconfined A_1 and confined B_1 jets

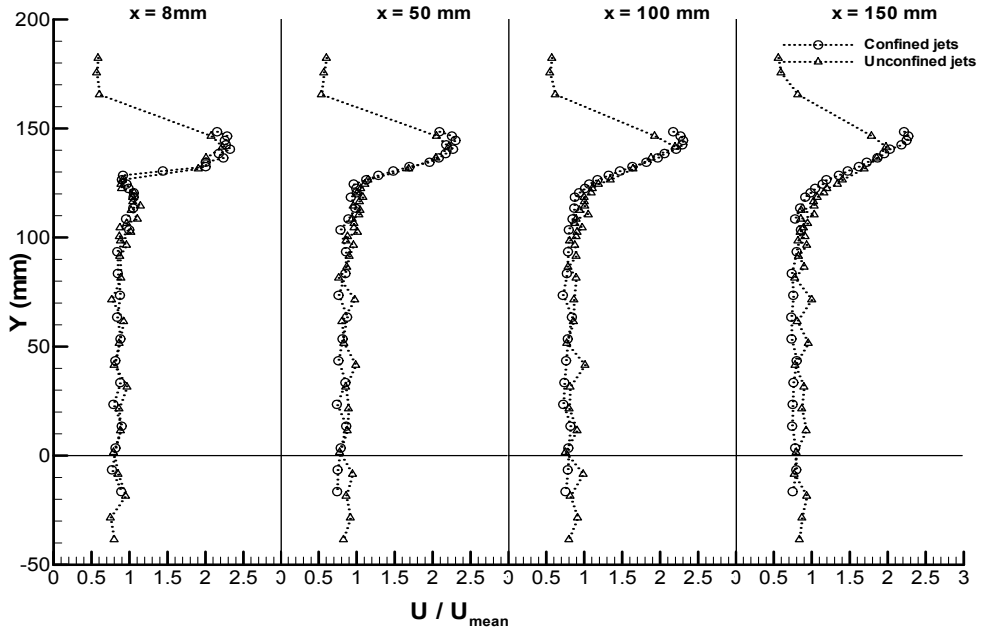

Figure 3.9. Vertical profiles of horizontal velocity for A_1 and B_1 test cases at stations x=8, 50, 100 and 150 mm.

Figure 3.9 shows the horizontal velocity results obtained for A_1 and B_1 test cases for the stations x=8, 50, 100 and 150 mm. In first station x=8 mm and for the B_1 confined test case the obtained values are within the $0.81<U/U_{mean}<2.32$, with its minor value verified at point y=3.5 mm and its major value verified at point y=140.50 mm. From y=148.5 to y=130.5 mm it is possible to identify the stronger outer jet values. At y=130.5 mm it is possible to identify the outer/inner jets shear layer. At this point there is loss of outer jet velocity in relation to its north and also a loss of the inner jet velocity related to its south, due to the very close jets division plate. Within $100 \leq y \leq 128.5$ mm range it is possible to observe a slightly velocity recuperation, due to momentum transfer, i.e., the faster U_o flow movement accelerates the slower U_i flow. Within $0 \leq y \leq 100$ range the values present $U/U_{mean}<0.90$. For

the A_1 unconfined test case, all the values are within $0.79<U/U_{mean}<2.22$. The minor value of this interval is verified at the point y=1.5 mm and the major value at the point y=141.50 mm. The highest velocity peak is lower than the observed for the confined jets case. At y=130.5 mm it is also possible to identify the outer/inner jets shear layer with a loss of outer and inner jets velocity. Within $0\leq y\leq 100$ range the obtained results are practically identical for both test cases.

For the station at x=50 mm the obtained results for both test cases are practically identical. The B_1 confined jets present its highest velocity peak of $U/U_{mean}=2.3$ at y=144.50 mm and its low velocity of $U/U_{mean}=0.74$ at y=23.50 mm. The A_1 unconfined jets present its highest velocity peak of $U/U_{mean}=2.21$ at y=141.50 mm and its low velocity of $U/U_{mean}=0.77$ at y=1.50 mm. In this stations, the y=130.5 mm point at the outer/inner jets mixture, there is no north and south verifications of velocity loss. In this region, the jets presents already a mixing ratio, which leads to a higher velocity attainment, the opposed to what happened in the previous station. Despite this mixture area verification, both jets present still their own well defined zone.

For the station x=100 mm the obtained results for both test cases remain practically identical. The B_1 confined jets present its highest velocity peak of $U/U_{mean}=2.3$ at y=144.50 mm and its low velocity of $U/U_{mean}=0.72$ at y=73.50 mm. The A_1 unconfined jets present its highest velocity peak of $U/U_{mean}=2.19$ at y=141.50 mm and its low velocity of $U/U_{mean}=0.75$ at y=1.50 mm.

The station x=150 mm verifies again the identical values for both test cases A_1 and B_1. The B_1 confined jets present its highest velocity peak of $U/U_{mean}=2.27$ at y=146.50 mm and its low velocity of $U/U_{mean}=0.73$ at y=73.50 mm. The outer jet higher velocity point is verified a little further north. The A_1 unconfined jets present its highest velocity peak of $U/U_{mean}=1.97$ at y=141.50 mm and its low velocity of $U/U_{mean}=0.79$ at y=1.5 mm. The highest outer jet velocity points remain practically the same for the unconfined figuration, regarding its evolution between first four measured stations (y=141.5 mm). The unconfined jet present a decrease evolution of the higher velocity values regarding the first four stations presented at Figure 3.9. The north wall confinement removal acted in the velocities and provoked an outer jet deflection.

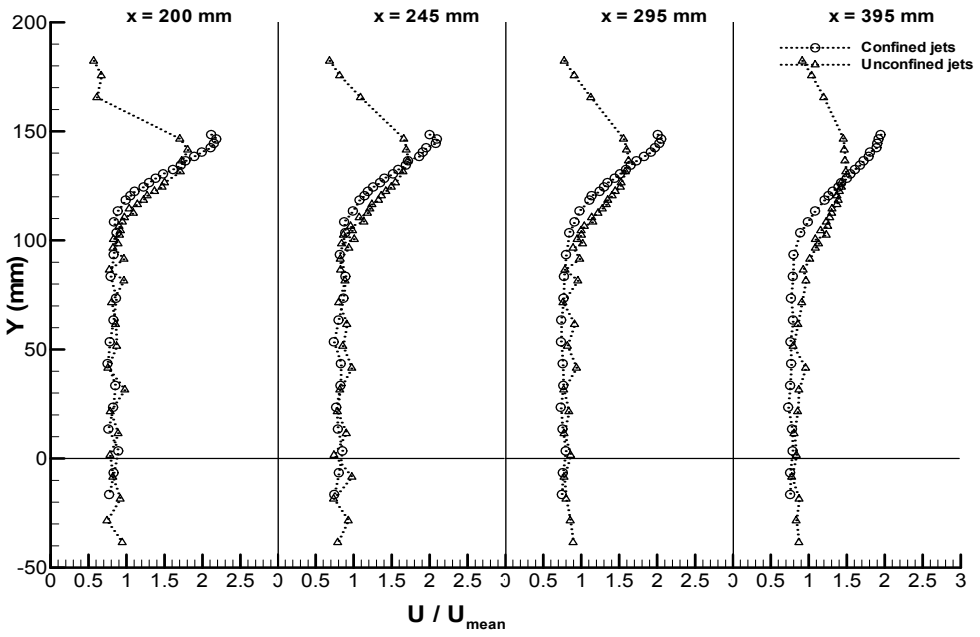

Figure 3.10. Vertical profiles of horizontal velocity for A_1 and B_1 test cases at stations x=200, 245, 295 and 395 mm.

In Figure 3.10 and for the station x=200 mm, both inner and the outer jet regions is still well defined, with region more close to point y=130.50 mm showing smother peak curves for both test cases. The outer jet velocity is already spread to y=110 mm north vicinity points. Besides, the highest velocities for both test cases, present lower values as well: related with the previous station the B_1 confined jets present its highest value downed from U/U_{mean}=2.27 for U/U_{mean}=2.1, with this value verified at the same point (y=146.50 mm). The lowest value is U/U_{mean}=0.74 at y=53.50 mm. Also related with the previous station the A_1 unconfined jets highest velocity value descend as well from U/U_{mean}=1.97 to U/U_{mean}=1.81 and remains at y=141.50 mm. The minor velocity verified is U/U_{mean}=0.78 at y=1.50 mm.

For the station x=245 mm, the outer jet influence extends from y=100 mm to all upwards measured values for both test cases. For the B_1 confined jet test case, the highest velocity is practically identical to the previous station, U/U_{mean}=2.09 at y=146.50 mm as well as the lowest value U/U_{mean}=0.73 at y=53.50 mm. For the A_1 unconfined jet test case, the highest velocity is U/U_{mean}=1.71 verified at different point y=136.50 mm and the lowest velocity is U/U_{mean}=0.74 at y=1.50 mm.

For the station x=295 mm the confined jet highest velocity is U/U_{mean}=2.05 at y=146.50 mm and the lowest velocity is U/U_{mean}=0.73 at y=53.50 mm. The unconfined jet test case highest velocity is U/U_{mean}=1.62 at y=136.50 mm and the lowest velocity is U/U_{mean}=0.76 to y=71.50 mm. The velocity amplitude is descending and the velocity curves are smoother, notably for the unconfined test case.

For the station x=395 mm and maintaining what has been observed along previous stations, the velocity amplitudes are smaller: for the confined jets the highest value is

U/U_{mean}=1.92 verified at the same point y=146.50 mm and the lowest velocity is U/U_{mean}=0.72 verified at y=23.50 mm. For the unconfined jet the highest value is U/U_{mean}=1.49 verified at a new point y=131.50 mm and the lowest velocity is U/U_{mean}=0.79 verified at y=51.50 mm.

Regarding the amplitude results evolution from x=8 mm to x=395 mm, B_1 test case $0.81<U/U_{mean}<2.32$ (U/U_{mean}=1.51 amplitude range) initial interval present values within the $0.72<U/U_{mean}<1.92$ (U/U_{mean}=1.2 amplitude range) at x=395 station mm, decreasing nearly 20%. Similarly, the A_1 test case $0.79<U/U_{mean}<2.22$ (U/U_{mean}=1.51 amplitude range) interval present values within the $0.79<U/U_{mean}<1.49$ (U/U_{mean}=0.7 amplitude range) at x=395 mm station, a closer 50% decreasing. Lower values are practically the same and higher values decreased.

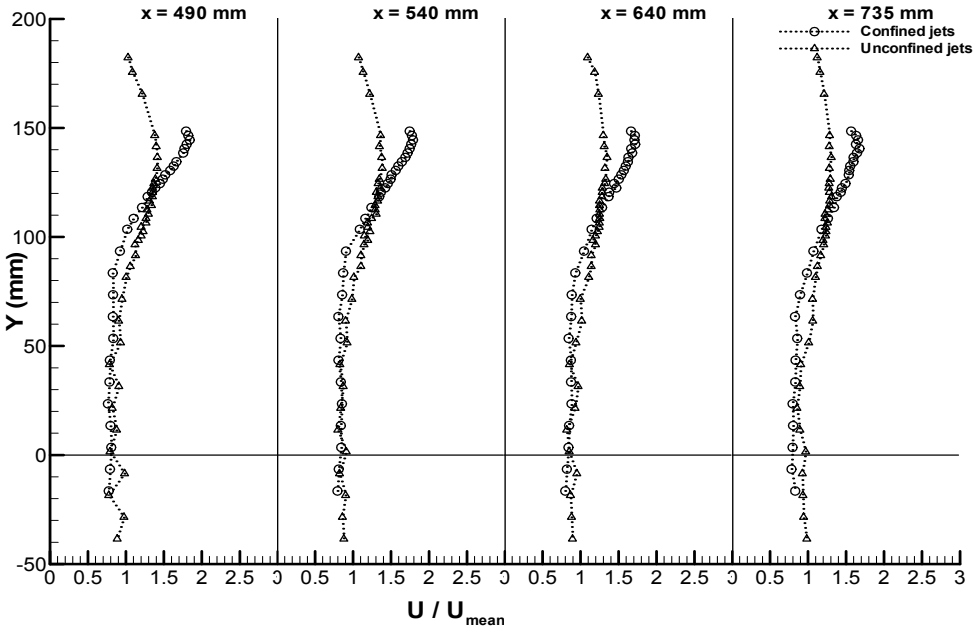

Figure 3.11. Vertical profiles of horizontal velocity for A_1 and B_1 test cases at stations x=490, 540, 640 and 735 mm.

At Figure 3.11, for the station x=490 mm the outer jet influence for confined test case is shown from north to near y=90 mm. For this case highest velocity is U/U_{mean}=1.84 at the same point y=146.50 mm. The lowest obtained value is U/U_{mean}=0.76 at y=23.50 mm. The unconfined case present its highest value of U/U_{mean}=1.41 at both points y=131.50 and 136.50 mm. The lowest value is U/U_{mean}=0.79 at point y=1.50 mm. The outer jet influence for this test case is shown from north to near y=80 mm.

For the station x=540 mm the velocity amplitudes continues to decrease for both test cases. For the confined jets, the highest value is U/U_{mean}=1.78 and is verified at a different point y=144.50 mm. Its minor value is U/U_{mean}=0.84 and appears at point y=13.50 mm. As for the unconfined test case, the highest values U/U_{mean}=1.38 appears at both points y=131.50 and y=136.50 mm. In upwards and downwards neighbourhood points of y=146.50 and 122.50

mm, the results shows weaker peaks with U/U_{mean}=1.36 value. The lowest value is U/U_{mean}=0.80 at y=11.50 mm.

For the station x=640 mm the velocity amplitude decrease continues: for the confined jet the highest velocity U/U_{mean}=1.71 is observed simultaneously at three points, y=146.50, 144.50 and 142.50 mm. The lowest velocity is U/U_{mean}=0.84 at y=13.50 mm. For the unconfined test case, the highest velocity is U/U_{mean}=1.35 at y=136.50 mm with several neighbourhood points registering very similar values. The lowest velocity is U/U_{mean}=0.85 at y=1.50 mm. The velocity amplitude for unconfined test case is almost half than the verified for the confined test case.

For the station x=735 mm the highest obtained velocity for the confined test case is U/U_{mean}=1.67 at y=140.50 mm with several surrounding points presenting similar values. The lowest value is U/U_{mean}=0.79 for y=3.50 mm. For the unconfined test case, the highest velocity is U/U_{mean}=1.30 at points y=136.50 and 118.50 mm. The lowest velocity is U/U_{mean}=0.85 at y=21.50 mm. The unconfined/confined velocity amplitude is like an half. The graphics shows that the horizontal velocity for the unconfined test case for station x=735 mm is practically a single velocity profile.

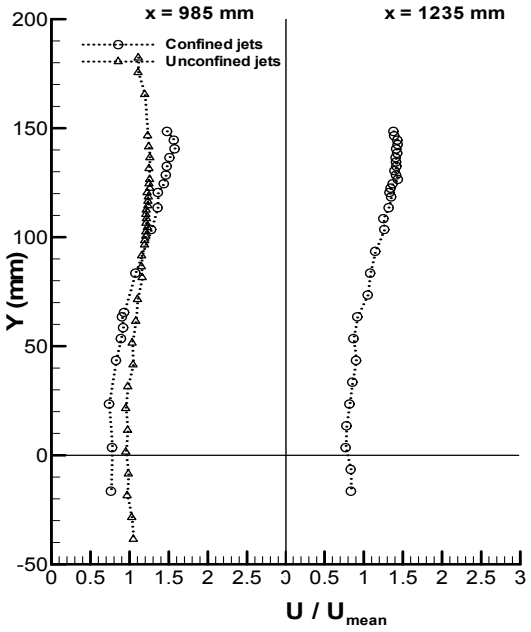

Figure 3.12. Vertical profiles of horizontal velocity for A_1 and B_1 test cases at stations x=985 and 1235 mm.

For the station x=985 mm in Figure 3.12, the highest velocity obtained for the confined test case is U/U_{mean}=1.57 at y=140.50 mm with several surrounding points presenting practically identical values. The lowest value is U/U_{mean}=0.73 and is verified at y=23.50 mm. For the unconfined jets test case, the highest value is U/U_{mean}=1.25 at y=126.50 mm. There are 18 points presenting values within $1.20<U/U_{mean}<1.25$ interval. The lowest velocity is

U/U_{mean}=0.95, almost the U_{mean} value. For the unconfined configuration the obtained results for this station, clearly shows a single velocity profile, that cannot present significant changes at any further station. For that it was decided to omit this test case for the next station.

Station x=1235 mm present the results for the confined test case. This station location is nearly 4.4 diameters distant from the jets exit. Highest velocity value is U/U_{mean}=1.43 at y=142.50 mm present 9 points with velocities within the $1.40<U/U_{mean}<1.43$ interval. The lowest velocity point is U/U_{mean}=0.77 at y=3.50 mm. This station is the farthest studied due to the traverse table railway end.

3.4.2. Unconfined A_2 and confined B_2 jets

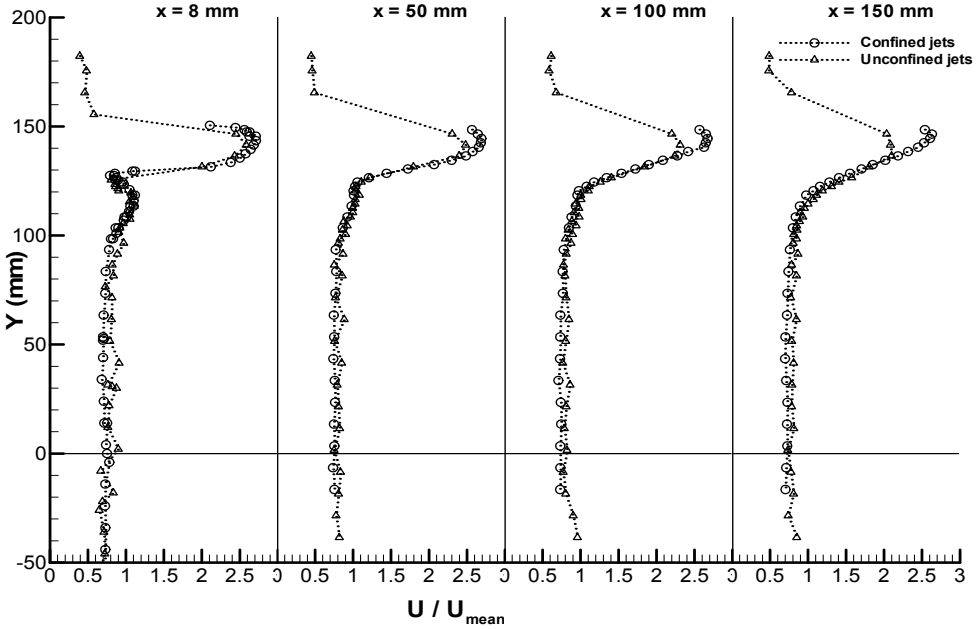

Figure 3.13. Vertical profiles of horizontal velocity for A_2 and B_2 test cases at stations x=8, 50, 100 and 150 mm.

Figure 3.13 shows the horizontal velocity results obtained for A_2 and B_2 test cases for the stations x=8, 50, 100 and 150 mm. For the first station x=8 mm and for the B_2 test case the obtained values are within the $0.68<U/U_{mean}<2.71$. The minor value of this interval is verified at the point y=34 mm and the major value at the point y=143.50 mm. Within the 130.50<y<148.5 mm interval it is possible to identify the stronger outer jet values. At y=130.5 mm it is possible to identify the outer/inner jets shear layer. At this point there is loss of outer jet velocity at related to its north and also a loss of the inner jet velocity related to its south, due to the very close jets division plate. From y=128.50 mm to y=100 mm it is possible to observe a slight velocity recuperation, due to momentum transfer as already found and referred for same station at Figure 3.9. For the same station in Figure 3.13, for the unconfined jets case all the values are within $0.76<U/U_{mean}<2.58$. The minor value of this interval is verified at the point y=12.0 and the major value at the point y=141.50 mm. The

highest velocity peak is lower than the confined jets case. For this first station, such as for the Figure 3.9 first station at y=130.5 mm it is also possible to identify the outer/inner jets shear layer with a loss of outer and inner jets velocity. From y=100 mm to symmetry axis for both cases all results are practically identical. Comparing the B_1 $0.81<U/U_{mean}<2.32$ and B_2 $0.68<U/U_{mean}<2.71$ amplitude results for this station, the velocity increasing show that higher and lower velocity results appear in the B_2 test case. At the same way, comparing the A_1 $0.79<U/U_{mean}<2.22$ and A_2 $0.76<U/U_{mean}<2.58$ amplitude results for this station, the velocity increasing show that higher and lower velocity results appear at A_2 test case.

For the station at x=50 mm the results for both test cases are practically identical. The confined jets present its highest velocity peak of $U/U_{mean}=2.69$ at y=144.50 mm and its lowest velocity of $U/U_{mean}=0.74$ at y=13.50 mm. The unconfined jets present its highest velocity peak of $U/U_{mean}=2.48$ at y=141.50 mm and its lowest velocity of $U/U_{mean}=0.75$ at y=1.50 mm. The verified outer/inner jets boundary velocity loss at y=130.50 mm in the previous station x=8 mm have lead to a both jets velocity mixture in this region and the result is a higher velocity attainment, the opposed to what happened in the previous station. Despite this mixture area verification, the jets are each at well defined zone.

For the station x=100 mm both test cases results are practically identical each other as well as in relation with the previous station. The highest velocity peak of the confined jets test case continues at y=144.50 mm and is $U/U_{mean}=2.67$, while the unconfined highest peak value is $U/U_{mean}=2.31$ at y=141.50 mm. The lowest values for the confined jets is $U/U_{mean}=0.73$ at y=3.50 mm and for the unconfined jets is $U/U_{mean}=0.78$ at y=11.50 mm. The highest velocity of unconfined jets is decreasing faster than the confined jets test case velocity peak.

For the station x=150 mm the unconfined jets highest velocity test case present a notorious decrease from $U/U_{mean}=2.31$ at the previous station to the value of $U/U_{mean}=2.10$ and that result is revealed at y=136.50 mm. For this test case, the lowest value is $U/U_{mean}=0.73$ at y=1.50 mm. The confined B_2 test case presents its highest velocity value of $U/U_{mean}=2.63$ at y=146.50 mm and its lowest velocity value of $U/U_{mean}=0.72$ at y=13.50 mm. The velocity amplitude intervals of unconfined/confined jets are nearly 71%. The velocity curve of the unconfined jets test case is smoother.

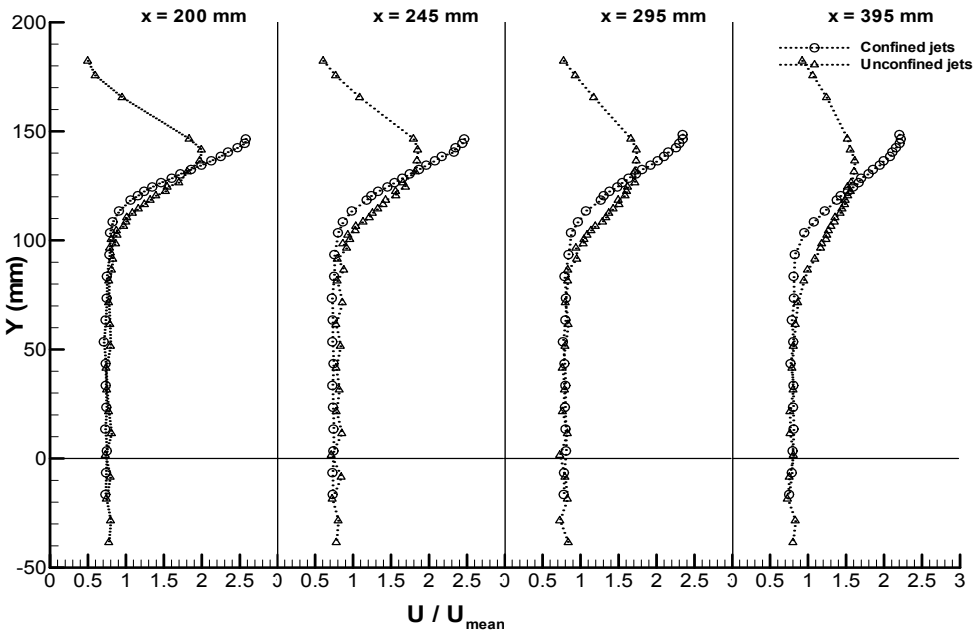

Figure 3.14. Vertical profiles of horizontal velocity for A_2 and B_2 test cases at stations x=200, 245, 295 and 395 mm.

In Figure 3.14, for the station x=200 mm the unconfined jets highest velocity test case presents is U/U_{mean}=1.99 at y=141.50 mm. The previous peak for this test case was at point y=136.50 mm. For this test case, the lowest value is U/U_{mean}=0.73 at y=1.50 mm. The confined jets test case present its highest velocity peak at y=146.50 mm and its values is U/U_{mean}=2.57 while the lowest value is U/U_{mean}=0.71 at y=53.50 mm. The influence of the outer jets velocity is visible form north to y=100 mm for both jets test cases. The velocity amplitude intervals of the unconfined/confined jets it is near 68%. The velocity curve of the unconfined jets test case is smoother.

For the station x=245, the confined jets test case present is highest velocity peak of U/U_{mean}=2.40 at y=146.50 mm. The lowest velocity is U/U_{mean}=0.79 at y=23.50 mm. The outer jet presents a slightly softer velocity curve than the same case at previous station. All values from y=100 to symmetry axis are practically identical since the first station. For the unconfined jets case, its higher velocity peak at this station is U/U_{mean}=1.85 at y=141.50 mm. The lowest velocity is U/U_{mean}=0.71 verified at y=1.50 mm. The velocity amplitude intervals of the unconfined/confined jets suffer a slight increase and it is near 71%. The outer jets curve for both cases is found smoother.

For the station X=295 mm the confined jets test case present is highest peak value of U/U_{mean}=2.34 at both y=146.50 and 148.50 mm, while the lowest value is U/U_{mean}=0.77 at y=53.50 mm. The outer jet presents a softer velocity curve than the same case at the previous station and its values are present from y=150 to y=90 mm. All values from y=90 mm to symmetry axis are practically identical since the first station. For the unconfined jets test case, the highest peak value is U/U_{mean}=1.73 at both y=136.50 and 131.50 mm points, while its

lowest value is U/U_{mean}=0.73 at y=1.50 mm. At this distance to the jets exit, the A_2 test case outer jet values are spread from y=182.25 mm near to y=90 mm, while the B_2 outer jets values are spread within the north wall at y=150 mm reaching y=100 mm. The velocity amplitude intervals of the unconfined/confined jets suffer a slight increase and it is near 64%. The outer jets curve for both cases is smoother.

For the station x=395 mm the confined jets test case present its highest peak value of U/U_{mean}=2.22 at y=146.50 mm, while the lowest value is U/U_{mean}=0.77 at y=43.50 mm. For this test case the outer jet evidence a smoothing velocity curve related to same case at previous station. When compared with the unconfined jets test case, it is more notable the velocity curves differences: while the unconfined jet is spread from y=182.25 mm to y=81.50 mm, the confined jet is spread from the north wall at y=150 mm to near y=100 mm. This reveals the jet flow attraction tendency to a nearby surface, i.e., the confinement of the outer flow retards the deflection due to the interaction between the boundary layer of the outer jet and the wall. The unconfined jets test case present its highest peak value of U/U_{mean}=1.61 at y=136.50 mm, while the lowest value is U/U_{mean}=0.76 at y=21.50 mm. When compared with previous station, the velocity amplitude intervals of the unconfined/confined jets suffer a nearly 58% values decrease.

Regarding the velocity amplitude intervals comparison between different velocities at station x=395 mm, the A_1 test case presents values within $0.7<U/U_{mean}<1.43$ while the A_2 test case presents $0.76<U/U_{mean}<1.61$. Lowest values are remaining practically the same, while highest values present a nearly 15% increase. The same situation is revealed when comparing the $0.72<U/U_{mean}<1.92$ B_1 with $0.77<U/U_{mean}<2.22$ B_2 amplitude intervals. Highest values present a nearly 17% increase. Regarding the amplitude results evolution from x=8 to x=395 mm station, B_2 test case $0.68<U/U_{mean}<2.71$ interval present values within the $0.77<U/U_{mean}<2.22$, a decrease of nearly 40%. At the same way, the amplitude results evolution for A_2 test case $0.76<U/U_{mean}<2.58$ interval present values within the $0.76<U/U_{mean}<1.61$, a decrease of nearly 47%. The unconfined test case amplitude velocity is decreasing faster than the confined test case.

Regarding the amplitude results evolution for the initial x=8 mm B_2 test case $0.68<U/U_{mean}<2.71$ interval present values within the $0.77<U/U_{mean}<2.22$ at x=395 mm station. At the same way, the amplitude results evolution for the initial x=8 A_2 test case $0.76<U/U_{mean}<2.58$ interval present values within the $0.76<U/U_{mean}<1.61$ at x=395 mm station. Lower values are practically the same, however higher values decreased: for the B_2 confined test case the amplitude along these stations varied from U/U_{mean}=2.03 to U/U_{mean}=1.45, decreasing nearly 29%. The A_2 unconfined test case present a much amplitude numbers, from U/U_{mean}=1.82 to U/U_{mean}=0.85, a closer 50% decreasing, all of this at the higher velocity values. The north wall confinement removal acted in the velocities and provoked an outer jet deflection.

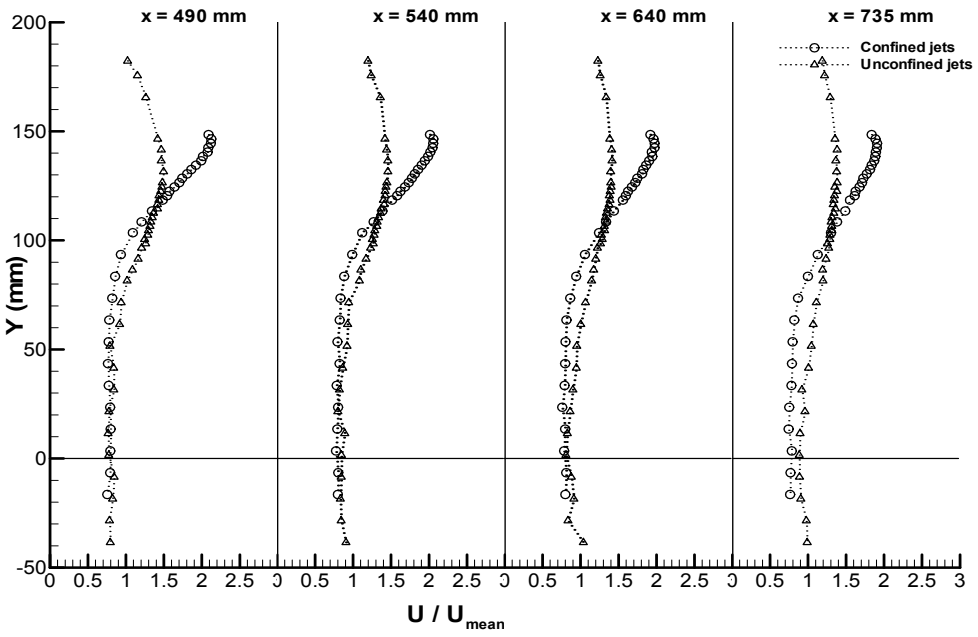

Figure 3.15. Vertical profiles of horizontal velocity for A_2 and B_2 test cases at stations x=490, 540, 640 and 735 mm.

For the station x=490 mm in the Figure 3.15, the confined jets presents its highest peak value of U/U_{mean}=2.12 at y=146.50 mm, while the lowest value is U/U_{mean}=0.76 at y=43.50 mm. The outer jet velocity is spread from the north wall y=150 to y=93.50 mm. The unconfined jets present its highest peak value of U/U_{mean}=1.50 at y=131.50 mm, while the lowest value is U/U_{mean}=0.77 at y=11.50 mm. The outer jet velocity for this test case is spread from the north wall y=182.25 mm to y=61.50 mm. When compared with previous station, the velocity amplitude intervals of the unconfined/confined jets suffer a slight decrease to a value near 54%.

For the station x=540 mm the confined jets present its highest peak value of U/U_{mean}=2.05 at y=146.50 mm, while the lowest value is U/U_{mean}=0.77 at y=3.50 mm. The outer jet velocity is spread from the north wall y=150 mm to y=83.50 mm. The unconfined jets present its highest peak value of U/U_{mean}=1.46 at y=131.50 mm and 126.50, with 10 obtained values within the $1.46<U/U_{mean}<1.40$ interval. The lowest value is U/U_{mean}=0.80 at y=21.50 mm. The outer jet velocity is spread from the north wall y=182.25 mm to y=41.50 mm. When compared with previous station, the velocity amplitude intervals of the unconfined/confined jets suffer a slight decrease to a value near 52%.

For the station x=640 mm, the confined jets present its highest peak value of U/U_{mean}=1.98 at both y=142.50 and y=140.50 mm points, while the lowest value is U/U_{mean}=0.78 at y=3.50 mm. The outer jet velocity is spread from the north wall y=150 mm to y=73.50 mm. The unconfined jets present its highest peak value of U/U_{mean}=1.41 at y=136.50 mm, with 10 obtained values within the $1.41<U/U_{mean}<1.37$ interval. The lowest value is U/U_{mean}=0.81 at y=1.50 mm. The outer jet velocity is spread from the north wall y=182.25 mm

to y=41.50 mm. When compared with previous station, the velocity amplitude intervals of the unconfined/confined jets suffer a slight decrease to a value near 50%.

For the station x=735 mm the confined jets present its highest peak value of U/U_{mean}=1.9 at both y=142.50 and y=140.50 mm points, while the lowest value is U/U_{mean}=0.74 at y=13.50 mm. The outer jet velocity is still spread from the north wall y=150 mm to y=73.50 mm. The unconfined jets present its highest peak value of U/U_{mean}=1.38 at both y=126.50 and 122.50 mm points, with 10 obtained values within the $1.38<U/U_{mean}<1.34$ interval. The lowest value is U/U_{mean}=0.88 at y=1.50 mm. The outer jet velocity is spread from the north wall y=182.25 mm to y=21.50 mm. When compared with previous station, the velocity amplitude intervals of the unconfined/confined jets suffer a decrease to a value near 44%.

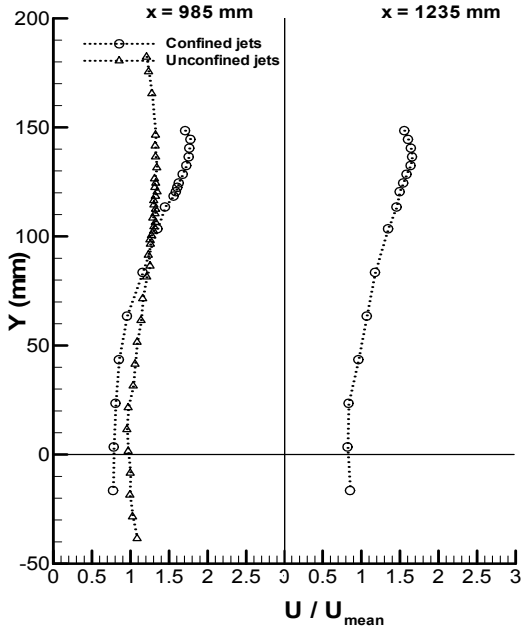

Figure 3.16. Vertical profiles of horizontal velocity for A_2 and B_2 test cases at stations x=985 and 1235 mm.

At Figure 3.16, for the station x=985 mm the confined jets presents its highest peak value of U/U_{mean}=1.77 at y=144.50 mm, while the lowest value is U/U_{mean}=0.78 at y=3.50 mm. The outer jet velocity is spread from the north wall y=150 mm to y=63.50 mm. The unconfined jets present its highest peak value of U/U_{mean}=1.34 at y=131.50 and y=120.50 mm, with 15 obtained values within the $1.34<U/U_{mean}<1.30$ interval. The lowest value is U/U_{mean}=0.95 at y=11.50 mm. The minimum obtained velocity is 0.95 U/U_{mean}. The graphic shows practically a single velocity profile instead of the two initial ones. For the unconfined test case for both A_1 and A_2 test cases (Figure 3.12 and Figure 3.16) for the station x=985 mm, this flow is fully developed. When compared with previous station, the velocity amplitude intervals of the unconfined/confined jets suffer a decrease to a value near 41%.

For the station x=1235 mm the confined jets present its highest peak value of U/U_{mean}=1.66 at both y=136.50 mm, while the lowest value is U/U_{mean}=0.83 at y=23.50 mm. The outer jet velocity is spread from the north wall y=150 mm to y=63.50 mm. This velocity amplitude interval is very similar to the unconfined case for the station x=540 mm and more than two times the interval of unconfined jets test case for x=985 mm.

3.4.3. Convergent 11° C_1 and convergent 22° D_1 jets

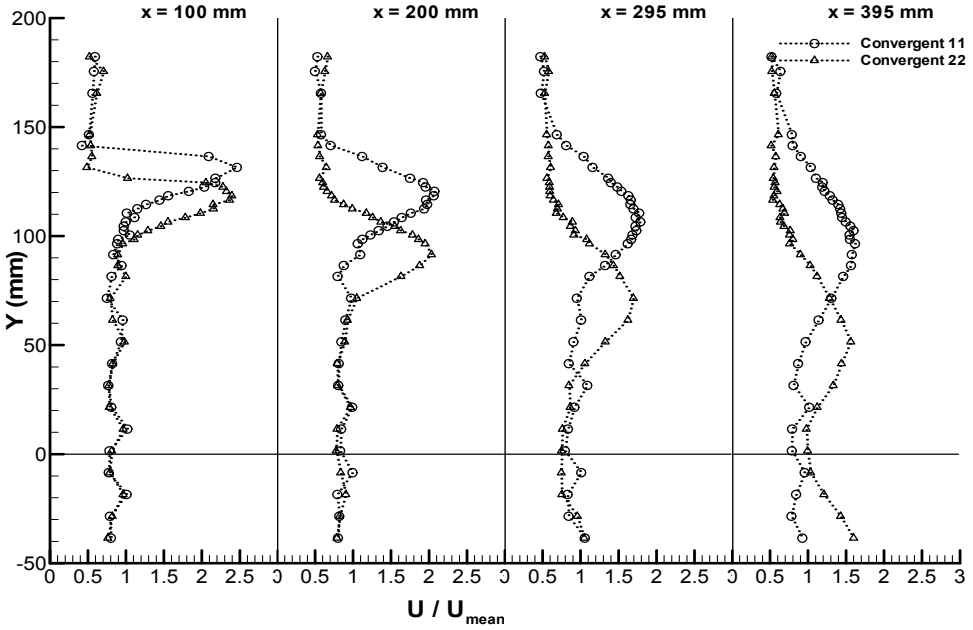

Figure 3.17. Vertical profiles of horizontal velocity for C_1 and D_1 test cases at stations x=100, 200, 295 and 395 mm.

Figure 3.17 shows the horizontal velocity results obtained for C_1 and D_1 test cases for the stations x=100, 200, 295 and 395 mm. At station x=100 mm both test cases shows differences only in their outer jet influence region. From y=150 mm upwards and from y=100 mm to symmetry axis plane, the obtained results for both C_1 and D_1 test cases are practically identical. For the C_1 test case, the outer jet velocity is spread within the 136.50<y<100 mm range, while for the D_1 test case the outer jet velocity is spread within the 126.50<y<96.50 mm range. The outer jet C_1 velocity peak is U/U_{mean}=2.46 at y=131.50 mm, while the outer jet D_1 velocity peak is U/U_{mean}=2.40 at y=118.50 mm. The outer/inner jet mixing is very low for both test cases. Vertical profiles differences are due to different inclination angles of outer jets.

For the station x=200 mm, from y=71.50 mm to symmetry axis plane and from y=150 mm upwards, the obtained results for both test cases are practically identical such as for the previous station. For the C_1 test case, at the 136.50<y<91.50 mm region, all obtained values are superior to U_{mean}, while for the D_1 test case, shows such values at the 110.50<y<71.50 mm region. The highest velocity registered for the C_1 test case is U/U_{mean}=2.07 at y=120.50 mm.

Observing the previous station, this C_1 test case value decreased from U/U_{mean}=2.46 to U/U_{mean}=2.07 and velocity peak point moved from y=131.50 mm to y=120.50 mm (moved 11 mm downwards) at this station. Regarding the D_1 test case, its highest value decreased from U/U_{mean}=2.40 at previous station for U/U_{mean}=2.03 in this one and the velocity peak point moved already to downwards, from y=118.50 mm in the previous station to y=91.50 mm in this one (moved 27 mm downwards). In the half south region of this station, for both test cases there is no jet mixing at all.

For the station x=295 mm, from y=41.50 mm to symmetry axis plane and from y=150 mm to north, the obtained results for both C_1 and D_1 test cases are practically identical such as for the previous station. For the C_1 test case, at the 136.50<y<81.50 mm region, all obtained values are superior to U_{mean}, while for the D_1 test case, shows such values at the 98.50<y<41.50 mm region. The highest velocity registered for the C_1 test case is U/U_{mean}=1.78 at y=106.50 mm. Observing the previous station, this C_1 test case value decreased from U/U_{mean}=2.07 to U/U_{mean}=1.78 and velocity peak point moved from y=120.50 mm to y=106.50 mm (moved 14 mm downwards) at this station. Regarding the D_1 test case, its highest value decreased from U/U_{mean}=2.03 at previous station for U/U_{mean}=1.70 in this one and the velocity peak point moved already from y=91.50 mm in the previous station to y=71.50 mm in this one (moved 20 mm downwards). Points from y=40 to symmetry axis plane, shows for both test cases, a very slight increase in the velocity values.

For the station x=395 mm, all the obtained results for both C_1 and D_1 test cases are different each other. For the C_1 test case, at the 131.50<y<61.50 mm region, all obtained values are superior to U_{mean}, while for the D_1 test case, shows such values at the 86.50<y<21.50 mm region. The highest velocity registered for the C_1 test case is U/U_{mean}=1.62 at y=96.50 mm. Observing the previous station, this C_1 test case value decreased from U/U_{mean}=1.78 to U/U_{mean}=1.62 and velocity peak point moved from y=106.50 mm to y=96.50 mm (moved 10 mm downwards) at this station. Regarding the D_1 test case, its highest value decreased from U/U_{mean}=1.70 at previous station for U/U_{mean}=1.56 in this one and the velocity peak point moved already from y=71.50 mm in the previous station to y=51.50 mm in this one (moved 20 mm downwards). At this station the C_1 test case results shows the highest obtained velocity at point y=96.50 mm and D_1 test case results shows the highest obtained velocity at point y=51.50 mm, which is close to the symmetry axis. For the D_1 test case this graphics shows that the jets are interacting completely. Since the first station x=100 mm to x=395 mm, the highest velocity peak of C_1 test case, moved 35 mm downwards and the same D_1 test case point moved 67 mm downwards.

The use of a convergent exit at the outer flow without the upper and lower plates provokes the merging of the flows. Regarding all the values at the station x=395 mm with special attention to the D_1 test case results and looking at its evolution since the first station it could be observed that the both south and north outer jets are not strong enough to turn

possible the idea of both outer jets joining at the symmetry axis even with high velocity peaks. That situation leads to a result that no recirculation zone could be detected.

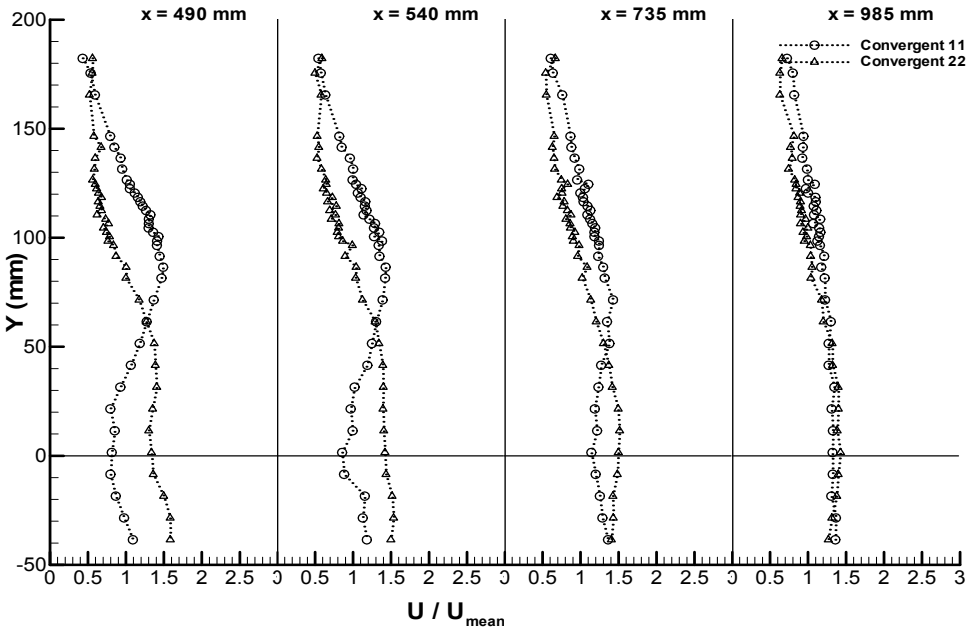

Figure 3.18. Vertical profiles of horizontal velocity for C_1 and D_1 test cases at stations x=490, 540, 735 and 985 mm.

In Figure 3.18, for the station x=490 mm all the obtained results for both C_1 and D_1 test cases are different each other. For the C_1 test case at the 126.50<y<41.50 mm region all obtained values are superior to U_{mean} while for the D_1 test case shows such values at the Y<81.50 mm region. The highest velocity registered for the C_1 test case is U/U_{mean}=1.49 at y=86.50 mm. Observing the previous station, this C_1 test case value decreased from U/U_{mean}=1.62 to U/U_{mean}=1.49 and velocity peak point moved from y=96.50 mm to y=86.50 mm (moved 10 mm downwards) at this station. Regarding the D_1 test case, its highest value decreased from U/U_{mean}=1.56 at previous station for U/U_{mean}=1.40 in this one and the velocity peak point moved already from y=51.50 mm in the previous station to y=31.50 mm in this one (moved 20 mm downwards).

For the station x=540 mm all the obtained results for both C_1 and D_1 test cases are different each other. For the C_1 test case, at the 126.50<y<41.50 mm region, all obtained values are superior to U_{mean}, while for the D_1 test case, shows such values at the Y<71.50 mm region. The highest velocity registered for the C_1 test case is U/U_{mean}=1.43 at y=86.50 mm. Observing the previous station, this C_1 test case value decreased from U/U_{mean}=1.49 to U/U_{mean}=1.43 and velocity peak point remains at y=86.50 mm at this station. Regarding the D_2 test case its highest value is U/U_{mean}=1.42, higher however very similar to U/U_{mean}=1.40 verified at the previous station. The velocity peak point moved from y=31.50 mm last station to y=1.50 mm in this one (moved 30 mm downwards).

For the station x=735 mm all the obtained results for both C_1 and D_1 test cases are different each other. For the C_1 test case at the y<122.50 mm region all obtained values are superior to U_{mean}, while the D_1 test case shows such values at the Y<86.50 mm region. The highest velocity registered for the C_1 test case is U/U_{mean}=1.42 at y=71.50 mm. Observing the previous station the highest value is identical and the velocity peak point moved from y=81.50 mm to y=71.50 mm (moved 10 mm downwards). Regarding the D_1 test case its highest value increased from U/U_{mean}=1.42 at previous station for U/U_{mean}=1.50 in this one and the velocity peak point moved from y=31.50 mm to y=1.50 mm in this one (moved 30 mm downwards).

For the station x=985 mm for the C_1 test case for the region y<120.50 mm all obtained values are superior to U_{mean}, while the D_1 test case shows an increment region values from previous station: y<86.50 mm region at previous station to the y<96.50 mm region at this station. The highest velocity registered for the C_1 test case is U/U_{mean}=1.32 at several points near the symmetry axis. Observing the previous station, this C_1 test case value decreased from U/U_{mean}=1.42 to U/U_{mean}=1.32 and the velocity peak disappeared. Regarding the D_1 test case, its highest value decreased from U/U_{mean}=1.50 at previous station for U/U_{mean}=1.43 in this one and the velocity peak disappeared too. Observing this station graphic, both test cases present very similar values.

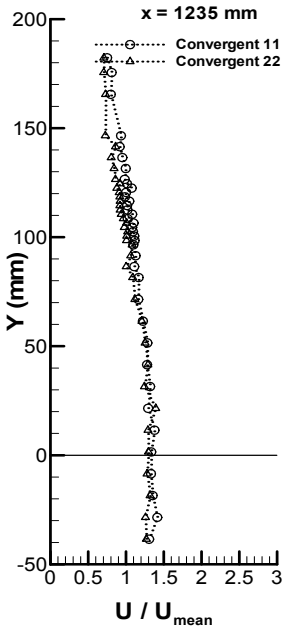

Figure 3.19. Vertical profiles of horizontal velocity for C_1 and D_1 test cases at station x=1235 mm.

Station x=1235 mm (Figure 3.19) shows the C_1 test case shows that at the Y<116.50 mm region all obtained values are superior to U_{mean}, while for the D_1 test case shows such values in y<102.50 mm region. The highest velocity registered for the C_1 test case is U/U_{mean}=1.37 at several points near the symmetry axis. Observing the previous station, this C_1 test case value increased from U/U_{mean}=1.32 to U/U_{mean}=1.37 and the velocity peak

disappeared. Regarding the D_1 test case, its highest value decreased from U/U_{mean}=1.43 at previous station for U/U_{mean}=1.40 in this one and the velocity peak disappeared too. Observing this station graphic, both test cases are practically identical.

3.4.4. Convergent 11° C_2 and convergent 22° D_2 jets

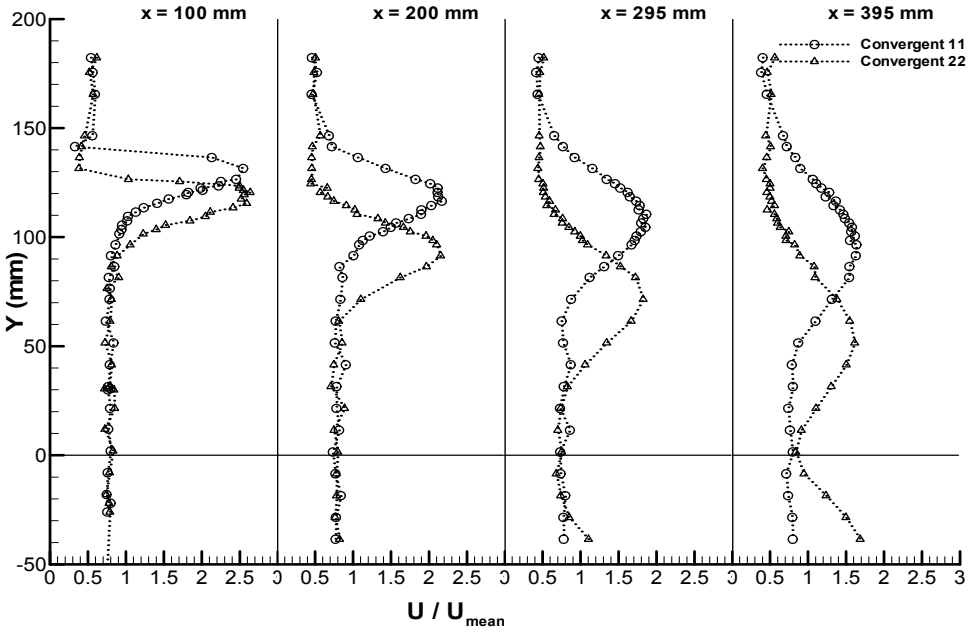

Figure 3.20. Vertical profiles of horizontal velocity for C_2 and D_2 test cases at stations x=100, 200, 295 and 395 mm.

Figure 3.20 shows the horizontal velocity results obtained for C_2 and D_2 test cases for the stations x=100, 200, 295 and 395 mm. Regarding station x=100 mm, both test cases shows differences only at the outer jet influence region. From y=140 mm upwards and from y=90 mm to symmetry axis plane the obtained results for both test cases are practically identical. For the C_2 test case the outer jet velocity is spread within the 136.50<y<107.50 mm, while for the D_2 test case the outer jet velocity is spread within the 126.50<y<96.50 mm. The outer jet C_2 velocity peak is U/U_{mean}=2.54 at y=131.50 mm, while the outer jet D_2 velocity peak is U/U_{mean}=2.63 at y=118.50 mm. The outer/inner jet mixing is very low for both test cases.

For the station x=200 mm, from y=61.50 mm to symmetry axis plane and from y=150 mm to north the obtained results are identical for both C_2 and D_2. For the C_2 test case, at the 136.50<y<91.50 mm region, all obtained values are superior to U_{mean}, while for the D_2 test case, shows such values at the 112.50<y<71.50 mm region. The highest velocity registered for the C_2 test case is U/U_{mean}=2.17 at y=116.50 mm. Observing the previous station, this C_2 test case value decreased from U/U_{mean}=2.54 to U/U_{mean}=2.17 and velocity peak point moved from y=131.50 mm to y=116.50 mm (moved 15 mm downwards) at this station. Regarding the D_2 test case, its highest value decreased from U/U_{mean}=2.63 at previous station for U/U_{mean}=2.15 in this one and the velocity peak point moved already from y=120.50 mm in the previous

station to y=91.50 mm in this one (moved 29 mm downwards). By comparing this two first stations with the same stations for the C_1 and D_1 test cases (Figure 3.17, x=100 and x=200 mm), the velocity peak points moved further axis plane; in the C_1 test case between the two stations it is verified that the highest velocity peak moved 11 mm to axis plane, while the C_2 test case present a 15 mm approach to symmetry axis plane. Similar situation is found for the D_1 and D_2 test cases, where the highest velocity peak point increases its migration from 27 to 29 mm approach to symmetry axis plane, between the two first stations. The velocity increase in both jets produces a faster outer/inner jets mixing.

For the station x=295 mm from y=31.50 mm and from y=150 mm to north the obtained results for both test cases are practically identical such as for the previous station. For the C_2 test case, at the 131.50<y<81.50 mm (50 mm zone) region, all obtained values are superior to U_{mean}, while for the D_2 test case, shows such values at the 98.50<y<41.50 region mm (57.50 mm zone). The highest velocity registered for the C_2 test case is U/U_{mean}=1.85 at y=104.50. Observing the previous station, C_2 test case values decreased from U/U_{mean}=2.17 to U/U_{mean}=1.85 and velocity peak point moved from y=116.50 mm to y=104.50 mm (moved 12 mm downwards) at this station. Regarding the D_2 test case, its highest value decreased from U/U_{mean}=2.15 at previous station for U/U_{mean}=1.82 in this one and the velocity peak point moved already to symmetry axis plane direction, from y=91.50 mm in the previous station to y=71.50 mm in this one (moved 20 mm downwards).

For the station x=395 mm all the obtained results for both test cases are different each other. For the C_2 test case, at the 126.50<y<61.50 mm region (65 mm zone) all obtained values are superior to U_{mean}, while for the D_2 test case shows such values at the 86.50<y<21.50 region mm (65 mm zone). The highest velocity registered for the C_2 test case is U/U_{mean}=1.64 at y=96.50 mm. Regarding the previous station, C_2 test case values decreased from U/U_{mean}=1.85 to U/U_{mean}=1.64 and velocity peak point moved from y=104.50 mm to y=96.50 mm (moved 8 mm downwards) at this station. Regarding the D_2 test case, its highest value decreased from U/U_{mean}=1.82 at previous station for U/U_{mean}=1.62 in this one and the velocity peak point moved already from y=71.50 mm in the previous station to y=51.50 mm in this one (moved 20 mm downwards). At this station the C_2 test case results shows the highest obtained velocity at point y=96.50 mm and D_2 test case results shows the highest obtained velocity at point y=51.50 mm, which is close to the symmetry axis plane. For the D_2 test case this graphics shows that the jets are interacting completely. Since the first station x=100 mm to x=395 mm, the highest velocity peak of C_2 test case, moved 35 mm downwards and the same D_2 test case point moved 67 mm downwards, identical values to C_1 and D_1 test cases between those stations.

Similarly to what is found at the same station x=395 mm for C_1 and D_1 test cases and by regarding the evolution values from x=100 mm to x=395 mm, for C_2 and D_2 test cases it could be observed that the both south and north outer jets are not strong enough to turn possible the idea of both outer jets joining at the symmetry axis even with high velocity

peaks. That situation leads to a result that no recirculation zone could be detected, since at this exit jets distance the velocity peaks decreased strongly and the outer jet influence is still far from reach the asymmetry axis.

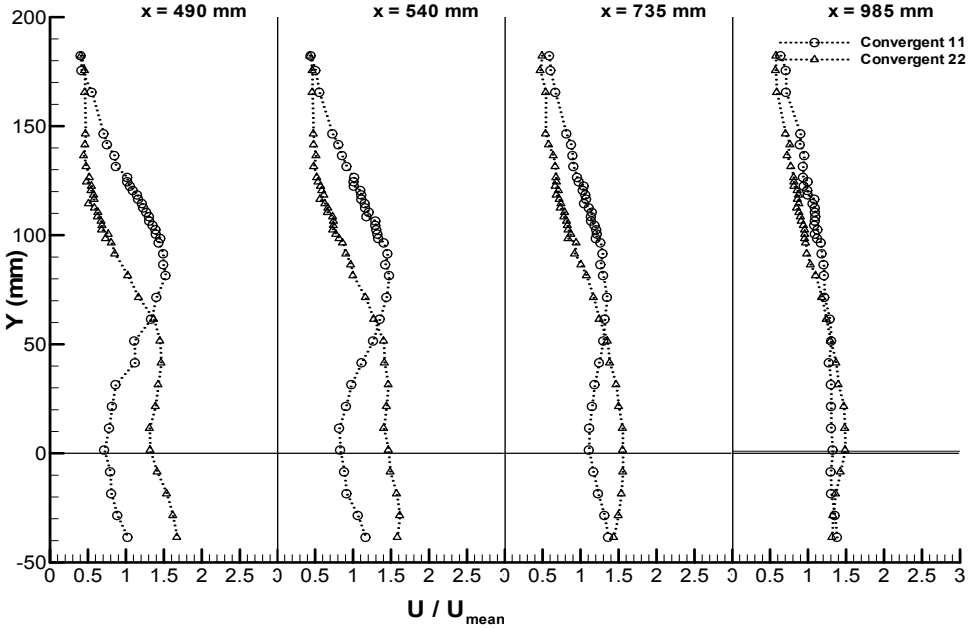

Figure 3.21. Vertical profiles of horizontal velocity for C_2 and D_2 test cases at stations x=490, 540, 735 and 985 mm.

In Figure 3.21, in the station x=490 mm all the obtained results for both test cases are different each other. Regarding C_2 test case, along the 126.50<y<41.50 mm region all obtained values are superior to U_{mean}, while D_2 test case shows such values at the y<81.50 mm region. The highest velocity registered for the C_2 test case is U/U_{mean}=1.52 at y=81.50 mm. Observing the previous station, C_2 test case value decreased from U/U_{mean}=1.64 to U/U_{mean}=1.52 and velocity peak point moved from y=96.50 mm to y=81.50 mm (moved 15 mm downwards) at this station. Regarding the D_2 test case, its highest value decreased from U/U_{mean}=1.62 at previous station for U/U_{mean}=1.47 at x=490 mm and the velocity peak point moved from y=51.50 mm in the previous station to y=41.50 mm in this one (moved 10 mm downwards).

For the station x=540 mm all the obtained results for both C_2 and D_2 test cases are different each other. For the C_2 test case, at the 126.50<y<41.50 mm region, all obtained values are superior to U_{mean}, while for the D_2 test case, shows such values at the y<71.50 mm region. The highest velocity registered for the C_2 test case is U/U_{mean}=1.47 at y=81.50 mm. Observing the previous station, this C_1 test case value decreased from U/U_{mean}=1.52 to U/U_{mean}=1.47 and velocity peak point remains at y=81.50 mm at this station. Regarding the D_2 test case its highest value is U/U_{mean}=1.46 practically identical to U/U_{mean}=1.47 verified at the

previous station. The velocity peak point moved from y=41.50 mm last station to y=31.50 mm in this one (moved 10 mm downwards).

For the station x=735 mm all the obtained results for both test cases are different each other. For the C_2 test case at the y<122.50 mm region all obtained values are superior to U_{mean}, while the D_2 test case shows such values at the y<86.50 mm region. The highest velocity registered for the C_2 test case is U/U_{mean}=1.35 at y=71.50 mm. Observing the previous station, C_2 value decreased from U/U_{mean}=1.47 to U/U_{mean}=1.35 and velocity peak point moved from y=81.50 mm to y=71.50 mm (moved 10 mm downwards). Regarding the D_2 its highest value increased from U/U_{mean}=1.46 at previous station for U/U_{mean}=1.55 in this one and the velocity peak point moved from y=31.50 mm to y=1.50 mm in this one (moved 30 mm downwards).

For the station x=985 mm, both test cases are tending to approach each other as a single one. The outer/inner jets velocity for both cases is very similar. For the C_2 test case for the region y<116.50 mm, all obtained values are superior to U_{mean}, while the D_2 test case shows same results at y<86.50 mm region The highest velocity registered for the C_2 test case is U/U_{mean}=1.32 at several points near the symmetry axis. Observing the previous station, this C_2 test case value decreased from U/U_{mean}=1.35 to U/U_{mean}=1.32 and the velocity peak disappeared. Regarding the D_2 test case, its highest value decreased from U/U_{mean}=1.55 at previous station for U/U_{mean}=1.49 in this one and the velocity peak disappeared too.

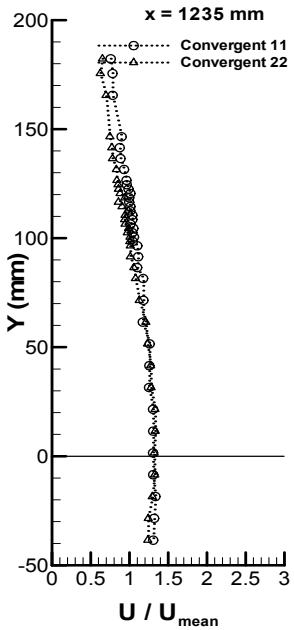

Figure 3.22. Vertical profiles of horizontal velocity for C_2 and D_2 test cases at station x=1235 mm.

For the station x=1235 mm (Figure 3.22) all obtained values are practically identical. The difference between both test cases is noted very slight at the north values. The C_2 test case shows that at the y<114.50 mm region all obtained values are superior to U_{mean}, while for

the D_2 test case shows such values in y<100.50 mm region. The highest velocity registered for the C_2 is U/U_{mean}=1.33 at several points near the symmetry axis. Observing the previous station, C_2 test case value decreased from U/U_{mean}=1.32 to U/U_{mean}=1.30 and the velocity peak disappeared. Regarding the D_2 test case, its highest value decreased from U/U_{mean}=1.49 at previous station for U/U_{mean}=1.33 in this one and the velocity peak disappeared too.

From the results of this subchapter 3.4 for the convergent jets tests cases it can be concluded that the use of a convergent exit at the outer flow without the upper and lower plates provokes the merging of the flows, but no recirculation zone could be detected.

3.5. Vertical profiles of vertical velocity

This subchapter presents all the obtained results for the vertical profiles of vertical velocity V, (dimensionless form by U_{mean}) distribution at the horizontal axis in each studied station, from y=200 mm to y=-50 mm. The vertical velocity distribution values are presented in both positive and negative values, from $-0.5 \leq V/U_{mean} \leq +0.5$. In some cases some graphics had to be presented from $-0.6 \leq V/U_{mean} \leq +0.4$ and $-0.8 \leq V/U_{mean} \leq +0.2$. However, and similar to subchapter 3.4 graphics, the verification velocity minus signal (-) and plus signal (+) were inverted: the minus verification signal is favouring the symmetry axis plane direction and the plus verification signal is favouring upwards. The confined jets values starts at y=148.50 mm, due to its wall confinement. The unconfined jets values starts at y=182.25 mm.

3.5.1. Unconfined A_1 and confined B_1 jets

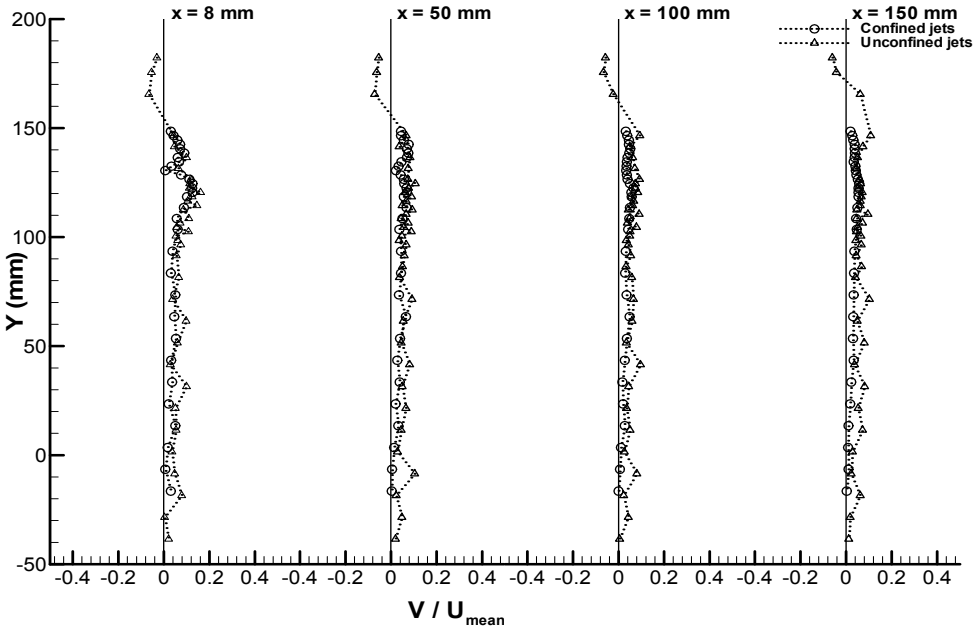

Figure 3.23. Vertical profiles of vertical velocity for A_1 and B_1 test cases at stations x=8, 50, 100 and 150 mm.

Figure 3.23 shows the vertical velocity results obtained for A_1 and B_1 test cases for the stations x=8, 50, 100 and 150 mm. For the first station x=8 mm for the B_1 test case the obtained values are within the $0.0067<V/U_{mean}<0.126$, with the minor value verified at the point y=130.50 mm at the outer/inner exit jets division and the major value at both points y=124.50 and 120.50 mm. The revealed positive values indicates that the vertical velocity favour the upwards until the north wall. Within $118.50\leq y\leq 128.50$ mm it is possible to observe $V/U_{mean}>0.1$ stronger vertical velocity results for this test case, being pulled into the outer jet. From the y=113.50 mm up to symmetry axis plane, all values are bellow 0.08 V/U_{mean}. The A_1 test case show similar results to B_1 test case. The north wall removal, show negative values at north pulled in the exterior jet direction, at points y=182.25, 175.50 and 165.50 mm. The obtained values are within the $0.06<V/U_{mean}<0.144$. The minor value of this interval is verified at the point y=131.50 mm at the outer/inner exit jets division and the major value at the point y=144.50 mm. Within $114.50\leq y\leq 126.50$ mm it is possible to observe the stronger $V/U_{mean}>0.1$ vertical velocity results for this test case being pulled into the outer jet. From the y=100.50 mm up to symmetry axis plane, all values are bellow 0.1 V/U_{mean}.

For the station x=50 mm for the B_1 test case the obtained values are within the $0.0137<U/U_{mean}<0.077$. The minor value of this interval is verified at the point y=3.50 mm at and the major value at point y=142.50 mm. The revealed positive values indicates that the vertical velocity favour the upwards until the north wall. The A_1 test case show similar results to B_1 test case. The north wall removal, show negative values at north pulled in the exterior jet direction, at points y=182.25, 175.50 and 165.50 mm. The obtained values are within the $-0.07<U/U_{mean}<0.106$. The minor value of this interval is verified at the point y=165.50 mm and the major value at the point y=124.50 mm. Both velocity amplitudes are lower than the obtained at x=8 mm and the outer/inner jet division values are smoother.

For the station x=100 mm for the B_1 test case, the obtained values are within the $0.01<V/U_{mean}<0.065$. The minor value of this interval is verified at the point y=3.50 mm and the major value at point y=122.50 mm. The revealed positive values indicates that the vertical velocity favour the upwards until the north wall. The jets A_1 test case show similar results to B_1 test case. The north wall removal, show negative values at north pulled in the exterior jet direction, at points y=182.25, 175.50 and 165.50 mm. The obtained values are within the $0.025<V/U_{mean}<0.096$. The minor value of this interval is verified at the point y=1.50 mm and the major value at the point y=41.50 mm. Both velocity amplitudes are lower than the obtained at both previous stations x=8 and x=50 mm.

For the station x=150 mm for the B_1 test case, the obtained values are within the $0.019<V/U_{mean}<0.054$. The minor value of this interval is verified at the point y=148.50 mm and the major value at points y=122.50, 12.50 and 118.50 mm. The revealed positive values indicates that the vertical velocity favour the upwards until the north wall. The A_1 test case show similar results to B_1 test case. The north wall removal, show negative values at north pulled in the exterior jet direction, at points y=182.25 and 175.50 mm. The obtained values

are within the $0.028<V/U_{mean}<0.108$. The minor value of this interval is verified at the point y=1.50 mm and the major value at the point y=146.50 mm. The confined jets test case velocity amplitudes are lower than the verified at all previous stations.

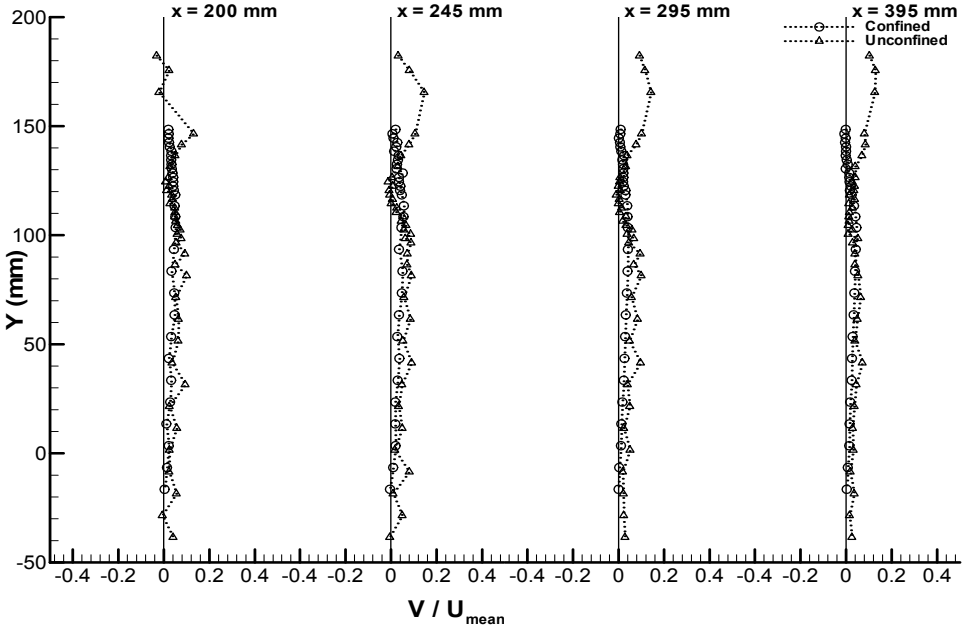

Figure 3.24. Vertical profiles of vertical velocity for A_1 and B_1 test cases at stations x=200, 245, 295 and 395 mm.

Figure 3.24 shows the vertical velocity results obtained for A_1 and B_1 test cases for the stations x=200, 245, 295 and 395 mm. For the station x=200 mm for the B_1 test case, the obtained values are within the $0.0137<V/U_{mean}<0.056$. The minor value of this interval is verified at the point y=138.50 mm and the major value at point y=113.50 mm. The revealed positive values indicates that the vertical velocity favour the upwards until the north wall. The A_1 test case show similar results to B_1 test case. The north wall removal, show negative values at north pulled in the exterior jet direction, at points y=182.25 and 165.50 mm. The obtained values are within the $0.0073<V/U_{mean}<0.13$. The minor value of this interval is verified at the point y=124.50 mm and the major value at the point y=146.50 mm. The exterior measured points for the unconfined test case are beginning to change their vertical velocity direction.

For the station x=245 mm for the B_1 test case, the obtained values are within the $0.006<V/U_{mean}<0.056$. The minor value of this interval is verified at the point y=146.50 mm and the major value at point y=113.50 mm. The revealed positive values indicates that the vertical velocity favour the upwards until the north wall. The A_1 test case show similar results to B_1 test case. The north wall removal, show positive values at north pulled the flow to outside direction, at points y=182.25, 175.50 and 165.50 mm. The higher velocity value at this test case is even at point y=165.50 mm, which is a point situated north to the outer jet.

The obtained values are within the $-0.0089<V/U_{mean}<0.144$. The minor value of this interval is verified at the point y=120.50 mm and the major value at the point y=165.50 mm. Three points at y=124.50, 120.50 and 118.50 mm reveals negative values, indicating that they are experiencing vertical velocities favouring the axis plane direction.

For the station x=295 mm, the B_1 test case obtained values are within the $0.01<V/U_{mean}<0.041$ with its minor value verified at point y=3.50 mm and its major value at both points y=103.5 and y=93.50 mm. The revealed positive values indicates that the vertical velocity favour the upwards until the north wall. The points from y=150 mm to y=100 mm reveals close to zero velocities. The A_1 test case show similar results to B_1 test case at axis plane and centre graphic regions. The north wall removal show positive values at north pulled the flow to outside direction, at points y=182.25, 175.50 and 165.50 mm. The obtained values are within the $-0.0015<V/U_{mean}<0.151$. The minor value of this interval is verified at both points y=122.50 mm and y=114.50 mm and the major value at the point y=165.50 mm.

For the station x=395 mm for the B_1 test case, from $130.50<y<148.50$ mm the obtained values are within the $-0.0076<V/U_{mean}<0$. This interval indicates that the vertical velocity is almost zero, with a very slight velocity favouring the axis plane direction. The minor value of this interval is verified at the point y=146.50 mm, and all other values are within $0<y<0.045$ mm with the major value at points y=103.50 mm. The jets A_1 test case show similar results to B_1 test case at axis plane and centre graphic regions. The north wall removal, show positive values at north pulled the flow to outside direction, at points y=182.25, 175.50 and 165.50 mm. The obtained values are within the $0.008<V/U_{mean}<0.13$. The minor value of this interval is verified at both points y=104.50 mm and y=114.50 mm and the major value at the point y=175.50 mm, the second exterior point.

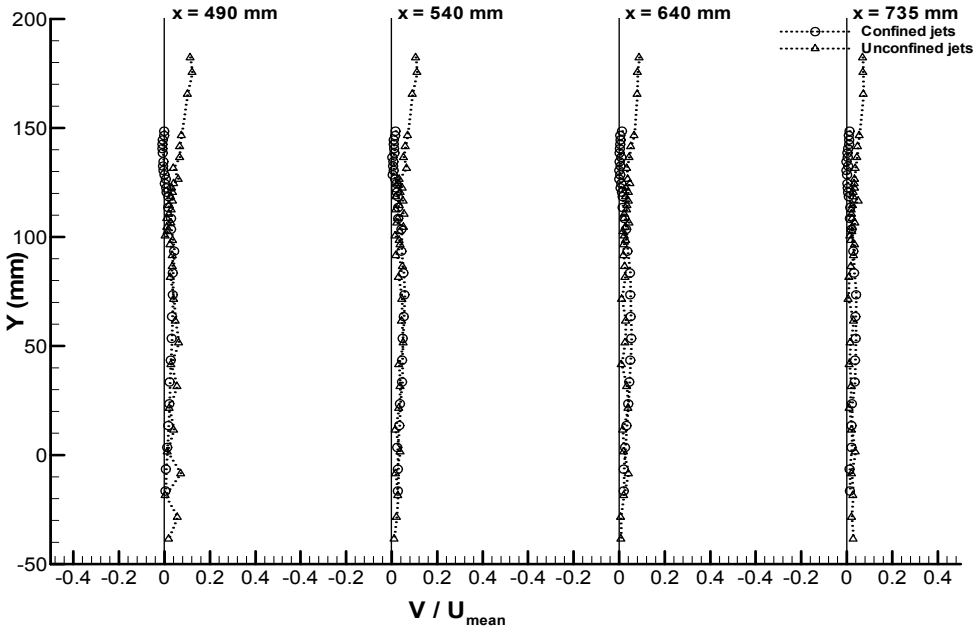

Figure 3.25. Vertical profiles of vertical velocity for A_1 and B_1 test cases at stations x=490, 540, 640 and 735 mm.

Figure 3.25 shows that for stations x=490, 540, 640 and 735 mm all the obtained results for both test cases are practically identical. As the station increases its distance to the exit jets all values tend to approach to zero value, except the north values for the unconfined test case, where the vertical velocity tend also to decrease but reveal vertical values that lead the exterior points y=182.50, 172.50 and 162.50 mm experiencing outside pushing.

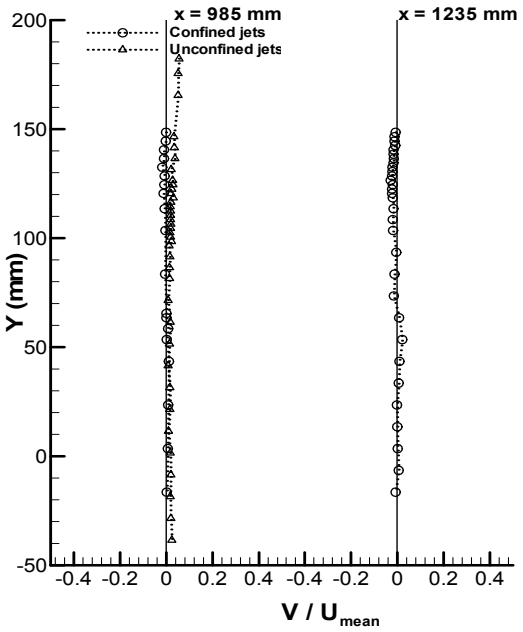

Figure 3.26. Vertical profiles of horizontal velocity for A_1 and B_1 test cases at stations x=985 and 1235 mm.

Figure 3.26 shows that for the stations x=985 mm, all the obtained results for both test cases are practically identical. All points reveal zero vertical velocities neighbourhood, with the exterior points of the unconfined jets still presenting outside pushing velocity. Station x=1235 mm shows only the confined test case, but all values are practically zero.

3.5.2. Unconfined A_2 and confined B_2 jets

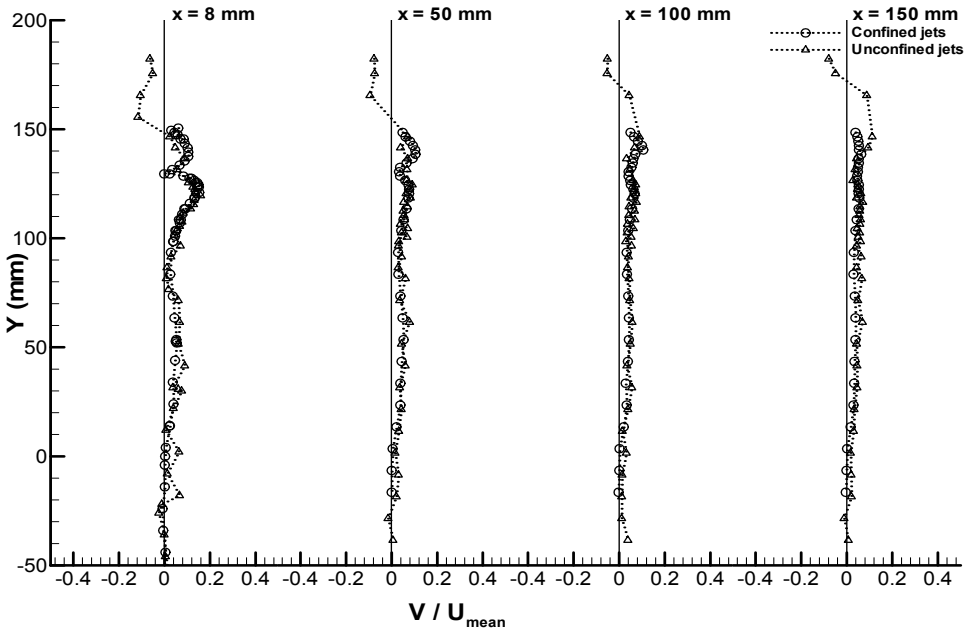

Figure 3.27. Vertical profiles of vertical velocity for A_2 and B_2 test cases at stations x=8, 50, 100 and 150 mm.

Figure 3.27 shows the vertical velocity results obtained for A_2 and B_2 test cases for the stations x=8, 50, 100 and 150 mm. For station x=8 mm the B_2 test case the obtained values are within $-0.001<V/U_{mean}<+0.15$. The minor value of this interval is verified at the point y=129.50 mm at the outer/inner exit jets division and the major value at point y=121.50 mm. The revealed positive values indicates that the vertical velocity favour the upwards until the north wall. From y=127.50 mm to y=116.0 mm it is possible to observe the stronger vertical velocity results for this test case, being pulled into the outer jet, $V/U_{mean}>0.1$. From the y=113.50 mm up to symmetry axis plane, all values are bellow 0.09 V/U_{mean}. The A_2 test case show similar results to B_2 test case. The north wall removal, show negative values at north pulled in the exterior jet direction, at points y=182.25, 175.50, 165.50 and 155.50 mm. The obtained values are within the $0.005<V/U_{mean}<0.159$. The minor value of this interval is verified at the point y=12.00 mm and the major value at the point y=119.50 mm. From y=125.50 mm to y=113.5 mm it is possible to observe the stronger vertical velocity results for this test case, being pulled into the outer jet, $V/U_{mean}>0.1$. From the y=110.50 mm up to symmetry axis plane, all values are bellow 0.08 V/U_{mean}. Generally, all obtained values for both test cases at this station are practically identical with exception for the four further north points for the unconfined jets test case. For both it is easy to identify the exterior and interior jets values.

For the station x=50 mm for the B_2 test case the obtained values are within the $0.0137<V/U_{mean}<0.077$. The minor value of this interval is verified at the point y=3.50 mm at

and the major value at both points y=142.50 mm. The revealed positive values indicates that the vertical velocity favour the upwards until the north wall. The A_1 test case show similar results to B_1 test case. The north wall removal, show negative values at north pulled in the exterior jet direction, at points y=182.25, 175.50 and 165.50 mm. The obtained values are within the $-0.07<V/U_{mean}<0.106$. The minor value of this interval is verified at the point y=165.50 mm and the major value at the point y=124.50 mm. Both velocity amplitudes are lower than the obtained at x=8 mm and the outer/inner jet division values are smoother.

For the station x=100 mm for the B_2 test case the obtained values are within the $0.0014<V/U_{mean}<0.106$. The minor value of this interval is verified at the point y=3.50 mm and the major value at point y=140.50 mm. The revealed positive values indicates that the vertical velocity favour the upwards until the north wall. The A_2 test case show similar results to B_2 test case. The north wall removal, show negative values at north pulled in the exterior jet direction, at points y=182.25 and 175.50 mm. The obtained values are within the $0.0324<V/U_{mean}<0.0930$. The minor value of this interval is verified at the point y=1.50 mm and the major value at the point y=41.50 mm. The outer/inner jet division values are practically disappeared.

For the station x=150 mm the obtained values for the B_2 test case is almost a very close to zero straight line. The outer/inner jets values division disappeared completely. For the unconfined jets A_2 test case, obtained values are very similar for same test case at the previous station, with exception to few north graphic points. Two exterior points presents negative values, indicating that their velocities are being pulled to the exterior jet.

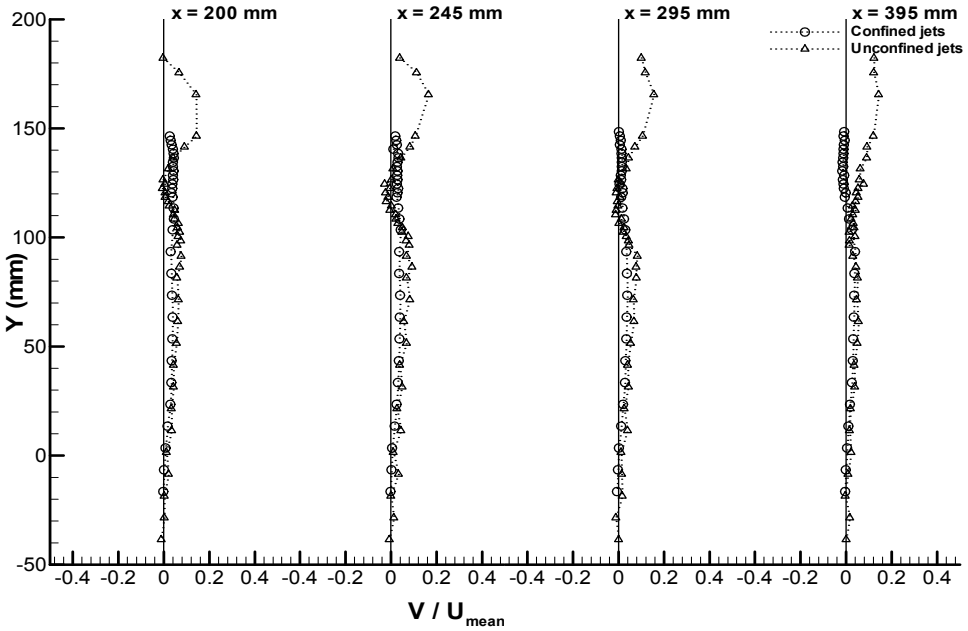

Figure 3.28. Vertical profiles of vertical velocity for A_2 and B_2 test cases at stations x=200, 245, 295 and 395 mm.

For the station x=200 mm (Figure 3.28) the B_2 test case values are within the $0.007<V/U_{mean}<0.0437$ interval. The A_2 unconfined jets test case exterior points at north are now being pushed away from exterior jet. Points y=126.50 and 122.50 mm present very slight negative velocity.

For the station x=245 mm the B_2 test case values are within the $0<V/U_{mean}<0.0350$ interval, practically identical to the obtained values for same test case at previous station. The A_2 test case present a positive region value from y=182.25 mm to y=126.50 mm, followed by a negative region value from y=124.50 mm to y=116.50 mm.

For the station x=295 mm the B_2 test case within the $142.50<y<148.50$ mm interval present positive V/U_{mean} values less than 0.01. The other remaining points present values practically identical to the obtained values for same test case at previous station. The A_2 test case present a positive region value from y=182.25 mm to y=124.50 mm, followed by a negative region value from y=122.50 mm to y=110.50 mm. Regarding the same test case at the previous station, the further north points are experiencing more velocity to north and the positive region value is somewhat wider.

For the station x=395 mm the B_2 test case within the $118.50<y<148.50$ mm interval present negative values, meaning that the velocity tendency is to symmetry axis plane. The other remaining points present values practically identical to the obtained values for same test case at previous station. The A_2 test case presents positive values for all measured points. Regarding the same test case at the previous station, the further north points are experiencing less velocity to north and the positive region value it is wider. At this station, both test cases are experiencing contrary vertical velocities at the $y>118.50$ mm region.

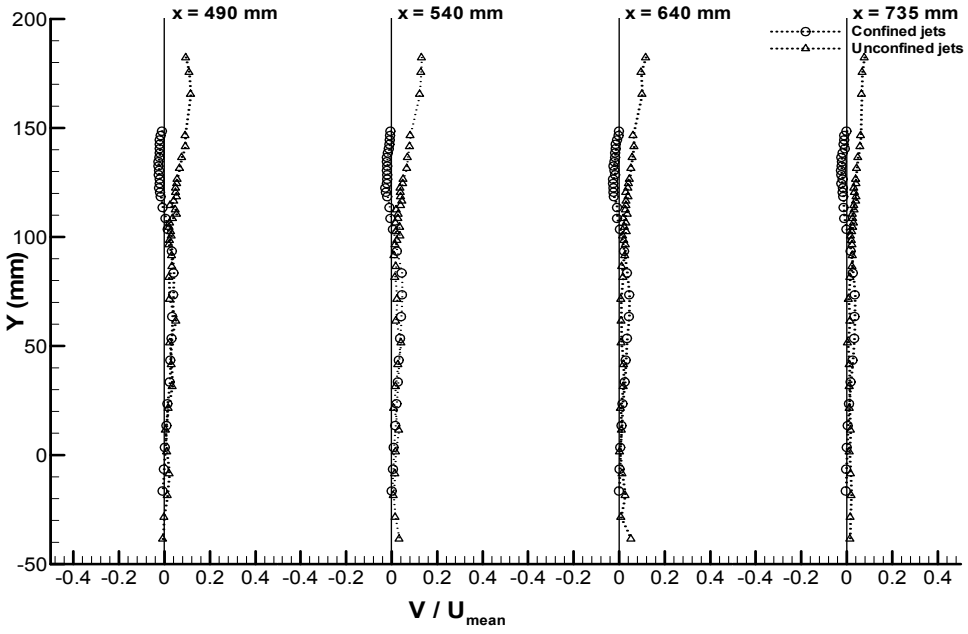

Figure 3.29. Vertical profiles of vertical velocity for A_2 and B_2 test cases at stations x=490, 540, 640 and 735 mm.

For the station x=490 mm (Figure 3.29) the B_2 test case present negative values within the 113.50<y<148.50 mm interval and the other remaining points present values practically identical to the obtained values for same test case at previous station. The A_2 test case presents positive values for all measured points. Regarding the same test case at the previous station, the further north points are experiencing less velocity to north and the positive region value it is wider. At this station, both test cases are experiencing contrary vertical velocities at the y>113.50 mm region. This region is experiencing velocity increasing and the absolute values differences seem to be decreasing.

For the station x=540 mm the B_2 test case present a negative value within the 108.50<y<148.50 mm interval and the other remaining points present values practically identical to the obtained values for same test case at previous station. The A_2 test case presents positive values for all measured points. Regarding the same test case at the previous station, the further north points are experiencing less velocity to north. At this station, both test cases are experiencing contrary vertical velocities at the y>108.50 mm region. Again, this region is experiencing velocity increasing and the absolute values differences seem to be decreasing.

Station x=640 mm presents previous station similar results. At this station, both test cases are experiencing contrary vertical velocities at the interval Y>108.50 mm region and the absolute values differences are decreasing.

At station x=735 mm the B_2 test case present a negative value within the 103.50<y<148.50 mm interval and the other remaining points present values closer to zero, regarding previous station. The A_2 unconfined jets test case present a positive values for all measured points. Regarding the same test case at the previous station, the further north points are experiencing less velocity to north. At this station, both test cases are experiencing contrary vertical velocities at the y>103.50 mm region. Again, this region is increasing and the absolute values differences are decreasing.

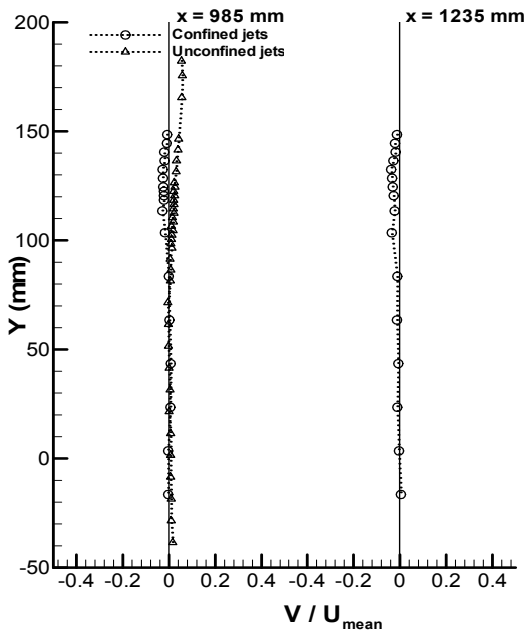

Figure 3.30. Vertical profiles of vertical velocity for A_2 and B_2 test cases at stations x=985 and 1235 mm.

The station x=985 mm (Figure 3.30) for the B_2 test case reveals only three points with positive vertical velocity at y=63.50, 43.50 and 23.50 mm. All values for this test case present a practically straight line at the zero vicinity. The A_2 unconfined jets test case reveals three point with negative velocity at y=71.50, 61.50 and 51.50 mm. Points to y<96.50 mm interval presents velocities near zero. The positive velocity at north is decreasing.

The station x=1235 mm presents an all negative velocity revealed profile for the confined jets test case. Values vary from V/U_{mean}=-0.004 at y=3.5 mm to V/U_{mean}=-0.034 at y=128.50 mm.

3.5.3. Convergent 11° C_1 and convergent 22° D_1 jets

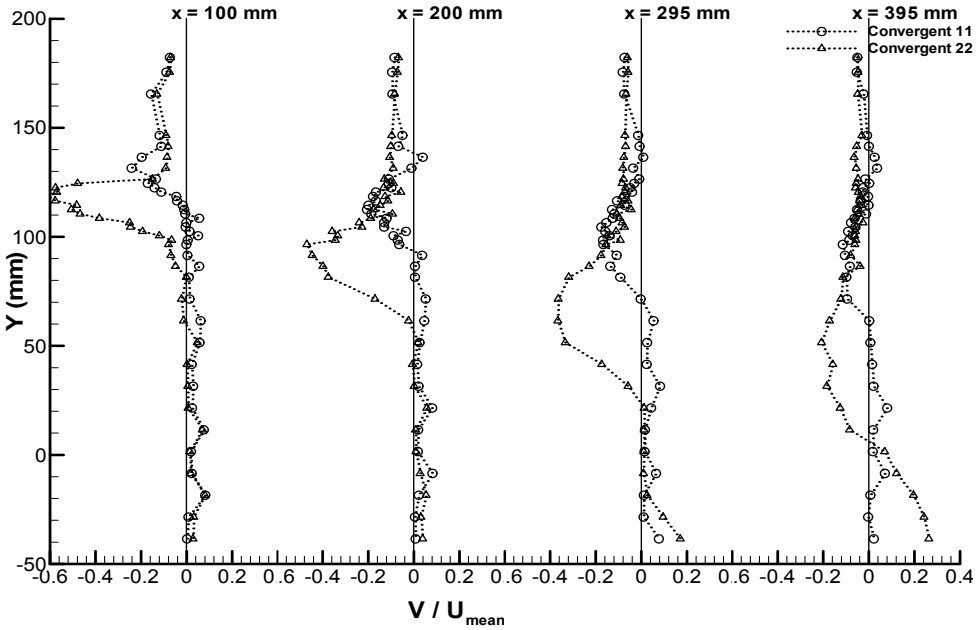

Figure 3.31. Vertical profiles of vertical velocity for C_1 and D_1 test cases at stations x=100, 200, 295 and 395 mm.

Figure 3.31 shows the vertical velocity results obtained for C_1 and D_1 test cases for the stations x=100, 200, 295 and 395 mm. For the station x=100 mm the C_1 test case presents negative values to y>148.50 mm. The exterior points are experiencing vertical velocities to symmetry axis plane direction. The stronger peak velocity for this test case is V/U_{mean}=-0.24 at y=131.50 mm at the outer jet exit. This jet is experiencing large vertical velocity turbulence due to the 11° convergent presence. Between 120.50<y<165.50 mm all obtained values are negative and greater than -0.1 V/U_{mean}. The other profile values are weaker than 0.08 V/U_{mean} and at the symmetry axis approaching the values are positive but close to zero. For the D_1 test case the obtained values reveals a very strong velocity peak of V/U_{mean}=-0.60 at y=118.50 and 116.50 mm respectively. This region is positioned at the inner jet exit, but the values are from the outer jet due to the presence of 22° convergent. Between 100.50<y<126.50 mm all obtained values are negative and greater than -0.1 V/U_{mean}. The other profile values are weaker than 0.08 V/U_{mean} and at the symmetry axis approaching the values are positive but close to zero. The D_1 test case presents negative values to y>148.50 mm as well as the C_1 case.

For the station x=200 mm the C_1 test case presents negative values to y>148.50 mm. The exterior points are experiencing vertical velocities to axis plane direction. The stronger peak velocity for this test case is V/U_{mean}=-0.20 at y=112.50 mm at the outer jet exit. Regarding the previous station, this peak moved 19 mm to axis plane. Between 104.50<y<126.50 mm all obtained values are negative and greater than -0.1 V/U_{mean}. The other profile values are weaker than 0.09 V/U_{mean} and at the symmetry axis approaching the

values are positive but close to zero. For the D_1 test case, the obtained values reveals a very strong velocity peak of V/U_{mean}=-0.469 at y=96.50 mm. Regarding the previous station, this peak moved to axis plane 20 to 22 mm. Between 71.50<y<141.50 mm all obtained values are negative and greater than -0.1 V/U_{mean}. The other profile values are weaker than 0.08 V/U_{mean} and at the symmetry axis approaching the values are positive but close to zero. The D_1 test case presents negative values to y>148.50 mm as well as the C_1 case.

For the station x=295 mm the C_1 test case presents negative values to y>148.50 mm. The exterior points are experiencing vertical velocities to axis plane direction. The stronger peak velocity for this test case is V/U_{mean}=-0.168 at y=98.50 mm at the outer jet exit. Regarding the previous station, this peak moved to axis plane 14 mm. Between 86.50<y<116.50 mm all obtained values are negative and greater than -0.1 V/U_{mean}. The other profile values are weaker than 0.09 V/U_{mean} and at the symmetry axis approaching the values are positive but close to zero. For the D_1 test case, the obtained values reveals a very strong velocity peak of V/U_{mean}=-0.366 at y=61.50 mm. By regarding previous station, this peak moved to axis plane 35 mm. Between 41.50<y<120.50 mm all obtained values are negative and greater than -0.1 V/U_{mean}. The other profile values are weaker than 0.09 V/U_{mean} and at the symmetry axis approaching the values are positive but close to zero. The D_1 test case presents negative values to y>148.50 mm as well as the C_1 case.

For the station x=395 mm the C_1 test case presents negative values to y>148.50 mm. The exterior points are experiencing vertical velocities to symmetry axis plane direction. Between 131.50<y<141.50 mm, this test case reveals positive velocities. The stronger peak velocity for this test case is V/U_{mean}=-0.15 at y=96.50 mm at the outer jet exit. Regarding the previous station, this peak moved 2 mm to axis plane. Between 91.50<y<96.50 mm all obtained values are negative and greater than -0.1 V/U_{mean}. The other profile values are weaker than 0.09 V/U_{mean} and at the symmetry axis approaching the values are positive but close to zero. For the D_1 test case, the obtained values reveals a very strong velocity peak of V/U_{mean}=-0.21 at y=51.50 mm. Regarding the previous station, this peak moved 10 mm up to symmetry axis plane. Between 21.50<y<81.50 mm all obtained values are negative and greater than -0.1 V/U_{mean}. The other profile values are weaker than 0.09 V/U_{mean} and at the symmetry axis approaching the values are positive but close to zero. The D_1 test case presents negative values to y>148.50 mm as well as the C_1 case. In fact only point y=1.5 mm of this test case revealed positive velocity.

The results evolution in these first four stations from x=100 mm to x=395 mm for the C_1 test case, the strong peak velocity observed at x=100 mm revealed at that station a value of V/U_{mean}=-0.24 at point y=131.50 mm. The peak revealed at station x=395 mm is V/U_{mean}=-0.15 at point 96.50 mm. This velocity peak is decreased from V/U_{mean}=-0.24 to V/U_{mean}=-0.15 and moved about 35 mm to symmetry axis plane. For the D_1 test case, these situation present V/U_{mean}=-0.60 at both points y=118.50 and y=116.50 mm at x=100 mm and V/U_{mean}=-0.21 at

point y=51.50 mm. This velocity peak is decreased from V/U_{mean}=-0.60 to V/U_{mean}=-0.21 and moved about 64/66 mm up to symmetry axis plane.

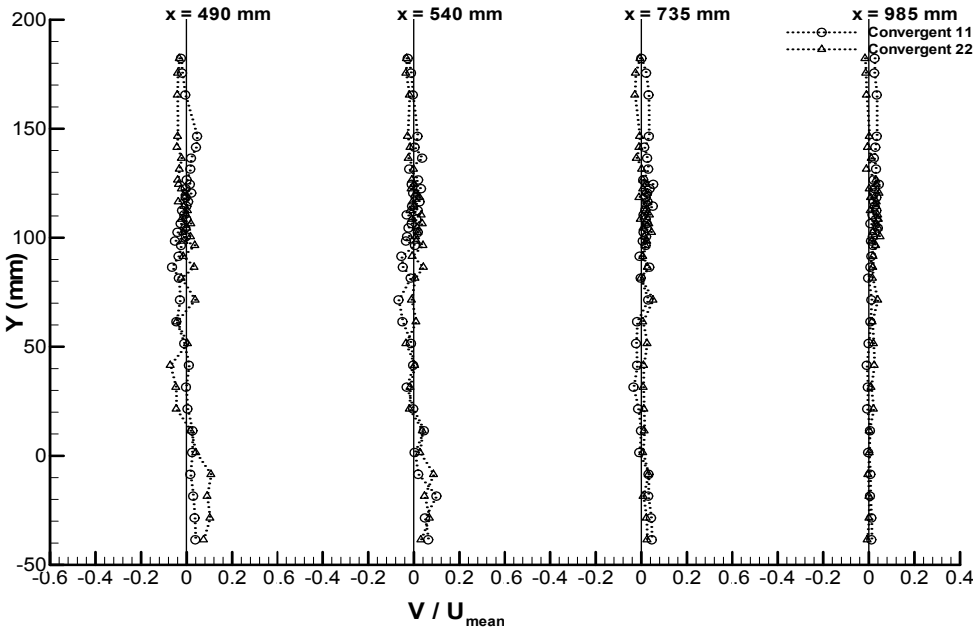

Figure 3.32. Vertical profiles of vertical velocity for C_1 and D_1 test cases at stations x=490, 540, 735 and 985 mm.

Figure 3.32 shows the vertical velocity results obtained for C_1 and D_1 test cases for the stations x=490, 540, 735 and 985 mm. For the station x=490 mm and for both test cases all obtained values are completely different from the ones observed at Figure 3.31 for the first four stations. The C_1 test case show three negative velocity points at north, a positive region at 124.50<y<146.50 mm followed by a negative region till y=31.50 mm. The vertical velocity oscillations vary from V/U_{mean}=0.045 at point y=141.50 mm to V/U_{mean}=-0.064 at point y=86.50 mm. The D_1 test case show a negative value region at 108.50<y<182.25 mm followed by a region positive/negative region till symmetry axis plane. The vertical velocity oscillations vary from V/U_{mean}=0.037 at point y=71.50 mm to V/U_{mean}=-0.072 at point y=41.50 mm.

The station x=540 mm presents similar results of the previous station with a little less vertical velocity oscillations for both test cases. Station x=735 mm presents very similar values for both test cases, with all values tending to zero. The same situation is visualized for station x=985 mm. For the station x=1235 mm (Figure 3.33) all values are practically identical. The vertical velocity values are practically a vertical straight line connecting points with vertical velocity at zero neighbourhoods.

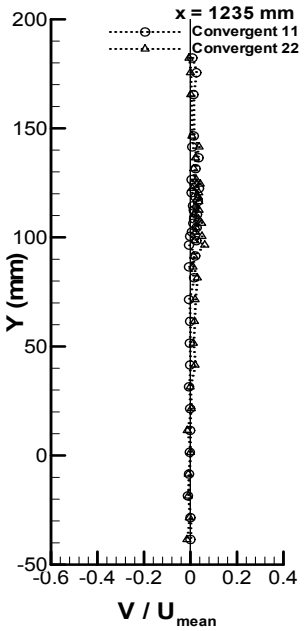

Figure 3.33. Vertical profiles of vertical velocity for C_1 and D_1 test cases at station x=1235 mm.

3.5.4. Convergent 11° C_2 and convergent 22° D_2 jets

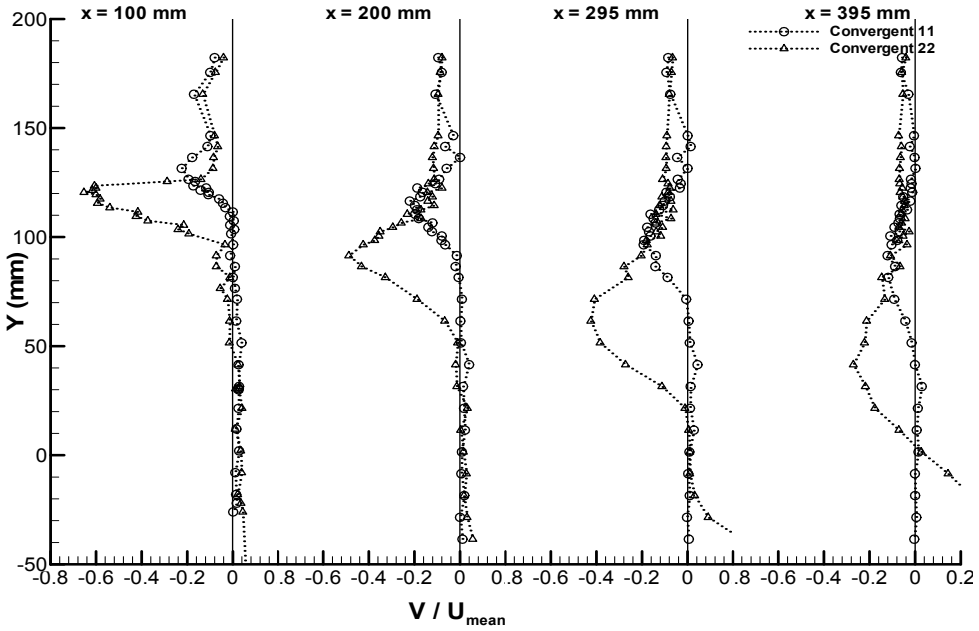

Figure 3.34. Vertical profiles of vertical velocity for C_2 and D_2 test cases at stations x=100, 200, 295 and 395 mm.

Figure 3.34 shows the vertical velocity results obtained for C_2 and D_2 test cases for the stations x=100, 200, 295 and 395 mm. For the station x=100 mm, both test case presents negative values to y>148.50 mm. The exterior points are experiencing vertical velocities to axis plane direction. The stronger peak velocity for C_2 test case is V/U_{mean}=-0.42 at y=121.50

mm at the outer jet exit. This jet is experiencing a vertical axis plane direction due to the 22º convergent presence. Between 119.50<y<141.50 mm all obtained values are negative and greater than -0.1 V/U_{mean}. This interval is practically half than the obtained for the C_1 test case (Figure 3.31): 120.50<y<165.50 mm. Higher velocities tend to concentrate the jet itself in their direction. Back to this station, the other C_2 profile values are weaker than 0.04 V/U_{mean} and at the symmetry axis approaching the values are positive but close to zero. For the D_2 test case, the obtained values reveals a very strong velocity peak of V/U_{mean} =-0.653 at y=120.50 mm. This region is positioned at the inner jet exit, but the values are from the outer jet due to the presence of 22º convergent. Between 100.50<y<126.50 mm all obtained values are negative and greater than -0.1 V/U_{mean}. This interval is practically identical to the obtained for the D_1 test case (Figure 3.31). The other profile values are weaker than 0.07 V/U_{mean} and at the symmetry axis approaching the values are positive but close to zero.

For the station x=200 mm, the C_2 test case presents negative values to Y>148.50 mm. The exterior points are experiencing vertical velocities to axis plane direction. The stronger peak velocity for this test case is V/U_{mean}=-0.198 at y=114.50 mm at the outer jet exit. Regarding the previous station, this peak moved to axis plane 7 mm. Between 102.50<y<124.50 mm all obtained values are negative and greater than -0.1 V/U_{mean}, practically the same as obtained for C_1 test case (Figure 3.31). The other profile values are weaker than 0.09 V/U_{mean} and at the symmetry axis approaching the values are positive but close to zero. For the D_2 test case, the obtained values reveals a very strong velocity peak of V/U_{mean}=-0.488 at y=91.50 mm. Regarding the previous station, this peak moved 29 mm up to symmetry axis plane. Between 71.50<y<141.50 mm, all obtained values are negative and greater than -0.1 V/U_{mean}, practically the same as obtained for D_1 test case (Figure 3.31). The other profile values are weaker than 0.08 V/U_{mean} and at the symmetry axis approaching the values are positive but close to zero.

For the station x=295 mm, the C_2 test case presents negative values to Y>148.50 mm. The exterior points are experiencing vertical velocities to axis plane direction. The stronger peak velocity for this test case is V/U_{mean}=-0.193 at y=96.50 mm at the outer jet exit. Regarding the previous station, this peak moved to axis plane 18 mm. Between 86.50<y<114.50 mm, all obtained values are negative and greater than -0.1 V/U_{mean}. The other profile values are weaker than 0.09 V/U_{mean} and at the symmetry axis approaching the values are positive but close to zero. For the D_2 test case, the obtained values reveals a very strong velocity peak of V/U_{mean}=-0.424 at y=61.50 mm. Regarding the previous station, this peak moved 30 mm up to symmetry axis plane. Between 31.50<y<100.50 mm, all obtained values are negative and greater than -0.1 V/U_{mean}. The other profile values are weaker than 0.09 V/U_{mean} and at the symmetry axis approaching the values are positive but close to zero. The D_2 test case presents negative values to y>148.50 mm.

For the station x=395 mm, the C_2 test case presents negative values to y>148.50 mm. The exterior points are experiencing vertical velocities in the symmetry axis plane direction.

The stronger peak velocity for this test case is V/U_{mean}=-0.12 at y=91.50 mm at the outer jet exit. Regarding the previous station, this peak moved 5 mm up to symmetry axis plane. Between 91.50<y<96.50 mm, all obtained values are negative and greater than -0.1 V/U_{mean}. The other profile values are weaker than 0.09 V/U_{mean} and at the symmetry axis approaching the values are positive but close to zero. For the D_2 test case, the obtained values reveals a very strong velocity peak of V/U_{mean}=-0.27 at y=41.50 mm. Regarding the previous station, this peak moved 20 mm up to symmetry axis plane. Between 21.50<y<81.50 mm, all obtained values are negative and greater than -0.1 V/U_{mean}. The other profile values are weaker than 0.09 V/U_{mean} and at the symmetry axis approaching the values are positive but close to zero. The D_2 test case presents negative values to y>148.50 mm as well as the C_2 case. The same way as D_1 test case at same station, only point y=1.5 mm of this test case revealed positive velocity.

Regarding the results evolution in these first four stations from x=100 mm to x=395 mm, for the C_2 test case, the strong peak velocity observed at x=100 mm revealed at that station a value of V/U_{mean}=-0.42 at point y=121.50 mm. The peak revealed at station x=395 mm is V/U_{mean}=-0.12 at point 91.50 mm. This velocity peak is decreased from V/U_{mean}=-0.42 to V/U_{mean}=-0.12 and moved 30 mm up to symmetry axis plane. For the D_2 test case, these situation present V/U_{mean}=-0.63 at point y=120.50 mm at x=100 mm and V/U_{mean}=-0.27 at point y=41.50 mm. This velocity peak is decreased from V/U_{mean}=-0.63 to V/U_{mean}=-0.27 and moved 79 mm up to symmetry axis plane.

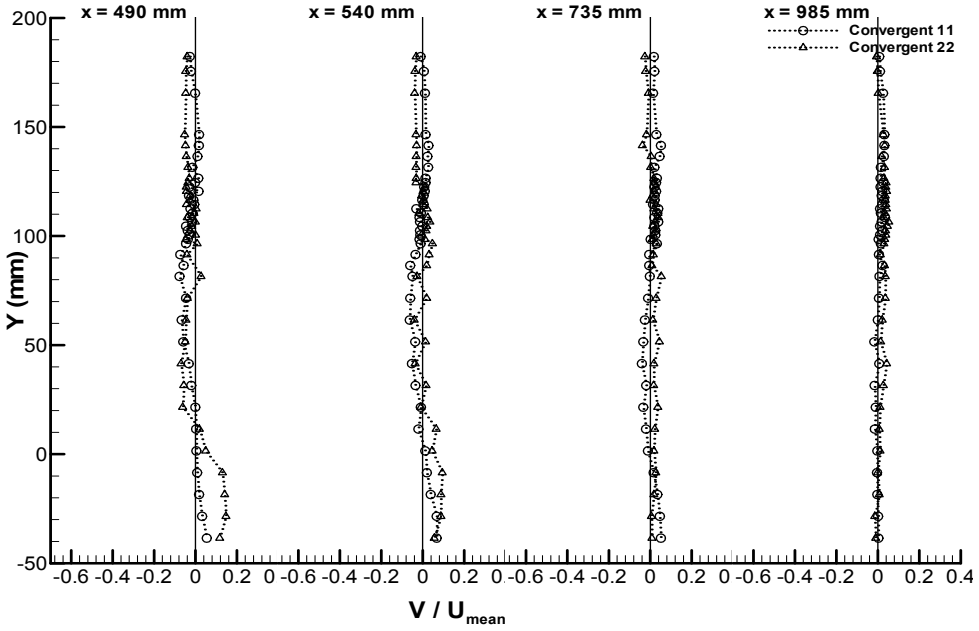

Figure 3.35. Vertical profiles of vertical velocity for C_2 and D_2 test cases at stations x=490, 540, 735 and 985 mm.

Figure 3.35 shows the vertical velocity results obtained for C_2 and D_2 test cases for the stations x=490, 540, 735 and 985 mm. The obtained results are very similar to Figure 3.32 for C_1 and D_1 test cases. For the station x=490 mm and for both test cases all obtained values are completely different from the ones observed at Figure 3.34 for the first four stations. The C_2 test case show three negative velocity points at north, a positive region at 136.50<y<146.50 mm followed by a negative region till y=21.50 mm. The vertical velocity oscillations vary from V/U_{mean}=0.0017 at point y=146.50 mm to V/U_{mean}=-0.077 at point y=81.50 mm. The D_2 test case show a negative value region at 114.50<y<182.25 mm followed by a region positive/negative region till symmetry axis plane. The vertical velocity oscillations vary from V/U_{mean}=0.048 at point y=1.50 mm to V/U_{mean}=-0.07 at point y=41.50 mm.

The station x=540 mm presents similar results of the previous station with a little less vertical velocity oscillations for both test cases. Stations x=735 mm and x= 985 mm present very similar values for both test cases with all values tending to zero vertical velocity.

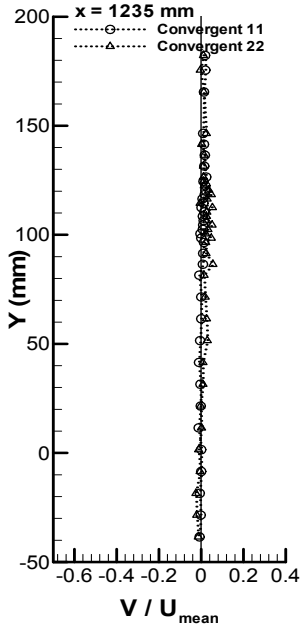

Figure 3.36. Vertical profiles of vertical velocity for C_2 and D_2 test cases at station at x=1235 mm.

At station x=1235 mm (Figure 3.36) all the vertical velocity values are practically identical for both test cases indicating a straight line connecting points with approximately zero.

Regarding the vertical velocity amplitude intervals results obtained at the jets exit, the unconfined test cases (A_1: 0.06<V/U_{mean}<0.144, with a V/U_{mean}=0.150 range interval; A_2: 0.005<V/U_{mean}<0.159, with a V/U_{mean}=0.164 range interval) and the confined test cases (B_1: 0.0067<V/U_{mean}<0.126, with a V/U_{mean}=0.1327 range interval; B_2: -0.0067<V/U_{mean}<0.15, V/U_{mean}=0.1567 range interval) are substantially smaller than the presented for the

convergent 11º (C_1: -0.24<V/U_{mean}<0.07, with a V/U_{mean}=0.31 range interval; C_2: -0.42<V/U_{mean}<0.04, with a V/U_{mean}=0.46 range interval) and for 22º test cases (D_1: -0.6<V/U_{mean}<0.07, with a V/U_{mean}=0.67 range interval; D_2: -0.653<V/U_{mean}<0.03, with a V/U_{mean}=0.656 range interval). All convergent amplitude intervals reveal negative values, due to its symmetry axis plane pushing direction.

3.6. Vertical profiles of streamwise fluctuation velocity

This subchapter presents all the obtained results for the vertical profiles of streamwise velocity fluctuation u'_{RMS} (dimensionless form by U_{mean}) distribution at the horizontal axis in each studied station, from y=200 mm to y=-50 mm. The vertical profiles of streamwise velocity fluctuation u'_{RMS} distribution values are presented from $0 \leq u'_{RMS}/U_{mean} \leq 4$. The confined jets values starts at y=148.50 mm, due to its wall confinement. The unconfined jets values starts at y=182.25 mm.

3.6.1. Unconfined A_1 and confined B_1 jets

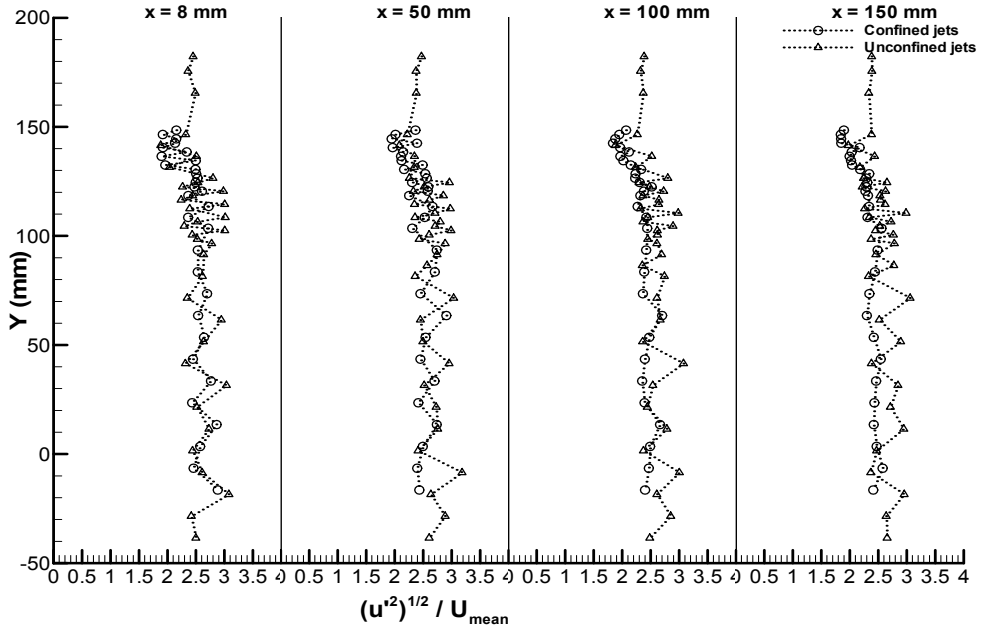

Figure 3.37. Vertical profiles of streamwise velocity fluctuation for A_1 and B_1 test cases at stations x=8, 50, 100 and 150 mm.

Figure 3.37 shows the streamwise velocity fluctuation results obtained for A_1 and B_1 test cases for the stations x=8, 50, 100 and 150 mm. For all stations referred at Figure 3.37, all values are very high since the obtained results are dimensionless form by the U_{mean}. For all presented stations the A_1 unconfined test case presents constant high amplitude oscillation between neighbouring points, a turbulent flow characteristic. At station x=8 mm, the B_1 confined test case present values within the 1.917<u'_{RMS}/U_{mean}<2.863, with an amplitude of u'_{RMS}/U_{mean}=0.946. The highest value is at y=13.50 mm and the lowest value is at y=146.50

mm. Great amplitude oscillation between neighbouring points is visible for all vertical profile. The A_1 test case reveals a higher amplitude interval in the obtained values: $1.881<u'_{RMS}/U_{mean}<3.035$, with amplitude of $u'_{RMS}/U_{mean}=1.154$. The highest obtained value is at y=31.50 mm and the lowest value is at y=141.50 mm. A_1 presents constant high amplitude oscillation between neighbouring points. The three exterior points at north seems to avoid oscillation compulsion of the flow.

For station x=50 mm the B_1 test case present values within the $1.947<u'_{RMS}/U_{mean}<2.907$, an amplitude of $u'_{RMS}/U_{mean}=0.960$, identical to the same test case regarding the previous station. The highest obtained value is at y=63.50 mm and the lowest value is at y=144.50 mm. Regarding previous station, the A_1 test case reveals a smaller amplitude interval in the obtained values: $2.083<u'_{RMS}/U_{mean}<3.034$, with amplitude of $u'_{RMS}/U_{mean}=0.951$. The highest obtained value is at y=71.50 mm and the lowest value is at y=141.50 mm. Both test cases show a constant oscillation between neighbouring points, with less amplitude in the confined test case. The three exterior points at north seems to avoid oscillation compulsion of the flow.

For station x=100 mm, the B_1 test case present values within the $1.838<u'_{RMS}/U_{mean}<2.700$. The highest obtained value is at y=73.50 mm and the lowest value is at y=142.50 mm. This interval shows an amplitude of $u'_{RMS}/U_{mean}=0.862$, smaller than $u'_{RMS}/U_{mean}=0.960$ obtained at the previous station. No velocity oscillation between neighbouring points is visible for this station. The A_1 test case reveals a higher amplitude interval in the obtained values when compared with same test case at previous station: $1.878<u'_{RMS}/U_{mean}<3.075$. This interval shows an amplitude of $u'_{RMS}/U_{mean}=1.197$, greater than $u'_{RMS}/U_{mean}=0.951$ obtained at the previous station. The highest obtained value is at y=41.50 mm and the lowest value is at y=141.50 mm. A_1 test case show a constant oscillation between neighbouring points. The three exterior points at north seems to avoid oscillation compulsion of the flow.

For station x=150 mm, the B_1 test case present values within the $1.842<u'_{RMS}/U_{mean}<2.557$, with amplitude of $u'_{RMS}/U_{mean}=0.715$, smaller than $u'_{RMS}/U_{mean}=0.862$ obtained at the previous station. The highest obtained value is at y=103.50 mm and the lowest value is at y=146.50 mm. No velocity oscillation between neighbouring points is visible for this station. The A_1 test case reveals a smallest amplitude interval in the obtained values when compared with same test case at previous station: $1.975<u'_{RMS}/U_{mean}<3.059$. This interval shows an amplitude of $u'_{RMS}/U_{mean}=1.084$, smaller than $u'_{RMS}/U_{mean}=1.197$ obtained at the previous station. The highest obtained value is at y=71.50 mm and the lowest value is at y=141.50 mm. A_1 test case show a constant oscillation between neighbouring points. The three exterior points at north seems to avoid oscillation compulsion of the flow.

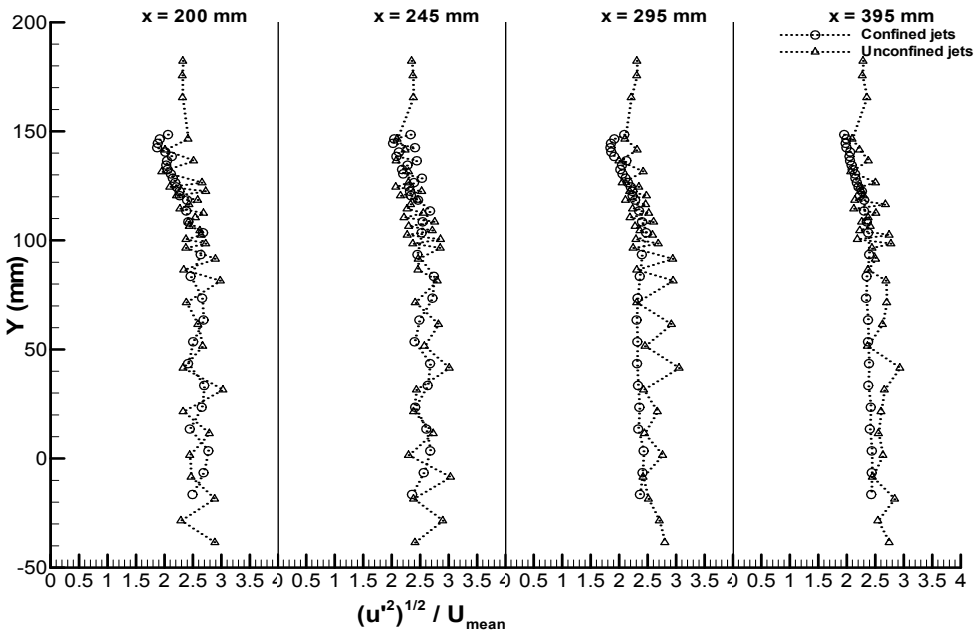

Figure 3.38. Vertical profiles of streamwise velocity fluctuation for A_1 and B_1 test cases at stations x=200, 245, 295 and 395 mm.

Figure 3.38 shows the streamwise velocity fluctuation results obtained for A_1 and B_1 test cases for the stations x=200, 245, 295 and 395 mm. For station x=200 mm, the B_1 test case present values within the $2.024<u'_{RMS}/U_{mean}<2.741$, with amplitude of $u'_{RMS}/U_{mean}=0.717$, identical than $u'_{RMS}/U_{mean}=0.715$ obtained at the previous station. The highest obtained value is at y=73.50 mm and the lowest value is at y=146.50 mm. The A_1 test case present values within the $1.953<u'_{RMS}/U_{mean}<3.026$, with amplitude of $u'_{RMS}/U_{mean}=1.073$, identical than $u'_{RMS}/U_{mean}=1.084$ obtained at the previous station. The highest obtained value is at y=31.50 mm and the lowest value is at y=131.50 mm. A_1 test case show a constant oscillation between neighbouring points. The three exterior points at north seems to avoid oscillation compulsion of the flow.

For station x=245 mm, the B_1 test case present values within the $2.04<u'_{RMS}/U_{mean}<2.677$. The highest obtained value is at y=3.50 and the lowest value is at y=146.50. This interval shows an amplitude of $u'_{RMS}/U_{mean}=0.653$, slightly smaller than $u'_{RMS}/U_{mean}=0.717$ obtained at the previous station. Below y=100 mm, the obtained values reveals less oscillation. The A_1 case present values within the $2.077<u'_{RMS}/U_{mean}<3.010$. This interval shows an amplitude of $u'_{RMS}/U_{mean}=0.933$, smaller than $u'_{RMS}/U_{mean}=1.073$ obtained at the previous station. The highest obtained value is at y=41.50 mm and the lowest value is at y=124.50 mm. A_1 test case show a constant oscillation between neighbouring points. The three exterior points at north seems to avoid oscillation compulsion of the flow.

For station x=295 mm, the B_1 test case present values within the $1.845<u'_{RMS}/U_{mean}<2.473$. The highest obtained value is at y=103.50 mm and the lowest value is at y=142.50 mm. This interval shows an amplitude of $u'_{RMS}/U_{mean}=0.628$, slightly smaller

than u'_{RMS}/U_{mean}=0.653 obtained at the previous station. Below y=100 mm, the obtained values reveals a straight line with practically no oscillation. The A_1 test case present values within the $1.997<u'_{RMS}/U_{mean}<3.050$. This interval shows an amplitude of u'_{RMS}/U_{mean}=1.053, greater than u'_{RMS}/U_{mean}=0.933 obtained at the previous station. The highest obtained value is at y=41.50 mm and the lowest value is at y=136.50 mm. A_1 test case show a constant oscillation between neighbouring points. The three exterior points at north seems to avoid oscillation compulsion of the flow.

For station x=395 mm, the B_1 test case present values within the $1.954<u'_{RMS}/U_{mean}<2.421$. The highest obtained value is at y=23.50 mm and the lowest value is at y=148.50 mm. This interval shows an amplitude of u'_{RMS}/U_{mean}=0.467, smaller than u'_{RMS}/U_{mean}=0.628 obtained at the previous station. Below y=100 mm, the obtained values continues to reveal a straight line with practically no oscillation. The A_1 test case present values within the $2.071<u'_{RMS}/U_{mean}<2.932$. This interval shows an amplitude of u'_{RMS}/U_{mean}=0.861, smaller than u'_{RMS}/U_{mean}=1.053 obtained at the previous station. The highest obtained value is at y=41.50 mm and the lowest value is at y=131.50 mm. A_1 test case show a constant oscillation between neighbouring points. The three exterior points at north seems to avoid oscillation compulsion of the flow.

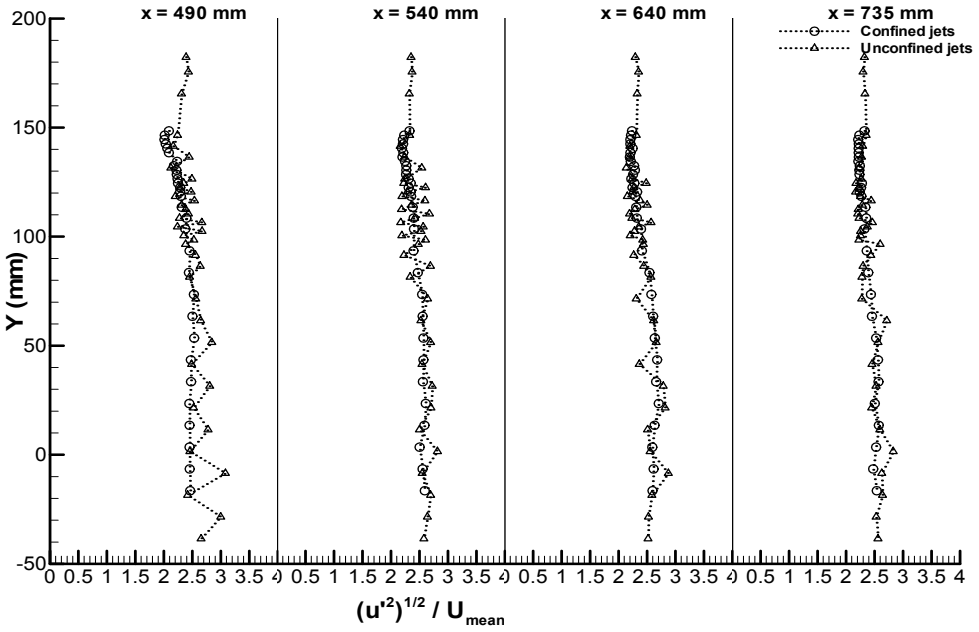

Figure 3.39. Vertical profiles of streamwise velocity fluctuation for A_1 and B_1 test cases at stations x=490, 540, 640 and 735 mm.

Figure 3.39 shows the streamwise velocity fluctuation results obtained for A_1 and B_1 test cases for the stations x=490, 540, 640 and 735 mm. For station x=490 mm, the B_1 test case present values within the $2.009<u'_{RMS}/U_{mean}<2.532$. The highest obtained value is at y=53.50 mm and the lowest value is at y=144.50 mm. This interval shows an amplitude of

u'_{RMS}/U_{mean}=0.523, slightly larger than u'_{RMS}/U_{mean}=0.427 obtained at the previous station. Below y=100 mm, the obtained values continues to reveal a straight line with practically no oscillation. The A_1 test case present values within the $2.123<u'_{RMS}/U_{mean}<2.840$. This interval shows an amplitude of u'_{RMS}/U_{mean}=0.717, smaller than u'_{RMS}/U_{mean}=0.861 obtained at the previous station. The highest obtained value is at y=51.50 mm and the lowest value is at y=131.50 mm. A_1 test case show a constant oscillation between neighbouring points.

For station x=540 mm, the B_1 test case present values within the $2.192<u'_{RMS}/U_{mean}<2.609$. The highest obtained value is at y=23.50 mm and the lowest value is at y=140.50 mm. This interval shows an amplitude of u'_{RMS}/U_{mean}=0.417, smaller than u'_{RMS}/U_{mean}=0.523 obtained at the previous station. Below y=100 mm, the obtained values continues to reveal a straight line with practically no oscillation. The A_1 test case present values within the $2.161<u'_{RMS}/U_{mean}<2.814$. This interval shows an amplitude of u'_{RMS}/U_{mean}=0.653, smaller than u'_{RMS}/U_{mean}=0.717 obtained at the previous station. The highest obtained value is at y=1.50 mm and the lowest value is at y=141.50 mm. The oscillations are decreasing. Most part of them are visible at 100<y<140 mm. Below y=100 mm for this station the unconfined test case reveals only very slight oscillations.

For station x=640 mm, the B_1 test case present values within the $2.198<u'_{RMS}/U_{mean}<2.704$. The highest obtained value is at y=23.50 mm and the lowest value is at y=136.50 mm. This interval shows an amplitude of u'_{RMS}/U_{mean}=0.506, slightly larger than u'_{RMS}/U_{mean}=0.417 obtained at the previous station. Below y=100 mm, the obtained values continues to reveal a straight line with practically no oscillation. The A_1 test case present values within the $2.135<u'_{RMS}/U_{mean}<2.817$. This interval shows an amplitude of u'_{RMS}/U_{mean}=0.682, identical than u'_{RMS}/U_{mean}=0.653 obtained at the previous station. The highest obtained value is at y=21.50 mm and the lowest value is at y=131.50 mm. Small oscillations are visible for all the entire vertical profile.

For station x=735 mm, the B_1 test case present values within the $2.212<u'_{RMS}/U_{mean}<2.574$. The highest obtained value is at y=13.50 mm and the lowest value is at y=144.50 mm. This interval shows an amplitude of u'_{RMS}/U_{mean}=0.312, smaller than u'_{RMS}/U_{mean}=0.506 obtained at the previous station. The entire vertical profile reveals very slight oscillations; all values are at u'_{RMS}/U_{mean}=2.5 neighbourhoods. The A_1 test case present values within the $2.169<u'_{RMS}/U_{mean}<2.827$. This interval shows an amplitude of u'_{RMS}/U_{mean}=0.658, identical than u'_{RMS}/U_{mean}=0.682 obtained at the previous station. The highest obtained value is at y=1.50 mm and the lowest value is at y=120.50 mm. Small oscillations are visible for all the entire vertical profile. With exception for four velocity points, all other values are identical to the B_1 test case.

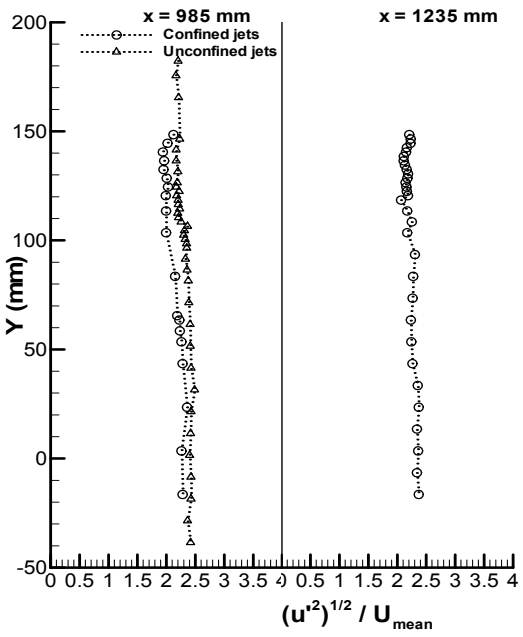

Figure 3.40. Vertical profiles of streamwise velocity fluctuation for A_1 and B_1 test cases at stations x=985 and 1235 mm.

Figure 3.40 shows the streamwise velocity fluctuation results obtained for A_1 and B_1 test cases for the stations x=985 and 1235 mm. For station x=985 mm, the B_1 test case present values within the $1.950<u'_{RMS}/U_{mean}<2.356$. The highest obtained value is at y=23.50 mm and the lowest value is at y=132.50 mm. This interval shows an amplitude of $u'_{RMS}/U_{mean}=0.406$, slightly larger than $u'_{RMS}/U_{mean}=0.312$ obtained at the previous station. The entire vertical profile reveals very slight oscillations; all values are bellow $u'_{RMS}/U_{mean}=2.5$. The A_1 test case present values within the $2.169<u'_{RMS}/U_{mean}<2.486$. This interval shows an amplitude of $u'_{RMS}/U_{mean}=0.317$, smaller than $u'_{RMS}/U_{mean}=0.658$ obtained at the previous station. The highest obtained value is at y=31.50 mm and the lowest value is at both y=136.50 mm and y=141.50 mm points. Small oscillations are visible for all the entire vertical profile. With exception for four velocity points, all other values are identical to the B_1 test case. The three exterior points at north seems to avoid oscillation compulsion of the flow. The graphics reveals practically a straight line with slightly higher values than the confined test case.

For station x=1235 mm, the B_1 test case present values within the $2.064<u'_{RMS}/U_{mean}<2.370$. The highest obtained value is at y=23.50 mm and the lowest value is at y=118.50 mm. This interval shows an amplitude of $u'_{RMS}/U_{mean}=0.306$, smaller than $u'_{RMS}/U_{mean}=0.406$ obtained at the previous station. The entire vertical profile reveals very slight oscillations; all values are bellow $u'_{RMS}/U_{mean}=2.5$.

3.6.2. Unconfined A_2 and confined B_2 jets

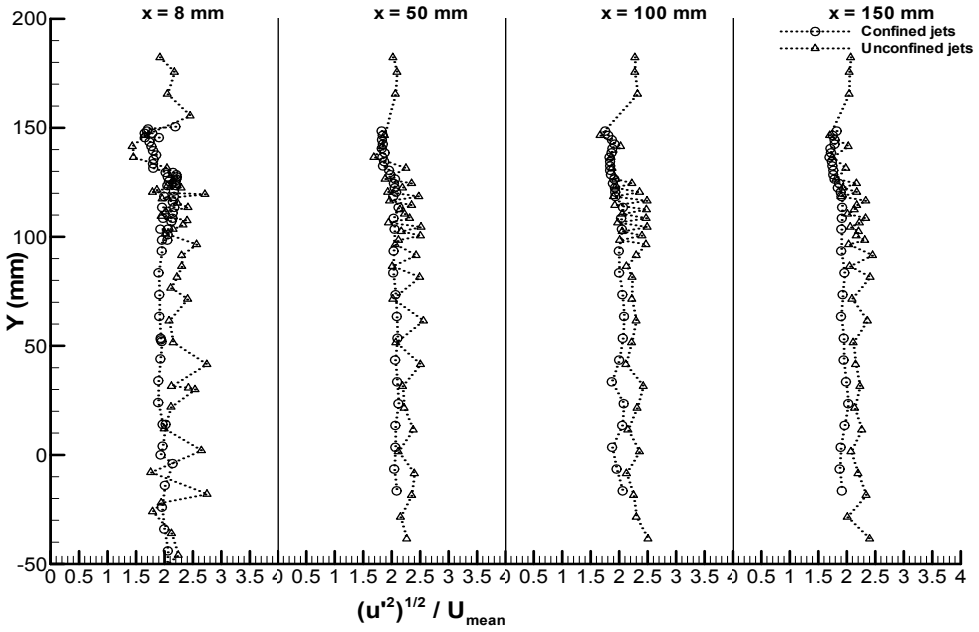

Figure 3.41. Vertical profiles of streamwise velocity fluctuation for A_2 and B_2 test cases at stations x=8, 50, 100 and 150 mm.

Figure 3.41 shows the streamwise velocity fluctuation results obtained for A_2 and B_2 test cases for the stations x=8, 50, 100 and 150 mm. For station x=8 mm, for both test cases A_2 and B_2 all values continue very high since the obtained results are dimensionless form by the U_{mean}. However these values are lower when compared with same station for A_1 and B_1 test cases. The B_2 test case present values within the $1.651<u'_{RMS}/U_{mean}<2.190$. The highest obtained value is at y=148.50 mm and the lowest value is at y=145.50 mm. This interval shows an amplitude of $u'_{RMS}/U_{mean}=0.539$ for this test case. The amplitude interval obtained for B_1 for this stations is of $u'_{RMS}/U_{mean}=0.946$. Comparing B_1 (Figure 3.37) to B_2 unconfined test cases, the increasing of horizontal velocity decreased the amplitude of streamwise fluctuation velocity. The graphic reveals that the increasing of horizontal velocity had stabilized the streamwise fluctuation velocity also for values below y=100 mm, where the great velocity oscillation disappeared. The A_2 test case reveals a higher amplitude interval in the obtained values: $1.434<u'_{RMS}/U_{mean}<2.648$. This interval shows an amplitude of $u'_{RMS}/U_{mean}=1.214$ for this test case, higher than the obtained for B_1 for this stations $u'_{RMS}/U_{mean}=1.154$. The highest obtained value is at y=2.00 mm and the lowest value is at y=141.50 mm. Such as what happened at A_1 test case for same station (Figure 3.37), great velocity oscillations between neighbouring points are visible for all vertical profile.

For station x=50 mm, for both test cases A_2 and B_2 all values are also lower when compared with same station for A_1 and B_1 test cases. The B_2 test case present values within the $1.822<u'_{RMS}/U_{mean}<2.121$. The highest obtained value is at y=113.50 mm and the lowest value is at y=148.50 mm. This interval shows a fine range of $u'_{RMS}/U_{mean}=0.299$ for this test

case. The amplitude interval obtained for B_1 for this stations is of $u'_{RMS}/U_{mean}=0.960$. Such as verified for the previous station, for y<100 mm the oscillations of streamwise fluctuation velocity disappeared. The A_2 test case reveals a $1.687<u'_{RMS}/U_{mean}<2.557$ range interval with an amplitude of $u'_{RMS}/U_{mean}=0.870$ for this test case, higher than the obtained for B_1 for this stations $u'_{RMS}/U_{mean}=0.951$. The highest obtained value is at y=61.50 mm and the lowest value is at y=136.50 mm. Such as what happened at A_1 test case for same station (Figure 3.37), great velocity oscillations between neighbouring points are visible for all vertical profile.

For station x=100 mm, for both test cases A_2 and B_2 all values are also lower when compared with same station for A_1 and B_1 test cases. The B_2 test case present values within the $1.754<u'_{RMS}/U_{mean}<2.084$. The highest obtained value is at y=63.50 mm and the lowest value is at y=148.50 mm. This interval shows a fine range of $u'_{RMS}/U_{mean}=0.330$ for this test case. The amplitude interval obtained for B_1 for this stations is of $u'_{RMS}/U_{mean}=0.862$. For Y<100 the oscillations of streamwise fluctuation velocity are very small. The A_2 test case reveals a $1.664<u'_{RMS}/U_{mean}<2.490$ range interval with an amplitude of $u'_{RMS}/U_{mean}=0.826$ for this test case, higher than the obtained for A_1 for this stations $u'_{RMS}/U_{mean}=1.197$. The highest obtained value is at y=104.50 mm and the lowest value is at y=146.50 mm. Streamwise velocity oscillations between neighbouring points are visible for all vertical profile.

For station x=150 mm, for both test cases A_2 and B_2 all values are also lower when compared with same station for A_1 and B_1 test cases. The B_2 test case present values within the $1.697<u'_{RMS}/U_{mean}<2.025$. The highest obtained value is at y=23.50 mm and the lowest value is at y=136.50 mm. This interval shows a fine range of $u'_{RMS}/U_{mean}=0.328$ for this test case. The amplitude interval obtained for B_1 for this stations is of $u'_{RMS}/U_{mean}=0.715$. For Y<100 mm, the oscillations of streamwise fluctuation velocity disappeared again. The A_2 test case reveals a $1.699<u'_{RMS}/U_{mean}<2.452$ range interval with an amplitude of $u'_{RMS}/U_{mean}=0.753$ for this test case, higher than the obtained for A_1 for this stations $u'_{RMS}/U_{mean}=1.084$. The highest obtained value is at y=91.50 mm and the lowest value is at y=146.50 mm. Streamwise velocity oscillations between neighbouring points are visible for all vertical profile.

By comparing the evolution results for A_1, B_1 test case and A_2, B_2 test cases between the stations x=8 mm to x=150 mm the results reveals that the streamwise fluctuation velocity presents a wider range for the A_1 and B_1 test cases. For the B_1 test case the amplitude of the results at these four stations decreased from $u'_{RMS}/U_{mean}=0.946$ at x=8 mm, to $u'_{RMS}/U_{mean}=0.715$ at x=150 mm. For the A_2 the amplitude of the results at these four stations decreased from $u'_{RMS}/U_{mean}=0.539$ at x=8 mm, to $u'_{RMS}/U_{mean}=0.328$ at x=150 mm. The obtained results reveal that for these first four stations, the pattern of streamwise fluctuation velocity for y<100 mm are completely different from the observed for A_1 and B_1 test cases. The horizontal velocity increase leads to a different behaviour for the confined jets. For the A_1 the amplitude of the results at these four stations were $u'_{RMS}/U_{mean}=1.154$ at x=8 mm, $u'_{RMS}/U_{mean}=0.951$ at x=50, $u'_{RMS}/U_{mean}=1.197$ at x=100 and $u'_{RMS}/U_{mean}=1.084$ at x=150 mm. For the confined jets test case A_2, the amplitude of the results at these four stations

decreased from u'_{RMS}/U_{mean}=1.234 at x=8 mm, to u'_{RMS}/U_{mean}=0.753 at x=150 mm. The obtained results reveal that for these first four stations, the pattern of streamwise fluctuation velocity for y<100 mm are practically equal to the observed for A_1 and B_1 test cases.

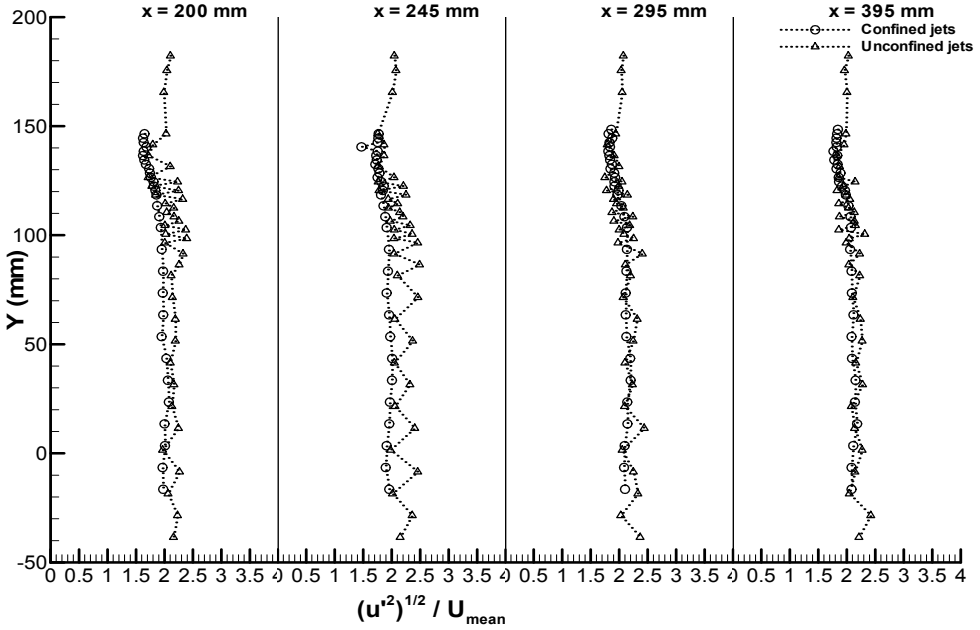

Figure 3.42. Vertical profiles of streamwise velocity fluctuation for A_2 and B_2 test cases at stations x=200, 245, 295 and 395 mm.

Figure 3.42 shows the streamwise velocity fluctuation results obtained for A_2 and B_2 test cases for the stations x=200, 245, 295 and 395 mm. For station x=200 mm for both test cases A_2 and B_2 all values are also lower when compared with same station for A_1 and B_1 test cases. The B_2 test case present values within the $1.623<u'_{RMS}/U_{mean}<2.077$. The highest obtained value is at y=23.50 mm and the lowest value is at y=144.50 mm. This interval shows a fine range of u'_{RMS}/U_{mean}=0.424 for this test case. The amplitude interval obtained for B_1 for this stations is of u'_{RMS}/U_{mean}=0.717. The oscillations of streamwise fluctuation velocity between neighbouring points disappeared. The A_2 test case reveals a $1.713<u'_{RMS}/U_{mean}<2.389$ range interval with an amplitude of u'_{RMS}/U_{mean}=0.676 for this test case, higher than the obtained for A_1 for this stations u'_{RMS}/U_{mean}=1.073. The highest obtained value is at y=98.50 mm and the lowest value is at y=126.50 mm. The oscillations of streamwise fluctuation velocity between neighbouring points are similar to B_2 test case for y<100 mm.

For station x=245 mm for both test cases A_2 and B_2 all values are also lower when compared with same station for A_1 and B_1 test cases. The B_2 test case present values within the $1.823<u'_{RMS}/U_{mean}<2.166$. The highest obtained value is at y=53.50 mm and the lowest value is at y=142.50 mm. This interval shows a fine range of u'_{RMS}/U_{mean}=0.343 for this test case. The amplitude interval obtained for B_1 for this stations is of u'_{RMS}/U_{mean}=0.653. The oscillations of streamwise fluctuation velocity between neighbouring points disappeared. The

A_2 test case reveals a $1.756<u'_{RMS}/U_{mean}<2.488$ range interval with an amplitude of $u'_{RMS}/U_{mean}=0.732$ for this test case, higher than the obtained for A_1 for this stations $u'_{RMS}/U_{mean}=0.933$. The highest obtained value is at y=86.50 mm and the lowest value is at y=146.50 mm. A_2 streamwise velocity reveals again strong neighbouring points oscillations for y<100 mm region.

For station x=295 mm, for both test cases A_2 and B_2 all values are also lower when compared with same station for A_1 and B_1 test cases. The B_2 test case present values within the $1.809<u'_{RMS}/U_{mean}<2.200$. The highest obtained value is at y=33.50 mm and the lowest value is at y=138.50 mm. This interval shows a fine range of $u'_{RMS}/U_{mean}=0.391$ for this test case. The amplitude interval obtained for B_1 for this stations is of $u'_{RMS}/U_{mean}=0.628$. For Y<100 mm, the oscillations of streamwise fluctuation velocity disappeared. The A_2 test case reveals a $1.777<u'_{RMS}/U_{mean}<2.437$ range interval with an amplitude of $u'_{RMS}/U_{mean}=0.660$ for this test case, higher than the obtained for A_1 for this stations $u'_{RMS}/U_{mean}=1.053$. The highest obtained value is at y=11.50 mm and the lowest value is at y=120.50 mm. Streamwise velocity reveals smoother neighbouring points oscillations for y<100 mm region.

For station x=395 mm, for both test cases A_2 and B_2 all values are also lower when compared with same station for A_1 and B_1 test cases. The B_2 test case present values within the $1.767<u'_{RMS}/U_{mean}<2.181$. The highest obtained value is at y=13.50 mm and the lowest value is at y=138.50 mm. This interval shows a fine range of $u'_{RMS}/U_{mean}=0.414$ for this test case. The amplitude interval obtained for B_1 for this stations is of $u'_{RMS}/U_{mean}=0.467$. For Y<100 mm, the oscillations of streamwise fluctuation velocity disappeared. The A_2 test case reveals a $1.829<u'_{RMS}/U_{mean}<2.314$ range interval with an amplitude of $u'_{RMS}/U_{mean}=0.485$ for this test case, higher than the obtained for A_1 for this stations $u'_{RMS}/U_{mean}=0.861$. The highest obtained value is at y=100.50 mm and the lowest value is at y=136.50 mm. Streamwise velocity reveals similarity to B_2 test case for y<100 mm. With exception to a few points, the obtained values are practically similar for both test cases.

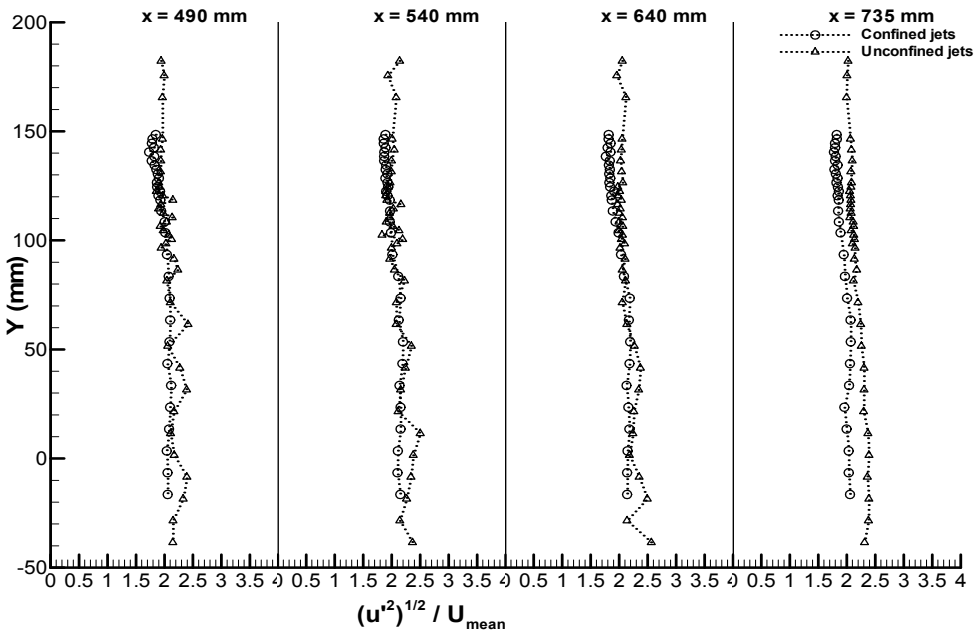

Figure 3.43. Vertical profiles of streamwise velocity fluctuation for A_2 and B_2 test cases at stations x=490, 540, 640 and 735 mm.

Figure 3.43 shows the streamwise velocity fluctuation results obtained for A_2 and B_2 test cases for the stations x=490, 540, 640 and 735 mm. For station x=490 mm, for both test cases A_2 and B_2 all values are also lower when compared with same station for A_1 and B_1 test cases. The B_2 test case present values within the $1.730<u'_{RMS}/U_{mean}<2.117$. The highest obtained value is at y=33.50 mm and the lowest value is at y=140.50 mm. This interval shows a fine range of $u'_{RMS}/U_{mean}=0.387$ for this test case. The amplitude interval obtained for B_1 for this stations is of $u'_{RMS}/U_{mean}=0.523$. For y<100 mm, the oscillations of streamwise fluctuation velocity disappeared. The A_2 test case reveals a $1.856<u'_{RMS}/U_{mean}<2.413$ range interval with an amplitude of $u'_{RMS}/U_{mean}=0.557$ for this test case, higher than the obtained for A_1 for this stations $u'_{RMS}/U_{mean}=0.717$. The highest obtained value is at y=61.50 mm and the lowest value is at y=122.50 mm. With exception to a few points, the obtained values are practically similar for both test cases.

Station x=540 mm reveals the previous station identical values for both test cases. At station x=640 mm, the values are practically similar to the both previous stations, with exception that the confined jets test case begin to present lower values than the unconfined jets test case for region 100<y<150 mm.

For station x=735 mm, the B_2 test case present values within the $1.776<u'_{RMS}/U_{mean}<2.069$. The highest obtained value is at y=53.50 mm and the lowest value is at y=140.50 mm. This interval shows a fine range of $u'_{RMS}/U_{mean}=0.293$ for this test case. The amplitude interval obtained for B_1 for this stations is of $u'_{RMS}/U_{mean}=0.312$. For all the entire vertical profile the oscillations of streamwise fluctuation velocity disappeared. The graphic reveals a line segment at $u'_{RMS}/U_{mean}=2$ neighbourhoods. The north values are slightly lower.

The A_2 test case reveals a $1.994<u'_{RMS}/U_{mean}<2.389$ range interval with an amplitude of $u'_{RMS}/U_{mean}=0.395$ for this test case, higher than the obtained for A_1 for this stations $u'_{RMS}/U_{mean}=0.658$. The highest obtained value is at y=1.50 mm and the lowest value is at y=165.50 mm, an exterior point. For all the entire vertical profile the oscillations of streamwise fluctuation velocity disappeared. The graphic reveals a line segment with values slightly superior to $u'_{RMS}/U_{mean}=2$. The north point's values are slightly lower. The unconfined jets test case reveals superior u'_{RMS}/U_{mean} values at this station.

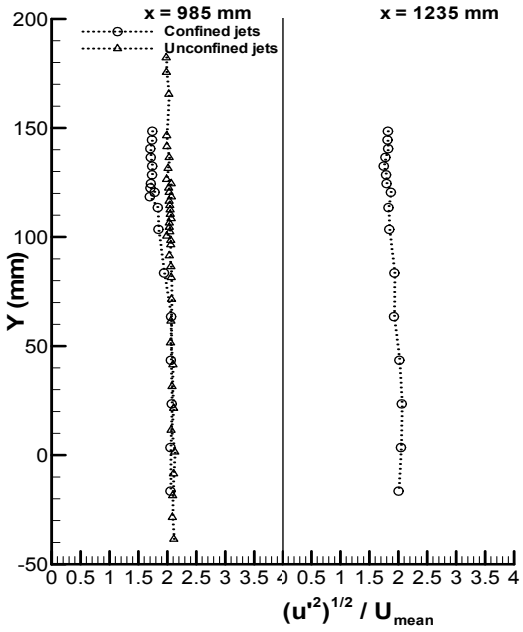

Figure 3.44. Vertical profiles of streamwise velocity fluctuation for A_2 and B_2 test cases at stations x=985 and 1235 mm.

For station x=985 mm (Figure 3.44), the B_2 test case present values within the $1.695<u'_{RMS}/U_{mean}<2.074$. The highest obtained value is at y=23.50 mm and the lowest value is at y=118.50 mm. This interval shows an amplitude of $u'_{RMS}/U_{mean}=0.379$. The entire vertical profile reveals very slight oscillations; all values are bellow $u'_{RMS}/U_{mean}=2.5$. The A_2 test case present values within the $1.986<u'_{RMS}/U_{mean}<2.127$. This interval shows an amplitude of $u'_{RMS}/U_{mean}=0.141$. The highest obtained value is at y=1.50 mm and the lowest value is at y=126.50 mm. The graphic reveals a straight line segment at $u'_{RMS}/U_{mean}=2$ neighbourhoods.

For station x=1235 mm, the B_2 test case present values within the $1.748<u'_{RMS}/U_{mean}<2.059$. The highest obtained value is at y=3.50 mm and the lowest value is at y=132.50 mm. This interval shows an amplitude of $u'_{RMS}/U_{mean}=0.311$. The entire vertical profile reveals very slight oscillations; all values are in $u'_{RMS}/U_{mean}=2$ vicinity.

3.6.3. Convergent 11° C_1 and convergent 22° D_1 jets

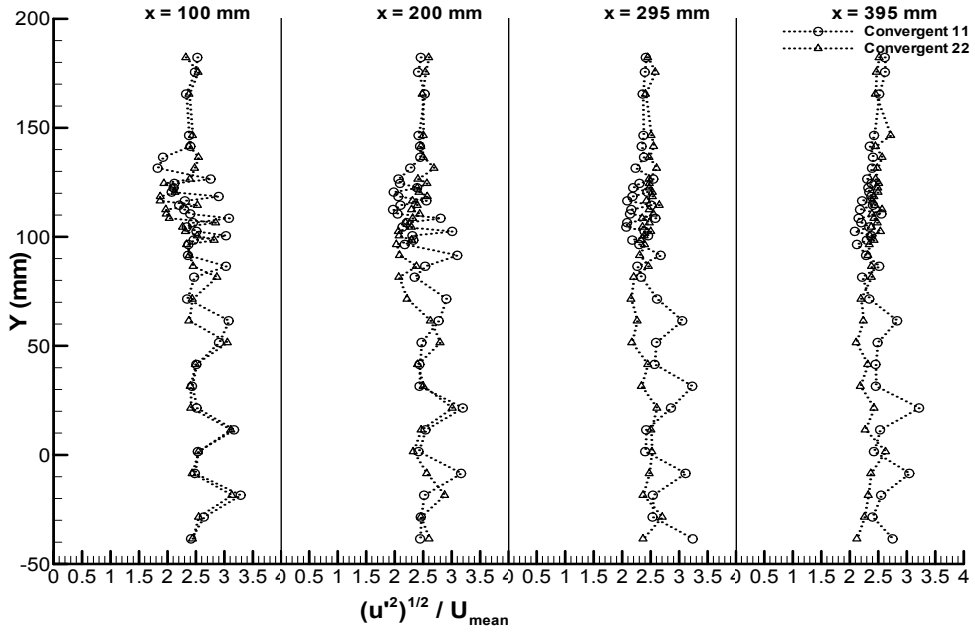

Figure 3.45. Vertical profiles of streamwise velocity fluctuation for C_1 and D_1 test cases at stations x=100, 200, 295 and 395 mm.

Figure 3.45 shows the streamwise velocity fluctuation results obtained for C_1 and D_1 test cases for the stations x=100, 200, 295 and 395 mm. For station x=100 mm, for both test cases C_1 and D_1 all values are very high since the obtained results are dimensionless form by the U_{mean}. Both test cases present neighbouring points amplitude oscillations. The C_1 test case present values within the $1.827<u'_{RMS}/U_{mean}<3.168$. The highest obtained value is at y=11.50 mm and the lowest value is at y=131.50 mm. This interval shows an amplitude of $u'_{RMS}/U_{mean}=1.341$. The D_1 test case present values within the $1.871<u'_{RMS}/U_{mean}<3.052$. The highest obtained value is at y=51.50 mm and the lowest value is at y=116.50 mm. This interval shows an amplitude of $u'_{RMS}/U_{mean}=1.181$. The three exterior points at north seems to avoid oscillation compulsion of the flow. The high amplitude streamwise intervals verified are due to convergent at the outer jets exit.

For station x=200 mm, for both test cases all values present a constant oscillation between neighbouring points. The C_1 test case present values within the $1.983<u'_{RMS}/U_{mean}<3.195$. The highest obtained value is at y=21.50 mm and the lowest value is at y=120.50 mm. This interval shows an amplitude of $u'_{RMS}/U_{mean}=1.212$. Comparing with the previous station the interval range narrowed from $u'_{RMS}/U_{mean}=1.341$ to $u'_{RMS}/U_{mean}=1.212$. The D_1 test case present values within the $2.030<u'_{RMS}/U_{mean}<3.010$. The highest obtained value is at y=21.50 mm and the lowest value is at y=96.50 mm. This interval shows an amplitude of $u'_{RMS}/U_{mean}=0.980$. Comparing with the previous station the interval range narrowed from $u'_{RMS}/U_{mean}=1.181$ to $u'_{RMS}/U_{mean}=0.980$. Great velocity oscillations are visible for all vertical profile. The three exterior points at north seems to avoid oscillation compulsion of the flow.

For station x=295 mm, both test cases continue to present neighbouring points oscillation. The C_1 test case present values within the $2.072<u'_{RMS}/U_{mean}<3.229$. The highest obtained value is at y=31.50 mm and the lowest value is at y=104.50 mm. This interval shows an amplitude of $u'_{RMS}/U_{mean}=1.157$. Comparing with the previous station the interval range narrowed from $u'_{RMS}/U_{mean}=1.212$ to $u'_{RMS}/U_{mean}=1.157$. The D_1 test case present values within the $2.153<u'_{RMS}/U_{mean}<2.607$. The highest obtained value is at y=21.50 mm and the lowest value is at y=71.50 mm. This interval shows an amplitude of $u'_{RMS}/U_{mean}=0.454$. Comparing with the previous station the interval range narrowed from $u'_{RMS}/U_{mean}=0.980$ to $u'_{RMS}/U_{mean}=0.454$ to nearly half. Great velocity oscillations are visible for all vertical profile for the test case C_1. Test case D_1 begin to presents smoother alterations. The three exterior points at north seems to avoid oscillation compulsion of the flow.

For station x=395 mm, for C_1 test case all values present a constant oscillation between neighbouring points, while for D_1 test case the streamwise fluctuation velocity are smoother. The C_1 test case present values within the $2.088<u'_{RMS}/U_{mean}<3.215$. The highest obtained value is at y=21.50 mm and the lowest value is at y=102.50 mm. This interval shows an amplitude of $u'_{RMS}/U_{mean}=1.127$. Comparing with the previous station the interval range is similar, moving from $u'_{RMS}/U_{mean}=1.157$ to $u'_{RMS}/U_{mean}=1.127$. The D_1 test case present values within the $2.112<u'_{RMS}/U_{mean}<2.718$. The highest obtained value is at y=146.50 mm and the lowest value is at y=51.50 mm. This interval shows an amplitude of $u'_{RMS}/U_{mean}=0.606$. Comparing with the previous station the interval ranged from $u'_{RMS}/U_{mean}=0.454$ to $u'_{RMS}/U_{mean}=0.606$. The three exterior points at north seems to avoid oscillation compulsion of the flow.

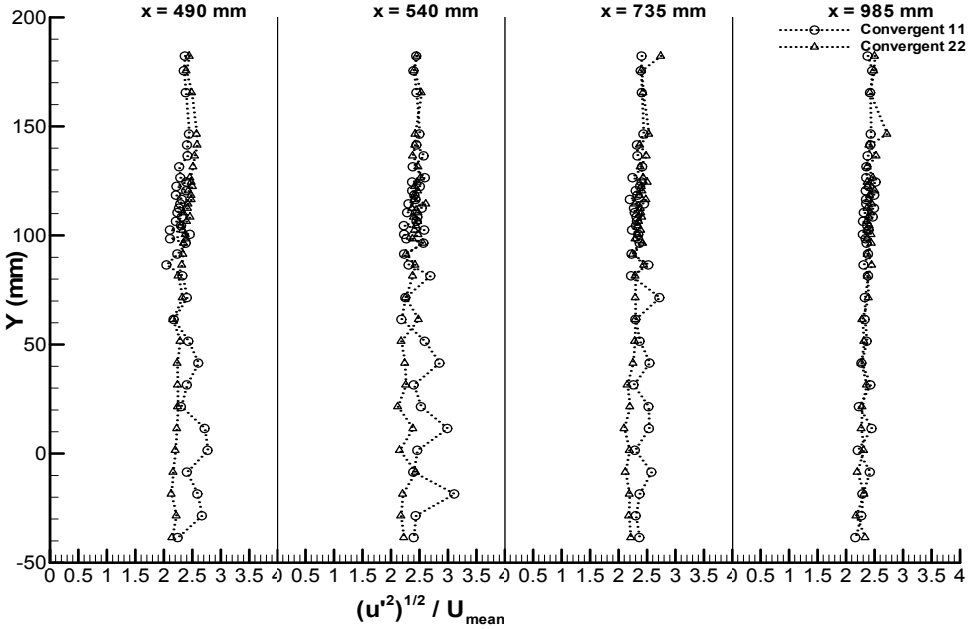

Figure 3.46. Vertical profiles of streamwise velocity fluctuation for C_1 and D_1 test cases at stations x=490, 540, 735 and 985 mm.

Figure 3.46 shows the streamwise velocity fluctuation results obtained for C_1 and D_1 test cases for the stations x=490, 540, 735 and 985 mm. For station x=490 mm, C_1 test case all values continue to present neighbouring points constant oscillation, while D_1 test case present practically a line segment. The C_1 test case present values within the $2.105<u'_{RMS}/U_{mean}<2.714$. The highest obtained value is at y=11.50 mm and the lowest value is at y=102.50 mm. This interval shows an amplitude of $u'_{RMS}/U_{mean}=0.609$. Comparing with the previous station the interval range is almost half ranged, moving from $u'_{RMS}/U_{mean}=1.127$ to $u'_{RMS}/U_{mean}=0.609$. The D_1 test case present values within the $2.155<u'_{RMS}/U_{mean}<2.581$. The highest obtained value is at y=141.50 mm and the lowest value is at y=61.50 mm. This interval shows an amplitude of $u'_{RMS}/U_{mean}=0.426$. Comparing with the previous station the interval ranged from $u'_{RMS}/U_{mean}=0.606$ to $u'_{RMS}/U_{mean}=0.426$. The three exterior points at north seems to avoid oscillation compulsion of the flow.

For station x=540 mm, both test cases presents higher oscillations than in the previous station. The C_1 test case present values within the $2.180<u'_{RMS}/U_{mean}<2.987$. The highest obtained value is at y=11.50 mm and the lowest value is at y=161.50 mm. This interval shows an amplitude of $u'_{RMS}/U_{mean}=0.807$. Comparing with the previous station the interval range become larger from $u'_{RMS}/U_{mean}=0.609$ to $u'_{RMS}/U_{mean}=0.807$. The D_1 test case present values within the $2.115<u'_{RMS}/U_{mean}<2.609$. The highest obtained value is at y=114.50 mm and the lowest value is at y=21.50 mm. This interval shows an amplitude of $u'_{RMS}/U_{mean}=0.494$. Comparing with the previous station the interval ranged from $u'_{RMS}/U_{mean}=0.426$ to $u'_{RMS}/U_{mean}=0.494$. The three exterior points at north seems to avoid oscillation compulsion of the flow.

For station x=735 mm, both test cases present similar values at Y>100 mm. For Y<100 mm the oscillation is stronger for C_1 regarding the previous station and is smoother for D_1 regarding the previous station. The C_1 test case present values within the $2.198<u'_{RMS}/U_{mean}<2.716$. The highest obtained value is at y=71.50 mm and the lowest value is at y=116.50 mm. This interval shows an amplitude of $u'_{RMS}/U_{mean}=0.518$. Comparing with the previous station the interval range become smaller from $u'_{RMS}/U_{mean}=0.807$ to $u'_{RMS}/U_{mean}=0.518$. The D_1 test case present values within the $2.095<u'_{RMS}/U_{mean}<2.529$. The highest obtained value is at y=146.50 mm and the lowest value is at y=11.50 mm. This interval shows an amplitude of $u'_{RMS}/U_{mean}=0.434$. Comparing with the previous station the interval ranged from $u'_{RMS}/U_{mean}=0.494$ to $u'_{RMS}/U_{mean}=0.434$. The three exterior points at north seems to avoid oscillation compulsion of the flow.

For station x=985 mm, both test cases present similar to each other at the entire vertical profile. The tendency is a straight line segment with values within the $u'_{RMS}/U_{mean}=2.3$ neighbourhoods. The C_1 test case present values within the $2.204<u'_{RMS}/U_{mean}<2.518$. The highest obtained value is at y=124.50 mm and the lowest value is at y=1.50 mm. This interval shows an amplitude of $u'_{RMS}/U_{mean}=0.314$. Comparing with the previous station the interval range become smaller from $u'_{RMS}/U_{mean}=0.518$ to $u'_{RMS}/U_{mean}=0.314$. The D_1 test case present

values within the $2.264<u'_{RMS}/U_{mean}<2.716$. The highest obtained value is at y=146.50 mm and the lowest value is at y=11.50 mm. This interval shows an amplitude of $u'_{RMS}/U_{mean}=0.452$. Comparing with the previous station the interval ranged from $u'_{RMS}/U_{mean}=0.434$ to $u'_{RMS}/U_{mean}=0.452$. The three exterior points at north seems to avoid oscillation compulsion of the flow.

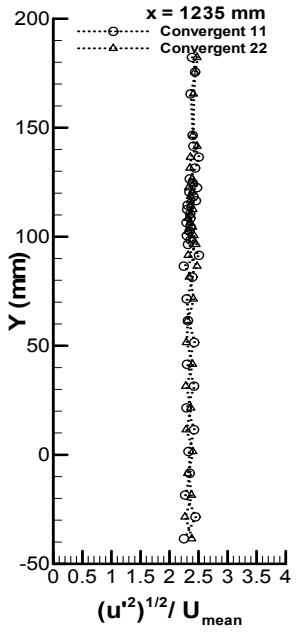

Figure 3.47. Vertical profiles of streamwise velocity fluctuation for C_1 and D_1 test cases at station x=1235 mm.

For station x=1235 mm (Figure 3.47) both test cases present practically a single streamwise fluctuation velocity profile that form a straight line at the $u'_{RMS}/U_{mean}=2.3$ neighbourhoods.

3.6.4. Convergent 11° C_2 and convergent 22° D_2 jets

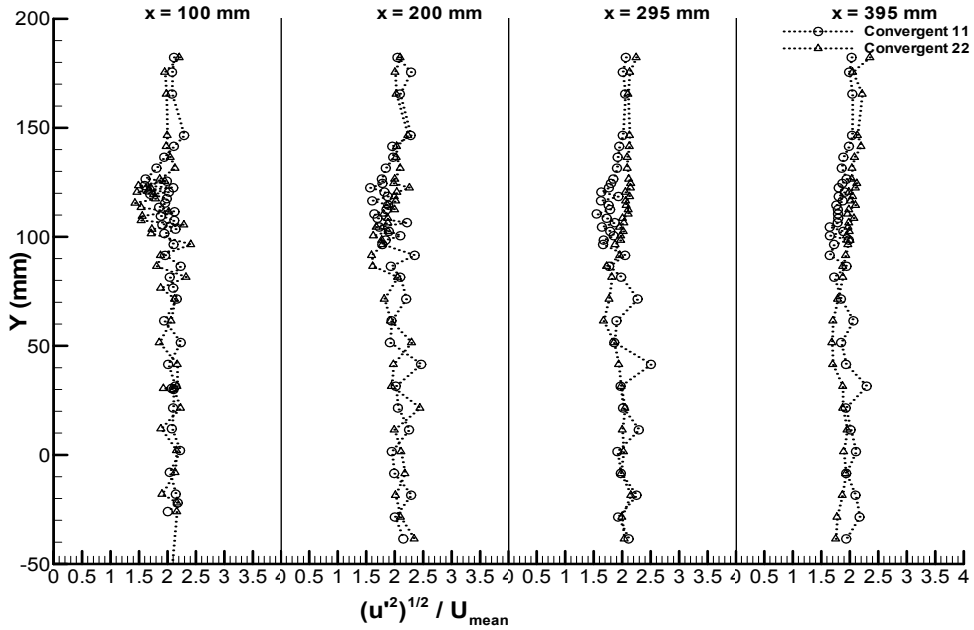

Figure 3.48. Vertical profiles of streamwise velocity fluctuation for C_2 and D_2 test cases at stations x=100, 200, 295 and 395 mm.

Figure 3.48 shows the streamwise velocity fluctuation results obtained for C_2 and D_2 test cases for the stations x=100, 200, 295 and 395 mm. For station x=100mm, for both C_2 and D_2 test cases all values present a constant neighbouring points amplitude oscillation. Regarding the C_1 and D_1 test cases for this station, the previous study present higher amplitude intervals of streamwise fluctuation velocity. The C_2 test case present values within the $1.615<u'_{RMS}/U_{mean}<2.233$. The highest obtained value is at y=51.50 mm and the lowest value is at y=126.50 mm. This interval shows an amplitude of $u'_{RMS}/U_{mean}=0.618$, less than half of $u'_{RMS}/U_{mean}=1.341$ obtained for C_1 at station x=100 mm. The D_2 test case present values within the $1.429<u'_{RMS}/U_{mean}<2.288$. The highest obtained value is at y=105.50 mm and the lowest value is at y=115.50 mm. This interval shows an amplitude of $u'_{RMS}/U_{mean}=0.859$, less than $u'_{RMS}/U_{mean}=1.181$ obtained for D_1 at station x=100 mm. The increase of horizontal velocity with exterior inclined jets, leads to minor amplitude range intervals of u'_{RMS}.

For station x=200 mm, both C_2 and D_2 test cases all values present a constant amplitude oscillation between neighbouring points. Regarding the C_1 and D_1 test cases for this station, the previous study present higher amplitude intervals of streamwise fluctuation velocity. C_2 test case present values within the $1.606<u'_{RMS}/U_{mean}<2.464$. The highest obtained value is at y=41.50 mm and the lowest value is at y=116.50 mm. This interval shows an amplitude of $u'_{RMS}/U_{mean}=0.858$, less than $u'_{RMS}/U_{mean}=1.212$ obtained for C_1 at station x=200 mm. The D_2 test case present values within the $1.595<u'_{RMS}/U_{mean}<2.442$. The highest obtained value is at y=11.50 mm and the lowest value is at y=91.50 mm. This interval shows an amplitude of $u'_{RMS}/U_{mean}=0.847$, less than $u'_{RMS}/U_{mean}=0.980$ obtained for D_1 at station x=200

mm. The increase of horizontal velocity leads to minor amplitude range intervals of u'_{RMS} at this station.

For station x=295 mm, D_2 test case presents smoother streamwise fluctuation velocity variations and the C_2 test case continue to present same amplitude variations. Regarding the C_1 and D_1 test cases for this station, the previous study present higher amplitude intervals of streamwise fluctuation velocity. The C_2 test case present values within the $1.551<u'_{RMS}/U_{mean}<2.291$. The highest obtained value is at y=11.50 mm and the lowest value is at y=110.50 mm. This interval shows an amplitude of $u'_{RMS}/U_{mean}=0.740$, less than $u'_{RMS}/U_{mean}=1.157$ obtained for C_1 at station x=295 mm. The D_2 test case present values within the $1.671<u'_{RMS}/U_{mean}<2.148$. The highest obtained value is at y=124.50 mm and the lowest value is at y=61.50 mm. This interval shows an amplitude of $u'_{RMS}/U_{mean}=0.477$, similar than $u'_{RMS}/U_{mean}=0.454$ obtained for D_1 at station x=295 mm. For the C_2 test case, the increase of horizontal velocity leads to minor amplitude range intervals of u'_{RMS} at this station.

For station x=395 mm, regarding previous station D_2 test case presents smoother streamwise fluctuation velocity variations and the C_2 test case continue to present same amplitude variations. Regarding the C_1 and D_1 test cases for this station, the previous study present higher amplitude intervals of streamwise fluctuation velocity. The C_2 test case present values within the $1.649<u'_{RMS}/U_{mean}<2.297$. The highest obtained value is at y=31.50 mm and the lowest value is at y=91.50 mm. This interval shows an amplitude of $u'_{RMS}/U_{mean}=0.648$, less than $u'_{RMS}/U_{mean}=1.127$ obtained for C_1 at station x=395 mm. The D_2 test case present values within the $1.685<u'_{RMS}/U_{mean}<2.197$. The highest obtained value is at y=141.50 mm and the lowest value is at y=51.50 mm. This interval shows an amplitude of $u'_{RMS}/U_{mean}=0.512$, slightly small than $u'_{RMS}/U_{mean}=0.606$ obtained for D_1 at station x=395 mm. For both test cases, the increase of horizontal velocity leads to minor amplitude range intervals of u'_{RMS} at this station.

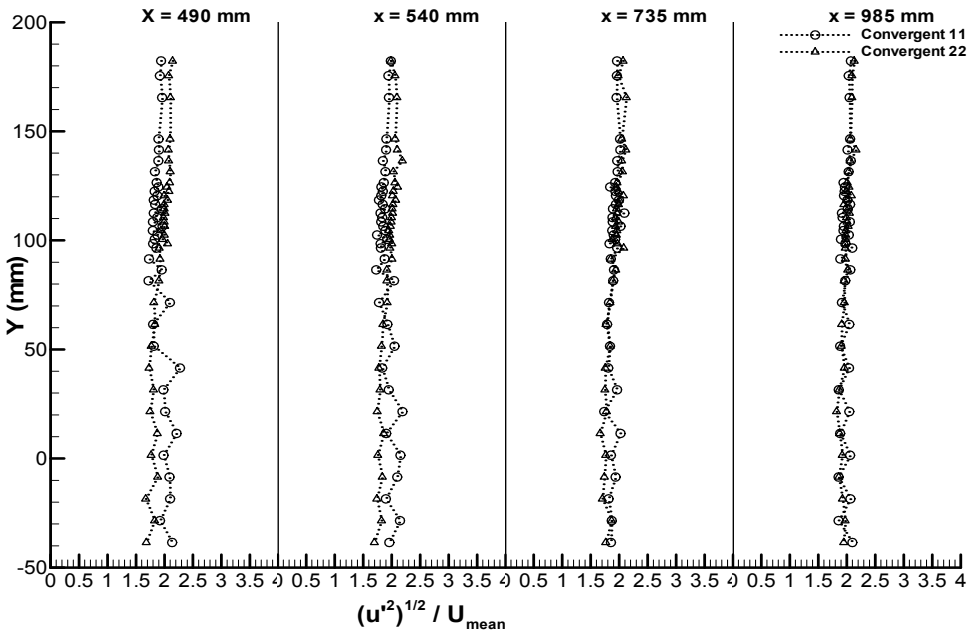

Figure 3.49. Vertical profiles of streamwise velocity fluctuation for C_2 and D_2 test cases at stations x=490, 540, 735 and 985 mm.

Figure 3.49 shows the streamwise velocity fluctuation results obtained for C_2 and D_2 test cases for the stations x=490, 540, 735 and 985 mm. At station x=490 mm and regarding previous station, C_2 and D_2 presents smoother streamwise fluctuation velocity variations. Regarding the C_1 and D_1 test cases for this station, the previous study present higher amplitude intervals of streamwise fluctuation velocity. The C_2 test case present values within the $1.720<u'_{RMS}/U_{mean}<2.273$. The highest obtained value is at y=41.50 mm and the lowest value is at y=81.50 mm. This interval shows an amplitude of $u'_{RMS}/U_{mean}=0.553$, less than $u'_{RMS}/U_{mean}=0.609$ obtained for C_1 at station x=490. The D_2 test case present values within the $1.728<u'_{RMS}/U_{mean}<2.079$. The highest obtained value is at y=122.50 mm and the lowest value is at y=41.50 mm. This interval shows an amplitude of $u'_{RMS}/U_{mean}=0.351$, slightly small than $u'_{RMS}/U_{mean}=0.426$ obtained for D_1 at station x=490 mm. For both test cases, the increase of horizontal velocity leads to minor amplitude range intervals of u'_{RMS} at this station.

Station x=540 mm presents practically the previous station results for both test cases. The C_2 test case present values within the $1.729<u'_{RMS}/U_{mean}<2.189$. The highest obtained value is at y=21.50 mm and the lowest value is at y=86.50 mm. This interval shows an amplitude of $u'_{RMS}/U_{mean}=0.460$ nearly $u'_{RMS}/U_{mean}=0.807$ from the obtained for C_1 test case at station x=540 mm. The D_2 test case present values within the $1.745<u'_{RMS}/U_{mean}<2.186$. The highest obtained value is at y=136.50 mm and the lowest value is at y=21.50 mm. This interval shows an amplitude of $u'_{RMS}/U_{mean}=0.441$, similar to $u'_{RMS}/U_{mean}=0.494$ obtained for D_1 test case.

For station x=735 mm, both test cases are tending to the same values, looking a single vertical profile. The C_2 test case present values within the $1.737<u'_{RMS}/U_{mean}<2.091$. The

highest obtained value is at y=112.50 mm and the lowest value is at y=21.50 mm. This interval shows an amplitude of u'_{RMS}/U_{mean}=0.354, less than u'_{RMS}/U_{mean}=0.518 obtained for C_1 test case at station x=735 mm. The D_2 test case present values within the $1.665<u'_{RMS}/U_{mean}<2.116$. The highest obtained value is at y=141.50 mm and the lowest value is at y=11.50 mm. This interval shows an amplitude of u'_{RMS}/U_{mean}=0.451, similar to u'_{RMS}/U_{mean}=0.434 obtained for C_1 test case at station x=735 mm.

For station x=985 mm, both test cases present similar to each other at the entire vertical profile. The tendency is a straight line segment with values within the u'_{RMS}/U_{mean}=2 neighbourhoods, lower than the tendency of u'_{RMS}/U_{mean}=2.3 for C_1 and D_1 test cases at station x=985 mm. The C_1 test case present values within the $1.859<u'_{RMS}/U_{mean}<2.071$. The highest obtained value is at y=131.50 mm and the lowest value is at y=31.50 mm. This interval shows an amplitude of u'_{RMS}/U_{mean}=0.212, less than u'_{RMS}/U_{mean}=0.314 for C_1 test case at station x=985. The D_2 test case present values within the $1.820<u'_{RMS}/U_{mean}<2.162$. The highest obtained value is at y=141.50 mm and the lowest value is at y=21.50 mm. This interval shows an amplitude of u'_{RMS}/U_{mean}=0.342, less than u'_{RMS}/U_{mean}=0.452 obtained for D_1 test case for station x=985 mm.

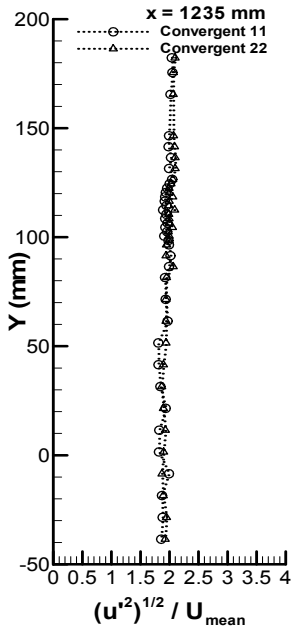

Figure 3.50. Vertical profiles of streamwise velocity fluctuation for C_2 and D_2 test cases at station x=1235 mm.

For station x=1235 mm, (Figure 3.50) both test cases present practically a single streamwise fluctuation velocity profile that form a straight line at the u'_{RMS}/U_{mean}=2 neighbourhoods, less than u'_{RMS}/U_{mean}=2.3 obtained at C_1 and D_1 test cases at station x=1235 mm.

3.7. Vertical profiles of transverse fluctuation velocity

This subchapter presents all the obtained results for the vertical profiles of transverse velocity fluctuation v'_{RMS}, (dimensionless form by U_{mean}) distribution at the horizontal axis in each studied station, from y=200 mm to y=-50 mm. The vertical profiles of transverse velocity fluctuation v'_{RMS} distribution values are presented from $0 \leq v'_{RMS}/U_{mean} \leq 1$. The confined jets values starts at y=148.50 mm, due to its wall confinement. The unconfined jets values starts at y=182.25 mm.

3.7.1. Unconfined A_1 and confined B_1 jets

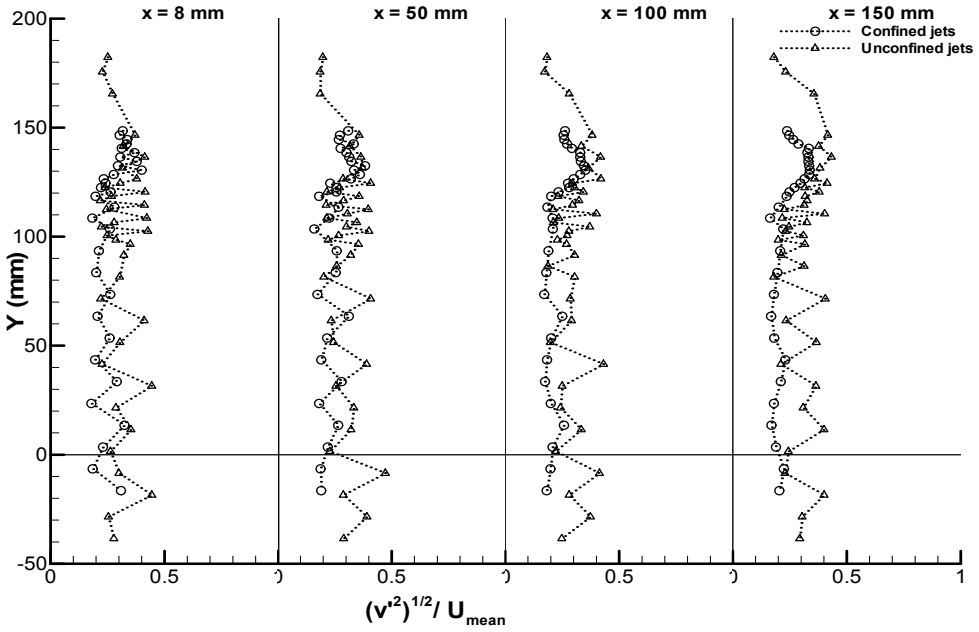

Figure 3.51. Vertical profiles of vertical velocity fluctuation for A_1 and B_1 test cases at stations x=8, 50, 100 and 150 mm.

Figure 3.51 shows vertical profiles of vertical velocity fluctuations for A_1 and B_1 test cases at stations x=8, 50, 100 and 150 mm. For station x=8 mm, for both test cases A_1 and B_1 all values are high since the obtained results are dimensionless form by the U_{mean}. For all presented stations the A_1 unconfined test case presents a constant high amplitude oscillation between neighbouring points. Regarding station x=8 mm, the B_1 test case present values within the $0.1788 < v'_{RMS}/U_{mean} < 0.4000$. The highest obtained value is at y=130.50 mm and the lowest value is at y=23.50 mm. This interval shows an amplitude of $v'_{RMS}/U_{mean}=0.2212$ for this test case. Transverse fluctuation velocity oscillations are visible for all vertical profile. The A_1 test case reveals an amplitude interval of $0.2185 < v'_{RMS}/U_{mean} < 0.4119$. This interval shows an amplitude of $v'_{RMS}/U_{mean}=0.1934$ for this test case. The highest obtained value is at y=141.50 mm and the lowest value is at y=116.50 mm. High transverse fluctuation velocity amplitude

oscillations between neighbouring points are visible for all vertical profile. The three exterior points at north seems to avoid oscillation compulsion of the flow.

For station x=50 mm, the B_1 test case present values within the $0.1606<v'_{RMS}/U_{mean}<0.3606$. The highest obtained value is at y=128.50 mm and the lowest value is at y=103.50 mm. This interval shows an amplitude of $v'_{RMS}/U_{mean}=0.2000$, less than $v'_{RMS}/U_{mean}=0.2212$ for the same test case regarding the previous station. Transverse fluctuation velocity oscillations are visible for all vertical profile. The A_1 test case present values within the $0.2022<v'_{RMS}/U_{mean}<0.4074$. The highest obtained value is at both y=124.50 and y=71.50 mm points. The lowest value is at y=81.50 mm. This interval shows an amplitude of $v'_{RMS}/U_{mean}=0.2052$, slightly higher than $v'_{RMS}/U_{mean}=0.1934$ obtained for the same test case regarding the previous station. Transverse fluctuation velocity oscillations between neighbouring points are visible for all vertical profile. All the three exterior points at north reveals minor transverse fluctuation velocity values.

For station x=100 mm, the B_1 test case present values within the $0.1712<v'_{RMS}/U_{mean}<0.3454$. The highest obtained value is at y=132.50 mm and the lowest value is at y=73.50 mm. This interval shows an amplitude of $v'_{RMS}/U_{mean}=0.1742$, less than $v'_{RMS}/U_{mean}=0.2000$ for the same test case regarding the previous station. Transverse fluctuation velocity oscillations are becoming weaker for all vertical profile. The A_1 test case present values within the $0.2022<v'_{RMS}/U_{mean}<0.4074$. The highest obtained value is at both y=124.50 and y=71.50 mm points. The lowest value is at y=81.50 mm. This interval shows an amplitude of $v'_{RMS}/U_{mean}=0.2052$, slightly higher than $v'_{RMS}/U_{mean}=0.1934$ obtained for the same test case regarding the previous station. Transverse fluctuation velocity oscillations between neighbouring points are visible for all vertical profile.

For station x=150 mm, the B_1 test case present values within the $0.1636<v'_{RMS}/U_{mean}<0.3379$. The highest obtained value is at y=130.50 mm and the lowest value is at y=108.50 mm. This interval shows an amplitude of $v'_{RMS}/U_{mean}=0.1743$, identical to $v'_{RMS}/U_{mean}=0.1742$ for the same test case regarding the previous station. The neighbouring points velocity oscillations disappeared. The A_1 test case present values within the $0.1801<v'_{RMS}/U_{mean}<0.4325$. The highest obtained value is at y=136.50 mm and the lowest value is at y=81.50 mm. This interval shows an amplitude of $v'_{RMS}/U_{mean}=0.2524$, slightly higher than $v'_{RMS}/U_{mean}=0.2333$ obtained for the same test case regarding the previous station. Transverse fluctuation velocity oscillations between neighbouring points are visible for all vertical profile.

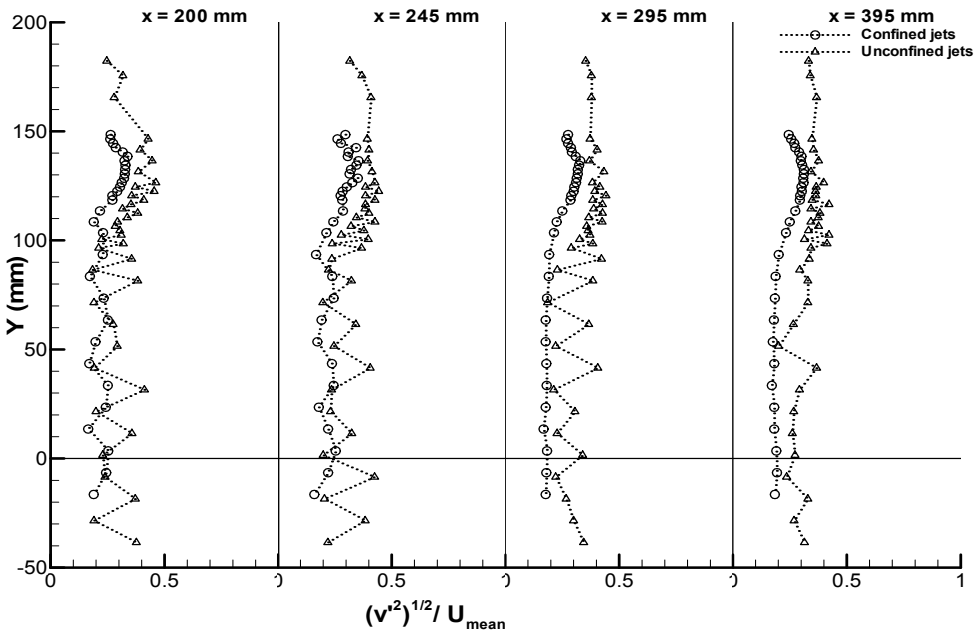

Figure 3.52. Vertical profiles of vertical velocity fluctuation for A_1 and B_1 test cases at stations x=200, 245, 295 and 395 mm.

Figure 3.52 shows vertical profiles of vertical velocity fluctuations for A_1 and B_1 test cases at stations x=200, 245, 295 and 395 mm. For station x=200 mm, the B_1 test case present values within the $0.1682<v'_{RMS}/U_{mean}<0.3545$. The highest obtained value is at y=136.50 mm and the lowest value is at y=93.50 mm. This interval shows an amplitude of $v'_{RMS}/U_{mean}=0.1863$ for this test case, slightly higher than $v'_{RMS}/U_{mean}=0.1743$ for the same test case regarding the previous station. The A_1 test case reveals an amplitude interval of $0.1904<v'_{RMS}/U_{mean}<0.4621$. This interval shows an amplitude of $v'_{RMS}/U_{mean}=0.2717$ for this test case, slightly higher than $v'_{RMS}/U_{mean}=0.2524$ for the same test case regarding the previous station. The highest obtained value is at y=126.50 mm and the lowest value is at y=71.50 mm. Transverse fluctuation velocity oscillations between neighbouring points are visible for all vertical profile.

For station x=245 mm, the B_1 test case present values within the $0.1701<v'_{RMS}/U_{mean}<0.3515$. The highest obtained value is at y=130.50 mm and the lowest value is at y=93.50 mm. This interval shows an amplitude of $v'_{RMS}/U_{mean}=0.1814$, slightly less than $v'_{RMS}/U_{mean}=0.1863$ for the same test case regarding the previous station. The A_1 test case reveals an amplitude interval of $0.1978<v'_{RMS}/U_{mean}<0.4629$. This interval shows an amplitude of $v'_{RMS}/U_{mean}=0.2451$ for this test case, slightly higher than $v'_{RMS}/U_{mean}=0.2717$ for the same test case regarding the previous station. The highest obtained value is at y=122.50 mm and the lowest value is at y=71.50 mm. Transverse fluctuation velocity oscillations between neighbouring points are visible for all vertical profile.

For station x=295 mm, the B_1 test case present values within the $0.1682<v'_{RMS}/U_{mean}<0.3255$. The highest obtained value is at y=136.50 mm and the lowest value is at y=13.50 mm. This interval shows an amplitude of $v'_{RMS}/U_{mean}=0.1573$, less than

v'_{RMS}/U_{mean}=0.1814 for the same test case regarding the previous station. Graphic shows practically a line segment between symmetry axis plane and y=100 mm point with identical values. The A_1 test case reveals an amplitude interval of $0.1860<v'_{RMS}/U_{mean}<0.4414$. This interval shows an amplitude of v'_{RMS}/U_{mean}=0.2554 for this test case, slightly higher than v'_{RMS}/U_{mean}=0.2451 for the same test case regarding the previous station. The highest obtained value is at y=120.50 mm and the lowest value is at y=71.50 mm. Transverse fluctuation velocity oscillations between neighbouring points are visible for all vertical profile.

For station x=395 mm, the B_1 test case present values within the $0.1712<v'_{RMS}/U_{mean}<0.3121$. The highest obtained value is at both y=132.50 and y=130.50 mm points. The lowest value is at y=33.50 mm. This interval shows an amplitude of v'_{RMS}/U_{mean}=0.1409, less than v'_{RMS}/U_{mean}=0.1573 for the same test case regarding the previous station. Graphic shows practically a line segment between symmetry axis and y=100 mm point with identical values. The A_1 test case reveals an amplitude interval of $0.2008<v'_{RMS}/U_{mean}<0.4222$. This interval shows an amplitude of u'_{RMS}/U_{mean}=0.2214 for this test case, less than v'_{RMS}/U_{mean}=0.2554 for the same test case regarding the previous station. The highest obtained value is present at both y=122.50 and y=116.50 mm points. The lowest value is at y=51.50 mm. Transverse fluctuation velocity oscillations between neighbouring points are smoother for all vertical profile.

By regarding all previous eight stations presented at subchapter 3.7, graphics reveals that for both A_1 and B_1 test cases, the transverse fluctuations velocity evolution range is decreasing for the y>100 mm region. For region y<100 mm, the A_1 test case reveals constant velocity oscillation, while for B_1 test case the oscillation range is quite small for stations x=295 mm and x=395 mm.

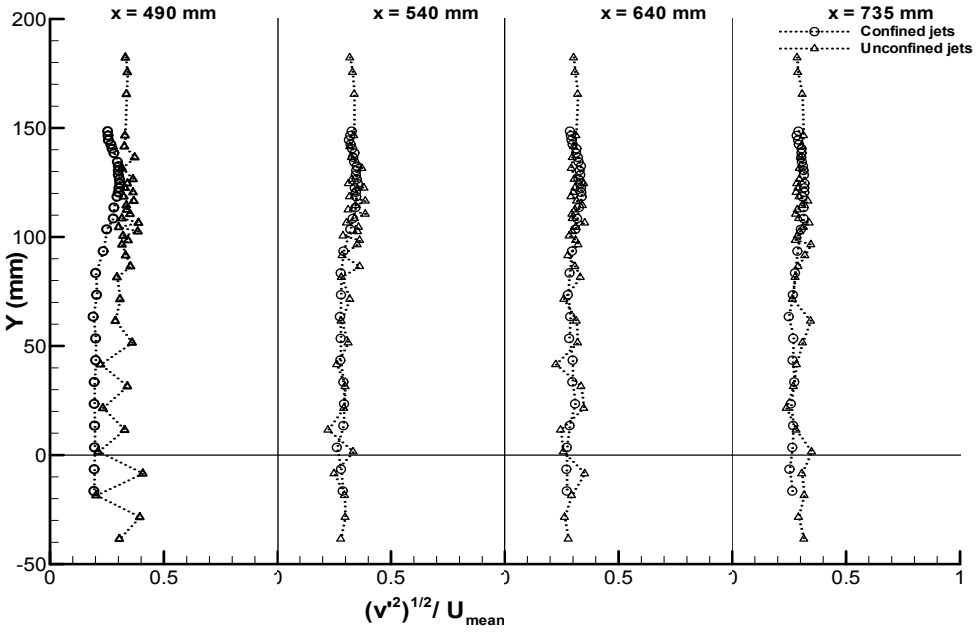

Figure 3.53. Vertical profiles of vertical velocity fluctuation for A_1 and B_1 test cases at stations x=490, 540, 640 and 735 mm.

Figure 3.53 shows vertical profiles of vertical velocity fluctuations for A_1 and B_1 test cases at stations x=490, 540, 640 and 735 mm. At station x=490 mm, the B_1 test case present values within the $0.1939<v'_{RMS}/U_{mean}<0.3060$. This interval shows an amplitude of $v'_{RMS}/U_{mean}=0.1121$ for this test case, less than $v'_{RMS}/U_{mean}=0.1409$ for the same test case regarding the previous station. The highest obtained value is at y=124.50 mm and the lowest value is both at y=13.50 and y=23.50 mm points. Transverse fluctuation velocity oscillations are very small. The A_1 test case reveals an amplitude interval of $0.2111<v'_{RMS}/U_{mean}<0.3882$. This interval shows an amplitude of $v'_{RMS}/U_{mean}=0.1771$ for this test case, less than $v'_{RMS}/U_{mean}=0.2214$ for the same test case regarding the previous station. The highest obtained value is at y=126.50 mm and the lowest value is at y=1.50 mm. Transverse fluctuation velocity oscillations between neighbouring points are smoother for all vertical profile.

For station x=540 mm, the B_1 test case present values within the $0.2621<v'_{RMS}/U_{mean}<0.3545$. The highest obtained value is at y=124.50 mm and the lowest value is at y=3.50 mm. This interval shows an amplitude of $v'_{RMS}/U_{mean}=0.0924$, less than $v'_{RMS}/U_{mean}=0.1121$ for the same test case regarding the previous station. Transverse fluctuation velocity oscillations are very small, revealing practically a vertical line segment at $v'_{RMS}/U_{mean}=0.3$ neighbourhoods. The A_1 test case reveals an amplitude interval of $0.2229<v'_{RMS}/U_{mean}<0.3868$. This interval shows an amplitude of $v'_{RMS}/U_{mean}=0.1639$ for this test case, slightly smaller than $v'_{RMS}/U_{mean}=0.1771$ for the same test case regarding the previous station. The highest obtained value is both at y=110.50 and y=116.50 mm points. The lowest value is at y=11.50 mm. Transverse fluctuation velocity oscillations are very small. Graphics reveals the same tendency values as the confined jets test case.

For station x=640 mm, the B_1 test case present values within the $0.2198<v'_{RMS}/U_{mean}<0.2704$ ($v'_{RMS}/U_{mean}=0.0506$ range interval, less than $v'_{RMS}/U_{mean}=0.0904$ for the same test case at the previous station). The highest obtained value is at y=23.50 mm and the lowest value is at y=136.50 mm. Transverse fluctuation velocity oscillations are very small, revealing practically a vertical line segment at $v'_{RMS}/U_{mean}=0.25$ neighbourhoods. The A_1 test case reveals an amplitude interval of $0.2244<v'_{RMS}/U_{mean}<0.3513$. This interval shows an amplitude of $v'_{RMS}/U_{mean}=0.1269$ for this test case, less than $v'_{RMS}/U_{mean}=0.1639$ for the same test case regarding the previous station. The highest obtained value is at y=106.50 mm and the lowest value is at y=41.50 mm. Transverse fluctuation velocity oscillations are visible for all vertical profile. Transverse fluctuation velocity oscillations are very small. Graphics reveals the same tendency values as the confined jets test case.

For station x=735 mm, the B_1 test case present values within the $0.2485<v'_{RMS}/U_{mean}<0.3182$. The highest obtained value is at y=124.50 mm. The lowest value is at y=63.50. This interval shows an amplitude of $v'_{RMS}/U_{mean}=0.0697$, slightly higher than $v'_{RMS}/U_{mean}=0.0506$ for the same test case regarding the previous station. Transverse fluctuation velocity oscillations are very small, revealing practically a vertical line segment at

v'_{RMS}/U_{mean}=0.3 neighbourhoods. The A_1 test case reveals an amplitude interval of 0.2775<v'_{RMS}/U_{mean}<0.3484. This interval shows an amplitude of v'_{RMS}/U_{mean}=0.0709 for this test case, less than v'_{RMS}/U_{mean}=0.1269 for the same test case regarding the previous station. The highest obtained value is at y=1.50 mm and the lowest value is at y=98.50 mm. Transverse fluctuation velocity oscillations are visible for all vertical profile. With some exception points, the transverse fluctuation velocity oscillations are very small revealing practically a vertical line segment at v'_{RMS}/U_{mean}=0.3 neighbourhoods.

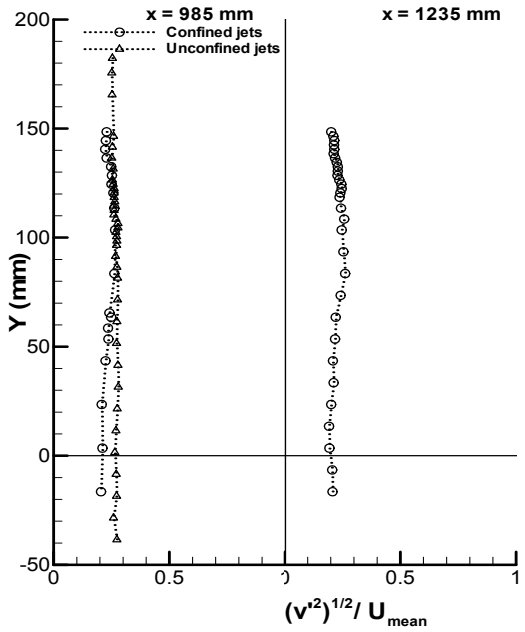

Figure 3.54. Vertical profiles of vertical velocity fluctuation for A_1 and B_1 test cases at stations x=985 and 1235 mm.

Figure 3.54 shows vertical profiles of vertical velocity fluctuations for A_1 and B_1 test cases at stations x=985 and 1235 mm. For station x=985 mm, the B_1 test case present values within the 0.2076<v'_{RMS}/U_{mean}<0.2651. The highest obtained value is at y=103.50 and the lowest value is at y=23.50. This interval shows an amplitude of v'_{RMS}/U_{mean}=0.0575, less than v'_{RMS}/U_{mean}=0.0697 for the same test case regarding the previous station. Transverse fluctuation velocity oscillations are very small, revealing practically a vertical line segment at v'_{RMS}/U_{mean}=0.25 neighbourhoods. The A_1 test case reveals an amplitude interval of 0.2510<v'_{RMS}/U_{mean}<0.2790. This interval shows an amplitude of v'_{RMS}/U_{mean}=0.0280 for this test case, less than v'_{RMS}/U_{mean}=0.0709 for the same test case regarding the previous station. The highest obtained value is at y=31.50 and the lowest value is at y=136.50. Transverse fluctuation velocity oscillations are visible for all vertical profile. Transverse fluctuation velocity oscillations are very small. Transverse fluctuation velocity oscillations are very small, revealing practically a vertical line segment at v'_{RMS}/U_{mean}=0.25 neighbourhoods.

For station x=1235 mm, the B_1 test case present values within the 0.1924<v'_{RMS}/U_{mean}<0.2621. The highest obtained value is at y=103.50. The lowest value is at

y=23.50. This interval shows an amplitude of v'_{RMS}/U_{mean}=0.0697, slightly higher than v'_{RMS}/U_{mean}=0.0575 for the same test case regarding the previous station. Transverse fluctuation velocity oscillations are very small, revealing practically a vertical line segment at v'_{RMS}/U_{mean}=0.2 neighbourhoods.

3.7.2. Unconfined A_2 and confined B_2 jets

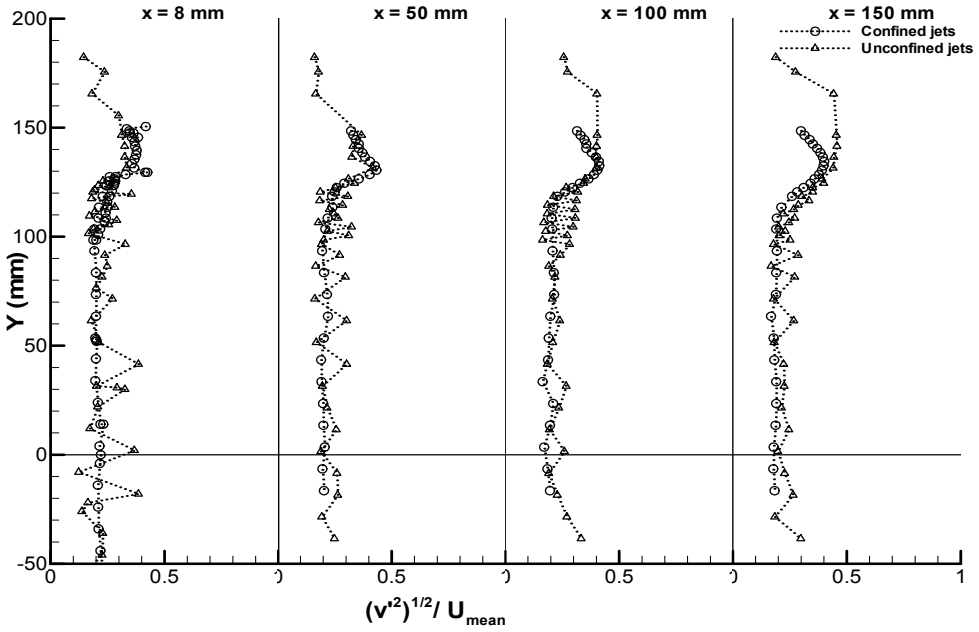

Figure 3.55. Vertical profiles of vertical velocity fluctuation for A_2 and B_2 test cases at stations x=8, 50, 100 and 150 mm.

Figure 3.55 shows vertical profiles of vertical velocity fluctuations for A_2 and B_2 test cases at stations x=8, 50, 100 and 150 mm. For station x=8 mm, the B_2 test case present values within the $0.1961<v'_{RMS}/U_{mean}<0.4247$, with amplitude of v'_{RMS}/U_{mean}=0.2286, very similar to v'_{RMS}/U_{mean}=0.2212 obtained for B_1 test case for x=8 mm. The highest obtained value is at y=129.50 mm and the lowest value is both at y=44.50 and y=63.50 mm. Despite the transverse fluctuation velocity range interval the obtained values reveals weak oscillations between neighbouring points. For y<100 mm the graphic reveals practically a vertical line segment in the v'_{RMS}/U_{mean}=0.2 neighbourhoods. The A_2 test case reveals an amplitude interval of $0.1665<v'_{RMS}/U_{mean}<0.3854$. This interval shows an amplitude of v'_{RMS}/U_{mean}=0.2189 for this test case, larger to v'_{RMS}/U_{mean}=0.1934 obtained for A_1 test case for x=8 mm. The highest obtained value is at y=41.50 mm and the lowest value is at y=101.50 mm. Transverse fluctuation velocity oscillations between neighbouring points are visible for all vertical profile.

For station x=50 mm, the B_2 test case present values within the $0.1905<v'_{RMS}/U_{mean}<0.4332$, with amplitude of v'_{RMS}/U_{mean}=0.2427 for this test case, larger to v'_{RMS}/U_{mean}=0.2212 obtained for B_1 test case for x=50 mm. The highest obtained value is at

y=130.50 mm and the lowest value is at y=43.50 mm. Despite the transverse fluctuation velocity range interval the obtained values reveals weak neighbouring points oscillations. For Y<100 mm, the graphic reveals practically a vertical line segment in the v'_{RMS}/U_{mean}=0.2 neighbourhoods. The A_2 test case reveals an amplitude interval of $0.1625<v'_{RMS}/U_{mean}<0.3371$. This interval shows an amplitude of v'_{RMS}/U_{mean}=0.1746 for this test case, larger to v'_{RMS}/U_{mean}=0.2052 obtained for A_1 test case for x=50 mm. The highest obtained value is at y=124.50 mm and the lowest value is at y=71.50 mm. Transverse fluctuation velocity oscillations between neighbouring points are visible for all vertical profile.

For station x=100 mm, the B_1 test case present values within the $0.1707<v'_{RMS}/U_{mean}<0.4120$, with amplitude of v'_{RMS}/U_{mean}=0.2413 for this test case, larger to v'_{RMS}/U_{mean}=0.1742 obtained for B_1 test case for x=100 mm. The highest obtained value is at y=132.50 mm and the lowest value is at y=3.50 mm. Despite the transverse fluctuation velocity range interval the obtained values reveals small oscillations between neighbouring points. The A_2 test case reveals an amplitude interval of $0.1692<v'_{RMS}/U_{mean}<0.4002$. This interval shows an amplitude of v'_{RMS}/U_{mean}=0.2310 for this test case, similar to v'_{RMS}/U_{mean}=0.2333 obtained for A_1 test case for x=100 mm. The highest obtained value is at y=131.50 mm and the lowest value is at y=106.50 mm. Transverse fluctuation velocity oscillations between neighbouring points are visible for all vertical profile.

For station x=150 mm, the B_2 test case present values within the $0.1679<v'_{RMS}/U_{mean}<0.4007$, amplitude of v'_{RMS}/U_{mean}=0.2328 for this test case, larger to v'_{RMS}/U_{mean}=0.1743 obtained for B_1 test case for x=150 mm. The highest obtained value is at y=134.50 mm and the lowest value is at y=63.50 mm. Despite the transverse fluctuation velocity range interval the obtained values reveals small oscillations between neighbouring points. The A_2 test case reveals an amplitude interval of $0.1679<v'_{RMS}/U_{mean}<0.4566$. This interval shows an amplitude of v'_{RMS}/U_{mean}=0.2887 for this test case, larger to v'_{RMS}/U_{mean}=0.2524 obtained for A_1 test case for x=150 mm. The highest obtained value is at y=141.50 mm and the lowest value is at y=86.50 mm. Transverse fluctuation velocity oscillations between neighbouring points are visible for all vertical profile.

By comparing the values evolution from stations x=8 mm to X=150 mm , the jets B_2 test case at all these stations reveals stabilized transverse fluctuations velocity for region below y=100 mm. For the same region, the A_2 test case reveals strong fluctuation values between neighbouring points. From x=8 mm to x=150 mm and at the 100<y<150 mm region the evolution values reveals that both test cases present smoother neighbouring points oscillations.

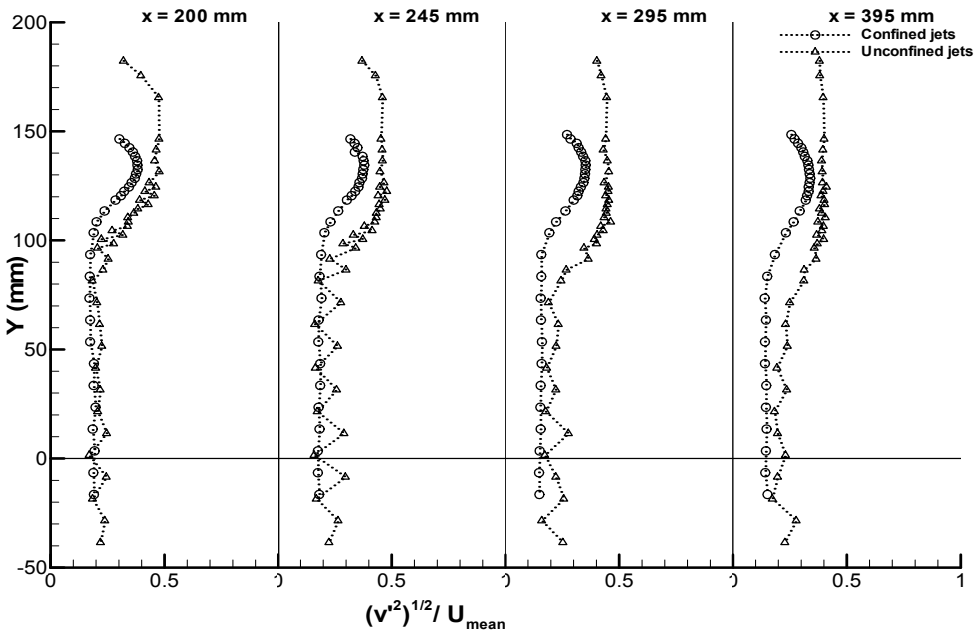

Figure 3.56. Vertical profiles of vertical velocity fluctuation for A_2 and B_2 test cases at stations x=200, 245, 295 and 395 mm.

Figure 3.56 shows vertical profiles of v'_{RMS}/U_{mean} for A_2 and B_2 test cases at stations x=200, 245, 295 and 395 mm. For station x=200 mm, the B_2 test case present values within the $0.1707<v'_{RMS}/U_{mean}<0.3824$, a $v'_{RMS}/U_{mean}=0.2117$ range interval, larger than $v'_{RMS}/U_{mean}=0.1863$ obtained for B_1 test case for x=200 mm. Despite this velocity range interval the obtained values reveals weak oscillations between neighbouring points. The highest obtained value is at y=132.50 mm and the lowest value is at y=73.50 mm. For y<100 mm, the graphic reveals practically a vertical line segment in the $v'_{RMS}/U_{mean}=0.2$ neighbourhoods. The A_2 test case reveals an amplitude interval of $0.1826<v'_{RMS}/U_{mean}<0.4754$. This interval shows an amplitude of $v'_{RMS}/U_{mean}=0.2928$ for this test case, larger to $v'_{RMS}/U_{mean}=0.2717$ obtained for A_1 test case for x=200 mm. The highest obtained value is at y=146.50 mm and the lowest value is at y=81.50 mm. The v'_{RMS}/U_{mean} stabilized for region 160>y>120 mm.

For station x=245 mm, the B_2 test case present values within the $0.1496<v'_{RMS}/U_{mean}<0.3626$, a $v'_{RMS}/U_{mean}=0.2130$ range interval, larger than $v'_{RMS}/U_{mean}=0.1814$ obtained for B_1 test case for x=245 mm. The highest obtained value is at y=132.50 mm and the lowest value is at both y=13.50 and y=3.50 mm points. Despite the transverse fluctuation velocity range interval the obtained values reveals weak oscillations between neighbouring points. For y<100 mm, the graphic reveals practically a vertical line segment in the $v'_{RMS}/U_{mean}=0.2$ neighbourhoods. The A_2 test case reveals an amplitude interval of $0.1598<v'_{RMS}/U_{mean}<0.4780$. This interval shows an amplitude of $v'_{RMS}/U_{mean}=0.3182$ for this test case, larger to $v'_{RMS}/U_{mean}=0.2451$ obtained for A_1 test case for x=245 mm. The highest obtained value is at y=122.50 mm and the lowest value is at y=1.50 mm. Transverse fluctuation velocity oscillations stabilized for region 160>y>100 mm.

For station x=295 mm, the B_2 test case present values within the $0.1510<v'_{RMS}/U_{mean}<0.3528$, with amplitude of $v'_{RMS}/U_{mean}=0.2018$ for this test case, larger than $v'_{RMS}/U_{mean}=0.1573$ obtained for B_1 test case for x=295 mm. The highest obtained value is at y=134.50 mm and the lowest value is at y=3.50 mm. Despite the transverse fluctuation velocity range interval the obtained values reveals weak oscillations between neighbouring points. For y<100 mm, the graphic reveals practically a vertical line segment in the $v'_{RMS}/U_{mean}=0.2$ neighbourhoods. The A_2 test case reveals an amplitude interval of $0.1732<v'_{RMS}/U_{mean}<0.4619$, with amplitude of $v'_{RMS}/U_{mean}=0.2887$ for this test case, larger to $v'_{RMS}/U_{mean}=0.2554$ obtained for A_1 test case for x=295 mm. The highest obtained value is at y=108.50 mm and the lowest value is at y=1.50 mm. Transverse fluctuation velocity oscillations stabilized for region 160>y>100 mm.

For station x=395 mm, the B_2 test case present values within the $0.1397<v'_{RMS}/U_{mean}<0.3401$, with a $v'_{RMS}/U_{mean}=0.2004$ range for this test case, larger than $v'_{RMS}/U_{mean}=0.1409$ obtained for B_1 test case for x=395 mm. The highest obtained value is at y=128.50 mm and the lowest value is at y=63.50 mm. Despite the transverse fluctuation velocity range interval the obtained values reveals weak oscillations between neighbouring points. For y<90 the graphic reveals practically a vertical line segment in the $v'_{RMS}/U_{mean}=0.2$ neighbourhoods. The A_2 test case reveals an amplitude interval of $0.1826<v'_{RMS}/U_{mean}<0.4109$. This interval shows an amplitude of $v'_{RMS}/U_{mean}=0.2288$ for this test case, similar to $v'_{RMS}/U_{mean}=0.2214$ obtained for A_1 test case for x=395 mm. The highest obtained value is at y=124.50 mm and the lowest value is at y=21.50 mm. Transverse fluctuation velocity oscillations stabilized for region 180>y>100 mm.

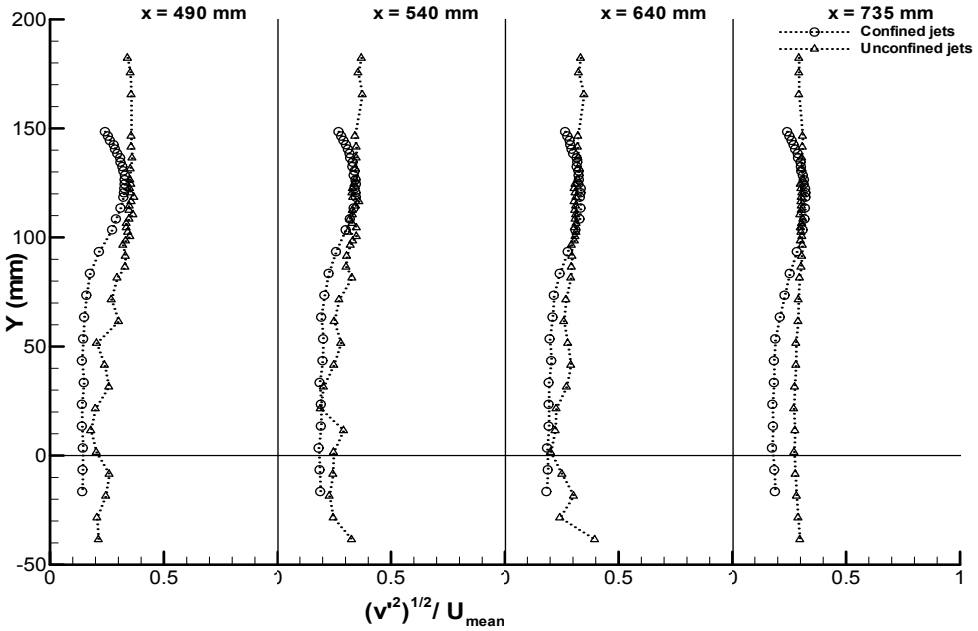

Figure 3.57. Vertical profiles of vertical velocity fluctuation for A_2 and B_2 test cases at stations x=490, 540, 640 and 735 mm.

Figure 3.57 shows vertical profiles of vertical velocity fluctuations for A_2 and B_2 test cases at stations x=490, 540, 640 and 735 mm. For station x=490 mm, the B_2 test case present values within the $0.1397<v'_{RMS}/U_{mean}<0.3288$. This interval shows an amplitude of $v'_{RMS}/U_{mean}=0.1858$ for this test case, larger to $v'_{RMS}/U_{mean}=0.1121$ obtained for B_1 test case for x=490 mm. The highest obtained value is at y=128.50 mm and the lowest value is at points y=13.50, y=23.50 and y=53.50 mm. Despite the transverse fluctuation velocity range interval the obtained values reveals weak oscillations between neighbouring points. For y<90 mm, the graphic reveals practically a vertical line segment in the $v'_{RMS}/U_{mean}=0.2$ neighbourhoods. The A_2 test case reveals an amplitude interval of $0.1786<v'_{RMS}/U_{mean}<0.3639$. This interval shows an amplitude of $v'_{RMS}/U_{mean}=0.1853$ for this test case, larger to $v'_{RMS}/U_{mean}=0.1771$ obtained for A_1 test case for x=490. The highest obtained value is at y=110.50 mm and the lowest value is at y=11.50 mm. Transverse fluctuation velocity oscillations stabilized for region 160>y>100 mm.

For station x=540 mm, the B_2 test case present values within the $0.1820<v'_{RMS}/U_{mean}<0.3457$. This interval shows an amplitude of $v'_{RMS}/U_{mean}=0.1637$ for this test case, larger to $v'_{RMS}/U_{mean}=0.0924$ obtained for B_1 test case for x=540 mm. The highest obtained value is at y=118.50 mm and the lowest value is at y=3.50 mm. Despite the transverse fluctuation velocity range interval the obtained values reveals weak oscillations between neighbouring points. For y<80 mm, the graphic reveals practically a vertical line segment in the $v'_{RMS}/U_{mean}=0.2$ neighbourhoods. The A_2 test case reveals an amplitude interval of $0.1893<v'_{RMS}/U_{mean}<0.3585$. This interval shows an amplitude of $v'_{RMS}/U_{mean}=0.1692$ for this test case, similar to $v'_{RMS}/U_{mean}=0.1639$ obtained for A_1 test case for x=540 mm. The highest obtained value is at y=116.50 mm and the lowest value is at y=21.50 mm. Transverse fluctuation velocity oscillations stabilized for region 180>y>100 mm.

For station x=640 mm, the B_2 test case present values within the $0.1863<v'_{RMS}/U_{mean}<0.3344$. This interval shows an amplitude of $v'_{RMS}/U_{mean}=0.1481$ for this test case, larger to $v'_{RMS}/U_{mean}=0.0506$ obtained for B_1 test case for x=540 mm. The highest obtained value is at y=122.50 mm and the lowest value is at y=3.50 mm. Despite the transverse fluctuation velocity range interval the obtained values reveals weak oscillations between neighbouring points. For y<70 mm the graphic reveals practically a vertical line segment in the $v'_{RMS}/U_{mean}=0.2$ neighbourhoods. The A_2 test case reveals an amplitude interval of $0.2014<v'_{RMS}/U_{mean}<0.3223$. This interval shows an amplitude of $v'_{RMS}/U_{mean}=0.1209$ for this test case, similar to $v'_{RMS}/U_{mean}=0.1269$ obtained for A_1 test case for x=640 mm. The highest obtained value is at y=136.50 mm and the lowest value is at y=1.50 mm. Transverse fluctuation velocity oscillations are weak at all vertical profile.

For station x=735 mm, the B_2 test case present values within the $0.1750<v'_{RMS}/U_{mean}<0.3217$. This interval shows an amplitude of $v'_{RMS}/U_{mean}=0.1467$ for this test case, larger to $v'_{RMS}/U_{mean}=0.0697$ obtained for B_1 test case for x=735 mm. The highest obtained value is both at y=120.50 and y=118.50 mm points. The lowest value is at y=3.50

mm. Despite the transverse fluctuation velocity range interval the obtained values reveals very weak oscillations between neighbouring points. The A_2 test case reveals an amplitude interval of $0.2699<v'_{RMS}/U_{mean}<0.3115$. This interval shows an amplitude of $v'_{RMS}/U_{mean}=0.0416$ for this test case, larger to $v'_{RMS}/U_{mean}=0.0709$ obtained for A_1 test case for x=735 mm. The highest obtained value is at y=126.50 mm and the lowest value is at y=21.50 mm. Transverse fluctuation velocity oscillations reveals practically a vertical line segment at the $v'_{RMS}/U_{mean}=0.3$ neighbourhoods.

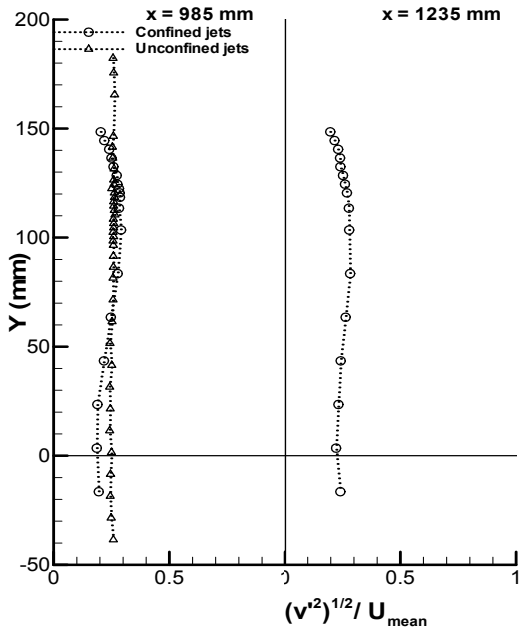

Figure 3.58. Vertical profiles of vertical velocity fluctuation for A_2 and B_2 test cases at stations x=985 and 1235 mm.

Figure 3.58 shows vertical profiles of vertical velocity fluctuations for A_2 and B_2 test cases at stations x=985 and 1235 mm. For station x=985 mm, the B_2 test case present values within the $0.1891<v'_{RMS}/U_{mean}<0.2907$. This interval shows an amplitude of $v'_{RMS}/U_{mean}=0.1016$ for this test case, larger to $v'_{RMS}/U_{mean}=0.0575$ obtained for B_1 test case for x=985 mm. The highest obtained value is at y=103.50 mm and the lowest value is at y=23.50 mm. Transverse fluctuation velocity oscillations reveals practically a vertical line segment at the $v'_{RMS}/U_{mean}=0.25$ neighbourhoods. The A_2 test case reveals an amplitude interval of $0.2417<v'_{RMS}/U_{mean}<0.2645$. This interval shows an amplitude of $v'_{RMS}/U_{mean}=0.0228$ for this test case, similar to $v'_{RMS}/U_{mean}=0.0280$ obtained for A_1 test case for x=985 mm. The highest obtained value is at y=110.50 mm and the lowest value is both at y=11.50 and y=31.50 mm points. Transverse fluctuation velocity oscillations reveals practically a vertical line segment at the $v'_{RMS}/U_{mean}=0.25$ neighbourhoods.

For station x=1235 mm, the B_2 test case present values within the $0.1975<v'_{RMS}/U_{mean}<0.2836$. This interval shows an amplitude of $v'_{RMS}/U_{mean}=0.0861$ for this test case, larger to $v'_{RMS}/U_{mean}=0.0697$ obtained for B_1 test case for x=1235 mm. The highest

obtained value is at y=83.50 mm and the lowest value is at y=148.50 mm. Despite the transverse fluctuation velocity range interval the obtained values reveals very weak oscillations between neighbouring points. Transverse fluctuation velocity oscillations reveals practically a vertical line segment at the v'_{RMS}/U_{mean}=0.25 neighbourhoods.

3.7.3. Convergent 11° C_1 and convergent 22° D_1 jets

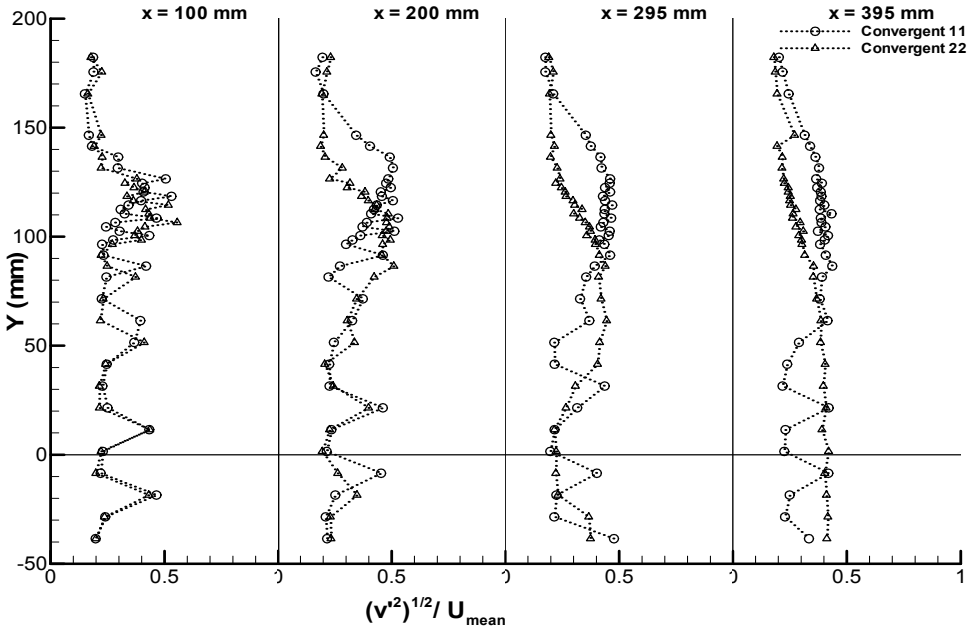

Figure 3.59. Vertical profiles of vertical velocity fluctuation for C_1 and D_1 test cases at stations x=100, 200, 295 and 395 mm.

Figure 3.59 shows vertical profiles of vertical velocity fluctuations for C_1 and D_1 test cases at stations station x=100, 200, 295 and 395 mm. At station x=100 mm, for both test cases C_1 and D_1 all values present a constant oscillation between neighbouring points. For this station, both test cases present similar oscillations range of transverse fluctuation velocity. The C_1 test case present values within the $0.1680<v'_{RMS}/U_{mean}<0.4647$. The highest obtained value is at y=108.50 and the lowest value is at y=146.50. This interval shows an amplitude of v'_{RMS}/U_{mean}=0.2967 for this test case. Transverse fluctuation velocity oscillations are visible for all vertical profile. The D_1 test case reveals an amplitude interval of $0.1908<v'_{RMS}/U_{mean}<0.4355$. This interval shows an amplitude of v'_{RMS}/U_{mean}=0.2447 for this test case. The highest obtained value is at y=11.50 and the lowest value is at y=141.50. Transverse fluctuation velocity oscillations are visible for all vertical profile.

For station x=200 mm, for both test cases C_1 and D_1, all values present a constant oscillation between neighbouring points. The C_1 test case present values within the $0.2229<v'_{RMS}/U_{mean}<0.4961$. This interval shows an amplitude of v'_{RMS}/U_{mean}=0.2732 for this test case, less than v'_{RMS}/U_{mean}=0.2967 obtained for C_1 test case at the previous station. Transverse fluctuation velocity oscillations are visible for all vertical profile. The highest

obtained value is at y=122.50 mm and the lowest value is at y=81.50 mm. The D_1 test case reveals an amplitude interval of $0.1878<v'_{RMS}/U_{mean}<0.4940$. This interval shows an amplitude of $v'_{RMS}/U_{mean}=0.3062$ for this test case, greater than $v'_{RMS}/U_{mean}=0.2447$ obtained for D_1 test case at the previous station. The highest obtained value is at y=141.50 mm and the lowest value is at y=98.50 mm. Transverse fluctuation velocity oscillations are visible for all vertical profile.

For station x=295 mm, for both test cases C_1 and D_1 all values present a constant oscillation between neighbouring points. The C_1 test case present values within the $0.2151<v'_{RMS}/U_{mean}<0.4694$. This interval shows an amplitude of $v'_{RMS}/U_{mean}=0.2543$ for this test case, less than $v'_{RMS}/U_{mean}=0.2732$ obtained for C_1 test case at the previous station. Transverse fluctuation velocity oscillations are visible for all vertical profile. The highest obtained value is at y=114.50 mm and the lowest value is at y=51.50 mm. The D_1 test case reveals an amplitude interval of $0.2001<v'_{RMS}/U_{mean}<0.4448$. This interval shows an amplitude of $v'_{RMS}/U_{mean}=0.2447$ for this test case, greater than $v'_{RMS}/U_{mean}=0.3062$ obtained for D_1 test case at the previous station. The highest obtained value is at y=61.50 mm and the lowest value is at y=146.50 mm. Transverse fluctuation velocity oscillations are visible for all vertical profile.

For station x=395 mm, the C_1 test case present values within the $0.2088<v'_{RMS}/U_{mean}<0.4364$. This interval shows an amplitude of $v'_{RMS}/U_{mean}=0.2276$ for this test case, less than $v'_{RMS}/U_{mean}=0.2543$ obtained for C_1 test case at the previous station. Transverse fluctuation velocity oscillations are more visible at symmetry axis plane, with the north values from 150>y>100 mm tending to stabilization values. The highest obtained value is at y=86.50 mm and the lowest value is at y=102.50 mm. The D_1 test case reveals an amplitude interval of $0.2153<v'_{RMS}/U_{mean}<0.4202$. This interval shows an amplitude of $v'_{RMS}/U_{mean}=0.2049$ for this test case, greater than $v'_{RMS}/U_{mean}=0.2447$ obtained for D_1 test case at the previous station. The highest obtained value is at y=1.50 mm and the lowest value is at y=131.50 mm. The y<70 mm region reveals that the transverse fluctuation velocity are stabilized. The neighbouring points oscillations disappeared.

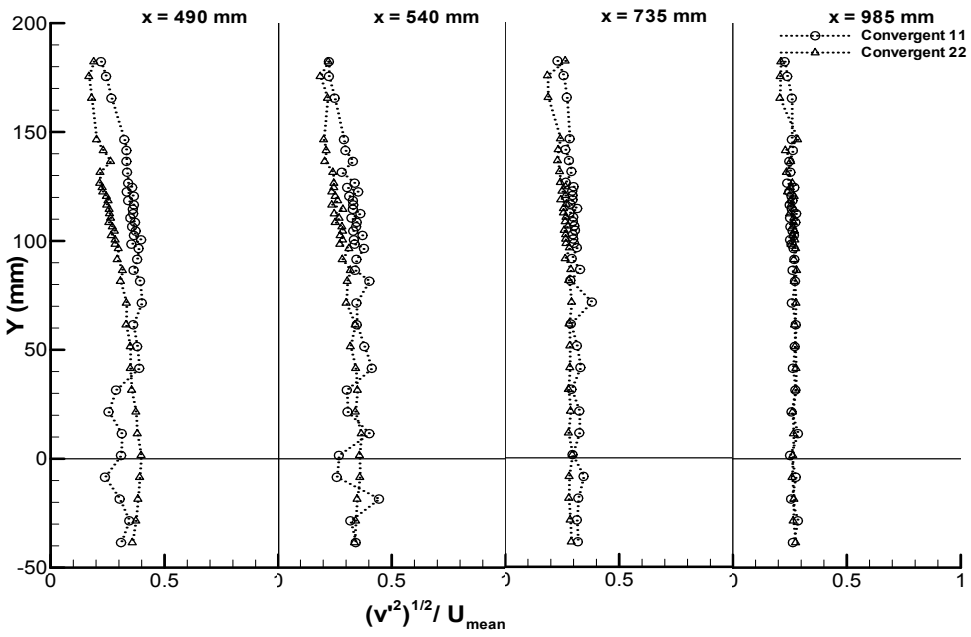

Figure 3.60. Vertical profiles of vertical velocity fluctuation for C_1 and D_1 test cases at stations x=490, 540, 735 and 985 mm.

Figure 3.60 shows vertical profiles of vertical velocity fluctuations for C_1 and D_1 test cases at stations x=490, 540, 735 and 985 mm. For station x=490 mm, the C_1 test case present values within the $0.2543<v'_{RMS}/U_{mean}<0.4003$, with $v'_{RMS}/U_{mean}=0.1460$ for this test case, less than $v'_{RMS}/U_{mean}=0.2276$ obtained for C_1 test case at the previous station. The 180>y>90 mm region is practically an inclined line segment with very low transverse fluctuation velocity oscillations. At the other axis plane region, points are experiencing small oscillations. The highest obtained value is at y=171.50 mm and the lowest value is at y=21.50 mm. The D_1 test case reveals an amplitude interval of $0.2016<v'_{RMS}/U_{mean}<0.3971$. This interval shows an amplitude of $v'_{RMS}/U_{mean}=0.1955$ for this test case, greater than $v'_{RMS}/U_{mean}=0.2049$ obtained for D_1 test case at the previous station. The highest obtained value is at y=1.50 mm and the lowest value is at y=146.50 mm. The 130>y>0 mm region is practically an inclined line segment with very low transverse fluctuation velocity oscillations. At the other axis plane region, points are experiencing small oscillations.

For station x=540 mm, the C_1 test case present values within the $0.2684<v'_{RMS}/U_{mean}<0.4129$. This interval shows an amplitude of $v'_{RMS}/U_{mean}=0.1445$ for this test case, similar than $v'_{RMS}/U_{mean}=0.1460$ obtained for C_1 test case at the previous station. The C_1 test case is experiencing very low transverse fluctuation velocity oscillations verified at the entire profile. The highest obtained value is at y=41.50 mm and the lowest value is at y=1.50 mm. The D_1 test case reveals an amplitude interval of $0.2016<v'_{RMS}/U_{mean}<0.3663$. This interval shows an amplitude of $v'_{RMS}/U_{mean}=0.1647$ for this test case, greater than $v'_{RMS}/U_{mean}=0.1955$ obtained for D_1 test case at the previous station. The highest obtained value is at y=11.50 mm and the lowest value is at y=146.50 mm. The D_1 test case is also

experiencing very low transverse fluctuation velocity oscillations verified at the entire profile.

For station x=735 mm, the C_1 test case present values within the $0.2826<v'_{RMS}/U_{mean}<0.3799$, with $v'_{RMS}/U_{mean}=0.0973$ for this test case, less than $v'_{RMS}/U_{mean}=0.1445$ obtained for C_1 test case at the previous station. The C_1 test case is experiencing very low transverse fluctuation velocity oscillations verified at the entire profile. The highest obtained value is at y=71.50 mm and the lowest value is at y=112.50 mm. The D_1 test case reveals an amplitude interval of $0.2293<v'_{RMS}/U_{mean}<0.2909$. This interval shows an amplitude of $v'_{RMS}/U_{mean}=0.0616$ for this test case, less than $v'_{RMS}/U_{mean}=0.1647$ obtained for D_1 test case at the previous station. The highest obtained value is at y=71.50 mm and the lowest value is at y=136.50 mm. The D_1 test case is also experiencing very low transverse fluctuation velocity oscillations verified at the entire profile.

For station x=985 mm, the C_1 test case present values within the $0.2204<v'_{RMS}/U_{mean}<0.2518$. This interval shows an amplitude of $v'_{RMS}/U_{mean}=0.0314$ for this test case, less than $v'_{RMS}/U_{mean}=0.0973$ obtained for C_1 test case at the previous station. The highest obtained value is at y=124.50 mm and the lowest value is at y=1.50 mm. The D_1 test case reveals an amplitude interval of $0.2355<v'_{RMS}/U_{mean}<0.2801$. This interval shows an amplitude of $v'_{RMS}/U_{mean}=0.0446$ for this test case, less than $v'_{RMS}/U_{mean}=0.0616$ obtained for D_1 test case at the previous station. The highest obtained value is at y=86.50 mm and the lowest value is at y=131.50 mm. Both test cases present an identical profile, with all values revealing a vertical line segment in the $v'_{RMS}/U_{mean}=0.25$ neighbourhoods.

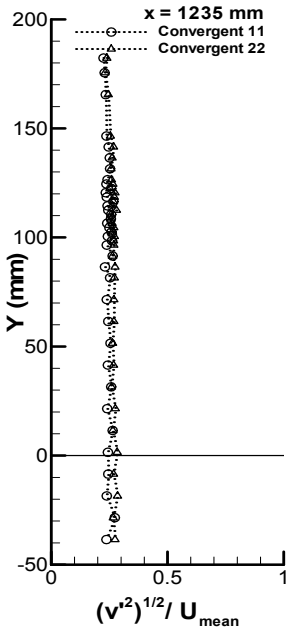

Figure 3.61. Vertical profiles of vertical velocity fluctuation for C_1 and D_1 test cases at station x=1235 mm.

Figure 3.61 shows vertical profiles of vertical velocity fluctuations for C_1 and D_1 test cases at station x=1235 mm. For station x=1235 mm, the C_1 test case present values within the $0.2245<v'_{RMS}/U_{mean}<0.2504$. This interval shows an amplitude of $v'_{RMS}/U_{mean}=0.0259$ for this test case, less than $v'_{RMS}/U_{mean}=0.0314$ obtained for C_1 test case at the previous station. The highest obtained value is at y=136.50 mm and the lowest value is at y=86.50 mm. The D_1 test case reveals an amplitude interval of $0.2539<v'_{RMS}/U_{mean}<0.2832$. This interval shows an amplitude of $v'_{RMS}/U_{mean}=0.0293$ for this test case, less than $v'_{RMS}/U_{mean}=0.0446$ obtained for D_1 test case at the previous station. The highest obtained value is at y=1.50 mm and the lowest value is at y=146.50 mm. Both test cases present an identical profile, with all values revealing a vertical line segment in the $v'_{RMS}/U_{mean}=0.25$ neighbourhoods.

3.7.4. Convergent 11° C_2 and convergent 22° D_2 jets

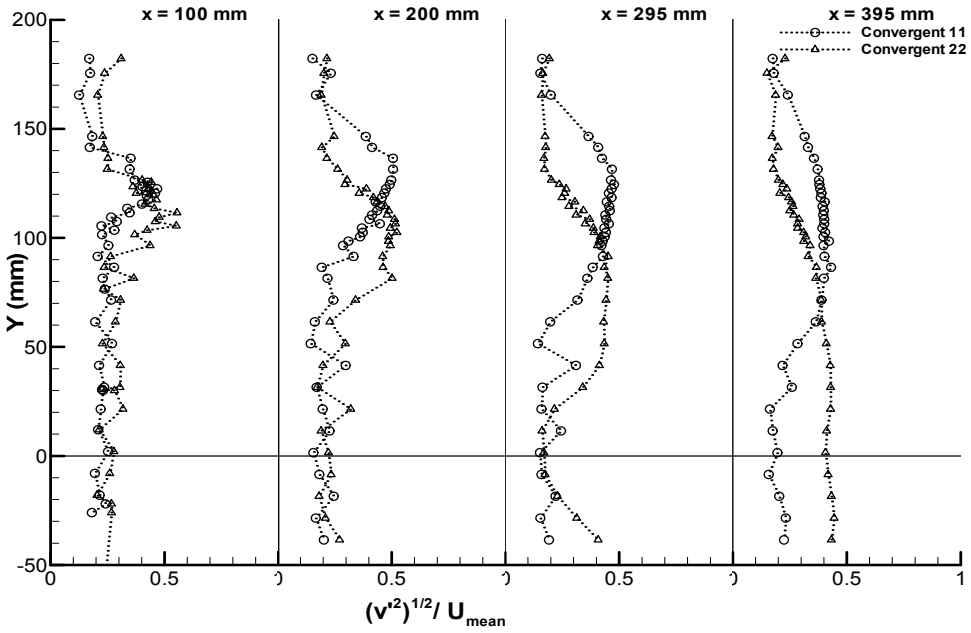

Figure 3.62. Vertical profiles of vertical velocity fluctuation for C_2 and D_2 test cases at stations x=100, 200, 295 and 395 mm.

Figure 3.62 shows vertical profiles of vertical velocity fluctuations for C_2 and D_2 test cases at stations x=100, 200, 295 and 395 mm. For station x=100 mm, for both test cases C_2 and D_2, all values present a constant oscillation between neighbouring points. For this station, both test cases present similar oscillations of transverse fluctuation velocity. The C_2 test case present values within the $0.1248<v'_{RMS}/U_{mean}<0.4678$. This interval shows an amplitude of $v'_{RMS}/U_{mean}=0.3430$ for this test case, larger than $v'_{RMS}/U_{mean}=0.2967$ obtained for 11° convergent C_1 test case for station x=100 mm. The highest obtained value is at y=122.50 mm and the lowest value is at y=165.50 mm. Transverse fluctuation velocity oscillations are visible for all vertical profile. Higher values are at y=120 mm neighbourhoods. The D_2 test

case reveals an amplitude interval of $0.2131<v'_{RMS}/U_{mean}<0.4645$. This interval shows an amplitude of $v'_{RMS}/U_{mean}=0.2514$ for this test case, slightly larger than $v'_{RMS}/U_{mean}=0.2447$ obtained for 11° convergent D_1 test case for station x=100 mm. The highest obtained value is at y=117.50 mm and the lowest value is at y=12.00 mm. Transverse fluctuation velocity oscillations are visible for all vertical profile. Higher values are at y=110 mm neighbourhoods.

For station x=200 mm, for both test cases C_2 and D_2 all values present a constant oscillation between neighbouring points. The C_2 test case present values within the $0.1444<v'_{RMS}/U_{mean}<0.5059$. This interval shows an amplitude of $v'_{RMS}/U_{mean}=0.3615$ for this test case, larger than $v'_{RMS}/U_{mean}=0.2732$ obtained for 11° convergent C_1 test case for station x=200 mm. The highest obtained value is at both y=131.50 mm and y=136.50 mm points. The lowest value is at y=71.50 mm. Higher values are at y=130 mm neighbourhoods. Transverse fluctuation velocity oscillations are visible for all vertical profile. The D_2 test case reveals an amplitude interval of $0.1720<v'_{RMS}/U_{mean}<0.5227$. This interval shows an amplitude of $v'_{RMS}/U_{mean}=0.3507$ for this test case, larger than $v'_{RMS}/U_{mean}=0.3062$ obtained for 11° convergent D_1 test case for station x=200 mm. The highest obtained value is at y=102.50 mm and the lowest value is at y=31.50 mm. Transverse fluctuation velocity oscillations are visible for all vertical profile. Higher values are at y=110 mm neighbourhoods.

For station x=295 the C_2 test case present values within the $0.1432<v'_{RMS}/U_{mean}<0.4770$, with $v'_{RMS}/U_{mean}=0.3338$ for this test case, larger than $v'_{RMS}/U_{mean}=0.2543$ obtained for C_1 test case for station x=295. The highest obtained value is at y=124.50 and the lowest value is at y=51.50. Higher values are at $40<y<90$ region. The D_2 test case reveals an amplitude interval of $0.1614<v'_{RMS}/U_{mean}<0.4513$. This interval shows an amplitude of $v'_{RMS}/U_{mean}=0.2899$ for this test case, larger than $v'_{RMS}/U_{mean}=0.2447$ obtained for D_1 test case for station x=295 mm. The highest obtained value is at y=91.50 mm and the lowest value is at y=11.50 mm. Higher values are at $100<y<130$ mm region.

For station x=395 mm, the C_2 test case present values within the $0.1630<v'_{RMS}/U_{mean}<0.4310$. This interval shows an amplitude of $v'_{RMS}/U_{mean}=0.2680$ for this test case, larger than $v'_{RMS}/U_{mean}=0.2276$ obtained for 11° convergent C_1 test case for station x=395 mm. The highest obtained value is at y=86.50 mm and the lowest value is at y=21.50 mm. Higher values are at y=70 mm neighbourhoods. The D_2 test case reveals an amplitude interval of $0.1734<v'_{RMS}/U_{mean}<0.4255$. This interval shows an amplitude of $v'_{RMS}/U_{mean}=0.2521$ for this test case, larger than $v'_{RMS}/U_{mean}=0.2049$ obtained for D_1 test case for station x=395 mm. The highest obtained value is at y=31.50 mm and the lowest value is at y=156.50 mm. Higher values are at $0<y<70$ mm region.

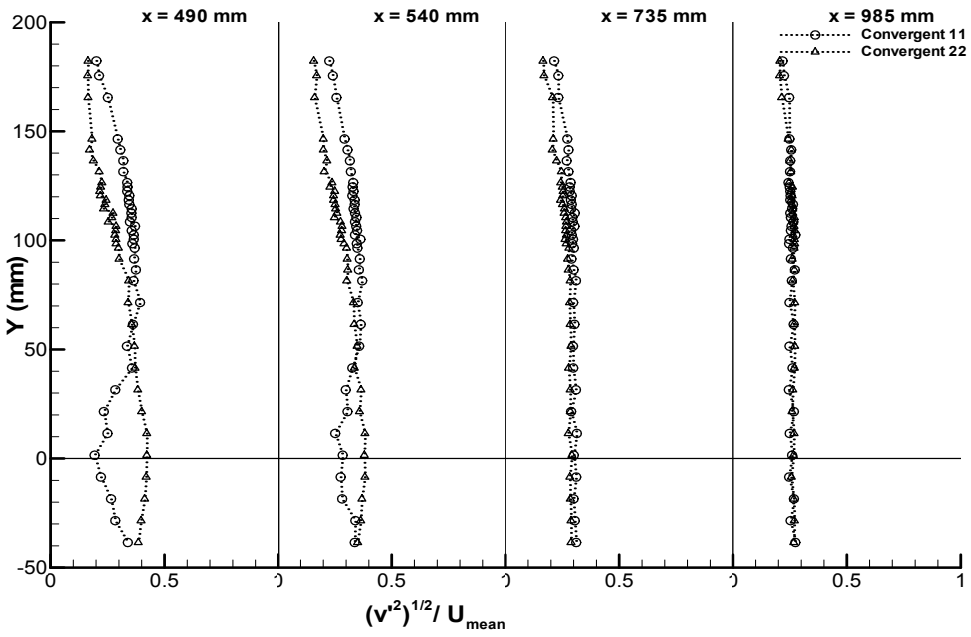

Figure 3.63. Vertical profiles of vertical velocity fluctuation for C_2 and D_2 test cases at stations x=490, 540, 735 and 985 mm.

Figure 3.63 shows vertical profiles of vertical velocity fluctuations for C_2 and D_2 test cases at stations x=490, 540, 735 and 985 mm. For station x=490 mm, the C_2 test case present values within the $0.1932<v'_{RMS}/U_{mean}<0.3929$. This interval shows an amplitude of $v'_{RMS}/U_{mean}=0.1997$ for this test case, larger than $v'_{RMS}/U_{mean}=0.1460$ obtained for C_1 test case for station x=490 mm. The highest obtained value is at y=71.50 mm and the lowest value is at y=1.50 mm. Higher values are at y=70 mm. From y=70 mm up to north, the obtained values reveals an inclined line segment. Lower values are at 0<y<50 mm region. The D_2 test case reveals an amplitude interval of $0.1641<v'_{RMS}/U_{mean}<0.4221$. This interval shows an amplitude of $v'_{RMS}/U_{mean}=0.2580$ for this test case, larger than $v'_{RMS}/U_{mean}=0.1955$ obtained for D_1 test case for station x=490 mm. The highest obtained value is both at y=1.50 mm and y=11.50 mm. The lowest value is at y=165.50 mm. The obtained values practically reveal an inclined line segment for the entire profile.

For station x=540 mm, the C_2 test case present values within the $0.2523<v'_{RMS}/U_{mean}<0.3706$. This interval shows an amplitude of $v'_{RMS}/U_{mean}=0.1183$ for this test case, larger than $v'_{RMS}/U_{mean}=0.1455$ obtained for C_1 test case for station x=540 mm. The highest obtained value is at y=11.50 mm and the lowest value is at y=165.50 mm. Higher values are at y=70 mm. From y=70 mm up to north, the obtained values reveals an inclined line segment. Lower values are at 0<y<50 mm region. The D_2 test case reveals an amplitude interval of $0.1614<v'_{RMS}/U_{mean}<0.3824$. This interval shows an amplitude of $v'_{RMS}/U_{mean}=0.2210$ for this test case, larger than $v'_{RMS}/U_{mean}=0.1647$ obtained for D_1 test case for station x=540 mm. The highest obtained value is at y=11.50 mm and the lowest value is at y=165.50 mm. The obtained values practically reveal an inclined line segment for the entire profile.

For station x=735 mm, the C_2 test case present values within the $0.2326<v'_{RMS}/U_{mean}<0.3141$. This interval shows an amplitude of $v'_{RMS}/U_{mean}=0.0815$ for this test case, larger than $v'_{RMS}/U_{mean}=0.0973$ obtained for C_1 test case for station x=735 mm. The highest obtained value is at y=11.50 mm and the lowest value is at y=165.50 mm. The D_2 test case reveals an amplitude interval of $0.2078<v'_{RMS}/U_{mean}<0.2975$. This interval shows an amplitude of $v'_{RMS}/U_{mean}=0.0.0847$ for this test case, larger than $v'_{RMS}/U_{mean}=0.0616$ obtained for D_1 test case for station x=735 mm. The highest obtained value is at y=1.50 mm and the lowest value is at y=165.50 mm. From $0<y<100$ mm the graphic reveals vertical line segments for both cases and with values approaching $v'_{RMS}/U_{mean}=0.3$. From $100<y<150$ mm, both test cases present slightly lower values.

For station x=985 mm, the C_2 test case present values within the $0.2444<v'_{RMS}/U_{mean}<0.2747$. This interval shows an amplitude of $v'_{RMS}/U_{mean}=0.0303$ for this test case, identical than $v'_{RMS}/U_{mean}=0.0314$ obtained for C_1 test case for station x=985 mm. The highest obtained value is at y=102.50 mm and the lowest value is at y=131.50 mm. The D_2 test case reveals an amplitude interval of $0.2144<v'_{RMS}/U_{mean}<0.2726$. This interval shows an amplitude of $v'_{RMS}/U_{mean}=0.0.0582$ for this test case, slightly larger than $v'_{RMS}/U_{mean}=0.0446$ obtained for D_1 test case for station x=985 mm. The highest obtained value is at y=104.50 mm and the lowest value is at y=165.50 mm. The graphic practically reveals a single profile. All values are identical for both test cases. The result is a vertical straight line with values at $v'_{RMS}/U_{mean}=0.27$ neighbourhoods.

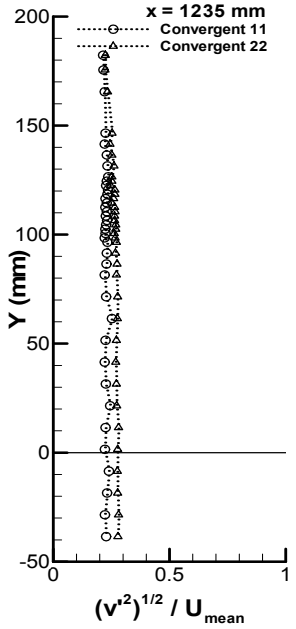

Figure 3.64. Vertical profiles of vertical velocity fluctuation for C_2 and D_2 test cases at station x=1235 mm.

Figure 3.64 shows vertical profiles of vertical velocity fluctuations for C_2 and D_2 test cases at station x=1235 mm. For station x=1235 mm, the C_2 test case present values within

the 0.2208<v'_{RMS}/U_{mean}<0.2523. This interval shows an amplitude of v'_{RMS}/U_{mean}=0.0315 for this test case, slightly larger than v'_{RMS}/U_{mean}=0.0259 obtained for C_1 test case for station x=1235 mm. The highest obtained value is at y=136.50 mm and the lowest value is at y=86.50 mm. The D_2 test case reveals an amplitude interval of 0.2329<v'_{RMS}/U_{mean}<0.2805. This interval shows an amplitude of v'_{RMS}/U_{mean}=0.0476 for this test case, slightly larger than v'_{RMS}/U_{mean}=0.0293 obtained for D_1 test case for station x=1235 mm. The highest obtained value is at y=11.50 mm and the lowest value is at y=165.50 mm. For the C_1 test case the graphic reveals a practically vertical line segment with values at v'_{RMS}/U_{mean}=0.23 neighbourhoods, while for the C_2 test case the graphic reveals a practically vertical line segment with values at v'_{RMS}/U_{mean}=0.26 neighbourhoods.

3.8. Vertical profiles of shear stress

This subchapter presents all obtained results for the vertical profiles of shear stress $\overline{u'v'}$, (dimensionless form by U_{mean}) distribution at the horizontal axis in each studied station, from y=200 mm to y=-50 mm. The vertical profiles of shear stress $\overline{u'v'}$ distribution values are presented from -0.2≤ $\overline{u'v'}/U_{mean}$≤+0.2. The confined jets values starts at y=148.50 mm, due to its wall confinement. The unconfined jets values starts at y=182.25 mm.

3.8.1. Unconfined A_1 and confined B_1 jets

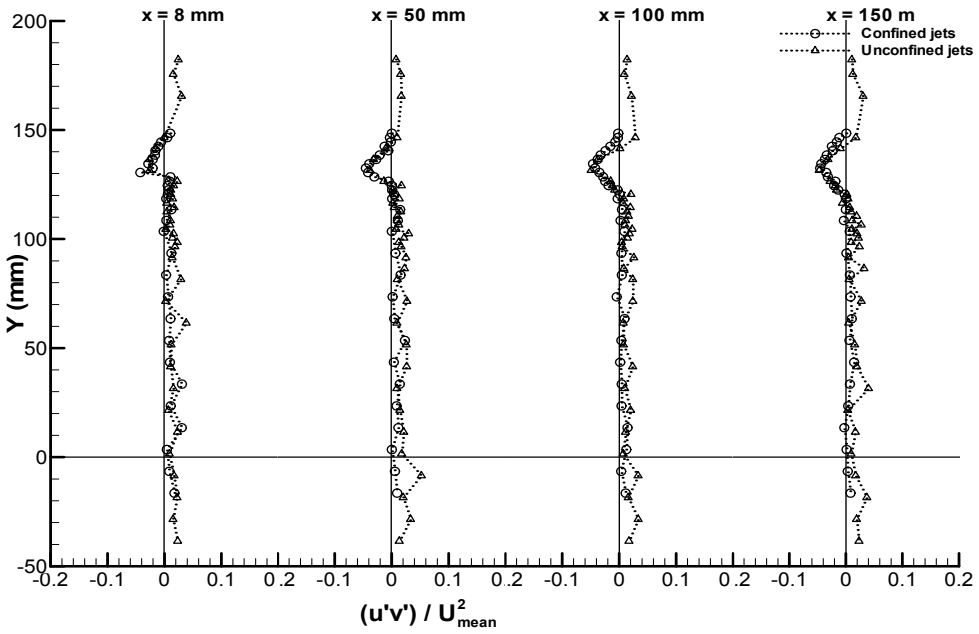

Figure 3.65. Vertical profiles of shear stress for A_1 and B_1 test cases at stations x=8, 50, 100 and 150 mm.

Figure 3.65 shows vertical profiles of shear stress for A_1 and B_1 test cases at stations x=8, 50, 100 and 150 mm, and reveals that all profiles present practically identical values for

both test cases along the first four stations. For station x=8 mm, the B_1 test case present values oscillating within the -0.04242<$\overline{u'v'}$<+0.03060 interval with amplitude range of $\overline{u'v'}$=0.07302. The highest peak obtained value is at y=33.50 mm and the lowest is at y=130.50 mm. The A_1 test case reveals an amplitude interval of -0.02648<$\overline{u'v'}$<+0.03824 with amplitude range of of $\overline{u'v'}$=0.06464, very similar to the B_1 test case interval for this station. The highest peak obtained value is at y=61.50 mm and the lowest value is at y=136.50 mm.

For station x=50 mm, the B_1 test case present values within -0.04524<$\overline{u'v'}$<+0.02321 interval with amplitude of $\overline{u'v'}$=0.06845, lower than $\overline{u'v'}$=0.07302 obtained at previous station. The highest peak obtained value is at y=53.50 mm and the lowest is at y=130.50 mm. The A_1 test case reveals an amplitude interval of -0.03805<$\overline{u'v'}$<+0.02665 with amplitude of $\overline{u'v'}$=0.06470, very slightly higher than the previous station interval. The highest peak obtained value is at y=74.50 mm and the lowest value is at y=131.50 mm.

For station x=100 mm, the B_1 test case present values within -0.04600<$\overline{u'v'}$<+0.01455 interval with amplitude of $\overline{u'v'}$=0.06055, lower than both obtained at previous stations. The highest peak obtained value is at y=13.50 mm and the lowest is at y=134.50 mm. The A_1 test case reveals an amplitude interval of -0.04927<$\overline{u'v'}$<+0.02377. This interval shows amplitude of $\overline{u'v'}$=0.07304 for this test case, higher than observed at both previous stations. The highest peak obtained value is at y=71.50 mm and the lowest value is at y=136.50 mm.

For station x=150 the mm, B_1 test case present values within -0.04533<$\overline{u'v'}$<+0.01455 interval with amplitude of $\overline{u'v'}$=0.05988, lower than obtained at all previous stations. The highest peak obtained value is at y=43.50 mm and the lowest is at y=132.50 mm. The A_1 test case reveals an amplitude interval of -0.04707<$\overline{u'v'}$<+0.04001. This interval shows amplitude of $\overline{u'v'}$=0.08708 for this test case, higher than observed at all previous stations. The highest peak obtained value is at y=31.50 mm and the lowest value is at y=131.50 mm.

Regarding the shear stress results evolution from stations x=8 mm up to x=150 mm for both test cases, the negative values region are present at the U_o/U_i jets division and its curve slope is becoming softer according to the jets exit distance increasing.

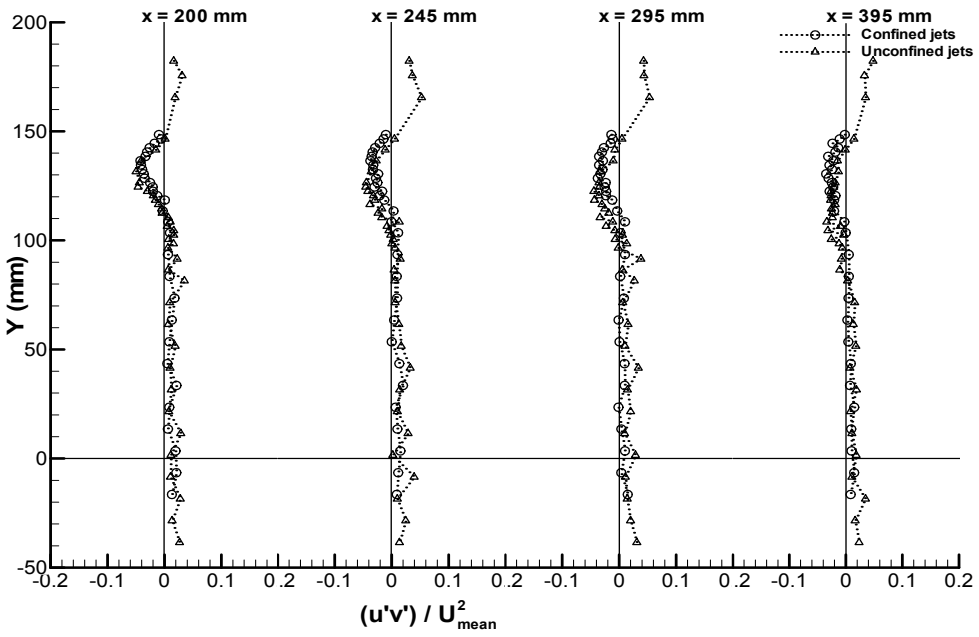

Figure 3.66. Vertical profiles of shear stress for A_1 and B_1 test cases at stations x=200, 245, 295 and 395 mm.

Figure 3.66 shows vertical profiles of shear stress for A_1 and B_1 test cases at stations x=200, 245, 295 and 395 mm and reveals that all profiles present practically identical values for both test cases along the first four stations. Exterior points are experiencing highest shear stress values. For station x=200 mm, the B_1 test case present values within -0.03728<$\overline{u'v'}$<+0.01979 interval with amplitude of $\overline{u'v'}$=0.05707, lower than obtained at all previous stations. The highest peak obtained value is at y=33.50 mm and the lowest is at y=136.50 mm. The A_1 test case reveals an amplitude interval of -0.05003<$\overline{u'v'}$<+0.02853 with amplitude of $\overline{u'v'}$=0.07856, lower than observed at previous station. The highest peak obtained value is at y=11.50 mm and the lowest value is at y=124.50 mm.

For station x=245 mm, the B_1 test case present values within -0.03728<$\overline{u'v'}$<+0.01972 interval with amplitude of $\overline{u'v'}$=0.05700, lower than obtained at all previous stations. The highest peak obtained value is at y=33.50 mm and the lowest is at y=136.50 mm. The A_1 test case reveals an amplitude interval of -0.04544<$\overline{u'v'}$<+0.03256 with amplitude of $\overline{u'v'}$=0.07800, slightly higher than observed at previous station. The highest peak obtained value is at y=41.50 mm and the lowest value is at y=124.50 mm.

For station x=295 mm, the B_1 test case present values within -0.03762<$\overline{u'v'}$<+0.01015 interval with amplitude of $\overline{u'v'}$=0.04777, lower than obtained at all previous stations since x=8 mm. The highest peak obtained value is at y=108.50 mm and the lowest is at y=128.50 mm. The A_1 test case reveals an amplitude interval of -0.04443<$\overline{u'v'}$<+0.03354 with amplitude of $\overline{u'v'}$=0.07797, identical than observed at previous station. The highest peak obtained value is at y=41.50 mm and the lowest value is at y=122.50 mm.

For station x=395 mm, the B_1 test case present values within -0.03484<$\overline{u'v'}$<+0.01487 interval with amplitude of $\overline{u'v'}$=0.04971, the first time increasing of amplitude verified since x=8 mm. The highest peak obtained value is at y=23.50 mm and the lowest is at y=130.50 mm. The A_1 test case reveals an amplitude interval of -0.03378<$\overline{u'v'}$<+0.01870 with amplitude of $\overline{u'v'}$=0.05248 for this test case, lower than $\overline{u'v'}$=0.07797 observed at previous station. The highest peak obtained value is at y=31.50 mm and the lowest value is at y=108.50 mm.

Regarding the shear stress results evolution from stations x=200 mm to x=395 mm for both test cases the negative peaks are becoming softer according to the jets exit distance increasing, and from x=245 mm to x=395 mm there is no observed peak but instead a region with very similar values.

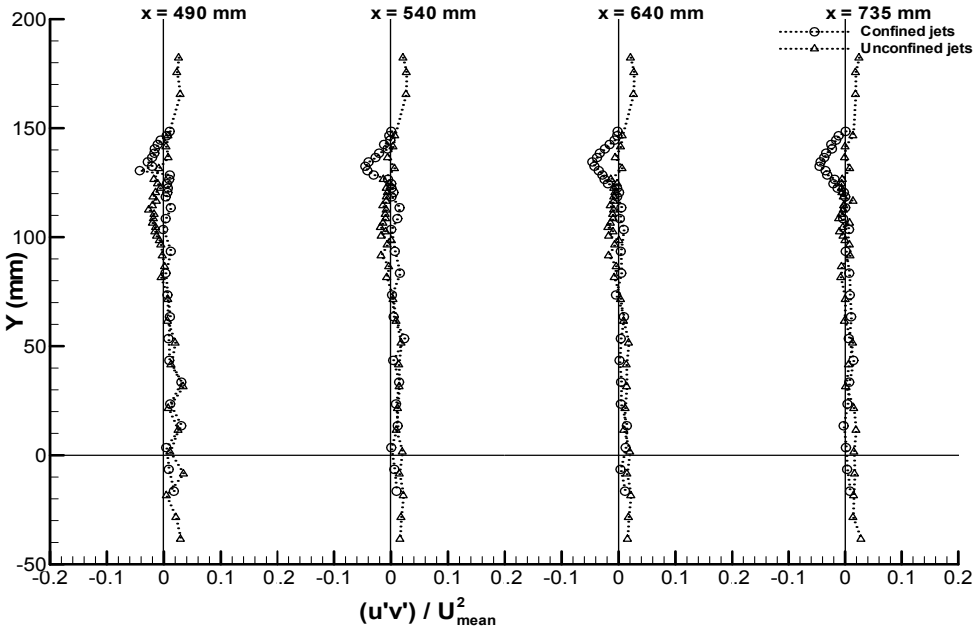

Figure 3.67. Vertical profiles of shear stress for A_1 and B_1 test cases at stations x=490, 540, 640 and 735 mm.

Figure 3.67 shows vertical profiles of shear stress for A_1 and B_1 test cases at stations x=490, 540, 640 and 735 mm and reveals that all profiles present slightly different values for both test cases along the first four stations. Exterior points are experiencing highest shear

For station x=490 mm, the B_1 test case present values within -0.03358<$\overline{u'v'}$<+0.01607 interval with amplitude of $\overline{u'v'}$=0.04604, the lower amplitude obtained so far since x=8 mm. The highest peak obtained value is at y=63.50 mm and the lowest is at y=124.50 mm. The A_1 test case reveals an amplitude interval within -0.02672<$\overline{u'v'}$<+0.03367 with amplitude of $\overline{u'v'}$=0.06039, higher than 0.05248 observed at previous station. The highest peak obtained value is at y=31.50 mm and the lowest value is at y=112.50 mm.

For station x=540 mm, the B_1 test case present values within -0.03253<$\overline{u'v'}$<+0.01083 interval with amplitude of $\overline{u'v'}$=0.04336, the B_1 lower amplitude obtained so far since x=8 mm. The highest peak obtained value is at y=51.50 mm and the lowest is at y=126.50 mm. The A_1

test case reveals an amplitude interval of -0.01878<$\overline{u'v'}$<+0.01748 with amplitude of $\overline{u'v'}$=0.03626, the A_1 lowest amplitude obtained so far since x=8 mm. The highest peak obtained value is at y=51.50 mm and the lowest value is at y=104.50 mm.

For station x=640 mm, the B_1 test case present values within -0.02754<$\overline{u'v'}$<+0.01623 interval with amplitude of $\overline{u'v'}$=0.04377, the similar to the previous station. The highest peak obtained value is at y=13.50 mm and the lowest is at y=130.50 mm. The A_1 test case reveals an identical amplitude interval of previous station, with exception of the three exterior points at north, all points presents low shear stress values.

For station x=735 mm, the B_1 test case present values within -0.01882<$\overline{u'v'}$<+0.0220 interval with amplitude of $\overline{u'v'}$=0.04102, the B_1 lower amplitude obtained so far since x=8 mm. The highest peak obtained value is at y=33.50 mm and the lowest is at y=130.50 mm. The A_1 test case reveals an identical amplitude interval of both previous stations, with exception of the three exterior points at north, all points presents low shear stress values.

Regarding the shear stress results evolution from x=490 mm up to x=735 mm, the amplitude intervals are higher for the unconfined test case; with exception for the three exterior points at north for this test case. The negative slope at region near y=130 it is present only for the confined test case.

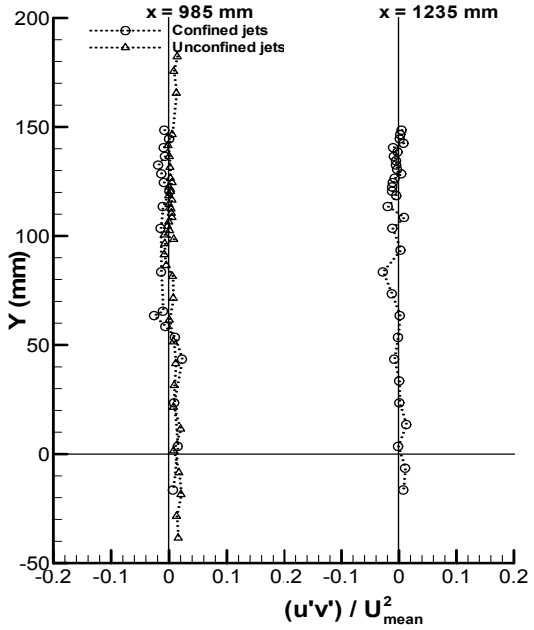

Figure 3.68. Vertical profiles of shear stress for A_1 and B_1 test cases at stations x=985 and 1235 mm.

Figure 3.68 reveals that for both test cases for station x=985 mm the negative peak disappeared completely and all values are approaching to a vertical line at the zero neighbourhood. For station x=1235 mm, the A_1 test case reveals identical results than the obtained at previous station with exception for points y=83.50 mm ($\overline{u'v'}$=-0.02816) and y=13.50 mm ($\overline{u'v'}$=+0.01249).

3.8.2. Unconfined A_2 and confined B_2 jets

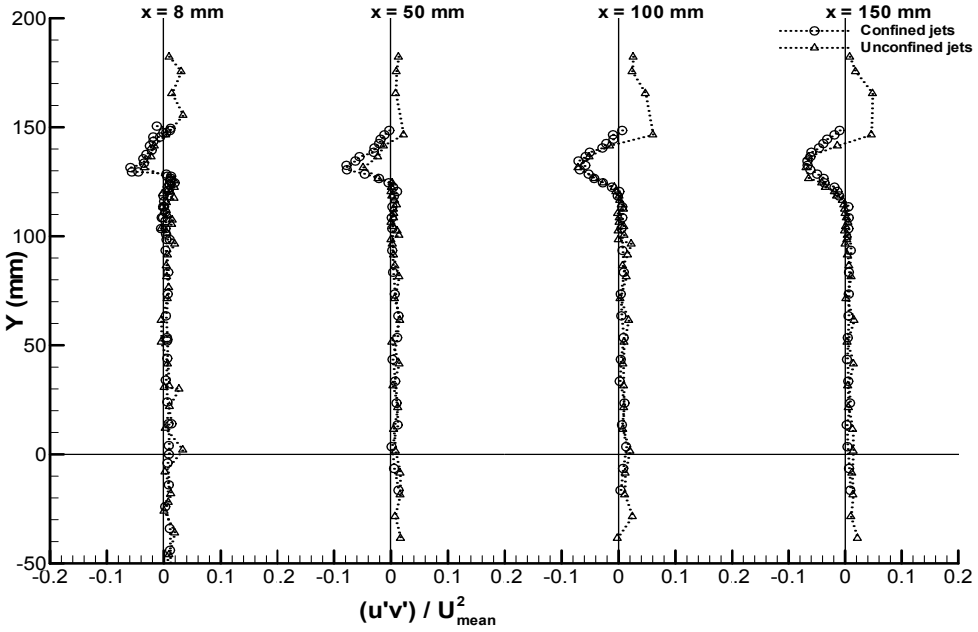

Figure 3.69. Vertical profiles of shear stress for A_2 and B_2 test cases at stations x=8, 50, 100 and 150 mm.

Figure 3.69 shows vertical profiles of shear stress for A_2 and B_2 test cases at stations x=8, 50, 100 and 150 mm, and reveals that all profiles present practically identical values for both test cases along the first four stations, such as verified at Figure 3.65 for A_1 and B_1 test cases. For station x=8 mm, the B_2 test case present values within -0.05885<$\overline{u'v'}$<+0.01897 interval with shows amplitude of $\overline{u'v'}$=0.07782, a little higher than the $\overline{u'v'}$=0.07302 obtained for B_1 test case at same station (Figure 3.65). The highest peak obtained value is at y=124.50 mm and the lowest is at y=131.50 mm. The A_2 test case reveals an amplitude interval of -0.03400<$\overline{u'v'}$<+0.03376 with amplitude of $\overline{u'v'}$=0.06716, little higher than the $\overline{u'v'}$=0.06464 obtained at A_1 test case interval for this station (Figure 3.65). The highest peak obtained value is at y=2.00 mm and the lowest value is at y=131.50 mm.

For station x=50 mm, the B_2 test case present values within -0.07821<$\overline{u'v'}$<+0.01284 interval, with amplitude of $\overline{u'v'}$=0.09105, a higher than the previous station value and higher than the obtained for B_1 test case at same station. The highest peak obtained value is at y=63.50 mm and the lowest is at y=132.50 mm. The A_2 test case reveals an amplitude interval of -0.04923<$\overline{u'v'}$<+0.01522. This interval shows amplitude of $\overline{u'v'}$=0.06449, little lower than the previous station value and similar to the A_1 test case interval for this station. The highest peak obtained value is at y=61.50 mm and the lowest value is at y=131.50 mm.

For station x=100 mm, the B_2 test case present values within -0.07036<$\overline{u'v'}$<+0.01330 interval. The highest peak obtained value is at y=3.50 mm and the lowest is at y=134.50 mm.

This interval shows amplitude of $\overline{u'v'}$=0.08366, lower than the previous station value and higher than the obtained for B_1 test case at same station. The A_2 test case reveals an amplitude interval of -0.07148<$\overline{u'v'}$<+0.06019. This interval shows amplitude of $\overline{u'v'}$=0.13167, more than two times the amplitude of previous station and higher than A_1 test case interval for this station. The highest peak obtained value is at y=146.50 mm and the lowest value is at y=131.50 mm.

For station x=150 mm, the B_2 test case present values within -0.06682<$\overline{u'v'}$<+0.01009 interval. The highest peak obtained value is at y=93.50 mm and the lowest is at y=134.50 mm. This interval shows amplitude of $\overline{u'v'}$=0.07691, lower than the previous station value and higher than the obtained for B_1 test case at same station. The A_2 test case reveals an amplitude interval of -0.06912<$\overline{u'v'}$<+0.04605. This interval shows amplitude of $\overline{u'v'}$=0.11517, lower than the amplitude of previous station and higher than A_1 test case interval for this station. The highest peak obtained value is at y=146.50 mm and the lowest value is at y=131.50 mm.

Regarding the shear stress results evolution and similarly to Figure 3.65, in Figure 3.69 from stations x=8 mm to x=150 mm for both test cases the negative values region are present at the U_o/U_i jets division and its curve slope is becoming softer according to the jets exit distance increasing.

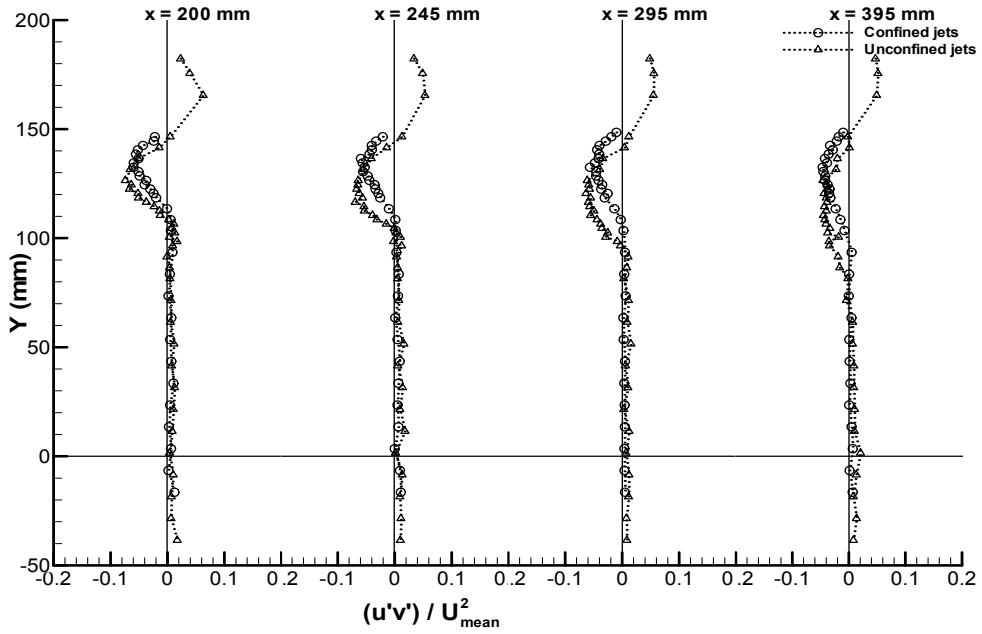

Figure 3.70. Vertical profiles of shear stress for A_2 and B_2 test cases at stations x=200, 245, 295 and 395 mm.

Figure 3.70 shows vertical profiles of shear stress for A_2 and B_2 test cases at stations x=200, 245, 295 and 395 mm, and reveals that all profiles present practically identical values for both test cases along all presented stations, presenting slight differences at the jets mixing areas. For station x=200 mm, the B_2 test case present values within -

0.05963<$\overline{u'v'}$<+0.01045 interval. The highest peak obtained value is at y=33.50 mm and the lowest is at y=138.50 mm. This interval shows amplitude of $\overline{u'v'}$=0.07008, lower than the previous station value and higher than the obtained for B_1 test case at same station. The A_2 test case reveals an amplitude interval of -0.07413<$\overline{u'v'}$<+0.06263. This interval shows amplitude of $\overline{u'v'}$=0.13676, higher than the amplitude of previous station and much higher than A_1 test case interval for this station. The highest peak obtained value is at y=165.50 mm and the lowest value is at y=126.50 mm.

For station x=245 mm, the B_2 test case present values within -0.05411<$\overline{u'v'}$<+0.00732 interval. The highest peak obtained value is at y=33.50 mm and the lowest is at y=138.50 mm. This interval shows amplitude of $\overline{u'v'}$=0.06142, lower than the previous station value and higher than the obtained for B_1 test case at same station. The A_2 test case reveals an amplitude interval of -0.06941<$\overline{u'v'}$<+0.05292. This interval shows amplitude of $\overline{u'v'}$=0.12233, lower than the amplitude of previous station and much higher than A_1 test case interval for this station. The highest peak obtained value is at y=165.50 mm and the lowest value is at y=116.50 mm.

For station x=295 mm, the B_2 test case present values within -0.05654<$\overline{u'v'}$<+0.00487 interval. The highest peak obtained value is at y=43.50 mm and the lowest is at y=132.50 mm. This interval shows amplitude of $\overline{u'v'}$=0.06141, similar than the previous station value and higher than the obtained for B_1 test case at same station. The A_2 test case reveals an amplitude interval of -0.06362<$\overline{u'v'}$<+0.05548. This interval shows amplitude of $\overline{u'v'}$=0.11910, lower than the amplitude of previous station and much higher than A_1 test case interval for this station. The highest peak obtained value is at y=175.50 mm and the lowest value is at y=120.50 mm.

For station x=395 mm, the B_2 test case present values within -0.04613<$\overline{u'v'}$<+0.00689 interval. The highest peak obtained value is at y=3.50 mm and the lowest is at y=132.50 mm. This interval shows amplitude of $\overline{u'v'}$=0.05302, lower than the previous station value and higher than the obtained for B_1 test case at same station. The A_2 test case reveals an amplitude interval of -0.04497<$\overline{u'v'}$<+0.04914. This interval shows amplitude of $\overline{u'v'}$=0.09411, lower than the amplitude of previous station and much higher than A_1 test case interval for this station. The highest peak obtained value is at y=165.50 mm and the lowest value is at y=110.50 mm.

Regarding the comparison between these four stations from x=200 mm to x=395 mm, it is visible that the curve slope tends to disappear in the last station. It is also visible that in the confined test case the shear stress negative values comprise a small region than the one in the unconfined test case for all four stations.

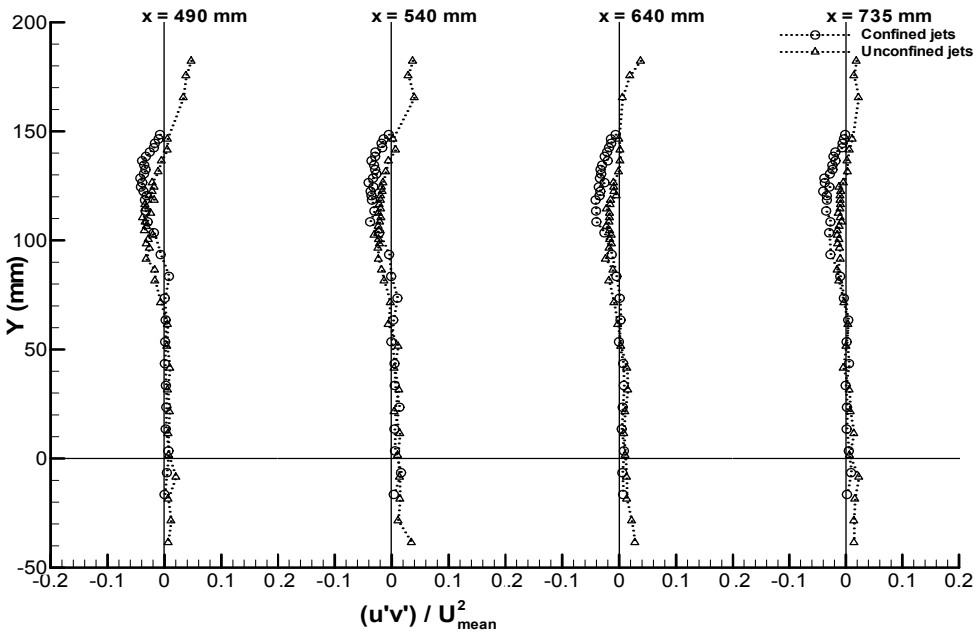

Figure 3.71. Vertical profiles of shear stress for A_2 and B_2 test cases at stations x=490, 540, 640 and 735 mm.

Figure 3.71 shows vertical profiles of shear stress for A_2 and B_2 test cases at stations x=490, 540, 640 and 755 mm, and reveals that all profiles present practically identical values for both test cases along all presented stations, presenting slight differences at the jets mixing areas. For station x=490 mm, the B_2 test case present values within -0.04243<$\overline{u'v'}$<+0.00786 interval. The highest peak obtained value is at y=83.50 mm and the lowest is at y=128.50 mm. This interval shows amplitude of $\overline{u'v'}$=0.05029, lower than the $\overline{u'v'}$=0.05302 previous station value and higher than the $\overline{u'v'}$=0.04604 obtained for B_1 test case at same station. The A_2 test case reveals an amplitude interval of -0.03825<$\overline{u'v'}$<+0.04667. This interval shows amplitude of $\overline{u'v'}$=0.08492, lower than the $\overline{u'v'}$=0.09411 amplitude of previous station and much higher than $\overline{u'v'}$=0.06039 A_1 test case this same station. The highest peak obtained value is at y=182.25 mm and the lowest value is at y=110.50 mm.

For station x=540 mm, the B_2 test case present values within -0.04060<$\overline{u'v'}$<+0.00999 interval. The highest peak obtained value is at y=83.50 mm and the lowest is at y=128.50 mm. This interval shows amplitude of $\overline{u'v'}$=0.05059, similar than the $\overline{u'v'}$=0.05029 previous station values and higher than the $\overline{u'v'}$=0.04336 obtained for B_1 test case at same station. The A_2 test case reveals an amplitude interval of -0.02425<$\overline{u'v'}$<+0.03960. This interval shows amplitude of $\overline{u'v'}$=0.06385, lower than the $\overline{u'v'}$=0.08492 amplitude of previous station and much higher than $\overline{u'v'}$=0.03626 A_1 test case this same station. The highest peak obtained value is at y=165.50 mm and the lowest value is at y=96.50 mm.

For station x=640 the B_2 test case present values within -0.04153<$\overline{u'v'}$<+0.00818 interval. The highest peak obtained value is at y=3.50 mm and the lowest is at y=118.50 mm.

This interval shows amplitude of $\overline{u'v'}$=0.04971, lower than the $\overline{u'v'}$=0.05059 previous station value and lower than the $\overline{u'v'}$=0.04377 obtained for B_1 test case at same station. The A_2 test case reveals an amplitude interval of -0.02418<$\overline{u'v'}$<+0.03738. This interval shows amplitude of $\overline{u'v'}$=0.06156, lower than the $\overline{u'v'}$=0.06385 amplitude of previous station and higher than $\overline{u'v'}$=0.05102 A_1 test case this same station. The highest peak obtained value is at y=182.25 mm and the lowest value is at y=91.50 mm.

For station x=735 mm, the B_2 test case present values within -0.04004<$\overline{u'v'}$<+0.00567 interval. The highest peak obtained value is at y=43.50 mm and the lowest is at y=122.50 mm. This interval shows amplitude of $\overline{u'v'}$=0.04571, lower than the $\overline{u'v'}$=0.05059 previous station value and higher than the $\overline{u'v'}$=0.02220 obtained for B_1 test case at same station. The A_2 test case reveals an amplitude interval of -0.01547<$\overline{u'v'}$<+0.02213. This interval shows amplitude of $\overline{u'v'}$=0.03760, lower than the $\overline{u'v'}$=0.06156 amplitude of previous station and higher than 0.03278 A_1 test case this same station. The highest peak obtained value is at y=165.50 mm and the lowest value is at y=86.50 mm.

Regarding the shear stress results obtained along these four stations it is visible that the two test cases pattern are very similar each other and there are present only very small alterations. From y=0 to y=80 the results between x=490 mm to x=735 mm are practically represented by a straight line at the zero neighbourhood.

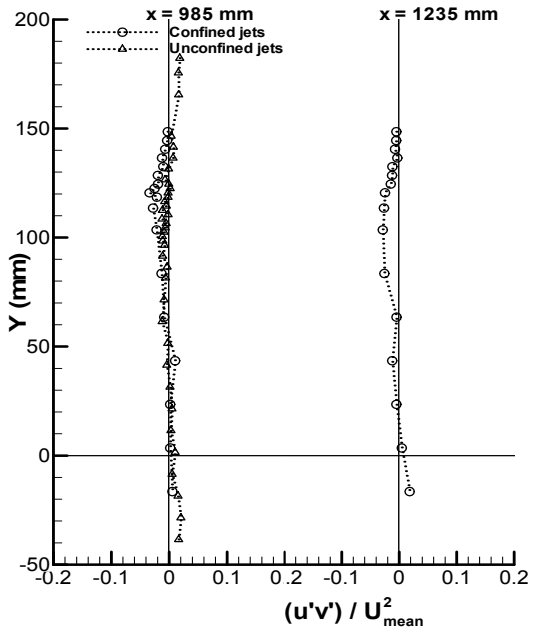

Figure 3.72. Vertical profiles of shear stress for A_2 and B_2 test cases at stations x=985 and 1235 mm.

For station x=985 mm (Figure 3.72), the B_2 test case present values within -0.03403<$\overline{u'v'}$<+0.01023 interval. The highest peak obtained value is at y=43.50 mm and the

lowest is at y=120.50 mm. This interval shows amplitude of $\overline{u'v'}$=0.04426, similar than the $\overline{u'v'}$=0.04571 previous station value and slightly lower than the $\overline{u'v'}$=0.04831 obtained for B_1 test case at same station. The A_2 test case reveals an amplitude interval of -0.01185<$\overline{u'v'}$<+0.01812. This interval shows amplitude of $\overline{u'v'}$=0.02997, lower than the $\overline{u'v'}$=0.03760 amplitude of previous station and similar than $\overline{u'v'}$=0.02830 A_1 test case this same station. The highest peak obtained value is at y=182.25 mm and the lowest value is at y=100.50 mm.

For station x=1235 mm, the B_2 test case present values within -0.02865<$\overline{u'v'}$<+0.00448 interval. The highest peak obtained value is at y=3.50 mm and the lowest is at y=103.50 mm. This interval shows amplitude of $\overline{u'v'}$=0.03313, lower than the $\overline{u'v'}$=0.04426 previous station value and lower than the $\overline{u'v'}$=0.04065 obtained for B_1 test case at same station.

3.8.3. Convergent 11º C_1 and convergent 22º D_1 jets

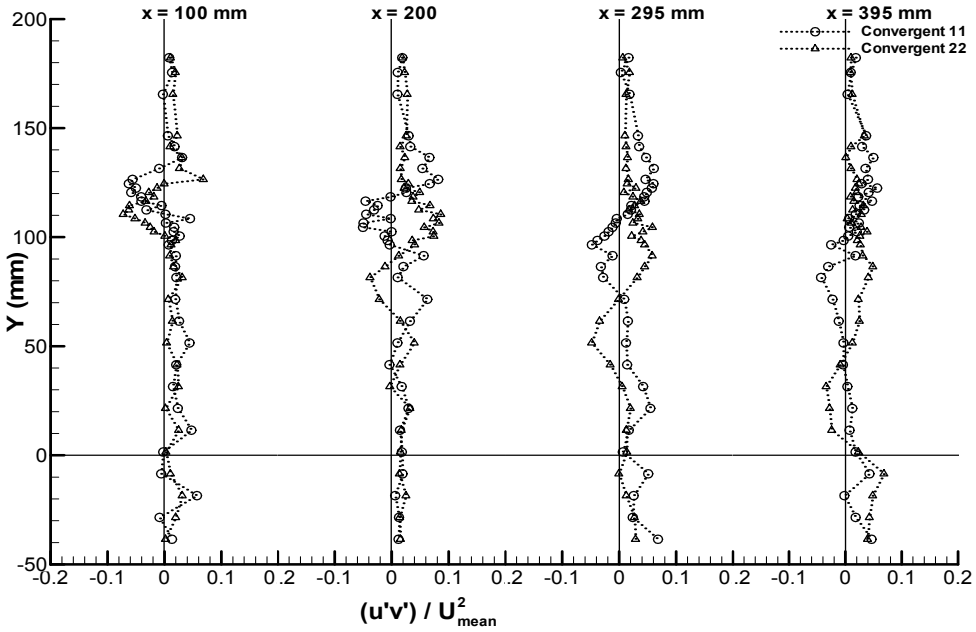

Figure 3.73. Vertical profiles of shear stress for C_1 and D_1 test cases at stations x=100, 200, 295 and 395 mm.

For the convergent C_1 and D_1 test cases the obtained shear stress oscillations for stations x=100, 200, 295 and 395 mm, are very different from all previous non convergent test cases, as illustrates Figure 3.73. Both these test cases present higher amplitude shear stress intervals than the confined B_1, B_2 and unconfined A_1, A_2 test cases. For station x=100 mm, the C_1 test case present values within -0.06257<$\overline{u'v'}$<+0.04729 interval. The highest peak obtained value is at y=11.50 mm and the lowest is at y=124.50 mm. This interval shows amplitude of 0.10986. The D_1 test case amplitude interval is -0.07260<$\overline{u'v'}$<+0.06817. This

interval shows amplitude of $\overline{u'v'}$=0.14077 for this test case. The highest peak obtained value is at y=126.50 mm and the lowest value is at y=110.50 mm.

For station x=200 mm, the C_1 test case present values within -0.05040<$\overline{u'v'}$<+0.08162 interval. The highest peak obtained value is at y=126.50 mm and the lowest is at y=104.50 mm. This interval shows amplitude of 0.13202, higher than the 0.10986 interval obtained at previous station. The D_1 test case reveals an amplitude interval of -0.03816<$\overline{u'v'}$<+0.08603. This interval shows amplitude of $\overline{u'v'}$=0.12419 for this test case, lower than $\overline{u'v'}$=0.14077 obtained at previous station. The highest peak obtained value is at y=110.50 mm and the lowest value is at y=81.50 mm.

For station x=295 mm, the C_1 test case present values within -0.04803<$\overline{u'v'}$<+0.06075 interval. The highest peak obtained value is at y=131.50 mm and the lowest is at y=96.50 mm. This interval shows amplitude of $\overline{u'v'}$=0.10878, lower than both intervals obtained at previous stations. The D_1 test case reveals an amplitude interval of -0.04851<$\overline{u'v'}$<+0.05829. This interval shows amplitude of $\overline{u'v'}$=0.10680 for this test case, lower than both intervals obtained at previous stations. The highest peak obtained value is at y=104.50 mm and the lowest value is at y=51.50 mm.

For station x=395 mm, the C_1 test case present values within -0.04322<$\overline{u'v'}$<+0.05646 interval. The highest peak obtained value is at y=122.50 mm and the lowest is at y=81.50 mm. This interval shows amplitude of $\overline{u'v'}$=0.09968, lower than three intervals obtained at previous stations. The D_1 test case reveals an amplitude interval of -0.03430<$\overline{u'v'}$<+0.04865. This interval shows amplitude of $\overline{u'v'}$=0.08295 for this test case, lower than three intervals obtained at previous stations. The highest peak obtained value is at y=86.50 mm and the lowest value is at y=31.50 mm.

Regarding the shear stress results evolution between the stations at Figure 3.73, the amplitude C_1 intervals are higher than D_1 at the first two stations; at station x=295 mm and x=395 mm, the reverse situation is observed and as the distance at the jets exit is increased the oscillating values regions are moving to axis plane.

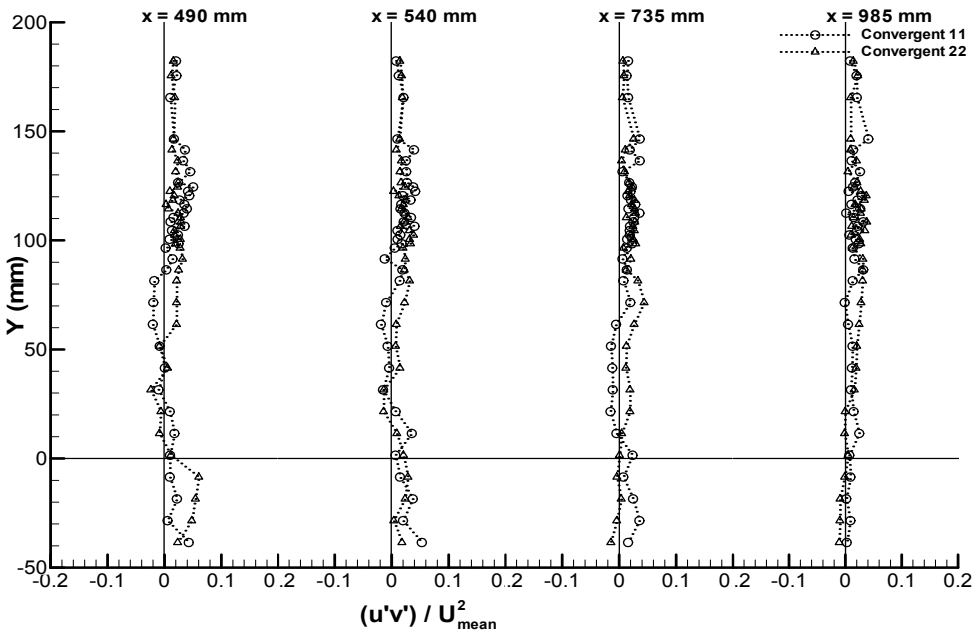

Figure 3.74. Vertical profiles of shear stress for C_1 and D_1 test cases at stations x=490, 540, 735 and 985 mm.

Figure 3.74 shows the shear stress results for C_1 and D_1 test cases at stations x=490, 540, 735 and 985 mm. For station x=490 mm, the C_1 test case present values within -0.02055<$\overline{u'v'}$<+0.05025 interval. The highest peak obtained value is at y=124.50 mm and the lowest is at y=61.50 mm. This interval shows amplitude of $\overline{u'v'}$=0.07080, lower than intervals obtained at previous stations. The D_1 test case reveals an amplitude interval of -0.02407<$\overline{u'v'}$<+0.03141. This interval shows amplitude of $\overline{u'v'}$=0.05548 for this test case, lower than intervals obtained at previous stations. The highest peak obtained value is at y=91.50 mm and the lowest value is at y=31.50 mm.

For station x=540 mm, the C_1 test case present values within -0.01900<$\overline{u'v'}$<+0.04125 interval. The highest peak obtained value is at y=122.50 mm and the lowest is at y=61.50 mm. This interval shows amplitude of $\overline{u'v'}$=0.06025, lower than three intervals obtained at previous stations. The D_1 test case reveals an amplitude interval of -0.01442<$\overline{u'v'}$<+0.03824. This interval shows amplitude of $\overline{u'v'}$=0.05284 for this test case, lower than three intervals obtained at previous stations. The highest peak obtained value is at y=102.50 mm and the lowest value is at y=21.50 mm.

For station x=735 mm, the C_1 test case present values within -0.01538<$\overline{u'v'}$<+0.03546 interval. The highest peak obtained value is at y=112.50 mm and the lowest is at y=21.50 mm. This interval shows amplitude of $\overline{u'v'}$=0.05084, lower than intervals obtained at previous stations. The D_1 test case reveals an all positive amplitude interval of +0.0004<$\overline{u'v'}$<+0.04365. This interval shows amplitude of $\overline{u'v'}$=0.04361 for this test case, lower than intervals obtained

at previous stations. The highest peak obtained value is at y=71.50 mm and the lowest value is at y=1.50 mm.

For station x=985 mm, the C_1 test case present values within -0.00128<$\overline{u'v'}$<+0.04064 interval. The highest peak obtained value is at y=146.50 mm and the lowest is at y=71.50 mm. This interval shows amplitude of $\overline{u'v'}$=0.04192, lower than intervals obtained at previous stations. The D_1 test case reveals an amplitude interval of -0.00158<$\overline{u'v'}$<+0.03705. This interval shows amplitude of $\overline{u'v'}$=0.03868 for this test case, lower than intervals obtained at previous stations. The highest peak obtained value is at y=120.50 mm and the lowest value is at y=11.50 mm.

Looking back to Figure 3.73 and comparing the Figure 3.74 obtained results, for both test cases the shear stress results oscillations are becoming more softer as the jets exit distance is increased and from station x=490 mm forward both test cases are tending to result equalization. All four stations presents amplitudes intervals lower for D_1 test case.

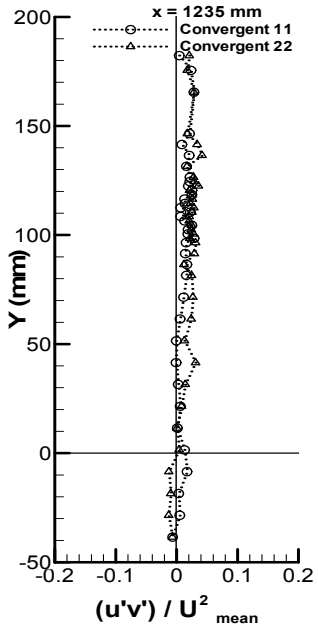

Figure 3.75. Vertical profiles of shear stress for C_1 and D_1 test cases at station x=1235 mm.

For station x=1235 mm (Figure 3.75), the C_1 test case present values within -0.00128<$\overline{u'v'}$<+0.02841 interval. The highest peak obtained value is at y=98.50 mm and the lowest is at y=71.50 mm. This interval shows amplitude of $\overline{u'v'}$=0.02969, lower than all intervals obtained at previous stations. The D_1 test case reveals an all positive amplitude interval of +0.00006<$\overline{u'v'}$<+0.04171. This interval shows amplitude of $\overline{u'v'}$=0.04165 for this test case, higher than obtained at previous station. The highest peak obtained value is at y=136.50 mm and the lowest value is at y=11.50 mm.

3.8.4. Convergent 11° C_2 and convergent 22° D_2 jets

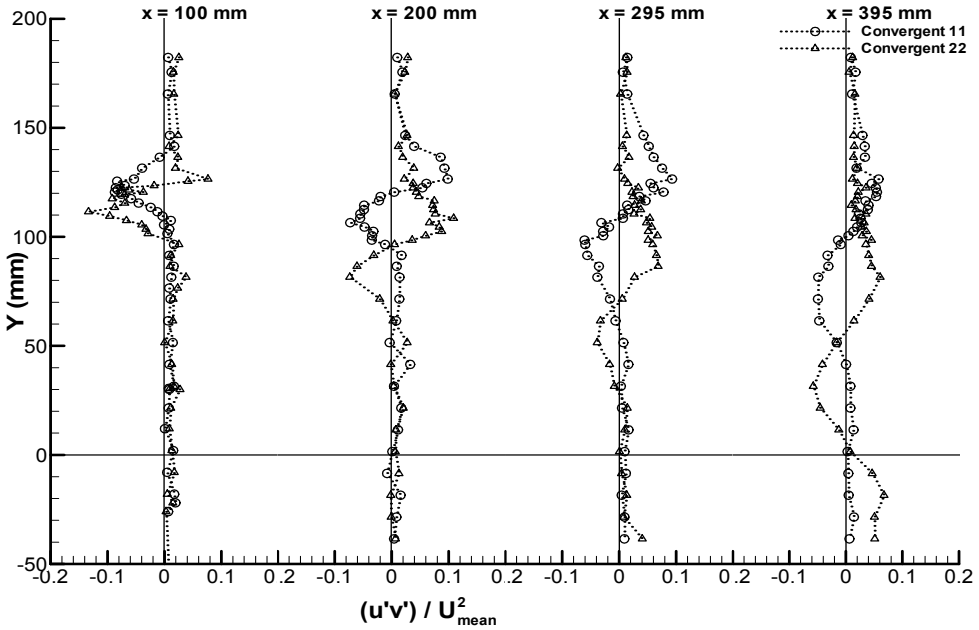

Figure 3.76. Vertical profiles of shear stress for C_2 and D_2 test cases at stations x=100, 200, 295 and 395 mm.

Figure 3.76 shows the vertical profiles of shear stress for C_2 and D_2 test cases at stations x=100, 200, 295 and 395 mm. For the convergent C_2 and D_2 test cases the obtained shear stress oscillations are very different as illustrates Figure 3.73, for the C_1 and D_1 test cases. For station x=100 mm, the C_2 test case present values within -0.08711<$\overline{u'v'}$<+0.01668 interval. The highest peak obtained value is at y=96.50 mm and the lowest is at y=120.50 mm. This interval shows amplitude of $\overline{u'v'}$=0.10379, higher than $\overline{u'v'}$=0.10986 obtained for C_1 test case and much higher than all other test cases. The D_2 test case reveals an amplitude interval of -0.13340<$\overline{u'v'}$<+0.07641. This interval shows amplitude of 0.20981 for this test case, the highest obtained interval for all test cases, even more than two times the C_2 interval at this station. The highest peak obtained value is at y=126.50 mm and the lowest value is at y=111.50 mm.

For station x=200 mm, the C_2 test case present values within -0.07282<$\overline{u'v'}$<+0.09831 interval. The highest peak obtained value is at y=126.50 mm and the lowest is at y=106.50 mm. This interval shows amplitude of 0.17113, the highest obtained for C_2 test case, only minor than the D_2 interval at previous station. The D_2 test case reveals an amplitude interval of -0.07353<$\overline{u'v'}$<+0.08777. This interval shows amplitude of $\overline{u'v'}$=0.16130 for this test case, lower than previous station and higher than those obtained for other test cases at this station. The highest peak obtained value is at y=102.50 mm and the lowest value is at y=81.50 mm.

For station x=295 mm, the C_2 test case present values within -0.06086<$\overline{u'v'}$<+0.09270 interval. The highest peak obtained value is at y=126.50 mm and the lowest is at y=98.50 mm. This interval shows amplitude of $\overline{u'v'}$=0.15356, lower than previous station and the highest obtained for this station for all test cases. The D_2 test case reveals an amplitude interval of -0.03867<$\overline{u'v'}$<+0.06828. This interval shows amplitude of $\overline{u'v'}$=0.10695 for this test case, much lower than previous station and higher than those obtained for other test cases at this station, similar to $\overline{u'v'}$=0.10680 obtained for C_1 test case and much higher than the intervals obtained for confined and unconfined test cases. The highest peak obtained value is at y=86.50 mm and the lowest value is at y=51.50 mm.

For station x=395 mm, the C_2 test case present values within -0.4944<$\overline{u'v'}$<+0.05794 interval. The highest peak obtained value is at y=126.50 mm and the lowest is at y=71.50 mm. This interval shows amplitude of $\overline{u'v'}$=0.10738, much lower than previous station and the higher than obtained for confined and unconfined test cases. The D_2 test case reveals an amplitude interval of -0.05765<$\overline{u'v'}$<+0.06056. This interval shows amplitude of $\overline{u'v'}$=0.11821 for this test case, slightly higher than previous station, higher than 0.08295 obtained for C_1 test case and much higher than the intervals obtained for confined and unconfined test cases. The highest peak obtained value is at y=81.50 mm and the lowest value is at y=31.50 mm.

Regarding the shear stress evolution results over this four stations, the highest interval of all measurements is verified for station x=100 mm for test case D_2 and the second highest interval of all is verified at x=200 mm for C_2 test case. As the jets exit distance is increased, the higher and lower observed peak are migrating to axis plane.

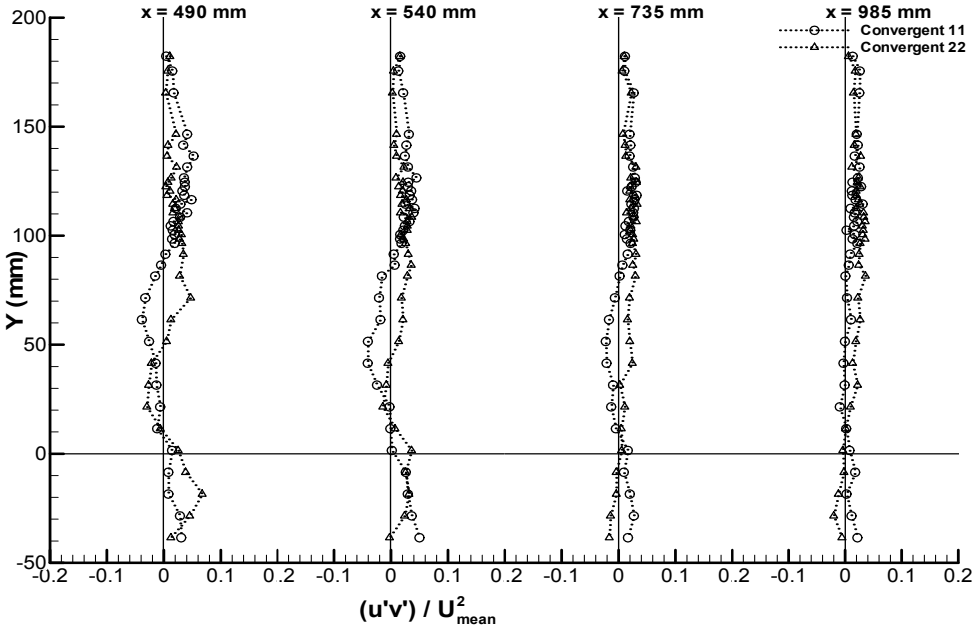

Figure 3.77. Vertical profiles of shear stress for C_2 and D_2 test cases at stations x=490, 540, 735 and 985 mm.

Figure 3.77 shows the vertical profiles of shear stress for C_2 and D_2 test cases at stations x=490, 540, 735 and 985 mm. For station x=490 mm, the C_2 test case present values within -0.03877<$\overline{u'v'}$<+0.04857 interval. The highest peak obtained value is at y=116.50 mm and the lowest is at y=51.50 mm. This interval shows amplitude of $\overline{u'v'}$=0.08731, much lower than all previous stations, higher than the C_1 test case and the higher than obtained for confined and unconfined test cases. The D_2 test case reveals an amplitude interval of -0.02991<$\overline{u'v'}$<+0.04688. This interval shows amplitude of $\overline{u'v'}$=0.07679 for this test case, much lower than $\overline{u'v'}$=0.11821 obtained at previous station, higher than $\overline{u'v'}$=0.05548 obtained for D_1 test case and higher than the intervals obtained for confined and unconfined test cases, except for the B_2 case interval ($\overline{u'v'}$=0.08492). The highest peak obtained value is at y=71.50 mm and the lowest value is at y=21.50 mm.

For station x=540 mm, the C_2 test case present values within -0.4107<$\overline{u'v'}$<+0.04455 interval. The highest peak obtained value is at y=126.50 mm and the lowest is at y=41.50 mm. This interval shows amplitude of $\overline{u'v'}$=0.08562, slightly lower than all previous stations, higher than the C_1 test case and the higher than obtained for confined and unconfined test cases. The D_2 test case reveals an amplitude interval of -0.01447<$\overline{u'v'}$<+0.03634. This interval shows amplitude of 0.05081 for this test case, lower than $\overline{u'v'}$=0.07679 obtained at previous station, slightly lower than $\overline{u'v'}$=0.05284 obtained for D_1 test case and higher than the intervals obtained for confined and unconfined test cases, except for the A_2 case interval ($\overline{u'v'}$=0.006385). The highest peak obtained value is at y=108.50 mm and the lowest value is at y=21.50 mm.

For station x=735 mm, the C_2 test case present values within -0.2248<$\overline{u'v'}$<+0.03162 interval. The highest peak obtained value is at y=118.50 mm and the lowest is at y=51.50 mm. This interval shows amplitude of $\overline{u'v'}$=0.05410, much lower than all previous stations, lower than the C_1 test case and the higher than obtained for confined and unconfined test cases. The D_2 test case reveals an all positive amplitude interval of +0.00203<$\overline{u'v'}$<+0.03250. This interval shows amplitude of $\overline{u'v'}$=0.03047 for this test case, lower than $\overline{u'v'}$=0.05081 obtained at previous station, lower than $\overline{u'v'}$=0.04361 all positive interval obtained for D_1 test case and lower than the intervals obtained for confined and unconfined test cases. The highest peak obtained value is at y=114.50 mm and the lowest value is at y=31.50 mm.

For station x=985 mm, the C_2 test case present values within -0.00946<$\overline{u'v'}$<+0.03091 interval. The highest peak obtained value is at y=114.50 mm and the lowest is at y=21.50 mm. This interval shows amplitude of $\overline{u'v'}$=0.04037, lower than all previous stations, slightly lower than the C_1 test case, higher than obtained for both unconfined test cases and lower than for both confined test cases. The D_2 test case reveals an amplitude interval of -0.00429<$\overline{u'v'}$<+0.03586. This interval shows amplitude of $\overline{u'v'}$=0.04015 for this test case, slightly higher than $\overline{u'v'}$=0.03047 obtained at previous station, slightly higher than

$\overline{u'v'}$=0.03863 obtained for D_1 test case higher than obtained for both unconfined test cases and lower than for both confined test cases. The highest peak obtained value is at y=81.50 mm and the lowest value is at y=1.50 mm.

Regarding the shear stress evolution results between Figure 3.76 and Figure 3.77 it is visible that the initially obtained higher and lower peaks at the jets division region are becoming softer and disappear as the jets exit distance is increased. At stations x=735 mm and x=985 mm the obtained profiles for both test cases reveals practically coincident results with exception at 30<y<90 mm region.

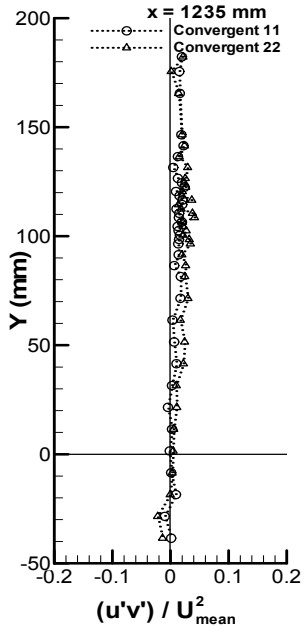

Figure 3.78. Vertical profiles of shear stress for C_2 and D_2 test cases at station x=1235 mm.

For station x=1235 mm (Figure 3.78), the C_2 test case present values within -0.00442<$\overline{u'v'}$<+0.02428 interval. The highest peak obtained value is at y=122.50 mm and the lowest is at y=21.50 mm. This interval shows amplitude of $\overline{u'v'}$=0.02870, lower than all previous stations, slightly lower than the C_1 test case and lower than obtained for confined test cases. The D_2 test case reveals an all positive amplitude interval of +0.00121<$\overline{u'v'}$<+0.04138. This interval shows amplitude of $\overline{u'v'}$=0.04017 for this test case, identical than $\overline{u'v'}$=0.04015 obtained at previous station, slightly lower than $\overline{u'v'}$=0.04165 obtained for D_1 test case, identical to B_1 test case and slightly higher than the B_2 test cases. The highest peak obtained value is at y=108.50 mm and the lowest value is at y=175.50 mm.

3.9. Vertical profiles of anisotropy

This subchapter presents all the obtained results for the vertical profiles of anisotropy $\sqrt{\overline{u'^2}}/\sqrt{\overline{v'^2}}$ distribution at the horizontal axis in each studied station, from y=200 mm to y=-50 mm. The anisotropy vertical profiles distribution values are presented from $0 \leq \sqrt{\overline{u'^2}}/\sqrt{\overline{v'^2}} \leq 20$. The confined jets values starts at y=148.50 mm, due to its wall confinement. The unconfined jets values starts at y=182.25 mm.

3.9.1. Unconfined A_1 and confined B_1 jets

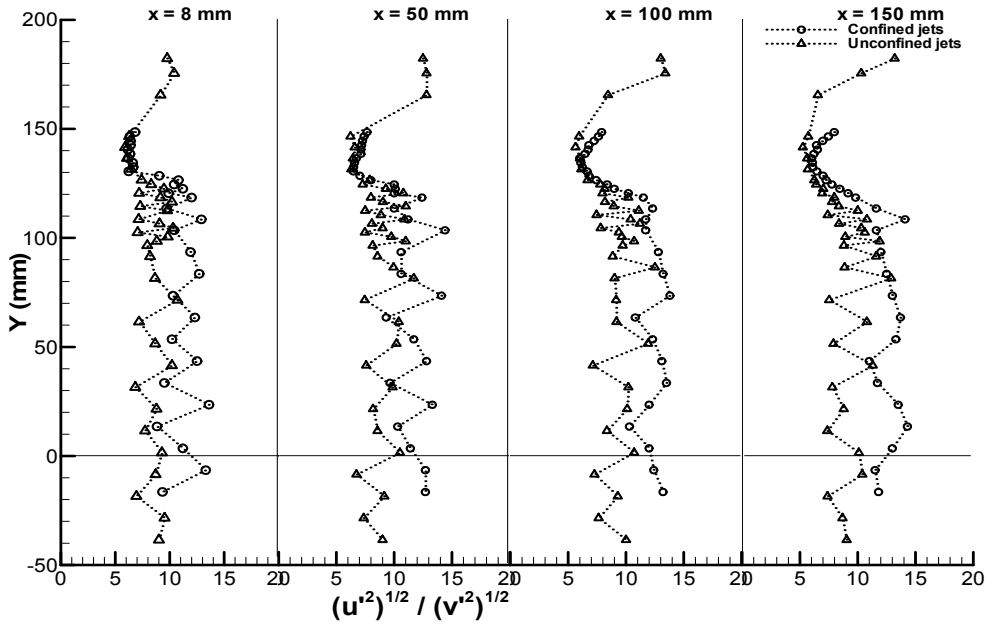

Figure 3.79. Vertical profiles of anisotropy for A_1 and B_1 test cases at stations x=8, 50, 100 and 150 mm.

Figure 3.79 shows vertical profiles of anisotropy for A_1 and B_1 test cases at stations x=8, 50, 100 and 150 mm, and reveals that all profiles present great oscillations between neighbouring points for all stations along 0<y<130 mm regions. For station x=8 mm, the B_1 test case present values within the $6.15<\sqrt{\overline{u'^2}}/\sqrt{\overline{v'^2}}<13.6$ interval with amplitude of $\sqrt{\overline{u'^2}}/\sqrt{\overline{v'^2}}$ =7.45. The highest obtained value is at y=23.50 mm and the lowest value is at y=142.50 mm. The A_1 test case reveals an amplitude interval of $5.90<\sqrt{\overline{u'^2}}/\sqrt{\overline{v'^2}}<10.7$, with amplitude of $\sqrt{\overline{u'^2}}/\sqrt{\overline{v'^2}}$ =4.9. The highest obtained value is at y=71.50 mm and the lowest value is at y=146.50 mm. The A_1 test case interval is almost 65% of the B_1 test case interval. The B_1 test case presents generically higher anisotropy values.

For station x=50 mm, the B_1 test case present values within the $6.47<\sqrt{\overline{u'^2}}/\sqrt{\overline{v'^2}}<14.4$ interval, with amplitude of $\sqrt{\overline{u'^2}}/\sqrt{\overline{v'^2}}$ =7.93. The highest obtained value is at y=108.50 mm and the lowest value is at y=130.50 mm. The A_1 test case reveals an amplitude interval of

6.22<$\sqrt{\overline{u'^2}}/\sqrt{\overline{v'^2}}$ <11.7, with amplitude of $\sqrt{\overline{u'^2}}/\sqrt{\overline{v'^2}}$ =5.48. The highest obtained value is at y=86.50 mm and the lowest value is at y=146.50 mm. The three exterior points at north, present the higher obtained values. The A_1 test case interval is almost 69% of the B_1 test case interval. The B_1 test case presents generically higher anisotropy values.

For station x=100 mm, the B_1 test case present values within the 5.99<$\sqrt{\overline{u'^2}}/\sqrt{\overline{v'^2}}$<13.8 interval, with amplitude of $\sqrt{\overline{u'^2}}/\sqrt{\overline{v'^2}}$ =7.81. The highest obtained value is at y=108.50 mm and the lowest value is at y=136.50 mm. The A_1 test case reveals an amplitude interval of 5.63<$\sqrt{\overline{u'^2}}/\sqrt{\overline{v'^2}}$<11.9, with amplitude of $\sqrt{\overline{u'^2}}/\sqrt{\overline{v'^2}}$ =6.27. The highest obtained value is at y=51.50 mm and the lowest value is at y=141.50 mm. The two exterior points at north, present the higher obtained values. The A_1 test case interval is almost 80% of the B_1 test case interval. The B_1 test case presents generically higher anisotropy values.

For station x=150 mm, the B_1 test case present values within the 6.02<$\sqrt{\overline{u'^2}}/\sqrt{\overline{v'^2}}$<14.3 interval, with amplitude of $\sqrt{\overline{u'^2}}/\sqrt{\overline{v'^2}}$ =8.28. The highest obtained value is at y=13.50 mm and the lowest value is at y=138.50 mm. The A_1 test case reveals an amplitude interval of 5.25<$\sqrt{\overline{u'^2}}/\sqrt{\overline{v'^2}}$<12.9, with amplitude of $\sqrt{\overline{u'^2}}/\sqrt{\overline{v'^2}}$ =7.65. The highest obtained value is at y=81.50 mm and the lowest value is at y=141.50 mm. Anisotropy oscillations are visible for all vertical profile. The farthest exterior point at north, present the higher obtained value. The A_1 test case interval is almost 92% of the B_1 test case interval. The B_1 test case presents generically higher anisotropy values. For these first four stations, the lowest values for both test cases are presented in the jets division zone.

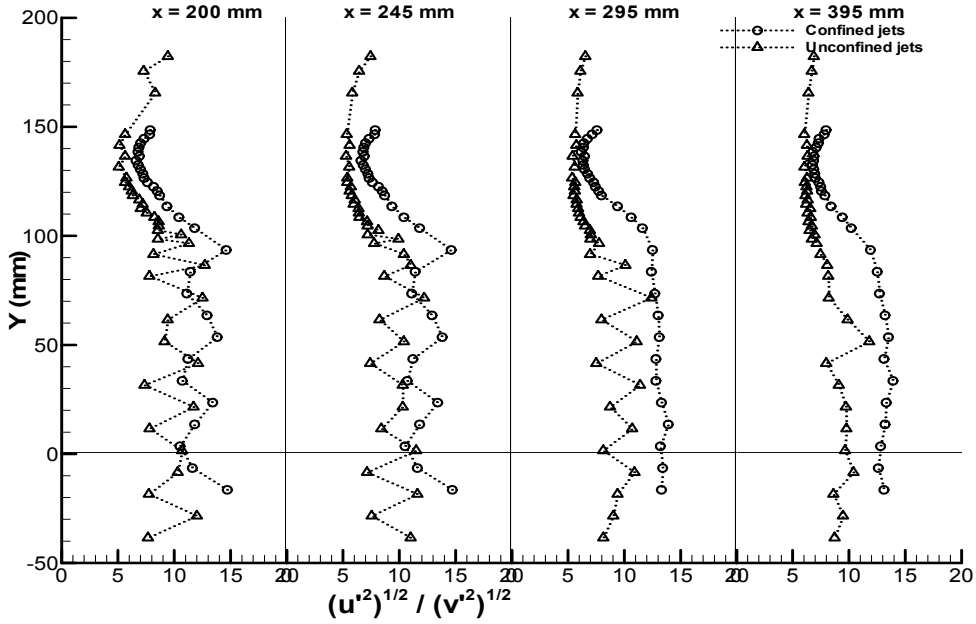

Figure 3.80. Vertical profiles of anisotropy for A_1 and B_1 test cases at stations x=200, 245, 295 and 395 mm.

Figure 3.80 shows vertical profiles of anisotropy for A_1 and B_1 test cases at stations x=200, 245, 295 and 395 mm, and reveals that all profiles present great oscillations between neighbouring points for all stations along 0<y<100 mm regions, with exceptions for confined test cases at stations x=295 and 395 mm. For station x=200 mm, the B_1 test case present values within the $6.60<\sqrt{\overline{u'^2}}/\sqrt{\overline{v'^2}}<14.60$ interval, with amplitude of $\sqrt{\overline{u'^2}}/\sqrt{\overline{v'^2}}$ =8.00 for this test case. The highest obtained value is at y=93.50 mm and the lowest value is at y=136.50 mm. Anisotropy oscillations are visible for all vertical profile. The A_1 test case reveals an amplitude interval of $5.07<\sqrt{\overline{u'^2}}/\sqrt{\overline{v'^2}}<12.7$, with amplitude of $\sqrt{\overline{u'^2}}/\sqrt{\overline{v'^2}}$ =7.63. The highest obtained value is at y=71.50 mm and the lowest value is at y=141.50 mm. Anisotropy oscillations are visible for all vertical profile. The A_1 test case interval is almost 95% of the B_1 test case interval. The B_1 test case presents generically higher anisotropy values.

For station x=245 mm, the B_1 test case present values within the $6.60<\sqrt{\overline{u'^2}}/\sqrt{\overline{v'^2}}<14.60$ interval, with amplitude of $\sqrt{\overline{u'^2}}/\sqrt{\overline{v'^2}}$ =8.00. The highest obtained value is at y=93.50 mm and the lowest value is at y=134.50 mm. Anisotropy oscillations are visible for all vertical profile. The A_1 test case reveals an amplitude interval of $5.27<\sqrt{\overline{u'^2}}/\sqrt{\overline{v'^2}}<12.20$, with amplitude of $\sqrt{\overline{u'^2}}/\sqrt{\overline{v'^2}}$ =6.93. The highest obtained value is at y=41.50 mm and the lowest value is at y=136.50 mm. Anisotropy oscillations are visible for all vertical profile. The A_1 test case interval is almost 87% of the B_1 test case interval. The B_1 test case presents generically higher anisotropy values.

For station x=295 mm, the B_1 test case present values within the $6.18<\sqrt{\overline{u'^2}}/\sqrt{\overline{v'^2}}<13.90$ interval, with amplitude of $\sqrt{\overline{u'^2}}/\sqrt{\overline{v'^2}}$ =7.72. The highest obtained value is at y=13.50 mm and the lowest value is at y=138.50 mm. Anisotropy oscillations are visible for all vertical profile. The A_1 test case reveals an amplitude interval of $5.37<\sqrt{\overline{u'^2}}/\sqrt{\overline{v'^2}}<11.40$. This interval shows amplitude of $\sqrt{\overline{u'^2}}/\sqrt{\overline{v'^2}}$ =6.03 for this test case. The highest obtained value is at y=41.50 mm and the lowest value is at y=136.50 mm. Anisotropy oscillations are visible for all vertical profile. The A_1 test case interval is almost 78% of the B_1 test case interval. The B_1 test case presents generically higher anisotropy values.

For station x=395 mm, the B_1 test case present values within the $6.74<\sqrt{\overline{u'^2}}/\sqrt{\overline{v'^2}}<13.90$ interval. The highest obtained value is at y=33.50 mm and the lowest value is at y=134.50 mm. This interval shows amplitude of $\sqrt{\overline{u'^2}}/\sqrt{\overline{v'^2}}$ =7.16. Anisotropy oscillations are visible for all vertical profile. The A_1 test case reveals an amplitude interval of $6.03<\sqrt{\overline{u'^2}}/\sqrt{\overline{v'^2}}<11.08$, with amplitude of $\sqrt{\overline{u'^2}}/\sqrt{\overline{v'^2}}$ =5.77. The highest obtained value is at y=61.50 and the lowest value is at y=146.50 mm. Anisotropy oscillations are visible for all vertical profile. The A_1 test case interval is almost 80% of the B_1 test case interval. The B_1 test case presents generically higher anisotropy values.

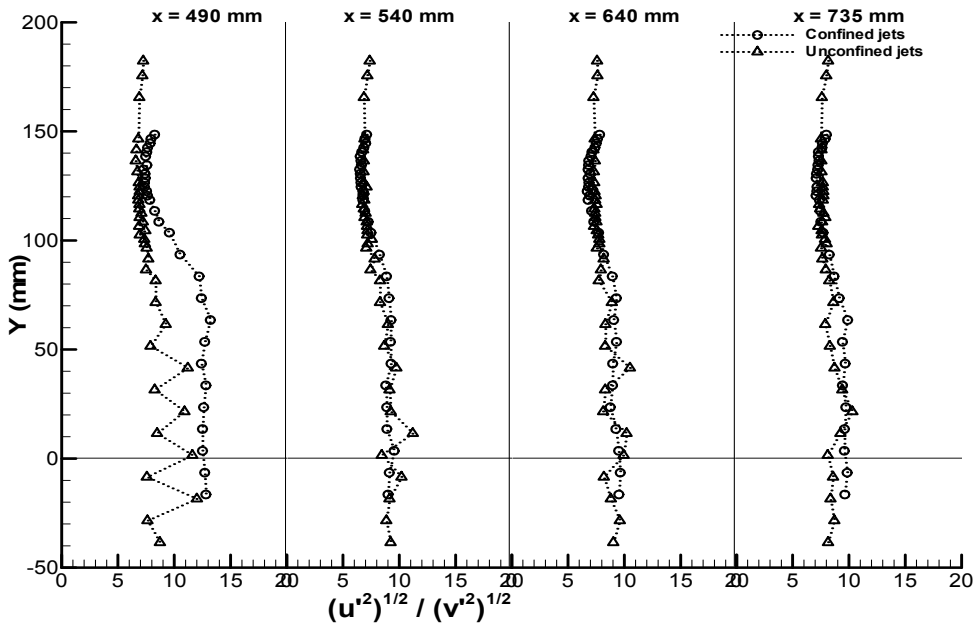

Figure 3.81. Vertical profiles of anisotropy for A_1 and B_1 test cases at stations x=490, 540, 640 and 735 mm.

Figure 3.81 shows vertical profiles of anisotropy for A_1 and B_1 test cases at stations x=490, 540, 640 and 735 mm and shows different anisotropy flow behaviours at station x=490 mm. At stations x=540, 640 and 735 mm the obtained results are tending to same values. For station x=490 mm, the B_1 test case present values within the $7.25<\sqrt{\overline{u}'^2}/\sqrt{\overline{v}'^2}<13.2$ interval, with amplitude of $\sqrt{\overline{u}'^2}/\sqrt{\overline{v}'^2}$ =5.95. The highest obtained value is at y=63.50 mm and the lowest value is at y=132.50 mm. Anisotropy oscillations are visible for all vertical profile. The A_1 test case reveals an amplitude interval of $6.57<\sqrt{\overline{u}'^2}/\sqrt{\overline{v}'^2}<11.6$, with amplitude of $\sqrt{\overline{u}'^2}/\sqrt{\overline{v}'^2}$ =5.03. The highest obtained value is at y=1.50 mm and the lowest value is at y=136.50 mm. Anisotropy oscillations are visible for all vertical profile. The A_1 test case interval is almost 84% of the B_1 test case interval. The B_1 test case presents generically higher anisotropy values.

For station x=540 mm, the B_1 test case present values within the $6.48<\sqrt{\overline{u}'^2}/\sqrt{\overline{v}'^2}<9.54$ interval. The highest obtained value is at y=3.50 mm and the lowest value is at y=132.50 mm. This interval shows amplitude of 3.06 for this test case. Anisotropy oscillations are very smooth for all vertical profile. The A_1 test case reveals an amplitude interval of $6.71<\sqrt{\overline{u}'^2}/\sqrt{\overline{v}'^2}<11.2$. This interval shows amplitude of $\sqrt{\overline{u}'^2}/\sqrt{\overline{v}'^2}$ =4.49. The highest obtained value is at y=11.50 mm and the lowest value is at y=116.50 mm. Anisotropy oscillations are also very smooth for all vertical profile. The A_1 test case interval is almost 147% of the B_1 test case interval. Both test cases present similar anisotropy values for the entire vertical profile.

For station x=640 mm, the B_1 test case present values within the $6.71<\sqrt{\overline{u}'^2}/\sqrt{\overline{v}'^2}<9.50$ interval. The highest obtained value is at y=3.50 mm and the lowest value is at y=122.50 mm.

This interval shows amplitude of $\sqrt{\overline{u'^2}}/\sqrt{\overline{v'^2}}$ =2.79 for this test case. Anisotropy oscillations are very smooth for all vertical profile. The A_1 test case reveals an amplitude interval of 7.26<$\sqrt{\overline{u'^2}}/\sqrt{\overline{v'^2}}$<10.50. This interval shows amplitude of $\sqrt{\overline{u'^2}}/\sqrt{\overline{v'^2}}$ =3.24. The highest obtained value is at y=41.50 mm and the lowest value is at y=141.50 mm. Anisotropy oscillations are also very smooth for all vertical profile. The A_1 test case interval is almost 116% of the B_1 test case interval. Both test cases present similar anisotropy values for the entire vertical profile.

For station x=735 mm, the B_1 test case present values within the 7.07<$\sqrt{\overline{u'^2}}/\sqrt{\overline{v'^2}}$<9.88 interval. The highest obtained value is at y=73.50 mm and the lowest value is at y=122.50 mm. This interval shows amplitude of $\sqrt{\overline{u'^2}}/\sqrt{\overline{v'^2}}$ $\sqrt{\overline{u'^2}}/\sqrt{\overline{v'^2}}$ =2.81 for this test case. Anisotropy oscillations are very smooth for all vertical profile. The A_1 test case reveals an amplitude interval of 7.35<$\sqrt{\overline{u'^2}}/\sqrt{\overline{v'^2}}$<10.3, with amplitude of $\sqrt{\overline{u'^2}}/\sqrt{\overline{v'^2}}$ =2.95. The highest obtained value is at y=21.50 mm and the lowest value is at y=116.50 mm. Anisotropy oscillations are also very smooth for all vertical profile. The A_1 test case interval is almost 105% of the B_1 test case interval. Both test cases present similar anisotropy values for the entire vertical profile.

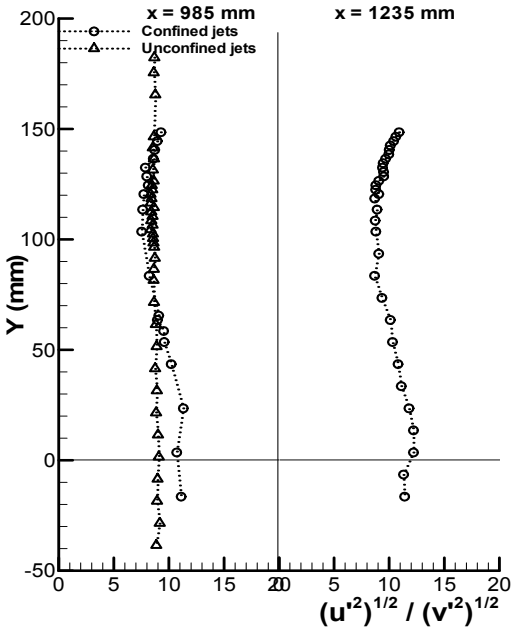

Figure 3.82. Vertical profiles of anisotropy for A_1 and B_1 test cases at stations x=985 and 1235 mm.

For station x=985 mm, Figure 3.82, the B_1 test case present values within the 7.52<$\sqrt{\overline{u'^2}}/\sqrt{\overline{v'^2}}$<11.3 interval. The highest obtained value is at y=23.50 mm and the lowest value is at y=113.50 mm. This interval shows amplitude of $\sqrt{\overline{u'^2}}/\sqrt{\overline{v'^2}}$ =3.78. Anisotropy oscillations are very smooth for all vertical profile. The A_1 test case reveals an amplitude interval of 8.34<$\sqrt{\overline{u'^2}}/\sqrt{\overline{v'^2}}$<9.08. This interval shows amplitude of $\sqrt{\overline{u'^2}}/\sqrt{\overline{v'^2}}$ =0.74 for this

test case. The highest obtained value is at y=1.50 mm and the lowest value is at y=104.50 mm. The graphic reveals practically a line segment for the anisotropy values. The A_1 test case interval is almost 19% of the B_1 test case interval. Both test cases present similar anisotropy values for the entire vertical profile.

For station x=1235 mm, the B_1 test case present values within the $8.67<\sqrt{\overline{u'^2}}/\sqrt{\overline{v'^2}}<12.2$ interval. The highest obtained value is at both y=3.50 mm and y=23.50 mm points. The lowest value is at y=83.50 mm. This interval shows amplitude of $\sqrt{\overline{u'^2}}/\sqrt{\overline{v'^2}}$ =3.53 for this test case. Anisotropy oscillations are very smooth for all vertical profile. The north values tend to become higher.

3.9.2. Unconfined A_2 and confined B_2 jets

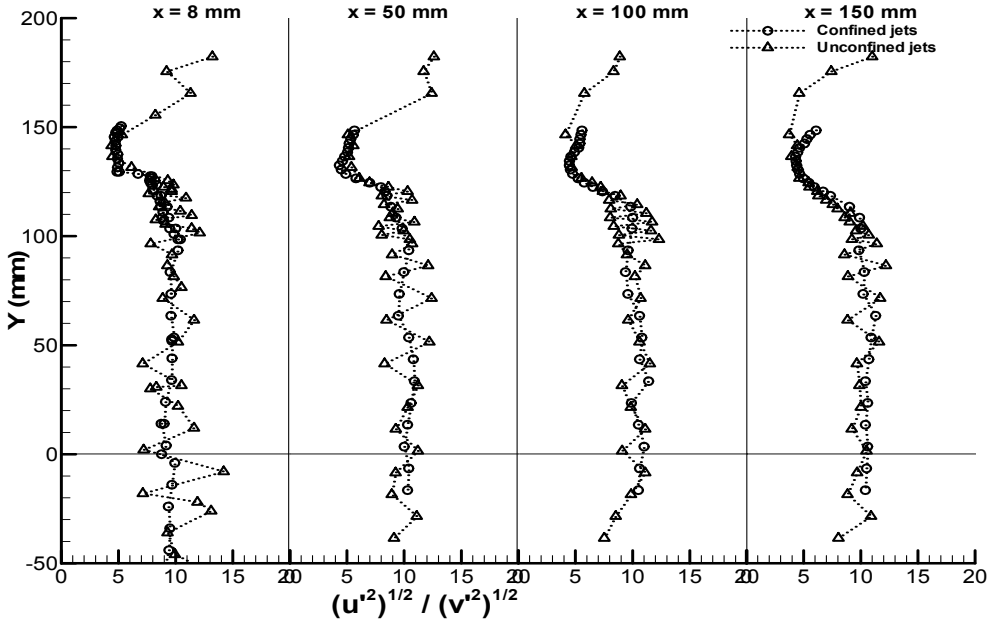

Figure 3.83. Vertical profiles of anisotropy for A_2 and B_2 test cases at stations x=8, 50, 100 and 150 mm.

Figure 3.83 shows vertical profiles of anisotropy for A_2 and B_2 test cases at stations x=8, 50, 100 and 150 mm. For station x=8 mm, the B_2 test case present values within the $4.63<\sqrt{\overline{u'^2}}/\sqrt{\overline{v'^2}}<10.4$ interval. The highest obtained value is at y=98.50 mm and the lowest value is at y=147.50 mm. This interval shows amplitude of $\sqrt{\overline{u'^2}}/\sqrt{\overline{v'^2}}$ =5.77 for this test case. Anisotropy irregular oscillations are visible for all vertical profile. Related with the B_1 test case at x=8 mm the interval decreased nearly 23% from $\sqrt{\overline{u'^2}}/\sqrt{\overline{v'^2}}$ =7.45 to $\sqrt{\overline{u'^2}}/\sqrt{\overline{v'^2}}$ =5.77. The A_2 test case reveals an amplitude interval of $4.41<\sqrt{\overline{u'^2}}/\sqrt{\overline{v'^2}}<12.1$, with amplitude of $\sqrt{\overline{u'^2}}/\sqrt{\overline{v'^2}}$ =7.69. The highest obtained value is at y=103.50 mm and the lowest value is at y=146.50 mm. Anisotropy irregular oscillations are visible for all vertical profile. Related with

the A_1 test case at x=8 the interval increased nearly 60% from $\sqrt{\overline{u'^2}}/\sqrt{\overline{v'^2}}$ =4.8 to $\sqrt{\overline{u'^2}}/\sqrt{\overline{v'^2}}$ =7.69. The A_2 test case interval is almost 133% of the B_2 test case interval.

For station x=50 mm, the B_2 test case present values within the 4.34<$\sqrt{\overline{u'^2}}/\sqrt{\overline{v'^2}}$<10.9 interval. The highest obtained value is at y=33.50 mm and the lowest value is at y=134.50 mm. This interval shows amplitude of $\sqrt{\overline{u'^2}}/\sqrt{\overline{v'^2}}$ =6.56 for this test case. Anisotropy irregular oscillations are visible for all vertical profile. Related with the B_1 test case at x=50 mm the interval decreased nearly 18% from $\sqrt{\overline{u'^2}}/\sqrt{\overline{v'^2}}$ =7.93 to $\sqrt{\overline{u'^2}}/\sqrt{\overline{v'^2}}$ =6.56. The A_2 test case reveals an amplitude interval of 5.09<$\sqrt{\overline{u'^2}}/\sqrt{\overline{v'^2}}$<12.40. This interval shows amplitude of $\sqrt{\overline{u'^2}}/\sqrt{\overline{v'^2}}$ =7.31 for this test case. The highest obtained value is at y=81.50 mm and the lowest value is at y=146.50 mm. Anisotropy irregular oscillations are visible for all vertical profile. Related with the A_1 test case at x=50 mm the interval increased nearly 33% from $\sqrt{\overline{u'^2}}/\sqrt{\overline{v'^2}}$ =5.48 to $\sqrt{\overline{u'^2}}/\sqrt{\overline{v'^2}}$ =7.31. The A_2 test case interval is almost 111% of the B_2 test case interval.

For station x=100 mm, the B_2 test case present values within the 4.47<$\sqrt{\overline{u'^2}}/\sqrt{\overline{v'^2}}$<11.4 interval. The highest obtained value is at y=33.50 mm and the lowest value is at y=132.50 mm. This interval shows amplitude of $\sqrt{\overline{u'^2}}/\sqrt{\overline{v'^2}}$ =6.93 for this test case. Anisotropy irregular oscillations are visible for all vertical profile. Related with the B_1 test case at x=100 mm the interval decreased nearly 12% from $\sqrt{\overline{u'^2}}/\sqrt{\overline{v'^2}}$ =7.81 to $\sqrt{\overline{u'^2}}/\sqrt{\overline{v'^2}}$ =6.93. The A_2 test case reveals an amplitude interval of 4.65<$\sqrt{\overline{u'^2}}/\sqrt{\overline{v'^2}}$<12.30. This interval shows amplitude of $\sqrt{\overline{u'^2}}/\sqrt{\overline{v'^2}}$ =7.65 for this test case. The highest obtained value is at y=86.50 mm and the lowest value is at y=141.50 mm. Anisotropy irregular oscillations are visible for all vertical profile. Related with the A_1 test case at x=100 mm the interval increased nearly 22% from $\sqrt{\overline{u'^2}}/\sqrt{\overline{v'^2}}$ =6.27 to $\sqrt{\overline{u'^2}}/\sqrt{\overline{v'^2}}$ =7.65. The A_2 test case interval is almost 110% of the B_2 test case interval.

For station x=150 mm the B_2 test case present values within the 4.30<$\sqrt{\overline{u'^2}}/\sqrt{\overline{v'^2}}$<11.30 interval. The highest obtained value is at y=53.50 mm and the lowest value is at y=136.50 mm. This interval shows amplitude of $\sqrt{\overline{u'^2}}/\sqrt{\overline{v'^2}}$ =7.00 for this test case. Anisotropy irregular oscillations are visible for all vertical profile. Related with the B_1 test case at x=150 mm the interval decreased nearly 15% from $\sqrt{\overline{u'^2}}/\sqrt{\overline{v'^2}}$ =8.28 to $\sqrt{\overline{u'^2}}/\sqrt{\overline{v'^2}}$ =7.00. The A_2 test case reveals an amplitude interval of 4.44<$\sqrt{\overline{u'^2}}/\sqrt{\overline{v'^2}}$<12.20. This interval shows amplitude of 7.76 for this test case. The highest obtained value is at y=86.50 mm and the lowest value is at y=141.50 mm. Anisotropy irregular oscillations are visible for all vertical profile. Related with the A_1 test case at x=150 mm the interval is similar (from $\sqrt{\overline{u'^2}}/\sqrt{\overline{v'^2}}$ =7.65 to $\sqrt{\overline{u'^2}}/\sqrt{\overline{v'^2}}$ =7.76). The A_2 test case interval is almost 110% of the B_2 test case interval.

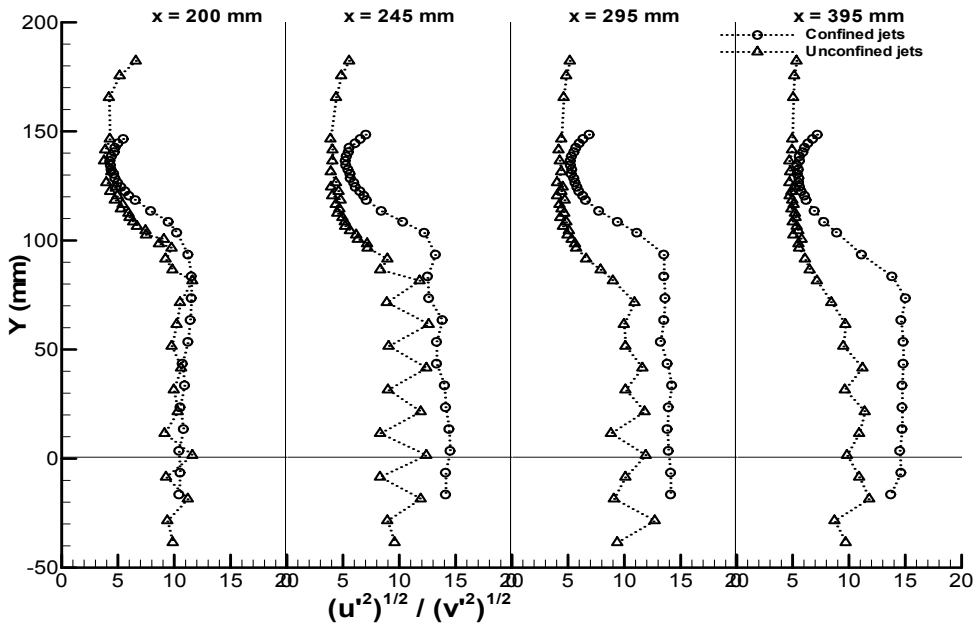

Figure 3.84. Vertical profiles of anisotropy for A_2 and B_2 test cases at stations x=200, 245, 295 and 395 mm.

Figure 3.84 shows vertical profiles of anisotropy for A_2 and B_2 test cases at stations x=200, 245, 295 and 395 mm. For station x=200 mm, the B_2 test case present values within the $4.28<\sqrt{\overline{u'^2}}/\sqrt{\overline{v'^2}}<11.50$ interval. The highest obtained value is at both y=73.50 mm and y=83.50 mm points. The lowest value is at y=136.50 mm. This interval shows amplitude of $\sqrt{\overline{u'^2}}/\sqrt{\overline{v'^2}}$ =7.22 for this test case. Related with the B_1 test case at x=200 mm the interval decreased nearly 10% from $\sqrt{\overline{u'^2}}/\sqrt{\overline{v'^2}}$ =8.00 to $\sqrt{\overline{u'^2}}/\sqrt{\overline{v'^2}}$ =7.22. Smallest values are at north for both test cases and highest are within the 0<y<100 mm region. The A_2 test case reveals an amplitude interval of $3.76<\sqrt{\overline{u'^2}}/\sqrt{\overline{v'^2}}<11.6$. This interval shows amplitude of $\sqrt{\overline{u'^2}}/\sqrt{\overline{v'^2}}$ =7.84 for this test case. The highest obtained value is at y=81.50 mm and the lowest value is at y=136.50 mm. Related with the A_1 test case at x=200 mm the interval is similar (from $\sqrt{\overline{u'^2}}/\sqrt{\overline{v'^2}}$ =7.63 to $\sqrt{\overline{u'^2}}/\sqrt{\overline{v'^2}}$ =7.84). The A_2 test case interval is almost 108% of the B_2 test case interval. Graphic reveals that the obtained values for both test cases at this station, tend to same pattern.

For station x=245 mm, the B_2 test case present values within the $5.20<\sqrt{\overline{u'^2}}/\sqrt{\overline{v'^2}}<14.50$ interval. The highest obtained value is at y=3.50 mm and the lowest value is at y=136.50 mm. This interval shows amplitude of $\sqrt{\overline{u'^2}}/\sqrt{\overline{v'^2}}$ =9.30 for this test case. Related with the B_1 test case at x=245 mm the interval increased nearly 16% from $\sqrt{\overline{u'^2}}/\sqrt{\overline{v'^2}}$ =8.00 to $\sqrt{\overline{u'^2}}/\sqrt{\overline{v'^2}}$ =9.30. Smallest values are at north for both test cases and highest are within the 0<y<100 mm region. The confined jets test case presents generically higher values than the unconfined test case. The A_2 test case reveals an amplitude interval of $3.88<\sqrt{\overline{u'^2}}/\sqrt{\overline{v'^2}}<12.6$. This interval shows amplitude of $\sqrt{\overline{u'^2}}/\sqrt{\overline{v'^2}}$ =8.72 for this test case. The

highest obtained value is at y=61.50 mm and the lowest value is at y=146.50 mm. Related with the A_1 test case at same station x=245 mm, the interval increased nearly 26% from $\sqrt{\overline{u'^2}}/\sqrt{\overline{v'^2}}$ =6.93 to $\sqrt{\overline{u'^2}}/\sqrt{\overline{v'^2}}$ =8.72. The A_2 test case interval is almost 93% of the B_2 test case interval.

For station x=295 mm, the B_2 test case present values within the $5.20<\sqrt{\overline{u'^2}}/\sqrt{\overline{v'^2}}<14.20$ interval. The highest obtained value is at y=33.50 mm and the lowest value is at y=136.50 mm. This interval shows amplitude of $\sqrt{\overline{u'^2}}/\sqrt{\overline{v'^2}}$ =9.0. Related with the B_1 test case at x=295 mm the interval increased nearly 16% from $\sqrt{\overline{u'^2}}/\sqrt{\overline{v'^2}}$ =7.72 to $\sqrt{\overline{u'^2}}/\sqrt{\overline{v'^2}}$ =9.00. Such as verified at previous station, the smallest values are at north for both test cases and highest are within the 0<y<100 mm region. The confined jets test case presents generically higher values than the unconfined test case. The A_2 test case reveals an amplitude interval of $4.03<\sqrt{\overline{u'^2}}/\sqrt{\overline{v'^2}}<11.9$. This interval shows amplitude of $\sqrt{\overline{u'^2}}/\sqrt{\overline{v'^2}}$ =7.87 for this test case. The highest obtained value is at y=1.50 and the lowest value is at both y=126.50 mm and y=120.50 mm points. Related with the A_1 test case at x=295 mm the interval increased nearly 30% from $\sqrt{\overline{u'^2}}/\sqrt{\overline{v'^2}}$ =6.03 to $\sqrt{\overline{u'^2}}/\sqrt{\overline{v'^2}}$ =7.87. The A_2 test case interval is almost 87% of the B_2 test case interval.

For station x=395 mm, the B_2 test case present values within the $5.37<\sqrt{\overline{u'^2}}/\sqrt{\overline{v'^2}}<15.0$ interval. The highest obtained value is at y=73.50 mm and the lowest value is at y=136.50 mm. This interval shows amplitude of $\sqrt{\overline{u'^2}}/\sqrt{\overline{v'^2}}$ =9.63 for this test case. Related with the B_1 test case at x=395 mm the interval increased nearly 35% from $\sqrt{\overline{u'^2}}/\sqrt{\overline{v'^2}}$ =7.16 to $\sqrt{\overline{u'^2}}/\sqrt{\overline{v'^2}}$ =9.63. Such as verified at previous station, the smallest values are at north for both test cases and highest are within the 0<y<100 mm region. The confined jets test case presents generically higher values than the unconfined test case. The A_2 test case reveals an amplitude interval of $4.70<\sqrt{\overline{u'^2}}/\sqrt{\overline{v'^2}}<11.4$. This interval shows amplitude of $\sqrt{\overline{u'^2}}/\sqrt{\overline{v'^2}}$ =6.7 for this test case. The highest obtained value is at y=21.50 mm and the lowest value is at y=136.50 mm. Related with the A_1 test case at x=395 mm the interval increased nearly 16% from$\sqrt{\overline{u'^2}}/\sqrt{\overline{v'^2}}$ = 5.77 to $\sqrt{\overline{u'^2}}/\sqrt{\overline{v'^2}}$ =6.7. The A_2 test case interval is almost 70% of the B_2 test case interval.

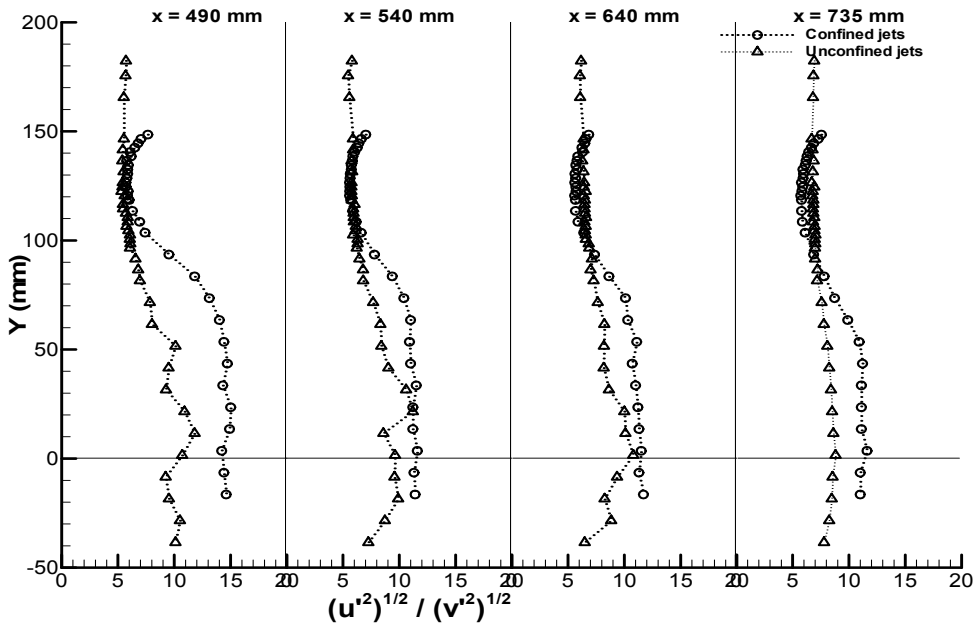

Figure 3.85. Vertical profiles of anisotropy for A_2 and B_2 test cases at stations x=495, 540, 640 and 735 mm.

Figure 3.85 shows vertical profiles of anisotropy for A_2 and B_2 test cases at stations x=495, 540, 640 and 735 mm. For station x=490 mm, the B_2 test case present values within the 5.70<$\sqrt{\overline{u'^2}}/\sqrt{\overline{v'^2}}$<15.0 interval, with amplitude of $\sqrt{\overline{u'^2}}/\sqrt{\overline{v'^2}}$=9.30. The highest obtained value is at y=23.50 mm and the lowest value is at y=128.50 mm. Related with the B_1 test case at x=490 mm the interval increased nearly 56% from $\sqrt{\overline{u'^2}}/\sqrt{\overline{v'^2}}$ =5.95 to $\sqrt{\overline{u'^2}}/\sqrt{\overline{v'^2}}$ =9.30. Such as verified at previous station, the smallest values are at north for both test cases and highest are within the 0<y<100 mm region. The confined jets test case presents generically higher values than the unconfined test case. The A_2 test case reveals an amplitude interval of 5.38<$\sqrt{\overline{u'^2}}/\sqrt{\overline{v'^2}}$<11.8. This interval shows amplitude of $\sqrt{\overline{u'^2}}/\sqrt{\overline{v'^2}}$ =6.42 for this test case. The highest obtained value is at y=11.50 and the lowest value is at y=141.50 mm. Related with the A_1 test case at x=490 mm, the interval increased nearly 27% from $\sqrt{\overline{u'^2}}/\sqrt{\overline{v'^2}}$ =5.03 to $\sqrt{\overline{u'^2}}/\sqrt{\overline{v'^2}}$ =6.42. The A_2 test case interval is almost 69% of the B_2 test case interval.

For station x=540 mm, the B_2 test case present values within the 5.49<$\sqrt{\overline{u'^2}}/\sqrt{\overline{v'^2}}$<11.6 interval. The highest obtained value is at y=3.50 mm and the lowest value is at y=122.50 mm. This interval shows amplitude of $\sqrt{\overline{u'^2}}/\sqrt{\overline{v'^2}}$ =6.01 for this test case. Related with the B_1 test case at x=540 mm the interval increased nearly 96% from $\sqrt{\overline{u'^2}}/\sqrt{\overline{v'^2}}$ =3.06 to $\sqrt{\overline{u'^2}}/\sqrt{\overline{v'^2}}$ =6.01. Such as verified at previous station, the smallest values are at north for both test cases and highest are within the 0<y<100 mm region. The confined jets test case presents generically higher values than unconfined test case. The A_2 test case reveals an amplitude interval of 5.45<$\sqrt{\overline{u'^2}}/\sqrt{\overline{v'^2}}$<11.2. This interval shows amplitude of $\sqrt{\overline{u'^2}}/\sqrt{\overline{v'^2}}$ =5.75 for this test case. The highest obtained value is at y=21.50 mm and the lowest value is at y=175.50 mm. Related

with the A_1 test case at x=540 mm the interval increased nearly 28% from $\sqrt{\overline{u'^2}}/\sqrt{\overline{v'^2}}$ =4.49 to $\sqrt{\overline{u'^2}}/\sqrt{\overline{v'^2}}$ =5.75. The A_2 test case interval is almost 95% of the B_2 test case interval.

For station x=640 mm the B_2 test case present values within the 5.60<$\sqrt{\overline{u'^2}}/\sqrt{\overline{v'^2}}$<11.5 interval. The highest obtained value is at y=3.50 mm and the lowest value is at y=126.50 mm. This interval shows amplitude of $\sqrt{\overline{u'^2}}/\sqrt{\overline{v'^2}}$ =5.9 for this test case. Related with the B_1 test case at x=640 mm the interval increased nearly 112% from $\sqrt{\overline{u'^2}}/\sqrt{\overline{v'^2}}$ =2.79 to $\sqrt{\overline{u'^2}}/\sqrt{\overline{v'^2}}$ =5.9. The A_2 test case reveals an amplitude interval of 6.05<$\sqrt{\overline{u'^2}}/\sqrt{\overline{v'^2}}$<10.8. This interval shows amplitude of $\sqrt{\overline{u'^2}}/\sqrt{\overline{v'^2}}$ =4.75 for this test case. The highest obtained value is at y=1.50 mm and the lowest value is at y=175.50 mm. Related with the A_1 test case at x=640 mm the interval increased nearly 46% from $\sqrt{\overline{u'^2}}/\sqrt{\overline{v'^2}}$ =3.24 to $\sqrt{\overline{u'^2}}/\sqrt{\overline{v'^2}}$ =4.75. The A_2 test case interval is almost 81% of the B_2 test case interval.

For station x=735 mm, the B_2 test case present values within the 5.72<$\sqrt{\overline{u'^2}}/\sqrt{\overline{v'^2}}$<11.6 interval. The highest obtained value is at y=3.50 mm and the lowest value is at y=120.50 mm. This interval shows amplitude of $\sqrt{\overline{u'^2}}/\sqrt{\overline{v'^2}}$ =5.88 for this test case. Related with the B_1 test case at x=735 mm the interval increased nearly 109% from $\sqrt{\overline{u'^2}}/\sqrt{\overline{v'^2}}$ =2.81 to $\sqrt{\overline{u'^2}}/\sqrt{\overline{v'^2}}$ =5.88. The A_2 test case reveals an amplitude interval of 6.68<$\sqrt{\overline{u'^2}}/\sqrt{\overline{v'^2}}$<8.81. This interval shows amplitude of $\sqrt{\overline{u'^2}}/\sqrt{\overline{v'^2}}$ =2.13 for this test case. The highest obtained value is at y=1.50 mm and the lowest value is at y=146.50 mm. Related with the A_1 test case at x=735 mm the interval decreased nearly 28% from $\sqrt{\overline{u'^2}}/\sqrt{\overline{v'^2}}$ =2.95 to $\sqrt{\overline{u'^2}}/\sqrt{\overline{v'^2}}$ =2.13. The A_2 test case interval is almost 36% of the B_2 test case interval. The unconfined test case reveals practically a vertical line segment.

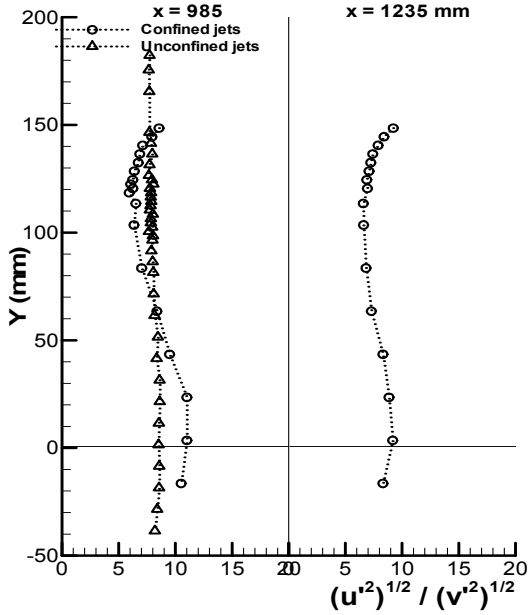

Figure 3.86. Vertical profiles of anisotropy for A_2 and B_2 test cases at stations x=985 and 1235 mm.

For station x=985 mm, (Figure 3.86) the B_2 test case present values within the $5.92<\sqrt{\overline{u'^2}}/\sqrt{\overline{v'^2}}<11.0$ interval. The highest obtained value is at y=3.50 mm and the lowest value is at y=120.50 mm. This interval shows amplitude of $\sqrt{\overline{u'^2}}/\sqrt{\overline{v'^2}}$ =5.08 for this test case. Related with the B_1 test case at x=985 mm the interval increased nearly 34% from $\sqrt{\overline{u'^2}}/\sqrt{\overline{v'^2}}$ =3.78 to $\sqrt{\overline{u'^2}}/\sqrt{\overline{v'^2}}$ =5.08. The A_2 test case reveals an amplitude interval of $7.67<\sqrt{\overline{u'^2}}/\sqrt{\overline{v'^2}}<8.62$. This interval shows amplitude of $\sqrt{\overline{u'^2}}/\sqrt{\overline{v'^2}}$ =0.95 for this test case. The highest obtained value is at y=21.50 mm and the lowest value is at y=100.50 mm. Related with the A_1 test case at x=985 mm the interval increased nearly 28% from $\sqrt{\overline{u'^2}}/\sqrt{\overline{v'^2}}$ =0.74 to $\sqrt{\overline{u'^2}}/\sqrt{\overline{v'^2}}$ =0.95. The A_2 test case interval is almost 18% of the B_2 test case interval. The unconfined test case reveals practically a vertical line segment.

For station x=1235 mm the B_2 test case present values within the $6.58<\sqrt{\overline{u'^2}}/\sqrt{\overline{v'^2}}<9.48$ interval. The highest obtained value is at y=148.50 mm and the lowest value is at y=120.50 mm. This interval shows amplitude of $\sqrt{\overline{u'^2}}/\sqrt{\overline{v'^2}}$ =2.90 for this test case. Related with the B_1 test case at x=1235 mm the interval decreased nearly 18% from $\sqrt{\overline{u'^2}}/\sqrt{\overline{v'^2}}$ =3.53 to $\sqrt{\overline{u'^2}}/\sqrt{\overline{v'^2}}$ =2.90.

For all test cases A_1, A_2, B_1 and B_2 it is verified that the flow has a completely anisotropic behaviour.

3.9.3. Convergent 11º C_1 and convergent 22º D_1 jets

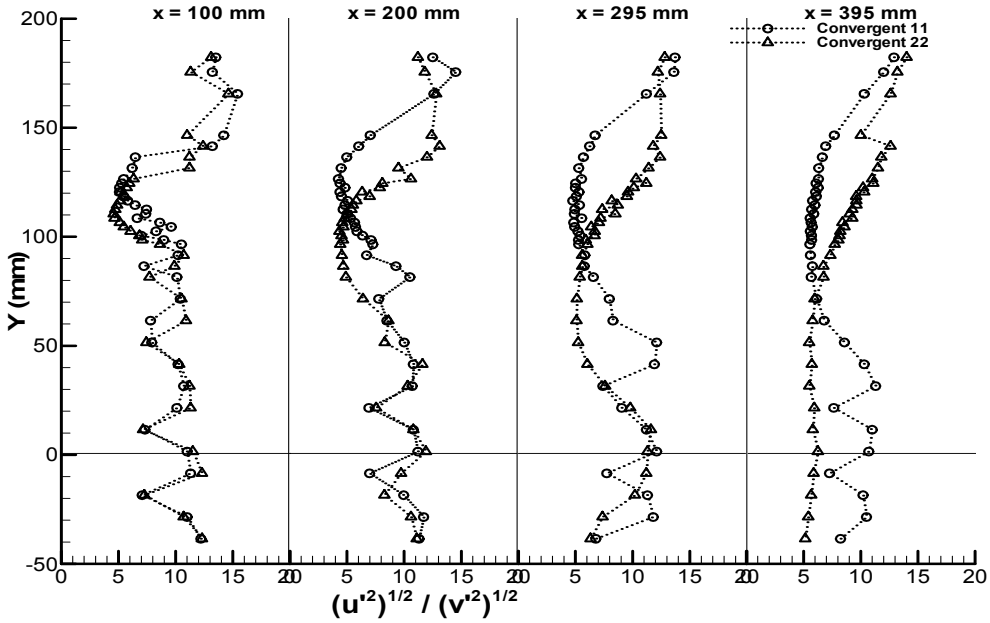

Figure 3.87. Vertical profiles of anisotropy for C_1 and D_1 test cases at stations x=100, 200, 295 and 395 mm.

Figure 3.87 shows vertical profiles of anisotropy for C_1 and D_1 test cases at stations x=100, 200, 295 and 395 mm. For station x=100 mm both test cases C_1 and D_1 all values present a constant oscillation between neighbouring points. For this station both test cases present similar anisotropy oscillations. The C_1 test case reveals values within $5.08<\sqrt{\overline{u'^2}}/\sqrt{\overline{v'^2}}<15.40$ which means an amplitude of $\sqrt{\overline{u'^2}}/\sqrt{\overline{v'^2}}$ =10.32. The highest obtained value is at y=165.50 mm and the lowest value is at y=120.50 mm. Lowest values are at y=120 mm neighbourhoods and highest values are at north points. The D_1 test case reveals values within $4.59<\sqrt{\overline{u'^2}}/\sqrt{\overline{v'^2}}<14.60$ which means an amplitude of $\sqrt{\overline{u'^2}}/\sqrt{\overline{v'^2}}$ =10.01 for this test case, similar to the C_1 test case for same station. These amplitudes are much higher when compared to A_1 and B_1 test cases, respectively $\sqrt{\overline{u'^2}}/\sqrt{\overline{v'^2}}$ =6.27 and $\sqrt{\overline{u'^2}}/\sqrt{\overline{v'^2}}$ =7.81 and also much higher when compared to A_2 and B_2 test cases, respectively $\sqrt{\overline{u'^2}}/\sqrt{\overline{v'^2}}$ =7.65 and $\sqrt{\overline{u'^2}}/\sqrt{\overline{v'^2}}$ =6.93. The highest obtained value is at y=165.50 mm and the lowest value is at y=110.50 mm. Lowest values are at y=120 mm neighbourhoods and highest values are at north points.

For station x=200 mm the C_1 test case present values within the $4.26<\sqrt{\overline{u'^2}}/\sqrt{\overline{v'^2}}<14.50$ interval. The highest obtained value is at y=175.50 mm and the lowest value is at y=126.50 mm. This interval shows amplitude of $\sqrt{\overline{u'^2}}/\sqrt{\overline{v'^2}}$ =10.24. Anisotropy oscillations are very high for all vertical profile. The D_1 test case reveals an amplitude interval of $4.34<\sqrt{\overline{u'^2}}/\sqrt{\overline{v'^2}}<13.10$. This interval shows amplitude of $\sqrt{\overline{u'^2}}/\sqrt{\overline{v'^2}}$ =8.76 for this test case. The highest obtained value is at y=136.50 mm and the lowest value is at y=162.50 mm. Anisotropy oscillations are also very high for all vertical profile. The C_1 test case interval is almost 116% of the D_1 test case interval. The lowest points observed for both test cases, are present at the jets intersection zone.

For station x=295 mm, the C_1 test case reveals values within the $4.85<\sqrt{\overline{u'^2}}/\sqrt{\overline{v'^2}}<13.70$ interval. The highest obtained value is at y=182.25 mm and the lowest value is at y=106.50 mm. This interval shows amplitude of $\sqrt{\overline{u'^2}}/\sqrt{\overline{v'^2}}$ =8.85. Anisotropy oscillations are very high for all vertical profile. The D_1 test case reveals an amplitude interval of $5.09<\sqrt{\overline{u'^2}}/\sqrt{\overline{v'^2}}<12.08$. This interval shows amplitude of $\sqrt{\overline{u'^2}}/\sqrt{\overline{v'^2}}$ =7.71. The highest obtained value is at y=182.25 mm and the lowest value is at y=71.50 mm. Anisotropy oscillations are also very high for all vertical profile. The C_1 test case interval is almost 113% of the D_1 test case interval. The lowest points observed for both test cases, are present at the jets intersection zone.

For station x=395 mm the C_1 test case present values within the $5.55<\sqrt{\overline{u'^2}}/\sqrt{\overline{v'^2}}<12.90$ interval. The highest obtained value is at y=182.25 mm and the lowest value is at y=96.50 mm. This interval shows amplitude of $\sqrt{\overline{u'^2}}/\sqrt{\overline{v'^2}}$ =7.35 for this test case. Anisotropy oscillations are very high for all vertical profile. The D_1 test case reveals an amplitude interval of $5.49<\sqrt{\overline{u'^2}}/\sqrt{\overline{v'^2}}<14.00$. This interval shows amplitude of $\sqrt{\overline{u'^2}}/\sqrt{\overline{v'^2}}$ =8.51 for this test case. The highest obtained value is at y=182.25 mm and the lowest value is at y=51.50

mm. Anisotropy oscillations are also very high for all vertical profile. The C_1 test case interval is almost 85% of the D_1 test case interval. For y<130 mm the D_1 test case practically reveals a line segment at the region. C_1 test case reveals higher values practically for all the vertical profile.

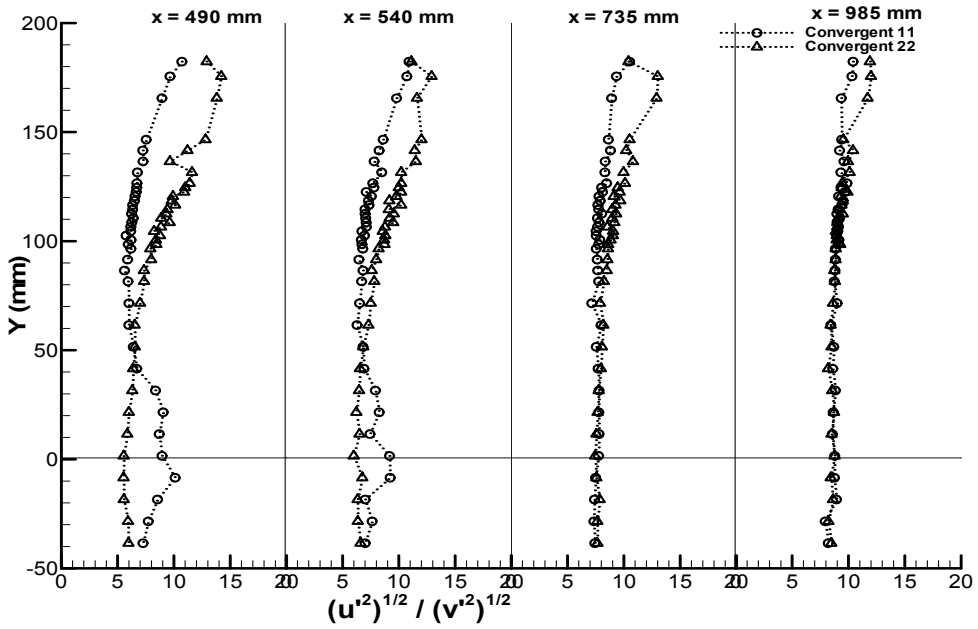

Figure 3.88. Vertical profiles of anisotropy for C_1 and D_1 test cases at stations x=490, 540, 735 and 985 mm.

Figure 3.88 shows vertical profiles of anisotropy for C_1 and D_1 test cases at stations x=490, 540, 735 and 985 mm. For station x=490 mm the C_1 test case present values within the $5.61<\sqrt{\overline{u'^2}}/\sqrt{\overline{v'^2}}<10.70$ interval. The highest obtained value is at y=182.25 mm and the lowest value is at y=86.50 mm. This interval shows amplitude of $\sqrt{\overline{u'^2}}/\sqrt{\overline{v'^2}}$ =5.09 for this test case. Anisotropy oscillations are very high for all vertical profile. The D_1 test case reveals an amplitude interval of $5.54<\sqrt{\overline{u'^2}}/\sqrt{\overline{v'^2}}<14.2$. This interval shows amplitude of $\sqrt{\overline{u'^2}}/\sqrt{\overline{v'^2}}$ =8.66 for this test case. The highest obtained value is at y=175.5 mm and the lowest value is at y=1.50 mm. Anisotropy oscillations are also very high for all vertical profile. The C_1 test case interval is almost 60% of the D_1 test case interval. For y<130 mm the D_1 test case practically reveals a line segment at the region. C_1 test case reveals higher values practically for all the vertical profile.

For station x=540 mm the C_1 test case present values within the $6.28<\sqrt{\overline{u'^2}}/\sqrt{\overline{v'^2}}<10.90$ interval. The highest obtained value is at y=182.25 mm and the lowest value is at y=61.50 mm. This interval shows amplitude of $\sqrt{\overline{u'^2}}/\sqrt{\overline{v'^2}}$ =4.62 for this test case. Anisotropy oscillations are high for all vertical profile. The D_1 test case reveals an amplitude interval of $5.99<\sqrt{\overline{u'^2}}/\sqrt{\overline{v'^2}}<12.9$. This interval shows amplitude of $\sqrt{\overline{u'^2}}/\sqrt{\overline{v'^2}}$ =6.91 for this test case. The highest obtained value is at y=175.5 mm and the lowest value is at y=1.50 mm. Anisotropy

oscillations are also high for all vertical profile. The C_1 test case interval is almost 67% of the D_1 test case interval. For y<130 mm the D_1 test case practically reveals a line segment at the region. C_1 test case reveals higher $\sqrt{\overline{u'^2}}/\sqrt{\overline{v'^2}}$ values practically for all the vertical profile.

For station x=735 mm the C_1 test case present values within the $7.15<\sqrt{\overline{u'^2}}/\sqrt{\overline{v'^2}}<10.50$ interval. The highest obtained value is at y=182.25 mm and the lowest value is at y=81.50 mm. This interval shows amplitude of $\sqrt{\overline{u'^2}}/\sqrt{\overline{v'^2}}$ =3.35 for this test case. The D_1 test case reveals an amplitude interval of $7.45<\sqrt{\overline{u'^2}}/\sqrt{\overline{v'^2}}<13.6$. This interval shows amplitude of $\sqrt{\overline{u'^2}}/\sqrt{\overline{v'^2}}$ =6.15 for this test case. The highest obtained value is at y=175.5 mm and the lowest value is at y=1.50 mm. The C_1 test case interval is almost 67% of the D_1 test case interval. For y<130 mm the D_1 test case practically reveals a line segment at the region. C_1 test case reveals higher values practically for all the vertical profile. From 0<y<70 mm both test cases presents identical values.

For station x=985 mm the C_1 test case present values within the $8.42<\sqrt{\overline{u'^2}}/\sqrt{\overline{v'^2}}<10.40$ interval. The highest obtained value is at y=182.25 mm and the lowest value is at y=61.50 mm. This interval shows amplitude of $\sqrt{\overline{u'^2}}/\sqrt{\overline{v'^2}}$ =1.98 for this test case. The D_1 test case reveals an amplitude interval of $8.18<\sqrt{\overline{u'^2}}/\sqrt{\overline{v'^2}}<12.0$. This interval shows amplitude of $\sqrt{\overline{u'^2}}/\sqrt{\overline{v'^2}}$ =3.82 for this test case. The highest obtained value is at y=175.5 mm and the lowest value is at y=41.50 mm. The C_1 test case interval is almost 52% of the D_1 test case interval. From 0<y<150 mm both test cases presents identical values.

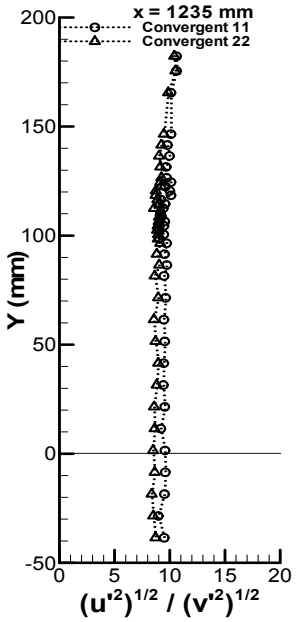

Figure 3.89. Vertical profiles of anisotropy for C_1 and D_1 test cases at stations station x=1235 mm.

For station x=1235 mm (Figure 3.89) the C_1 test case present values within the $9.05<\sqrt{\overline{u'^2}}/\sqrt{\overline{v'^2}}<10.60$ interval. The highest obtained value is at y=182.25 mm and the lowest value is at y=102.50 mm. This interval shows amplitude of $\sqrt{\overline{u'^2}}/\sqrt{\overline{v'^2}}$ =1.55 for this test case. The D_1 test case reveals an amplitude interval of $8.48<\sqrt{\overline{u'^2}}/\sqrt{\overline{v'^2}}<10.5$. This interval shows amplitude of $\sqrt{\overline{u'^2}}/\sqrt{\overline{v'^2}}$ =2.02 for this test case. The highest obtained value is at y=175.5 mm and the lowest value is at y=1.50 mm. The C_1 test case interval is almost 76% of the D_1 test case interval. For both test cases, the vertical profile shows similar values. Graphic reveals two vertical line segments at the 9 neighbourhoods.

3.9.4. Convergent 11° C_2 and convergent 22° D_2 jets

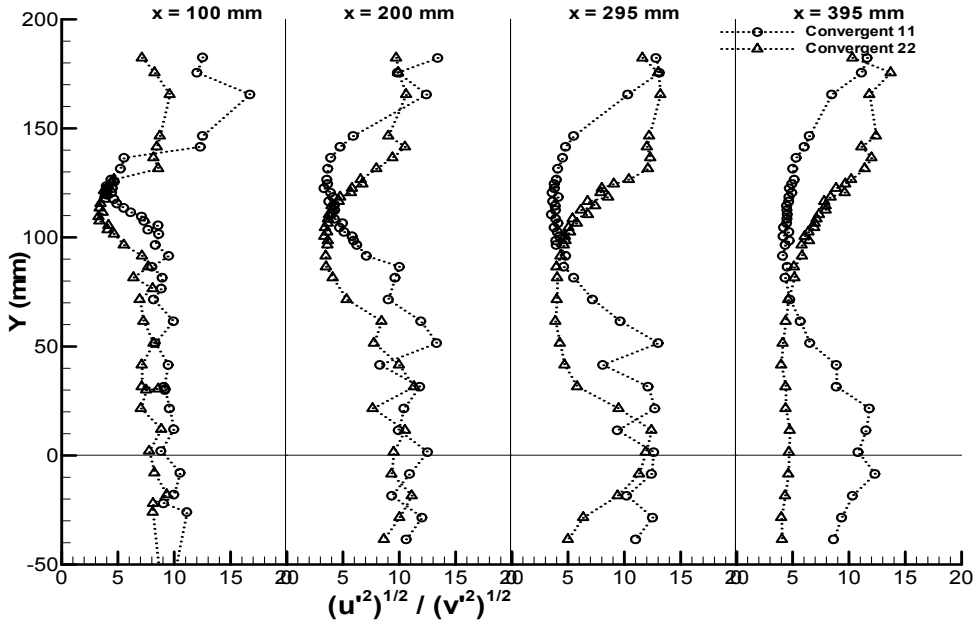

Figure 3.90. Vertical profiles of anisotropy for C_2 and D_2 test cases at stations x=100, 200, 295 and 395 mm.

Figure 3.90 shows vertical profiles of anisotropy for C_2 and D_2 test cases at stations x=100, 200, 295 and 395 mm. For station x=100 mm for both test cases C_2 and D_2 all values present a constant oscillation between neighbouring points. The C_2 test case reveals values within $3.91<\sqrt{\overline{u'^2}}/\sqrt{\overline{v'^2}}<16.7$ which means an amplitude of $\sqrt{\overline{u'^2}}/\sqrt{\overline{v'^2}}$ =12.79 for this test case. This amplitude is the highest verified in this work. The highest (y=165.50 mm) and the lowest (y=121.50 mm) anisotropy values of the entire work is verified at this station for C_1 test case. Lowest values are at the jets intersection for both test cases. Related with the C_1 test case at x=100 mm the interval increased nearly 24% from $\sqrt{\overline{u'^2}}/\sqrt{\overline{v'^2}}$ =10.32 to $\sqrt{\overline{u'^2}}/\sqrt{\overline{v'^2}}$ =12.79. The D_2 test case reveals values within $3.27<\sqrt{\overline{u'^2}}/\sqrt{\overline{v'^2}}<9.58$ interval which means an amplitude of $\sqrt{\overline{u'^2}}/\sqrt{\overline{v'^2}}$ =6.31. Related with the D_1 test case at x=100 mm the interval decreased nearly

37% from $\sqrt{\overline{u'^2}}/\sqrt{\overline{v'^2}}$ =10.01 to $\sqrt{\overline{u'^2}}/\sqrt{\overline{v'^2}}$ =6.31. The C_2 test case interval is almost 203% of the D_2 test case interval.

For station x=200 mm for both test cases C_2 and D_2 all values present a constant neighbouring points oscillation. The C_2 test case reveals values within 3.56<$\sqrt{\overline{u'^2}}/\sqrt{\overline{v'^2}}$<13.4 interval which means an amplitude of $\sqrt{\overline{u'^2}}/\sqrt{\overline{v'^2}}$ =9.84 for this test case. The highest value is at y=165.5 mm and the lowest at y=121.50 mm. Lowest values are at the jets intersection for both test cases. Related with the C_1 test case at same station x=200 mm, the interval decreased nearly 4% from $\sqrt{\overline{u'^2}}/\sqrt{\overline{v'^2}}$ =10.24 to $\sqrt{\overline{u'^2}}/\sqrt{\overline{v'^2}}$ =9.84. The D_2 test case reveals values within 3.34<$\sqrt{\overline{u'^2}}/\sqrt{\overline{v'^2}}$<11.3 interval which means an amplitude of $\sqrt{\overline{u'^2}}/\sqrt{\overline{v'^2}}$ =7.96. Related with the D_1 test case at x=200 mm the interval decreased nearly 10% from $\sqrt{\overline{u'^2}}/\sqrt{\overline{v'^2}}$ =8.76 to $\sqrt{\overline{u'^2}}/\sqrt{\overline{v'^2}}$ =7.96. The C_2 test case interval is almost 123% of the D_2 test case interval.

For station x=295 mm for both test cases C_2 and D_2 all values present a constant neighbouring points oscillation. The C_2 test case reveals values within 3.53<$\sqrt{\overline{u'^2}}/\sqrt{\overline{v'^2}}$<13.1 interval which means amplitude of $\sqrt{\overline{u'^2}}/\sqrt{\overline{v'^2}}$ =9.57 for this test case. The highest value is at y=175.5 mm and the lowest at y=110.50 mm. Lowest values are at the jets intersection for both test cases. Related with the C_1 test case at x=295 mm the interval increased nearly 8% from $\sqrt{\overline{u'^2}}/\sqrt{\overline{v'^2}}$ =8.85 to $\sqrt{\overline{u'^2}}/\sqrt{\overline{v'^2}}$ =9.57. The D_2 test case reveals values within 3.87<$\sqrt{\overline{u'^2}}/\sqrt{\overline{v'^2}}$<13.2 interval which means an amplitude of $\sqrt{\overline{u'^2}}/\sqrt{\overline{v'^2}}$ =9.33. Related with the D_1 test case at x=295 mm the interval increased nearly 21% from $\sqrt{\overline{u'^2}}/\sqrt{\overline{v'^2}}$ =7.71 to $\sqrt{\overline{u'^2}}/\sqrt{\overline{v'^2}}$ =9.33. The C_2 test case interval is almost identical of the D_2 test case interval.

For station x=395 mm the D_2 test case present a vertical line segment graphic for the region y<70 mm. The C_2 test case reveals values within 4.10<$\sqrt{\overline{u'^2}}/\sqrt{\overline{v'^2}}$<11.8 interval which means amplitude of $\sqrt{\overline{u'^2}}/\sqrt{\overline{v'^2}}$ =7.7 for this test case. The highest value is at y=31.5 mm and the lowest at y=91.50 mm. Related with the C_1 test case at x=395 mm the interval increased nearly 5% from $\sqrt{\overline{u'^2}}/\sqrt{\overline{v'^2}}$ =7.35 to $\sqrt{\overline{u'^2}}/\sqrt{\overline{v'^2}}$ =7.7. The D_2 test case reveals values within 3.98<$\sqrt{\overline{u'^2}}/\sqrt{\overline{v'^2}}$<13.7 interval which means an amplitude of $\sqrt{\overline{u'^2}}/\sqrt{\overline{v'^2}}$ =9.72. Related with the D_1 test case at x=395 mm the interval increased nearly 14% from $\sqrt{\overline{u'^2}}/\sqrt{\overline{v'^2}}$ =8.51 to $\sqrt{\overline{u'^2}}/\sqrt{\overline{v'^2}}$ =9.72. The C_2 test case interval is almost 74% of the D_2 test case interval.

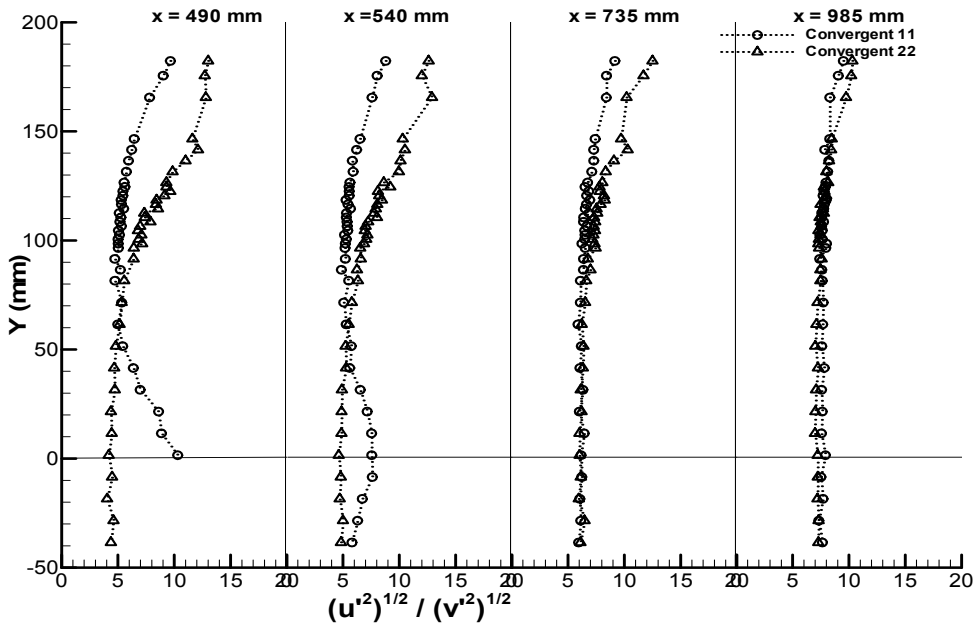

Figure 3.91. Vertical profiles of anisotropy for C_2 and D_2 test cases at stations x=490, 540, 735 and 985 mm.

Figure 3.91 shows vertical profiles of anisotropy for C_2 and D_2 test cases at stations x=490, 540, 735 and 985 mm. For station x=490 mm the D_2 test case present a vertical line segment graphic for the region y<130 mm. The C_2 test case reveals values within 4.72<$\sqrt{\overline{u'^2}}/\sqrt{\overline{v'^2}}$<10.3 interval which means amplitude of $\sqrt{\overline{u'^2}}/\sqrt{\overline{v'^2}}$ =5.58 for this test case. The highest value is at y=1.5 mm and the lowest at y=91.50 mm. Related with the C_1 test case at x=490 mm the interval increased nearly 10% from $\sqrt{\overline{u'^2}}/\sqrt{\overline{v'^2}}$ =5.09 to $\sqrt{\overline{u'^2}}/\sqrt{\overline{v'^2}}$ =5.58. The D_2 test case reveals values within 4.18<$\sqrt{\overline{u'^2}}/\sqrt{\overline{v'^2}}$<13.0 which means amplitude of $\sqrt{\overline{u'^2}}/\sqrt{\overline{v'^2}}$ =8.82. Related with the D_1 test case at x=490 mm the interval increased nearly 2% from $\sqrt{\overline{u'^2}}/\sqrt{\overline{v'^2}}$ =8.66 to$\sqrt{\overline{u'^2}}/\sqrt{\overline{v'^2}}$ = 8.82. The C_2 test case interval is almost 63% of the D_2 test case interval.

For station x=540 mm the D_2 test case present a vertical line segment graphic for the region Y<150 mm. The C_2 test case reveals values within 4.86<$\sqrt{\overline{u'^2}}/\sqrt{\overline{v'^2}}$<8.79 which means an amplitude of $\sqrt{\overline{u'^2}}/\sqrt{\overline{v'^2}}$ =3.93 for this test case. The highest value is at y=182.25 mm and the lowest at y=86.50 mm. Related with the C_1 test case at x=540 mm the interval decreased nearly 15% from $\sqrt{\overline{u'^2}}/\sqrt{\overline{v'^2}}$ =4.62 to $\sqrt{\overline{u'^2}}/\sqrt{\overline{v'^2}}$ =3.93. The D_2 test case reveals values within 4.62<$\sqrt{\overline{u'^2}}/\sqrt{\overline{v'^2}}$<12.9 interval which means amplitude of $\sqrt{\overline{u'^2}}/\sqrt{\overline{v'^2}}$ =8.28. Related with the D_1 test case at x=540 mm the interval increased nearly 19% from $\sqrt{\overline{u'^2}}/\sqrt{\overline{v'^2}}$ =6.91 to $\sqrt{\overline{u'^2}}/\sqrt{\overline{v'^2}}$ =8.28. The C_2 test case interval is almost 47% of the D_2 test case interval.

For station x=735 mm both test cases present an identical vertical line segment graphic for the region y<100 mm. The C_2 test case reveals values within 5.89<$\sqrt{\overline{u'^2}}/\sqrt{\overline{v'^2}}$<9.16

interval which means an amplitude of $\sqrt{\overline{u'^2}}/\sqrt{\overline{v'^2}}$ =3.27 for this test case. The highest value is at y=182.25 mm and the lowest at y=61.50 mm. Related with the C_1 test case at x=735 mm the interval is practically identical, from $\sqrt{\overline{u'^2}}/\sqrt{\overline{v'^2}}$ =3.35 to $\sqrt{\overline{u'^2}}/\sqrt{\overline{v'^2}}$ =3.27. The D_2 test case reveals values within 6.02<$\sqrt{\overline{u'^2}}/\sqrt{\overline{v'^2}}$<12.5 interval which means amplitude of $\sqrt{\overline{u'^2}}/\sqrt{\overline{v'^2}}$ =6.48. Related with the D_1 test case at x=735 mm the interval increased nearly 5% from 6.15 to 6.48. The C_2 test case interval is almost 50% of the D_2 test case interval.

For station x=985 mm both test cases present an identical vertical line segment graphic for the region y<150 mm. The C_2 test case reveals values within 7.40<$\sqrt{\overline{u'^2}}/\sqrt{\overline{v'^2}}$<9.50 interval which means an amplitude of $\sqrt{\overline{u'^2}}/\sqrt{\overline{v'^2}}$ =2.10 for this test case. The highest value is at y=182.25 mm and the lowest at y=96.50 mm. Related with the C_1 test case at x=985 mm the interval increased nearly 7%, from $\sqrt{\overline{u'^2}}/\sqrt{\overline{v'^2}}$ =1.98 to $\sqrt{\overline{u'^2}}/\sqrt{\overline{v'^2}}$ =2.10. The D_2 test case reveals values within 6.98<$\sqrt{\overline{u'^2}}/\sqrt{\overline{v'^2}}$<10.3 interval which means amplitude of $\sqrt{\overline{u'^2}}/\sqrt{\overline{v'^2}}$ =3.32. Related with the D_1 test case at same station x=985 mm, the interval decreased nearly 14% from $\sqrt{\overline{u'^2}}/\sqrt{\overline{v'^2}}$ =3.82 to $\sqrt{\overline{u'^2}}/\sqrt{\overline{v'^2}}$ =3.32. The C_2 test case interval is almost 63% of the D_2 test case interval.

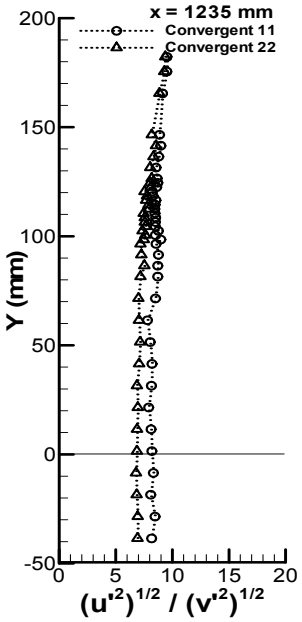

Figure 3.92. Vertical profiles of anisotropy for C_2 and D_2 test cases at station x=1235 mm.

For station x=1235 mm (Figure 3.92) both test cases present similar vertical line segment graphic for entire vertical profile. The C_2 test case reveals values within 7.80<$\sqrt{\overline{u'^2}}/\sqrt{\overline{v'^2}}$<9.52 interval which means an amplitude of $\sqrt{\overline{u'^2}}/\sqrt{\overline{v'^2}}$ =1.72 for this test case. The highest value is at y=182.25 mm and the lowest at y=61.50 mm. Related with the C_1 test case at x=1235 mm the interval increased nearly 10%, from $\sqrt{\overline{u'^2}}/\sqrt{\overline{v'^2}}$ =1.55 to $\sqrt{\overline{u'^2}}/\sqrt{\overline{v'^2}}$ =1.72. The D_2 test case reveals values within 6.87<$\sqrt{\overline{u'^2}}/\sqrt{\overline{v'^2}}$<9.37 interval which means an

amplitude of $\sqrt{\overline{u'^2}}/\sqrt{\overline{v'^2}}$ =2.50. Related with the D_1 test case at x=1235 mm the interval decreased nearly 25% from $\sqrt{\overline{u'^2}}/\sqrt{\overline{v'^2}}$ =2.02 to $\sqrt{\overline{u'^2}}/\sqrt{\overline{v'^2}}$ =2.50. The C_2 test case interval is almost 76% of the D_2 test case interval.

3.10. Vertical profiles of correlation coefficient

This subchapter presents all the obtained results for the correlation coefficient $\frac{\overline{u'v'}}{\sqrt{\overline{u'^2}}\sqrt{\overline{v'^2}}}$ distribution at the horizontal axis in each studied station, from y=200 mm to y=-50 mm. This correlation factor values are presented from -0.15≤$\frac{\overline{u'v'}}{\sqrt{\overline{u'^2}}\sqrt{\overline{v'^2}}}$≤+0.15. The confined jets values starts at y=148.50 mm, due to its wall confinement. The unconfined jets values starts at y=182.25 mm.

3.10.1. Unconfined A_1 and confined B_1 jets

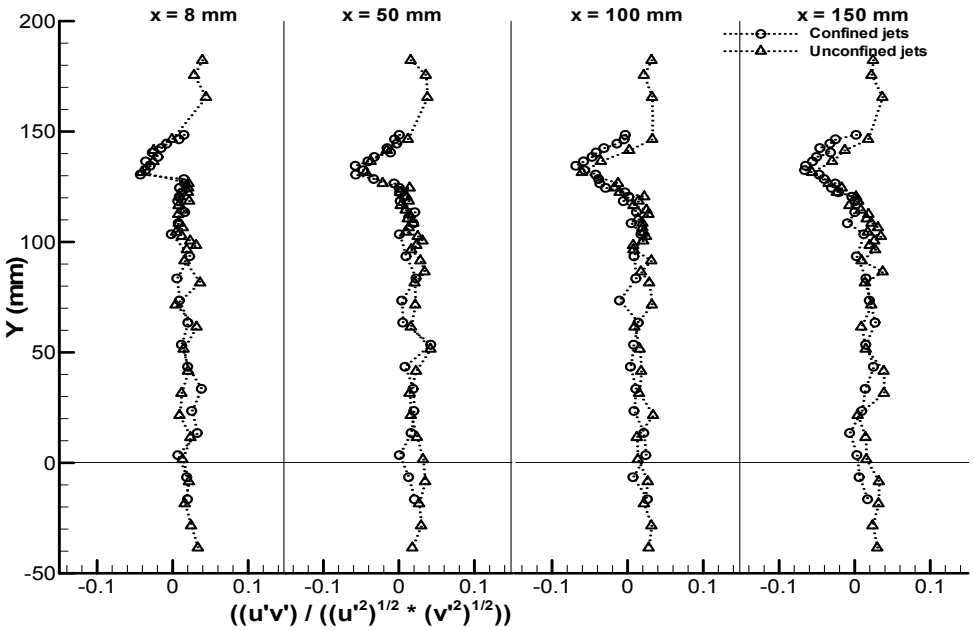

Figure 3.93. Vertical profiles of correlation coefficient for A_1 and B_1 test cases at stations x=8, 50, 100 and 150 mm.

Figure 3.93 shows vertical profiles of correlation coefficient for A_1 and B_1 test cases at stations x=8, 50, 100 and 150 mm, and reveals that both test cases present very similar profiles for all presented stations. For station x=8 mm the B_1 test case present values within -0.0426<$\frac{\overline{u'v'}}{\sqrt{\overline{u'^2}}\sqrt{\overline{v'^2}}}$<+0.0381 interval. The highest obtained value is at y=33.50 mm and the lowest value is at y=130.50 mm. This interval shows amplitude of 0.0807. Correlation factor oscillations are practically identical for both test cases at this station. The A_1 test case

reveals an amplitude interval of -0.0406<$\frac{\overline{u'v'}}{\sqrt{\overline{u'^2}}\sqrt{\overline{v'^2}}}$<+0.0441. This interval shows amplitude of 0.0847 for this test case, very similar to the B_1 test case interval for this station. The highest obtained value is at y=165.50 mm and the lowest value is at y=131.50 mm. Correlation factor presents very low values for both test cases.

For station x=50 mm the B_1 test case present values within -0.0577<$\frac{\overline{u'v'}}{\sqrt{\overline{u'^2}}\sqrt{\overline{v'^2}}}$<+0.0421 interval. The highest obtained value is at y=134.50 mm and the lowest value is at y=33.50 mm. This corresponds to an amplitude interval of 0.0988 for this test case. Correlation factor oscillations are practically identical for both test cases at this station, such as for previous station. The A_1 test case reveals values within -0.0437<$\frac{\overline{u'v'}}{\sqrt{\overline{u'^2}}\sqrt{\overline{v'^2}}}$<+0.0377. This interval shows amplitude of 0.0814. The highest obtained value is at y=165.50 and the lowest value is at y=131.50 mm. Correlation factor presents very low values for both test cases. The A_1 correlation factor amplitude interval corresponds to nearly 83% of the B_1 amplitude interval.

For station x=100 mm the B_1 test case present values within -0.0686<$\frac{\overline{u'v'}}{\sqrt{\overline{u'^2}}\sqrt{\overline{v'^2}}}$<+0.0239 interval. The highest obtained value is at y=134.50 mm and the lowest value is at y=3.50 mm. This corresponds to an amplitude interval of 0.0925 for this test case. Correlation factor oscillations are practically identical for both test cases at this station, such as for previous stations. The A_1 test case reveals values within -0.0605<$\frac{\overline{u'v'}}{\sqrt{\overline{u'^2}}\sqrt{\overline{v'^2}}}$<+0.0336. This interval shows amplitude of 0.0941. The highest obtained value is at y=21.50 mm and the lowest value is at y=131.50 mm. Correlation factor presents very low values for both test cases. The A_1 correlation factor amplitude interval is similar to B_1 amplitude interval.

For station x=150 mm the B_1 test case present values within -0.0663<$\frac{\overline{u'v'}}{\sqrt{\overline{u'^2}}\sqrt{\overline{v'^2}}}$<+0.0269 interval. The highest obtained value is at y=73.50 mm and the lowest value is at y=132.50 mm. This corresponds to an amplitude interval of 0.0932 for this test case. Correlation factor oscillations are practically identical for both test cases at this station, such as for previous stations. The A_1 test case reveals values within -0.0566<$\frac{\overline{u'v'}}{\sqrt{\overline{u'^2}}\sqrt{\overline{v'^2}}}$<+0.0388. This interval shows amplitude of 0.0954. The highest obtained value is at y=21.50 mm and the lowest value is at y=131.50 mm. Correlation factor presents very low values for both test cases. The A_1 correlation factor amplitude interval is similar to B_1 amplitude interval. Looking for obtained correlation factor results evolution from station x=8 mm to x=150 mm, the lowest results are at y=130 mm vicinity, near the jets division.

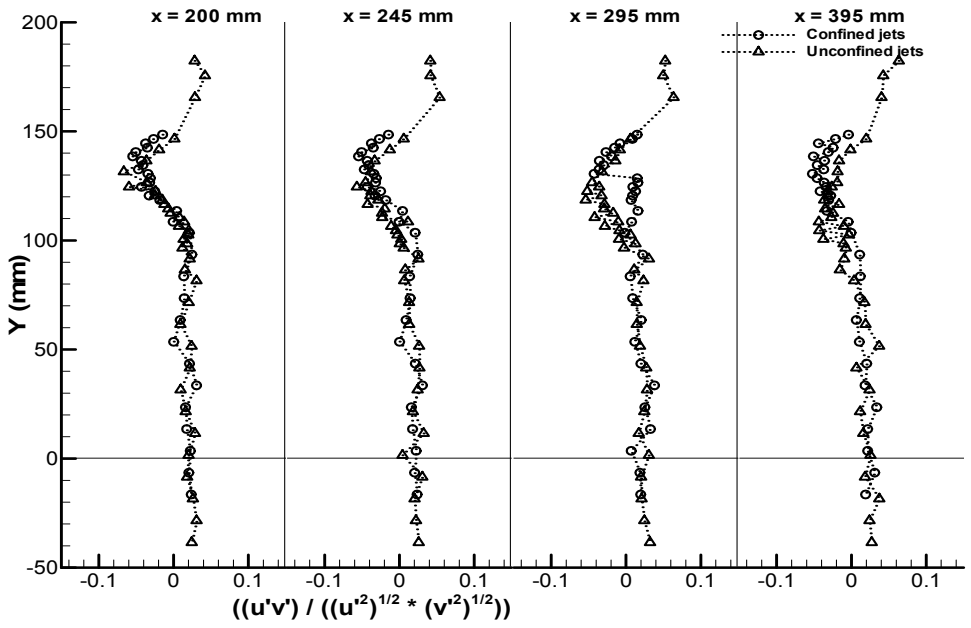

Figure 3.94. Vertical profiles of correlation coefficient for A_1 and B_1 test cases at x=200, 245, 295 and 395 mm.

Figure 3.94 shows vertical profiles of correlation coefficient for A_1 and B_1 test cases at x=200, 245, 295 and 395 mm. For station x=200 mm the B_1 test case present values within -0.0547<$\frac{\overline{u'v'}}{\sqrt{\overline{u}^2}\sqrt{\overline{v}^2}}$<+0.0306 interval. The highest obtained value is at y=33.50 mm and the lowest value is at y=138.50 mm. This interval shows amplitude of 0.0853 for this test case. Correlation factor oscillations are practically identical for both test cases at this station. The A_1 test case reveals an amplitude interval of -0.0665<$\frac{\overline{u'v'}}{\sqrt{\overline{u}^2}\sqrt{\overline{v}^2}}$<+0.0420. This interval shows amplitude of 0.1085 for this test case. The B_1 amplitude interval is nearly 78% to the A_1 test case interval for this station. The highest obtained value is at y=175.50 mm and the lowest value is at y=131.50 mm. Correlation factor presents very low values for both test cases.

For station x=245 mm the B_1 test case present values within -0.0497<$\frac{\overline{u'v'}}{\sqrt{\overline{u}^2}\sqrt{\overline{v}^2}}$<+0.0296 interval. The highest obtained value is at y=33.50 mm and the lowest value is at y=138.50 mm. This interval shows amplitude of 0.0793 for this test case. Correlation factor oscillations are practically identical for both test cases at this station. The A_1 test case reveals an amplitude interval of -0.0569<$\frac{\overline{u'v'}}{\sqrt{\overline{u}'^2}\sqrt{\overline{v}'^2}}$<+0.0537. This interval shows amplitude of 0.1106. The B_1 amplitude interval is nearly 71% to the A_1 test case interval for this station. The highest obtained value is at y=165.50 mm and the lowest value is at y=124.50 mm. Correlation factor presents very low values for both test cases.

For station x=295 mm the B_1 test case present values within -0.0538<$\frac{\overline{u'v'}}{\sqrt{\overline{u}'^2}\sqrt{\overline{v}'^2}}$<+0.0636 interval. The highest obtained value is at y=165.50 mm and the lowest value is at y=118.50

mm. This interval shows amplitude of 0.1174 for this test case. Correlation factor oscillations are practically identical for both test cases at this station. The A_1 test case reveals an amplitude interval of -0.0599<$\frac{\overline{u'v'}}{\sqrt{\overline{u'^2}}\sqrt{\overline{v'^2}}}$<+0.0230. This interval shows amplitude of 0.0829 for this test case. The B_1 amplitude interval is nearly 71% to the A_1 test case interval for this station. The highest obtained value is at y=33.50 mm and the lowest value is at y=138.50 mm. Correlation factor presents very low values for both test cases.

For station x=395 mm the B_1 test case present values within -0.0521<$\frac{\overline{u'v'}}{\sqrt{\overline{u'^2}}\sqrt{\overline{v'^2}}}$<+0.0338 interval. The highest obtained value is at y=23.50 mm and the lowest value is at y=130.50 mm. This interval shows amplitude of 0.0859 for this test case. Correlation factor oscillations are practically identical for both test cases at this station. The A_1 test case reveals an amplitude interval of -0.0436<$\frac{\overline{u'v'}}{\sqrt{\overline{u'^2}}\sqrt{\overline{v'^2}}}$<+0.0633. This interval shows amplitude of 0.1069 for this test case. The B_1 amplitude interval is nearly 80% to the A_1 test case interval for this station. The highest obtained value is at y=182.25 mm and the lowest value is at y=108.50 mm. Correlation factor presents very low values for both test cases. Regarding the evolution values from station x=200 mm to x=395 mm, at this last station there is peak point observation near the y=130 mm region.

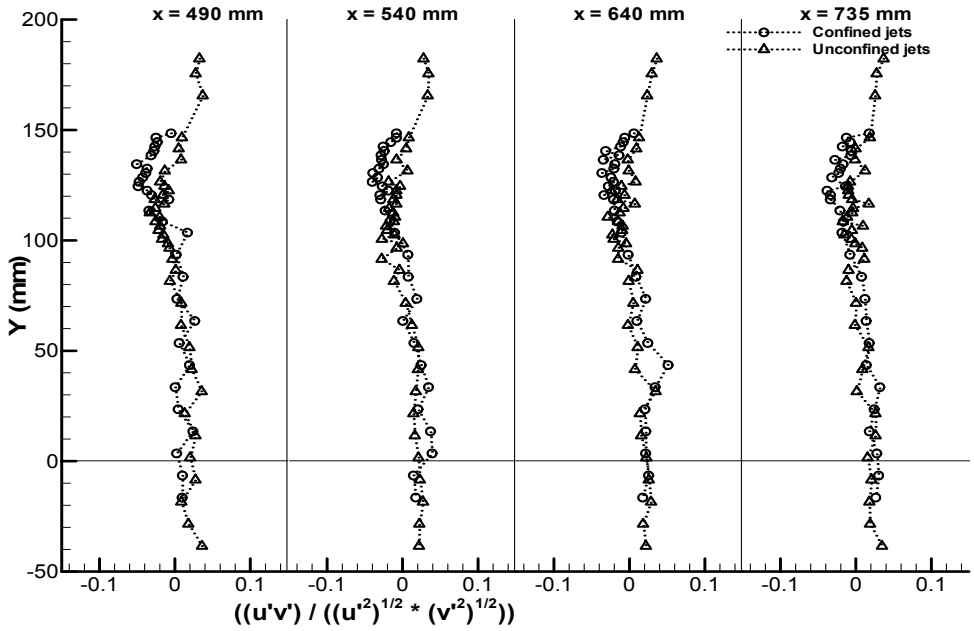

Figure 3.95. Vertical profiles of correlation coefficient for A_1 and B_1 test cases at x=495, 540, 640 and 735 mm.

Figure 3.95 shows vertical profiles of correlation coefficient for A_1 and B_1 test cases at x=495, 540, 640 and 735 mm. For station x=490 mm the B_1 test case present values within -0.0513<$\frac{\overline{u'v'}}{\sqrt{\overline{u'^2}}\sqrt{\overline{v'^2}}}$<+0.0267 interval. The highest obtained value is at y=73.50 mm and the lowest

value is at y=182.25 mm. This interval shows amplitude of 0.0780 for this test case. Correlation factor oscillations are similar for both test cases at this station. The A_1 test case reveals an amplitude interval of -0.0269<$\frac{\overline{u'v'}}{\sqrt{\overline{u}'^2}\sqrt{\overline{v}'^2}}$<+0.369. This interval shows amplitude of 0.0638 for this test case. The B_1 amplitude interval is nearly 122% to the A_1 test case interval for this station. The highest obtained value is at y=165.50 mm and the lowest value is at y=118.50 mm. Correlation factor presents very low values for both test cases.

For station x=540 mm the B_1 test case present values within -0.0402<$\frac{\overline{u'v'}}{\sqrt{\overline{u}'^2}\sqrt{\overline{v}'^2}}$<+0.0391 interval. The highest obtained value is at y=3.50 mm and the lowest value is at y=126.50 mm. This interval shows amplitude of 0.0793 for this test case. Correlation factor oscillations are similar for both test cases at this station. The A_1 test case reveals an amplitude interval of -0.0278<$\frac{\overline{u'v'}}{\sqrt{\overline{u}'^2}\sqrt{\overline{v}'^2}}$<+0.341. This interval shows amplitude of 0.0619 for this test case. The B_1 amplitude interval is nearly 128% to the A_1 test case interval for this station. The highest obtained value is at y=175.50 mm and the lowest value is at y=96.50 mm. Correlation factor presents very low values for both test cases.

For station x=640 mm the B_1 test case present values within -0.0366<$\frac{\overline{u'v'}}{\sqrt{\overline{u}'^2}\sqrt{\overline{v}'^2}}$<+0.0512 interval. The highest obtained value is at y=43.50 mm and the lowest value is at y=130.50 mm. This interval shows amplitude of 0.0878 for this test case. Correlation factor oscillations are similar for both test cases at this station. The A_1 test case reveals an amplitude interval of -0.0287<$\frac{\overline{u'v'}}{\sqrt{\overline{u}'^2}\sqrt{\overline{v}'^2}}$<+0.361. This interval shows amplitude of 0.0648 for this test case. The B_1 amplitude interval is nearly 135% to the A_1 test case interval for this station. The highest obtained value is at y=182.25 mm and the lowest value is at y=110.50 mm. Correlation factor presents very low values for both test cases.

For station x=735 mm the B_1 test case present values within -0.0383<$\frac{\overline{u'v'}}{\sqrt{\overline{u}'^2}\sqrt{\overline{v}'^2}}$<+0.0317 interval. The highest obtained value is at y=33.50 mm and the lowest value is at y=122.50 mm. This interval shows amplitude of 0.0700 for this test case. Correlation factor oscillations are similar for both test cases at this station. The A_1 test case reveals an amplitude interval of -0.0174<$\frac{\overline{u'v'}}{\sqrt{\overline{u}'^2}\sqrt{\overline{v}'^2}}$<+0.317. This interval shows amplitude of 0.0541. The B_1 amplitude interval is nearly 129% to the A_1 test case interval for this station. The highest obtained value is at y=182.25 mm and the lowest value is at y=110.50 mm. Correlation factor presents very low values for both test cases.

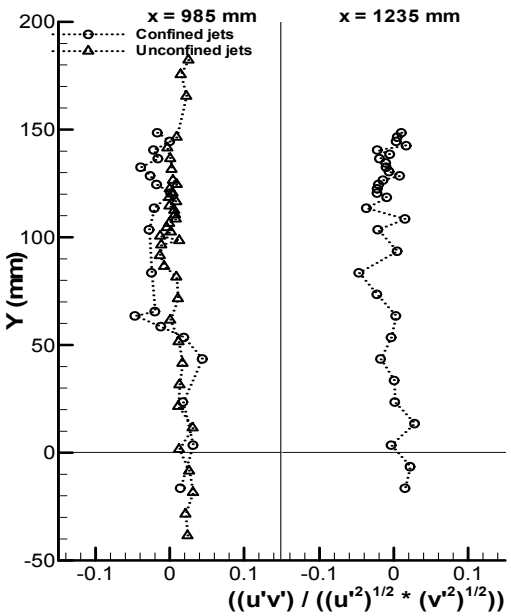

Figure 3.96. Vertical profiles of correlation coefficient for A_1 and B_1 test cases at x=985 and 1235 mm.

For station x=985 mm (Figure 3.96) the B_1 test case present values within -0.0470<$\frac{\overline{u'v'}}{\sqrt{\overline{u}'^2}\sqrt{\overline{v}'^2}}$<+0.0437 interval. The highest obtained value is at y=43.50 mm and the lowest value is at y=63.50 mm. This interval shows amplitude of 0.907 for this test case. The A_1 test case reveals an amplitude interval of -0.0134<$\frac{\overline{u'v'}}{\sqrt{\overline{u}'^2}\sqrt{\overline{v}'^2}}$<+0.280. This interval shows amplitude of 0.0384 for this test case. The B_1 amplitude interval is nearly 236% to the A_1 test case interval for this station. The highest obtained value is at y=182.25 mm and the lowest value is at y=91.50 mm. Correlation factor presents very low values for both test cases.

For station x=1235 mm the B_1 test case present values within -0.0473<$\frac{\overline{u'v'}}{\sqrt{\overline{u}'^2}\sqrt{\overline{v}'^2}}$<+0.0278 interval. The highest obtained value is at y=13.50 mm and the lowest value is at y=83.50 mm. This interval shows amplitude of 0.751 for this test case. Correlation factor presents very low values for this test case.

3.10.2. Unconfined A_2 and confined B_2 jets

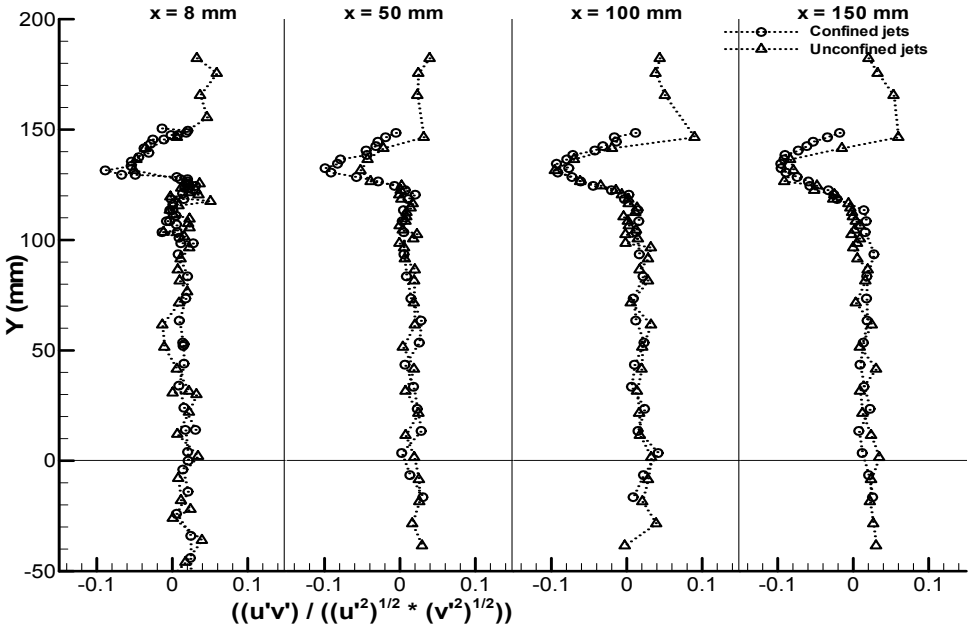

Figure 3.97. Vertical profiles of correlation coefficient for A_2 and B_2 test cases at stations x=8, 50, 100 and 150 mm.

Figure 3.97 shows vertical profiles of correlation coefficient for A_2 and B_2 test cases at stations x=8, 50, 100 and 150 mm, and reveals that both test cases present very similar profiles for all presented stations. For station x=8 mm the B_2 test case present values within the -0.0890<$\frac{\overline{u'v'}}{\sqrt{\overline{u'^2}}\sqrt{\overline{v'^2}}}$<+0.0308 interval. The highest obtained value is at y=124.50 mm and the lowest value is at y=131.50 mm. This interval shows amplitude of 0.1198 for this test case. Related with the B_1 test case at x=8 mm the interval increased nearly 48% from 0.0807 to 0.1198. The A_2 test case reveals an amplitude interval of -0.0508<$\frac{\overline{u'v'}}{\sqrt{\overline{u'^2}}\sqrt{\overline{v'^2}}}$<+0.0589. This interval shows amplitude of 0.1097. The highest obtained value is at y=175.50 mm and the lowest value is at y=131.50 mm. Related with the A_1 test case at x=8 the interval increased nearly 29% from 0.0847 to 0.1097. The A_2 test case interval is almost 91% of the B_2 confined test case interval. Practically all obtained values are identical for both test cases.

For station x=50 mm the B_2 test case present values within -0.0993<$\frac{\overline{u'v'}}{\sqrt{\overline{u'^2}}\sqrt{\overline{v'^2}}}$<+0.0281 interval. The highest obtained value is at y=13.50 mm and the lowest value is at y=132.50 mm. This interval shows amplitude of 0.1274 for this test case. Related with the B_1 test case at x=50 mm the interval increased nearly 28% from 0.0988 to 0.1274. The A_2 test case reveals an amplitude interval of -0.0524<$\frac{\overline{u'v'}}{\sqrt{\overline{u'^2}}\sqrt{\overline{v'^2}}}$<+0.0393. This interval shows amplitude of 0.0917 for this test case. The highest obtained value is at y=182.25 mm and the lowest value is at y=131.50 mm. Related with the A_1 test case at x=50 mm the interval increased nearly 13%

from 0.0814 to 0.0917. The A_2 test case interval is almost 71% of the B_2 confined test case interval. Practically all obtained values are identical for both test cases at this station.

For station x=100 mm the B_2 test case present values within -0.0932<$\frac{\overline{u'v'}}{\sqrt{\overline{u'^2}}\sqrt{\overline{v'^2}}}$<+0.0416 interval. The highest obtained value is at y=3.50 mm and the lowest value is at y=134.50 mm. This interval shows amplitude of 0.1348. Related with the B_1 test case at x=100 mm the interval increased nearly 45% from 0.0925 to 0.1348. The A_2 test case reveals an amplitude interval of -0.0954<$\frac{\overline{u'v'}}{\sqrt{\overline{u'^2}}\sqrt{\overline{v'^2}}}$<+0.0898. This interval shows amplitude of 1.852. The highest obtained value is at y=146.50 mm and the lowest value is at y=131.50 mm. Related with the A_1 test case at x=100 mm the interval increased nearly 97% from 0.0941 to 0.1852. The A_2 test case interval is almost 137% of the B_2 confined test case interval. Practically all obtained values are identical for both test cases at this station.

For station x=150 mm the B_2 test case present values within -0.0959<$\frac{\overline{u'v'}}{\sqrt{\overline{u'^2}}\sqrt{\overline{v'^2}}}$<+0.0275 interval. The highest obtained value is at y=93.50 mm and the lowest value is at y=134.50 mm. This interval shows amplitude of 0.1234 for this test case. Related with the B_1 test case at x=150 mm the interval increased nearly 32% from 0.0932 to 0.1234. The A_2 test case reveals an amplitude interval of -0.0915<$\frac{\overline{u'v'}}{\sqrt{\overline{u'^2}}\sqrt{\overline{v'^2}}}$<+0.0597. This interval shows amplitude of 0.1512 for this test case. The highest obtained value is at y=146.50 mm and the lowest value is at y=126.50 mm. Related with the A_1 test case at x=150 mm the interval increased nearly 58% from 0.0954 to 0.1512. The A_2 test case interval is almost 122% of the B_2 confined test case interval. Practically all obtained values are identical for both test cases at this station.

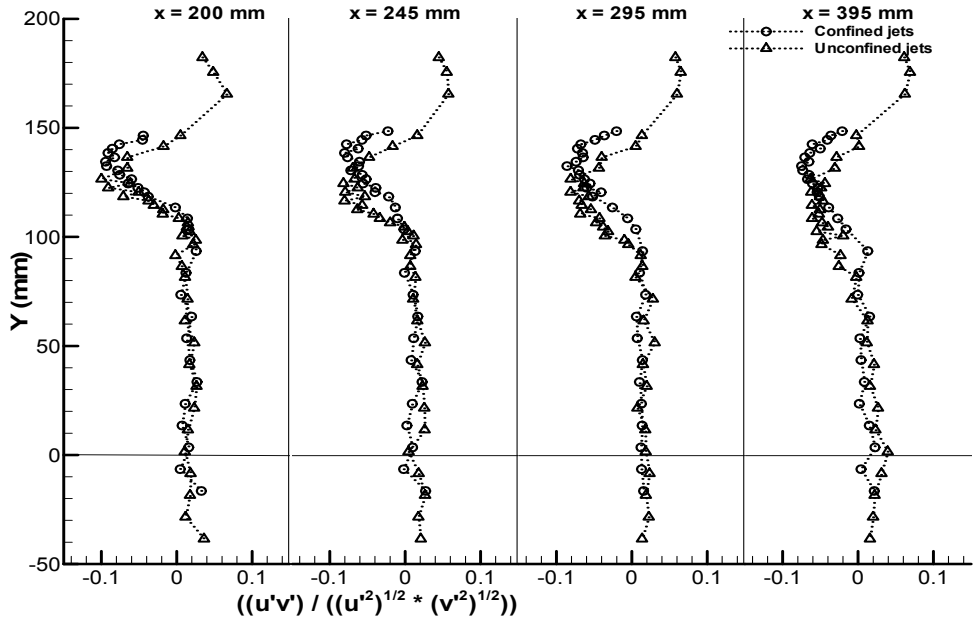

Figure 3.98. Vertical profiles of correlation coefficient for A_2 and B_2 test cases at stations x=200, 245, 295 and 395 mm.

Figure 3.98 shows vertical profiles of correlation coefficient for A_2 and B_2 test cases at stations x=200, 245, 295 and 395 mm, and reveals that both test cases present very similar profiles for all presented stations, with exception for the outer(inner jets interaction region. For station x=200 mm the B_2 test case present values within $-0.0945<\frac{\overline{u'v'}}{\sqrt{\overline{u'^2}}\sqrt{\overline{v'^2}}}<+0.0268$ interval. The highest obtained value is at y=33.50 mm and the lowest value is at y=134.50 mm. This interval shows amplitude of 0.1213. Related with the B_1 test case at x=200 the interval increased nearly 42% from 0.0853 to 0.1213. The A_2 test case reveals an amplitude interval of $-0.0910<\frac{\overline{u'v'}}{\sqrt{\overline{u'^2}}\sqrt{\overline{v'^2}}}<+0.0665$. This interval shows amplitude of 0.1575. The highest obtained value is at y=165.50 mm and the lowest value is at y=22.50 mm. Related with the A_1 test case at x=200 mm the interval increased nearly 45% from 0.1085 to 0.1575. The A_2 test case interval is almost 129% of the B_2 confined test case interval. Practically all obtained values are identical for both test cases at this station. The lowest observed peak values are beginning to differentiate its positions for both test cases.

For station x=245 mm the B_2 test case present values within $-0.0803<\frac{\overline{u'v'}}{\sqrt{\overline{u'^2}}\sqrt{\overline{v'^2}}}<+0.0225$ interval. The highest obtained value is at y=33.50 mm and the lowest value is at y=138.50 mm. This interval shows amplitude of 0.1028 for this test case. Related with the B_1 test case at x=245 mm the interval increased nearly 42% from 0.0793 to 0.1028. The A_2 test case reveals an amplitude interval of $-0.0819<\frac{\overline{u'v'}}{\sqrt{\overline{u'^2}}\sqrt{\overline{v'^2}}}<+0.0573$. This interval shows amplitude of 0.1392 for this test case. The highest obtained value is at y=145.50 mm and the lowest value is at y=124.50 mm. Related with the A_1 test case at x=245 mm the interval increased nearly 25% from 0.1106 to 0.1392. The A_2 test case interval is almost 135% of the B_2 confined test case interval. Practically all obtained values are identical for both test cases at this station. Observing both test cases, the lowest observed peak values are increasing its distance.

For station x=295 mm the B_2 test case present values within $-0.0860<\frac{\overline{u'v'}}{\sqrt{\overline{u'^2}}\sqrt{\overline{v'^2}}}<+0.0143$ interval. The highest obtained value is at y=93.50 mm and the lowest value is at y=132.50 mm. This interval shows amplitude of 0.1003. Related with the B_1 test case at x=295 the interval increased nearly 20% from 0.0829 to 0.1003. The A_2 test case reveals an amplitude interval of $-0.0813<\frac{\overline{u'v'}}{\sqrt{\overline{u'^2}}\sqrt{\overline{v'^2}}}<+0.0649$. This interval shows amplitude of 0.1462 for this test case. The highest obtained value is at y=175.50 mm and the lowest value is at y=120.50 mm. Related with the A_1 test case at x=295 mm the interval increased nearly 24% from 0.1174 to 0.1462. The A_2 test case interval is almost 146% of the B_2 confined test case interval. Observing both test cases, the lowest observed peak values are increasing its distance, a tendency observed initially at station x=200 mm.

For station x=395 mm the B_2 test case present values within $-0.0750<\frac{\overline{u'v'}}{\sqrt{\overline{u'^2}}\sqrt{\overline{v'^2}}}<+0.0224$ interval. The highest obtained value is at y=3.50 mm and the lowest value is at y=132.50 mm.

This interval shows amplitude of 0.0974 for this test case. Related with the B_1 test case at x=395 mm the interval increased nearly 14% from 0.0859 to 0.0974. The A_2 test case reveals an amplitude interval of -0.0622<$\frac{\overline{u'v'}}{\sqrt{\overline{u}'^2}\sqrt{\overline{v}'^2}}$<+0.0688. This interval shows amplitude of 0.1310 for this test case. The highest obtained value is at y=175.50 mm and the lowest value is at y=120.50 mm. Related with the A_1 test case at x=395 mm the interval increased nearly 23% from 0.1069 to 0.1310. The A_2 test case interval is almost 135% of the B_2 confined test case interval. Observing both test cases, the lowest observed peak values continue to increase its distance, a tendency observed initially at station x=200 mm.

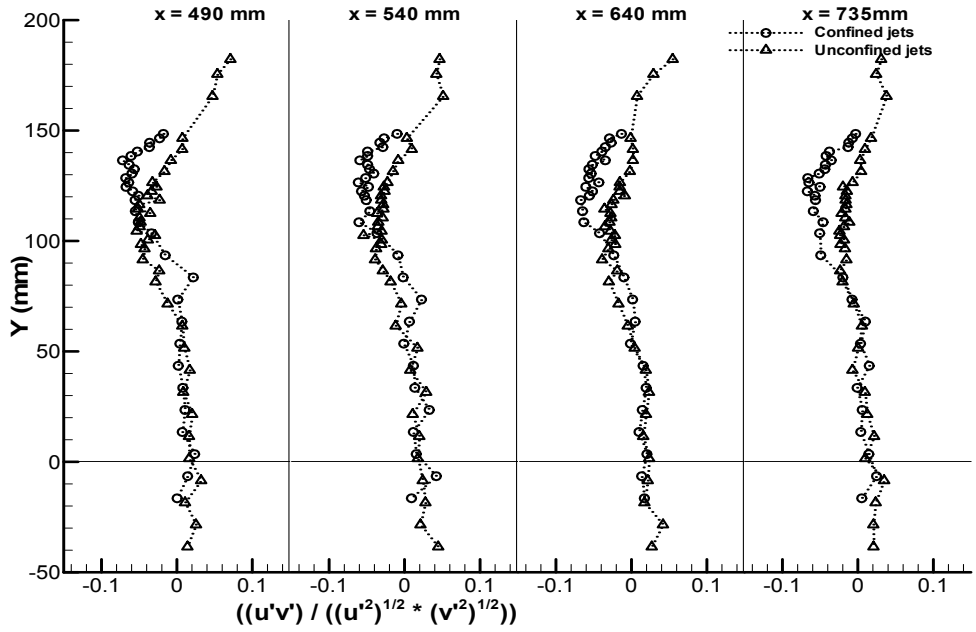

Figure 3.99. Vertical profiles of correlation coefficient for A_2 and B_2 test cases at stations x=490, 540, 640 and 735 mm.

Figure 3.99 shows vertical profiles of correlation coefficient for A_2 and B_2 test cases at stations x=490, 540, 640 and 735 mm. For station x=490 mm the B_2 test case present values within -0.0720<$\frac{\overline{u'v'}}{\sqrt{\overline{u}'^2}\sqrt{\overline{v}'^2}}$<+0.0235 interval. The highest obtained value is at y=3.50 mm and the lowest value is at y=136.50 mm. This interval shows amplitude of 0.0955. Related with the B_1 test case at x=490 mm the interval increased nearly 22% from 0.0780 to 0.0955. The A_2 test case reveals an amplitude interval of -0.0534<$\frac{\overline{u'v'}}{\sqrt{\overline{u}'^2}\sqrt{\overline{v}'^2}}$<+0.0709. This interval shows amplitude of 0.1243. The highest obtained value is at y=182.25 mm and the lowest value is at y=104.50 mm. Related with the A_1 test case at x=490 mm the interval increased nearly 95% from 0.0638 to 0.1243. The A_2 test case interval is almost 130% of the B_2 confined test case interval. Observing both test cases, the lowest observed peak values continue to increase its distance, a tendency observed initially at station x=200 mm.

For station x=540 mm the B_2 test case present values within -0.0613<$\frac{\overline{u'v'}}{\sqrt{\overline{u'^2}}\sqrt{\overline{v'^2}}}$<+0.0327 interval. The highest obtained value is at y=3.50 mm and the lowest value is at y=118.50 mm. This interval shows amplitude of 0.0940. Related with the B_1 test case at x=540 mm the interval increased nearly 19% from 0.0793 to 0.0940. The A_2 test case reveals an amplitude interval of -0.0545<$\frac{\overline{u'v'}}{\sqrt{\overline{u'^2}}\sqrt{\overline{v'^2}}}$<+0.0511. This interval shows amplitude of 0.1056. The highest obtained value is at y=165.50 mm and the lowest value is at y=102.50 mm. Related with the A_1 test case at x=540 mm the interval increased nearly 70% from 0.0619 to 0.1056. The A_2 test case interval is almost 112% of the B_2 confined test case interval. Observing both test cases, the lowest observed peak values disappeared almost completely.

For station x=640 mm the B_2 test case present values within -0.0673<$\frac{\overline{u'v'}}{\sqrt{\overline{u'^2}}\sqrt{\overline{v'^2}}}$<+0.0205 interval. The highest obtained value is at y=3.50 mm and the lowest value is at y=118.50 mm. This interval shows amplitude of 0.0878. Related with the B_1 test case at x=640 mm the interval is exactly equal to 0.0878. The A_2 test case reveals an amplitude interval of -0.0389<$\frac{\overline{u'v'}}{\sqrt{\overline{u'^2}}\sqrt{\overline{v'^2}}}$<+0.0547. This interval shows amplitude of 0.0936. The highest obtained value is at y=182.25 mm and the lowest value is at y=91.50 mm. Related with the A_1 test case at same station x=640 mm, the interval increased nearly 44% from 0.0648 to 0.0936. The A_2 test case interval is almost 107% of the B_2 confined test case interval.

For station x=735 mm the B_2 test case present values within -0.0671<$\frac{\overline{u'v'}}{\sqrt{\overline{u'^2}}\sqrt{\overline{v'^2}}}$<+0.0150 interval. The highest obtained value is at y=43.50 mm and the lowest value is at y=122.50 mm. This interval shows amplitude of 0.0821 for this test case. Related with the B_1 test case at x=735 mm the interval increased nearly 17% from 0.700 to 0.0821. The A_2 test case reveals an amplitude interval of -0.0245<$\frac{\overline{u'v'}}{\sqrt{\overline{u'^2}}\sqrt{\overline{v'^2}}}$<+0.0379. This interval shows amplitude of 0.0624 for this test case. The highest obtained value is at y=165.50 mm and the lowest value is at y=104.50 mm. Related with the A_1 test case at x=735 mm the interval increased nearly 44% from 0.0541 to 0.0624. The A_2 test case interval is almost 76% of the B_2 confined test case interval.

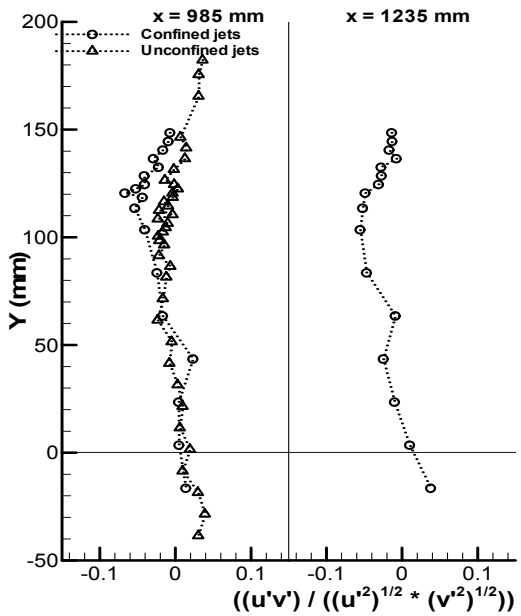

Figure 3.100. Vertical profiles of correlation coefficient for A_2 and B_2 test cases at stations x=985 and 1235 mm.

For station x=985 mm (Figure 3.100), he B_2 test case present values within -0.0671<$\frac{\overline{u'v'}}{\sqrt{\overline{u}'^2}\sqrt{\overline{v}'^2}}$<+0.0229 interval. The highest obtained value is at y=43.50 mm and the lowest value is at y=120.50 mm. This interval shows amplitude of 0.0900. Related with the B_1 test case at x=985 mm the interval is practically identical (from 0.0907 to 0.0900). The A_2 test case reveals an amplitude interval of -0.0237<$\frac{\overline{u'v'}}{\sqrt{\overline{u}'^2}\sqrt{\overline{v}'^2}}$<+0.0357. This interval shows amplitude of 0.0594 for this test case. The highest obtained value is at y=182.25 mm and the lowest value is at y=61.50 mm. Related with the A_1 test case at same station x=985 mm, the interval increased nearly 52% from 0.0384 to 0.0594. The A_2 test case interval is almost 66% of the B_2 confined test case interval.

For station x=1235 mm the B_2 test case present values within -0.0556<$\frac{\overline{u'v'}}{\sqrt{\overline{u}'^2}\sqrt{\overline{v}'^2}}$<+0.0098 interval. The highest obtained value is at y=3.50 mm and the lowest value is at y=103.50 mm. This interval shows amplitude of 0.0654 for this test case. Related with the B_1 test case at x=1235 mm the interval decreased nearly 14% from 0.0751 to 0.0654.

3.10.3. Convergent 11° C_1 and convergent 22° D_1 jets

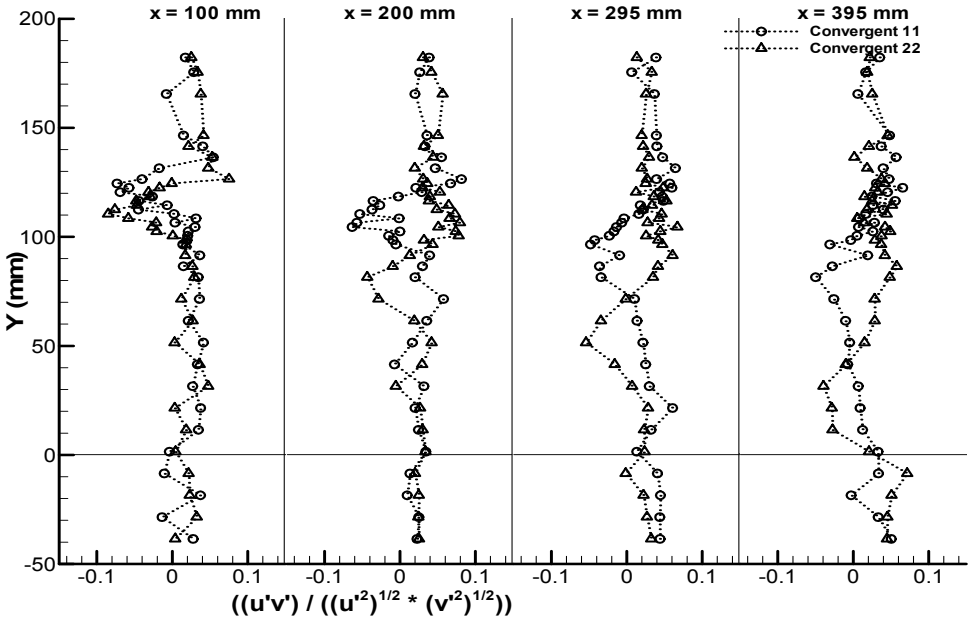

Figure 3.101. Vertical profiles of correlation coefficient for C_1 and D_1 test cases at stations x=100, 200, 295 and 395 mm.

Figure 3.101 shows vertical profiles of correlation coefficient for A_1 and B_1 test cases at stations x=100, 200, 295 and 395 mm. For station x=100 mm, for both test cases C_1 and D_1 all values present a constant oscillation between neighbouring points. For this station both test cases present same shape of obtained correlation factor results. The 11° convergent C_1 test case present values within the -0.0692<$\frac{\overline{u'v'}}{\sqrt{\overline{u'^2}}\sqrt{\overline{v'^2}}}$ <+0.0542 which means an amplitude of 0.1234. The highest obtained value is at y=136.50 mm and the lowest value is at y=120.50 mm. The D_1 test case reveals values within -0.0854<$\frac{\overline{u'v'}}{\sqrt{\overline{u'^2}}\sqrt{\overline{v'^2}}}$<+0.0752 interval which means an amplitude of 0.1606 for this test case, nearly 30% greater than the C_1 test case for same station. These amplitudes are much higher when compared to A_1 and B_1 test cases, respectively 0.0847 and 0.0807 and also higher when compared to A_2 and B_2 test cases, respectively 0.1092 and 0.1198. The highest obtained value is at y=126.50 mm and the lowest value is at y=110.50 mm. Lowest values are at y=120 mm vicinity for C_1 test case and at y=110 mm for D_1 test case, at the respective jets division regions.

For station x=200 mm the C_1 test case present values within the -0.0634<$\frac{\overline{u'v'}}{\sqrt{\overline{u'^2}}\sqrt{\overline{v'^2}}}$ <+0.0814 interval which means an amplitude of 0.1448. The highest obtained value is at y=126.50 mm and the lowest value is at y=104.50 mm. The D_1 test case reveals values within -0.0435<$\frac{\overline{u'v'}}{\sqrt{\overline{u'^2}}\sqrt{\overline{v'^2}}}$<+0.0794 interval which means an amplitude of 0.1229 for this test case, nearly 17% smaller than the C_1 test case for same station. The highest obtained value is at

y=106.50 mm and the lowest value is at y=81.50 mm. Lowest values are at y=100 mm vicinity for C_1 test case and at y=80 mm for D_1 test case, at the respective jets division regions.

For station x=295 mm the C_1 test case present values within the -0.0481<$\frac{\overline{u'v'}}{\sqrt{\overline{u'^2}}\sqrt{\overline{v'^2}}}$<+0.0644 interval which means an amplitude of 0.1125 for this test case. The highest obtained value is at y=131.50 and the lowest value is at y=96.50 mm. The D_1 test case present values within -0.0540<$\frac{\overline{u'v'}}{\sqrt{\overline{u'^2}}\sqrt{\overline{v'^2}}}$<+0.0670 interval which means an amplitude of 0.1210 for this test case, nearly 8% greater than the C_1 test case for same station. The highest obtained value is at y=104.50 mm and the lowest value is at y=51.50 mm. Lowest values are at y=90 mm vicinity for C_1 test case and at y=50 mm for D_1 test case, at the respective jets division regions.

For station x=395 mm the C_1 test case present values within the -0.0499<$\frac{\overline{u'v'}}{\sqrt{\overline{u'^2}}\sqrt{\overline{v'^2}}}$<+0.0655 interval which means an amplitude of 0.1154. The highest obtained value is at y=122.50 mm and the lowest value is at y=81.50 mm. The D_1 test case present values within -0.0395<$\frac{\overline{u'v'}}{\sqrt{\overline{u'^2}}\sqrt{\overline{v'^2}}}$<+0.0577 interval which means an amplitude of 0.0972 for this test case, nearly 18% smaller than the C_1 test case for same station. The highest obtained value is at y=86.50 mm and the lowest value is at y=31.50 mm. Lowest values are at y=80 mm vicinity for C_1 test case and at y=30 mm for D_1 test case, at the respective jets division regions.

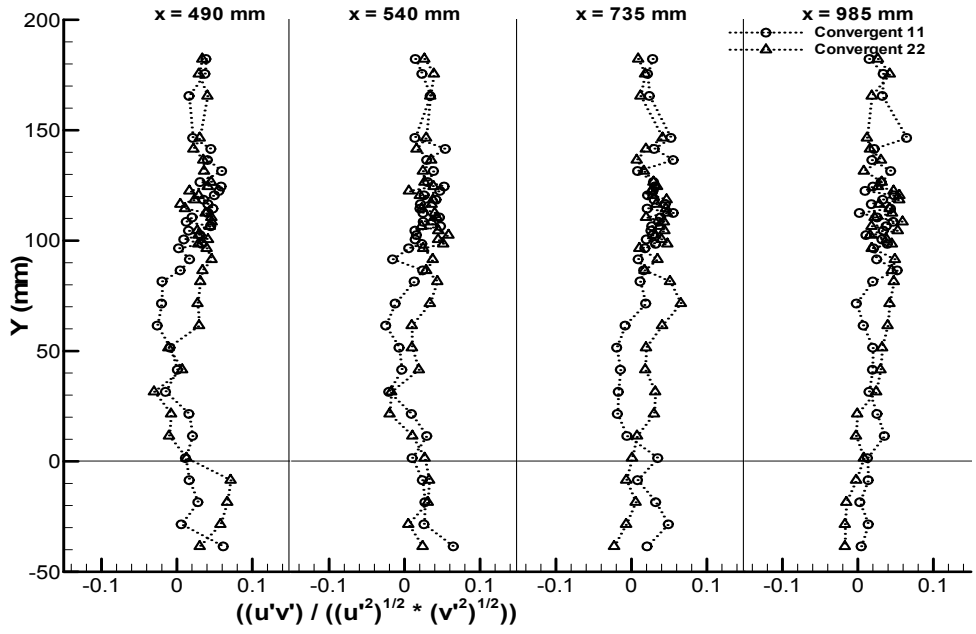

Figure 3.102. Vertical profiles of correlation coefficient for C_1 and D_1 test cases at stations x=490, 540, 735 and 985 mm.

Figure 3.102 shows vertical profiles of correlation coefficient for A_1 and B_1 test cases at stations x=490, 540, 735 and 985 mm. For station x=490 mm the C_1 test case present values within the -0.0261<$\frac{\overline{u'v'}}{\sqrt{\overline{u'^2}}\sqrt{\overline{v'^2}}}$<+0.0593 interval which means an amplitude of 0.0854 for this test case. The highest obtained value is at y=131.50 mm and the lowest value is at y=61.50 mm. The D_1 test case present values within -0.0303<$\frac{\overline{u'v'}}{\sqrt{\overline{u'^2}}\sqrt{\overline{v'^2}}}$<+0.0461 which means an amplitude of 0.0764 for this test case, nearly 11% smaller than the C_1 test case for same station. The highest obtained value is at y=108.50 mm and the lowest value is at y=31.50 mm. The lowest peaks are tending to vanish for both test cases.

For station x=540 mm the C_1 test case present values within the -0.0251<$\frac{\overline{u'v'}}{\sqrt{\overline{u'^2}}\sqrt{\overline{v'^2}}}$<+0.0539 which means an amplitude of 0.0790. The highest obtained value is at y=141.50 mm and the lowest value is at y=61.50 mm. The D_1 test case reveals values within -0.0200<$\frac{\overline{u'v'}}{\sqrt{\overline{u'^2}}\sqrt{\overline{v'^2}}}$<+0.0582 interval which means an amplitude of 0.0782 for this test case, nearly identical than the C_1 test case for same station. The highest obtained value is at y=102.50 mm and the lowest value is at y=21.50 mm. The lowest peaks are completely vanishing for both test cases.

For station x=735 mm the C_1 test case present values within the -0.0196<$\frac{\overline{u'v'}}{\sqrt{\overline{u'^2}}\sqrt{\overline{v'^2}}}$<+0.0553 interval which means an amplitude of 0.0749 for this test case. The highest obtained value is at y=136.50 mm and the lowest value is at y=51.50 mm. The D_1 test case reveals values within +0.0069<$\frac{\overline{u'v'}}{\sqrt{\overline{u'^2}}\sqrt{\overline{v'^2}}}$<+0.0655 interval which means an amplitude of 0.0586 for this test case, the first all positive values interval. The D_1 test case is at about 78% of the C_1 test case for same station. The highest obtained value is at y=71.50 mm and the lowest value is at y=136.50 mm. The lowest peaks are completely vanishing for both test cases.

For station x=985 mm the C_1 test case present values within the -0.0021<$\frac{\overline{u'v'}}{\sqrt{\overline{u'^2}}\sqrt{\overline{v'^2}}}$<+0.0645 interval which means an amplitude of 0.0666 for this test case. The highest obtained value is at y=146.50 mm and the lowest value is at y=71.50 mm. The D_1 test case reveals values within -0.0026<$\frac{\overline{u'v'}}{\sqrt{\overline{u'^2}}\sqrt{\overline{v'^2}}}$<+0.0591 which means an amplitude of 0.0617 for this test case. The D_1 test case is at about 92% of the C_1 test case for same station. The highest obtained value is at y=108.50 mm and the lowest value is at y=11.50 mm. The lowest peaks are completely vanishing for both test cases.

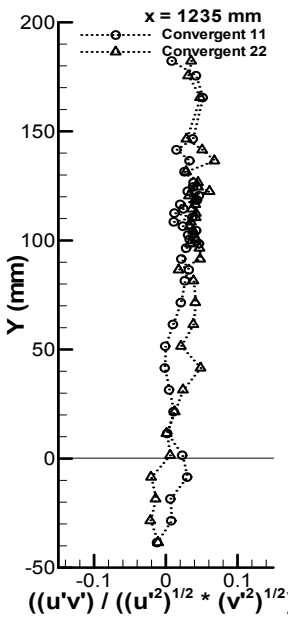

Figure 3.103. Vertical profiles of correlation coefficient for C_1 and D_1 test cases at station x=1235 mm.

For station x=1235 mm (Figure 3.103) the C_1 test case present values within the -0.0016<$\frac{\overline{u'v'}}{\sqrt{\overline{u'^2}}\sqrt{\overline{v'^2}}}$<+0.0513 interval which means an amplitude of 0.529 for this test case. The highest obtained value is at y=165.50 mm and the lowest value is at y=41.50 mm. The D_1 test case reveals values within +0.0009<$\frac{\overline{u'v'}}{\sqrt{\overline{u'^2}}\sqrt{\overline{v'^2}}}$<+0.0676 which mean an amplitude of 0.0667 for this test case, the second all positive values interval. The highest obtained value is at y=136.50 mm and the lowest value is at y=11.50 mm. The D_1 test case is at about 126% of the C_1 test case for same station. The highest obtained value is at y=136.50 mm and the lowest value is at y=11.50 mm.

3.10.4. Convergent 11° C_2 and convergent 22° D_2 jets

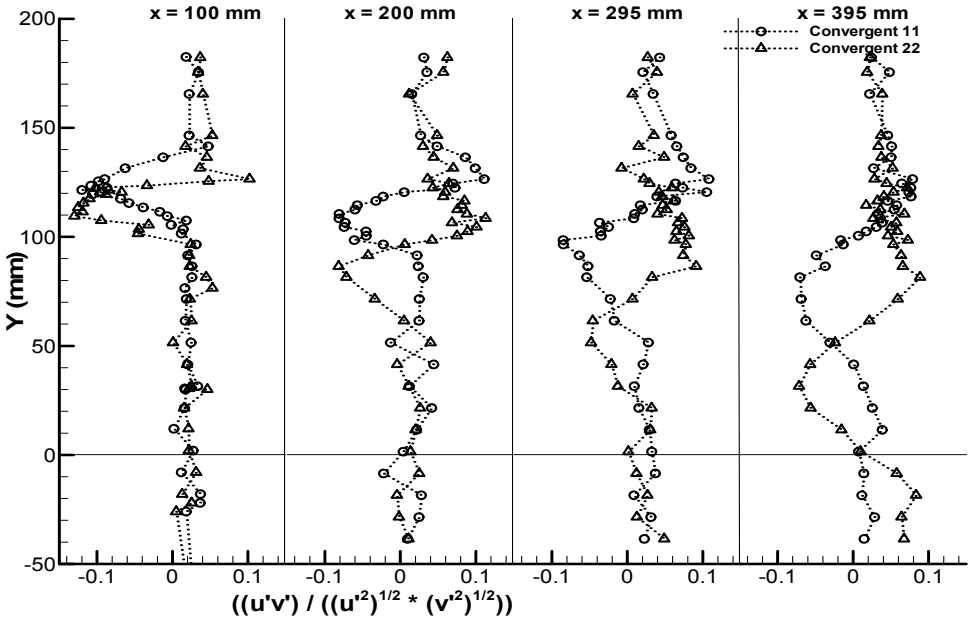

Figure 3.104. Vertical profiles of correlation coefficient for C_2 and D_2 test cases at stations x=100, 200, 295 and 395 mm.

Figure 3.104 shows vertical profiles of correlation coefficient for C_2 and D_2 test cases at stations x=100, 200, 295 and 395 mm. For station x=100 mm for both test cases present very similar results with exception to the jets division region. Lowest values are at the jets intersection for both test cases. The C_2 test case present values within the -0.120<$\frac{\overline{u'v'}}{\sqrt{\overline{u'^2}}\sqrt{\overline{v'^2}}}$<+0.0472 which means an amplitude of 0.1672. The highest obtained value is at y=141.50 mm and the lowest value is at y=121.50 mm. Related with the C_1 test case at same station x=100, the interval increased nearly 35% from 0.1234 to 0.1672. The D_2 test case reveals values within -0.130<$\frac{\overline{u'v'}}{\sqrt{\overline{u'^2}}\sqrt{\overline{v'^2}}}$<+0.102 interval which means an amplitude of 0.2320. The highest obtained value is at y=126.50 mm and the lowest value is at y=109.50 mm. Related with the D_1 test case at same station x=100 mm the interval increased nearly 44% from 0.1606 to 0.2320. The C_2 test case interval is almost 138% of the D_2 test case interval.

For station x=200 mm both test cases present always different results. The jets division region moved slightly to axis plane. Lowest values are at the jets intersection for both test cases. The C_2 test case present values within the -0.0812<$\frac{\overline{u'v'}}{\sqrt{\overline{u'^2}}\sqrt{\overline{v'^2}}}$<+0.111 Interval which means an amplitude of 0.1922 for this test case. The highest obtained value is at y=126.50 mm and the lowest value is at y=108.50 mm. Related with the C_1 test case at same station x=200 mm the interval increased nearly 33% from 0.1448 to 0.1922. The D_2 test case reveals values within -0.0818<$\frac{\overline{u'v'}}{\sqrt{\overline{u'^2}}\sqrt{\overline{v'^2}}}$<+0.113 which means an amplitude of 0.1948. The

highest obtained value is at y=108.50 and the lowest value is at y=86.50 mm. Related with the D_1 test case at same station x=200 mm the interval increased nearly 58% from 0.1229 to 0.1948. The C_2 test case interval is practically identical to D_2 test case interval.

For station x=295 mm both test cases present always different results. The jets division region moved again slightly to axis plane. Lowest values are at the jets intersection for both test cases. The C_2 test case present values within the $-0.0851<\frac{\overline{u'v'}}{\sqrt{\overline{u'^2}}\sqrt{\overline{v'^2}}}<+0.108$ Interval which means an amplitude of 0.1931. The highest obtained value is at y=126.50 mm and the lowest value is at y=98.50 mm. Related with the C_1 test case at same station x=295 the interval increased nearly 33% from 0.1448 to 0.1931. The D_2 test case reveals values within $-0.0481<\frac{\overline{u'v'}}{\sqrt{\overline{u'^2}}\sqrt{\overline{v'^2}}}<+.00911$ which means an amplitude of 0.1392. The highest obtained value is at y=86.50 mm and the lowest value is at y=51.50 mm. Related with the D_1 test case at same station x=295 mm, the interval increased nearly 15% from 0.1210 to 0.1392. The C_2 test case interval is almost 72% of the D_2 test case interval.

For station x=395 mm both test cases present always different results. The jets division region moved again slightly to axis plane. Lowest values are at the jets intersection for both test cases. The C_2 test case present values within the $-0.0706<\frac{\overline{u'v'}}{\sqrt{\overline{u'^2}}\sqrt{\overline{v'^2}}}<+0.0787$ Interval which means an amplitude of 0.1493. The highest obtained value is at y=126.50 mm and the lowest value is at y=81.50 mm. Related with the C_1 test case at same station x=395 mm the interval increased nearly 29% from 0.1154 to 0.1493. The D_2 test case reveals values within $-0.0717<\frac{\overline{u'v'}}{\sqrt{\overline{u'^2}}\sqrt{\overline{v'^2}}}<+0.0806$ which means an amplitude of 0.1603. The highest obtained value is at y=81.50 mm and the lowest value is at y=31.50 mm. Related with the D_1 test case at same station x=395 mm the interval increased nearly 64% from 0.0972 to 0.1603. The C_2 test case interval is almost 93% of the D_2 test case interval. By observing Figure 3.104, the results evolution reveals that the correlation factor lowest values are present at the jets division and are migrating to axis plane as the distance of the jets exit is increasing.

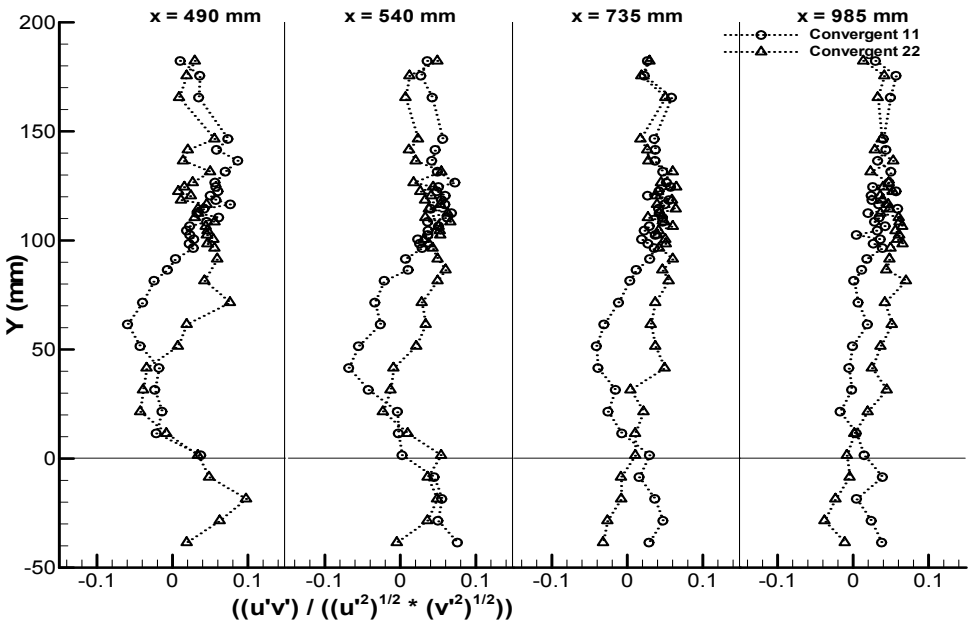

Figure 3.105. Vertical profiles of correlation coefficient for C_2 and D_2 test cases at stations x=490, 540, 735 and 985 mm.

Figure 3.105 shows vertical profiles of correlation coefficient for C_2 and D_2 test cases at stations x=490, 540, 735 and 985 mm. For station x=490 mm both test cases present always different results. The jets division region disappeared. The C_2 test case reveals values within -0.0596<$\frac{\overline{u'v'}}{\sqrt{\overline{u'^2}}\sqrt{\overline{v'^2}}}$<+0.0864 which means an amplitude of 0.1460. The highest obtained value is at y=136.50 mm and the lowest value is at y=61.50 mm. Related with the C_1 test case at same station x=490 mm the interval increased nearly 70% from 0.0854 to 0.1460. The D_2 test case reveals values within -0.0429<$\frac{\overline{u'v'}}{\sqrt{\overline{u'^2}}\sqrt{\overline{v'^2}}}$<+0.0761 which means an amplitude of 0.1190. The highest obtained value is at y=71.50 mm and the lowest value is at y=21.50 mm. Related with the D_1 test case at same station x=490 mm the interval increased nearly 55% from 0.0764 to 0.1190. The C_2 test case interval is almost 122% of the D_2 test case interval.

For station x=540 mm for both test cases present always different results. It is not visible the jets division region. The C_2 test case reveals values within -0.0685<$\frac{\overline{u'v'}}{\sqrt{\overline{u'^2}}\sqrt{\overline{v'^2}}}$<+0.0722 which means an amplitude of 0.1407. The highest obtained value is at y=126.50 mm and the lowest value is at y=41.50 mm. Related with the C_1 test case at x=540 mm the interval increased nearly 79% from 0.0790 to 0.1407. The D_2 test case reveals values within -0.0231<$\frac{\overline{u'v'}}{\sqrt{\overline{u'^2}}\sqrt{\overline{v'^2}}}$<+0.0663 which means an amplitude of 0.0894. The highest obtained value is at y=108.50 mm and the lowest value is at y=21.50 mm. Related with the D_1 test case at same station x=540 mm the interval increased nearly 15% from 0.0782 to 0.0894. The C_2 test case interval is almost 157% of the D_2 test case interval.

For station x=735 mm both test cases present always different results. The jets division region disappeared. The C_2 test case reveals values within -0.0412<$\frac{\overline{u'v'}}{\sqrt{\overline{u'^2}}\sqrt{\overline{v'^2}}}$<+0.0584 which means an amplitude interval of 0.0996. The highest obtained value is at y=165.50 mm and the lowest value is at y=51.50 mm. Related with the C_1 test case at x=735 mm the interval increased nearly 32% from 0.0749 to 0.0996. The D_2 test case reveals values within +0.0102<$\frac{\overline{u'v'}}{\sqrt{\overline{u'^2}}\sqrt{\overline{v'^2}}}$<+0.0647 which means an all positive values amplitude interval of 0.0545. The highest obtained value is at y=124.50 mm and the lowest value is at y=11.50 mm. Related with the D_1 test case at x=735 mm the interval decreased nearly 7% from 0.0586 to 0.0545. The C_2 test case interval is almost 183% of the D_2 test case interval.

For station x=985 mm both test cases present always different results. The jets division region disappeared. The C_2 test case reveals values within -0.0173<$\frac{\overline{u'v'}}{\sqrt{\overline{u'^2}}\sqrt{\overline{v'^2}}}$<+0.0589 Interval which means an amplitude of 0.0762 for this test case. The highest obtained value is at y=114.50 mm and the lowest value is at y=21.50 mm. Related with the C_1 test case at x=985 mm the interval increased nearly 15% from 0.0666 to 0.0762. The D_2 test case reveals values within -0.0084<$\frac{\overline{u'v'}}{\sqrt{\overline{u'^2}}\sqrt{\overline{v'^2}}}$<+0.0700 which means a 0.0784 amplitude interval. The highest obtained value is at y=81.50 mm and the lowest value is at y=1.50 mm. Related with the D_1 test case at x=985 mm the interval decreased nearly 27% from 0.0617 to 0.0784. The C_2 test case interval is almost 97% of the D_2 test case interval.

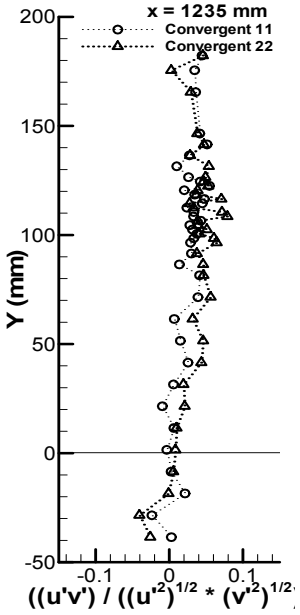

Figure 3.106. Vertical profiles of correlation coefficient for C_2 and D_2 test cases at station x=1235 mm.

For station x=1235 mm (Figure 3.106) both test cases present always different results. The jets division region disappeared. The C_2 test case reveals values within -

$0.0093<\frac{\overline{u'v'}}{\sqrt{\overline{u'^2}}\sqrt{\overline{v'^2}}}<+0.0546$ Interval which means an amplitude of 0.0639 for this test case. The highest obtained value is at y=122.50 mm and the lowest value is at y=21.50 mm. Related with the C_1 test case at x=1235 mm the interval increased nearly 20% from 0.0529 to 0.0639. D_2 test case reveals values within $+0.0026 <\frac{\overline{u'v'}}{\sqrt{\overline{u'^2}}\sqrt{\overline{v'^2}}}<+0.0790$ which gives a 0.0764 all positive amplitude interval. The highest obtained value is at y=108.50 mm and the lowest value is at y=175.50 mm. Related with the D_1 test case at x=1235 mm the interval decreased nearly 15% from 0.0667 to 0.0764. The C_2 test case $\frac{\overline{u'v'}}{\sqrt{\overline{u'^2}}\sqrt{\overline{v'^2}}}$ interval is almost 83% of the D_2 test case interval.

Chapter 4. Conclusions

The main objective of this work was to achieve high mixing zones by new aerodynamic processes instead of swirl or bluff bodies. In combustion applications it is desirable to achieve the complete fuel-air mixing in the shortest possible length in order to get better efficiencies. One way to achieve this rate is ranging highlight the difference in speed between the two flows. And this application in fuel injection systems is quite interesting due to better mixing of fuel-air mixture, leading it to better yields and efficiencies. In the specific case of the turbofan engines there has a particular interest in reducing the temperature gradient between the jet engine to be output and ambient temperature, thus achieving a lower formation of noise. In all the applications the key issue is to get the maximum mixing in the shortest distance possible. The ultimate goal of this work was to produce a recirculation zone by means of high velocity and turbulence intensities ratios, together with confinement and deflection of the outer flow. This hypothesis rose up from a previous study (Barata *et al*. 2007, 2007a, 2009) performed for an axisymmetric geometry, which confirmed the possibility of controlling the generation, size and location of a recirculation zone by aerodynamic parameters. In this axisymmetric case, it was found that the pressure gradient plays an important role, probably due to the area variation in the radial direction, but the authors did not considered it as a major parameter.

To isolate any axisymmetric effect in the present study a two-dimensional geometry was adopted without sidewalls to allow any vortex present to grow in the third direction. The width of inner and outer jets selected in the present work is proportional to those of the Ahmed and Sharma (2000) work. In this experimental work, it was decided to study the behavior of the confined and unconfined planar jets. Since no recirculation zone emerged from the measurements of those configurations and with the previous acknowledgement that for this jets ratios and velocity ratios λ>1 the outer jet is predominant due mainly to its high turbulence intensity levels, it was then decided to vary the outer jets angle toward the inner jet in a way to accelerate the mixing propagation between jets with different velocities and thus to obtain measurements of a recirculating flow. The idea was to confirm if it is it possible to generate experimentally the recirculation zone detected numerically for near zero pressure gradient. To investigate this hypothesis, the present work used a two-dimensional configuration with three parietal jets representing the inner and outer flows. Different velocity ratios between the inner and the outer jets were used, confinement was also investigated, as well as the inclination of the outer jets.

The measurements have shown that the smaller velocity ratio is characterized by an initial decrease of the horizontal velocity component in the vertical plane of symmetry from the exit value (U/U_{mean}=1) to about 75%, and then remains practically constant. The confinement (upper plate) reduces the mean horizontal velocity component, but only about 5% which is not sufficient to create a flow reversal. The effect of the outer jet flow growing

towards the centre due to the confinement is opposed to the momentum transfer upwards to compensate the energy dissipation near the wall. As a consequence the blockage of the central flow is no so effective and no recirculation zone could be generated. Increasing the velocity of the outer jet by 25% was found to change both effects in the same way, and the result was similar. The use of convergents forces the outer jets to collide at nearly 25 exit heights (about 500mm), and in the initial region a reduction of 25% of the horizontal velocity was observed, and this was independent of the initial angle (11º or 22º).

The mean vertical velocity component does not change in the downstream direction with values of about 5% of the average velocity (U_{mean}). The sign is consistently negative (upwards) revealing the presence of the bottom wall during all the tests. With the smaller convergent the value of the mean vertical velocity component approaches zero when the outer jets collide, but no significant differences from the parallel unconfined geometries (test cases A) can be observed. For the larger convergent angle the negative values double at the collision distance, which indicates that the outer jet is even more deflected upwards due to the vertical favourable pressure gradient that is generated.

The use of confinement keeps the outer flow attached to the wall, while for the unconfined test cases the north wall confinement removal acted on the velocities and provoked an outer jet deflection. It looks like in the confined test cases the confinement of the outer flow retards the deflection due to the interaction between the boundary layer of the outer jet and the wall. The unconfined test cases reveal that the interior and exterior jets mixed themselves more quickly.

For the convergent jets tests cases it can be concluded that the use of both 11º and 22º convergent exits at the outer flow without the upper and lower plates provokes the complete merging of the flows and no recirculation zone could be produced.

With both convergents, the horizontal velocity component is similar near x=0, but then increase clearly further downstream (about 50%). This effect is more pronounced for the greater convergent angle of 22º. The outer jet velocity was found not to represent a control parameter because the mean horizontal velocity component remains about the same. The mean vertical velocity component is nearly zero for all the cases studied. The more efficient way of creating a downward velocity corresponds to the increase of the convergent angle. Nevertheless, the peak is only about 10% of U_{mean} at x=500 mm (see Figure 3.8) and it is insufficient to generate a recirculation zone: This is also confirmed by the vertical profiles of the mean horizontal velocity that exhibit for all the test cases without convergent that does not change its vertical location. The use of deflectors were expected to produce higher vertical velocity fluctuations, but the horizontal velocity fluctuations are predominant with levels of anisotropy, $\sqrt{\overline{u'^2}}/\sqrt{\overline{v'^2}}$ >10.

The obtained results of this Thesis and their main conclusions suggested a consequent future study on testing a new 2 D experimental study for the same configurations for a velocity ratio of λ = 6.0 with the outer and inner jets fed with independent admissions.

References

Abrosimov, I. A., Turilov, A. M., Kosterin, V. A., "Control of coaxial jet mixing", *Journal Russian Aeronautics* (Iz Vuz), Vol. 50, No. 1, pp. 98-100, 2007.

Ahmed, A., Bangahh, Z. A., "Experimental investigation of axisymmetric coaxial synthetic jets", *Experimental Thermal and Fluid Science*, Vol. 33, No. 8, pp. 1142-1148, 2009.

Ahmed, M. R., Sharma S. D., "Effect of velocity ratio on the turbulent mixing of confined, co-axial jets", *Experimental Thermal and Fluid Science*, Vol. 22, No. 1-2, pp. 19-33, 2000.

Ahmed, M. R., Sharma, S. D., "Turbulent mixing enhancement with a 10° chute mixer", *Journal of Aircraft Engineering and Aerospace Technology*, Vol. 77, No. 5, pp. 404-414, 2005.

Ahmed, M. R., Sharma, S. D., "Turbulent mixing enhancement with a 20° chute mixer", *Experimental Thermal and Fluid Science*, Vol. 30, No. 3, pp. 161-174, 2006.

Akselvoll, K., Moin, P., "Large-Eddy Simulation of Turbulent Confined Coannular Jets", *Journal of Fluid Mechanics,* Vol. 315, pp. 387-411, 1996.

Albagli, D., Levy, Y., "Two-phase flow measurements in confined coaxial jets", *International Journal of Multiphase Flow*, Vol. 16, No. 5, pp. 929-932, 1990.

Albayrak, K., Eralp, O. C., Celen, B., "An investigation on the mixing region of co-axial jets", *Modelling, Simulation Control*, Part B, Vol. 33, No. 2, pp. 49-64, 1990.

Alekseenko, S. V., Kuibin, P. A., Okulov, V. L., Shtork, S. I., "Helical vortices in swirl flow", *Journal of Fluid Mechanics*, Vol. 382, No. 1, pp. 195–243, 1999.

Alekseenko, S. V., Dulin, V. M., Kozorezov, Y. S, Markovich, D. M., "Effect of axisymmetric forcing on the structure of a swirling turbulent jet", *International Journal of Heat and Fluid Flow*, Vol. 29, No. 6, pp. 1699-1715, 2008.

Alpinieri, J. L., "Turbulent Mixing of Coaxial Jets", *AIAA Journal*, Vol. 2, No. 9, pp. 1560-1567, 1964.

Altgeld, H., Jones, W. P., Wilhelmi, J., "Velocity measurements in a confined swirl driven recirculating flow", *Experiments in Fluids*, Vol. 1, No. 2, pp. 73-78, 1983.

Anderson, Jr., J. D., Fundamentals of Aerodynamics, 3rd Ed., ISBN: 0-07-237335-0, McGraw-Hill Hill Higher Education, Aeronautical and Aerospace Engineering, 2001.

Antonia, R. A., Bilger, R. W., "An Experimental investigation of an Axisymmetric Jet in a Co-Flowing Air Stream", *Journal of Fluid Mechanics*, Vol. 61, No. 4, pp. 805-822, 1973.

Antonia, R. A., Bilger, R. W., "The Heated Round Jet in a Coflowing Stream", *AIAA Journal*, Vol. 14, No. 11, pp. 1541-1546, 1976.

Areal, P. M., Palma, J. M. L. M., "LES of turbulent mixing in a confined coaxial jet with 0.8 velocity ratio", *Springer Proceedings in Physics*, ISSN 0930-8989, Vol. 117, pp. 313-315, 2007.

Au, H., Ko, N. W. M., "Coaxial jets of different mean velocity ratios", *Journal of Sound and Vibration*, Vol. 100, pp. 211-232, 1985.

Balarac, G., Métais, O., "Coherent vortices in coaxial jets", *Advance in Turbulence X*, CIMNE, Barcelona, Spain, pp. 149-152, 2004.

Balarac, G., Si-Ameur, M., "Mixing and coherent vortices in turbulent coaxial jets", *Comptes Rendus Mécanique*, Vol. 333, No. 8, pp. 622-627, 2005.

Balarac, G., Métais, O., "The near field of coaxial jets: A numerical study", *Physics of Fluids*, Vol. 17, No. 6, pp. 065102-065102-14, 2005.

Balarac, G., Métais, O., Lesieur M., "Mixing enhancement in coaxial jets through inflow forcing: A numerical study", *Physics of Fluids*, Vol. 19, No. 7, pp. 075102-075102-17, 2007.

Barata, J. M. M., "Estudo Numérico e Experimental de Jactos Incidentes Sobre Placas Através de um escoamento Cruzado", PhD Thesis, Instituto Superior Técnico, Lisboa, Portugal, 1989.

Barata, J. M. M., Durão, D. F. G., "Laser-Doppler measurements of a highly curved flow", *AIAA Journal*, Vol. 43, No. 12, pp. 2652-2655, 2005.

Barata, J. M. M., Neves, F. M. S. P., Silva A. R. R., "Estudo numérico do efeito do nível de turbulência inicial na mistura de jactos coaxiais confinados – Parte I", *Engenharias '07 I&D, Ubiengenharias,* Universidade da Beira Interior, Covilhã, Portugal, 2007.

Barata, J. M. M., Neves, F. M. S. P., Silva A. R. R., "Estudo numérico do efeito do nível de turbulência inicial na mistura de jactos coaxiais confinados – Parte II", *Engenharias '07 I&D, Ubiengenharias,* Universidade da Beira Interior, Covilhã, Portugal, 2007a.

Barata, J. M. M., Neves, F. M. S. P., Silva A. R. R., "Numerical study of mixing co-axial jets", *AIAA-2009-1250, 47th Aerospace Sciences Meeting*, 5-8 January, Orlando, Florida, 2009.

Barchilon, M., Curtet, R., "Some details of the structure of an axisymmetric confined jet with backflow", *Transactions of the ASME, Journal of Basic Engineering,* Vol. 86, pp. 777-787, 1964.

Bardina, J. E., Huang, P. G., Coakley, T. J., "Turbulence Modeling Validation, Testing and Development", *NASA Technical Memorandum-110446*, 1997.

Barlow, J. B., Rae, W. H., Jr., A. Pope, A., Low-Speed Wind Tunnel Testing", 3rd Ed., ISBN: 978-0-471-55774-6, John Willey & Sons, Inc., 1999.

Batchelor, G. K., The Theory of Homogeneous Turbulence, Cambridge University Press, New York, 1953.

Becker, H. A., Hottel, H. C., Williams, G. C., "Mixing and flow in ducted turbulent jets", *Proceedings of the 9th International Symposium of Combustion*, Vol. 9, No 1, pp. 7-20, 1963.

Bell, J. H., Mehta, R. D., "Contraction design for small low-speed wind tunnels" *NASA Contractor Report*-182747, 1988.

Ben Cheikh, H., Kriaa, W., Mhiri, H., "Etude numérique de la structure et la dynamicque d'un jet coaxial turbulent", *18éme Congrès Français de Mecanique*, 27-31 August, Grenoble, France, 2007.

Bender, C., Büchner, H., "Noise Emissions from a Premixed Swirl Combustor", *Proceedings of the 12th International Congress on Sound and Vibration,* ICSV 12, 11-14 July, Lisbon, Portugal, 2005.

Billant, P., Chomaz, J.-C., Huerre, P., "Experimental study of vortex breakdown in swirling jets", *Journal of Fluid Mechanics*, Vol. 376, No. 1, pp. 183-219, 1998.

Bitting, J. W., Nikitopoulos, D. E., Gogineni, S. P., Gutmark, E. J., "Visualization and two-colour DPIV measurements of flow in circular and square coaxial nozzles", *Experiments in Fluids*, Vol. 31, No. 1, pp. 1-12, 2001.

Brederode, V., Fundamentos de Aerodinâmica Incompressível, ISBN: 972-97402-0-8, IDMEC, Instituto Superior Técnico, Lisboa, 1997.

Brown, G. L., Lopez, J. M., "Axisymmetric vortex breakdown part 2, Physical Mechanism" *Journal of Fluid Mechanics*, Vol. 221, pp. 553-576, 1990.

Brücker, C., Althaus, W., "Study of vortex breakdown by particle tracking velocimetry (PTV), Part 1: Bubble-type vortex breakdown", *Journal of Experiments in Fluids*, Vol. 13, No. 5, pp. 339-349, 1992.

Brücker, C., "Study of vortex breakdown by particle tracking velocimetry, Part 2 PTV: Spiral-type vortex breakdown", *Journal of Experiments in Fluids*, Vol. 14, No. 1-2, pp. 133-139, 1993.

Brücker, C., Althaus, W., "Study of vortex breakdown by particle tracking velocimetry (PTV), Part 3: Time-dependent structure and development of vortex breakdown-modes", *Journal of Experiments in Fluids*, Vol. 18, No. 3, pp. 174-186,1995.

BSA Flow Software-Installation & User's guide, Vol.1, 2002.

Bucchave, P., "The Measurement of Turbulence with the Burst Type-Laser Doppler Anemometer-Errors and Corrections Méthods", PhD Thesis, State University of New York, United States, 1979.

Buresti, G., Talamelli, A., Petagna, P., "Experimental characterization of the velocity field of a coaxial jet configuration", *Experimental Thermal and Fluid Science*, Vol. 9, No. 2, pp. 135–146, 1994.

Buresti, G., Talamelli, A., Petagna, P., "Experimental investigation on the turbulent near-field of coaxial jets", *Experimental Thermal and Fluid Science*, Vol. 17, No. 1-2, pp. 18-36, 1998.

Cassidy, J. J., Falvey, H. T., "Observation of Unsteady Flow Arising After Vortex Breakdown", *Journal of Fluid Mechanics*, Vol. 41, No. 4, pp. 727-736, 1970.

Castro, I. P., Bradshaw, P. "The turbulence structure of a highly curved mixing layer", *Journal of Fluid Mechanics*, Vol. 73, No. 2, pp. 265-304, 1976.

Castro, P., "Estudo Experimental da Interacção de um Jacto de Parede e uma Camada Limite", Projecto Final de Curso, Departamento de Ciências Aeroespaciais, Universidade da Beira Interior, Covilhã, 2004.

Cenedese, A., Doglia, G., Romano, G. P., De Michele, G., Tanzini, G., "LDA and PIV velocity measurements in free jets", *Experimental Thermal and Fluid Science*, Vol. 9, No 1, pp. 125-134, 1994.

Champagne, F. H., Wygnanski, I. J., "An experimental investigation of coaxial turbulent jets", *International Journal of Heat Mass Transfer*, Vol. 14, No. 9, 1445-1464, 1971.

Champagne, F. H., Kromat, S., "Experiments on the formation of a recirculation zone in swirling coaxial jets", *Experiments in Fluids*, Vol. 29, No. 5, pp. 494-504, 2000.

Chang, T. H., Kim, H. Y., "An investigation of swirling flow in a cylindrical tube", *(KSME) Korean Society of Mechanical Engineers International Journal*, Vol. 15, No. 12, pp. 1892-1899, 2001.

Chen, Y., Kim, S. W., "Computation of turbulent flows using an extended k-ε turbulence closure model", *NASA Contractor Report-179204*, 1987.

Chigier, N. A., Beer, J. M., "The Flow Region near the Nozzle in Double Concentric Jets", *Journal of Basic Engineering*, Vol. 4, pp. 797-804, 1964.

Chigier, N. A., Chervinsky, A., "Experimental Investigation of Swirling Vortex Motion in Jet", *Transactions of the ASME, Journal of Applied Mechanics*, Vol. 34, No. 2, pp. 443-451, 1967.

Cohen, J., Wygnanski, I., "The evolution of instabilities in the axisymmetric jets Part 1. The linear growth of disturbances near the nozzle", *Journal of Fluid Mechanics*, Vol. 176, pp. 191-219, 1987.

Craya, A., Curtet, R., "On the spreading of a confined jet", *Comptes-Rendus, Academie des Sciences*, Paris, Vol. 241, No. 1, pp. 621–622, 1955.

Crow, S. C., Champagne, F. H., "Orderly structures in jet turbulence", *Journal of Fluid Mechanics*, Vol. 48, No. 3, pp. 547-591, 1971.

Curtet, R., "Confined jets and recirculations phenomena with cold-air", *Combustion and Flame*, Vol. 2, No. 4, pp. 383-411, 1958.

Curtet, R., Ricou, F. P., "On the tendency of self-preservation in jets", *Transactions of the ASME, Series D, Journal of Basic Engineering,* Vol. 86, No. 4, pp. 765-776, 1964.

Dahm, W. J. A., Dimotakis, P. E., "Measurements of entrainment and mixing in turbulent jets", *AIAA Journal*, Vol. 25, No. 9, pp. 1216-1223, 1987.

Dahm, W. J. A., Frieler, C. E., Tryggvason, G., "Vortex structure and dynamics in the near-field of a coaxial jet", *Journal of Fluid Mechanics*, Vol. 241, pp. 371-402, 1992.

Davies, P. O. A. L., Fisher, M., Barrat, M., "The characteristics of turbulence in the mixing region of a round jet", *Journal of Fluid Mechanics*, Vol. 15, No. 3, pp. 337-367, 1963.

Deconink, H., Dick, E., Computational Fluid Dynamics, e-ISBN: 978-3-540-92779-2, Proceedings of the Fourth International Conference on Computational Fluid Dynamics, ICCFD4, 10–14 July 2006, Ghent, Belgium, Springer-Verlag Berlin Heidelberg, 2009.

Del Taglia, C., Blum, L., Gass, J., Ventikos, Y., Poulikakos, D., "Numerical and experimental investigation of an annular jet flow with large blockage", *Journal of Fluids Engineering*, Vol. 126, No. 3, pp. 375-384, 2004.

Dianat, M., Yang, Z., Jiang, D., McGuirck, J. J., "Large eddy simulation of scalar mixing in a coaxial confined jet", *Flow Turbulence and Combustion*, Vol. 77, No. 1-4, pp. 205-227, 2006.

Dryden, H. L., "The theory of isotropic turbulence", *AIAA Journal Special Supplement: Centennial of Powered Flight*, reprinted from *Journal of the Aeronautical Sciences*, Vol. 4, No 7, pp. 273-280, 1937.

Durão, D., Whitelaw, J. H., "Turbulent mixing in the developing region of coaxial jets", *Transactions of the ASME, Journal of Fluids Engineering*, Vol. 95, pp. 467–473, 1973.

Durst, F., Whitelaw, J. H., "Optimization of optical anemometers", *Proceedings of the Royal Society*, London, A 12, Vol. 324, No. 1557, pp. 157-181, 1971.

Durst, F., Melling, A., Whitelaw, J. H., Principles and Practice of Laser-Doppler Anemometry, 2nd Ed., ISBN: 0-12-225260-8, Academic Press Inc (London) LTD, 1981.

Durst, F., Fluid Mechanics: An Introduction to the Theory of Fluid Flows, ISBN: 978-3-540-71342-5, Springer-Verlag Berlin Heidelberg, 2008.

Dziomba, B., Fiedler, H. E., "Effect of initial conditions on two dimensional free shear layers", *Journal of Fluid Mechanics*, Vol. 152, pp. 419-442, 1985.

Elghobashi, S. E., Pun W. N., Spalding, D. B., "Concentration Fluctuations in Isothermal Turbulent Confined Coaxial Jets", *Chemical Engineering Science*, Vol. 32, No. 2, pp. 161-166, 1977.

Emmons, H. W., "The laminar-turbulent transition in boundary layer-Part I", *AIAA Journal Special Supplement: Centennial of Powered Flight,* reprinted from *Journal of the Aeronautical Sciences*, Vol. 18, No. 7, pp. 490-498, 1951.

Erhard, P., Etling, D., Müller, U., Riedel, U., Sreenivasan, K. R., Warnatz, J., Prandtl-Essentials of Fluid Mechanics (Applied Mathematical Sciences, Vol. 158), 3rd Ed., e-ISBN: 978-1-4419-1564-1, Springer Science+Business Media, LLC, 2010.

Escudier, M. P., Keller, J. J., "Recirculation in swirling flow: A manifestation of vortex breakdown", *AIAA Journal*, Vol. 23, No. 1, pp. 111–116, 1985.

Faler, J. H., Leibovich, S., "Disrupted states of vortex flow and vortex breakdown", *Physics of Fluids*, Vol. 20, No. 9, pp. 1385–1400, 1977.

Fan, J. R., Shi, J. M., Zhang, X. Y., Cen, K. F., "Numerical simulation of the effect of velocity ratio on the flow characteristics in a coaxial jet", *Chemical Engineering Communications*, Vol. 147, No. 1, pp. 85-98, 1996.

Favre-Marinet, M., Camano, E. B., Sarboch, J., "Near-field of coaxial jets with large density differences", *Experiments in Fluids*, Vol. 26, No. 1-2, pp. 97-106, 1999.

Favre-Marinet, M., Schettini, E. B. C., "The density field of coaxial jets with large velocity ratio and large density differences", *International Journal of Heat and Mass Transfer*, Vol. 44, No. 10, pp. 1913–1924, 2001.

FCO 12 & 14 Micromanometers user's guide, No. 3, Furness Controls Limited, East Sussex, England, 1996.

Fink, L. E., "Influence of external turbulence on mixing of axisymmetric co-axial jets", *Proceedings of the First Symposium on Turbulent Shear Flows*, Pennsylvania State University, Vol. 1, pp. 2.11–2.21, April 18-20, 1977.

Flowlite 2 D, Installation & user's guide, 2nd Ed., Dantec Dynamics A/S, Denmark, 2002.

Forstall, W., Shapiro A. H., "Momentum and mass transfer in coaxial gas jets", *Transactions of the ASME, Journal of Applied Mechanics*, Vol. 17, pp. 399-408, 1950.

Foster, P. J., MacInnes, J. M., Schubnell, F., "Approximate similarity of confined turbulent coaxial jets", *Transactions of the ASME, Fluids Engineering*, Vol. 123, No. 3, pp. 707-709, 2001.

Fröhlich, J., Garcia-Villaba, M., Rodi, W., "Scalar mixing and large-scale coherent structures in a turbulent swirling jet", *Flow, Turbulence and Combustion*, Vol. 80, No. 1, pp. 47-59, 2008.

Garg, A. K., Leibovich, S., "Spectral characteristics of vortex breakdown flowfields", *Physics of Fluids*, Vol. 22, No. 11, pp. 2053-2064, 1979.

Ghia, K. N., Torda, T. P., Lavan, Z., "Turbulent mixing in the initial region of heterogeneous axisymmetric coaxial confined jets", *NASA Contractor Report-1615*, 1970.

Giannadakis, A., Perrakis, K., Panidis, Th., "A swirling jet under the influence of a coaxial flow", *Experimental Thermal and Fluid Science*, Vol. 32, No. 8, pp. 1548-1563, 2008.

Gibson, M. M., "Hydrodynamics of confined co-axial jets", *Encyclopedia of Fluid Mechanics*, Vol. 2, pp. 367-390, 1986.

Gladnick, P. G., Enotiadis, A. C., LaRue, J. C., Samuelsen, G. S., "Near-field characteristics of a turbulent coflowing jet", *AIAA Journal*, Vol. 28, No. 8, pp. 1405-1414, 1990.

Grandmaison, E. W., Becker, H. A., "Turbulent mixing in free swirling jets", *The Canadian Journal of Chemical Engineering*, Vol. 60, pp. 76-82, 1982.

Grandmaison, E. W., Becker, H. A., Zettler, N. L., "Scalar mixing in turbulent concentric round jets", *The Canadian Journal of Chemical Engineering*, Vol. 74, No.4, pp. 433-447, 1996.

Gupta, N. R., Wakelyn, N. T., "Theoretical study of reactive and nonreactive turbulent coaxial jets", *NASA Technical Note D-8127*, 1976.

Habib, M. A., Whitelaw, J. H., "Velocity characteristics of confined coaxial jets", *Journal of Fluids Engineering*, Vol. 101, No. 2-3, pp. 521-529, 1979.

Habib, M. A., Whitelaw, J. H., "Velocity characteristics of confined co-axial jets with and without swirl", *Transactions of the ASME, Journal of Fluids Engineering.*, Vol. 102, No. 3, pp. 47–53, 1980.

Habib, M. A., Whitelaw, J. H., "Calculations of confined coaxial-jet flows", *5th Turbulent Shear Flows*, pp. 5.20-5.26, 1985.

Hall, M. G., "Vortex breakdown", *Annual Review of Fluid Mechanics*, Vol. 4 pp. 195-217, 1972.

Hanson, S., "Broadening of the measured frequency spectrum in a differential laser anemometer due to interference plane gradients", *Journal of Physics D: Applied Physics*, Vol. 6, No. 2, pp. 164–171, 1973.

Hanson, S., "Visualization of alignment errors and heterodyning constraints in laser Doppler velocimeters", *The accuracy of flow measurements by laser Doppler methods; Proceedings of the LDA-Symposium*, 25-28 August, Copenhagen, Denmark, 1975.

Harvey, J. K., "Some observations on vortex breakdown phenomenon", *Journal of Fluid Mechanics*, Vol. 14, pp. No. 4, pp. 585-592, 1962.

Hassel, E., Janke, S., kornev, N., Tkachenko, I., Zhdanov, V., "Large-eddy simulation and laser diagnostic measurements of mixing in a coaxial jet mixer", *Chemical Engineering Science*, Vol. 61, No. 9, pp. 2908-2912, 2006.

Hattori, N., Arai, Y., Sugiyama, A., "Experimental study of coaxial double pipe air jets at different temperatures", *Heat Transfer-Japanese Research*, Vol. 27**,** No**.** 6, pp. 431-446, 1998.

Hill, P. G., "Turbulent Jets in Ducted Streams", *Journal of Fluid Mechanics*, Vol. 22, part 1, pp. 161-186, 1965.

Hinze, J. O., Van Der Hegge Zijnen, B. G., "Transfer of heat and matter in the turbulent mixing zone of an axially symmetrical jet", *Applied Scientific Research*, Vol. 1, No. 1, pp. 435-461, 1949.

Hinze, J. O., Turbulence, 2nd Ed., ISBN: 0070290377, McGraw-Hill, New York, 1975.

Hoffmann, K. A., Chiang, S. T. L., Siddiqui, M. S., Papadakis, M., Fundamental Equations of Fluid Mechanics, ISBN: 0-9623731-9-2, Engineering Education System, 1996.

Huang, F. R., Tsai, F. C., "Flow field characteristics of swirling double concentric jets", *Experimental Thermal and Fluid Science*, Vol. 25, No. 3-4, pp. 151-161, 2001.

Hussain, A. K. M. F., "Coherent Structures and Turbulence", *Journal of Fluid Mechanics,* Vol. 173, pp. 303-356, 1986.

Ivanic T., Foucault, E., Pecheux, J., Gilard, V., "Instabilities in coaxial rotating jets", *Journal of Thermal Science,* Vol. 9, No. 4, pp. 322-326, 2000.

Ivanic, T., Foucault, E., Pecheux, J., "Dynamics of swirling jet flows", *Experiments in Fluids*, Vol. 35, pp. 317-324, 2004.

Jackson, T. W., Lilley, D. G., "Turbulence characteristics of swirling jets", *NASA Contractor Report-174918*, 1985.

Jahnke, S., Kornev, N., Tkatchenko, I., Hassel, E., Leder, A., "Numerical study of influence of different parameters on mixing in a coaxial jet mixer using LES", *Heat and Mass Transfer*, Vol. 41, pp. 471-481, 2005.

Jensen, K. D., "Flow Measurements", *Journal of the Brazilian Society of Mechanical Sciences and Engineering,* Vol. 26, No. 4, pp. 400-419, ISSN 1678-5878, 2004.

Jochmann, P., Sinigersky, A., Hehle, M., Schäfer, O., Koch, R., Bauer, H-J., "Numerical simulation of a precessing vortex breakdown", *International Journal of Heat and Fluid Flow*, Vol. 27, No. 2, pp. 192-203, 2006.

Johnson, B. V., Clark, J. W., "Experimental study of multi-component coaxial flow-jets in short chambers", *NASA Contractor Report-1190*, 1968.

Johnson, B. V., Bennett, J. C., "Mass and momentum turbulent transport experiments with confined coaxial jets", *NASA Contractor Report-165574*, 1981.

Johnson, B. V., Bennett, J. C., "Statistical characteristics of velocity, concentration, mass transport, and momentum transport for coaxial jet mixing in a confined duct", *Journal of Engineering for Gas Turbines and Power*, Vol. 106, No. 1, pp. 121-127, 1984.

Johnson, B. V., Roback, R., "Turbulent transport and length scale measurement experiments with confined coaxial jets", *NASA Contractor Report-174831*, 2004.

Johnson, R. W., "Prediction of turbulent coaxial streams of constant and variable density", *Journal of Propulsion and Power*, Vol. 9, No. 4, pp. 588-596, 1993.

Jones, W. P., Launder, B. E., "The prediction of laminarization with a two-equation model of turbulence", *International Journal of Heat and Mass Transfer*, Vol. 15, pp. 301-314, 1972.

Kamath, R. V., "Numerical Analysis and Experimental Investigation of Ejectors", PhD Thesis, Department of Aerospace Engineering, Indian Institute of Technology, Bombay, India, 1996.

Kandakure, M. T., Patkar, V. C., Patwardhan, A. W., "Characteristics of turbulent confined jets", *Chemical Engineering and Processing: Process Intensification*, Vol. 47, No. 8, pp. 1234-1245, 2008.

Kerhervé, F., Fitzpatrick, J., "The frequency dependence of the characteristics of coaxial jet flows", *13th International symposium on applications of laser techniques to fluid mechanics*, Lisbon, 26, 29 June, 2006.

Khodadadi, J. M., Vlachos, N. S., "Experimental and numerical study of confined coaxial turbulent jets", *AIAA Journal*, Vol. 27, No. 5, pp. 532-541, 1989.

Kiwata, T., Okajima, A., Kimura, S., "Flow visualization of vortex structure of an excited coaxial jet", *Journal of Visualization*, Vol. 4, No. 1, pp 99–107, 2001.

Kiwata, T., Ishii, T., Kimura S., Okajima A., Miyazaki, K., "Flow visualization and characteristics of a coaxial jet with a tabbed annular nozzle", *Japan Society Mechanical Engineering International Journal*, Series B, Vol. 49, No. 4, pp. 906-913, 2006.

Ko, N. W. M., Kwan A. S. H., "The initial region subsonic coaxial jets", *Journal of Fluid Mechanics*, Vol. 73, No. 2, pp. 305–332, 1976.

Ko, N. W. M., Chan, W. T., "The inner regions of annular jets", *Journal of Fluid Mechanics*, Vol. 93, No. 3, pp. 549-584, 1979.

Ko, N. W. M., Au, H., "Initial region of subsonic coaxial jets of high mean velocity ratio", *Transactions of the ASME, Journal of Fluids Engineering*, Vol. 103, pp. 335–338, 1981.

Ko, N. W. M., Au, H., "Spreading rate and reattachment of coaxial jets of high-mean velocity ratio", *Transactions of the ASME, Journal of Fluids Engineering*, Vol. 104, No. 3, pp. 400-401, 1982.

Ko, N. W. M., Chan, W. T., "Similarity in the initial region of annular jets: three configurations", *Journal of Fluid Mechanics*, Vol. 84, No. 4, pp. 641–656, 1984.

Ko, N. W. M., Au, H., "Coaxial jets of different mean velocity ratios - Part 2", *Journal of Sound and Vibration*, Vol. 116, No. 3, pp. 427-443, 1987.

Kornev, N., Tkatchenko, I., Zhdanov, V., Hassel, E., Jahnke, S., "Simulations and measurement of flow phenomena in a coaxial jet mixer", *Chemical Engineering Science*, Vol. 61, No. 9, pp. 2908-2912, 2006.

Kornev, N., Tkatchenko, I., Zhdanov, V., Hassel, E., Jahnke, S., "LES simulation and measurement of separation flow phenomena in a confined coaxial jet with large inner to outer velocity ratio", *Advances and Applications in Fluid Mechanics*, Vol. 2, No. 1, pp. 1–28, 2007.

Kornev, N., Zhdanov, V., Hassel, E., "Study of scalar macro-and microstructures in a confined jet", *International Journal of Heat and Fluid Flow*, Vol. 29, No. 3, pp. 665-674, 2008.

Krasnov, N. F., Aerodinámica en Preguntas y Problemas, ISBN: 5-03-000665-6, Editorial Mir, Moscú, 1989.

Kuethe, A. M., "Investigations on Turbulent Mixing Regions", PhD Thesis, California Institute of Technology, United States, 1933.

Kulik, R. A., Leithem, J. J., Weinstein, H., "Effect of Free Stream Turbulence on Coaxial Mixing", *NASA Contractor Report-1336*, 1969.

Kulik, R. A., Leithem, J. J., Weinstein, H., "Turbulence measurements in a ducted coaxial flow", *AIAA Journal*, Vol. 8, No. 9, pp. 1694-1696, 1970.

Kriaa, W., Mhiri, H., Le Palec, G., Bournot, P., "Numerical study of the interaction between two laminar and coaxial plane jets with variable density in an ambient fluid", *Energy Conversion and Management*, Vol. 44, No. 12, pp. 2037–2057, 2003.

Kuzmin, A., Computational Fluid Dynamics 2010, ISBN: 978-3-642-17883-2, Proceedings of the Sixth International Conference on Computational Fluid Dynamics, ICCFD6, July 12-16, St Petersburg, Russia, 2010.

Kwan, A. S. H., Ko, N. W. M., "Coherent structures in subsonic coaxial jets", *Journal of Sound and Vibration*, Vol. 48, No. 2, pp. 203-219, 1976.

Kwan, A. S. H., Ko, N. W. M., "Covariance measurements in the initial region of coaxial jets", *Journal of Sound and Vibration*, Vol. 52, pp. 567-578, 1977.

Kwan, A. S. H., Ko, N. W. M., "The initial region subsonic coaxial jets. Part 2", *Journal of Fluid Mechanics*, Vol. 82, No. 2, pp. 273–287, 1977a.

Launder, B. E., Spalding, D. B, "The numerical computation of turbulent flows", *Computer Methods in Applied Mechanics and Engineering*, Vol.3, No. 2, pp. 269-289, 1974.

Launder, B. E., Reece, G. J., Rodi, W., "Progress in the development of a Reynolds-stress turbulent closure", *Journal of Fluid Mechanics*, Vol. 68, No. 3, pp. 537-566, 1975.

Leibovich, S., "The structure of a vortex breakdown", Annual *Review of Fluid Mechanics*, Vol. 10, pp. 221-246, 1978.

Leithem, J. J., Kulik, R. A., Weinstein H., "Turbulence in the mixing region between ducted coaxial streams", *NASA Contractor Report-1335*, 1969.

Lesieur, M., Turbulence in Fluids-Fluid Mechanics and its Applications, 4th Ed., ISBN: 978-1-4020-6435-7, Springer, 2008.

Lima, M., Palma, J., "Mixing in coaxial confined jets of large velocity ratio", *11th Proceedings of the International Symposia on Applications of Laser Techniques to Fluid Mechanics*, Lisbon, 2002.

Lin, C. A., "Modeling a confined swirling coaxial jet", *Center for Turbulent Research, Annual Research Briefs*, pp. 211-219, 1998.

Lopez, J. M., "Axisymmetric vortex breakdown part 1. Confined swirling flow" *Journal of Fluid Mechanics*, Vol. 221, pp. 533-552, 1990.

Lucca-Negro, O., O'Doherty, T., "Vortex breakdown: A Review", *Progress in Energy Combustion Science*, Vol. 27, No. 4, pp. 431– 481, 2001.

Mahesh, K., "A model for the onset of breakdown in an axisymmetric compressible vortex", *Physics of Fluids*, Vol. 8, pp. 3338-3345, 1996.

Malalasekera, W., Ranga-Dinesh, K. K. J., Ibrahim, S. S., Masri, A. R., "LES of recirculation and vortex breakdown in swirling flames", *Combustion Science and Technology*, Vol. 180, No. 5, pp. 809-832, 2008.

Martin Magnum 800, User's Guide, Version 1.0, Martin Professionals A/S, Denmark, 2003.

Massey, B. S., Mecânica dos Fluidos, ISBN 972-31-0945-X, Fundação Calouste Gulbenkian, Lisboa 2002.

Matsumoto, R., Kimoto, K., Tsuchimoto, N., "A study on double concentric jets", *Bulletin of The Japan Society of Mechanical Engineers*, Vol. 16, No. 93, pp. 529-540, 1973.

Mehta, R. D., "The aerodynamic design of blower tunnels with wide-angle diffusers", *Progress in Aerospace Sciences*, Vol. 18, pp. 59-120, 1979.

Mehta R. D., Bradshaw, P., "Design rules for small low speed wind tunnels", *Journal of the Royal Aeronautical Society*, Vol. 83, No. 827, pp. 443-449, 1979a.

Mehta R. D., "Turbulent boundary layer perturbed by a screen", *AIAA Journal*, Vol. 23, No. 9, 1985.

Menter, F. R., "Zonal two equation k-ω turbulence models for aerodynamic flows", AIAA-93-2906*, 24th Fluid Dynamics Conference*, 6-9 July, Orlando, Florida, 1993.

Mergheni, M. A., Boushaki, T., Sautet, J-C., Godard, G., Ticha, H. B., Nasrallah, S. B., "Effects of different mean velocity ratios on dynamics characteristics of a coaxial jet", *Thermal Science*, Vol. 12, No. 2, pp. 49-58, 2008.

Meunier, P., Villermaux, E., "How vortices mix", *Journal of Fluid Mechanics*, Vol. 476, pp 213-222, 2003.

Mikhail, S., "Mixing of co-axial streams inside a closed conduit", *Journal of Mechanical Engineering Science*, Vol. 2, No. 1, pp. 59-68, 1960.

Mitsuishi, A., Fukagata, K., Kasagi, N., "Near-field development of large-scale vortical structures in a controlled confined coaxial jet", *Journal of Turbulence*, Vol. 8, No. 23, pp 1-27, 2007.

Moon, L. F., "Pressure and velocity in a developing coaxial jet", *AIAA Journal*, Vol. 14, No. 1, pp. 43-49, 1976.

Montealegre, A. P., Weinstein, H., "The mixing of homogeneous co-axial streams", *Israel Journal of Technology*, Vol. 9, No. 1-2, pp.141-150, 1971.

Morel, T., "Comprehensive design of axisymmetric wind tunnel contractions", *Transactions of the ASME, Journal of Fluids Engineering*, Vol. 95, pp. 225-233, 1975.

Morel, T., "Design of two-dimensional wind tunnel contractions", *Transactions of the ASME, Journal of Fluids Engineering*, Vol. 99, pp. 371-378, 1977.

Mortensen, M., Orciuch, W., Bouaifi, M., Andersson, B., 2003, "Mixing of a jet in a pipe", *Chemical Engineering Research and Design*, Vol. 81, No. 3, pp. 357-363, 2004.

Munson, B. R., Young, D. F., Okiishi, T. H., Huebsch, W. W., Fundamentals of Fluid Mechanics, 6th Ed., ISBN: 978-0470-26284-9, John Wiley & Sons, Inc., New York, 2009.

Nallasamy, M., "Computation of confined turbulent coaxial jet flows", *AIAA-86-0218, 24th Aerospace Sciences Meeting*, 6-9 January, Reno, Nevada, pp. 11, 1986.

Nallasamy, M., "Prediction of recirculation zones in isothermal coaxial jet flows relevant to combustors", *NASA Contractor Report-4064*, 1987.

Narasimh, K. S., Sastri, R. S., "Mixing in double concentric jets", *Journal of the Institute of Fuel*, Vol. 45, pp. 460-462, 1972.

Neves, F. M. S. P., Barata, J. M. M., Silva, A. R. R., "Numerical study of the mixing of co-axial jets", *International Review of Mechanical Engineering*, Vol. 5, No. 5, pp. 876-883, ISSN: 1970-8734, 2011.

Neves, F. M. S. P., Barata, J. M. M., Silva, A. R. R., " Experimental Study of 2D Turbulent Parietal Jets", *II LAETA Young Researchers Meeting*, FEUP, Porto, 10/11 April, 2012.

Neves, F. M. S. P., Barata, J. M. M., Silva, A. R. R., "Experimental Study of 2D Shear Layers, "*The Eleventh Inretnational Conference on Combustion and Energy Utilization (11th ICCEU)*", Coimbra, 9/13 May, 2012.

Nikitopoulos, D. E., Bitting, J. W., Gogineni, S., "Comparisons of initially turbulent, low-velocity-ratio circular and square coaxial jets", *AIAA Journal*, Vol. 41, No. 2, pp. 230-239, 2003.

Nikjooy, M., Karki, K. C., Mongia, H. C., McDonell, V. G., Samuelsen, G. S., "A numerical and experimental study of coaxial jets", *International Journal of Heat and Fluid Flow*, Vol. 10, No. 3, pp. 253-261, 1989.

Owen, F. K., "Measurements and observations of turbulent recirculating jet flows", *AIAA Journal*, Vol. 14, No. 11, pp. 1556-1562, 1976.

Panda, J., McLaughlin D. K., "Experiments on the instabilities of a swirling jet", *Physics of Fluids*, Vol. 6, No. 1, pp. 263-276, 1994.

Park, C. J., Chen, L. D., "Experimental investigation of confined turbulent jets I-Single-phase data, *AIAA Journal*, Vol. 27, No. 11, pp. 1506-1510, 1989.

Park, C. J., Chen, L. D., "Experimental investigation of confined turbulent jets II-Particle-laden flow data", *AIAA Journal*, Vol. 27, No. 11, pp. 1511-1516, 1989a.

Pierce, C. D., Moin, P., "Large eddy simulation of a confined coaxial jet with swirl and heat release", *AIAA 98-2892, 29th AIAA Fluid Dynamics Conference*,15-18 June, Albuquerque, New México, 1998.

Piquet, J., Turbulent Flows, Models and Physics, ISBN: 3-540-65411-9 Springer-Verlag Berlin Heidelberg New York, 1999.

Pope, S. B., Whitelaw, J. H., "The calculation of near-wake flows", *Journal of Fluid Mechanics*, Vol. 73, No. 1, pp. 9-32, 1976.

Pope, S. B., Turbulent Flows, Cambridge University Press, ISBN: 0-521-59125-2, Cambridge, U.K., 2000.

Rahman, M., Mechanics of Real Fluids, ISBN: 978-1-84564-502-1, Southampton, WIT Press, 2011.

Rajaratnam, N., Turbulent Jets, Developments in Water Science, Volume 5, ISBN: 0-444-41372 -3, Elsevier Scientific Publishing Company, Amsterdam, 1976.

Ranga Dinesh, K. K. J., Malalasekera, W., Ibrahim, S. S., Kirkpatrick, M. P., "*Large eddy simulation of Isothermal swirling flow*", *Proceedings of the 5th Asia-Pacific Conference on Combustion*, the University of Adelaide, Adelaide, Australia, pp. 93-96, 17-20 July, 2005.

Ranga Dinesh, K. K. J., Kirkpatrick, M. P., "Study of jet precession, recirculation and vortex breakdown in turbulent swirling jets using LES", *Computers & Fluids*, Vol. 38, No. 6, pp. 1232-1242, 2009.

Ranga Dinesh, K. K. J., Savill, A. M., Jenkins, K. W., Kirkpatrick, M. P., "A study of mixing and intermittency in a coaxial turbulent jet", *Journal of Fluid Dynamics Research*, Vol. 42, No. 2, 025507, 2010.

Razinsky, E., Brighton, J. A., "Confined jet mixing for non-separating conditions", *Transactions of the ASME, Journal of Basic Engineering*, Vol. 93, No. 3, pp. 333-349, 1971.

Rehab, H., Villermaux, E., Hopfinger, E. J., "Flow regimes of large velocity-ratio coaxial jets", *Journal of Fluid Mechanics*, Vol. 345, pp. 357-381, 1997.

Resagk, C., du Puis, R., Thess, A., "Error estimation of laser-Doppler anemometry measurements in fluids with spatial inhomogeneities of the refractive index" *Experiments in Fluids*, Vol. 35, No. 4, pp. 357-363, 2003.

Revuelta, A., Sánchez, A. L., Liñan, A., "Confined axissymmetric laminar jets with large expansion ratios", *Journal of Fluid Mechanics*, Vol. 456, pp. 319-352, 2002.

Reynier, P., Ha Minh, H., "Numerical prediction of unsteady compressible turbulent coaxial jets", *Computers & Fluids*, Vol. 27, No. 2, pp. 239-254, 1998.

Ribeiro, M. M. R., Whitelaw, J. H., "Turbulent mixing of coaxial jets with particular reference to the near-exit region", *Transactions of the ASME, Journal of Fluids Engineering*, Vol. **98**, pp. 284–291, 1976.

Ribeiro, M. M. R., Whitelaw, J. H., "Coaxial jets with and without swirl", *Journal of Fluid Mechanics*, Vol. 96, No. 4, pp. 769-795, 1980.

Ribeiro, M. M. R., Whitelaw, J. H., "The structure of turbulent jets", *Proceedings of the Royal Society, Series A: Mathematical and Physical Sciences*, Vol. 370, No. 1742, pp. 281-301, 1980a.

Riellor, G. L., "Comments on "turbulent mixing of coaxial jets"", *AIAA Journal*, Vol. 3, No. 4, pp. 798-799, 1965.

Roback, R., Johnson, B. V., "Mass and momentum turbulent transport experiments with confined swirling coaxial jets", *NASA Contractor Report-168252*, 1983.

Roshko, A., "Structure of turbulent shear flows: a new look", *AIAA Special Supplement: Centennial of Powered Flight*, reprinted from *AIAA Journal*, Vol. 4, No. 10, pp. 1349-1357, 1976.

Rozenman, T., Weinstein, H., "Recirculation patterns in the initial region of co-axial jets", *NASA Contractor Report-1595*, 1970.

Rubel, A., "Swirling jet turbulent mixing and combustion computations", *NASA Contractor Report-2231*, 1973.

Ruck, B., "Distortion of LDA fring pattern by tracer particles", *Experiments in Fluids*, Vol. 10, pp. 349-354, 1991.

Ruith, M. R., Chen, P., Meiburg, E., Maxworthy, T., "Three-dimensional vortex breakdown in swirling jets and wakes: direct numerical simulation", *Journal of Fluid Mechanics*, Vol. 486, pp. 331-378, 2003.

Sadr, R., Klewicki, J. C., "An experimental investigation of the near-field flow development in coaxial jets", *Physics of Fluids*, Vol 15, No. 5, pp. 1233-1246, 2003.

Salvetti, M. V., Orlandi, P., Verzicco, R., "Numerical simulations of transitional axisymmetric coaxial jets", *AIAA Journal*, Vol. 34, No. 4, pp. 736-743, 1996.

Salvetti, M. V., Orlandi, P., Verzicco, R., "Effects of velocity ratio on vorticity dynamics and mixing in coaxial jet flow", *1st International Congress in Turbulent Shear Flows Phenomena*, 2000.

Samet, M., Einav, S., "Mean value measurements of a turbulent swirling-jet", *AIAA Journal*, Vol. 26, No. 5, pp. 619-621, 1988.

Sarpkaya, T., "On stationary and travelling vortex breakdowns", *Journal of Fluid Mechanics*, Vol. 45, No. 3, pp. 545–559, 1971.

Sarpkaya, T., "Turbulent vortex breakdown", *Physics of Fluids*, Vol. 7, No. 10, pp. 2301-2303, 1995.

Sharma, S. D., Ahmed, M. R., "Mixing of coaxial jets with small annular area in a short duct", *AIAA Journal*, Vol. 36, No. 9, pp. 1740-1742, 1998.

Schlichting, H., Gersten, K., *Boundary Layer Theory, 8th Revised and Enlarged Ed.*, ISBN: 3-540-66270-7, Springer Verlag, 1999.

Sheen, H. J., Chen, W. J., Jeng, S. Y., "Recirculation zones of unconfined and confined annular swirling jets", *AIAA Journal*, Vol. 34, No. 3, pp. 572-579, 1996.

Shmyglevskii, Y. D., "On "Vortex Breakdown"", *Fluid Dynamics*, Vol. 30, No. 3, pp. 477-478, 1995.

Silva, C. B., Balarac, G., Métais, O., "Transition in high velocity ratio coaxial jets analysed from direct numerical simulations", *Journal of Turbulence*, Vol. 4, No. 1, pp. 24, 2003.

Silva, A. R. R., "Experimental and Numerical Study of Physical Aspects of Fuel Processes", PhD Thesis, Universidade da Beira Interior, Covilhã, Portugal, 2007.

Singh, S. N., Agrawal, D. P., Malhotra, R. C., Raghava, A. K., "Mean-velocity distributions of contra-swirling coaxial, confined jets", *Experiments in Fluids*, Vol. 7, No. 7, pp 501-504, 1989.

So, R. M. C., Ahmed, S. A., Mongia, H. C., "Jet characteristics in confined swirling flows", *Experiments in Fluids*, Vol. 3, No. 1, pp. 221-230, 1985.

Srinivasan, R., Mongia, H. C., "Numerical Computations of Swirling Recirculating Flow Final Report", *NASA Contractor Report-165196*, 1980.

Stark, S. B., "Mixing of gas streams in a flame", *Zhurnal Tecknicheskoy Fisiki*, Vol. 23, pp. 1802–1819, 1953.

Syed, S. A., Sturgess, G. J., "Validation studies of turbulence and combustion models for aircraft gas turbine combustor", *Momentum and Heat Transfer Process in Recirculating Flows* (ASME, HTD, New York) Vol. 13, pp. 71-89, 1980.

Talamelli, A., Gavarini, I., "Linear instability characteristics of incompressible coaxial jets" *Flow, Turbulence and Combustion*, Vol. 76, No. 3, pp. 221-240, 2006.

Taylor, G. I., "The statistical theory of isotropic turbulence", *AIAA Journal Spcecial Supllement: Centennial of Powered Flight,* reprinted from *Journal of the Aeronautical Sciences*, Vol. 4, No. 8, pp- 311-315, 1931.

Tenekees, H., Lumley, J. L., A First Course in Turbulence, 8th Ed, ISBN: 0-262-20019-8 (hardcover), MIT Press, Cambridge, 1982.

Tenekees, H., Lumley, J. L., Turbulência em Fluidos, ISBN: 978-972-31-1347-1, Fundação Calouste Gulbenkian, Lisboa, 2010.

Tinney, C. E., Jordan, P., "The near pressure field of co-axial subsonic jets", *Journal of Fluid Mechanics*, Vol. 611, No. 1, pp. 175-204, 2008.

Tkatchenko, I., Kornev, N., Jahnke, S., Steffen, G., Hassel, E., "Performances of LES and RANS models for simulation of complex flows in a coaxial jet mixer", *Flow, Turbulence and Combustion*, Vol. 78, No. 2 pp. 111-127, 2007.

Townsend, A. A., The Structure of Turbulent Shear Flow, 2nd Ed., ISBN: 0-521-29819-9, Cambridge University Press, 1980.

Tropea, C., Yarin, A. L., Foss, J. F., Springer Handbook of Experimental Fluid Mechanics, e-ISBN: 978-3-540-30299-5, Springer-Verlag Berlin Heidelberg 2007.

Tulapurkara, E. G., Bhalla, V. V. K., "Experimental investigation of Morel's method for wind tunnel contractions", *Journal of Fluids Engineering*, Vol. 110, No. 1, pp. 45-48, 1988.

Villermaux, E., "Mixing and spray formation in coaxial jets", *Journal of Propulsion and Power*, Vol. 14, No. 5, pp. 807-817, 1998.

Villermaux, E., Rehab, H., "Mixing in coaxial jets", *Journal of Fluid Mechanics*, Vol. 425, pp. 161-185, 2000.

Von Kármán, Th., "Turbulence and skin friction", *AIAA Journal Special Supplement: Centennial of Powered Flight,* reprinted from the *Journal of the Aeronautical Sciences*, Vol. 1, No. 1 pp. 1-20, 1934.

Von Kármán, Th., "The fundamentals of the statistical theory of turbulence", *AIAA Journal Special Supplement: Centennial of Powered Flight*, reprinted from the *Journal of Aeronautical Sciences*, Vol. 4, No. 4, pp. 131-137, 1937.

Von Kármán, Th., Howarth, L., "On the Statistical Theory of Isotropic Turbulence", *Proceedings of the Royal Society, series A: Mathematical, Physical & Engineering Sciences*, Vol. 164, pp. 192-215, 1938.

Von Kármán, Th., "Progress in the statistical theory of turbulence", *Proceedings of the National Academy of Sciences of the United States of America*, Vol. 34, No. 11, pp. 530-539, 1948.

Von Kármán, Th., von Mises, R., Advances in Applied Mechanics, Vol. I, Academic Press Inc., Publishers, New York, 1948.

Von Kármán, Th., Aerodynamics, ISBN: 07-067602-X, McGraw-Hill Book Company, New York, 1963.

Xu, H., Khalid, M., Pollard, A., "Large eddy simulation of turbulent flow in a confined square coaxial jet", *International Journal of Computational Fluid Dynamics*, Vol. 17, No. 5, pp. 339-356, 2003.

Yamashita, H., Kushida, G., Takino, T., "An experimental study on transition and mixing processes in a coaxial jet", *Proceedings of the 9th Symposium on Turbulent Shear Flows*, 16-18 August, Kyoto, Japan, pp. 212-1-4, 1993.

Yang, X., Ma, H., "Linear and nonlinear eddy-viscosity turbulence models for a confined swirling coaxial jet", *Numerical Heat Transfer*, Part B, Vol. 43, pp. 289-305, 2003.

Yanta, Z., Smith, R. A., "Measurements of turbulent-transport properties with Laser-Doppler velocimeter", *AIAA-73-0169, 11th Aerospace Sciences Meeting*, Washington, 1978.

Yeh, Y., Cummins, H. Z., "Localized fluid flow measurements with an He-Ne Laser spectrometer" Applied Physics Letters, Vol. 4, pp. 176-178, 1964.

Young, D. L., Liao, C. B., Sheen, H. J., "Computations of recirculation zones of a confined annular swirling flow", *International Journal for Numerical Methods in Fluids*, Vol. 29, No. 7, pp. 791–810, 1999.

Yu, S. C., Chua, L., Wang, X., "Measurements in the near field of a confined coaxial square jet", *AIAA Journal*, Vol. 42, No. 5, pp. 965-972, 2004.

Wang, P., Bai, X. S., "Large eddy simulation and experimental studies of a confined turbulent swirling flow", *Physics of Fluids*, Vol. 16, No. 9, pp. 3306-3324, 2004.

Warda, H. A., Kassab S. Z., Elshorbagy, K. A., Elsaadawy E. A., "An experimental investigation of the near field region of free turbulent round central and annular jet", *Flow Measurements and Instrumentation*, Vol. 10, pp. 1–14, 1999.

Warda, H. A., Kassab, S. Z., Elshorbagy, K. A., Elsaadawy E. A., "An experimental investigation of the near-field region of a free turbulent coaxial jet using LDA", *Flow Measurements and Instrumentation*, Vol. 10, No. 1, pp. 15-26, 1999a.

Warda, H. A., Kassab, S. Z., Elshorbagy, K. A., Elsaadawy, E. A., "Influence of the magnitude of the two initial velocities on the flow field of a coaxial turbulent jet", *Flow Measurements and Instrumentation*, Vol. 12, pp. 29-35, 2001.

White, F. M., Fluid Mechanics, 6th ed., ISBN: 978-0071286466, McGraw Hill Book Company, New York, 2006.

Wicker, R. B., Eaton, J. K., "Near field of a coaxial jet with and without axial excitation," *AIAA Journal*, Vol. 32, No. 3, pp. 542-546, 1994.

Wicker, R. B., Eaton, J. K., "Structure of a swirling, recirculating coaxial free jet and its effect on particle motion", *International Journal of Multiphase Flow*, Vol. 27, No. 6, pp. 949-970, 2001.

Wieghardt, K. E. G., "On the resistance of screens", *The Aeronautical Quarterly*, Vol. IV, pp. 186–192, 1953.

Wygnanski, I., Fiedler, H., "Some measurements in the self-preservating jet", *Journal of Fluid Mechanics*, Vol. 38, part 3, pp. 577-612, 1969.

Zawacki, T. S., Weinstein, H., "Experimental investigation of turbulence in the mixing region between co-axial streams", *NASA Contractor Report-959*, 1968.

Zhang, Zh., Eisele, K., "On the broadening of the flow turbulence due to fringe distortion in LDA measurement volumes", *Proceedings of the 7th International Conference Laser Anemometry, Advances and Applications*, 8-11 September, University of Karlsruhe, Germany, pp. 351–357, 1997.

Zhang, Zh., Eisele, K., "On the overestimation of the flow turbulence due to fringe distortion in LDA measurement volumes", *Journal of Experimental Fluids*, Vol. 25, pp. No. 4, pp. 371–374, 1998.

Zhang, Zh., LDA Application Methods, Laser Doppler Anemometry Fluid Dynamics, e-ISBN: 978-3-642-13514-9, Springer-Verlag Berlin Heidelberg, 2010.

Zhdanov, V., Kornev, N., Hassel, E., Chorny, A., "Mixing of confined coaxial flows", *International Journal of Heat and Mass Transfer*, Vol. 49, pp. 3942-3956, 2006.

Zhdanov, V., Kornev, N., Hassel, E., "Flow structure of a recirculation zone in a coaxial jet mixer", *Proceeding of 5th International Symposium on Turbulence, Heat and Mass Transfer*, pp. 26-29, 2006.

Zhu, J., Shih, T.-H., "A numerical study of confined turbulent jets", *NASA Technical Memorandum-106197*, 1993.

Zhu, J., Shih, T.-H., "Computation of confined coflow jets with three turbulence models", *International Journal for Numerical Methods in Fluids*, Vol. 19, No. 10, pp. 939-956, 1994.

Zhu, J. Y., "Laser Doppler Velocimetry for Flow Measurements in Pulp and Paper Research", IPST Technical Paper Series Number 618, *TAPPI Engineering Conference,* 16-19 September, Chicago, USA, 1996.